

Bo Li
Lei Shu
Deze Zeng (Eds.)



237

LNICST

Communications and Networking

12th International Conference, ChinaCom 2017
Xi'an, China, October 10–12, 2017
Proceedings, Part II

Part 2



 Springer

Lecture Notes of the Institute for Computer Sciences, Social Informatics and Telecommunications Engineering

237

Editorial Board

Ozgur Akan

Middle East Technical University, Ankara, Turkey

Paolo Bellavista

University of Bologna, Bologna, Italy

Jiannong Cao

Hong Kong Polytechnic University, Hong Kong, Hong Kong

Geoffrey Coulson

Lancaster University, Lancaster, UK

Falko Dressler

University of Erlangen, Erlangen, Germany

Domenico Ferrari

Università Cattolica Piacenza, Piacenza, Italy

Mario Gerla

UCLA, Los Angeles, USA

Hisashi Kobayashi

Princeton University, Princeton, USA

Sergio Palazzo

University of Catania, Catania, Italy

Sartaj Sahni

University of Florida, Florida, USA

Xuemin Sherman Shen

University of Waterloo, Waterloo, Canada

Mircea Stan

University of Virginia, Charlottesville, USA

Jia Xiaohua

City University of Hong Kong, Kowloon, Hong Kong

Albert Y. Zomaya

University of Sydney, Sydney, Australia

More information about this series at <http://www.springer.com/series/8197>

Bo Li · Lei Shu
Deze Zeng (Eds.)

Communications and Networking

12th International Conference, ChinaCom 2017
Xi'an, China, October 10–12, 2017
Proceedings, Part II

Editors

Bo Li
Northwestern Polytechnical University
Xi'an
China

Deze Zeng
China University of Geosciences
Wuhan, Hubei
China

Lei Shu
Guangdong Pharmaceutical University
Guangzhou
China

ISSN 1867-8211 ISSN 1867-822X (electronic)
Lecture Notes of the Institute for Computer Sciences, Social Informatics
and Telecommunications Engineering
ISBN 978-3-319-78138-9 ISBN 978-3-319-78139-6 (eBook)
<https://doi.org/10.1007/978-3-319-78139-6>

Library of Congress Control Number: 2018937372

© ICST Institute for Computer Sciences, Social Informatics and Telecommunications Engineering 2018
This work is subject to copyright. All rights are reserved by the Publisher, whether the whole or part of the material is concerned, specifically the rights of translation, reprinting, reuse of illustrations, recitation, broadcasting, reproduction on microfilms or in any other physical way, and transmission or information storage and retrieval, electronic adaptation, computer software, or by similar or dissimilar methodology now known or hereafter developed.

The use of general descriptive names, registered names, trademarks, service marks, etc. in this publication does not imply, even in the absence of a specific statement, that such names are exempt from the relevant protective laws and regulations and therefore free for general use.

The publisher, the authors and the editors are safe to assume that the advice and information in this book are believed to be true and accurate at the date of publication. Neither the publisher nor the authors or the editors give a warranty, express or implied, with respect to the material contained herein or for any errors or omissions that may have been made. The publisher remains neutral with regard to jurisdictional claims in published maps and institutional affiliations.

Printed on acid-free paper

This Springer imprint is published by the registered company Springer International Publishing AG
part of Springer Nature
The registered company address is: Gewerbestrasse 11, 6330 Cham, Switzerland

Preface

The 12th International Conference on Communications and Networking in China (CHINACOM 2017) was successfully held in Xi'an, China, during October 10–12, 2017. The aim of CHINACOM is to bring together Chinese and international researchers and practitioners, from over the world, to exchange original ideas and share R&D advances in communications and networking.

ChinaCom 2017 consisted of 16 technical tracks and one workshop: Wireless Communications and Networking, Next-Generation WLAN, Big Data Network, Cloud Communications and Networking, Ad-Hoc and Sensor Networks, Satellite and Space Communications and Networking, Optical Communications and Networking, Information and Coding Theory, Multimedia Communications and Smart Networking, Green Communications and Computing, Signal Processing for Communications, Network and Information Security, Machine-to-Machine and Internet of Things, Communication QoS, Reliability and Modeling, Cognitive Radio and Networks, E-Health, and Workshop on Advances and Trends of V2X Networks. CHINACOM has become one of the major events in these areas in the Asia-Pacific region. It has been successful in encouraging interactions among participants, exchanging novel ideas, and disseminating knowledge.

Following the great success of the past CHINACOM events held during 2006–2016, CHINACOM 2017 received more than 178 submitted papers, out of which 112 papers were selected for presentation. The Technical Program Committee (TPC) did an outstanding job in organizing a diverse technical program consisting of 25 symposia that covered a broad range of research areas in information and communication technologies. Under the excellent leadership of TPC Co-chairs Prof. Pinyi Ren, Prof. Yunsong Li, and Prof. Chilian Chen, the TPC members handled the reviews of papers, with more than three reviews per paper on average.

The technical program featured five outstanding keynote speakers, who presented their vision of wireless communication systems in theory and practice: Prof. Jian-Nong Cao, Hong Kong Polytechnic University, Hong Kong, SAR China; Prof. Bob Li, University of Electronic Science and Technology of China, China; Prof. Jian-Dong Li, Xidian University, China; Prof. Ying-Chang Liang, University of Electronic Science and Technology of China, China; and Prof. Ping Zhang, Beijing University of Posts and Telecommunications, China.

We would like to thank the TPC co-chairs, TPC members, all the reviewers, the workshop co-chairs, the Web chairs, the publication chair, the local chairs, and all the members of the Organizing Committee, for their assistance and efforts to make the conference succeed. The continuing sponsorship by EAI and Springer is gratefully acknowledged. We also express our appreciation to the conference keynote speakers, tutorial speakers, paper presenters, and authors.

Organization

Steering Committee

Imrich Chlamtac	EAI/Create-Net, Italy
Hsiao-Hwa Chen	National Cheng Kung University, Taiwan
Ya-Bin Ye	Huawei Europe Research Center
Zheng Zhou	Beijing University of Posts and Telecommunications, China
Bo Li	Hong Kong University of Science and Technology, SAR China
Andreas F. Molisch	University of South California, USA
Jun Zheng	Southeast University, China
Zhi-Feng Zhao	Zhejiang University, China

Organizing Committee

General Chair

Bo Li	Northwestern Polytechnical University, China
-------	--

General Co-chairs

Pinyi Ren	Xi'an Jiaotong University, China
Yunsong Li	Xidian University, China
Chilian Chen	China Electronics Technology Group Corporation, China

TPC Chair

Lei Shu	EAI China Office, China/Guangdong University of Petrochemical Technology, China/University of Lincoln, UK
---------	---

TPC Co-chairs

Shuai Wan	Northwestern Polytechnical University, China
Lin Zhang	Beijing University of Posts and Telecommunications, China
Song Xiao	Xidian University, China

Local Chair

Zhongjiang Yan	Northwestern Polytechnical University, China
----------------	--

Workshop Co-chairs

Lijun Qian Prairie View A&M University, USA
Daji Qiao Iowa State University, USA

Publicity and Social Media Chairs/Co-chairs

Der-Jiunn Deng Changhua University of Education, Taiwan
Hongwei Zhao Northwestern Polytechnical University, China

Publications Chair

Deze Zeng China University of Geosciences, China

Web Chair

Mao Yang Northwestern Polytechnical University, China

Panels Chair

Lei Wang Dalian University of Technology, China

Sponsorship and Exhibits Chairs

Xiaoya Zuo Northwestern Polytechnical University, China
Ming Hao China Electronics Technology Group Corporation (CETC),
20th Institute, China
Luohui Su Aviation Industry Corporation of China (AVIC),
Xi'an Flight Automatic Control Research Institute,
China
Li Yan Guangdong University of Petrochemical Technology,
China

Tutorials Chair

Weipeng Jing Northeast Forestry University, China

Demos Chairs

Yuanfang Chen Guangdong University of Petrochemical University, China
Jianhua Zhang China Academy of Space Technology (CAST),
Xi'an Branch, China

Poster and PhD Track Chairs

Mithun Mukherjee Guangdong University of Petrochemical University, China
Yunjie Yuan China North Industries Group Corporation (CNIGC),
206th Institute

Industrial Exhibition Co-chairs

Chaoxing Su (Director)	Zhongke Industrial Park of Western Guangdong Province, China
Jun Feng (Deputy Director)	Zhongke Industrial Park of Western Guangdong Province, China
Meiquan Ou	Zhongke Industrial Park of Western Guangdong Province, China
Tianping Chen	Zhongke Industrial Park of Western Guangdong Province, China

Conference Manager

Dominika Belisova	European Alliance for Innovation (EAI)
-------------------	--

Technical Program Committee**Track Chairs****Wireless Communications and Networking**

Zheng Ma	Southwest Jiaotong University, China
Zhenyu Xiao	Beijing University of Aeronautics and Astronautics, China
Min Zhu	Xidian University, China

Special Session on the Next-Generation WLAN

Yingpei Lin	Huawei Technologies Co., China
Yunbo Li	Huawei Technologies Co., China

Big Data Network

Yong Li	Tsinghua University, China
Xiang Chen	Sun Yat-sen University, China

Cloud Communications and Networking

Chungang Yang	Xidian University, China
Yichen Wang	Xi'an Jiaotong University, China

Ad-hoc and Sensor Networks

Shihai Shao	University of Electronic Science and Technology of China
Chengbing He	Northwestern Polytechnical University, China

Satellite and Space Communications and Networking

Jinglun Shi	South China University of Technology, China
Mingwu Yao	Xidian University, China
Song Xiao	Xidian University, China

Optical Communications and Networking

Xiaoyan Pang	Northwestern Polytechnical University, China
Jie Lian	University of Virginia, USA

Information and Coding Theory

Jialiang Lu Shanghai Jiao Tong University, China
Zhengchuan Chen Singapore University of Technology and Design,
Singapore

Multimedia Communications and Smart Networking

Fuzheng Yang Xidian University, China
Hui Yuan Shandong University, China

Green Communications and Computing

Jianchao Du Xidian University, China
Guomei Zhang Xi'an Jiaotong University, China
Yiming Liu China Academy of Electronics and Information
Technology, China

Signal Processing for Communications

Hongxing Guo Huazhong University of Science and Technology, China
Wentao Shi Northwestern Polytechnical University, China
Qinghe Du Xi'an Jiaotong University, China

Network and Information Security

Yongqiang Hei Xidian University, China
Chengkai Tang Northwestern Polytechnical University, China
Pinyi Ren Xi'an Jiaotong University, China

Machine-to-Machine and Internet of Things

Shaohui Mei Northwestern Polytechnical University, China
Yongqian Du Northwestern Polytechnical University, China

Communication QoS, Reliability, and Modeling Symposium

Zhong Shen Xidian University, China
Guifang Li Northwestern Polytechnical University, China

Cognitive Radio and Networks Symposium

Yong Niu Beijing Jiaotong University, China
Li Sun Xi'an Jiaotong University, China

e-Health

Zhongjin Liu Coordination Center of China
He Guan Northwestern Polytechnical University, China

Contents – Part II

Multimedia Communications and Smart Networking

WSN Routing Algorithm Based on Energy Approximation Strategy	3
<i>Yuexia Zhang, Hang Chen, and Tianrun Gao</i>	
SIFT Based Monocular SLAM with GPU Accelerated.	13
<i>Tonghui Wang, Guoyun Lv, Shikai Wang, Haili Li, and Baicen Lu</i>	
Combining Computer Graphics and Feature for 3D Camera Tracking Based on CAD Model	23
<i>Linlin Wang, Guoyun Lv, Ningxin Zhang, and Yanggege Yu</i>	
Performance Analysis of CBRP, AODV and DSR Routing Protocols in VANETs Based on IDM-IM.	33
<i>Luqi Wu and Xia Wang</i>	
DOA Estimation for Far-Field Sources in Mixed Signals with Gain-Phase Error Array	41
<i>Jiaqi Zhen and Yanchao Li</i>	
Sparse Reconstruction in Frequency Domain and DOA Estimation for One-Dimensional Wideband Signals.	51
<i>Jiaqi Zhen and Yanchao Li</i>	
Radar Burst Control Based on Constrained Ordinal Optimization Under Guidance Quality Constraints	61
<i>Bo Li, Qingying Li, and Daqing Chen</i>	
An Overview of CCMANET: Content Centric MANET.	72
<i>Yuehua Huo, Weiqiang Fan, Yinlong Liu, and Dong Li</i>	
A Cooperative Broadcast Algorithm Based on the Successful Broadcasting Ratio and Residual Energy of Neighbor Nodes in Mobile Ad Hoc Networks	82
<i>Yichen Deng, Yanping Yu, and Zhengqing Yan</i>	

Signal Processing for Communications

Joint User Association and ABS for Energy-Efficient eICIC in Heterogeneous Cellular Network	95
<i>Jie Zheng, Ling Gao, Hai Wang, Jinping Niu, Xiaoya Li, and Jie Ren</i>	

Transmissions and Network Management of Multiple 100 GB/s Based on Stacking Technology <i>Xin Huang, Kaixiong Zhou, Chaoxiang Shi, Jianxin Chang, and Meng Gao</i>	102
Topology-Transparent Scheduling in Mobile Ad Hoc Networks with Unidirectional Links <i>Yiming Liu, Zhi Fu, and Mao Yang</i>	112
Carrier Synchronizator in Nonbinary LDPC Coded Modulation Systems <i>Qiang Zhang, Zhong-yang Yu, and Baoming Bai</i>	122
An Assessment Method of Pilot Situation Awareness in Manned/Unmanned-Aerial-Vehicles Team <i>Jun Chen, Qilin Zhang, Xunjie Qiu, and Bo Hou</i>	132
Minimum Interference Beam Selection for Millimeter Wave BeamSpace MIMO System <i>Dantao Li, Xiaohui Li, Bin Zhou, Yanbin Zhao, and Danfeng Meng</i>	141
An Efficient Algorithm for Constructing Underwater Sensor Barrier <i>Weiqliang Shen, Chuanlin Zhang, Min-Rong Chen, Jinglun Shi, and Guo-Qiang Zeng</i>	153
Distributed Coverage Hole Detection Algorithm Based on Čech Complex <i>Wang Yuchen, Lu Jialiang, and Philippe Martins</i>	165
An Energy-aware Routing Protocol Based on Network Coding for Wireless Sensor Networks <i>Panpan Cui, Song Xiao, and Lei Li</i>	176
Detecting Hierarchical and Overlapping Community Structures in Social Networks Using a One-Stage Memetic Algorithm <i>Chun-Cheng Lin, Der-Jiunn Deng, Jung-Chao Wu, and Liang-Yi Lu</i>	182
Optimal ZF Precoder Under per Antenna Power with Conjugate Beamforming for MU Massive MIMO Systems <i>James Kweku Nkrumah Nyarko and Christian Ango Mbom</i>	189
Butterfly-Flow-Graph Based MAP Decoding Algorithm for Channel Quality Information in 3GPP-LTE <i>Qi Li, He Wang, Yunchuan Yang, Bin Yu, and Chengjun Sun</i>	199
Group-Based Layered Scheduling of ADMM Decoding for LDPC Codes <i>Xing-Long Zhang, Meng Niu, Luo-Hui Su, and Ke-Pu Song</i>	207

LUT-Based Efficient Impulse Shaping for Direct Synthesizing Digital Communication Signals at Arbitrary Symbol Rate. 215
Ziyao Liu, Zhijie Wang, Jun Wang, Di Huang, and Nangen Zhang

An Adaptive Step-Size Prediction Joint OMP Algorithm for Beam Tracking in Millimeter Wave Systems. 227
Xu Yang, Xiaohui Li, Bin Zhou, Yanbin Zhao, and Ruiyang Yuan

Priority-Based Multi-carrier Access Schemes for Safety Message Transmission in Vehicular Networks 239
Huichao Wang, Longjiang Li, Fan Wu, Ke Zhang, and Supeng Leng

V2V Resource Allocation Schemes for Non-safety Service in Cellular Vehicular Networks. 250
Lei Jiang, Fan Wu, Ke Zhang, and Lixiang Ma

Adaptive Slot Assignment for TDMA Based Dynamic Airborne Ad Hoc Networks 260
Yueyan Qian, Mingwu Yao, and Liang Zhang

On Low-Pass Phase Noise Mitigation in OFDM System for mmWave Communications 271
Xiaoming Chen, Wei Fan, and Anxue Zhang

Network and Information Security

Secure Algorithm via Hybrid Relaying Scheme and Resource Allocation for OFDM Networks 283
Xianwen Zhou, Pinyi Ren, and Qinghe Du

Dynamic Group Behavior Analysis and Its Application in Network Abnormal Behavior Detection. 292
Yan Tong, Jian Zhang, Wei Chen, Mingdi Xu, and Tao Qin

A Simplifying Logic Approach for Gate Level Information Flow Tracking. . . 302
Yu Tai, Wei Hu, Dejun Mu, Baolei Mao, Lantian Guo, and Maoyuan Qin

A Cloud-Based Distance Bounding Protocol for RFID Conforming to EPC-C1 G2 Standards 312
Zhenjiang Dong, Xinluo Wang, Miao Lei, Wei Wang, and Hui Li

Research on the Monitoring Method of the Road Communication Network Quality Based on Vehicle Borne Internet of Things. 323
Baihua Ji, Xiao Liu, Tenghui Ke, Rongjie Kuang, Zibin Gao, and Daoce Wang

A Negotiation-Based Collision Avoidance Scheme for Autonomous Mobile Robots	331
<i>Zhaoxuan Chen, Pin Lv, Siyu Pan, and Jia Xu</i>	
Intelligent Access Scheme for Internet of Things Supported by 5G Wireless Network	341
<i>Yingshuan Song, Heli Zhang, Xi Li, Chunsheng Zhu, and Hong Ji</i>	
Fast Group Paging Algorithm for Large-Scale MTC Systems	352
<i>Si Huang, Xiaohui Li, Bin Zhou, Yanbin Zhao, and Ruiyang Yuan</i>	
A Honeyfarm Data Control Mechanism and Forensic Study	362
<i>Wei Yin, Hongjian Zhou, and Chunlei Yang</i>	
Environment-Related Information Security Evaluation for Intrusion Detection Systems	373
<i>Ran Cheng, Yueming Lu, and Jiefu Gan</i>	
A Novel Accurate Source Number Estimation Method Based on GBSA-MDL Algorithm	383
<i>Taha Bouras, Di He, Fei Wen, Peilin Liu, and Wenxian Yu</i>	
Communication QoS, Reliability and Modeling	
A Green Load Balancing Algorithm for Dynamic Spatial-Temporal Traffic Distribution in HetNets	395
<i>Jichen Jiang, Xi Li, and Hong Ji</i>	
Research on the Construction of Radio Environment Map (REM) Based on Spatial Interpolation	405
<i>Ran Zi, Jun Chang, Rong Zong, Ruonan Wang, and Guiwen Liao</i>	
Resource Allocation in OFDM-Based Cognitive Radios Under Proportional Rate Constraint	416
<i>Hongzhi Wang, Yongfei Yan, and Mingyue Zhou</i>	
Capacity Analysis of Secondary User System in Cognitive MIMO Networks Based on NOMA	426
<i>Han Liao</i>	
A Novel Energy Aware Coded Opportunistic Routing for Social Cognitive Radio Networks	440
<i>Shoubai Xiao, Renhao Lu, and Xiaoxiong Zhong</i>	
Research on Anti PUE Attack Based on CAF Spectrum and Repeated-Game	450
<i>Hong Chang and Yong Li</i>	

Multi-modal Transmission Strategies with Obstacle Avoidance for Healthcare Applications	463
<i>Tiong Hoo Lim</i>	
A BP Neural Network Based Self-tuning for QoS Support in AVB Switched Ethernet	474
<i>Dong Chen and Ang Gao</i>	
Optimal Power Splitting in a Full-Duplex Wireless Powered Network with a Bidirectional Relay	485
<i>Yingting Liu, Hongwu Yang, Chunman Yan, and Li Cong</i>	
Advances and Trends of V2X Networks	
Design and Implementation of an Intelligent Shipborne Terminal System. . . .	497
<i>Wenqiu Chen, Rongbin Yao, Jincai Ye, Xin Tang, and Xiaohuan Li</i>	
A Positioning Method Based on RSSI and Power Spectrum Waveform Distinction	509
<i>Yuyang Lin, Zunwen He, Jiang Yu, and Yan Zhang</i>	
A Network Coding Collaborative Download Scheme for Platoon-Based VANETs	519
<i>Jincai Ye, Xuwen Huang, Xiaohuan Li, Guan Wang, Rongbin Yao, and Xin Tang</i>	
Analysis of Conditional Connectivity Based on Two Lanes for VANETs. . . .	532
<i>Bin Pan and Hao Wu</i>	
Optimized Workload Allocation in Vehicular Edge Computing: A Sequential Game Approach.	542
<i>Dongdong Ye, Maoqiang Wu, Jiawen Kang, and Rong Yu</i>	
Navigation Route Based Stable Clustering for Vehicular Ad Hoc Networks	552
<i>Zhiwei Yang, Weigang Wu, Yishun Chen, Xiaola Lin, and Xiang Chen</i>	
A Social-Aware Routing Protocol for Two Different Scenarios in Vehicular Ad-Hoc Network	563
<i>Zhixiao Zhu, Binjie Hu, Haina Song, and Xiaotao Liu</i>	
Author Index	577

Contents – Part I

Wireless Communications and Networking

A Throughput Enhanced JTIDS Waveform Design	3
<i>Yingjie Song, Meng Zhang, and Ming Hao</i>	
Design and Application of Aperture-Coupled-Patch Frequency Selective Surfaces	13
<i>Yu Wang</i>	
Radar Cross Section Reduction Based on Metasurface	21
<i>Xing-Long Zhang, Meng Niu, Luo-Hui Su, and Ke-Pu Song</i>	
Joint Direction-of-Departure and Two-Dimensional Direction-of-Arrival Estimation with Automatic Pairing in Massive MIMO Systems.	27
<i>Yuan Zhou, Xiang Ji, and Man Dai</i>	
Non-orthogonal Multi-carrier Technology for Space-Based Internet of Things Applications.	37
<i>Mengdi Zhao, Hongxing Li, Yi Li, Li Fang, and Ping Chen</i>	
A Novel GPS Spoofing Algorithm Based on Modifying Navigation Message	46
<i>Qiong Yang, Yi Zhang, and Chengkai Tang</i>	
Implementation of Narrowband Interference Suppression Technology for DSSS Systems in Time Domain and Frequency Domain.	54
<i>Xiongfei Li, Xiangyang Meng, and Pan Liu</i>	
Spinal Codes Based Efficient Rateless Transmission Scheme for Massive MIMO System with Imperfect CSI	64
<i>Liangliang Wang, Yin Sun, Xuming Lu, Xiang Chen, and Hongzhou Tan</i>	
Low-Cost Topology Design for Wireless Ad Hoc Networks with Connectivity Constraint	75
<i>Mengmeng Xu, Qinghai Yang, and Hengzhou Xu</i>	
Waveform Design of UNB Modulation and Performance Analysis	84
<i>Aoqin Duan, Qinghe Du, and Bo Sun</i>	
System-Level Simulation Platform for Device-to-Device Communications in 5G Networks	95
<i>Zhihao Ding, Pinyi Ren, and Qinghe Du</i>	

Joint Algorithm for MIMO-OFDM System Based on the Idea of Layered Iteration	106
<i>Juan Wei, Shixuan Feng, and Lihong Wang</i>	
Improved UWB Indoor Positioning Algorithms Based on BP Neural Network Model.	114
<i>Haojie Liu, Zhonghua Liang, Danli Liu, and La'ning Ma</i>	
Performance of Transmitted Reference UWB Communication System with Time-Hopping Multiple Access	125
<i>Danli Liu, Wenjing Wu, Zhonghua Liang, Jinjin Liu, and Xiaojun Yang</i>	
Improved Ultra-wideband Pulse Shaping Technique Based on Spectrum Shifted Gaussian Waveforms	135
<i>Danli Liu, Zhonghua Liang, La'ning Ma, and Huansheng Song</i>	
An Uplink SCMA Scheme Combined with Interleaving.	146
<i>Fei Yang and Zhisong Bie</i>	
Integer-Forcing Detection of Generalized Spatial Modulation	155
<i>Guoquan Li, Ying Zhou, Xiangyun Zhou, Jinzhao Lin, Yu Pang, Jiacheng Wang, and Hongyu Zhu</i>	
Design of Dynamic TDMA Protocols for Tactical Data Link	166
<i>Lei Liu, Yiming Liu, Zhaowei Wang, and Chunxu Liu</i>	
Estimation Under Staggered Frame Structure for Multi-cell Multi-user Massive MIMO Systems	176
<i>Mengjun Zhang, Gang Xie, and Jinchun Gao</i>	
A Time-Domain Combined Anti-jamming Preprocess Method for DOA Estimation in DSSS System	186
<i>Shuyun Li, Sheng Ke, and Yuan Chai</i>	
An Efficient Wireless Backhaul Algorithm for User-Centric Ultra-Dense Networks	195
<i>Hong Feng, Xi Li, and Hong Ji</i>	
Stochastic Optimal Control for Power Allocation and Link Selection in Energy-Harvesting Three-Node Relay Network	206
<i>Qianyun Gong, Qinbo Chen, Hui Cai, Maoxin Tian, and Sai Zhao</i>	
Parallel Symbol Timing Recovery Using FPGA for 600 Mpsps QPSK	216
<i>Di Huang, Zhijie Wang, Jun Wang, and ZiYao Liu</i>	
Joint Fingerprinting and Curve Fitting Scheme with NLOS Identification for Indoor Localization	226
<i>Ruiyang Yuan, Xiaohui Li, Yanbin Zhao, Bin Zhou, and Si Huang</i>	

Fairness-Aware Scheduling for Millimeter Wave Backhaul Networks	240
<i>Danfeng Meng, Xiaohui Li, Yanbin Zhao, Bin Zhou, and Dantao Li</i>	
Lyapunov Optimization for NOMA Wireless Transmission with Energy Harvesting and Storage	254
<i>Qinbo Chen, Qianyun Gong, Maoxin Tian, Hui Cai, and Xiancai Chen</i>	
SEA: SDN-Based Evolution Architecture for 5G Network	264
<i>Chen He and Xiaofeng Qiu</i>	
A Method of Link Margin Analysis for Aeronautical Communication Systems in LOS Environment.	274
<i>Guofeng Jiang, Yangyu Fan, Hongbo Yuan, and Gang Zhou</i>	
Study on Handover of High Speed Railway by Rate-Splitting and Interference Cancellation	284
<i>Bo Zhang, Hui Liu, Hai Zhu, and Hengzhou Xu</i>	
Satellite and Space Communications and Networking	
A Novel Wavelet Denoising Algorithm Based on 2-Fold Cross Validation for BDS GEO Code Multipath Bias	297
<i>Peng Wu, Baowang Lian, Zesheng Dan, and Qiong Yang</i>	
Multi Block Overlapping Zero Padding Algorithm for Weak Signal Acquisition.	307
<i>Jinhua Sun, Shanshan Lv, and Hao Wang</i>	
A Partially Repeated Scheme for Polar Codes.	317
<i>Daolong Wu</i>	
Performance Bound Analysis on Hamming-Weight-Analysis Algorithm for Blind Recognition of Linear Block Codes	323
<i>Di Mao</i>	
An Efficient Algorithm for Refining Position and Velocity Outputs of Space Borne GNSS Receivers.	332
<i>Shuhao Chang, Xi Chen, and Menglu Wang</i>	
Fountain-Coding Aided Symmetrical Encryption for Secure Wireless Transmission	341
<i>Chao Lyu, Pinyi Ren, Qinghe Du, and Li Sun</i>	
A New Anti-blackout Communication Method Based on Carrier Aggregation of OFDMA and Frequency Diversity.	351
<i>Jieqi Li, Xiaoya Zuo, Yong Zhang, Zhengxue Li, Shaohui Mei, and Zhongqi Tian</i>	

Real-Time Indoor Positioning System Based on Background Training Model Using IR-UWB Radar 361
Hui-Seon Gang, June-Buem Park, and Jae-Young Pyun

Bandwidth Adaptive Image Communication via Similarity Based Auto-Selection 372
Jieqi Li, Mingyang Ma, Yong Zhang, Zhengxue Li, Shaohui Mei, and Shuai Wan

Hyperspectral Image Fusion Based on Multistage Guided Filter 381
Wenqian Dong, Song Xiao, Jiahui Qu, and Lizhao Li

Adaptive Long-Term Object Tracking for Real-Time Visual Search in Multimedia Surveillance. 388
Lei Li, Song Xiao, and Feiyang Tan

Multi-objective Optimization and Design of LEO Satellite Broadband Networks 398
Dawei Yan, Cong Liu, Peng You, and Shaowei Yong

Routing Protocol Design for LEO Satellite Networks with Uni-directional Links 409
Juan Wei, Lihong Wang, and Shixuan Feng

Measuring Quality of Experience of Novel 360-Degree Streaming Video During Stalling 417
Wenjie Zou and Fuzheng Yang

A Realizable and Efficient Approach for Building Software Defined Satellite Network 425
Wei Ma, Leifang Hui, Hanwen Sun, and Zhe Zhao

Proactive Edge Caching Strategy Based on Mobility Prediction in Dense Small Cell Networks 433
Tianming Song, Heli Zhang, Xi Li, Chunsheng Zhu, and Hong Ji

The Minimum of GDOP for Satellite Navigation System 443
Xuetao Yang, Jianchao Du, and Weibin Li

A SDN Security Transmission Service Using Multi-connection and Time-Slot Scheduling 448
Shiqi Zhou, Rongheng Lin, Shuquan Fan, Hua Zou, and Budan Wu

Construction of Quasi-Cyclic LDPC Codes with Diagonal Structure of Parity-Check Matrices 460
Hengzhou Xu, Huaan Li, Min Zhu, Bo Zhang, and Baoming Bai

Analyzing the Impact of Redundant Paths on Multistage Switch Performance. 470
Gao Ya, Pan Weitao, and Zheng Ling

Big Data Network Track

Positive and Unlabeled Learning for Mobile App User and Server Interaction Prediction. 481
Binbin Wang, Ke Yu, Xiaofei Wu, Fang Wei, Wan Jiang, and Di Pan

Game-Based Mobile Traffic Sharing with WiFi 492
Rong Wang, Zhifei Wang, Jibing Wu, Hongbin Huang, Su Deng, and Yahui Wu

Continuous Cell Zooming Algorithm Towards Energy Efficient in Random Heterogeneous Cellular Networks 502
Jie Sheng, Yang You, Dong Ma, Canyan Zhu, and Fan Xu

D2D Assisted MU-MIMO Precoding to Enhance LTE Network 512
Yanqiu Zhang, Shu Fang, Yuanchao Han, and Yu Zeng

High Concurrent Elastic Resource Allocation in Hadoop YARN. 524
Yang Peng, Danyan Luo, Jian Dong, and Zhibo Wu

An Autoencoder-Based Learning Method for Wireless Communication Protocol Identification 535
Jie Ren, Zulin Wang, and Mai Xu

A Novel Path Selection Algorithm Based on Graph-Cut to Ensure Security in SDN 546
Shuquan Fan, Rongheng Lin, Shiqi Zhou, Hua Zou, Budan Wu, and Yun Su

Secure and Reliable Transmission for Dense HetNets Based on Secure Energy Efficiency Optimization 557
Yunjia Xu, Kaizhi Huang, and Yi Zou

Author Index 567

Multimedia Communications and Smart Networking



WSN Routing Algorithm Based on Energy Approximation Strategy

Yuexia Zhang^{1,2(✉)}, Hang Chen^{1,2}, and Tianrun Gao¹

¹ School of Information and Communication Engineering,
Beijing Information Science & Technology University, Beijing, China
zhangyuexia@bistu.edu.cn, chenhang813@163.com,
gaotr2009@126.com

² Beijing Key Laboratory of High Dynamic Navigation Technology,
University of Beijing Information Science & Technology, Beijing, China

Abstract. In the routing protocol of wireless sensor networks, the traditional LEACH algorithm is too random, and the cluster head selection of it is not ideal. To solve this problem, it proposes a WSN routing algorithm based on energy approximation strategy. It chooses a series of nodes with high energy and high density to form cluster candidate clusters, and then selects the farthest node as the cluster head from the candidates by using the energy approximation strategy. The algorithm is simple and easy to implement, and the cluster head selection of it is ideal. Using Matlab software for simulation, the results show that it is less energy consuming than the LEACH algorithm, and the lifetime of the whole network is prolonged.

Keywords: Wireless sensor network · Routing algorithm · Cluster head
Energy approximation

1 Introduction

Wireless sensor network (WSN) is a network system composed of many different types of sensor nodes [1, 2]. It can collaboratively sense, collect, and process the relevant information in a specific area by using these different functions, self-organized sensor nodes. And finally the information are sent to the observer of the network system. WSN can be widely used in national defense and military, modern medical, intelligent transportation and environmental monitoring and many other fields. However, the energy of sensor node in WSN networks is very small due to the size and other factors. Therefore, it is important to reduce energy consumption and extend the life cycle of the network.

Routing protocol is one of the key technologies of WSN, which can be classified into four types: hierarchical, data center, geo-location and energy-aware routing protocols. LEACH algorithm is the first cluster-based routing protocol [3, 4], it choose the cluster head through the relationship between the node generated random number and threshold. The LEACH algorithm has a longer life cycle than planar routing protocol [5]. However, the randomness of the LEACH algorithm cluster-head selection is too large, it may cause the cluster head node to be distributed unevenly in the network

system and increase the energy loss of the network [6, 7]. The LEACH algorithm does not take into account the current density of the node itself, energy status and other factors, and its cluster head selection is not reasonable that would affect the network system life cycle. Therefore, the traditional LEACH algorithm has been unable to meet the needs of efficient use of WSN system. Literature [8] proposed a self-configuring cluster head fault detection mechanism based on LEACH algorithm. This mechanism can replace the fault cluster head node in time and effectively prolong the network lifetime, but it does not fundamentally the cluster head selection and can not effectively reduce the energy consumption of the network. Literature [9] proposed a routing algorithm that uses the energy delay index to select the cluster head. This algorithm improves the cluster head selection mechanism and improves the network energy utilization rate, but it does not take into account the cluster information path, and the selected cluster head may not be the optimal cluster head on the network communication path. Literature [10] proposed a fuzzy C-means algorithm for the optimum number of the cluster head and its location. It is greatly increasing the complexity of the algorithm although the algorithm increases the lifetime of the network.

In this paper, a new routing algorithm named Routing Algorithm for Energy Approximation Strategy (RA-EAS) is proposed to solve the shortcomings of existing routing protocols. RA-EAS chooses a series of nodes with high energy density and high density to form cluster candidate groups, and then selects the farthest node as the cluster head from the candidates by energy approximation strategy. RA-EAS algorithm is simple and easy to choose, and its cluster-head selection is ideal. RA-EAS algorithm can effectively save the residual energy of network and prolongs the network life-cycle than the LEACH algorithm through the simulation experiments.

2 Traditional LEACH Algorithm

Traditional LEACH algorithm is presented in the form of “round” [11]. Each round includes the cluster head creation phase and the information transmission phase. The traditional LEACH algorithm chooses the nodes as cluster heads randomly in each round, and repeats the process of creating cluster heads.

In the initial stage of cluster head establishment, the traditional LEACH algorithm establishes a threshold $T(i)$ first, which is defined as:

$$T(i) = \begin{cases} p/(1 - p \cdot (n \bmod (1/p))), & i \in G \\ 0, & \text{other} \end{cases} \quad (1)$$

Where p is the ratio of the number of clusters in the network to the number of whole nodes in the network, n is the number of cluster head selections. And G is the group of cluster selections that are not selected as cluster for $1/p$ times.

Every sensor node randomly generates a value RN that between 0 and 1, and then compare with the value RN and the threshold value $T(i)$. If $RN < T(i)$, this sensor node can be regarded as the cluster head; otherwise, the node is not selected as cluster head.

In the information transmission phase, sensor node that selected as the cluster head sends broadcast information to all normal nodes within its own coverage. According to

the strength of the received signal, the normal node judges to join the appropriate cluster and sends the join request. After receiving the request, the cluster head makes a TDMA schedule for all nodes in its own cluster, and all nodes send information to the cluster head by according this schedule.

After the above, the cluster head processes the data fusion and send it to the base station through the multi-hop transmission between others cluster heads to finish one round of information transmission. In the traditional LEACH algorithm, the cluster head is chosen according to the relationship of the generated value RN and the threshold value [12, 13]. All nodes in the network are selected as cluster heads with equal probability in each round, and new cluster head is selected for each round.

It is too random to select the cluster head in each round of LEACH algorithm, and the selection of the cluster head is not reasonable. Traditional LEACH algorithm does not consider the actual situation of every sensor node, these factors have a direct impact on the advantages and disadvantages of cluster head selection. It would increase the energy consumption of network systems and shorten the life cycle if inappropriate nodes are selected as the cluster head.

3 RA-EAS Algorithm

In RA-EAS algorithm, WSN network distribution diagram shown in Fig. 1. The Cartesian coordinate system is established with the known base station position as the coordinate origin. The WSN network is composed of known base station and N sensor nodes that randomly distributed around the known base station. The coordinate of the base station is $(0, 0)$, the coverage network radius is R , and the coverage radius of all the sensor nodes is $r, r < R$.

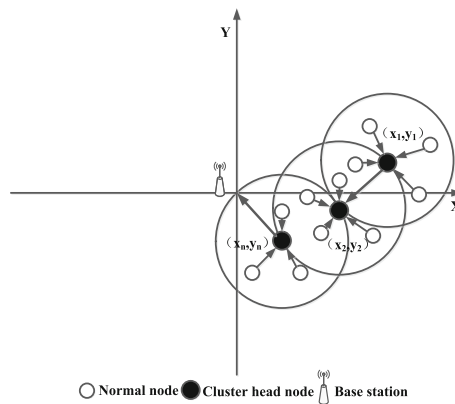


Fig. 1. WSN network distribution diagram

The probability value $P(i)$ of each node selected as cluster head can be calculated by using the residual energy of surviving nodes and the density of surviving nodes in the coverage radius. The value $P(i)$ is:

$$P(i) = c_1 \frac{E(i)}{E_{ave}} + c_2 \frac{N_{neigh}(i)}{N_{alive}} \quad (2)$$

Where c_1 , c_2 are the proportional coefficient. $E(i)$ refers to the current node itself carries the remaining energy value. E_{ave} represents the average remaining energy of all surviving nodes in the WSN network. $N_{neigh}(i)$ refers to the intensity of the current node that the number of surviving nodes within its coverage radius r . N_{alive} is the number of surviving nodes in the current network.

The probability value of every nodes selected as cluster heads can be calculated by formula (2). A probability threshold is set in advance, when $P(i) > V$, then the node i is selected as the candidate group of cluster heads.

In order to avoid the high complexity of the algorithm due to the Sub-region selection of the cluster head, and the chosen cluster head in the current region is not necessarily the best cluster head in the whole network, which brings about extra energy consumption. Therefore, the RA-EAS algorithm adopts cluster head selection method based on energy approximation strategy, a series of nodes that can cover the whole area and are farthest from each other are selected as cluster heads in the candidate group of cluster heads.

Suppose the coordinates of cluster head from far to near are $(x_1, y_1), (x_2, y_2) \cdots (x_i, y_i) \cdots (x_l, y_l)$, then the coordinates of cluster head satisfy the following conditions:

1. Every selected cluster head position is closer to the known base station position than the previous one. So, the absolute value of the vertical and horizontal coordinates of the current cluster head is smaller than that of the last selected cluster head in the Cartesian coordinate system. That is:

$$\begin{cases} R > |x_1| > |x_2| > \cdots > |x_l| > 0 \\ R > |y_1| > |y_2| > \cdots > |y_l| > 0 \end{cases} \quad (3)$$

2. The distance between adjacent cluster heads must less than the coverage radius r in order to meet the basic communication requirements between cluster heads, That is:

$$\sqrt{(x_i - x_{i-1})^2 + (y_i - y_{i-1})^2} < r \quad (4)$$

3. In order to make the distance between the adjacent cluster heads farthest for the optimal information transmission path, the position of the current cluster head is at the coverage of the overlap between the previous cluster head and the latter cluster in the Cartesian coordinate system. That is:

$$\begin{cases} |x_{i-1}| - r < |x_i| < |x_{i+1}| + r \\ |y_{i-1}| - r < |y_i| < |y_{i+1}| + r \end{cases} \quad (5)$$

4. When the known base station lies within the coverage radius of the selected cluster head, it is not necessary to continue selecting the cluster head any longer. That is:

$$\begin{cases} 0 < |x_l| \leq r \\ 0 < |y_l| \leq r \end{cases} \quad (6)$$

5. The sum of the distances between all adjacent cluster heads is greater than R that in order to satisfy all the nodes within the coverage radius R of known base station can complete the information transmission. That is:

$$R \leq \sum_{i=2}^n \left(\sqrt{(x_i - x_{i-1})^2 + (y_i - y_{i-1})^2} + \dots + \sqrt{(x_l)^2 + (y_l)^2} \right) + r \quad (7)$$

In summary, the coordinates of cluster head must meet the following constraints:

$$\begin{cases} R > |x_1| > |x_2| > \dots > |x_l| > 0 \\ R > |y_1| > |y_2| > \dots > |y_l| > 0 \\ |x_{i-1}| - r < |x_i| < |x_{i+1}| + r \\ |y_{i-1}| - r < |y_i| < |y_{i+1}| + r \\ \sqrt{(x_i - x_{i-1})^2 + (y_i - y_{i-1})^2} < r \\ 0 < |x_l| \leq r \\ 0 < |y_l| \leq r \\ R \leq \sum_{i=2}^n \left(\sqrt{(x_i - x_{i-1})^2 + (y_i - y_{i-1})^2} + \dots + \sqrt{(x_l)^2 + (y_l)^2} \right) + r \end{cases} \quad (8)$$

When one cluster head is selected from the candidate group of cluster heads, the others nodes within its coverage become the normal nodes automatically. The cluster head sends broadcast messages to all normal nodes within its own coverage radius r , and the normal nodes choose to join the appropriate cluster according to the information received. At this point, clustering is completed, and RA-EAS algorithm clustering process flow diagram shown in Fig. 2.

The clustering process of RA-EAS algorithm is described as follows:

Step 1. Establishing the Cartesian coordinate system by using the known base station position as the coordinate origin.

Step 2. Calculating the probability value $P(i)$ that the node is elected as cluster head by using formula (2).

Step 3. Determining the cluster head candidate group though the pre-set probability threshold V .

Step 4. Judging energy approximation of constraint conditions in the candidate group of cluster heads. The cluster head is selected as the cluster head if the constraint condition is satisfied, otherwise it becomes the normal node.

Step 5. Every node completes its own task according to the routing protocol after determining the cluster head node and the normal node. The cluster head sends a broadcast message to all normal nodes within the coverage radius of r that cluster itself as the center. And the normal nodes select join into a suitable cluster according to the strength of the broadcast information received.

Step 6. At this point, a complete cluster structure assignment end up.

Then, steps 4 and 5 are repeated to complete the subsequent clustering steps. And cluster-based cooperative communication centered on cluster-head is realized in the WSN network finally. Every cluster-head receives the information of the normal node in the cluster and fuses the information to transmit to the base station in multi-hop mode. Thus, a complete round of information transmission end up. Cycle to carry out the above steps to complete each round of the cluster process and information transfer process.

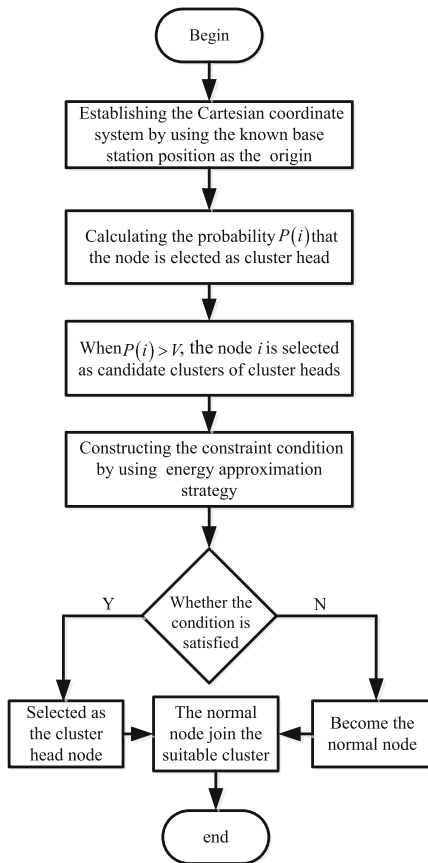


Fig. 2. RA-EAS algorithm clustering process flow diagram

4 Performance Analysis

The number of dead nodes and the energy consumption between traditional LEACH algorithm and RA-EAS algorithm are simulated to verify the effectiveness of RA-EAS algorithm. The experimental parameters [14] in the simulation environment are shown in Table 1.

Table 1. The experimental parameters in the simulation environment

Parameters	Symbol	Value
Number of nodes	N	100
Initial energy	E_0	0.5 J
Proximal energy consumption coefficient	E_{fs}	10 pJ/bit/m ²
Remote energy consumption coefficient	E_{amp}	0.0013 pJ/bit/m ⁴
Transmit and receive energy consumption	E_{elec}	50 nJ/bit
Packet size	k	4000 bits
Control packet size	L_{ctrl}	100 bits
Data aggregation energy	E_{da}	5 pJ/bit/report
Cluster head probability threshold	V	0.05
Network area	$M \times M$	100 m \times 100 m

100 nodes are randomly distributed in WSN network area which area is 100 m 100 m. Figure 3 shows the distribution of nodes in this network area, and the origin of Cartesian coordinate system is the known base station location.

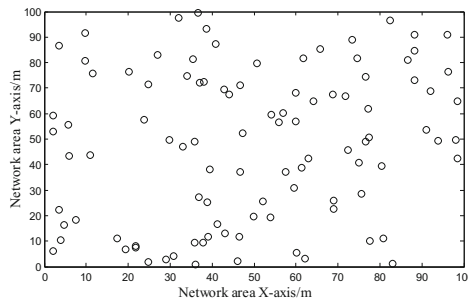


Fig. 3. The distribution of nodes in the network area

Figure 4 gives the comparison between the number of network death nodes and the rounds of selection in LEACH algorithm and EA-RAS algorithm. The network life cycle is defined as the dead time of the first network node. The first death node in the LEACH algorithm network in Fig. 4 appears in 946 rounds, while the RA-EAS algorithm appears in 1189 rounds. The RA-EAS algorithm prolongs the lifetime of the network system by 26% compared with the LEACH algorithm. This is because the

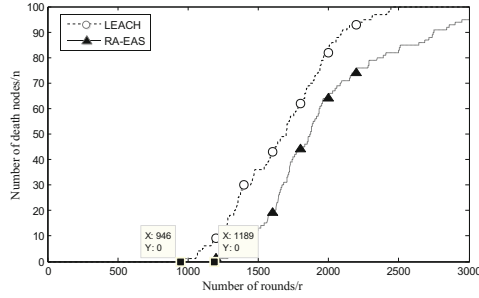


Fig. 4. The comparison between the number of network death nodes and the rounds of selection

LEACH algorithm selects the cluster head randomly, but the RA-EAS algorithm has taken into account the current node’s own energy and density in the selection of cluster head, makes that the preferably nodes become cluster heads.

Figure 5 shows the comparison between the number of surviving nodes in the network and the rounds of selection in the cluster. It can be seen that the nodes in RA-EAS algorithm begin to die are later than that in LEACH algorithm, so that the RA-EAS algorithm prolongs the network life cycle than LEACH algorithm.

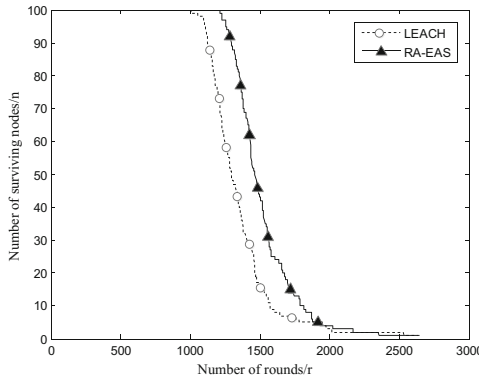


Fig. 5. The comparison between the number of surviving nodes and the rounds of selection

Figure 6 exhibits the network energy consumption comparison between LEACH algorithm and EA-RAS algorithm. It can be seen that the energy consumption per round of the network system in the EA-RAS algorithm is less than that in the LEACH algorithm under the same conditions. The network energy consumption of both algorithms tends to be stable after 2500 rounds, this is because most of the nodes in the network are dead at this time. It is also shows that the total energy consumption in the EA-RAS algorithm is lower than that in the LEACH algorithm. That is, the EA-RAS algorithm can more save the residual energy of the network than LEACH algorithm.

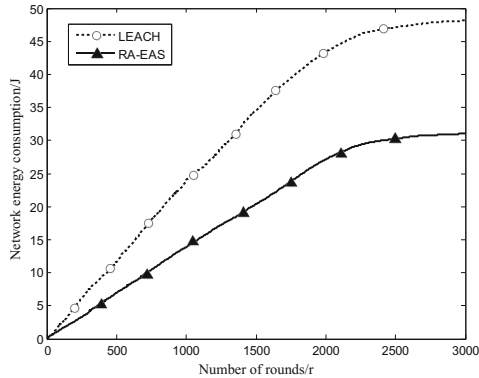


Fig. 6. The network energy loss comparison between LEACH and EA-RAS

5 Conclusions

This study proposes a WSN routing algorithm of EA-RAS that based on energy approximation strategy. The EA-RAS algorithm is simple and the cluster-head selection is ideal. And the RA-EAS algorithm is more effective in extending the life cycle of the network system and saving the residual energy compared with the LEACH algorithm that simulation results show.

References

1. Pantazis, N.A., Nikolidakis, S.A., Vergados, D.D.: Energy-efficient routing protocols in wireless sensor networks: a survey. *IEEE Commun. Surv. Tutor.* **15**(2), 551–591 (2013)
2. Borges, L.M., Velez, F.J., Lebres, A.S.: Survey on the characterization and classification of wireless sensor network applications. *IEEE Commun. Surv. Tutor.* **16**(4), 1860–1890 (2014)
3. Dhawan, H., Waraich, S.: A comparative study on LEACH routing protocol and its variants in wireless sensor networks: a survey. *Int. J. Comput. Appl.* **95**(8), 21–27 (2014)
4. Lee, W.S., Ahn, T.W., Song, C.Y.: A study on improvement of energy efficiency for LEACH protocol in WSN. *J. Inst. Electron. Inf. Eng.* **52**(3), 213–220 (2015)
5. Nayak, P., Devulapalli, A.: A fuzzy logic-based clustering algorithm for WSN to extend the network lifetime. *IEEE Sens. J.* **16**(1), 137–144 (2016)
6. Han, Z., Wu, J., Zhang, J., et al.: A general self-organized tree-based energy-balance routing protocol for wireless sensor network. *IEEE Trans. Nucl. Sci.* **61**(2), 732–740 (2014)
7. Zhang, D., Li, G., Zheng, K., et al.: An energy-balanced routing method based on forward-aware factor for wireless sensor networks. *IEEE Trans. Ind. Inform.* **10**(1), 766–773 (2014)
8. Izadi, D., Abawajy, J., Ghanavati, S.: An alternative clustering scheme in WSN. *IEEE Sens. J.* **15**(7), 4148–4155 (2015)
9. Thakkar, A., Kotecha, K.: Cluster head election for energy and delay constraint applications of wireless sensor network. *IEEE Sens. J.* **14**(8), 2658–2664 (2014)
10. Bouyer, A., Hatamlou, A., Masdari, M.: A new approach for decreasing energy in wireless sensor networks with hybrid LEACH protocol and fuzzy c-means algorithm. *Int. J. Commun. Netw. Distrib. Syst.* **14**(4), 400–412 (2015)

11. Long, C.Z., Lin, H., Huang, C.H., et al.: Improved LEACH multi-hop algorithm based on residual energy and region distribution. *J. Inf. Comput. Sci.* **11**(9), 2955–2964 (2014)
12. Dong, S., Li, C.: The improvement of LEACH algorithm in wireless sensor networks. *Int. J. Online Eng. (iJOE)* **12**(11), 46–51 (2016)
13. Mottaghi, S., Zahabi, M.R.: Optimizing LEACH clustering algorithm with mobile sink and rendezvous nodes. *AEU-Int. J. Electron. Commun.* **69**(2), 507–514 (2015)
14. Fu, C., Jiang, Z., Wei, W.E.I., et al.: An energy balanced algorithm of LEACH protocol in WSN. *Int. J. Comput. Sci.* **10**(1), 354–359 (2013)



SIFT Based Monocular SLAM with GPU Accelerated

Tonghui Wang, Guoyun Lv^(✉), Shikai Wang, Haili Li, and Baicen Lu

School of Electronics and Information, Northwestern Polytechnical University,
Xi'an, China

nwpuwth@qq.com, 178510887@qq.com, 1748710855@qq.com,
735110965@qq.com, 992159044@qq.com

Abstract. With the rapid development of computer vision technology, 3D Reconstruction based on monocular SLAM (Simultaneous Localization and Mapping) has got more and more attention for its simple requirements, low cost, easy to implement, convenient to carry. ORB-SLAM is a kind of monocular SLAM method based on feature point. ORB feature can meet the real-time requirements for SLAM, but it does not have scale invariance. In this paper, we proposed a monocular SIFT-SLAM, in which a SIFT (Scale Invariant Feature Transform) algorithm based on GPU is used to replace the ORB algorithm, to implement 3D Reconstruction. We show the experiment result of SIFT-SLAM in this paper, which gets some improvement.

Keywords: SLAM · Monocular · SIFT · GPU · 3D Reconstruction

1 Introduction

1.1 Monocular Visual SLAM

In recent years, SLAM based 3D Reconstruction method has become a hot issue in the field of computer vision [1, 2]. SLAM [3] is a process in which the mobile robot senses the surrounding environment through the sensor carried by itself, and uses the information obtained by the perception to carry on the self-localization process. Compared with the expensive and complex shortcomings such as laser sensors, ordinary visual sensors have advantages such as a wide range of measurement, rich information collection, cost-effective, versatile, convenient to carry and so on. In addition, the visual SLAM is real-time system. Based on these advantages monocular vision SLAM technology becomes the direction of SLAM development [3, 10–12].

At present, the vision-based SLAM technique is divided into two types: feature-based method and direct method. The direct method uses all the pixels in the image for map reconstruction based on the gray scale invariant assumption of the object feature point, so the extraction of the feature points is avoided and reduce the computational complexity, and ensure the real-time performance of the algorithm. The main representative is LSD-SLAM (Large-Scale Direct Monocular SLAM) [4] proposed by Jakob Engle and others of the University of Munich, Germany. The feature point method considers the feature point as the fixed point of the fixed three-dimensional space,

calculates the three-dimensional coordinate transformation matrix of the feature point according to the matching of different image feature points, and implement the object reconstruction, the representative method is the ORB-SLAM [5] algorithm proposed by Mur-Artal et al. At present, the visual SLAM algorithm based on feature point matching is still the mainstream research direction of SLAM field. But the traditional feature point method still has obvious shortcomings. ORB (Oriented BRIEF) [6] feature point, which uses FAST as the feature point and detection operator BRIEF as a feature descriptor, has the advantages of rotation invariance, affine invariance, translation invariance. But ORB does not have good robustness for noise and scale invariance. In 2004, David proposed the SIFT (Scale Invariant Feature Transform) [7] feature point, which has translation invariance, rotation invariance, scale invariance, affine invariance, and the robustness for noise and light are better. However, the SIFT algorithm has high complexity and large computational complexity, which leads to poor algorithm performance and cannot be directly used in real-time visual SLAM system.

This paper presents the calculation of SIFT algorithm on the GPU platform [11] to solve the real-time problem of SIFT algorithm. The accelerated SIFT algorithm is used to replace the ORB algorithm in ORB-SLAM system, to realize the SIFT-SLAM system based on monocular vision. This paper gives the results of the accelerated SIFT algorithm, and evaluates the feasibility and effectiveness of the SIFT-SLAM system.

1.2 GPU and CUDA

The rapid development of semiconductor technology, make CPU and GPU with faster and faster computing speed. But the CPU and GPU have their own unique advantages. The difference between CPU and GPU are as Fig. 1.

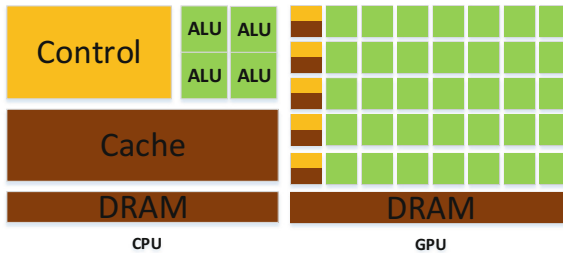


Fig. 1. CPU and GPU structure diagram. CPU has bigger Control area and smaller ALU area, which makes CPU be more capable in logic control. GPU has more ALU which means GPU has faster computing speed.

The CPU facilitates a large number of programs including loops, branches, logical decisions, and complex instructions; the GPU is more advantageous for processing with programs that have high parallelism, large data volumes, low data coupling, high computational density, and less interaction with the CPU.

NVIDIA has released a CUDA parallel computing platform that makes heterogeneous programming based on CPU and GPU easy to implement. The CPU is called Host, and GPU is called Device. In this heterogeneous model, the CPU is responsible for the logic control and serial computing. The GPU is responsible for the highly parallel computing of large-scale data in the system. A part of the parallel processing of a CUDA program is done by the kernel function. CUDA threads are divided into three levels: grid, block, thread. Every thread of every block in every grid has a unique thread index, which we named it as `threadIdx`. The `threadIdx` ensures that each thread can read the corresponding data in the memory space to ensure that the parallelization of the normal calculation. CUDA reduces the use of loop structures by parallel computation, as a result this saves a lot of time.

2 ORB-SLAM Framework

ORB-SLAM can run on computer in real time with good system robustness. The overall framework of the ORB-SLAM system is shown in Fig. 2. The whole system is divided into three parts:

Tracking. The tracking part mainly extracts the ORB feature from the image, performs the pose estimation according to the previous frame, or initializes the pose through the global positioning, optimizes the position, and then confirm the new key frame according to some rules.

Local Mapping. This part mainly completes the local map construction, including the insertion of the new key frame, verifies and filters the newly generated map points, and generates the correct map points. After that, the local Bundle Adjustment (BA) is used to filter the inserted key frame and remove redundant key frames.

Loop Closing. This part is divided into two parts, loop closing detection and loop closing correction. Loop closing detection is first performed using a Bag of Words [8] and then simulated by Sim3. Loop closing correction, mainly closed-loop fusion and g2o (general graph optimization) [9] optimization.

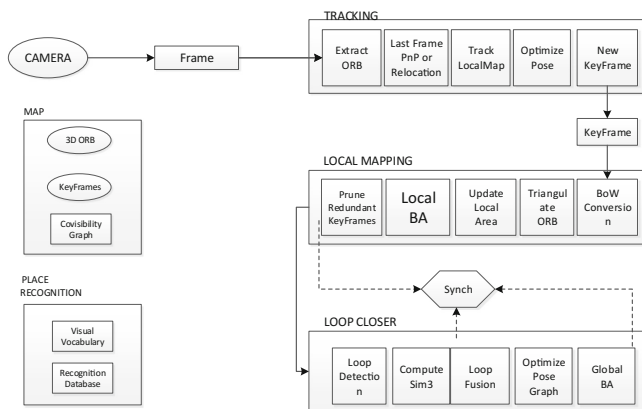


Fig. 2. The framework of ORB-SLAM.

From the Fig. 2, it can be seen that ORB-SLAM extracted the ORB feature points from the picture taken by the camera. In this paper, we use the SFIT algorithm after GPU acceleration to extract the feature points, so we can get a real-time SLAM system under the premise of a good 3D Reconstruction result.

3 Accelerated SIFT Algorithm

3.1 SIFT Algorithm

David G. Lowe proposed the Scale-Invariant Feature in 1999 to carry out object recognition and image matching. In 2004, he proposed the Scale Invariant Feature Transform (SIFT) algorithm for development and refinement.

The SIFT algorithm contains four parts: the scale space is built and the extreme points are detected, the feature points are selected and positioned, and the direction values are determined for the feature points (Fig. 3).

First, the original image is layered by using Gaussian filters of different scales, and then the adjacent Gaussian filtered image is subtracted to obtain the difference of Gaussian (DoG) pyramid. Then we select the extreme point from the scale space. The feature points with lower contrast and the feature points located at the edge position are removed, leaving the remaining feature points which meet the threshold requirements. In the discrete function extremum points can represent the mathematical characteristics of the discrete function. The maximum gradient modulus value of each pixel at the feature point and its neighborhood will be the main direction of the feature point.

Select a rectangular block pixels around a key-point, and divided it into $16 = 4 \times 4$ sub regions as suggested in Lowe's paper [7]. We draw the cumulative value for each gradient direction, forming a key point, which include 8-way vector information. As a result, one feature point can generate a $4 \times 4 \times 8$ dimensional data, which means, a total of 128-dimensional data to form a 128-dimensional SIFT feature vector.

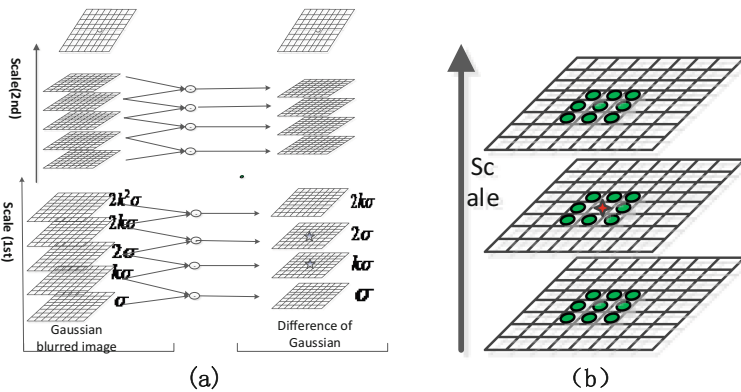


Fig. 3. (a) is the figure of Gaussian and Difference of Gaussian. (b) is extreme point value detection in Gaussian scale-space, the red point means the feature point, the green point represents the pixels wait to be compared. (Color figure online)

3.2 Accelerate SIFT with GPU

Create Difference of Gaussian Pyramid. The SIFT algorithm creates the scale space by Gaussian blur, uses the Gaussian function to compute the fuzzy template. Then the template is used to do convolution with the original image.

The equation of the two - dimensional Gaussian function $G(x, y)$ is as follows:

$$G(x, y) = \frac{1}{2\pi\sigma^2} e^{-\frac{(x-m/2)^2 + (y-n/2)^2}{2\sigma^2}} \quad (1)$$

m represents the width of image and n represents the height of image, σ represents deviation of normal distribution. x, y represent the pixel coordinates.

When we calculate the DoG pyramid, each blurred image obtained is based on the original image to take different σ values to achieve. The coordinates of each layer in the octave are calculated as follows:

$$\sigma(s) = \sqrt{(k^m \sigma_0)^2 - (k^{m-1} \sigma_0)^2} \quad (2)$$

m represents the index of an interval in an octave, σ_0 represents the initial value of σ .

So we can put the process of creating a scale space into the GPU. Assuming that the Gaussian pyramid has N octaves, each octave contains M intervals, then in the GPU the kernel will create $N \times M$ threads, giving each thread a different σ value. Through a parallel calculation, the Gaussian blurred images can be calculated. Afterwards adjacent image is subtracted to obtain a difference of Gaussian pyramid.

Extreme Point Detection. In the Gaussian scale-space, each pixel is compared with pixels in its $3 * 3$ neighborhood at its interval and the adjacent interval. When it is an extreme value, the feature point is stored.

For a difference of Gaussian pyramid with N octaves, each group of M internals, the number of pixels between the different octave are different and independent with each other. The kernel function is performed separately from the feature point detection between the octaves. The kernel function performs the feature point calculation of a set of Gaussian blurred images at a time, and loop N times to complete all the calculations.

Define Direction for Key-Point. In order to make the descriptor have rotational invariance, it is necessary to use the local feature of the image to assign a reference direction for each key-point. Using the method of calculating image gradient to find the stable direction of local feature. For the key-points detected in the DOG pyramid, the gradient and direction distribution of the pixels in the neighborhood window of the Gaussian pyramid image are calculated.

The formulas used to calculate the modulus value and direction of gradient as follows:

$$m(x, y) = \sqrt{(L(x+1, y) - L(x-1, y))^2 + (L(x, y+1) - L(x, y-1))^2} \quad (3)$$

$$\theta(x, y) = \tan^{-1}(L(x, y+1) - L(x, y-1)) / (L(x+1, y) - L(x-1, y)) \quad (4)$$

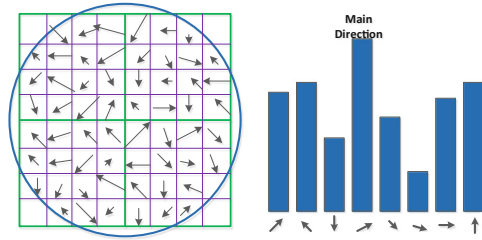


Fig. 4. Gradient direction of Key-point and histogram of gradient modulus value (For simplicity, only eight bins are show in the histogram).

$m(x, y)$ and $\theta(x, y)$ represent the modulus and direction of the gradient, respectively. L represents the scale space of the key points.

After completing the gradient calculation of the key-points, we use the histogram to measure the gradient and direction of the pixels in the neighborhood. The gradient histogram divides the range of 0 to 360° into 36 columns (bins), 10° per column. As shown in Fig. 4, the peak direction of the histogram represents the main direction of the key-point [7].

The peak of the direction histogram represents the direction of the neighborhood gradient at the key-point, and the maximum value in the histogram is taken as the main direction of the key-point. According to the calculation process, the gradient direction and the gradient modulus of all the points in the neighborhood of the key-point are put into GPU. Assuming there are n points in the neighborhood, the GPU kernel function create n CUDA threads, and executes the calculation process. And then the search of main direction and auxiliary direction is calculated in CPU.

Generates Feature Point Descriptors. Through the above steps, for each key, there are three information: location, scale and direction. The next step is to create a descriptor for each key, and describes the key point with a set of vectors so that it does not change with various changes, such as changes in light, changes in perspective, and so on.

We rotate the coordinate axis to the main direction of the key point to make the rotation invariance. Then we draw the cumulative value for each gradient direction, forming a key point, which include 8-way vector information. As a result, one feature point can generate a $4 \times 4 \times 8$ dimensional data, which means, a total of 128-dimensional data to form a 128-dimensional SIFT feature vector (Fig. 5).

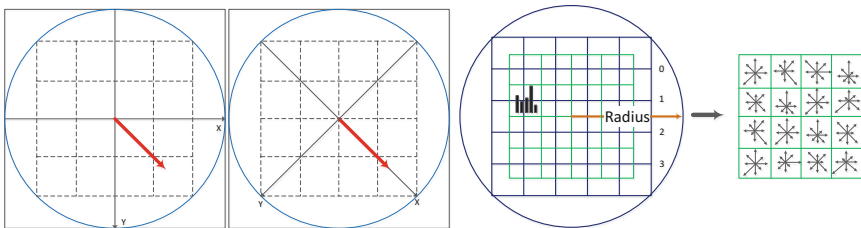


Fig. 5. Rotate the axis towards the main direction of key-point and the descriptor of SIFT feature

In the calculation, rotating the axis is carried out in the CPU, and when the eight degrees of freedom in the 16 sub-regions are calculated, the kernel function in the GPU is opened with 128 threads, and the feature points are generated together.

4 Experiment and Results

4.1 Experiment Platform

In this test the hardware platform we used is the Intel Core I7-6700, GPU for the NVIDIA GTX 1060. The specific test environment is shown in Table 1.

Table 1. Parameters of experiment platform

Class	Contents
System	Linux Ubuntu 14.04 and 64
CPU	Intel(R) Core(TM) i7-6700 CPU @ 2.40 GHz
RAM	16 GB
GPU	NVIDIA GeForce GTX 1060
CUDA version	8.0
OpenCV version	3.0

This section selects three sets of images with different resolutions and scales in Fig. 6(a), (b) and (c) for experiments.

We use three different images of different images to experiment, Fig. 6(a), (b) and (c) three different resolution images, the second image of each group has angle translation and scale transformation relative to the first image. Respectively, with the ORB algorithm in OpenCV, the SIFT algorithm in OpenCV, the accelerated GPU-SIFT algorithm to test 10 times, take the average. The final results are shown in Table 2 and Fig. 6(d).

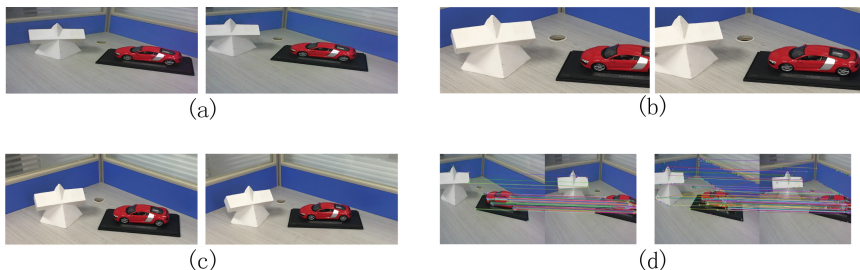


Fig. 6. (a) Image resolution 640×480 ; (b) Image resolution 1280×720 ; (c) Image resolution 1920×1080 ; (d) is the result of ORB algorithm and GPU-SIFT algorithm.

The Time Cost above is used to extract the feature points of two pictures and match them. From the experimental results, we get the follow conclusions:

Conclusion A. Compared with the original SIFT algorithm, the GPU-accelerated SIFT algorithm has obvious acceleration effect at the speed of the feature points extraction. For 640×480 resolution images, the time cost is reduced by nearly 20 times, while for 1920×1080 resolution images, the time cost is reduced by nearly 70 times. From this we can see that when the GPU is dealing with parallel computation of large data, the acceleration effect is very obvious.

Conclusion B. Compared with the traditional ORB algorithm, GPU-accelerated SIFT algorithm in the feature point extraction speed makes up for their own shortcomings, timeliness problems have been resolved. Besides SIFT algorithm gets more feature points than ORB algorithm, which means the match will be more accurate.

Conclusion C. The above experimental results are not considered in the CPU-GPU heterogeneous programming platform, the time spent with the data transfer in the host memory and graphics memory. So in the actual SIFT-SLAM system, the use of time-consuming will increase (Fig. 7).

Table 2. Experiments based on NVIDIA GeForce GTX 1060 and result

Image resolution	Algorithm	Number of feature		Match feature	Time cost
640×480	ORB	500	500	200	21 ms
	SIFT	359	409	132	270 ms
	GPU-SIFT	346	371	128	14 ms
1280×720	ORB	500	500	175	65 ms
	SIFT	1273	1403	609	878 ms
	GPU-SIFT	1187	1276	593	18.8 ms
1920×1080	ORB	500	500	51	114 ms
	SIFT	2206	2361	126	1870 ms
	GPU-SIFT	1962	2289	107	26.9 ms



Fig. 7. The left picture shows the source picture. And the right one is the result of SIFT-SLAM algorithm.

4.2 SIFT-SLAM Experiment

In this experiment, we collected the video sequence through the camera as the data source, which was tested in the monocular ORB-SLAM system and monocular SIFT-SLAM system respectively.

In the experiment, we use ORB-SLAM and SIFT-SLAM to rebuild the building. As the result, the SIFT feature gets more feature points than ORB, and we get a clearer silhouette with SIFT-SLAM.

So we get the conclusion that SIFT feature is more suitable for 3D Reconstruction in feature-based slam system than ORB feature. But in the experiment, SIFT-SLAM is a little slow than ORB-SLAM, which we still need to optimize.

5 Conclusions

In this paper, we proposed a method, using the GPU to accelerate SIFT algorithm for real-time calculations. Combined with mature ORB-SLAM, we use accelerated SIFT algorithm to replace ORB algorithm, and we propose a SIFT based monocular SLAM system. As experiment results show, the accelerated SIFT algorithm can make feature detection run on real-time. Besides SIFT feature has greater advantages in scale invariance and robustness compared with ORB algorithm. The SIFT-SLAM monocular system generate a sparse point cloud map, which is enough for simple 3D Reconstruction.

Acknowledgments. This work is sponsored by the Seed Foundation of Innovation and Creation for Graduate Students in Northwestern Polytechnical University (No. Z2017139).

References

1. Smith, R., Self, M., Chessman, P.: Estimating uncertain spatial relationships in robotics. In: Proceedings of the Uncertainty in Artificial Intelligence (1988)
2. Davison, A.J., Nobuyuki, K.: 3D simultaneous localization and map building using active vision for a robot moving on undulating terrain. In: Proceedings of the IEEE International Conference on Computer Vision and Recognition, Hawaii, pp. 384–391 (2001)
3. Andersen, D.R., Cuykendall, R., Regan, J.J.: SLAM - vectorized calculation of refraction and reflection for a Gaussian beam at a nonlinear interface in the presence of a diffusive Kerr-like nonlinearity. *Comput. Phys. Commun.* **48**(2), 255–264 (1988)
4. Engel, J., Schöps, T., Cremers, D.: LSD-SLAM: large-scale direct monocular SLAM. In: Fleet, D., Pajdla, T., Schiele, B., Tuytelaars, T. (eds.) ECCV 2014. LNCS, vol. 8690, pp. 834–849. Springer, Cham (2014). https://doi.org/10.1007/978-3-319-10605-2_54
5. Mur-Artal, R., Montiel, J.M.M., Tardos, J.D.: ORB-SLAM: a versatile and accurate monocular SLAM system. *IEEE Trans. Robot.* **31**(5), 1147–1163 (2015)
6. Rublee, E., Rabaud, V., Konolige, K.: ORB: an efficient alternative to SIFT or SURF. In: Proceedings, vol. 58, no. 11, pp. 2564–2571 (2011)
7. Lowe, D.G.: Distinctive image features from scale-invariant key-points. *J. Comput. Vis.* **2** (60), 91–110 (2004)

8. Nister, D., Stewenius, H.: Scalable recognition with a vocabulary tree. In: IEEE Computer Society Conference on Computer Vision and Pattern Recognition, NY, USA, pp. 2161–2168 (2006)
9. Kümmerle, R., Grisetti, G., Strasdat, H., Konolige, K., Burgard, W.: g2o: a general framework for graph optimization. In: International Conference on Robotics and Automation (ICRA) (2011)
10. Klein, G., Murray, D.: Parallel tracking and mapping for small AR workspaces. In: Proceedings of the IEEE and ACM International Symposium on Mixed and Augmented Reality, Nara, Japan, pp. 225–234 (2007)
11. Klein, G., Murray, D.: Improving the agility of keyframe-based SLAM. In: Forsyth, D., Torr, P., Zisserman, A. (eds.) ECCV 2008. LNCS, vol. 5303, pp. 802–815. Springer, Heidelberg (2008). https://doi.org/10.1007/978-3-540-88688-4_59
12. Mur Artal, R., Tardos, J.D.: Fast relocalisation and loop closing in keyframe-based SLAM. In: Proceedings of the IEEE International Conference on Robotics and Automation, New Orleans, LA, pp. 846–853 (2014)



Combining Computer Graphics and Feature for 3D Camera Tracking Based on CAD Model

Linlin Wang, Guoyun Lv^(✉), Ningxin Zhang, and Yanggege Yu

School of Electronics and Information, Northwestern Polytechnical University,
Xi'an, China

534183837@qq.com, 178510887@qq.com, 2568117320@qq.com,
376151248@qq.com

Abstract. A real-time 3D tracking system based on CAD model is proposed in this paper. The strategy in the tracking process includes both template-based and keypoint-based approaches. Compared with traditional CAD model-based tracking, a more accurate initial camera pose can be provided for the following feature-based operation which can accelerate the convergence of camera pose estimation. Using template-based method reduces the demand for textures of the tracking object to improve the universality of the system. Furthermore, adaptive visual feature extraction within the feature-based tracking is adopted in the experiment, and feature homogenization and other methods is also chosen to enhance the robustness and interference immunity of the system. Finally, the effectiveness and stability of the methods proposed in this paper is verified through the experiment of tracking targets in the image sequence.

Keywords: Template-based tracking · Feature-based tracking
CAD model

1 Introduction

The recognition and tracking of objects have always been the hot issue in machine vision. With the rapid development of related research in recent years, many related studies have already been applied in various domains such as robotics, AR (Augmented Reality), industry applications and so on. The 2D plane tracking is to get the object location in the image coordinate system among continuous image sequence. While in 3D tracking, the goal is to obtain the position and orientation of object relative to the camera, which is also called camera pose. Nowadays, there are a variety of related methods to solve the problem of real-time 3D object tracking and camera pose estimation. The CAD model are also widely used as a priori knowledge in these methods. These methods can be divided into the following categories: *edge-based*, *keypoint-based*, *template-based* and *hybrid-based*. For most objects, feature points and edges can easily be extracted, so the 3D visual tracking based on feature is widely used.

In the methods of *edge-based* tracking, the estimation of the pose is achieved by aligning projective edges of 3D CAD line model and edges extracted from current frame. Harris proposed a matching algorithm which matches the projective edges of CAD with the corresponding edges in the image [1]. Drummond eliminate the

influence of outliers by using a robust estimator [2]. Goued proposed a real-time tracking system based on the method of Wuest [3] and get a more stable tracking result by using multi-constraint conditions [4]. In addition, a relatively stable initial camera pose should be ensured when introducing edge-based tracking. And if the pose has large deviation, it will be difficult to get the correct value in subsequent optimal estimation process.

In *keypoint-based* methods, pose estimation is performed by matching the corresponding feature points of the reference image and the current image. The corner detection algorithm delivered by Harris is highly efficient [5]. Lowe proposed an AR system built by using the scale-invariable feature point named SIFT (Scale-invariant Feature Transform) [6]. Bay proposed an optimization algorithm for SIFT, which could reduce the computation cost [6]. In addition, Rabaud thought about another new way on the 3D visual tracking, based on scale-invariable feature ORB [7]. The 3D CAD model of the object needs to be pre-built, and it is easy to estimate the camera pose when the correspondences between 3D points and the 2D image features are known.

Hybrid-based approach is a combination of methods that mentioned above. It is proposed to solve the instability caused by using a single method in practical applications. Vacchetti raised methods which fuse feature points and edges under multiple hypothesis [8]. Similarly, Marchand presented method that combine the texture information and edge tracking, and integrated M-estimator in the minimization process to improve system stability [9]. Christensen came up with an approach integrating Global Pose Estimation (GPE) with Local Pose Estimation (LPE) for tracking [10].

But each approach has its strengths and weakness. When the target has obvious edge features and poor textures, edge-based tracking method is very efficient and stable even under the influence of illumination and specular material. Since the edge features are not invariant, the approach cannot get superior results when the textures of the object are rich or the environment is complicated. Feature points have strong characteristic, which makes them invariant to both rotation and affine transformation. However, as illumination can change the gray-level of the image, the keypoint-based tracking is greatly affected. The blurred image caused by fast movement of camera influences the extraction and matching of feature points. Moreover, keypoint-based tracking is not always beneficial, because the amount of computation is expensive and it cannot achieve real-time effects in the application.

This paper has mentioned to achieve 3D object tracking and camera pose estimate-on by the way of combining template and feature points. A more accurate initial pose is obtained by using template-based initialization method. After initialization, keypoint-based method is employed to continue the tracking and estimation. The initial value of the object pose is estimated by matching the template image rendered from CG (Computer Graphics) with image sequence which only uses the geometric information of the object. Therefore, this method can acquire the accurate initial pose for object with rich or poor texture. The video frame which has been matched successfully with the CAD model rendered by CG is set as a reference frame. And then we can get the correspondences between 3D coordinates and 2D feature points in the reference frame based on the initial pose. In the subsequent process, as

long as obtaining the transformation between the reference frame and the current video frame, the camera position can be obtained by updating the corresponding relationship between 2D feature points and 3D coordinates.

In the remainder of this paper, the theory basis is introduced in Sect. 2. The system implementation process is introduced in Sect. 3. The Sect. 4 describes the experiments and evaluation of the system. Section 5 summarizes the paper.

2 Theoretical Background

The essential of the pin-hole camera model used in this paper is a perspective projection model. The intrinsic matrix presents the relationship between the image coordinate and the camera coordinate. The coordination of any object can be transformed from a world coordinate to a camera coordinate through rigid body transformation, which is called camera extrinsic matrix \mathbf{M} . A series of 3D points $p_i = (x_i, y_i, z_i)^t$ that are non-coplanar in the world coordinate can be transformed to the points $p'_i = (x'_i, y'_i, z'_i)^t$ in the camera coordinate by the formula (1).

$$p'_i = rp_i + t \quad (1)$$

$r = (r_x, r_y, r_z)^t$ is a rotation vector, while $t = (t_x, t_y, t_z)^t$ is a translation vector. The rotation vector can be converted to the corresponding rotation matrix \mathbf{R} by the Rodriguez transformation. The camera's extrinsic matrix is constituted of the rotation matrix \mathbf{R} and the translation vector t .

$$\mathbf{M} = \begin{bmatrix} \mathbf{R} & t \\ 0^T & 1 \end{bmatrix} \quad (2)$$

These parameters are closely related to the problem of camera pose estimation. According to the theoretical relationship mentioned above, the relationship between the 2D point g_i of the image coordinate and its corresponding 3D point p_i in the pinch model is:

$$g_i = \mathbf{K}\mathbf{M}p_i \quad (3)$$

The critical issue of pose estimation is to determine 6-DOF (Degree of Freedom) parameters, which means to find the correspondence between 3D and 2D points observed in image plane. The current pose of object, called camera pose, can be calculated by the pre-computed camera pose and the transformation between the reference frame and the current frame. Usually the camera pose is obtained by minimizing accumulation of errors, such as the least-squares method and the Gauss-Newton method (Fig. 1).

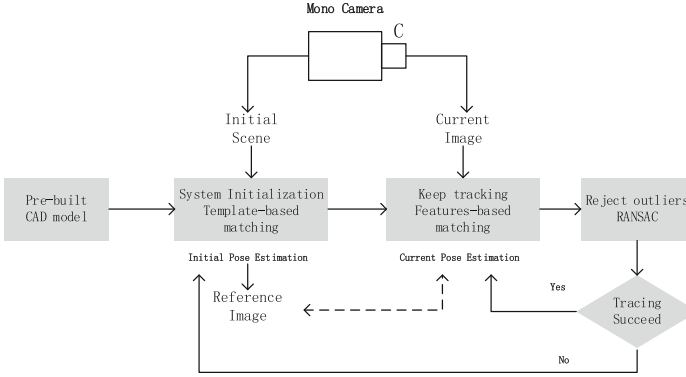


Fig. 1. The framework of tracking system. The initial pose of object is estimated by template-based matching. On the basis of the initial pose, the pose of the object is consecutively estimated by SURF key-points matching.

3 Proposed Approach

3.1 System Initialization Using Optimized Template-Based Matching

Tracking through the visual features of an object, the correctness of subsequent tracking is based on the accurate initial pose. The method of common initialization includes not only the manual calibration of corresponding 2D and 3D points, but also feature-based matching. These methods are suitable for objects with rich texture or for simple background situation, otherwise, it might influence the subsequent tracking because of inaccurate initial pose caused by mismatching. We use CAD model rendered by Computer Graphics matched with the current image. There is only geometric information in the current frame after processed, which does not contain the texture information and background of the object. Using OpenGL to render the CAD model of the object, as the camera intrinsic parameters \mathbf{K} and extrinsic parameters \mathbf{M} are known, the template image can be rendered. The initial pose is estimated by matching the current image with the template image.

In this paper, a CAD model is pre-built and a camera has been calibrated in advance, the intrinsic matrix \mathbf{K} has been fixed and the value in extrinsic matrix \mathbf{M} can be set while rendering. We can get the rendering image T using OpenGL as the first row in Fig. 2.

Simultaneously, we can capturing a series of images I' using camera with a series of unknown extrinsic parameter matrixes \mathbf{M}' . In order to obtain the extrinsic parameter matrix \mathbf{M}' of the image currently captured by the camera, we need to minimizing the difference between image $T(\mathbf{M})$ and the image of the current frame $I(\mathbf{M}')$:

$$\Delta = T(\mathbf{M}) - I(\mathbf{M}') \quad (4)$$

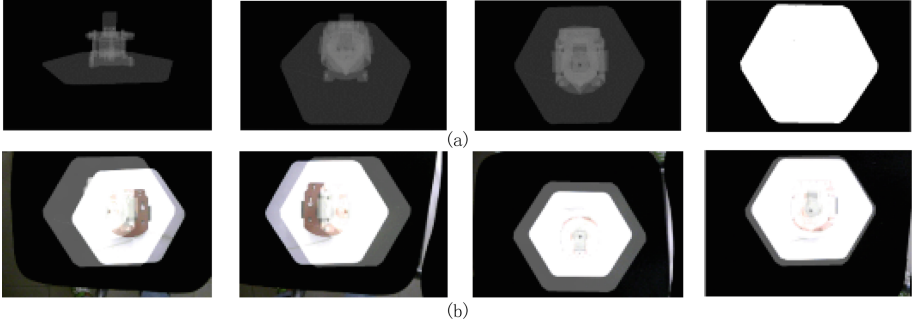


Fig. 2. Template-based matching using CG images. The images rendered by different extrinsic parameter shown in the first row (a). The last image in first row show the preprocessed image which eliminate the texture information from input image. The second row (b) shows the image difference between the template and the current image from a real camera.

The similarity of the matching is usually described by using the squared difference of the gray value of the video frame sub-region and the template image.

$$D(i, j) = \sum_{m=1}^M \sum_{n=1}^N [I_{ij}(m, n) - T_{ij}(m, n)]^2 ((i, j) \in l(i, j)) \quad (5)$$

In the above equation, the $D(i, j)$ is similar matrix, and $l(i, j)$ is the upper left corner coordinate of the region with the most similarity. The best matching pose found in D is the point $\varepsilon_1 = \min\{d_{ij}\}$ with smallest value. To ensure the accuracy of the matching, it is found in the experiment that the correctness of choosing points fallen in $\varepsilon_1 \sim 2\varepsilon_1$ matching is up to 98%. Therefore, the modified similar matrix $D'(i, j)$ can be determined by using $\varepsilon_2 = 2\varepsilon_1$ as the upper bound of the similarity of the matching point. The value d'_{ij} is:

$$d'_{ij} = \begin{cases} 1 & (d_{ij} > \varepsilon_2) \\ d_{ij} & (d_{ij} \leq \varepsilon_2) \end{cases} \quad (6)$$

The modified similarity matrix can accelerate the convergence rate. We found that when the rendered image is similar with specific region of the current frame, the value will converge quickly. We take advantage of this distribution characteristic to carry out the coarse scan to lock the approximate area, and then using square error to describe the similarity of two regions that matched, the time for matching will decrease significantly. The method mentioned above is usually an iterative process. When the error is less than the threshold, the two are thought to be matching successfully.

3.2 Feature-Based Tracking

After initialization, we can get the correspondences between the 2D features in the reference frame and the 3D coordinates. The main target of subsequent tracking is to

generate a new 3D-2D correspondences to update pose, based on the matching SURF features extracted from reference image and current image. And the RANSAC algorithm is used to remove the distortions. The new correspondences of 3D-2D can be generated according to the pre-computed camera pose and the new 2D transformation determined from feature-based matching. \mathbf{H}_{ij} is a homography matrix, d_i and d_j is the feature points extracted from the reference frame and the current frame. The relationship among the feature points can be defined as:

$$d_i = \mathbf{H}_{ij}d_j \quad (7)$$

As for the follow-up feature-based tracking, richness of texture among objects impacts the quality and number of extracted features, which is the key factor in pose calculation and follow-up matching. Therefore, for the object with different texture, the sufficient feature points should be obtained by self-adaptive, which increases the robustness of the system and can also achieve better performance for various objects. The value of Hessian determinant is the primary gist for filtering the feature points. Therefore, we proposed self-adaptive method for extracting SURF features. Since the amount of the feature points can be obtained in the current image $F_{num}(I_i)$, and the quantitative range of feature points $\delta_1 \sim \delta_2$ is achieved in accordance with the test in advance, the method to adaptively extract SURF feature points from different objects is as follows:

$$\begin{cases} \rho_+(\det(\mathbf{Hessian})_{thre}) & F_{num}(I_i) > \delta_2 \\ \rho_-(\det(\mathbf{Hessian})_{thre}) & F_{num}(I_i) < \delta_1 \end{cases} \quad (8)$$

ρ_+ and ρ_- are the functions used to dynamically adjust the Hessian determinant threshold. In order to decrease the computing time, the threshold is only adjusted at the beginning of feature-based tracking, and the acceptable maximum times of adjustment is set as well. When the times of iteration are over to maximum times but do not meet the conditions, the current threshold will be deemed to be the parameters of extracted SURF features.

Because the texture information of an object is concentrated in a small area, when the region is disturbed by the environment, the tracking and subsequent calculation would be affected seriously. The situation such as partial cover or outflow boundary of the object is inevitable during tracking process. And when it occurs, we hope that the remaining part can be used for tracking. As we know, the extracted feature points tend to focus on the richly-textured regions of the object, so a method to solve this problem is to weaken the dense distribution of feature points. Only when the feature points are scattered, the remaining parts of the object which is sheltered or out of boundary can also have feature points to continue tracking. In order to solve the problem above, we propose an algorithm on the basis of SURF algorithm which are obtained by segmenting the image and using multi-threshold.

The current image is divided into N pieces, respectively named as P_1, P_2, \dots, P_N . The number of the pieces is usually set as 4 or 9. Then the feature points can be detected from the image which has been segmented. Its descriptors need to be extracted and merged:

$$F = \{f_1\} \cup \{f_2\} \dots \cup \{f_n\} \quad (9)$$

The distribution of feature is more dispersed after segmentation. But if each input frame is processed, it will undoubtedly increase computation. After initialization and self-adaptive feature extraction of the object, the number of features in the current frame can be used as the threshold. Once the area with rich textures on the object is affected, the number of feature points will decrease sharply. When the number of feature points in the current frame and the previous frame meet the (10), the input image will be processed by segmentation and feature extraction by multi-threshold:

$$F_{\text{num}}(I'_j) < \sigma F_{\text{num}}(I_j) \quad (10)$$

σ is related to the proportion of texture-rich area in total area, and the better results can be achieved when the value of σ is 0.6.

3.3 Robustness of System

Comparing 3D tracking with 2D tracking, the visual features are different while the viewpoint changes. It's necessary to change reference image. When the quantity of matching points is lower than the threshold we set, we can say that the current frame has not been tracked correctly. The video frame which can get the correct camera posture before tracking failure ought to be saved as the new reference frame. Moreover, if the amount of matching points in the next 20 frames still cannot reach the threshold, the process of tracking failed, and the system will return to the initial state and restart. To sum up, the methods proposed in this paper can be utilized for a variety of objects, and they have strong anti-jamming in the tracking process. Situations such as image blur caused by high movement, object covered, out of bond and so on, the system can run without manual intervention.

4 Experiments and Results

In this paper, not only the method proposed has been tested in practice, but also the results of the tracking and pose estimation have been evaluated. The hardware platform used in this experiment is Intel Core i7-4720 2.6 GHz and software platform is visual studio 2010, with OpenCV and OpenGL as additional Dependencies. The Gsou USB monocular camera is adopted in the experiment, whose frame rate of image sequence is 25 frame/s, and resolution of video image is 640×480 pixels.

Thus we will translate CAD model data into a format of OBJ text file, in order to complete the system through the language C more conveniently.

4.1 Initialization Test

Through this experiment, it can be verified the initial pose is achieved by matching the video frame with the template image, which is a CAD model rendered by CG. The object we chose is a pedestal of mechanical arm in the experiment. The camera's six degrees of freedom parameters $E = [r_x, r_y, r_z, t_x, t_y, t_z]$ can be used to represent the position of the camera, where r_x , r_y , and r_z respectively represent rotation angles around the x , y and z axes. Similarly t_x , t_y and t_z respectively represent translation.

We set the initial pose in the matrix $E_0 = [0, 0, 0, 0, 0, 0]$, which is used to render the CAD model to get the template image. After the video sequence frame matches the template image successfully, it can be regarded as initializing successfully and that the location of the object L_0 is recorded meanwhile. Afterwards, we keep the location of camera and move the object until 200 frames. On the premise of correct tracking, the new camera pose E_{end} and the final position of the object L_{end} should be recorded by the system, then finish tracking. We keep the camera and object motionless, the camera pose E_{end} is used to reinitialize the system. At this moment, the template image obtained by rendering the CAD model in the current state must match the input video frame successfully.

With the location of camera still fixed, we move the object to the initial position, and get the corresponding pose $E'_0 = [-0.1, 0.4, 0, 0.3, -0.5, 0.6]$, which has small deviation with the initial given pose. Therefore, the method of initialization based on the template matching can complete estimating the initial pose.

4.2 Tracking Results and Re-initialization Test

In the experiment, the camera pose, which is estimated above, is used to render a virtual cube model. The accuracy of tracking and pose estimation was determined by judging whether the cube is fit with the being tracked object and the movement trend is consistent with the actual situation. Two different video sequences are used to verify the system stability of the subsequent tracking. In the first video sequence, the camera and the tracked object are always static. The Fig. 3 respectively express rotation and translation parameters calculated by the system according to the sequence. In the case of fixed position, the trend of the six parameter values is approximately referred as a straight line in the Fig. 3(a), which meets the physical situation. In addition, the pictures in Fig. 4(a) are the 50th, 80th, 150th and 180th frame after rendering the virtual cube in the first sequence and we find that the state of virtual cube model has not changed. The second video sequence is obtained by rotating, translating and scaling the tracked object. We can find the 6-DOF parameters in Fig. 3(b) without burr which prove the estimation is accurate. Separately, the pictures in Fig. 4(b) are the 50th, 150th, 200th and 240th frame after rendering the virtual cube by 6-DOF parameters in second sequence. In the experiment, the virtual cube is basically accord with the state of the object, even with the problems like out of boundary and partial occlusion.

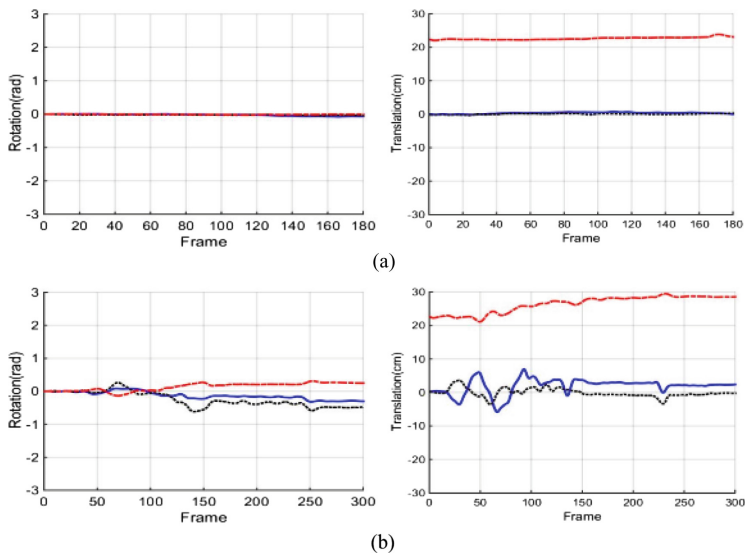


Fig. 3. 6-DOF pose of the pedestal of mechanical arm in tracking test. The first row (a) shows the rotation and translation of the first sequence while the camera and object are always static. The second row (b) shows the parameters of the second sequence while the motion of object is random. (blue solid = x-axis, black dotted = y-axis, red dashed = z-axis) (Color figure online)

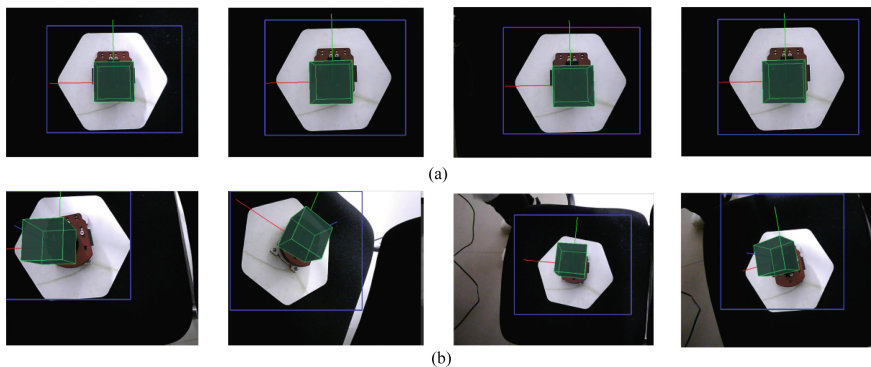


Fig. 4. Results on different input sequences. The first row (a) from the first sequence shows the virtual cube is changeless. The second row (b) from the second sequence the virtual cube is consistent with the movement of object.

5 Conclusions

In this paper, we have proposed a robust tracking system for 3D object recognition and tracking based on the combination of two different approaches. By using template-based matching in initialization, we can give an accurate initial pose for

marker-less visual tracking. Based on the initialization, we use SURF descriptors in remainder tracking to achieve the system robust against the changes of rotation and scale. The system has been tested on real scene and show good results. There is still some work that we should be done to reduce the computation. We hope that the system can be applied to more scenes.

Acknowledgments. The work is sponsored by the Seed Foundation of Innovation and Creation for Graduate Students in Northwestern Polytechnical University (No. Z2017139).

References

1. Harris, C.: Tracking with Rigid Objects. MIT Press, Cambridge (1992)
2. Drummond, T., Cipolla, R.: Real-time visual tracking of complex structures. *IEEE Tran. Pattern Anal. Mach. Intell.* **24**(7), 932–946 (2002)
3. Wuest, H., Stricker, D.: Adaptive line tracking with multiple hypotheses for augmented reality. In: Proceedings of the Fourth IEEE and ACM International Symposium on Mixed and Augmented Reality, pp. 62–69 (2005)
4. Gouet, B.L.V.: SAP: a robust approach to track objects in video streams with snakes and points. In: 15th British Machine Vision Conference, vol. 2, pp. 737–746 (2004)
5. Harris, C., Stephens, M.: A Combined corner and edge detector. In: Proceedings of the Fourth Alvey Vision Conference, pp. 147–151 (1988)
6. Bay, H., Tuytelaars, T.: SURF: speeded up robust features. *Comput. Vis. Image Underst.* **110**(3), 346–359 (2008)
7. Rubble, E., Rabaud, V.: ORB: an efficient alternative to SIFT or SURF. In: International Conference on Computer Vision, vol. 11, no. 58, pp. 2564–2571 (2012)
8. Vacchetti, L., Lepetit, V., Fua, P.: Combining edge and texture information for real-time accurate 3D camera tracking. In: International Symposium on Mixed and Augmented Reality, pp. 48–57 (2004)
9. Marchand, E., Chaumette, F.: Real-time markerless tracking for augmented reality: the virtual visual servoing framework. *IEEE Trans. Vis. Comput. Graph.* **12**(4), 615–628 (2002)
10. Choi, C., Christensen, H.I.: Real-time 3D model-based tracking using edge and keypoint features for robotic manipulation. In: IEEE International Conference on Robotics and Automation (ICRA), Alaska, USA (2010)



Performance Analysis of CBRP, AODV and DSR Routing Protocols in VANETs Based on IDM-IM

Luqi Wu^(✉) and Xia Wang

School of Electronics and Information Engineering,
Xi'an Jiaotong University, Xi'an, China
wuluqi_567@163.com, wangxia@mail.xjtu.edu.cn

Abstract. Due to multi-lanes, speed limit, buildings around corners and traffic lights, Vehicular Ad Hoc Networks (VANETs) with urban areas especially in intersections have more complicated network topology, resulting in standard flat routing protocols inapplicable in VANETs. Theoretically hierarchy based routing protocol such as CBRP (Clustering Based Routing Protocol) can achieve better performance in VANETs. To the best of our knowledge, there is no literature reporting network performance tests on CBRP in VANETs. Existing Network Simulator (NS) does not contain CBRP, therefore this paper firstly implements CBRP into NS-2.35 and then aims to compare and analyze performance of CBRP against AODV (Ad Hoc On-demand Distance Vector) and DSR (Dynamic Source Routing) in VANETs based on IDM-IM (Intelligent Driver Model with Intersection Management) modeled by VanetMobiSim. Simulation results reveal that CBRP performs well compared to AODV and DSR in terms of delay, packet loss ratio and route costs.

Keywords: VANETs · CBRP · AODV · DSR · Network performance

1 Introduction

Over the past few years, advances and development of Intelligent Transport System (ITS) [1] have brought a new type of Mobile Ad Hoc Network (MANET) which is known as Vehicular Ad Hoc Network (VANET). VANETs can improve driver safety, reduce traffic accident and avoid road congestion by obtaining state of adjacent vehicles, road environment, traffic condition and entertainment information through communications between Vehicle to Vehicle (V2V) and Vehicle to Infrastructure (V2I) [2]. So, unlike MANETs, due to the complex network environment characterized by features of vehicles, VANETs are far more difficult and challengeable. The specific details can be concluded as:

- Instability of wireless channel: Because of shared wireless channel in VANETs, communication quality can be easily affected by factors such as weather state, road condition, traffic lights and buildings around the corners at an intersection.
- Dynamic and rapid change of topology: High speed of vehicles frequently lead to rapid change of network topology and short life of wireless link in VANETs.

- Limitation of network capacity: Given the fact that vehicles are constrained by predefined layout of streets, so the network capacity in VANETs is more restricted than traditional ad hoc networks.
- Unpredictability of traffic density: Network performance can be relatively poor when traffic density is either high or low. During the rush hours, number of vehicles sharply increase causing traffic jam and broadcast storm. On the contrary, sparse density may lead to high data packet loss ratio and sudden linkage interrupt of communication.

Such characteristics often make typical flat routing protocols, in which all nodes are equal and involved in routing process, such as AODV (Ad Hoc On-demand Distance Vector) and DSR (Dynamic Source Routing), unusable or inefficient in VANETs. One of the critical disadvantages of the flat routing protocols is that network scalability is limited and thus they do not perform well under dense networks. One way to solve this problem is hierarchical routing. With the cluster structure, the processing of data packet and routing information can only be restricted to a few nodes known as Cluster Heads (CHs). The rest mobile nodes are either Undecided or Cluster Members (CMs). In other words, the cluster routing can help reduce routing space and route costs. Hence, CBRP (Clustering Based Routing Protocol), as one of the typical hierarchy based routing protocol, can be able to provide better network scalability theoretically.

Although many clustering algorithms based on CBRP have been proposed, modified and testified, either network performance in VANETs has not been done or nodes' mobility model cannot reflect realistic vehicles' traveling traces. Therefore, in this paper, we firstly implement CBRP into NS2 and then combine with VanetMobiSim so as to analyze typical flat and clustering routing protocols in delay, packet loss ratio and route costs.

2 Related Work

In the perspective of network structure, routing protocols can be divided into flat and hierarchy-based routing. Typical flat routing protocols include AODV and DSR. But with expansion of network scalability, especially in the case of rapid mobility of nodes, flat routing protocols can achieve huge route costs and poor scalability which restrict the application scenarios. The basic idea of hierarchy based routing protocols, such as CBRP, is dividing mobile nodes into different clusters and each node is assigned either CM or CH. The work in [4] confirms that CBRP present better network performance in terms of packet delivery ratio, average delay and throughput than AODV, DSR and DSDV routing protocols in MANETs.

Researchers have been working on CH selection algorithm based on CBRP with the Lowest-ID (LD) algorithm [5–7]. Efficient Cluster Based Routing Protocol (ECBRP) implementing Efficient Clustering Scheme (ECS) [5] has been proposed and verified that ECBRP can provide better performance than CBRP in MANETs, however, whether CBRP or ECBRP can achieve better performance in VANETs is not clear.

Different from LD algorithm, mobility based clustering scheme MOBIC [6] selects the node with smallest variance of relative mobility as CH. Simulation results show MOBIC algorithm can achieve more stable cluster structure in MANETs. Compared to MOBIC, Affinity Propagation for Vehicular Networks (APROVE) [7] utilizing the affinity propagation algorithm in a distributed manner display obviously higher stability in cluster maintenance than MOBIC in VANETs under highway scenarios. But the performance tests under urban VANETs is not considered. Also some clustering algorithms have been proposed in [8–10], and they put emphasis on cluster stability as in [6, 7], however, none of those was imposed on a reasonable VANETs model and performance analysis of the proposed algorithms has not been done.

Traffic accidents usually happen near an intersection in urban areas causing V2V communication a severe problem. A Multi-vehicle Select Broadcast (MSB) protocol in [11] is brought forward to broadcast safety messages to vehicles at an intersection with all directions. But the simulation work is based on a USC mobility generator [12] which cannot reflect real behavior of vehicular mobility. Because of those features in VANETs described in Sect. 1, setdest, a tool of NS2, being used to generate randomly wireless network mobile scenes based on Random Way Point (RWP) for general MANETs, cannot present specific vehicular movement patterns. Therefore in this paper VanetMobiSim [13], release 1.1, is selected for producing vehicles mobility in urban intersections as much close as possible in realistic scenarios and generating corresponding mobility traces for NS2 based on IDM-IM (Intelligent Driver Model with Intersection Management). As an advanced version of Car Following Model (CFM), IDM characterizes drivers' behavior based on action of front vehicles by smoothly changing the instantaneous acceleration.

The rest of this paper is organized as follows. Section 2 introduces related research on hierarchy-based routing protocols. Section 3 describes simulation model and network performance metrics. In Sect. 4, simulation results and analysis are presented. Finally, we come to a brief conclusion in Sect. 5.

3 Simulation Model and Performance Metrics

3.1 Simulation Model

Simulation scenario in $2000 \times 1000 \text{ m}^2$ with intersections, multi-lanes and traffic lights is modeled in VanetMobiSim. Random Initial Position Generator, Random Trip Generator and IDM_IM mobility model is adopted in our simulation. Specific parameters setting in VANETs is showed in Table 1. Figure 1 shows mobile scenario with 30 vehicles. Mobility topology file can be obtained in the xml script by adding

```
<extension  
class="de.uni_stuttgart.informatik.canu.mobisim.extension  
s.NSOutput" output="filename"/>
```

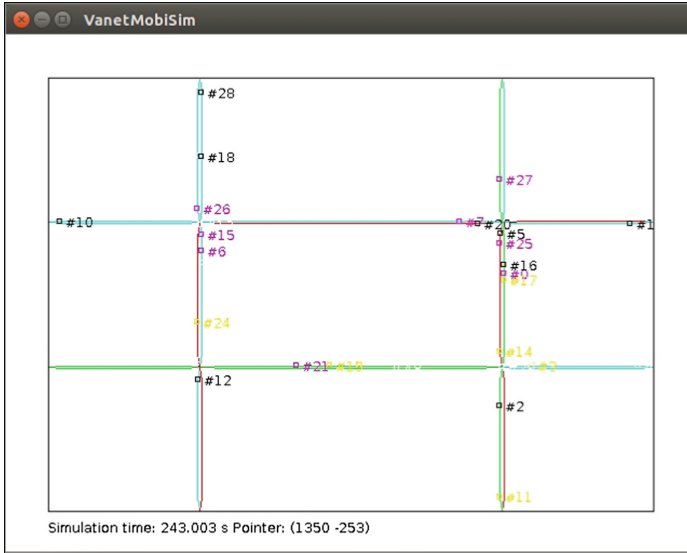


Fig. 1. Simulation topology scenario with 30 vehicles and four different colors of vehicles is used to distinguish vehicles traveling in four different lanes.

Table 1. Simulation parameters in VANETs modeled by VanetMobiSim

Parameters	Values
Simulation dimension	2000 × 1000 m ²
Simulation time	1000 s
Number of intersections	4
Number of lanes	4
Traffic lights/intersection	4
Traffic lights switching time	30 s
Number of vehicles	20–100
Maximum speed	30 km/h
Initial position model	Random
Trip model	Random
Mobility model	IDM-IM

NS2, release 2.35, is used to evaluate network performances with trace file generated by VanetMobiSim. Although CBRP is proposed long before, CBRP is not taken in NS2, thus the very first step is to implement CBRP into NS-2.35. CBRP implement has been done in early version with NS2, but the implement in update version NS-2.35 is more complicated. The implement work mainly include building ‘CBRP’ and adding it into ns-2.35 directory. Files needed to be built in ‘CBRP’ include cbrpagent.h/cbrpagent.cc, ntable.h/ntable.cc, hdr_cbrp.h/hdr_cbrp.cc and cbrp_packet.h. And then ‘CBRP’ has to be created parallel with ‘AODV’ and ‘DSR’ under the ns-2.35 directory. After that there are some files in NS-2.35 needed to be changed accordingly:

- (1) Define a new type of packet in common/packet.h by adding

```
#define HDR_CBRP(p) (hdr_cbrp::access(p))
.....
static const packet t PT_CBRP = 73;
.....
name [PT_CBRP]="CBRP";
```

- (2) Add a function declaration ‘ void format cbrp(Packet *p, int offset);’ in trace/cmu-trace.h and its definition in trace/cmu-trace.cc.

```
void format cbrp(Packet *p, int offset)
{
Hdr_cbrp *cbrph = HDR_CBRP(p);
Hdr_ip *_ph = HDR_IP(p);
sprintf(pt ->buffer() + offset,
 "[%d #%d %d->%d] [%d #%d %d %d %d->%d]
 [%d %d] [%d %d %d %d->%d]",
.....
}
```

- (3) To unite CBRP and Otcl, in tcl/lib/ns-packet.tcl, add

```
Set protolist{
.....
HDLC
CBRP
}
```

- (4) Change Makefile and Makefile.in by adding (Table 2).

```
`cbrp/hdr cbrp.o cbrp/ntable.o cbrp/cbrpagent.o n`
```

Table 2. Simulation parameters in network simulator

Parameters	Values
Simulation time	100 s
Transmission range	300 m
MAC protocol	IEEE 802.11p
Routing protocol	CBRP/AODV/DSR
Propagation model	TwoWayGround
Packet type	CBR
Packet size	512 bytes

3.2 Performance Metrics

The network performance of CBRP is compared against AODV and DSR by the following metrics:

- (1) Average End-to-End Delay: it defines the whole sum of possible average time such as taken by discovering path, retransmitting time in MAC layer and delivering efficient data packets from source nodes to destination nodes.
- (2) Packet Loss Ratio: it is ratio of total number of packets dropped from source nodes to the number of packets sent from source nodes.
- (3) Route Costs: it is ratio of routing control packets to data packets of CBR.

4 Simulation Results

In this section, the network performance of CBRP compared to AODV and DSR is presented and discussed. To obtain a proper evaluation on the performance differences, ten groups of experiment were conducted. Simulation results is showed in Figs. 2, 3 and 4.

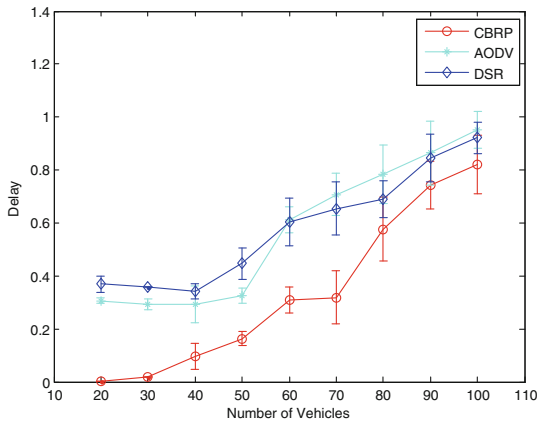


Fig. 2. Average end-to-end delay vs. number of vehicles

As number of vehicles increase from 20 to 100, traffic density changes from low to high, packets delivering time from source vehicles to destination vehicles increase resulting delay time in Fig. 2 increase accordingly. Packet loss ratio in Fig. 3 increases as a result of packet congestion caused by vehicles growth. In Fig. 2, CBRP present lowest delay. The experimental data shows that, in sparse vehicle density, delay of AODV and DSR is higher 5–20 times that of CBRP. In Fig. 3, in low density CBRP, AODV and DSR can achieve pretty close performance, while in high density, CBRP present better packet loss ratio. In Fig. 4, both AODV and DSR increase slowly in low density, while increase sharply in high density. However, in either sparse or dense

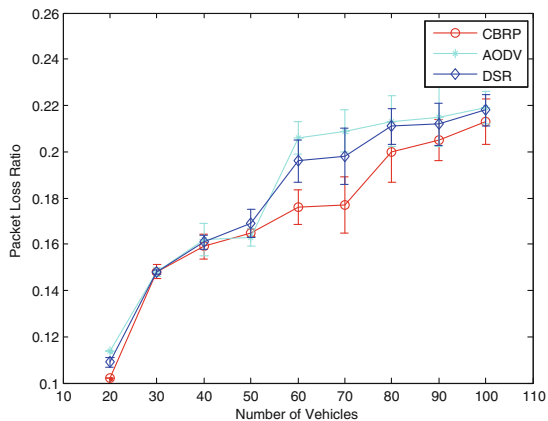


Fig. 3. Average packet loss ratio vs. number of vehicles

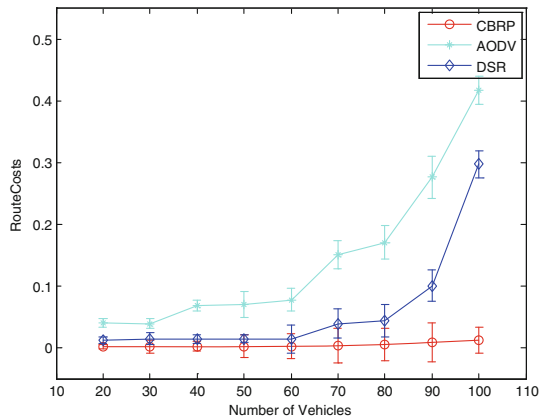


Fig. 4. Average route costs vs. number of vehicles

network, CBRP displays smallest, stable and robust route costs. Especially in high density, route costs of AODV and DSR is 10–40 times that of CBRP. In conclusion, simulation results and analysis of experimental data prove the advantage of CBRP in terms of delay, packet loss ratio and route costs.

5 Conclusions

In this paper, we present difficulties and challenges in VANETs, discuss flat and hierarchy-based routing protocols and analyze existing models being used. Our simulation scenario is modeled by VanetMobiSim and network performance of CBRP, AODV and DSR is analyzed in NS2. Simulation results indicate that, delay, packet loss

ratio and route costs of the former is much better than that of the latter two, which evidences, not only in theory but also in practice, the stronger robust performance of CBRP especially under high density of VANETs.

References

1. Karagiannis, G., Altintas, O., Ekici, E., Heijenk, G., Jarupan, B., Lin, K., Weil, T.: Vehicular networking: a survey and tutorial on requirements, architectures, challenges, standards and solutions. *IEEE Commun. Surv. Tutor.* **13**, 584–616 (2011)
2. Bilgin, B.E., Gungor, V.C.: Performance comparison of IEEE 802.11p and IEEE 802.11b for vehicle-to-vehicle communications in highway, rural, and urban areas. *Int. J. Veh. Technol.* **2013** (2013)
3. Kumar, A., Singh, P., Kumar, V., Tyagi, N.: Performance comparison of IEEE 802.11p and IEEE 802.11b for vehicle-to-vehicle communications in highway, rural, and urban areas. *Int. J. Comput. Netw. Inf. Secur.* **5** (2013)
4. Jiang, M., Li, J., Tay, Y.C.: Cluster Based Routing Protocol (CBRP) Function Specifications (2008)
5. Yu, J.Y., Chong, P.H.J., Zhang, M.: Performance of efficient CBRP in mobile ad hoc networks (MANETS). In: *Vehicular Technology Conference, VTC 2008-Fall*, pp. 1–7. IEEE Press (2008)
6. Basu, P., Khan, N., Little, T.D.C.: A mobility based metric for clustering in mobile ad hoc networks. In: *International Workshop on Wireless Networks and Mobile Computing*, pp. 413–418 (2012)
7. Shea, C., Hassanabadi, B., Valaee, S.: Mobility-based clustering in VANETs using affinity propagation. In: *Global Telecommunications Conference, GLOBECOM*, pp. 1–6 (2010)
8. Souza, E., Nikolaidis, I., Gburzynski, P.: A new aggregate local mobility (ALM) clustering algorithm for VANETs. In: *IEEE International Conference on Communications*, pp. 1–5 (2010)
9. Maglaras, L.A., Katsaros, D.: Distributed clustering in vehicular networks. In: *International Workshop on Vehicular Communications and Networking*, pp. 593–599 (2012)
10. Chatterjee, M., Das, S.K., Turgut, D.: An on-demand weighted clustering algorithm (WCA) for ad hoc networks. In: *Global Telecommunications Conference, GLOBECOM 2000*, vol. 3, pp. 1697–1701, IEEE (2000)
11. Cho, J., Shin, S., Copeland, J.: Fast broadcast at the intersection in VANET. In: *Consumer Communications and Networking Conference*, pp. 65–69 (2011)
12. Bai, F., Sadagopan, N., Helmy, A.: User Manual for Important Mobility Tool Generators in NS-2 Simulator. University of Southern California (2004)
13. Fiore, M., Harri, J., Filali, F., Bonnet, C.: Vehicular mobility simulation for VANETs. In: *Simulation Symposium, ANSS 2007*, pp. 301–309. IEEE (2007)



DOA Estimation for Far-Field Sources in Mixed Signals with Gain-Phase Error Array

Jiaqi Zhen^(✉) and Yanchao Li

College of Electronic Engineering, Heilongjiang University,
Harbin 150080, China
zhenjiaqi2011@163.com

Abstract. Most of the super-resolution direction finding algorithms often require the accurate array manifold, but the gain-phase of the channels is often inconsistent in practical applications, which will lead to the estimation performance deterioration. Therefore, a new method for direction of arrival (DOA) estimation of far-field sources in mixed far-field and near-field signals with gain-phase error array is presented. First, fast Fourier transformation (FFT) is performed on the received data, then matrix transformation is used for simplifying the spectrum function, at last, DOA of far-field signals can be acquired by finding the roots of corresponding polynomial. There is no need to calibrate the array, simulations have shown that the proposed algorithm is effective.

Keywords: Direction of arrival · Gain-phase error · Far-field signals
Near-field signals · Wideband signals

1 Introduction

Super-resolution direction finding is one of the major researches in array signal, it is extensively applied in radio monitoring [1–3], internet of things [4, 5] and military [6, 7]. Generally speaking, knowing the exact array manifold is the precondition to the estimation, but the gain and the length of the channels are often not the same, which will lead to the estimation performance deterioration, so it is necessary to correct the array.

In general, calibration methods in array signal processing can be classified into using source and self correction. The former are realized by utilizing the assistant signal whose location is known; The latter are usually based on some optimization functions to calculate the directions and perturbation parameters of the array iteratively. Some of these methods have their distinct advantages: Lee [8] proposed a covariance approximation method for near-field direction finding using a uniform linear array, it estimated

J. Zhen—This work was supported by the National Natural Science Foundation of China under Grant Nos. 61501176 and 61505050, University Nursing Program for Young Scholars with Creative Talents in Heilongjiang Province (UNPYSCT-2016017), China Postdoctoral Science Foundation (2014M561381), Heilongjiang Province Postdoctoral Foundation (LBH-Z14178), Heilongjiang Province Natural Science Foundation (F2015015), Outstanding Young Scientist Foundation of Heilongjiang University (JCL201504) and Special Research Funds for the Universities of Heilongjiang Province (HDRCCX-2016Z10).

DOA, together with unknown sensor gains and phases in the uncalibrated portion of the array; Liu [9] presented an eigenstructure approach which synchronously obtained the DOA and gain-phase perturbations without joint iteration; Cao and Ye [10] proposed a calibration method for channel gain-phase uncertainty based on fourth-order cumulant technique, it adapts to the background of non-Gaussian signals and Gaussian noise; Han [11] considered the problem of DOA estimation based on a nonuniform linear nested array, which is known to provide $O(N^2)$ degrees of freedom using only N sensors, and the gain-phase errors can also be calculated by different subsequent processing.

In recent years, many experts have developed some DOA estimation algorithms of mixed far-field and near-field sources (FFS and NFS), Liang [12] proposed a two-stage dimensional multiple signal classification (MUSIC) algorithm with cumulant which averted high-dimensional searching and parameters matching; Wang [13] presented a novel localization algorithm for the mixed sources based on the polynomial decomposing method and high-order cumulant technique, but the computation is very complex; In [14], a new mixed NFS and FFS localization algorithm based on sparse signal recovery is addressed, it can provide the improved estimation accuracy comparing with the traditional algorithm. All the methods above only adapt to narrowband signals, but there are rare published literatures of gain-phase uncertainty calibration for mixed wideband signals.

In this paper, a novel method for DOA estimation of far-field sources in mixed far-field and near-field wideband signals in the presence of gain-phase uncertainty is proposed. First, fast Fourier transformation (FFT) is performed on the received data, then matrix transformation is used for simplifying the spectrum function, at last, DOA of far-field signals can be acquired by finding the roots of corresponding polynomial. There is no need to calibrate the array, so as to improve the calculation efficiency on the premise of ensuring some level of precision and it is suitable for wideband coherent signals as well.

2 Array Signal Model

2.1 Ideal Signal Model

It is shown in Fig. 1, there are N_1 far-field linear frequency modulation wideband signals $s_{n_1}(t)(n_1 = 1, 2, \dots, N_1)$ and N_2 near-field wideband signals $s_{n_2}(t)(n_2 = 1, 2, \dots, N_2)$ with the same energy arriving at the uniform linear array composed of $2M + 1$ sensors, DOA of these signals are $[\theta_1, \dots, \theta_{N_1}, \theta_{N_1+1}, \dots, \theta_N]$, where $N = N_1 + N_2$, the distance of adjacent sensors is d , it is equal to half of the wavelength of the center frequency of these sources, suppose N_1, N_2 is known in advance. The 0-th sensor is deemed to be the reference. The frequency of all signals is limited in $[f_{\text{Low}}, f_{\text{High}}]$, J points of fast Fourier transformation (FFT) are employed for the output of the array, then we can model the signal as

$$\mathbf{X}(f_i) = \mathbf{A}(f_i, \theta)\mathbf{S}(f_i) + \mathbf{E}(f_i) \quad (i = 1, 2, \dots, J) \quad (1)$$

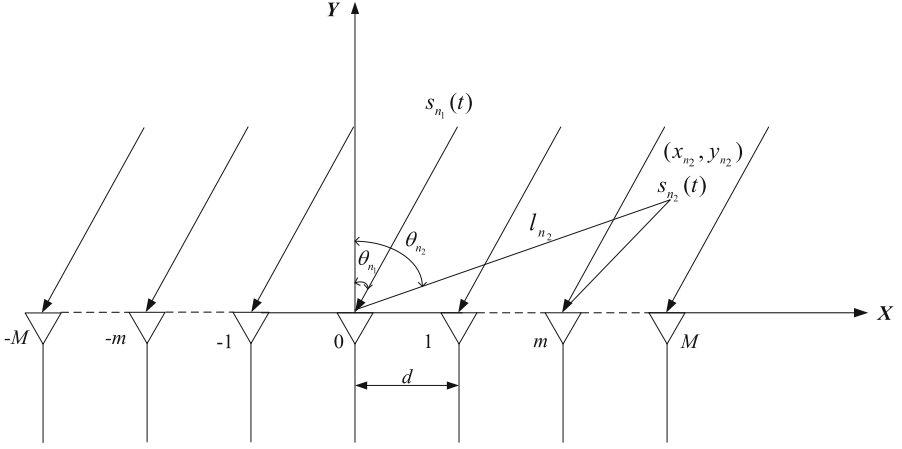


Fig. 1. Array signal model

where $f_{\text{Low}} \leq f_i \leq f_{\text{High}}$, $\mathbf{X}(f_i) = [\mathbf{X}(f_i, 1), \dots, \mathbf{X}(f_i, z), \dots, \mathbf{X}(f_i, Z)]$, Z is the sampling times at every frequency, and

$$\mathbf{X}(f_i, z) = [X_{-M}(f_i, z), \dots, X_{-m}(f_i, z), \dots, X_0(f_i, z), \dots, X_m(f_i, z), \dots, X_M(f_i, z)]^T \quad (2)$$

here $X_m(f_i, z)$ is the z -th sampling data on the m -th sensor at f_i , $\mathbf{A}(f_i, \theta)$ is the array manifold at f_i

$$\begin{aligned} \mathbf{A}(f_i, \theta) &= [\mathbf{a}_{FS}(f_i, \theta_1), \dots, \mathbf{a}_{FS}(f_i, \theta_{n_1}), \dots, \mathbf{a}_{FS}(f_i, \theta_{N_1}), \mathbf{a}_{NS}(f_i, \theta_{N_1+1}), \dots, \mathbf{a}_{NS}(f_i, \theta_{n_2}), \dots, \mathbf{a}_{NS}(f_i, \theta_N)] \\ &= [\mathbf{A}_{FS}(f_i), \mathbf{A}_{NS}(f_i)] \quad (i = 1, 2, \dots, J) \end{aligned} \quad (3)$$

where $\mathbf{A}_{FS}(f_i) = [\mathbf{a}_{FS}(f_i, \theta_1), \dots, \mathbf{a}_{FS}(f_i, \theta_{n_1}), \dots, \mathbf{a}_{FS}(f_i, \theta_{N_1})]$ is the array manifold of FFS at f_i ideally, and $\mathbf{a}_{FS}(f_i, \theta_{n_1})$ is the corresponding far-field steering vector of $s_{n_1}(t)$; $\mathbf{A}_{NS}(f_i) = [\mathbf{a}_{NS}(f_i, \theta_{N_1+1}), \dots, \mathbf{a}_{NS}(f_i, \theta_{n_2}), \dots, \mathbf{a}_{NS}(f_i, \theta_N)]$ is the array manifold of NFS at f_i ideally, and $\mathbf{a}_{NS}(f_i, \theta_{n_2})$ is the corresponding near-field steering vector of $s_{n_2}(t)$, so we have

$$\begin{aligned} \mathbf{a}_{FS}(f_i, \theta_{n_1}) &= [\exp(-j2\pi f_i \tau_{-M}(\theta_{n_1})), \dots, \exp(-j2\pi f_i \tau_{-m}(\theta_{n_1})), \dots, 1, \dots, \\ &\quad \exp(-j2\pi f_i \tau_m(\theta_{n_1})), \dots, \exp(-j2\pi f_i \tau_M(\theta_{n_1}))]^T \quad (n_1 = 1, 2, \dots, N_1) \end{aligned} \quad (4)$$

where

$$\tau_m(\theta_{n_1}) = m \frac{d}{c} \sin \theta_{n_1} \quad (m = -M, \dots, -m, \dots, 0, \dots, m, \dots, M; n_1 = 1, 2, \dots, N_1) \quad (5)$$

is the propagating delay for the n_1 -th ($n_1 = 1, 2, \dots, N_1$) FFS arriving at the m -th sensor with respect to the reference of the array, similarly

$$\mathbf{a}_{NS}(f_i, \theta_{n_2}) = [\exp(-j2\pi f_i \tau_{-M}(\theta_{n_2})) \cdots, \exp(-j2\pi f_i \tau_{-m}(\theta_{n_2})), \cdots, 1, \cdots, \exp(-j2\pi f_i \tau_m(\theta_{n_2})), \cdots, \exp(-j2\pi f_i \tau_M(\theta_{n_2}))]^T \quad (n_2 = 1, 2, \dots, N_2) \quad (6)$$

Combing geometrical relationship in Fig. 1, we have

$$\tau_m(\theta_{n_2}) = \frac{l_{n_2} - \sqrt{l_{n_2}^2 + (md)^2 - 2l_{n_2}md \sin \theta_{n_2}}}{c} \quad (7)$$

It is the propagating delay for the NFS $s_{n_2}(t)$ arriving at the m -th sensor with respect to the reference of the array, combing Fourier series, we can expand (7) [15]

$$\tau_m(\theta_{n_2}) = -\frac{m^2 d^2}{4l_{n_2} c} \cos 2\theta_{n_2} + \frac{1}{c} md \sin \theta_{n_2} - \frac{m^2 d^2}{4l_{n_2} c} \quad (8)$$

In (1), there is

$$\begin{aligned} \mathbf{S}(f_i) &= [\mathbf{S}_{FS}(f_i), \mathbf{S}_{NS}(f_i)]^T \\ &= [\mathbf{S}_1(f_i), \cdots, \mathbf{S}_{n_1}(f_i), \cdots, \mathbf{S}_{N_1}(f_i), \mathbf{S}_{N_1+1}(f_i), \cdots, \mathbf{S}_{n_2}(f_i), \cdots, \mathbf{S}_N(f_i)]^T \quad (9) \\ &\quad (i = 1, 2, \dots, J) \end{aligned}$$

it is the signal vector at f_i , where $\mathbf{S}_{FS}(f_i) = [\mathbf{S}_1(f_i), \cdots, \mathbf{S}_{n_1}(f_i), \cdots, \mathbf{S}_{N_1}(f_i)]^T$ is the vector of FFS, $\mathbf{S}_{NS}(f_i) = [\mathbf{S}_{N_1+1}(f_i), \cdots, \mathbf{S}_{n_2}(f_i), \cdots, \mathbf{S}_N(f_i)]^T$ is that of NFS. $\mathbf{E}(f_i)$ is the noise vector with mean 0 and variance $\sigma^2(f_i)$, then the ideal covariance matrix at f_i is

$$\begin{aligned} \mathbf{R}(f_i) &= \frac{1}{Z} \mathbf{X}(f_i) \mathbf{X}^H(f_i) \\ &= \frac{1}{Z} \mathbf{A}(f_i, \theta) \mathbf{S}(f_i) \mathbf{S}^H(f_i) \mathbf{A}^H(f_i, \theta) + \sigma^2(f_i) \mathbf{I}_{(2M+1) \times (2M+1)} \quad (i = 1, 2, \dots, J) \quad (10) \\ &= \mathbf{R}_{FS}(f_i) + \mathbf{R}_{NS}(f_i) + \sigma^2(f_i) \mathbf{I}_{(2M+1) \times (2M+1)} \end{aligned}$$

Here the covariance matrix of FFS is $\mathbf{R}_{FS}(f_i) = \frac{1}{Z} \mathbf{A}_{FS}(f_i) \mathbf{S}_{FS}(f_i) \mathbf{S}_{FS}^H(f_i) \mathbf{A}_{FS}^H(f_i)$, and that of NFS is $\mathbf{R}_{NS}(f_i) = \frac{1}{Z} \mathbf{A}_{NS}(f_i) \mathbf{S}_{NS}(f_i) \mathbf{S}_{NS}^H(f_i) \mathbf{A}_{NS}^H(f_i)$.

2.2 Array Error Model

When there is gain-phase error in the array, the perturbation at f_i can be expressed by

$$\mathbf{W}(f_i) = \text{diag}\left([W_{-M}(f_i), \dots, W_{-m}(f_i), \dots, 1, \dots, W_m(f_i), \dots, W_M(f_i)]^T\right) \quad (11)$$

$(i = 1, 2, \dots, J)$

where

$$W_m(f_i) = \rho_m(f_i)e^{j\phi_m(f_i)}, m = -M, \dots, -m, \dots, 0, \dots, m, \dots, M \quad (i = 1, 2, \dots, J) \quad (12)$$

is the gain-phase perturbation of the m -th sensor at f_i , and $\rho_m(f_i)$, $\phi_m(f_i)$ are the gain and phase of the m -th sensor with respect to the 0-th sensor, at the moment, the steering vector of the n -th signal at f_i is

$$\begin{aligned} \mathbf{a}'(f_i, \theta_n) &= \begin{bmatrix} W_{-M}(f_i)e^{-j2\pi f_i \tau_{-M}(\theta_n)}, \dots, W_{-m}(f_i)e^{-j2\pi f_i \tau_{-m}(\theta_n)}, \dots, 1, \dots, \\ W_m(f_i)e^{-j2\pi f_i \tau_m(\theta_n)}, \dots, W_M(f_i)e^{-j2\pi f_i \tau_M(\theta_n)} \end{bmatrix}^T \\ &= \text{diag}\left([W_{-M}(f_i), \dots, W_{-m}(f_i), \dots, 1, \dots, W_m(f_i), \dots, W_M(f_i)]^T\right) \mathbf{a}(f_i, \theta_n) \\ &= \mathbf{W}(f_i) \mathbf{a}(f_i, \theta_n) \quad (n = 1, 2, \dots, N) \end{aligned} \quad (13)$$

The corresponding array manifold is

$$\begin{aligned} \mathbf{A}'(f_i, \theta) &= [\mathbf{a}'_{FS}(f_i, \theta_1), \dots, \mathbf{a}'_{FS}(f_i, \theta_{n_1}), \dots, \mathbf{a}'_{FS}(f_i, \theta_{N_1}), \mathbf{a}'_{FS}(f_i, \theta_{N_1+1}), \dots, \mathbf{a}'_{FS}(f_i, \theta_{n_2}), \dots, \mathbf{a}'_{FS}(f_i, \theta_N)] \\ &= [\mathbf{A}'_{FS}(f_i), \mathbf{A}'_{FS}(f_i)] \\ &= \mathbf{W}(f_i) \mathbf{A}(f_i, \theta) \end{aligned} \quad (14)$$

where $\mathbf{A}'_{FS}(f_i) = \mathbf{W}(f_i) \mathbf{A}_{FS}(f_i) = [\mathbf{a}'_{FS}(f_i, \theta_1), \dots, \mathbf{a}'_{FS}(f_i, \theta_{n_1}), \dots, \mathbf{a}'_{FS}(f_i, \theta_{N_1})]$ is the array manifold of FFS, $\mathbf{a}'_{FS}(f_i, \theta_{n_1})$ is the corresponding steering vector of $s_{n_1}(t)$; $\mathbf{A}'_{NS}(f_i) = \mathbf{W}(f_i) \mathbf{A}_{NS}(f_i) = [\mathbf{a}'_{NS}(f_i, \theta_{N_1+1}), \dots, \mathbf{a}'_{NS}(f_i, \theta_{n_2}), \dots, \mathbf{a}'_{NS}(f_i, \theta_N)]$ is the array manifold of NFS, $\mathbf{a}'_{NS}(f_i, \theta_{n_2})$ is the corresponding steering vector of $s_{n_2}(t)$, then output of the array at present is

$$\mathbf{X}'(f_i) = \mathbf{A}'(f_i, \theta) \mathbf{S}(f_i) + \mathbf{E}(f_i) = \mathbf{W}(f_i) \mathbf{A}(f_i, \theta) \mathbf{S}(f_i) + \mathbf{E}(f_i) \quad (i = 1, 2, \dots, J) \quad (15)$$

For the sake of simplicity, we also define the gain-phase uncertainty vector of the array as

$$\mathbf{w}(f_i) = [\rho_{-M}(f_i)e^{j\phi_{-M}(f_i)}, \dots, \rho_{-m}(f_i)e^{j\phi_{-m}(f_i)}, \dots, 1, \dots, \rho_m(f_i)e^{j\phi_m(f_i)}, \dots, \rho_M(f_i)e^{j\phi_M(f_i)}]^T \quad (16)$$

3 Estimation Theory

First, the covariance matrix at f_i in the presence of gain-phase perturbation is solved by

$$\begin{aligned}
\mathbf{R}'(f_i) &= \frac{1}{Z} \mathbf{X}'(f_i) (\mathbf{X}'(f_i))^H \\
&= \frac{1}{Z} \mathbf{A}'(f_i, \theta) \mathbf{S}(f_i) \mathbf{S}^H(f_i) (\mathbf{A}'(f_i, \theta))^H + \sigma^2(f_i) \mathbf{I}_{(2M+1) \times (2M+1)} \\
&= \frac{1}{Z} \mathbf{W}(f_i) \mathbf{A}(f_i, \theta) \mathbf{S}(f_i) \mathbf{S}^H(f_i) \mathbf{A}^H(f_i, \theta) \mathbf{W}^H(f_i) + \sigma^2(f_i) \mathbf{I}_{(2M+1) \times (2M+1)} \\
&= \mathbf{R}'_{FS}(f_i) + \mathbf{R}'_{NS}(f_i) + \sigma^2(f_i) \mathbf{I}_{(2M+1) \times (2M+1)}
\end{aligned} \tag{17}$$

Where the covariance matrix of the FFS in the presence of gain-phase perturbation is $\mathbf{R}'_{FS}(f_i) = 1/Z \times \mathbf{W}(f_i) \mathbf{A}_{FS}(f_i) \mathbf{S}_{FS}(f_i) \mathbf{S}_{FS}^H(f_i) \mathbf{A}_{FS}^H(f_i) \mathbf{W}^H(f_i)$, that of the NFS is $\mathbf{R}'_{NS}(f_i) = 1/Z \times \mathbf{W}(f_i) \mathbf{A}_{NS}(f_i) \mathbf{S}_{NS}(f_i) \mathbf{S}_{NS}^H(f_i) \mathbf{A}_{NS}^H(f_i) \mathbf{W}^H(f_i)$. Eigen-decomposition is performed on $\mathbf{R}'(f_i)$, we can obtain its eigenvector $\mathbf{U}'(f_i) = [\mathbf{U}'_S(f_i) \mathbf{U}'_E(f_i)]$, here $\mathbf{U}'_S(f_i)$ is the signal eigenvector and $\mathbf{U}'_E(f_i)$ is the noise eigenvector, the former can be utilized to transform the received data on the focusing frequency

$$\mathbf{R}''(f_0) = \frac{1}{J} \sum_{i=1}^J \mathbf{T}(f_i) \mathbf{R}'(f_i) \mathbf{T}^H(f_i) \tag{18}$$

Where $\mathbf{T}(f_i) = \mathbf{U}'_S(f_0) (\mathbf{U}'_S(f_i))^H$ is the focusing matrix, here the center frequency can be used as f_0 . Similarly, Eigen-decomposition is performed on $\mathbf{R}''(f_0)$, its noise eigenvector $\mathbf{U}_E(f_0)$ is obtained, then combining multiple signal classification algorithm, we can establish the following spatial spectrum

$$\begin{aligned}
P_{MU-F}(\theta) &= \frac{1}{(\mathbf{a}'_{FS}(f_0, \theta))^H \mathbf{U}_E(f_0) \mathbf{U}_E^H(f_0) \mathbf{a}'_{FS}(f_0, \theta)} \\
&= \frac{1}{\mathbf{a}_{FS}^H(f_0, \theta) \mathbf{W}^H(f_0) \mathbf{U}_E(f_0) \mathbf{U}_E^H(f_0) \mathbf{W}(f_0) \mathbf{a}_{FS}(f_0, \theta)} \\
&= \frac{1}{Y}
\end{aligned} \tag{19}$$

Perform the following transformation on the denominator of the function above

$$Y = \sum_{n_1=1}^{N_1} \mathbf{a}_{FS}^H(f_0, \theta_{n_1}) \mathbf{W}^H(f_0) \mathbf{U}_E(f_0) \mathbf{U}_E^H(f_0) \mathbf{W}(f_0) \mathbf{a}_{FS}(f_0, \theta_{n_1}) \tag{20}$$

Simplify (20), we have

$$\begin{aligned}
 Y &= \sum_{n_1=1}^{N_1} \mathbf{a}_{FS}^H(f_0, \theta_{n_1}) \mathbf{W}^H(f_0) \mathbf{U}_E(f_0) \mathbf{U}_E^H(f_0) \mathbf{W}(f_0) \mathbf{a}_{FS}(f_0, \theta_{n_1}) \\
 &= \sum_{n_1=1}^{N_1} \mathbf{w}^H(f_0) \left\{ (\text{diag}(\mathbf{a}_{FS}(f_0, \theta_{n_1})))^H \mathbf{U}_E(f_0) \mathbf{U}_E^H(f_0) \text{diag}(\mathbf{a}_{FS}(f_0, \theta_{n_1})) \right\} \mathbf{w}(f_0) \\
 &= \mathbf{w}^H(f_0) \mathbf{D}(f_0, \theta) \mathbf{w}(f_0)
 \end{aligned} \tag{21}$$

Where $\mathbf{D}(f_0, \theta) = \sum_{n_1=1}^{N_1} \left\{ (\text{diag}(\mathbf{a}_{FS}(f_0, \theta_{n_1})))^H \mathbf{U}_E(f_0) \mathbf{U}_E^H(f_0) \text{diag}(\mathbf{a}_{FS}(f_0, \theta_{n_1})) \right\}$, the

DOA of FFS can be solved by minimizing (21). As $\mathbf{w}(f_0) \neq \mathbf{0}$, $\mathbf{w}^H(f_0) \mathbf{D}(f_0, \theta) \mathbf{w}(f_0)$ will equal zero only if $\mathbf{D}(f_0, \theta)$ is singular, then θ corresponds to the actual DOA at the moment, so $\theta_1, \dots, \theta_{N_1}$ can be estimated by solving N_1 roots of the following polynomial

$$|\mathbf{D}(f_0, \theta)| = 0 \tag{22}$$

The proposed method is suitable for far-field sources in mixed wideband signals, so we can call it FMW method.

4 Simulations

Here, some simulations are presented for the method, consider some wideband chirp signals impinge on a uniform linear array with 11 omnidirectional sensors, the sixth sensor is defined as the reference, three FFS and two NFS arriving at the array from $(25^\circ, 35^\circ, 45^\circ)$ and $(5^\circ, 15^\circ)$ synchronously. The frequency of these wideband signals is limited in $[0.1 \text{ GHz}, 0.12 \text{ GHz}]$, and spacing d between adjacent sensors is equal to half of the wavelength of the center frequency, the signal band is divided into 30 bins. Here we will simplify the generation of the error, so the gain and phase of the every sensor relative to the reference are respectively selected in $[0, 1.6]$ and $[-24^\circ, 24^\circ]$, the average of 200 Monte-Carlo trials is regarded as the result. EGP [10], MFN [16], two-sided correlation transformation (TCT) [17] and FMW are respectively utilized for the estimation.

4.1 DOA Estimation for Narrowband Signals

Figure 2 is the estimation errors versus SNR at 0.11 GHz when sampling times Z is 20; Fig. 3 presents that versus sampling times Z at 0.11 GHz when SNR is 6 dB. It can be seen from Figs. 2 and 3, estimation errors decrease with the increase of SNR or sampling times, and they are convergent finally. MFN can not apply to the gain-phase perturbation, even though SNR is high or sampling times is large, a large error can not be avoided all the same; EGP has to calibrate the array before estimating FFS, which will also bring some uncertainty; By contrast, FMW is not necessary to correct the array before calculating FFS, so it performs better than the other two methods.

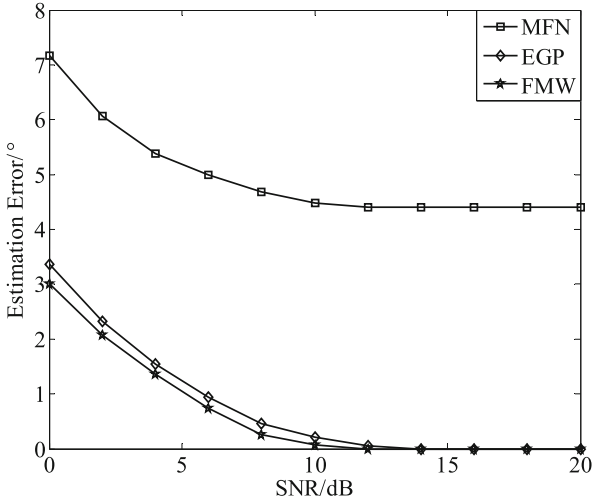


Fig. 2. DOA estimation errors at 0.11 GHz versus SNR

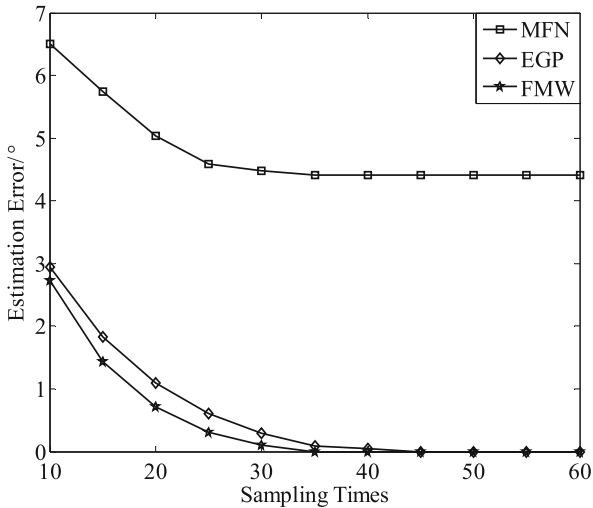


Fig. 3. DOA estimation errors at 0.11 GHz versus sampling times

4.2 DOA Estimation for Wideband Signals

Figure 4 shows estimation error versus SNR of wideband coherent signals when sampling times Z is 20; and Fig. 5 verifies that versus sampling times Z of wideband coherent signals when SNR is 6 dB.

From Figs. 4 and 5 we know that FMW is still effective to wideband coherent signals by focusing, and there are no obvious differences comparing with the circumstance of narrowband signals; though TCT is also suitable for wideband signals, it has failed owing to the array error.

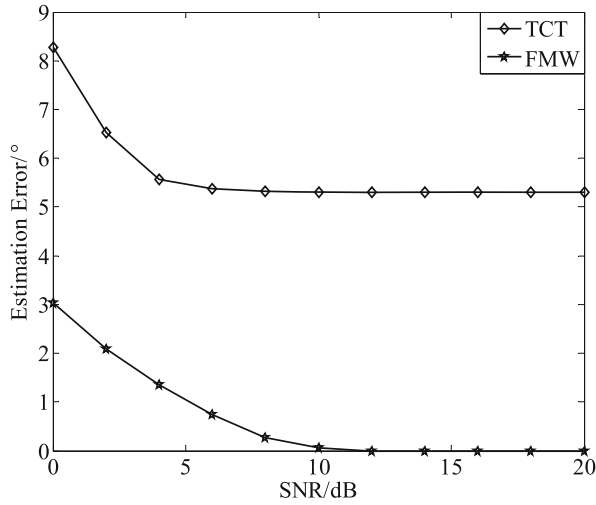


Fig. 4. DOA estimation errors of wideband coherent signals versus SNR

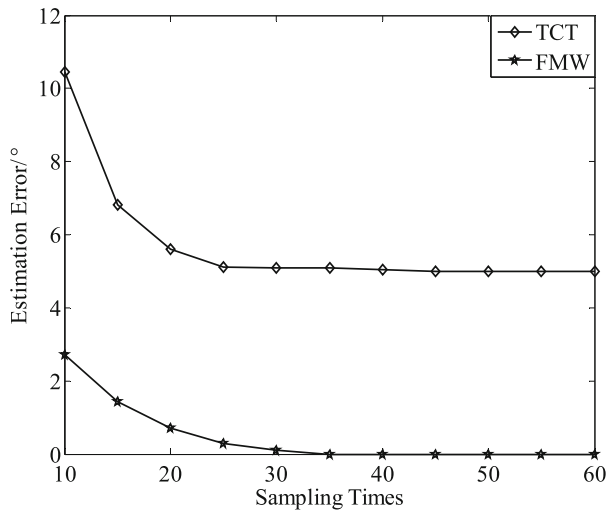


Fig. 5. DOA estimation errors of wideband coherent signals versus sampling times

5 Conclusion

In the paper, a new method of estimating DOA of FFS in mixed FFS and NFS with gain-phase error array is provided. It both applies to narrowband and wideband coherent signals. In the meantime, it averts spectrum searching by directly finding roots of the polynomial according to the special structure of the array, so the computational efficiency is improved to a great extent.

Acknowledgments. I would like to thank Heilongjiang province ordinary college electronic engineering laboratory and post doctoral mobile stations of Heilongjiang University.

References

1. Otte, W.R., Gokhale, A., Schmidt, D.C.: Efficient and deterministic application deployment in component-based enterprise distributed real-time and embedded systems. *Inf. Softw. Technol.* **55**, 475–488 (2013)
2. Shafiq, M., Hussain, G.A.: Partial discharge diagnostic system for smart distribution networks using directionally calibrated induction sensors. *Electr. Power Syst. Res.* **119**, 447–461 (2015)
3. Yusuke, H., Jihoon, H., Tomoaki, O.: Activity recognition using array antenna. In: 2015 IEEE International Conference on Communications, pp. 507–511. IEEE Press, Hangzhou (2015)
4. Sanchez, L., Munoz, L., Galache, J.A.: SmartSantander: IoT experimentation over a smart city testbed. *Comput. Netw.* **61**, 217–238 (2014)
5. Han, G., Wan, L., Shu, L., Feng, N.: Two novel DOA estimation approaches for real-time assistant calibration systems in future vehicle industrial. *IEEE Syst. J.* **99**, 1–12 (2015)
6. Li, J., Zhao, Y.J., Li, D.H.: Accurate single-observer passive coherent location estimation based on TDOA and DOA. *Chin. J. Aeronaut.* **27**, 913–923 (2014)
7. Fabrizio, G., Heitmann, A.: A multipath-driven approach to HF geolocation. *Sig. Process.* **93**, 3487–3503 (2013)
8. Lee, J., Chen, Y., Yeh, C.: A covariance approximation method for near-field direction finding using a uniform linear array. *IEEE Trans. Sig. Process.* **43**, 1293–1298 (1995)
9. Liu, A.F., Liao, G.S., Zeng, C.: An eigenstructure method for estimating DOA and sensor gain-phase errors. *IEEE Trans. Sig. Process.* **59**, 5944–5956 (2011)
10. Cao, S.H., Ye, Z.F., Hu, N.: DOA estimation based on fourth-order cumulants in the presence of sensor gain-phase errors. *Sig. Process.* **93**, 2581–2585 (2013)
11. Han, K.Y., Yang, P., Nehorai, A.: Calibrating nested sensor arrays with model errors. *IEEE Trans. Antennas Propag.* **63**, 4739–4748 (2015)
12. Liang, J.L., Liu, D.: Passive localization of mixed near-field and far-field sources using two-stage MUSIC algorithm. *IEEE Trans. Sig. Process.* **58**, 108–120 (2010)
13. Wang, K., Wang, L., Shang, J.R.: Mixed near-field and far-field source localization based on uniform linear array partition. *IEEE Sens. J.* **16**, 8083–8090 (2016)
14. Ye, T., Sun, X.Y.: Mixed sources localisation using a sparse representation of cumulant vectors. *IET Sig. Process.* **8**, 606–611 (2014)
15. Vleck, E.B.V.: The influence of Fourier's serious upon the development of mathematics. *Science* **39**, 113–124 (1914)
16. He, J., Swamy, M.N.S., Ahmad, M.O.: Efficient application of MUSIC algorithm under the coexistence of far-field and near-field sources. *IEEE Trans. Sig. Process.* **60**, 2066–2070 (2012)
17. Valaee, S., Kabal, P.: Wideband array processing using a two-sided correlation transformation. *IEEE Trans. Sig. Process.* **43**, 160–172 (1995)



Sparse Reconstruction in Frequency Domain and DOA Estimation for One-Dimensional Wideband Signals

Jiaqi Zhen^(✉) and Yanchao Li

College of Electronic Engineering, Heilongjiang University,
Harbin 150080, China
zhenjiaqi2011@163.com

Abstract. Previous recovery methods in the literature are usually based on grid partition, which will bring about some perturbation to the eventual result. In the paper, a novel idea for one-dimensional wideband signals by sparse reconstruction in frequency domain is put forward. Firstly, Discrete Fourier Transformation (DFT) is performed on the received data. Then the data of the frequency with the most power is expressed by Fourier series coefficients. On this basis, the optimization functions and corresponding dual problems are solved. After that the support set is calculated, and the primary sources of this frequency and direction of arrival (DOA) can also be acquired. Comparing with the traditional methods, the proposed approach has further improved the estimation accuracy.

Keywords: Direction of arrival · Sparse reconstruction · Frequency domain Wideband signals

1 Introduction

Direction of arrival (DOA) estimation methods based on sparse recovery is a hot topics in recent years [1–7], and some good ideas have been put forward successively. Li [8] made full use of the frequency distribution of a received signal to generate the over-complete dictionary and it required no spectral decomposition or focusing. Xu [9] used the Capon spectrum to design a weighted ℓ_1 -norm penalty for choosing a proper regularization parameter. He [10] provided a low complexity method for DOA estimation via array covariance matrix sparse representation, the method showed an extended-aperture and led to a significant improvement in the resolution limit.

J. Zhen—This work was supported by the National Natural Science Foundation of China under Grant Nos. 61501176 and 61505050, University Nursing Program for Young Scholars with Creative Talents in Heilongjiang Province (UNPYSCT-2016017), China Postdoctoral Science Foundation (2014M561381), Heilongjiang Province Postdoctoral Foundation (LBH-Z14178), Heilongjiang Province Natural Science Foundation (F2015015), Outstanding Young Scientist Foundation of Heilongjiang University (JCL201504) and Special Research Funds for the Universities of Heilongjiang Province (HDRCCX-2016Z10).

Based on different optimization problems which were solvable using second-order cone (SOC) programming, Hu [11] introduced a perspective for DOA estimation without knowing the signal number. Jagannath [12] derived a Bayesian Cramer-Rao bound for the grid mismatch problem with the errors in variables model and proposed a block sparse estimator for grid matching and sparse recovery, decreasing the computation complexity properly. Amin [13] established the role of sparse arrays and sparse sampling in antijam global navigation satellite systems and showed that both jammer DOA estimation methods and mitigation techniques benefited from the design flexibility of sparse arrays and their extended virtual apertures or coarrays.

DOA estimation by sparse reconstruction has lowered the demand for SNR and number of snapshots to a large extent. But previous recovery methods in the literature are usually based on grid division, which will bring about some perturbation to the eventual result. Candes [14, 15] discussed the sparse recovery in continuous domain, averted errors when signals were recovered in discrete domain, the estimation precision had been improved greatly, it is a development of the application of compressed sensing, but they did not tell us how to implement super-resolution direction finding for wideband signals.

In the paper, a novel idea for one-dimensional wideband sources by sparse reconstruction in frequency domain is put forward, Firstly, Discrete Fourier Transformation (DFT) is performed on the received data. Then the data of the frequency with the most power is expressed by Fourier serious coefficients. On this basis, the optimization functions and corresponding dual problems are solved. After that the support set is calculated, and the primary sources of this frequency and DOA can also be acquired. Comparing with the traditional methods, the proposed approach has further improved the estimation accuracy.

2 Signal Model

Consider N far field wideband signals $s_n(t)$ ($n = 1, 2, \dots, N$) with the same energy arriving at the uniform linear array formed by M sensors from $\theta_1, \dots, \theta_N$, it is illustrated as Fig. 1, the interval of adjacent sensors is d , which equals half of the wavelength of center frequency, here N is known in advance. The signals and noise are

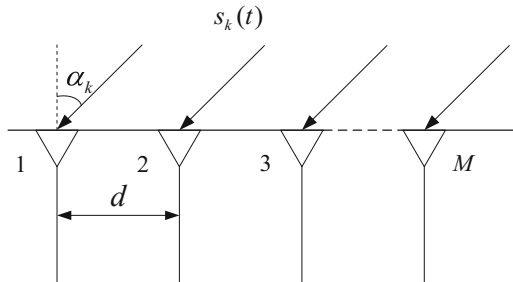


Fig. 1. Array signal model

assumed to be Gaussian distribution, and independent of each other, the first sensor is regarded as the reference, then output of the array can be modeled as

$$\mathbf{y}(t) = \left[\sum_{n=1}^N s_n(t), \dots, \sum_{n=1}^N s_n \left(t - (m-1) \frac{d}{c} \sin(\theta_n) \right), \dots, \sum_{n=1}^N s_n \left(t - (M-1) \frac{d}{c} \sin(\theta_n) \right) \right]^T + [b_1(t), \dots, b_m(t), \dots, b_M(t)]^T \quad (1)$$

Assume that number of the subbands is K , perform DFT on $\mathbf{y}(t)$, the wideband sources can be partitioned into K parts:

$$\mathbf{Y}(f_k) = \mathbf{A}(f_k) \mathbf{S}(f_k) + \mathbf{B}(f_k) \quad k = 1, \dots, K \quad (2)$$

Here, $\mathbf{B}(f_k)$ is the noise vector at f_k with mean 0 and variance $\sigma^2(f_k)$, and the steering vector matrix at f_k is determined as

$$\begin{aligned} \mathbf{A}(f_k) &= [\mathbf{a}(f_k, \theta_1), \dots, \mathbf{a}(f_k, \theta_N)] \\ &= \begin{bmatrix} 1 & \dots & 1 \\ \vdots & & \vdots \\ e^{-j2\pi f_k m \frac{d}{c} \sin(\theta_1)} & \dots & e^{-j2\pi f_k m \frac{d}{c} \sin(\theta_N)} \\ \vdots & & \vdots \\ e^{-j2\pi f_k (M-1) \frac{d}{c} \sin(\theta_1)} & \dots & e^{-j2\pi f_k (M-1) \frac{d}{c} \sin(\theta_N)} \end{bmatrix} \end{aligned} \quad (3)$$

Here, $\mathbf{a}(f_k, \theta_n)$ is the direction vector of wideband source coming from θ_n ($n = 1, \dots, N$) at frequency f_k . Suppose $\mathbf{S}(f_k)$ is sparse, for example, the signal vector is composed by some spikes [14], it can be expressed as the sparse model:

$$\mathbf{S}(f_k) = \begin{bmatrix} S_1(f_k) \\ \vdots \\ S_n(f_k) \\ \vdots \\ S_N(f_k) \end{bmatrix} = \begin{bmatrix} v_1^2(f_k) \delta_{\varphi_1(f_k)} \\ \vdots \\ v_n^2(f_k) \delta_{\varphi_n(f_k)} \\ \vdots \\ v_N^2(f_k) \delta_{\varphi_N(f_k)} \end{bmatrix} \quad (4)$$

Where

$$\varphi_n(f_k) = \frac{df_k}{c} (1 - \sin(\theta_n)) \quad (5)$$

And $\delta_{\varphi_n(f_k)}$ is a dirac measure at $\varphi_n(f_k)$, define $\{\varphi_1(f_k), \dots, \varphi_N(f_k)\}$ as the sparse support set of $\mathbf{S}(f_k)$, where $\varphi_n(f_k)$ contains direction of the n th signal, $v_n(f_k)$ is corresponding amplitude.

3 Estimation Theory

3.1 Infinite Samples

Assume that information of f_0 has the more power than that of the other frequencies, the covariance matrix at f_0 is

$$\begin{aligned}\mathbf{R}_Y(f_0) &= E[\mathbf{Y}(f_0)\mathbf{Y}^H(f_0)] \\ &= \mathbf{A}(f_0)\mathbf{R}_S(f_0)\mathbf{A}^H(f_0) + \mathbf{\Omega}(f_0) \\ &= \sum_{n=1}^N v_n^2(f_0) \mathbf{a}(f_0, \theta_n) \mathbf{a}^H(f_0, \theta_n) + \mathbf{\Omega}(f_0)\end{aligned}\quad (6)$$

Where

$$\mathbf{R}_S(f_0) = E[\mathbf{S}(f_0)\mathbf{S}^H(f_0)] = \text{diag}(\mathbf{\Sigma}_S(f_0)) = \text{diag}\left([v_1^2(f_0), \dots, v_N^2(f_0)]^T\right) \quad (7)$$

Here, $\mathbf{\Sigma}_S(f_0) = [v_1^2(f_0), \dots, v_N^2(f_0)]^T$, and

$$\mathbf{\Omega}(f_0) = E[\mathbf{B}(f_0)\mathbf{B}^H(f_0)] = \text{diag}\left([\sigma^2(f_0), \dots, \sigma^2(f_0)]_{1 \times M}^T\right) \quad (8)$$

Vectoring (6), we have

$$\mathbf{p}(f_0) = \text{vec}(\mathbf{R}_Y(f_0)) = \mathbf{\Theta}(f_0)\mathbf{\Sigma}_S(f_0) + \mathbf{\Gamma}(f_0) \quad (9)$$

Where $\mathbf{\Gamma}(f_0) = [\sigma^2(f_0)\mathbf{e}_1^T, \dots, \sigma^2(f_0)\mathbf{e}_M^T]^T$, \mathbf{e}_m is the vector with all zero elements, except for the m th element, which equals one, and

$$\mathbf{\Theta}(f_0) = \mathbf{A}^*(f_0) \odot \mathbf{A}(f_0) = [\mathbf{a}^*(f_0, \theta_1) \otimes \mathbf{a}(f_0, \theta_1), \dots, \mathbf{a}^*(f_0, \theta_N) \otimes \mathbf{a}(f_0, \theta_N)] \quad (10)$$

Get rid of duplicate items in (9), then arrange them in order, we have

$$\bar{\mathbf{p}}(f_0) = \bar{\mathbf{\Theta}}(f_0)\mathbf{\Sigma}_S(f_0) + \bar{\mathbf{\Gamma}}(f_0) \quad (11)$$

Where

$$\bar{\mathbf{\Theta}}(f_0) = \begin{bmatrix} e^{(-j2\pi f_0(2M-1)\frac{d}{c}\sin(\theta_1))} & \dots & e^{(-j2\pi f_0(2M-1)\frac{d}{c}\sin(\theta_N))} \\ e^{(-j2\pi f_0(2M-2)\frac{d}{c}\sin(\theta_1))} & \dots & e^{(-j2\pi f_0(2M-2)\frac{d}{c}\sin(\theta_N))} \\ \vdots & \ddots & \vdots \\ e^{(j2\pi f_0(2M-1)\frac{d}{c}\sin(\theta_1))} & \dots & e^{(j2\pi f_0(2M-1)\frac{d}{c}\sin(\theta_N))} \end{bmatrix} \quad (12)$$

$\bar{\mathbf{\Gamma}}(f_0)$ is acquired after rearranging $\mathbf{\Gamma}(f_0)$. Given a measure $S(\varphi)$ with $\varphi \in [0, 1]$, the Fourier series coefficients of $S^2(\varphi)$ can be expressed as

$$q(m) = \int_0^1 \exp(-j2\pi m\varphi) S^2(\varphi) d\varphi \quad m = -(2M-1), -(2M-2), \dots, (2M-1) \quad (13)$$

Combine (4) and (13)

$$q(m, f_0) = \sum_{n=1}^N \exp(-j2\pi m\varphi_n(f_0)) v_n^2(f_0), \quad m = -(2M-1), -(2M-2), \dots, (2M-1) \quad (14)$$

So we have

$$\mathbf{Q}(f_0) = \mathbf{F}(f_0) \boldsymbol{\Sigma}_S(f_0) \quad (15)$$

Where

$$\mathbf{Q}(f_0) = [q(-(2M-1), f_0), q(-(2M-2), f_0), \dots, q((2M-1), f_0)]^T \quad (16)$$

and

$$\mathbf{F}(f_0) = \begin{bmatrix} e^{j2\pi(2M-1)\varphi_1(f_0)} & \dots & e^{j2\pi(2M-1)\varphi_N(f_0)} \\ e^{j2\pi(2M-2)\varphi_1(f_0)} & \dots & e^{j2\pi(2M-2)\varphi_N(f_0)} \\ \vdots & \ddots & \vdots \\ e^{-j2\pi(2M-1)\varphi_1(f_0)} & \dots & e^{-j2\pi(2M-1)\varphi_N(f_0)} \end{bmatrix} \quad (17)$$

In order to reconstruct primary sources, it is possible to solve the following question

$$\min_{\boldsymbol{\Sigma}_S(f_0)} \|\boldsymbol{\Sigma}_S(f_0)\|_{\text{TV}}, \text{ s.t. } \mathbf{Q}(f_0) = \mathbf{F}(f_0) \boldsymbol{\Sigma}_S(f_0) \quad (18)$$

where $\|\boldsymbol{\Sigma}_S(f_0)\|_{\text{TV}} = \sum_{n=1}^N v_n^2(f_0)$, then we can recover the source $\mathbf{S}(f_0)$ if the interval between $\varphi_\alpha(f_0)$ and $\varphi_\beta(f_0)$ is wider than $2/f_0$ for $1 \leq \alpha, \beta \leq N$ [14].

3.2 Finite Samples

In real systems, suppose the sampling times at every frequency is KP , the covariance matrix can be acquired by

$$\hat{\mathbf{R}}_Y(f_0) = \frac{1}{KP} \sum_{kp=1}^{KP} \mathbf{Y}(f_0) \mathbf{Y}^H(f_0) \quad (19)$$

Get rid of the noise item, we have

$$\hat{\mathbf{R}}_Y(f_0) - \sigma^2(f_0)\mathbf{I} = \mathbf{A}(f_0)\mathbf{R}_S(f_0)\mathbf{A}^H(f_0) + \mathbf{D}(f_0) \quad (20)$$

Where $\mathbf{D}(f_0)$ is the corresponding error, $\sigma^2(f_0)$ can be estimated according to the eigenvalue, then

$$\hat{\mathbf{p}}(f_0) = \text{vec}(\hat{\mathbf{R}}_Y(f_0)) = \boldsymbol{\Theta}(f_0)\boldsymbol{\Sigma}_S(f_0) + \boldsymbol{\Gamma}(f_0) + \boldsymbol{\Psi}(f_0) \quad (21)$$

Here $\boldsymbol{\Psi}(f_0) = \text{vec}(\mathbf{D}(f_0))$, take out repeated items in (21) and arrange them in sequence, we have

$$\bar{\mathbf{p}}(f_0) = \bar{\boldsymbol{\Theta}}(f_0)\boldsymbol{\Sigma}_S(f_0) + \bar{\boldsymbol{\Gamma}}(f_0) + \bar{\boldsymbol{\Psi}}(f_0) \quad (22)$$

Where $\bar{\boldsymbol{\Psi}}(f_0)$ can be obtained by rearranging $\boldsymbol{\Psi}(f_0)$. Referring to (4), the linear transform of (22) is

$$\begin{aligned} q(m, f_0) &= \exp\left(-j2\pi m \frac{df_0}{c}\right) (\bar{\mathbf{p}}_m(f_0) - \bar{\boldsymbol{\Gamma}}_m(f_0)) \\ &= \exp\left(-j2\pi m \frac{df_0}{c}\right) \left(\sum_{n=1}^N \exp\left(j2\pi m \frac{df_0}{c} \sin(\theta_n)\right) v_n^2(f_0) + \bar{\boldsymbol{\Psi}}(m, f_0) \right) \\ &= \sum_{n=1}^N \exp\left(-j2\pi m \frac{df_0}{c} (1 - \sin \theta_n)\right) v_n^2(f_0) + \exp\left(-j2\pi m \frac{df_0}{c}\right) \bar{\boldsymbol{\Psi}}(m, f_0) \\ &= \sum_{n=1}^N \exp(-j2\pi m \varphi_n(f_0)) v_n^2(f_0) + \boldsymbol{\omega}(m, f_0) \end{aligned} \quad (23)$$

Where $\boldsymbol{\omega}(m, f_0) = \exp(-j2\pi m \frac{df_0}{c}) \bar{\boldsymbol{\Psi}}(m, f_0)$, so we have

$$\mathbf{Q}(f_0) = \mathbf{F}(f_0)\boldsymbol{\Sigma}_s(f_0) + \boldsymbol{\omega}(f_0) \quad (24)$$

Where $\boldsymbol{\omega}(f_0) = [\boldsymbol{\omega}(-(2M-1), f_0), \dots, \boldsymbol{\omega}(m, f_0), \dots, \boldsymbol{\omega}((2M-1), f_0)]$, similarly, primary sources can be recovered by the question (25)

$$\min_{\boldsymbol{\Sigma}_S(f_0)} \|\boldsymbol{\Sigma}_S(f_0)\|_{\text{TV}} \text{ s.t. } \|\mathbf{Q}(f_0) - \mathbf{F}(f_0)\boldsymbol{\Sigma}_s(f_0)\|_2 \leq |\varsigma(f_0)| \quad (25)$$

It can be recast as the formula below [14]

$$\begin{aligned} &\max_{\boldsymbol{\Phi}(f_0), \mathbf{Z}} \text{Re}[\mathbf{Q}^*(f_0)\boldsymbol{\Phi}(f_0)] - \varsigma(f_0)\|\boldsymbol{\Phi}(f_0)\|_2 \text{ s.t.} \\ &\begin{bmatrix} \mathbf{Z} & \boldsymbol{\Phi}(f_0) \\ \boldsymbol{\Phi}^*(f_0) & \mathbf{1} \end{bmatrix} \succ 0, \|\mathbf{F}^*(f_0)\boldsymbol{\Phi}(f_0)\|_{L_\infty} \leq 1 \end{aligned} \quad (26)$$

Where $\sum_{\alpha=1}^{4M+1-\beta} \mathbf{Z}_{\alpha, \alpha+\beta} = \begin{cases} 1 & \beta = 0 \\ 0 & \beta = 1, 2, \dots, 4M \end{cases}$, $\mathbf{Z} \in C^{(4M-1) \times (4M-1)}$ is a Hermitian matrix, and $\Phi(f_0) \in C^{(4M-1) \times 1}$ is the corresponding Lagrangian matrix for $\mathbf{Q}(f_0) = \mathbf{F}(f_0)\Sigma_s(f_0) + \omega(f_0)$, it can be acquired according to some softwares [16, 17].

We can use the equation below [15] to state the relationship between (25) and (26):

$$(\mathbf{F}^* \Phi)(f_0) = \text{sign}(\|\Sigma_s(f_0)\|_{\text{TV}}) \quad (27)$$

So

$$|\mathbf{F}^{\text{H}}(n, f_0) \Phi(f_0)| = 1, \quad (n = 1, \dots, N) \quad (28)$$

Then DOA can be determined by integrating (5), (17) and (28), then the primary sources can also be reconstructed according to (4). As the proposed sparse reconstruction method is implemented in frequency domain, and suitable for one-dimensional sources, we can call it SFO method for short.

4 Simulations

Here, some simulations are presented, consider some wideband sources impinge on a uniform linear array with 12 omnidirectional sensors, the frequencies of these sources are 4 GHz–5 GHz, frequency bins $K = 10$, sparse recovery methods in discrete domain (SRD) [18] and SFO are respectively employed, $\varepsilon(f_0)$ in the sparse reconstruction method is taken as 1.2. The grids in discrete domain are partitioned according to $\sin(\theta)$, the step size is 0.004, 300 Monte-Carlo simulations have run for each condition.

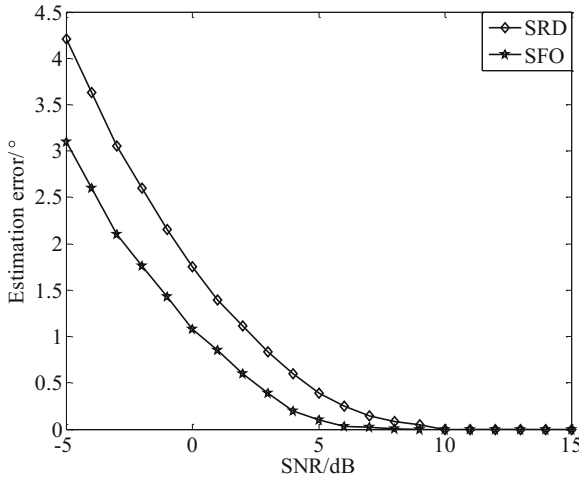


Fig. 2. Estimation error versus SNR

4.1 Estimation Error Versus SNR

Suppose that four far-field wideband sources simultaneously arrive at the array with the same energy from $\sin(\theta) = [0.213, 0.459, 0.576, 0.624]$, Fig. 2 shows the estimation errors versus signal to noise ratio (SNR) when sampling times at every frequency is 20; Fig. 3 provides that versus sampling times at every frequency when SNR is 4 dB, and we can see from the simulations, the estimation precision of SFO method is higher than SRD.

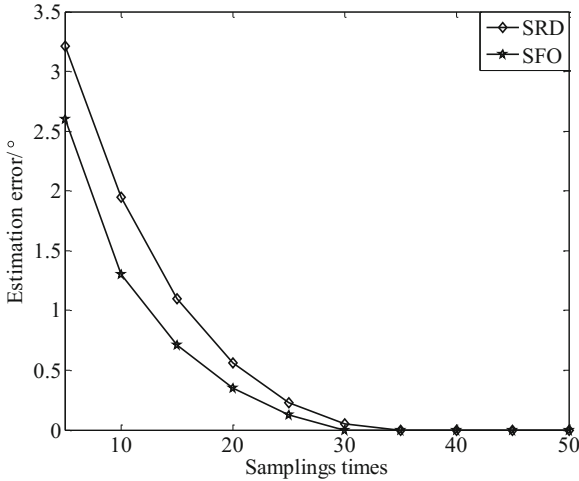


Fig. 3. Estimation error versus sampling times

4.2 Resolution

Suppose that two wideband sources simultaneously impinge at the array with the same energy from $\sin(\theta) = [0.76, 0.82]$, SNR is 6 dB, sampling times at every frequency is 20,

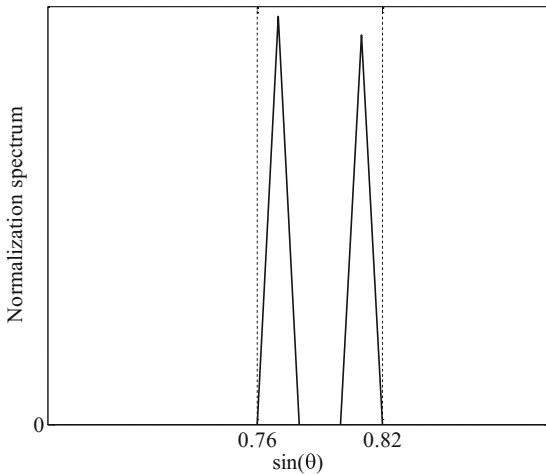


Fig. 4. Normalization spectrum of SRD for near sources

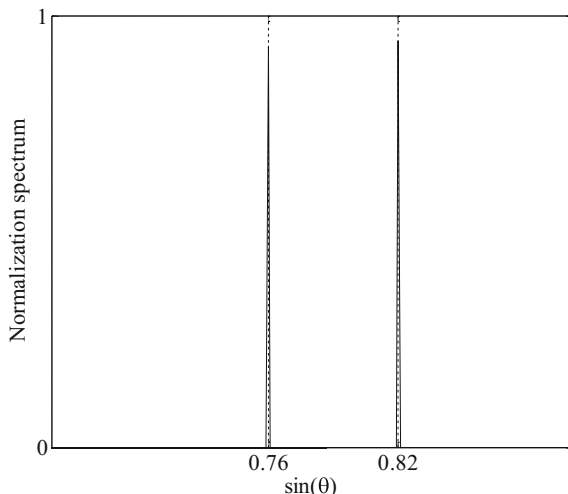


Fig. 5. Normalization spectrum of SFO for near sources

the normalization spectrum are illustrated in Figs. 4 and 5. It is seen that when the two sources are near to each other, SFO can still resolve them more accurately than SRD.

5 Conclusion

The DOA estimation for one-dimensional wideband sources by sparse reconstruction in frequency domain is put forward in this paper, only the information of the frequency with the most energy is used. This method averts the uncertainty brought by sparse reconstruction based on grid partition, and it still has a good property when the sampling times are not enough or SNR is low.

Acknowledgments. I would like to thank Professor Qun Ding, Heilongjiang province ordinary college electronic engineering laboratory and post doctoral mobile stations of Heilongjiang University.

References

1. Luis, S., Luis, M., Jose, A.G.: SmartSantander: IoT experimentation over a smart city testbed. *Comput. Netw.* **61**, 217–238 (2014)
2. Verdouw, C.N., Beulens, A.J., Vandervorst, M.J.G.A.J.: Virtualisation of floricultural supply chains: a review from an Internet of things perspective. *Comput. Electron. Agric.* **99**, 160–175 (2013)
3. Li, J., Zhao, Y.J., Li, D.H.: Accurate single-observer passive coherent location estimation based on TDOA and DOA. *Chin. J. Aeronaut.* **27**, 913–923 (2014)
4. Giuseppe, F., Andrew, H.: A multipath-driven approach to HF geolocation. *Sig. Process.* **93**, 3487–3503 (2013)

5. He, Z.Q., Shi, Z.P., Huang, L.: Underdetermined DOA estimation for wideband signals using robust sparse covariance fitting. *IEEE Sig. Process. Lett.* **22**, 435–439 (2015)
6. Tan, Z., Yang, P., Nehorai, A.: Joint-sparse recovery method for compressed sensing with structure dictionary mismatches. *IEEE Trans. Sig. Process.* **62**, 4997–5008 (2014)
7. Azais, J.M., Castro, Y.D., Gamboa, F.: Spike detection from inaccurate samplings. *Appl. Comput. Harmonic Anal.* **38**, 177–195 (2015)
8. Li, P., Zhang, M., Zhong, Z.: Integrative wideband DOA estimation method based on sparse representation. *Electron. Lett.* **47**, 1251–1252 (2011)
9. Xu, X., Wei, X.H., Ye, Z.F.: DOA estimation based on sparse signal recovery utilizing weighted l_1 -norm penalty. *IEEE Sig. Process. Lett.* **19**, 155–158 (2012)
10. He, Z.Q., Liu, Q.H., Jin, L.N.: Low complexity method for DOA estimation using array covariance matrix sparse representation. *Electron. Lett.* **49**, 228–230 (2013)
11. Hu, N., Ye, Z.F., Xu, X.: DOA estimation for sparse array via sparse signal reconstruction. *IEEE Trans. Aerosp. Electron. Syst.* **49**, 760–773 (2013)
12. Jagannath, R., Hari, K.V.S.: Block sparse estimator for grid matching in single snapshot DoA estimation. *IEEE Sig. Process. Lett.* **20**, 1038–1041 (2013)
13. Amin, M.G., Wang, X.R., Zhang, Y.D.: Sparse arrays and sampling for interference mitigation and DOA estimation in GNSS. *Proc. IEEE* **104**, 1302–1317 (2016)
14. Candes, E.J., Fernandez, G.C.: Towards a mathematical theory of super-resolution. *Communication* **67**, 906–956 (2012)
15. Candes, E.J., Fernandez, G.C.: Super-resolution from noisy data. *J. Fourier Anal. Appl.* **19**, 1229–1254 (2013)
16. Boyd, S., Vandenberghe, L.: *Convex Optimization*. Cambridge University Press, Cambridge (2004)
17. CVX: Matlab software for disciplined convex programming, version 1.22. <http://cvxr.com/cvx>
18. Hu, N., Xu, X., Ye, Z.F.: DOA estimation for wideband signals based on sparse signal reconstruction using prolate spheroidal wave functions. *Sig. Process.* **96**, 395–400 (2014)



Radar Burst Control Based on Constrained Ordinal Optimization Under Guidance Quality Constraints

Bo Li¹, Qingying Li^{1(✉)}, and Daqing Chen²

¹ School of Information and Electronics, Northwestern Polytechnical University, Xi'an, China

liqingying2015@mail.nwpu.edu.cn

² School of Engineering, London South Bank University, London, England

Abstract. Radar burst control has come into use in order to improve the survivability of combat aircraft and ensure operational effectiveness in the increasingly harsh electronic warfare environment. The critical factor in radar burst control is the radar burst timing. In this paper, a novel method is proposed to determine the optimal timing based on constrained ordinal optimization. Taking the combat effectiveness of air-to-air missile as the constraint condition, the constrained ordinal optimization method is applied to the radar burst detection of hybrid control. The optimal burst timing can be selected quickly and efficiently while making the combat effectiveness maximized. Simulation results indicate that the proposed method can significantly improve the searching efficiency of the optimal radar burst timing.

Keywords: Radar optimal burst timing · Hybrid control
Constrained ordinal optimization · Operational effectiveness

1 Introduction

In order to improve the combat effectiveness and survivability of a combat aircraft in the increasingly harsh electronic warfare environment, [1] proposed a radar burst control technology based on airborne multi-sensor coordination. In the area of the airborne multi-sensor co-tracking and radiation control, a significant research effort has been made. [2] proposed a joint detection filter, a measurement of measuring uncertainty with multiple sensors and single target tracking in the presence of clutter. In [3], a distributed multi-sensor collaborative management method was proposed. [4–6] focused on the sensor tracking, radiation control algorithm, and tracking accuracy. However, to improve the overall combat effectiveness, the sensor needs to coordinate with other units of command and control, communication and weapons. In the literature [7], a coordinated tracking method of airborne multi-sensor system based on radiation control was discussed. The main idea of this method is to apply a real-time control into radar switch machine in order to generate the radar intermittently radiate electromagnetic waves. However, the radar burst detection problem is a complex optimization problem which involves various random factors, computational time

constrain, and an NP-hard type problem, and it cannot be expressed as an explicitly definite optimization function. As such it is difficult to utilize the commonly used optimization algorithms to the problem. As well-known, the Ordinal Optimization theory can greatly reduce the computational complexity while ensuring a reasonably good solution at a sufficiently high probability. Compared with the Ordinal Optimization method, the selection set of the constrained ordinal optimization (COO) [8] is smaller, and the computation time is greatly reduced.

In this paper, a hybrid control method is proposed for the radar burst detection control. This method can effectively reduce the computational complexity caused by calculating the residual norm in each measurement update. At the same time, the multi-sensor information fusion tracking performance is linked with the combat effectiveness. The effect of the radar burst detection technology on the combat effectiveness is studied by using the air-to-air missile target intercept probability as the combat effectiveness evaluation method. All the feasibility models are selected by using the target probability of air-to-air missiles as the constraint condition, and then the ordinal optimization method is used in the candidate solution set to determine the optimal timing of the radar burst under the given combat effectiveness constraints.

This remainder of the paper is organized as follows: Sects. 2 and 3 are about the principle of radar burst detection and its various control modes. Section 4 introduces the method of determining the optimal burst timing of the radar under the guidance of quality constraint. In Sect. 5 the determination of the optimal burst time of radar based on COO method is discussed. The simulation results are discussed in Sect. 6 and the performance of the proposed approach is evaluated. Finally, in Sect. 7 the main contribution of this paper and the relevant future work are highlighted.

2 Radar Burst Detection

The so-called radar burst detection is a detection method when performing a probing task during commission operations, the radar no longer continuously sends electromagnetic signals, but uses the periodic (or aperiodic) switch machine model. When a probe signal is turned on, the frequency and the waveform of the transmitted signal are also pseudo-random agility in the pulse. This makes it look like a radar were working at different frequencies, and therefore, enables the system to have a low detectability so to avoid being detected by other systems. Essentially it is a way of radar radiation control.

Figure 1 shows the working principle of the fire control radar burst detection. Its essence is to moderate the normal radar working waveform by adding a control signal to it. The burst time interval of the radar depends on the time interval of the control signal T_c . The number of burst pulses N is determined by the pulse width of the burst signal τ_c and the pulse width of the normal operating waveform τ , i.e., $N = \tau_c/\tau$. The radar burst control signal is based on tracking accuracy or control system requirements to determine the size of T_c and τ_c by the radar computer.

In order for the radar to find target more quickly and accurately in the use of burst detection mode, we can let the radar work under the guidance of other airborne sensors. This requires the radar to work with other sensors, and among them, is the multi-sensor coordination radar burst detection tracking, and its process is shown in Fig. 2.

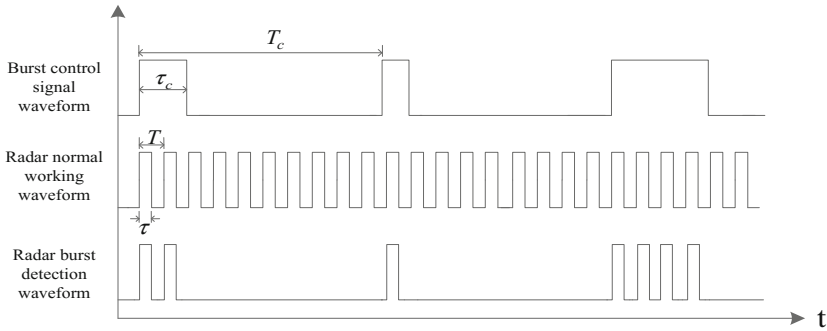


Fig. 1. Radar burst detection working principle diagram

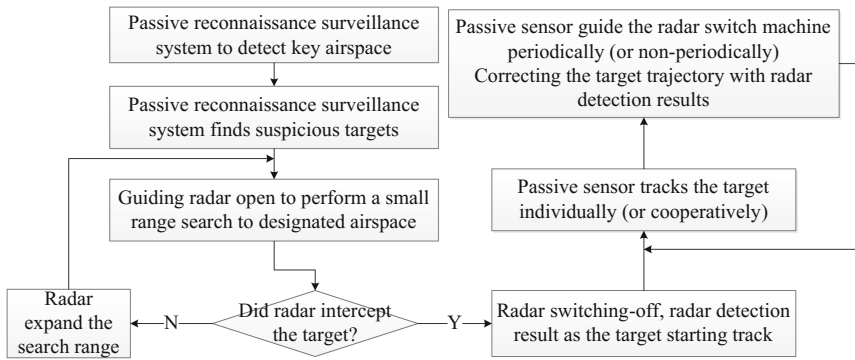


Fig. 2. Radar burst detection process under multi-sensor coordination

3 Radar Burst Detection Control Method

To ensure the quality of the target tracking, the radar start-up time and the length of each radiation must be strictly controlled. The method of determining the size of τ_c can be found in [9]. In terms of the radar burst control technology, there are three main ways to control the radar burst time as discussed below.

3.1 Equal Interval Control

The equal interval control method uses a fixed radar burst control signal interval T_c in order for the radar to perform periodic burst detection. This control method is simple and easy to implement. However, the off-line calculation process of the optimal radar burst interval with different tracking accuracies is time-consuming, and the time interval cannot be adjusted in real-time during the tracking process.

3.2 Real-Time Control

The basic idea of the real-time burst control is: according to a real-time tracking quality assessment of the target being tracked by the sensor system, we can determine if the radar burst is to be used to detect the target. This method has a great flexibility.

In [7], a radar real-time burst control method based on target residual norm was discussed, which uses the comparison results of the target filter residual norm and a given threshold to control the radar switch in real-time, and accordingly makes the radar intermittently radiate electromagnetic waves. Consider the target residual norm as

$$d(k) = \mathbf{v}_k^T \mathbf{S}_k^{-1} \mathbf{v}_k \quad (1)$$

where \mathbf{v}_k is the filter residual (innovation), \mathbf{S}_k is innovation covariance, and $d(k)$ obeys the chi-square distribution with a degree of freedom m (m is the observed dimension). We have

$$\begin{aligned} E[d(k)] &= m \\ \sigma[d(k)] &= \sqrt{2m} \end{aligned} \quad (2)$$

Hence, the problem of whether the radar is turned on by the filter residual control can be considered a hypothetical testing problem to test whether $d(k)$ is in a confidence interval centered at m .

When

$$m - k\sigma_{d(k)} < d(k) < m + k\sigma_{d(k)} \quad (3)$$

holds, the radar is to be turned off, and no external radiation; otherwise, the radar is on to detect. In Eq. (3) k is the coefficient that determines the length of the confidence interval, called burst control factor, and its size is selected according to the actual situation.

3.3 Hybrid Control

Each of the two methods discussed above has its own advantages. In practical applications, these two control methods can be combined to use, that is, with a fixed interval cycle T_c use the target residual norm to determine whether to turn the radar on. In this way, we can not only avoid the problem of poor flexibility due to burst detection at fixed cycles, but also reduce the computational complexity of calculating the residual norm for each measurement update. This method can have a good balance between flexibility and computational complexity compared with the other two control methods. This paper adopts this method.

4 Determining the Optimal Radar Burst Timing Under Guidance Quality Constraint

For the equal interval control, real-time control and hybrid control discussed above, it is necessary to determine the burst control signal interval T_c or the burst control factor k in advance to establish a pre-defined database, and then select appropriate T_c or

k according to the specific problem in the actual commission delivery process. For the problem of air-to-air missile combat guidance under multi-sensor coordination, the theoretical analysis shows that the combat effectiveness of air-to-air missile is positively correlated with radar burst detection times. For this reason, with the goal of maximizing the air-to-air missile operational effectiveness and the radar burst detection times after missile launch, we establish an optimization problem in respect to T_c or k by solving different target values under different conditions, and build a database to be used for actual operations.

When the multi-sensor co-tracking a target, the timing of radar burst detection will directly affect the tracking quality. And corresponding to the specific air-to-air missile guidance process, this timing directly affects the guidance accuracy, and hence affects seeker interception probability of the missile handover phase between midcourse guidance and terminal guidance, and ultimately affects the operational effectiveness of an air-to-air missile. This paper uses the missile intercept target probability P_c to reflect the air-to-air missile operational effectiveness. To unify the different combat situations and radar radiation durations of a missile guidance process under a certain air-to-air missile launch distance, we define the radar burst boot rate as

$$\alpha = \frac{\delta n_e}{t_g} \quad (4)$$

to reflect the radar burst boot frequency of a combat process guided by an air-to-air missile under multi-fighter multi-sensor coordination, where n_e is the radar burst detection times during the guidance, the duration of each detection is δ ; and t_g indicates the missile guidance duration, from the missile launch to the handover phase between the midcourse guidance and the terminal guidance.

For the combat problem guided by an air-to-air missile under multi-fighter multi-sensor cooperative, it is more convenient to reduce the airborne radar burst detection times by as much as possible while maintaining the operational effectiveness of air-to-air missiles. Therefore, the following constraint optimization problem can be established:

For equal interval control,

$$\begin{cases} \min \alpha = f_1(T_c) \\ \text{s.t. } P_c = g_1(T_c) \geq p \end{cases} \quad (5)$$

For real-time control,

$$\begin{cases} \min \alpha = f_2(k) \\ \text{s.t. } P_c = g_2(k) \geq p \end{cases} \quad (6)$$

For hybrid control,

$$\begin{cases} \min \alpha = f_3(T_c, k) \\ \text{s.t. } P_c = g_3(T_c, k) \geq p \end{cases} \quad (7)$$

Note that for the above optimization problems, the objective function $f(\bullet)$ and the constraint condition $g(\bullet)$ cannot be expressed by an explicit function. We therefore use air combat simulations to generate the relevant output results as the function output values. As such, the above optimization problem is based on experimental optimization.

5 Determination of the Optimal Radar Burst Timing Based on COO Method

We explore the advantages of using the Ordinal Optimization theory to solve the complex simulation optimization problems we are facing.

5.1 Ordinal Optimization Theory

The Ordinal Optimization (OO) theory consists of two basic ideas: sorting comparison and target softening. In a simple way, the ordinal optimization method divides the problem optimization process into two phases: establishing a rough model in the first stage based on known information and the understanding of the characteristics for selecting a better performance solution from a large search space, and make the number of solutions to be considered within a manageable scale. And then in the second stage the real model is to be used to evaluate the performance of the solutions selected in the first stage.

5.2 Constrained Ordinal Optimization

The traditional ordinal optimization only considers an unconstrained optimization problem of a single objective. To address this limitation, a Constrained Ordinal Optimization has been proposed by Zhao [8] to solve the problem of simulation optimization with constraints.

The basic idea of the Constrained Ordinal Optimization is: First, the feasibility model is used to scan and obtain a feasible solution, and then apply OO in the estimated feasible solution set. The COO requires a smaller set of selection than the direct application of OO without the feasibility model. At the same time, the size of the selection set also depends on the accuracy of the feasibility model. The step of determining the radar burst timing method based on COO is as follows (shown in Fig. 3):

Step 1. Establish the air-to-air missile guidance combat simulation model under multi-fighter multi-sensor cooperation. On this basis, a feasibility analysis model is created based on the constraint condition function $g(\bullet)$, and the objective function of the accurate calculation model is built up based on the objective function $f(\bullet)$. At the same time, this objective function is used to determine the rough calculation model;

Step 2. Sample from the effective range of T_c or k values evenly at a regular interval to form a decision solution set Θ ;

Step 3. Use the feasibility model, randomly extract N feasible solutions (i.e., the solution of $P_c \geq p$) from Θ according to the principle of equal opportunity to form a feasible solution set Φ ;

Step 4. Use the blind selection rule and the rough calculation model to calculate the feasible solution set Φ .

Step 5. Order the feasible solution set Φ by rough calculation solutions to estimate the type of ordered performance curve, and constitute a sub-decision set S_f according to the top s_f feasible solutions from the sorted solutions. In accordance of the relevant theory in the literature [10], the size of s_f is determined by

$$s_f = e^z k^\rho g^\gamma + \eta \tag{8}$$

where z , ρ , γ and η can be found from the regression table in [10], g is the number of elements in the sufficient subset G , and k is the number of elements in the intersection of the sub-decision set S_f and the sufficient subset G .

Step 6. Simulate the s_f feasible schemes selected from the sub-decision set S_f , and sort out the results.

Step 7. Analyze the previously sorted k_s feasible solutions of the exact simulation results, the values of T_c and k corresponding to the radar burst optimal timing are determined. Verify whether they are satisfied the constraint conditions.

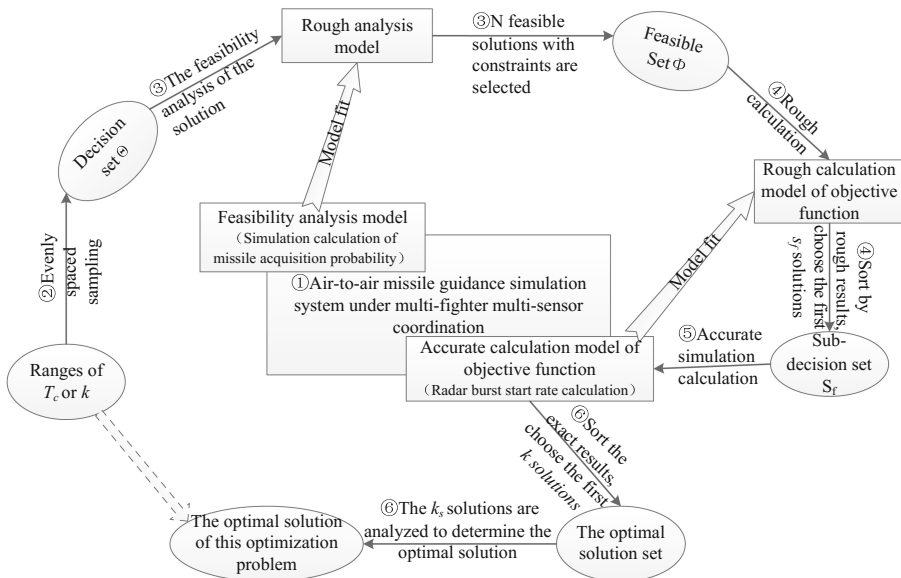


Fig. 3. The process of determining optimal radar burst timing based on the COO method

In the above process, the establishment of an appropriate and reliable simulation model is the first step to solve the optimization problem, and it is the most important step. Below are the relevant simulation models to be adopted:

- (1) Air combat simulation model based on multi-sensor cooperative
The model includes the basic combat aircraft model, air-to-air missile model, sensor model, weapon fire control model, and detailed sensor management model and tracking filter model.
- (2) Feasibility analysis model
The feasibility analysis model is based on the constraint function $g(\bullet)$. For the optimization problem of the optimal radar timing, the solution of the feasibility analysis model is the air-to-air missile target intercept probability calculation model. For air-to-air missile target intercept probability, the most commonly used method is Monte Carlo simulation.
- (3) Accurate calculation model of objective function
The exact calculation model is a detailed calculation model of the radar burst rate based on the objective function $f(\bullet)$. According to the definition of radar burst detection rate, it is necessary to record the number of radar bursts detected during the period from the missile launch to the beginning of handing over the midcourse to the terminal guidance. This process is carried out in combat simulation guided by air-to-air missile under multi-fighter multi-sensor coordination. Due to the randomness of the sensor measurement process, the statistical results obtained by the single simulation have a significant uncertainty. Therefore, to make the statistical results more reliable, it is usually necessary to conduct Monte Carlo simulation several times repeatedly, then take the average of the results of the multiple experiments.
- (4) Rough calculation model
Due to the limitation of the computational capacity and the evaluation time, it is not feasible to use the simulation model to evaluate each feasible solution in real time. According to the order comparison characteristics of the ordinal optimization theory, we only need to establish the rough model of the evaluation function, and make a quick assessment of each option. Therefore, we propose to use a partial sample value obtained by the simulation model to fit the precise model and using the fitted model as a rough model for a rapid assessment.
We use an $n-2n-2$ three-layer error back propagation (BP) network model shown in Fig. 4 to fit the simulation model. The network contains $2n$ hidden nodes (n is the number of the network input nodes), and the activation function of each hidden node is a sigmoid function. The node on the output layer adopts a linear activation function. The network parameters will be determined throughout training with the partial data obtained by the simulation evaluation model. Compared with the rough calculation using the simulation model, the BP network after fitting can not only reduce the time of rough calculation, but also ensure the validity of the calculated data.

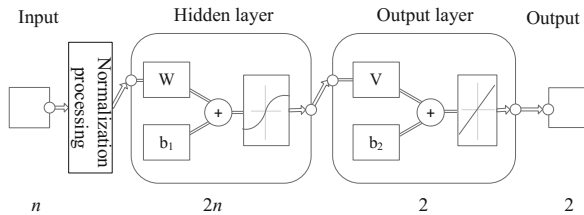


Fig. 4. BP network structure for rough calculation

6 Simulation Experiment

In our simulation, the burst period of an airborne radar was assumed to be controlled within 0.1 s–10.0 s. A proper radar burst period was determined based on the requirements that the target intercept probability would not less than 85% and the burst rate would take the minimum when the air-to-air missile has been launched within 60 km–80 km.

Sampling the radar burst cycle by 0.1 s step length, missile launch distance by 1 km step gives a total of $100 \times 21 = 2100$ combination groups. It is not advisable to do scheme optimization by traversal search, since it is very time-consuming using Monte Carlo approach to determine the missile intercept probability. Our simulation experiments have shown that: when taking 1 s as the simulation step, completing a missile intercept probability calculation usually requires 70.59 s of CPU time, even without considering the time of scenario edit and simulation framework start-up. The simulation time would be about 132 s when the radar burst period was optimized by 0.2 s step. To complete more than 2000 sets of simulation calculation, it would take about 70 h. Therefore, the COO method proposed in this paper was used to optimize:

- (1) Rough calculation and evaluation model. From the above-mentioned 2100 combinations, 50 (10×5) groups were extracted by $T_c = 1, 2, \dots, 10$ s and $D = 60, 65, \dots, 80$ km, respectively. Calculating the corresponding missile intercept probabilities and radar burst boot rates by step 1 s, and training a BP network with the resultant data. The inputs of the BP network were the radar burst period and the missile launch distance, and the output was the missile intercept probability and the radar burst boot rate. The process took about 1 h.
- (2) Using the trained BP network to roughly calculate the 2100 combinations quickly. The process was completed in a minute.
- (3) According to the rough calculation results, selecting any combination of the missile intercept probability that satisfies $P_c > 83\%$ (considering the possible impact of the model fitting error on the result, so to relax the constraints). Then the selected combinations were merged together according to the radar burst period, and sorted by the average radar burst rate from small to large.
- (4) Selecting the five radar burst periods of the forward order to do accurate calculation by simulation step 1 s. At this time, a total of $5 \times 21 = 105$ groups of experiments were conducted, consuming about 4 h.

- (5) Comparing and analyzing the accurate simulation results, the radar burst period $T_c = 3.6$ s corresponding to the minimum average radar burst boot rate and satisfying the target intercept probability not less than 85% when the missile launch distance is within 60 km–80 km. Table 1 shows the target intercept probability corresponding to the partial launch distance at $T_c = 3.6$ s, all of which meet the requirements.

From the steps described above, it is evident that the COO method has greatly reduced the workload in determining the radar optimal burst timing. Making the duration of calculations reduced from more than 70 h of CPU time to 5 h. Hence, the ordinal optimization method has a great advantage in solving the problem of simulation optimization.

Table 1. A part of the target capture probability corresponding to the launch distance when $T_c = 3.6$ s

Transmitting distance/km	60	64	68	72	76	80
Target capture probability	88.2%	87.5%	87.0%	86.4%	85.9%	85.3%

7 Conclusion

This paper presents a method to determine the radar optimal burst timing based on Constrained Ordinal Optimization, and has applied it to air-to-air missile guidance process. Simulation results indicate that using the Constrained Ordinal Optimization method to determine the optimal radar burst timing can greatly improve the searching probability under the conduction that the combat effectiveness is maximized, and therefore effectively control the radar radiation and improve the stability and viability of combat aircraft. In the future, we can use parallel computing technology to further improve the searching efficiency.

Acknowledgments. This research was supported by The Fundamental Research Funds for the Central Universities under grant No. 3102016CG002.

References

1. Xue-quan, L., Bo, L., Kai-fang, W., et al.: Study on radar burst technology based on multi-sensor synergy. *J. Civ. Aviat. Univ. China* **30**(6), 17–20 (2012)
2. Vo, B.T., See, C.M., Ma, N., et al.: Multi-sensor joint detection and tracking with the Bernoulli filter. *IEEE Trans. Aerosp. Electron. Syst.* **48**(2), 1385–1402 (2012)
3. Frey, T.: Cooperative sensor resource management for improved situation awareness. In: *Infotech@ Aerospace 2012* (2012)
4. Toupet, O., How, J.: Collaborative sensor fusion and management for multiple UAVs. In: *AIAA Infotech@ Aerospace Conference* (2011)
5. Deng, R., Chen, J., Yuen, C., et al.: Energy-efficient cooperative spectrum sensing by optimal scheduling in sensor-aided cognitive radio networks. *IEEE Trans. Veh. Technol.* **61**(2), 716–725 (2012)

6. Kenefic, R.J.: Sensor rotation bias removal for multiple hypothesis tracking applications. *J. Aerosp. Inf. Syst.* **10**(5), 250–257 (2013)
7. Wei, W., Yi, L., Guo-hong, W., et al.: Active and passive synergy tracking technique with emission constraint. *Inf. Control* **40**(3), 418–423 (2011)
8. Ho, Y.-C., Zhao, Q.-C., Jia, Q.-S.: *Ordinal Optimization: Soft Optimization for Hard Problems*. Springer, New York (2007)
9. Liu, X.-Q., Li, B., Wan, K.-F., et al.: Analysis and application of AN/ APG-77 radar remote guidance search mode. In: *The Proceedings of the Academic Annual Meeting of Fire and Command Control in 2013*, 11 (2013)
10. Lau, T.W.E., Ho, Y.C.: Universal alignment probabilities and subset selection for ordinal optimization. *J. Optim. Theory Appl.* **93**(3), 455–489 (1997)



An Overview of CCMANET: Content Centric MANET

Yuehua Huo¹, Weiqiang Fan², Yinlong Liu³(✉), and Dong Li¹

¹ Center of Modern Education Technology,
China University of Mining and Technology, Beijing, Beijing 100083, China
{huoyh, lidong}@cumtb.edu.cn

² School of Mechanical Electronic and Information Engineering,
China University of Mining and Technology, Beijing, Beijing 100083, China
fan_weiqiang@163.com

³ Institute of Information Engineering, Chinese Academy of Sciences,
Beijing 100093, China
532806957@qq.com

Abstract. Due to CCN has the advantages of content-centric, unstructured, chunk-level and multipath, the Content Centric Mobile Ad-hoc Network (CCMANET) applies the advantages of Content Centric Network (CCN) to Mobile Ad-hoc Network (MANET). The method solves the problems of low efficiency and unstable in transmission, which caused by nodes movement, dynamical changes of topology, limited node capacity, instability of wireless channel. This paper provides an overview of the existing technologies in CCMANET. Firstly, the paper introduces the basic principle and the new features of CCMANET. Secondly, the key techniques, such as caching, routing, mobility management and security are visited. From this, some important remaining challenges are raised.

Keywords: CCMANET · Content centric network · MANET
Routing · Mobility management · Security

1 Introduction

Mobile Ad-Hoc Networks (MANETs) [1] can provide efficient content sharing among mobile nodes (MNs), but there are many shortcomings that limit the application of the MANET in practice. MANETs are composed of MNs autonomous network, equipped with wireless communication interface, between nodes can communicate directly, without relying on any infrastructure. The network is particularly suitable for self-organizing mobile scenes, including battlefields, vehicular networks and disaster recovery [2, 3]. However, routing uncertainty and flexibility caused by node mobility will pose a huge challenge to MANET. At present, traditional wireless protocols and IP networks tend to perform poorly due to high mobility and compromise channels. So safe and reliable content distribution is a key challenge in a destructive environment.

Based on the traditional network, the researchers have carried out extensive research on various forms of MANET [4, 5]. However, the traditional host-based transport mechanism limits the mobility management of the supporting nodes.

As most of the MANET applications are “content-centric” information sharing, such as picture, video, etc., don’t care about the content hosted in which node and provided by which node. Therefore, the content delivery efficiency of the MANET is expected to be improved effectively by using content-centric routing protocol than using host-centric TCP/IP routing protocol. To validate, some researchers [6–8] have used the idea of content centric network (CCN) to MANNET, and proved that the method is a reasonable and effective.

CCN as a network example [9], its purpose is to allow content and services such as access and transmission of resources to become the basic driving force of network design. CCN uses the content name as the address instead of the IP-based host address. It publishes the content request primarily by broadcasting, including the interest grouping (IntPs) of the name of the requested content. Its IntPs is the node with the data, through the intermediate node to the sender of the request to send data packets (DatPs). The requesting node is able to receive multiple answers and select the “best” answer. Each node used to transfer data is able to cache data for the same local request. The local cache distributes the same content across multiple nodes, so the requesting node can retrieve the content from multiple nodes and select the best node to transmit the data. This basic paradigm “decouples” the resources with the hosts on which it resides, enabling the network to efficiently locate and deliver the resources requested by the endpoint.

Reference [10] investigated ad-hoc networking via CCN, and the authors of [8] designed a video sharing system of Smartphone over content-centric networks, their results demonstrate that the CCMANET is stable and reduce traffic overhead. In order to improve the performance of CCMANET, a lot of researches about the caching, routing, mobility management and security have been carried on. Moreover, in [11], the CCN was introduced into the military network and emergency MANETs. Experimental results, CCN can provide simple content search and system delivery in battlefield and first aid situations.

The main purpose of this paper is to overview of the CCMANET. The basic structure of the rest is as follows. Section 2 mainly introduces the basic principle and characteristics of CCMANET. Section 3 visits the key techniques of CCMANET. Section 4 presents several challenging research directions in this subject, and finally Sect. 5 concludes this paper.

2 CCMANET: Content Centric MANET

In this section, we review the general concept of CCN, and introduce the principle and features of CCMANET.

2.1 Content Centric Network

In the CCN, each node maintains three data structures, including content storage (CS), forwarding information base (FIB), and pending interest table (PIT). When a node needs content, it only broadcasts a request packet, called the Interest package, which contains the content name. When a node receives an Interest, it first searches for the

contents of the locally cached content of the CS content and matches the content. If it is found, which will send a DatP as a reply. Otherwise, PIT try to see if the pending request is waiting for the same content by matching. If a match is found, the new interface identifier is included in the PIT. When a DatP is received, it will be sent on all node interfaces with entries in the PIT. If both CS and PIT can't match, the node will search in FIB. If a match is complete, the node appends a new entry to PIT and forwards the interest. Data forwarding is simple; the packet follows the interest chain to return to the original requester. Each node that transmits data performs data caching later for the same local request.

CCN mainly through the host from the separation of resources, and focus on data transfer rather than end-to-end coverage. Because of this innovative concept, CCNs are expected to benefit from efficient MANETs retrieval and generate new interest.

2.2 Basic Principle of CCMANET

In CCMANET, if the node is interested in its contents, the node will broadcast IntPs to all its neighbor nodes, as illustrated in Fig. 1, step ①. The name of the content is included in the IntP.

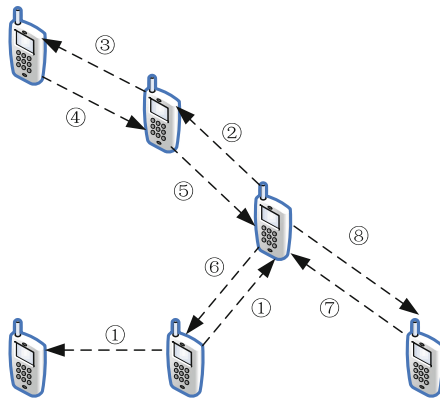


Fig. 1. CCMANET overview

Any node that receives IntP does the following: (1) To send the DatP and discard the IntP, if the content is in the Content Store; (2) To discard the IntP, if IntP has been seen; (3) If you do not see IntP, IntP adds an invisible entry to the PIT and forwards the interest to the neighbor node (steps ②–③).

When a node receives the interest, any content node that contains its content store will issue a DatP with a name that matches the name in IntP. DatP is forwarded to the node of interest (step ④).

Any node that receives DatP will follow the following behavior: (1) The DatP is relayed to the interface of the upstream node according to the DatP content name (steps ⑤–⑥) on the PIT. If you are interested in forwarding DatP, delete interest in PIT.

(2) According to the cache strategy, decide whether to cache or cache the contents of the Content Store. If the cache is available, the subsequent request for the same object can be answered from the node (as shown in steps ⑦–⑧, as shown in Fig. 1).

2.3 New Features of CCMANET

CCN can provide some benefits for MANETs, and is a host-centered effective alternative to the Internet paradigm, but this will not be conducive to the dynamic nature of the mobile environment. In CCMANET, the mobile node can communicate according to its own required data, rather than calculating a specific path for a particular node. This greatly simplifies the implementation of CCMANET, and has the following new features.

First, the CCN paradigm eliminates the need to assign an IP address or identifier to each node; the node can transfer Interests and DatPs to each other through the application data name. Static configuration is not possible because nodes such as node mobility and Mobile IP are unsatisfactory [12]. Therefore, the CCN paradigm is very useful in dynamic environments.

Second, there is no routing loop for this data name-based design, so IntPs can forward multiple routes to multiple data paths; by analyzing the requested data in multiple directions, the node can evaluate which path gives Out of the best performance, and only to the future direction of interest to send the same interest. This multi-path approach eliminates the critical dependency on a single path that is pre-computed, and the routing update and routing state consistency between all nodes are not critical.

Third, in-network caching and cache fragments of application data techniques can be match the nature of MANET. For MANET, in the mobile environment, the traditional cache method can't meet all condition that the stability of the routing path and the byte cache node to obtain the exact path to follow the packet. Therefore they can't work properly. On the contrary, in the CCN, even if the path is neither stable nor predictable, CCN can also be implemented cache. In view of the uniqueness of the identity of the content, if the other node requests it, it can also be reused and can be cached in any node that forwards it.

Finally, the CCN itself can support asynchronous data exchange between end nodes. When internal caching data is used, the mobile node can be used as a link between the disconnected areas, and can be communicated even in the case of intermittent connections.

3 Overview Existing Key Technologies of CCMANET

Extending the CCN paradigm to MANETs will mainly lead to scalability and mobility-related issues, so these issues must be properly addressed. Therefore, many investigators have done some researches on the key technologies of CCMANET and acquired many novel accomplishments. In this section, we will anatomize and conclude researching achievement in the way, so as to impel the relative research to be in deeper development.

The CCMANET mainly includes the following 4 technologies. The purpose and characteristics of each technology are as follows in Table 1.

Table 1. Purpose and characteristics of the four technologies

Technology	Purpose	Present situation and characteristics
Caching	The CCMANET is to provide efficient content retrieval to mobile nodes without the support of any communication infrastructure. As a result, efficient caching schemes in CCMANET are of significant interests	Combining CCN with MANET is one of the keys to CCMANET. Because CCN and MANET can't use caching schemes in CCMANET, this also poses new challenges for CCMANET's caching solution
Routing	In the CCN, when the node chooses an interface to broadcast IntP, the corresponding DatP follows IntP's bread-traces and returns to the data consumer. Therefore, the CCMANET efficient forwarding design is of great significance	In CCMANET, one challenge is that torrents will cause additional bandwidth and power consumption; another challenge is the caching of clips. In a typical MANET deployment, a node uses only one interface, and the interface selective design causes all nodes to flood all of the IntPs it receives. At the same time there is no predictability of IntP destination connectivity and block completion status, so the existing single-path routing algorithm will continue to find the first location to send data packets, and ultimately may lead to most of the IntP re-overflow
Mobility management	To assess the effects of the node mobility of CCMANET	The mobility of the source node (SN) and the client node (CN) is the two main mobility types of CCMANET
Security	The CCMANET mainly through its unique name to protect the content itself, in other words to ensure that it claims a content item. Therefore, CCMANET for the application of security issues, mainly from the content of the manufacturer's trust and data integrity of the two aspects to consider	Theoretical analysis, any node has the ability to publish a service content, resulting in the existence of malicious node manipulation routing. Obviously, because this approach can require nodes to expose their interest to the network, so it can introduce privacy challenges. If a third party is able to map identifiers to possible common content items, it may cause serious damage to the user's privacy. In addition, there are other routing-related security issues that have not yet been fully explored

3.1 Caching Technology

The present situation and characteristics of caching schemes made new challenges, such as, no center, self-organized, name-centric routing, multi-path transmission and in-network caching. In [10], the NDN (aka CCN) is introduced to improve the validity and efficiency of MANET, and it is shown that NDN is a new research direction of ad hoc network. However, the basic caching algorithm used in this article, and through the content stored in the CCN to cache all the content passed. If this design function was used in MANETs, it will bring too much duplicate content to the network.

In order to reduce the redundancy of contents in networks, Zeng introduced a parameter, data interval, in DatP [13]. The value at which the node holding the content sends data is set to the data interval, which determines the cache interval of the data forwarding path. When the DatP is forwarded by the intermediate node, the value of the data interval is decremented by one. If the data interval is equal to 0, the contents are cached in the node's content store and the data interval is reset. If the data interval is not 0, the DatP will be relayed immediately. Experiments show that the network with cache design can improve the performance, and the performance of the proposed cache strategy is always superior to the traditional Ad-hoc On-demand distance vector (AODV).

Different from the above research, the literature [14] mainly focused on how to improve the performance of content replacement, and through the use of named data to provide maximum content delivery information, and proposed a cache replacement strategy, the strategy can not only identify the content popularity and also consider the overlap of information, more suitable for MANET.

3.2 Routing Technology

A single physical node usually holds a complete data object, and the cache typically retains only some data objects. Based on Listen First & Broadcast Later (LFBL), a non-topology-independent data center forwarding protocol for wireless ad hoc networks is proposed [15]. Where the consumer decides the flood content request and the intermediate node eavesdropping the packet to find out if they qualify for the transponder. The receiver maintains the minimum state quantity in each node to perform all forwarding decisions. In order to avoid collisions, the data exchange phase should follow the distance-based forwarding rules. Experimental results show that LFBL is superior to AODV protocol in highly dynamic environment.

The NAIF is an NDM forwarding protocol [16], which aims to reduce the high overhead of CCMANET routing design. In general, NAIF and NDNF are compatible with all relevant relays, while LFBL implicitly selects the path between the consumer and the data holder. By evaluating the performance of NAIF as well as the existing CCMANET routing mechanism for NDNF and LFBL. Experiments show that in the multi-consumer data retrieval program, NDNF and NAIF completion rate higher than LFBL 30–60%. In both simulation and simulation, both NDNF and NAIF can reduce bandwidth usage by as much as 54%, keep the average response time and completion time close. Thus, NAIF can reload the data service as a starting point based on the name forwarding method and design reliable naming data MANET.

Although above mentioned researchers have proposed different routing technologies for MANETs, seldom system exploits them. Therefore, Yao et al. have implemented a wireless ad-hoc content-centric network over smartphone and proposed a loop-free name-based routing protocol [8]. Several smartphones are connected through free Wi-Fi interface, and share their video and Internet resources. Data are exchanged by name, not by IP again. The experimental results demonstrated that the wireless ad-hoc content-centric network performs better than IP-based protocol, and is very suitable in wireless ad-hoc networks.

3.3 Mobility Management Technology

The mobility of the source node (SN) and the mobility of the client node (CN) are two mobile types of CCMANET. For static grid topologies, Alfano and Garetto have set up an ad-hoc networks with asymptotic delay-throughput trade-off based on content-centric scenarios [17]. Experiments show that the mobility of the system often leads to the decline of system performance, and the content of the characteristics of the popularity of the system performance has an important impact.

3.3.1 The Source Node (SN) Mobility

The SN mobility has brought many problems, such as frequent routing updates and low routing aggregation. In other words, the speed of the routing of all related content routers is very slow due to the mobility of the content source. In order to decrease the adverse effect on the system performance from the SN mobility, [18] proposed a mobility management scheme based on a partially extended route update method. In the CCN environment, this method is used in mobile consumer devices with content data, which can reduce the number of routing table entries and network convergence time. The operation of the partial path expansion (PPx) scheme consists of three steps: movement indication, path extension and path update & revocation.

3.3.2 The Client Node (CN) Mobility

The CN mobility led to the DatPs cannot be relayed to the CN since the SN or other intermediate nodes have no idea about the movement of the CN. To receive the content, the CN has to send the Interest again from the new location. This incurs huge control overhead for the network and delay experienced by the CN as the Interests need to be retransmitted again every time the CN changes its location. To solve the problem, there have been few schemes such as the Proxy-based mobility management [19], flow mobility management architecture [20], tunnel-based routing architecture [21] and architectures for solving the mobility issues in mobile ad-hoc networks for smart phones [20] and in the emergency networks [11].

In the proxy-based scheme [19], a fixed physical proxy is configured as an overlay architecture over IP networks. This scheme maintains the overall working of CCN limited between mobile nodes and physical proxies while the communication between the proxies is carried out using the normal Internet architecture. In [20], the flow mobility management architecture on Proxy Mobile Internet Protocol (PMIPv6) has been proposed. The architecture used physical mapping agent to solve the CN mobility issue. This scheme is cost inefficient like proxy-based scheme with regard to extra

physical mapping agents and could also have some memory issues. Tunnel based routing scheme [21] outperforms the basic CCN in terms of control overhead, hit ratio and content delivery time. This scheme tunnels the interest and data between the old and new CN location. This scheme has triangular routing issues which have not been catered yet.

3.4 Security Technology

Currently, existing security schemes [22] have been considered inefficient, unavailable, and difficult to deploy, such as in public key encryption, PKI, and mobile application scenarios. In particular, PKI services are not available in applications where there is no infrastructure for in-vehicle networks. So CCMANET requires a more practical and flexible mechanism, and can verify the relationship between the public-key binding and the identity of the user.

In [23], the SECON of introducing CR and CRS was established. The function of CRS includes not only support the content cache, intentional resolution and forwarding of content-centric networks, but also supports descriptions of metadata from different data patterns, translations, and other interesting names that CRS can't perform. In SECON, users provide content-centric security solutions by using peer-to-peer exchange of information. Where the data owners can share encrypted published data items with others without having to predict which potential users are interested. And the proposed architecture supports several features, including secure intentional naming of messages, content announcements, and retrieval.

In [24], a security scheme based on social networks is proposed, which is used to solve the problem of the authenticity and integrity of network applications centered on mobile information. In a reliable social network, it allows the requester to verify the identity of the content creator and the public-key binding relationship through identity binding retrieval. The program has been validated on small-scale artificial networks and has demonstrated scalability in large real life social networks.

4 Challenges and Open Questions

Because of the limited space of the article, some important topics such as naming rules, name look up and CCMANET applications. Related reference may be made to other relevant literature, e.g. [25].

At present, there are still some challenges and open issues in achieving reliable and efficient content sharing for CCMANET, such as the following aspects.

- Topology control. The dynamically changing topology is one of the most significant features of MANET, which has an important impact on the performance of the network. But there is no relevant public coverage for the relationship between topologies and CCMANET performance. Therefore, there is an urgent need to study the impact of topology on CCMANET performance and design topology control mechanisms to optimize network performance.

- Joint caching and routing. Usually, caching and routing are designed independently, because caching primarily decides whether to cache resources, and routing is primarily improved by improving the network performance based on the identified resources and replicas. However, there are two aspects of the inevitable coupling. For example, under different caching algorithms, the same routing algorithm may show significant differences, and vice versa. In addition, in the future, the integrated design of multipath routing and co-caching is a challenging issue in CCMANET.
- True opportunities and economy models. It is important that the economic and engineering benefits of traditional MANET were quantified using CCN. In addition, the need to develop the underlying network economic model to meet the business community on the CCMANET comfort needs.

5 Conclusion

At present, the study of CCMANET field shows explosive growth, this article is difficult to cover all related issues. Therefore, in this paper, we have a systematic summary of CCMANET, and focus on the basic principles, new features, key technologies and remaining challenges. This will provide a complete understanding of CCMANET for researchers and practitioners.

Acknowledgements. This work was supported by the Foundation for National Key R&D Program of China plan under Grant 2016YFC0801800.

References

1. Conti, M., Giordano, S.: Mobile ad hoc networking: milestones, challenges, and new research directions. *IEEE Commun. Mag.* **52**(1), 85–96 (2014)
2. Chandravanshi, K., Mishra, D.K.: Minimization of routing overhead on the bases of multipath and destination distance estimation mechanism under MANET. *IEEE Commun. Mag.* **46**(11), 55–61 (2017)
3. Tran, T.X., Hajisami, A., Pandey, P., et al.: Collaborative mobile edge computing in 5G networks: new paradigms, scenarios, and challenges. *IEEE Commun. Mag.* **55**(4), 54–61 (2017)
4. Chen, K., Shen, H., Zhang, H.: Leveraging social networks for P2P content-based file sharing in disconnected MANETs. *IEEE Trans. Mob. Comput.* **13**(2), 235–249 (2014)
5. Singal, G., Laxmi, V., Gaur, M.S., et al.: Moralism: mobility prediction with link stability based multicast routing protocol in MANETs. *Wirel. Netw.* **23**(3), 663–679 (2017)
6. Vijayalakshmi, M., Sreenivasarao, D.: Dynamic quality of service stability based multicast routing protocol for MANETs (DQSMRP). In: *International Conference on Computer Science, Information Technology and Applications*, pp. 159–173 (2017)
7. Li, B., Ma, M., Yang, X.: Perceptive forwarding in content-centric networks. *IEEE Access* **99**, 1 (2017)
8. Yao, S., Zhang, X., Lao, F.: MobileCCN: wireless ad-hoc content-centric networks over smartphone. In: *Proceeding of ACM International Conference on Future Internet Technologies*, 5–7 June, pp. 1–2 (2013)

9. Bosunia, M.R., Kwon, S., Jeong, S.H.: A CCN-based multi-source and multi-path transport mechanism for wireless mobile networks. In: IEEE International Conference on Information Networking, pp. 30–34 (2017)
10. Jia, S., Xu, C., Vasilakos, A.V.: Reliability-oriented ant colony optimization-based mobile peer-to-peer VoD solution in MANETs. *Wirel. Netw.* **20**(5), 1185–1202 (2014)
11. Guo, H., Wang, X., Cheng, H., et al.: A routing defense mechanism using evolutionary game theory for Delay Tolerant Networks. *Appl. Soft Comput.* **38**, 469–476 (2016)
12. Zettervall, S.L., Lu, J., Kuang, X., et al.: IP075. Elective open abdominal aortic aneurysm repair following prior EVAR with unsatisfactory results is not associated with increased mortality or major morbidity. *J. Vasc. Surg.* **65**(6), 76S (2017)
13. Liu, S., Ölveczky, P.C., Meseguer, J.: A framework for mobile ad hoc networks in real-time maude. In: Escobar, S. (ed.) WRLA 2014. LNCS, vol. 8663, pp. 162–177. Springer, Cham (2014). https://doi.org/10.1007/978-3-319-12904-4_9
14. Yuan, M., Yang, Z., Huang, G., et al.: Feature selection by maximizing correlation information for integrated high-dimensional protein data. *Pattern Recogn. Lett.* **92**, 17–24 (2017)
15. Chen, H.L., Lou, L.: Contact expectation based routing for delay tolerant networks. *Ad Hoc Netw.* **36**, 244–257 (2016)
16. Li, S., Hu, D., Fang, W., et al.: Protocol oblivious forwarding (POF): software-defined networking with enhanced programmability. *IEEE Netw.* **31**(2), 58–66 (2017)
17. Hines, P.D.H., Dobson, I., Rezaei, P.: Cascading power outages propagate locally in an influence graph that is not the actual grid topology. *IEEE Trans. Power Syst.* **32**(2), 958–967 (2017)
18. Ren, F., Qin, Y., Zhou, H., et al.: Mobility management scheme based on software defined controller for content-centric networking. In: IEEE Computer Communications Workshops, pp. 193–198 (2016)
19. Chen, Y., Qu, Z., Rastogi, V.: System and Method for Proxy-Based Data Access Mechanism in Enterprise Mobility Management. US20170076103 (2017)
20. Guo, J., Chen, I.R., Tsai, J.J.P.: A hierarchical cloud architecture for integrated mobility, service, and trust management of service-oriented IoT systems. In: IEEE Sixth International Conference on Innovative Computing Technology, pp. 72–77 (2017)
21. Ramadza, I., Ozegovic, J., Pekic, V.: Class based tunnel exclusion router architecture. In: IEEE International Conference on Software, Telecommunications and Computer Networks, pp. 274–278 (2015)
22. Hassouna, M., Barry, B., Bashier, E.: A new level 3 trust hierarchal certificateless public key cryptography scheme in the random oracle model. *Int. J. Netw. Secur.* **19**, 551–558 (2017)
23. Wang, G.Q., Tong, W.: System and method for a context layer switch. US, US9319311 (2016)
24. Younes, E.B.E.I., Fatma, E.M., Nisrine, M.: A security approach for social networks based on honeypots. In: IEEE International Colloquium on Information Science and Technology, pp. 638–643 (2017)
25. Tan, Y., Zhu, S.: Efficient name lookup scheme based on hash and character trie in named data networking. In: IEEE Web Information System and Application Conference, pp. 130–135 (2015)



A Cooperative Broadcast Algorithm Based on the Successful Broadcasting Ratio and Residual Energy of Neighbor Nodes in Mobile Ad Hoc Networks

Yichen Deng, Yanping Yu^(✉), and Zhengqing Yan

College of Information and Electronic Engineering,
Zhejiang Gongshang University, Hangzhou 310018, China
ycdeng26@163.com, yuyanping@zjgsu.edu.cn,
1162865308@qq.com

Abstract. In order to suppress the broadcast storm, balance the energy consumption of the nodes and provide certain reliability, we propose a cooperative broadcast algorithm based on the successful broadcasting ratio and residual energy of neighbor nodes (BSRREN). In this algorithm, each node in a network calculates the broadcasting coefficient according to the successful broadcasting ratio and residual energy. Then, the broadcasting coefficient encapsulated in the broadcast packets is exchanged between neighbor nodes. Each node constructs a neighbor information table (NIT) to store the broadcasting coefficient. Each node dynamically selects up to four neighbor nodes which have the highest broadcast coefficients as the forwarding nodes. The addresses of the four forwarding nodes which are designated as the next hop forwarding nodes are encapsulated in the broadcast packet headers. The transmissions of each node are randomly delayed to reduce the probability of channel contention and message collision. The simulation results show the BSRREN algorithm has lower forwarding node ratio and higher network lifetime, which indicates the algorithm can effectively suppress broadcast storm and balance the energy consumption.

Keywords: Mobile ad hoc networks · Broadcast algorithms · Broadcast storm
Broadcast reliability · Energy balance · Successful broadcasting ratio

1 Introduction

Mobile ad hoc networks are a type of wireless communication networks which are composed of a group of mobile nodes with wireless communication transceivers. They are also called multi-hop and self-organizing networks. Broadcast is a technology by which a source node sends the same message to all nodes in a network. It is widely used in resource scheduling, transmission of network control information, route discovery and maintenance, sending alarm signals and other applications in mobile ad hoc networks.

Flooding is one of the simplest broadcasting schemes in mobile ad hoc networks. In flooding, each node transmits a broadcast packet to its neighbor node immediately

when the node receives the broadcast packet for the first time. But traditional flooding introduces a large number of redundant transmissions which is usually referred to as broadcast storm problem [1, 2]. Broadcast storm has a serious impact on network throughput, channel utilization, QoS (Quality of Service) and other network performance. Meanwhile, channel contending and packet collisions may exist during the transmissions which lead to the unreliable broadcast problem [3]. In addition, due to the limited energy of nodes, how to prolong the network lifetime is another issue that is needed to be considered [4].

Currently, most researches are focused on suppressing the broadcast storm [5]. The broadcast suppression schemes are basically classified as the probabilistic schemes, neighbor information based schemes, hybrid schemes. All of them aim to suppress the broadcast storm to certain extent. The probabilistic scheme is simple but it introduces the problem of lower coverage problem. The neighbor information based scheme is effective but complex. Some schemes need GPS (Global Positioning System) to determine the distance or location, which leads to limited applications.

Broadcast unreliability may be caused by channel contending, packet collision, channel and noise interruption. Broadcast unreliability may lead to the failure of network routing, etc. Therefore, improving broadcast reliability is essential in ad hoc networks [3]. Reliable broadcast algorithms are classified into the following categories: acknowledgment based algorithms [6], spanning tree based broadcasting (such as RMST [7]), time-division based broadcasting (such as RAPID reliable probability broadcast algorithm [8]), and hybrid reliable broadcasting.

In the mobile Ad hoc network, each node is equipped with a battery whose energy is limited. In order to prolong the lifetime of the entire network as much as possible, it is important to improve the energy efficiency. The most common strategies to prolong the network lifetime is minimizing energy consumption [4] and balancing the energy consumption [9].

The BSRN algorithm can adjust the forwarding probability of the current node in real time according to the averaged successful broadcasting ratio of the neighbor nodes [10]. The algorithm can improve the network reachability and reduce the network delay. But the strategy might cause the traffic concentrating to some nodes, which results in unevenly energy consumption of nodes and thus a shorter network lifetime. In the BSREB algorithm, a node determines its own forwarding probability according to the node's successful broadcasting ratio and the residual energy [9]. It does not need any neighbor information. The algorithm can balance the energy consumption. However, the forwarding probability is only determined by its own successful broadcasting ratio and residual energy which leads to the lower reachability of BSREB than that of BSRN. In the DP algorithm, a node dynamically adjusts its own forwarding probability according to the number of neighbors [11]. So it can mitigate the redundant retransmission. However, the forwarding probability does not associate with the load of the network. The improvement of performance in terms of reachability is limited.

In order to suppress broadcast storm, balance the energy consumption of a network and provide network reliability, a cooperative broadcast algorithm based on the successful broadcasting ratio and residual energy of neighbor nodes (BSRREN) in mobile ad hoc networks is proposed in this paper.

The rest of the paper is organized as follows: BSRREN is described in detail in Sect. 2. The simulation scenarios and simulation results are presented in Sect. 3. Section 4 concludes this paper.

2 BSRREN

In BSRREN, each node in a network needs to calculate its own broadcast coefficient is determined by the successful broadcasting ratio and the residual energy before sending a broadcast packet and encapsulate the broadcast coefficient into the broadcast packet header.

Each node in the network maintains a NIT (Neighbor Information Table) which is used to record the most recent broadcast coefficient of the neighbor nodes. After receiving a broadcast packet, a node first judges the addresses of four forwarding nodes. If its own address matches one of the addresses of the four forwarding nodes in the packet header, the node will forward the packet just received. Or, if all of the addresses of four forwarding nodes in the packet header are special addresses (254.255.255.255), the packet is forwarded according to the probability. Before sending the packet, the current node needs to select up to four next hop forwarding nodes according to the broadcast coefficients of neighbor nodes which are stored in NIT. Because the degree of usual networks is generally around four, up to four forwarding nodes are selected.

2.1 Calculation of Parameters

Take node k as an example, N_k denotes the number of packets broadcasted. Set S_k denotes the number of packets that have been successfully broadcasted. Suppose the initial value of N_k and S_k are 0. Increment N_k by one after the node k broadcasts a packet and increment S_k by one after node k sends a broadcast packet successfully. R_k denotes the successful broadcasting ratio which is initialized as $A(0 < A \leq 1)$.

$$R_k = S_k / N_k (N_k > 0, S_k \geq 0). \quad (1)$$

$R_k \in [0, 1]$, the greater the value of R_k is, the higher the reliability of the network is.

Assume the maximum energy of each node is E_{\max} . E_{kc} denotes the energy consumed by node k and E_k denotes the residual energy of node k . Then the residual energy of the node is calculated as in Eq. (2).

$$E_k = E_{\max} - E_{kc}. \quad (2)$$

Assume that the energy consumed by the node when sending a broadcast packet is E_{ks} , the energy consumed by the node when receiving a broadcast packet is E_{kr} . Then,

$$E_k = E_{\max} - (M_{ks}E_{ks} + M_{kr}E_{kr}). \quad (3)$$

Here M_{ks} is the number of the broadcast packets sent from node k . M_{kr} is the number of broadcast packets received by node k .

We set a threshold of residual energy E_{th} under which the node is not allowed to forward any packet to save energy for receiving packets.

Node k , according to the successful broadcasting ratio R_k and the residual energy E_k , calculates its own broadcast coefficient B_k as shown in Eq. (4)

$$B_k = \begin{cases} (1 - \alpha)R_k + \alpha \frac{E_k}{E_{\max}} & E_k \geq E_{th} \\ 0 & E_k < E_{th} \end{cases} \quad (4)$$

Where α is the weighting coefficient ($0 < \alpha < 1$). The smaller the value of α is, the more the forwarding probability is determined by the successful broadcasting ratio of the node, which means more attention is paid to the broadcast reliability. The greater the value of α is, the more the forwarding probability is determined by the residual energy of the node, which means more attention is paid to the energy consumption and the network lifetime.

2.2 Table Maintaining

The format of NIT is shown in Table 1. When a node receives a broadcast packet from a neighbor node, it creates a new entry in the NIT for the neighbor node if it receives a broadcast packet from this neighbor node for the first time. Otherwise, it updates the corresponding entry for the neighbor node in the NIT. Meanwhile, set the timeout in the entry for the neighbor node. The timeout is set to the initial value after the entry is established or updated. If an entry in NIT is not refreshed within the timeout period, it is not considered as the neighbor node of the current node neighbor node. Therefore, the corresponding entry is removed from the NIT.

Table 1. The format of NIT in a node

IP address (node: k)
IP address (neighbor 1: k_1)
B_{k1}
t_{k1}
IP address (neighbor 2: k_2)
B_{k2}
t_{k2}
.....

where:

IP address (current node: k): the IP address of node k ;

IP address (neighbor node: j): the IP address of the j th neighbor node of node k ;

B_{kj} : the broadcast coefficient of the j th neighbor node of node k ;

t_{kj} : the timeout of the j th neighbor node of node k .

The record table of broadcast packet received and sent is shown in Table 2.

Table 2. The record format of broadcast packet received and sent

IP address (current node: k)
IP address (source node: i)
Packet sequence number x (from source node i)
Be received (Yes or No)
Be broadcasted (Yes or No)
Be successfully broadcasted (Yes or No)
IP address (current node: m)
Packet sequence number y (from source node: m)
Be received (Yes or No)
Be broadcasted (Yes or No)
Be successfully broadcasted (Yes or No)
.....

Where,

IP address (current node: k): IP address of the current node k .

IP address (source node: i): IP address of the source node i .

Packet sequence number x (from source node i): the broadcast packet with sequence number x sent from the source node i .

Be received: whether the broadcast packet has been received, “Yes” indicates that it has been received, “No” indicates that it has not been received.

Be broadcasted: whether the broadcast packet has been broadcasted, “Yes” indicates that it has been broadcasted, “No” indicates that it has not been broadcasted.

Be successfully broadcasted: whether the broadcast packet has been successfully broadcasted, “Yes” indicates that it has been successfully broadcasted, “No” indicates that it has not been successfully broadcasted.

2.3 Sending Process of a Source Node

When the source node i receives a broadcast packet from the upper layer, it firstly determines whether there is a NIT at node i . If not, use 254.255.255.255 as the addresses of four forwarding nodes. Or, at most four neighbor nodes whose broadcasting coefficients are maximum are selected as the forwarding nodes when the number of neighbor nodes is greater than 4. Otherwise, all of neighbor nodes are selected as forwarding nodes when the number of neighbor nodes is less than or equal to 4. Then, node i calculates its own broadcast coefficient according to its successful broadcasting ratio and the residual energy. After that, node i encapsulates the source node address, the broadcast packet sequence number, the address of current node i , the broadcast coefficient of node i and addresses of four forwarding nodes. Finally, node i ends out the packet with probability 1. After that, node i updates the residual energy of

the node i , and increments the number of the packets broadcasted N_i by one, updates the record of the packets broadcasted in the table of broadcast packet received and sent.

After sending the broadcast packet, the source node adopts the retransmission mechanism when it does not receive the packet it originated to improve the reliability. Whenever the source node i sends its own broadcast packet, it initializes response time T_{ack} , which is the sum of the broadcast packet transmission time, the maximum waiting delay for forwarding and twice of the propagation delay. That the node does not receive the broadcast packet it originates within T_{ack} indicates the broadcast packet transmission is unsuccessful and it is necessary to retransmit the broadcast packet. Otherwise, the packet broadcast transmission is successful. Thus, increment the number of the broadcast packet successfully transmitted S_i by one, update the table of the broadcast packet received and sent, and record the packet which has been successfully broadcasted by the source node, stop the timer of T_{ack} . In this algorithm, the maximum retransmission number of the source node is one.

2.4 Processing Process of a Relay Node

After a relay node k receives a packet from a neighbor node j , it processes as follows.

- (1) Node k updates its own residual energy after receiving the broadcast packet from the neighbor node j .
- (2) If node k receives the broadcast packet from the neighbor node j for the first time, it extracts IP address of the upstream neighbor node and the broadcast coefficient B_j from the header of the received broadcast packet, establishes a new entry in the NIT of node k . Then, the IP address of the neighbor node, the broadcast coefficient of the neighbor node and the timeout t_{kj} are written into the new entry established, jump to (3). Otherwise, the current node updates the broadcast coefficient and the timeout t_{kj} in the corresponding entry of node j in the NIT, jump to (3). If the timeout t_{kj} expired, the entry of node j in the NIT is required to be deleted.
- (3) Comparing the IP address of the source node and the sequence number of the broadcast packet to the records in the record table of broadcast packet received and sent, judge whether the current node has received the packet. If yes, jump to (6). If not, it indicates that the current node received the packet for the first time. Then, the current node first records that the packet has been received in the record table of broadcast packet received and sent. Next, judge whether the addresses of the four forwarding nodes in the received broadcast packet header are all 254.255.255.255. If yes, node k forwards the packet with probability of 0.7. Node k uses a uniformly distributed function to generate a random number α . If $\alpha > 0.7$, discard the packet directly and jump to (8). If $\alpha < 0.7$, the node forwards the broadcast packet and then turn to (5).
- (4) If all addresses of four forwarding node in the broadcast packet header are not 254.255.255.255, node k judge whether the address of node k matches one of the four addresses. If not, discard the packet and jump to (8). If yes, continues.
- (5) Node k selects up to four neighbors as the forwarding nodes which have the maximum broadcast coefficient. If the number of neighbors is less than or equal to 4, all of these neighbors are selected as the forwarding nodes. If the number of

neighbors is greater than four, exclude the node with the broadcast coefficient which is 0, select the four neighbor nodes with the highest broadcast coefficient as the forwarding nodes from the rest of neighbors, calculate the broadcast coefficient of node k according to its own successful broadcasting ratio and residual energy, encapsulate the packet and send the broadcast packet. After that, record the packet which has been broadcasted in the record table of packet received and sent, update the number of packets broadcasted N_k and the residual energy E_k , jump to (8).

- (6) If the *broadcast* packet received has been received for more than one time, node k judges whether the broadcast packet has been broadcasted in the record table of packet received and sent. If not, it illustrates that the packet has been received but not been broadcasted. This time it is processed in the same way. So discard the packet directly, jump to (8).
- (7) If the broadcast packet has been received and broadcasted, judge whether the packet has been successfully broadcasted according to the record table of packet received and sent. If not, node k records that the packet has been successfully broadcasted in the record table of packet received and sent, increments S_k by 1, discards the packet received. If yes, node k discards the packet received.
- (8) End.

3 Simulation

3.1 The Simulation Scenario and Parameter Setting

To verify the performance of BSRREN, we conducted the simulations. BSRN, BSREB and DP are used for comparison. The simulation parameters are set as follows. A network covers an area of 1.0 km * 1.0 km. The rate of wireless interface is 11 Mb/s. Each node in the network uses IEEE802.11DCF as the MAC layer protocol. Nodes in a network are randomly evenly distributed. Each source node uses the constant bit rate (CBR) to send the broadcast packets. The size of each broadcast packet is 64 bytes, and the simulation time is 3 h. The wireless coverage of every node is 250 m. The mobility model of nodes is the random waypoint model [12]. In this simulation, the node pause time is 20 s, and the movement speed is selected from 0 to 10 m/s randomly.

Scenario 1: The value of weight coefficient α is 0.5. CBR of sources is set to 4 packets/s. The number of network nodes is 30, 60, 90, 120 and 150, respectively.

Scenario 2: All parameters are the same as those in the Scenario 2 with exception that the weight coefficient α is 0.3.

The simulations are conducted to acquire the performance in terms of ratio of forwarding nodes, network lifetime, averaged end-to-end delay and reachability.

- (1) Ratio of forwarding nodes
Ratio of forwarding nodes is defined as the ratio of the number of nodes participating in forwarding to the total number of nodes in the network during the

simulation. The lower ratio of forwarding nodes is, the lower the number of redundant transmission is, the less channel contending and the less collision have.

(2) Network lifetime

Network lifetime is the duration from the beginning of the simulation to the time when a node first depletes its energy. Assume the total energy of each node in a network is equal, and the energy consumed by each node for sending or receiving a broadcast packet is equal.

(3) Average end-to-end delay

Average end-to-end delay is the averaged delay between the time when a source node sending a broadcast packet to the time when each destination receiving the packet.

(4) Reachability

Reachability is the ratio of the number of broadcast packets actually received by all destination nodes to the number of broadcast packets that should be received by all destinations. Assume the number of nodes in the network is N , the number of the broadcast packets sent by the source node i is M , and the number of the broadcast packets received by node k is D_k . The reachability of the network is

$$REA_{aver} = \sum_{k=0 \& k \neq i}^{N-1} D_k / (M * (N - 1)). \quad (5)$$

3.2 Simulation Results and Analysis

(1) Ratio of forwarding nodes

Figure 1 shows the ratio of forwarding nodes versus the number of nodes in a network. As is seen, BSRREN and DP have better performance than BSRN and BSREB in terms of the ratio of forwarding nodes. In the BSRREN algorithm, maximum four nodes with high successful broadcasting ratio and high residual energy are selected to forward the broadcast packets. It can effectively avoid that too many nodes involve in forwarding broadcast packets. Thus, BSRREN can effectively reduce the transmission redundancy and channel contending which may lead to the broadcast storm. The DP algorithm can adjust the forwarding probability of nodes in real time according to the density of network nodes, and thus ratio of forwarding nodes is reduced.

(2) Network lifetime

Figure 2 presents the network lifetime versus the number of network nodes. From Fig. 2, we can see that the network lifetime drops down with the increase of the number of nodes in the network. The network lifetime of BSRREN is much larger than that of BSRN and BSREB and is slightly larger than that of DP. The first reason is that less energy is consumed since fewer nodes involve in forwarding. Secondly, the energy balance strategy is adopted in BERREN, which prolongs the network lifetime. Thirdly, higher successful broadcasting ratio is one of the factors when determining forwarding nodes. As a result, fewer channel contending and packet collision occur, which also leads to a longer network lifetime. Instead,

BSRN, BSREB and DP are all probabilistic algorithm. More forwarding nodes involve in forwarding. Thus they have shorter network lifetime.

(3) Average end-to-end delay

Figure 3 is the average end-to-end delay versus the number of nodes in a network. From Fig. 3, the average end-to-end delay of BSRREN is larger than that of the other three algorithms. This can be explained by observing that packets do not usually travel over the shortest path since fewer nodes are selected as the forwarding nodes in BSRREN. The other three algorithms, however, are probabilistic algorithms which are more likely to select shorter path for packet forwarding.

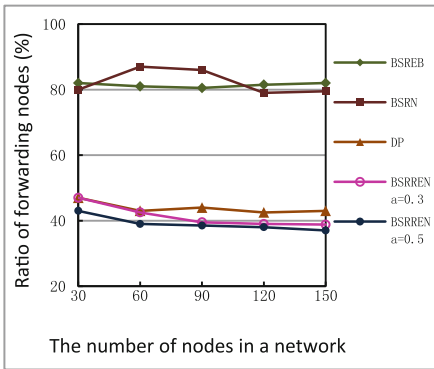


Fig. 1. Ratio of forwarding nodes versus the number of nodes in a network

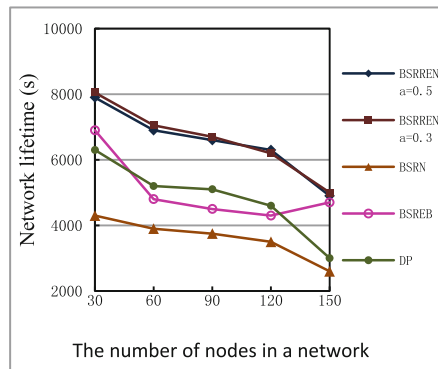


Fig. 2. Network lifetime versus the number of nodes in a network

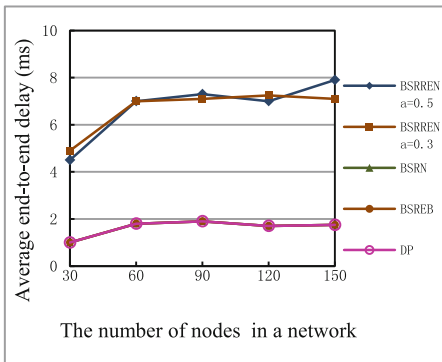


Fig. 3. Average end-to-end delay versus the number of nodes in a network

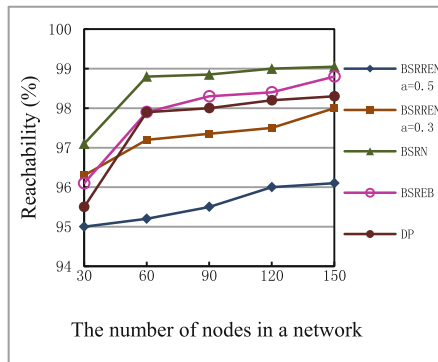


Fig. 4. Reachability versus the number of nodes in a network

(4) Reachability

Figure 4 shows the reachability of the four algorithms versus the number of nodes in a network. When α is 0.3, the reachability of BSRREN is comparable to that of BSREB, but it is still lower than that of BSRN and DP. The reason is that fewer nodes involve in forwarding in BSRREN and therefore less broadcast coverage is acquired.

4 Conclusions

In this paper, to suppress the broadcast storm, balance energy consumption and provide broadcast reliability, a cooperative broadcast algorithm based on the successful broadcasting ratio and residual energy of neighbor nodes in mobile ad hoc networks is presented. Simulation results show that BSRREN is effective to suppress broadcast storm, prolong network lifetime and provide broadcast reliability to certain extent.

Acknowledgments. The work is partially supported by The Graduate Science and Technology Innovation Project of Zhejiang Gongshang University (virtual force based cooperative broadcast algorithm in wireless ad hoc networks).

References

1. Williams, B., Camp, T.: Comparison of broadcasting techniques for mobile ad hoc networks. In: The 3rd ACM International Symposium on Mobile Ad Hoc Networking and Computing, New York, pp. 194–205 (2002)
2. Tseng, Y.C., Ni, S.Y., Chen, Y.S., Sheu, J.P.: The broadcast storm problem in a mobile ad hoc network. *Wirel. Netw.* **8**(2/3), 153–167 (2002)
3. Vollset, E., Ezhilchelvan, P.: A survey of reliable broadcast protocols for mobile ad hoc networks. Technical report CS-TR-792. University of Newcastle upon Tyne (2003)
4. Wan, P.J., Călinescu, G., Li, X.Y., Frieder, O.: Minimum-energy broadcast routing in static ad hoc wireless networks. *Wirel. Netw.* **8**, 607–617 (2002)
5. Reina, D.G., Toral, S.L., Johnson, P., Barrero, F.: A survey on probabilistic broadcast schemes for wireless ad hoc networks. *Ad Hoc Netw.* **25**(Part A), 263–292 (2015)
6. Lou, W., Wu, J.: A reliable broadcast algorithm with selected acknowledgements in mobile ad hoc network. In: IEEE Global Telecommunications Conference, vol. 6, pp. 3536–3541 (2003)
7. Lipman, J., Paul, B., Joe, C.: Reliable optimised flooding in ad hoc networks. In: Proceedings of the IEEE 6th Circuits and Systems Symposium on Emerging Technologies: Frontiers of Mobile and Wireless Communication, vol. 2, pp. 521–524 (2004)
8. Drabkin, V., Friedman, R., Kliot, G., Segal, M.: RAPID: reliable probabilistic dissemination in wireless ad-hoc networks. In: 26th IEEE International Symposium on Reliable Distributed Systems, pp. 13–22 (2007)
9. Liu, K.: Research on Broadcast Algorithm Based on Successful Broadcasting Ratio and Energy Balance of Nodes in Mobile Ad Hoc Networks. Zhejiang Gongshang University, Hangzhou, Zhejiang (2015). (in Chinese)
10. Yu, Y.: Research on Broadcast Algorithm Based on Successful Broadcasting Ratio of Neighbor Nodes. Zhejiang Gongshang University, Hangzhou, Zhejiang (2015). (in Chinese)

11. Hanashi, A.M., Siddique, A., Awan, I., Woodward, M.: Performance evaluation of dynamic probabilistic broadcasting for flooding in mobile ad hoc networks. *Simul. Model. Pract. Theory* **17**, 364–375 (2009)
12. Bettstetter, C., Resta, G., Santi, P.: The node distribution of the random waypoint mobility model for wireless ad hoc networks. *IEEE Trans. Mobile Comput.* **2**, 257–261 (2003)

Signal Processing for Communications



Joint User Association and ABS for Energy-Efficient eICIC in Heterogeneous Cellular Network

Jie Zheng¹(✉) , Ling Gao²(✉), Hai Wang¹, Jinping Niu¹, Xiaoya Li¹,
and Jie Ren¹

¹ School of Information and Technology, Northwest University, Xi'an 710127, China
jzheng@nwu.edu.cn

² Xi'an Polytechnic University and Northwest University, Xi'an 710071, China
gl@nwu.edu.cn

Abstract. In the work, we design a novel EE-eICIC algorithm to deal with determining the amount of almost blank subframes (ABS) and user should associate with pico or macro from energy efficiency perspective. Using a generalized fractional programming theory and the convex programming, we propose an iterative and relaxed-rounding algorithm to deal with the problem. Numerical experiments show that the proposed EE-eICIC method can obtain superior performance comparing with state-of-the-art algorithms in terms of energy efficiency of system.

Keywords: Energy efficiency (EE)
Enhanced inter-cell interference coordination (eICIC) · Load balancing
Heterogeneous cellular network (HetNet)

1 Introduction

The 3GPP standard has proposed the eICIC that macrocell make its down-link transmission silent in specific time frames, namely almost blank subframes (ABSs) [1]. The user associated with small cell can transmit at a higher data rate for ABSs due to much less interference.

The eICIC allocation is related with the user association, i.e., the allocation of ABS and user association rule decide the airtime resources and the allocated user to macro or pico. Most exsist works [2–4] have focused on different dynamic ABS configuration schemes for load balancing between macro cell and small cell with the dynamic variations of load. But these works almost pay more attention to improving the network throughput but neglect the energy efficiency (EE). And only ABS configuration cannot meet the need to reduce cross-tier interference significantly when the number of picocell is large [5]. The work [6] has point out that bias setting for per-tier is not efficient for EE on load balancing. It reveals that the user association for EE is quite different from that for load balancing investigated for system capacity on interference management.

Interference management together with reducing energy consumption should be considered jointly in HetNets [7]. However, the association of UE is predetermined with SINR in the downlink between macro and pico. Therefore, we propose an energy-efficient joint UE association and ABS scheme for eICIC.

2 System Model

We consider the TDD system in two-tiers HetNets, where the subframe and ABS for eICIC are configured dynamically. For the purpose of signal to interference plus noise ratio (SINR) model, we distinguish downlink association into two categories: pico-associated and macro-associated. Table 1 gives the expression of variables.

Table 1. The expression of variables

Notation	Description
$P_{Rx}(u)$	The received power of user
$P_{BS}(u)$	The received interference from BS (pico or macro)
N_{sf}	The number of ABS-period
N_m	Non-ABS subframes used by pico
A_p	ABS subframes used by pico
x_u	Airtime in non-ABS subframes for user
$y_{u,A(nA)}$	Airtime in ABS (non-ABS) subframes for user
p_u^{BS}	The transmit power of BS (macro or pico)
p_{ref}^{macro}	The broadcast signals power for macro over ABS subframes

The SINR of user associated with pico is

$$SINR_{pico}(u) = \begin{cases} \frac{P_{Rx}(u)}{P_{pico}(u) + N_0} & \text{for ABS} \\ \frac{P_{Rx}(u)}{P_{pico}(u) + P_{macro}(u) + N_0} & \text{for non-ABS} \end{cases} \quad (1)$$

The SINR of user associated with macro is

$$SINR_{macro}(u) = \frac{P_{Rx}(u)}{P_{pico}(u) + P_{macro}(u) + N_0} \text{for non-ABS} \quad (2)$$

So, we obtain the data rate for user from Shannon capacity formulation.

3 Optimization Problem Formulation

Our objective is to maximize the EE of network and still satisfies the basic rate requirements of all the users. Naturally, we jointly optimize these variables

$\psi = \{R_u, P_u, x_u, y_{u,A}, y_{u,nA}, A_p, N_m\}$ to obtain the EE-eICIC algorithm by the following optimization problem (OP1). The problem variables are denoted in Table 1.

$$\max_{\psi} \frac{\sum_u R_u}{\sum_u P_u} \quad (3)$$

$$R_u \leq r_u^{macro} \cdot x_u + r_{u,A}^{pico} \cdot y_{u,A} + r_{u,nA}^{pico} \cdot y_{u,nA} \quad (4)$$

$$P_u \leq p_u^{macro} \cdot x_u + (p_u^{pico} + P_{ref}^{macro}) \cdot y_{u,A} + p_u^{pico} \cdot y_{u,nA} \quad (5)$$

$$x_u \cdot (y_{u,A} + y_{u,nA}) = 0 \quad (6)$$

$$A_p + N_m \leq N_{sf}, \forall p, m \in I_{BS} \quad (7)$$

$$\sum_{u \in U_m} x_u \leq N_m, \forall m \in M \quad (8)$$

$$\sum_{u \in U_p} y_{u,A} \leq A_p, \forall p \in P \quad (9)$$

$$\sum_{u \in U_p} y_{u,A} + y_{u,nA} \leq N_{sf}, \forall p \in P \quad (10)$$

$$x_u \geq 0, y_{u,A} \geq 0, y_{u,nA} \geq 0 \quad (11)$$

$$A_p, N_m \leq N^+, \forall p, m \in I_{BS} \quad (12)$$

where N^+ denotes the positive integers.

The (4) and (5) state the rate and power consumption for a user is limited the airtimes obtained from macro or pico. The (6) denotes association constraint, which user only associates with either macro or pico, but not both. The (7) ensures that the ABS subframes used by pico in I_{BS} , where $I_{BS}, BS \in \{macrocell, picocell\}$ denotes that the set of basestation interfered with each other. The (8) states that airtime used by user from macro is less than the total ABS N_m . The (9) states airtime allocated to the UE from a pico is less than the total available ABS subframes A_p . The (10) states airtime allocated to the UE from a pico is less than the period of ABS N_{sf} .

Since the OP1 is a mixed integer programming problem, the solution to OP1 is generally NP-hard [8]. We solve it in a suboptimal way. The structure of (3) is exploited to reformulate with generalized fractional programming [9]. The optimization problem (OP2) can be solved in Algorithm 1 for a given η (e.g., η_k at iteration k) is

$$\begin{aligned} & \max_{\psi} (R_u - \eta P_u) \\ & \text{s.t.} \quad (4) - (12) \end{aligned} \quad (13)$$

But it is hard to solve (13) for a given η . Even with in a single pico and a single interfering macro, the OP2 problem is also NP-hard [1].

Algorithm 1. Iterative Algorithm for EE-eICIC

```

1: Set the error tolerance  $\varepsilon > 0$  and the maximum iteration number  $K_{max}$ 
2: while Stop == 0 and  $k \leq K_{max}$  do
3:   Solve the problem OP2 for a given  $\eta_{EE}^k$ 
4:   if  $|\eta_{EE}^k| = |(R_u^k - \eta_{EE}^k P_u^k)| < \varepsilon$  then
5:     Stop = 1;
6:     return the optimal EE-eICIC configuration policy  $\psi^{opt}$  and maximal  $\eta_{EE}^{opt}$ 
7:   else
8:     set  $\eta_{EE} = \frac{R_u}{P_u}$  and  $k = k + 1$ , Stop = 0.
9:   end if
10: end while

```

4 Algorithm for Nonlinear Program

In the section, we introduce two stages algorithm in polynomial time to deal with the OP2. The description is as follows in detail.

4.1 Solution for the Relaxed Problem OP3

Firstly, we solve the relaxed problem OP3 from OP2. The OP3 is computed by ignoring the constraints (6) and relaxing the (12) on N_m and A_p into positive real numbers. The OP3 can be denoted as:

$$\begin{aligned}
 & \max_{\psi} R_u - \eta P_u \\
 & \text{s.t.} \quad (4) - (5) \text{ and } (7) - (11) \\
 & \quad A_p, N_m \in R^+, \forall p, m \in I_{BS}
 \end{aligned} \tag{14}$$

where R^+ denotes the positive real numbers. The relaxed OP3 is a convex programming, so we introduce the CVX tools [10] to solve the OP3, which is defined as Algorithm 2. Algorithm 2: CVX with (14).

4.2 Interger Rounding the Result of Algorithm 2

To get the feasible solution of N_m and A_p for OP2, we adopt the rounding method:

$$Rnd(x) = \begin{cases} \text{floor}(x) & x < \frac{N_{sf}}{2} \\ \text{ceil}(x) & x \geq \frac{N_{sf}}{2} \end{cases} \tag{15}$$

where floor is round down and ceil is round up. The rounding and EE-association scheme are shown in Algorithm 3.

5 Numerical Results

For the purpose of this study, Tx power of macros and pico are set to 36 dBm and 30 dBm, and the broadcast signals power from macro in ABS is set to 23 dBm.

Algorithm 3. The rounding and association Algorithm

- 1: *EE-ABS Rounding*: To make N_m^* and A_p^* integer values. $N_m^* = \text{Rnd}(N_m')$ and $A_p^* = \text{Rnd}(A_p')$, where N_m' and A_p' are results of Algorithm 2.
- 2: *UE EE-Association for Downlink*:

$$R_u^{\text{macro}} = r_u^{\text{macro}} \cdot \tilde{x}_u, P_u^{\text{macro}} = p_u^{\text{macro}} \cdot \tilde{x}_u \quad (16)$$

$$R_u^{\text{pico}} = r_{u,A}^{\text{pico}} \cdot \tilde{y}_{u,A} + r_{u,nA}^{\text{pico}} \cdot \tilde{y}_{u,nA}, P_u^{\text{pico}} = (p_u^{\text{pico}} + P_{\text{ref}}^{\text{macro}}) \cdot \tilde{y}_{u,A} + p_u^{\text{pico}} \cdot \tilde{y}_{u,nA} \quad (17)$$

where $\tilde{x}_u, \tilde{y}_{u,A}, \tilde{y}_{u,nA}$ is output of Algorithm 2. Computing $\eta_u^{\text{pico}} = \frac{R_u^{\text{pico}}}{P_u^{\text{pico}}}$, $\eta_u^{\text{macro}} = \frac{R_u^{\text{macro}}}{P_u^{\text{macro}}}$. If $\eta_u^{\text{macro}} > \eta_u^{\text{pico}}$, user can connect with macro, or with pico.

- 3: *Energy-Efficient Computation*:

For each user, calculate the time scale of frame

$$\hat{x}_u = \frac{\tilde{x}_u \cdot N_m^*}{X_m}, \hat{y}_{u,A} = \frac{\tilde{y}_{u,A} \cdot A_p^*}{Y_{p,A}}, \hat{y}_{u,nA} = \frac{\tilde{y}_{u,nA} \cdot (N_{sf} - A_p^*)}{Y_{p,nA}} \quad (18)$$

Finally, the rate and power consumption of user are computed in macrocell or picocell. For $u \in U_m^*$, $R_u^* = r_u^{\text{macro}} \cdot \hat{x}_u$, $P_u^* = p_u^{\text{macro}} \cdot \hat{x}_u$. For $u \in U_p^*$, $R_u^* = r_{u,A}^{\text{pico}} \cdot \hat{y}_{u,A} + r_{u,nA}^{\text{pico}} \cdot \hat{y}_{u,nA}$, $P_u^* = (p_u^{\text{pico}} + P_{\text{ref}}^{\text{macro}}) \cdot \hat{y}_{u,A} + p_u^{\text{pico}} \cdot \hat{y}_{u,nA}$. So the EE of user: $\eta_u^* = \frac{R_u^*}{P_u^*}$.

For comparison, three methods we use are as follows: (1) Max sum rate with eICIC (MaxSUMRate) [11], (2) Max log rate with eICIC (MaxSUMlogRate) [1], (3) Proposed method Max EE with eICIC (MaxEE).

In Fig. 1, we plot the convergence evolution of the overall convergence rate of EE-eICIC Algorithm under the system of one macrocell, two picocells and thirty users. It is observed that it converges typically in ten steps.

Figure 2 shows the effect of the number of users on energy efficiency of system, with the number of macro is 1 and the number pico is 2. In Fig. 3, it is shown that MaxEE achieves significant energy efficiency gain over MaxSUMlogRate and MaxSUMRate. The proposed scheme MaxEE is improve the energy efficiency gain average by 21.4% and 43.6%, compared to MaxSUMRate and

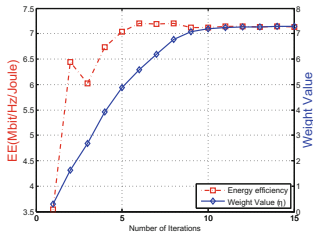


Fig. 1. Convergence of EE-eICIC algorithm

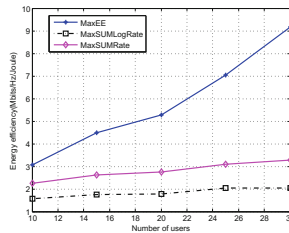


Fig. 2. Energy efficiency vs. users

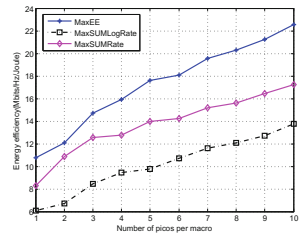


Fig. 3. Energy efficiency vs. picos

MaxSUMlogRate respectively. We can see that the eICIC need to be design from energy efficiency perspective.

In Fig. 3, we can see that the proposed MaxEE obtains the best EE performance, which has the EE gain by about 23.44% and 64.71% over the MaxSUM-Rate and MaxSUMlogRate on average. Moreover, the EE gain increases with the number of picos, which mean that the small cell is energy efficiency for HetNets.

6 Conclusion

In the work, we have formulated a novel framework for EE-eICIC in HetNet. To deal with this mixed-integer fractional programming problem, an iterative algorithm is proposed firstly by using fractional programming theory. And then we solve the problem through simplifying the UEs association and ABS allocation in a two-step relaxed-round algorithm to reduce the computational complexity. Our numerical results show that the energy efficiency of joint UEs association and ABS allocation can obtain a significant gain on energy efficiency of system.

Acknowledgement. This work was supported in part by the National Natural Science Foundation of China (Grants nos. 61701400, 61672426, 61501372, 61572401, 41601353), by the Postdoctoral Foundation of China (Grants nos. 2017M613188 and 2017M613186), by the Natural Science Special Foundation of Shaanxi (Grant nos. 2017JQ6052, 2017JQ4003 and 17JK0783).

References

1. Deb, S., Monogioudis, P., Miernik, J., Seymour, J.P.: Algorithms for enhanced inter-cell interference coordination (eICIC) in LTE HetNets. *IEEE/ACM Trans. Netw.* **22**, 137–150 (2014)
2. Cierny, M., Wang, H., Wichman, R., Ding, Z., Wijting, C.: On number of almost blank subframes in heterogeneous cellular networks. *IEEE Trans. Wirel. Commun.* **12**(10), 5061–5073 (2013)
3. Vasudevan, S., Pupala, R.N., Sivanesan, K.: Dynamic eICIC - a proactive strategy for improving spectral efficiencies of heterogeneous LTE cellular networks by leveraging user mobility and traffic dynamics. *IEEE Trans. Wirel. Commun.* **12**(10), 4956–4969 (2013)
4. Zhou, H., Ji, Y., Wang, X., Yamada, S.: Joint spectrum sharing and ABS adaptation for network virtualization in heterogeneous cellular networks. In: *IEEE Global Communications Conference*, pp. 1–6. IEEE Press (2014)
5. Mei, W., Hailun, X., Chunyan, F.: Joint eICIC and dynamic point blanking for energy-efficiency in heterogeneous network. In: *International Conference on Wireless Communications Signal Processing*, pp. 1–6. IEEE Press (2015)
6. Kuang, Q., Utschick, W.: Energy management in heterogeneous networks with cell activation, user association, and interference coordination. *IEEE Trans. Wirel. Commun.* **15**(6), 3868–3879 (2016)
7. Chungang, Y., Jiandong, L., Qiang, N., Alagan, A., Mohsen, G.: Interference-aware energy efficiency maximization in 5G ultra-dense networks. *IEEE Trans. Commun.* **65**(2), 728–739 (2017)

8. Vanderbei, R.J.: *Linear Programming: Foundations and Extensions*, 3rd edn. Springer, Heidelberg (2008). <https://doi.org/10.1007/978-1-4614-7630-6>
9. Crouzeix, J.P., Ferland, J.A.: Algorithms for generalized fractional programming. *Math. Program.* **52**(2), 191–207 (1991)
10. Grant, B., Boyd, S.: CVX: Matlab software for disciplined convex programming, Stanford, April 2011. <http://cvxr.com/cvx/>
11. Ye, Q., Alshalashy, M., Caramanis, C., Andrews, J.G.: On/off macrocells and load balancing in heterogeneous cellular networks. In: *Proceedings IEEE Globecom*, pp. 3814–3819. IEEE Press (2013)



Transmissions and Network Management of Multiple 100 GB/s Based on Stacking Technology

Xin Huang^{1(✉)}, Kaixiong Zhou¹, Chaoxiang Shi¹, Jianxin Chang²,
and Meng Gao²

¹ School of Communication and Information Engineering,
Chongqing University of Posts and Telecommunications, Chongqing 400065, China
hsjcn666@163.com, zhoukaixiong1992@163.com, shicx@cqupt.edu.cn

² CNMP Networks, Inc., Beijing, China
jxchang@cnmpnetworks.net, mgao@cnmpnetworks.net

Abstract. We have previously proposed and implemented a small form factor and low cost 100G optical transmission system using inverse-multiplexing technology and MLD (Multiplex-Lane Distribution) mechanism [1]. Based on this 100G system, we will further implement a transmission and network management system for multiple 100G application via stacking technology. This technology can incrementally realize the standard 100G OTN or 100G Ethernet capacity expansion with a centralized network element management at one node. The stacking system contains both network management port stacking and optical wavelength stacking. Our test results show that we can stack at least four devices with stable performance, which means a maximum transmission capacity of 400G, but with one IP address or one NE (network element) network management. This technology has a significant advantage comparing with a large rack equipment in term of device cost and flexible 100G bandwidth addition, as well as simple management function.

Keywords: 100G · Multiple 100G · Stacking · Capacity expansion
Network element management

1 Introduction

In recent years, with the advent and popularity of broadband services of the terminal users, such as 4G/5G services, Internet video, high-quality Internet Protocol TV (IPTV), cloud computing, big data, etc., the demands of bandwidth in data networks are showing the scale of exponential growth, which drives the development of high-capacity optical transmission network. Data center switch and router are upgrading to 100GbE interfaces, and the mainstream transmission equipment has developed to single-wavelength 100G capacity from 10G due to the bottleneck of 10G networks. As the support network, the transmission

network is entering an accelerating era of 100G or beyond 100G. On current projections, the transmission capacity of metropolitan area network (MAN) will increase five-fold in 2017 comparing with 2012 [1, 2].

However, how to further improve the bandwidth in backbone network and achieve the access to a variety of services are forever topics. Although beyond 100G optical transmission systems have been the hot subject of recent research efforts, remaining the immature standard and some unresolved technical problems, and it will still adopt PDM (Polarization Division Multiplexed) and fast DSP technology which is not very appropriated for low-end application.

On the other hand, high-capacity optical transmission requires effective network management. A network management implementation should be capable of handling configuration, traffic, fault, alarm and security [3]. Traditionally, network element is managed independently. In the meantime, the increasing NEs (network equipment) add to pressure on network management, which will make it complicated. Therefore, it is essential to reduce the number of logical devices utilizing virtualization, through which network topology can be simplified for network management.

We have proposed and implemented a low cost 100G transmission platform which is based on Inverse-Multiplexing technology and MLD (Multiplex-Lane Distribution) mechanism [1, 4]. It is an effective low cost solution for 100GE transmission in MAN, access network, especially for data center 100G interconnection applications. In this paper, in order to support application for multiple 100G transmissions on one node and do centralized management of multiple physical devices, we further propose a novel scheme to implement multiple 100G transmissions based on stacking technology. When we do network expansion based on 100G transmission platform, it will increase complexities of OAM management due to the addition of NEs. Most communication manufactures generally manage and configure network element equipment independently, which results in a waste of IP resources and makes a complicated network management system. And this traditional method just interconnects multiple devices to increase available ports, but does not reduce the logical NEs, so it cannot simplify network structure actually [5]. To solve this problem, we propose to use virtual stacking technology to realize high port density as well as unification of equipment management for beyond 100G. It is implemented by connecting multiple 100G physical devices through physical ports of stackable subcards with switch chips, and virtualizing them into single logical equipment after some necessary software configurations. It is different from the general scheme applying to a whole beyond 100G system since it can implement multiple 100G via simpler 10G technology, and stacking is usually used among switches while rarely used on transmission devices like our proposed system. The stacking system consisting of multiple devices only has one external IP/MAC address, and there is one master device and at least one slave device in the system. These devices communicate with each other via Ethernet protocol and data packet forwarding at layer two. It is notable that implementation of stacking is consisted of network management port stacking and optical wavelength stacking.

2 Experiment Setup

2.1 100G Transmission Platform

The 100G transmission platform is a low cost, 1RU device (1.75 in. height and 19 in. width), which has the most small form factor and lowest power consumption (100 W) in the world until now [1]. The prototype picture and block diagram of 100G main board are shown in Fig. 1(a) and (b) respectively. The 100G system provides 10 wavelengths for 100GE point to point and long distance transmission. It has three EDFA slots which can be any combinations of pre-amplifier and boost amplifier, and it can also support OLP (Optical Line Protection) card, FBG (Fiber Bragg Grating) based DCM (Dispersion Compensator Module) card and Band-Filter card for stacking application. 100GE traffic from switch or router is fed into CFP module by 4×25 or 10×10 WDM optical signal. In this application, CFP module is used at client side and it converts 100GE traffic to $10 - lane \times 10.3125$ GB/s electrical CAUI interface defined by IEEE 802.3ba standard [6]. For better performance and network management, ten 10G OTN frames are designed to provide FEC and PM (Performance Monitor) function. Each lane of CAUI signal is transparently mapped into 10G OTN frame, and then sent to integrated DWDM SFP+ module for electronic to optical modulation process and long haul transmission. Through SFP+, optical signals are multiplexed into one fiber via a 10-channel DWDM MUX from the transmitter, and are de-multiplexed via DEMUX at the receiver.

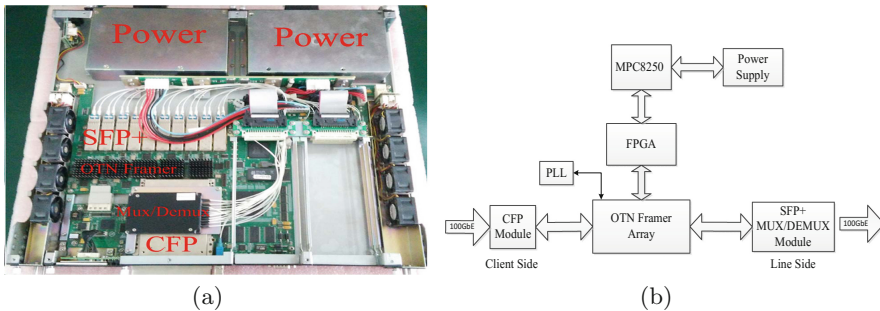


Fig. 1. (a) Prototype picture of a 100G optical transmission device; (b) Block diagram of 100G main board

2.2 Transmission System for Multiple 100G

Figure 2 shows experiment set up for multiple 100G stacking application. It is a typical structure of two devices stacking connection, in which devices link up by up/down Ethernet ports of STK subcard. We call every 100G device as a shelf. Each shelf has its already configured shelf number which is saved in flash. According to different shelf numbers, shelves in a stacking system can be divided

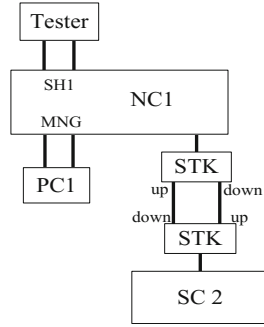


Fig. 2. Multiple 100G stacking application diagram

into NC and SC. NC is node controller and SC is a shelf controller. NC is directly operated by users which should be able to obtain necessary performance data from SC devices, and its shelf number is one. SC needs to send data to NC and its shelf number cannot be one. There is only one NC while the others are SC devices in a stacking system. In stack application in term of 100G system, the number of SC can reach three, so maximum up to 400G total stacking capacities. The stacking card STK mainly involves a highly integrated 3-port switch chip with PHYs, among which up/down ports represent stack ports, and they are physical interfaces to send or receive messages between 100G shelves. STK subcard is presented in Fig. 3.

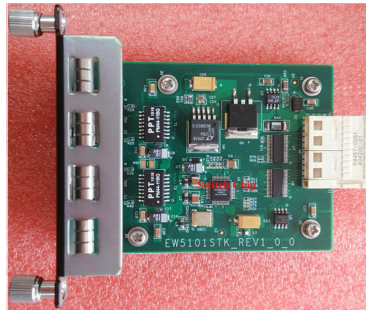


Fig. 3. STK subcard

3 Stack Application for Multiple 100G Optical Transmission System

3.1 Stack of Network Management Port

Network management port stacking refers to a method of connecting two or more physical switch chips to build a larger system that behaves as a single

logical entity. Stackable and chassis network equipment are two approaches to address high port density and unified management demands. In order to support application for more 100G signals on one node instead of adding new nodes to expand capacity, the 100G optical transmission device can stack at least 4 mini-chassis, which means it can support at least $4 \times 100\text{G}$ transmission traffic. Stack of network management port is the foremost part in the system which is realized by STK subcard.

The STK subcard has two 10/100M physical layer transceivers and three MAC units with an integrated layer 2 managed switch. On the media side, this module supports IEEE 802.3 10BASE-T and 100BASE-TX on both PHY ports. The two 10/100M management ports are used for network management stacking. STK subcards are attached to each stacking 100G mini-chassis through Ethernet interface, i.e., SMC (Simple Management Card) slot. And then connect UP port to DOWN port of each STK subcard in order, which makes software management and configuration management for each individual 100G mini-chassis flexible and easy. Figure 4 shows the application of network management port stacking.

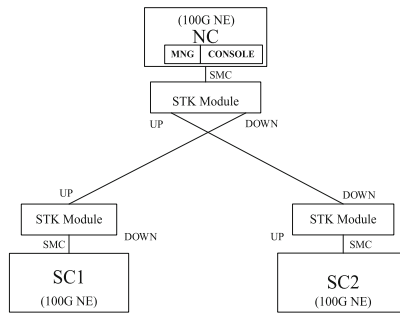


Fig. 4. Stack of network management port

In multiple 100G stacking application, the whole system has been used MPC8250 microprocessor as control unit, which provides many simultaneously available CPMs (Communication Process Module). MPC8250 has three FCCs (Fast Communication Control) and FCC1 is applied in management port stacking as the communication interface with STK. FCC supports entire Ethernet standard through MII (Media Independent Interface). In term of hardware, FCC1 is connected to SMC slot through CPLD (Complex Programmable Logic Device), and then attached to switch chip in STK module. Specific interconnection structure is shown in Fig. 5 below. The reduced media independent interface (RMII) specifies a low pin count Media Independent Interface (MII). RMII provides a common interface between physical layer and MAC layer devices. It operates in MAC mode in this connection.

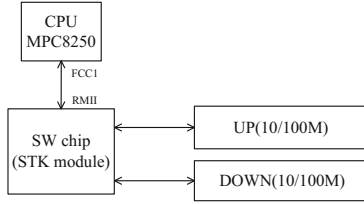


Fig. 5. Interaction between CPU and switch chip of STK

3.2 Stack of Optical Wavelength

Optical wavelength stacking is implemented by sub-band multiplexing/demultiplexing card, i.e., wavelength band filter card. The one shown in Fig. 6 supports two sub-bands stacking. Band filter card for CWDM/DWDM platform is the new type of optical wavelength stacking application. It is a small scalable device with high-density and integrated slots. It allows the wavelength to be divided into several sub-bands and can support up to four wavelength sub-bands. Hence, numbers of 100G equipment can be stacked together for the ease of network expansion purpose. The network capacity can be enhanced up to 400G. Figure 7 below summarizes the functionality of a band filter.



Fig. 6. Band filter card

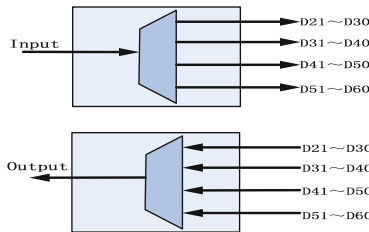


Fig. 7. Block diagram of band filter card

In example of 400G stack system shown in Fig. 8, band filter card can divide DWDM wavelengths of C band into sub-band 1 to sub-band 4, which are in accord with ITU-T G.692 [7] wavelength standard. Each sub band includes ten wavelengths and every 100G mini-chassis supports one sub-band. Therefore, four mini-chassis can be stacked to support 400G transmission. For details, at the

line side, the received stacked optical signals enter into band filter card and output into four group sub-bands. The sub bands are then sent to each individual 100G shelf respectively via output ports of band filter card. Finally, ten different optical wavelengths are split through in-built DEMUX of each 100G shelf. After two multiplexing/de-multiplexing stages, four devices are stacked in one node to support maximum 400G transmission.

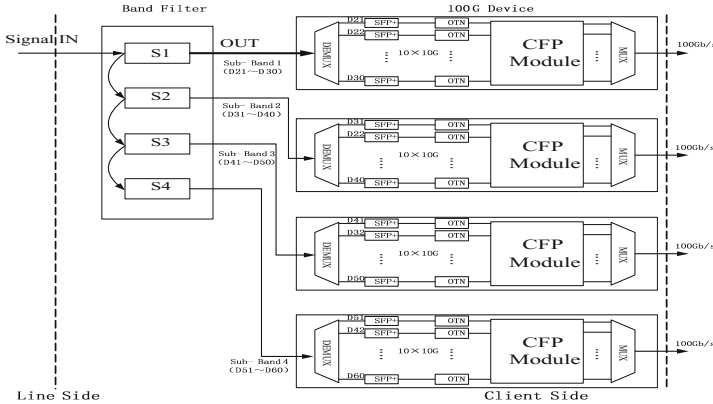


Fig. 8. Block diagram of optical wavelength stack

3.3 Experiment Results of Stack Application

Next, we test the performance of 100G system. The major parameters are receiver sensitivity and dispersion penalty, which represent system performance. Figure 9(a) uses 20 dB attenuator while (b) uses 80 km SM fiber. We can get receiver power by adjusting the variable attenuator. The BER (Bit Error Rate) polylines against to the receiver power are shown in Fig. 10. The total receiving power (receiver sensitivity) of Fig. 10(a) and (b) is about -15.76 dBm and -13.51 dBm respectively around the BER at 10^{-12} . We can see that the receiver sensitivity increases with 80 km SM fiber because of the transmission performance degradation caused by the fiber dispersion. The dispersion penalty is about 2.3 dB.

Based on the 100G BER tests above, we further test function of multiple 100G system according to stacking experiment set up shown in Fig. 2. We use a

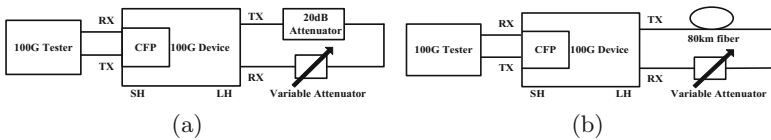


Fig. 9. (a) Line side test diagram with 20 dB attenuator; (b) Line side test diagram with 80 km fiber

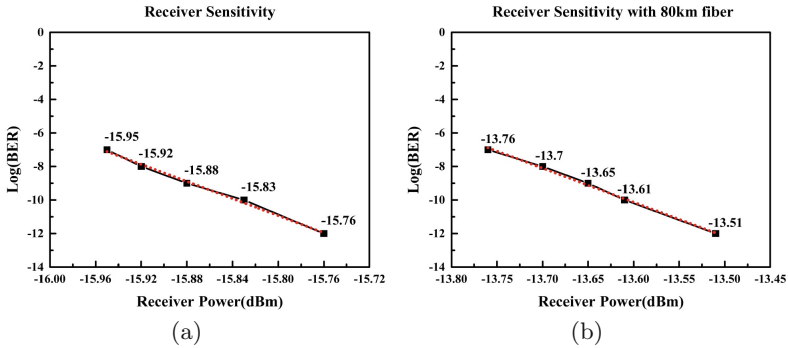


Fig. 10. (a) LH receiver sensitivity with 20 dB attenuator; (b) LH receiver sensitivity with 80 km SM fiber

PC to manage multiple shelves in the system and monitor them through console. NC can control and configure all SC devices via CLI (Command Line) of software. Moreover, console of NC show the status data of SC. The test results are presented in following Figs. 11, 12 and 13 respectively.



Fig. 11. (a) NC starting up test; (b) SC sync process with NC; (c) SC starting up test; (d) Image synchronization

Figure 11(a), (b) and (c) show NC and SC starting up process and SC sync process with NC. NC will synchronize its DB (Data Base) and RTC (Real Time Clock) information to SC when NC starts up. Figure 11(d) presents SC image upgrading process when we download a new version to NC. It clearly indicates that SC is always under the control of NC.

Figure 12(a) and (b) show shelf status of NC and SC. Figure 12(c) show the real-time display of SC by NC. The status of SC is the same as which we get from NC. This proves that NC can monitor all shelves status in stacking system.

Figure 13(a), (b) and (c) illustrate the configuration sync process from NC to SC. NC configures long haul admin of SC into disabled status, we can see the

```
*192.168.0.58:> show shelf status
<shelf/1>
Shelf status: registered
Mac address: 0001-0000-0000
Serial number:
System up time: 01:51:00
<shelf/2>
Shelf status: registered
Mac address: 0002-0000-0000
Serial number:
System up time: 01:51:00
```

(a)

```
0.0.0.0:> show shelf status
<shelf/2>
Shelf status: registered
Mac address: 0002-0000-0000
Serial number:
System up time: 01:51:00
```

(b)

```
192.168.0.178:> show linecard status
No Status Alarm Hard Type Description SN Service
-----
1/1 IS NoDetect MR VCard VCard gbe
1/2 OOS Missing O/P - - -
1/3 IS NoDetect B-EDFA oM43178B - -
1/4 IS NoDetect MR VCard VCard gbe
2/1 OOS NoConfig - - -
2/2 OOS NoConfig - - -
2/3 OOS NoConfig - - -
3/1 OOS - MR VCard - - gbe
```

(c)

Fig. 12. (a) Shelf status of NC; (b) Shelf status of SC; (c) Linecard status of NC and SC

```
*192.168.0.58:> configure interface 2/1/1 lh administration disable
*192.168.0.58:> show configuration ram
User configuration file: shM432193
Date: 2017/04/19
Time: 20:35:16
Manage Mac Address: 0000-3233-6443
West Mac Address: 0000-7738-9900
East Mac Address: 0002-3311-2211
Software Version: 1.00.12 beta29
ip manage 192.168.0.58 255.255.255.0
-Interface 2/1/1 lh administration disable-
```

(a)

```
*192.168.0.178:> show interface 2/1/1 sh
<Interface SH 2/1/1>
Alias Admin : Disable
Name :
Speed : 10g lan
Tx-sync : Disable
LLF : Disable
Mode : Disable
Normal
```

(b)

```
0.0.0.0:> show interface 2/1/1 lh
<Interface LH 2/1/1>
Admin : Disable
Alias Name :
Speed : 10g lan
Tx-sync : Disable
LLF : Disable
Mode : Normal
Service Status : OOS
Alarm : Supporting Port Disabled
```

(c)

Fig. 13. (a) NC configuring SC process; (b) Configuration result in NC; (c) Effective configuration in SC

successful information in configuration ram of NC, NC also shows the configuration result of SC, and then the command takes effect in SC to make the admin disable, which verifies effective management function of the whole system.

4 Conclusions

In this paper, we have proposed and developed a novel scheme for multiple 100G transmission applications via stacking technology, which is based on our previously proposed low cost and small form factor 100G transmission system [1, 4]. The stacking application consists of both network management stacking and optical wavelength stacking. It can support incrementally transmission capacity expansion as well as centralized management of multiple physical devices. The test results show that stacking system for multiple 100G transmissions can operate with stable performance and normal function, at least four 1RU devices can be stacked for 400G optical transmission and with one IP or one NE network management. This technology has a great device cost and size advantage comparing with a large rack equipment, and especially on its advantage with incremental cost/bandwidth addition as well as one IP or one NE with simple management function.

References

1. Yang, O., Dong, C., Liu, Q.C., Shi, C.X.: A small form factor and low cost 100 GB/s optical transmission system based on inverse-multiplexing technology. In: International Conference on Communications and Networking in China, pp. 85–89. IEEE Press, Shanghai (2015)
2. Borowiec, A.: High Capacity Transport-100G and Beyond. Invited talk, Photonics North (2015)
3. Doverspike, R.D., Yates, J.: Optical network management and control. *J. Proc. IEEE* **100**(5), 1092–1104 (2012)
4. Jia, Z., He, W., Shi, C., Chang, J., Gao, M.: Design and implementation of link loss forwarding in 100G optical transmission system. In: Chen, Q., Meng, W., Zhao, L. (eds.) *ChinaCom 2016. LNICST*, vol. 209, pp. 403–411. Springer, Cham (2018). https://doi.org/10.1007/978-3-319-66625-9_39
5. Liu, T.B., Liu, Y., Zhao, S.B.: Technical principle and application of H3C IRF. *J. Adv. Mater. Res.* **1044–1045**, 1375–1379 (2014)
6. Fu, K., Ma, Z.Q., Li, X.S.: Standard research of IEEE P802.3ba in 40 GB/s, 100 GB/s ethernet. *Opt. Commun. Technol.*, **33**(11) (2009)
7. ITU-T Recommendation G.692, Interfaces for the Optical Transport Networks (2009)



Topology-Transparent Scheduling in Mobile Ad Hoc Networks with Unidirectional Links

Yiming Liu¹✉, Zhi Fu¹, and Mao Yang²

¹ China Academy of Information and Electronics Technology,
Beijing 100041, People's Republic of China
liuyiming09@tsinghua.org.cn

² School of Electronics and Information, Northwestern Polytechnical University,
Xi'an, China

Abstract. In this paper, a novel efficient transmission scheduling algorithm for multihop mobile ad hoc networks (MANETs) with unidirectional links (ULs) is introduced. We propose an algorithm employing topology-transparent scheduling and erasure coding to support throughput guarantee over ULs in multihop MANETs. Our proposed algorithm can work over both unidirectional and bidirectional links, for both unicast and broadcast scenarios. We analytically study the performance of the proposed algorithm and achieve the maximum guaranteed throughput, for both unicast and broadcast scenarios. Simulations show that the proposed algorithm performs better than other topology-transparent algorithms over unidirectional links.

Keywords: Topology-transparent scheduling · Erasure coding
Unidirectional links

1 Introduction

Unidirectional links exist commonly in ad hoc networks for many reasons, such as heterogeneous transmission powers [14], interference, and stealth considerations [12]. Almost all medium access control (MAC) protocols do not function well over unidirectional links, due to the nonexistence of feedback links and more serious hidden terminal problem [14, 16].

Recently, many routing protocols [7, 12, 16] have been proposed to employ ULs to improve the throughput of ad hoc networks. However, there are very few efforts on channel access protocols capable of efficient and reliable data transmissions over unidirectional links.

Transmission scheduling protocols can be divided into two categories, namely, contention-based protocols and schedule-based protocols. Contention-based approaches, such as Carrier Sense Multiple Access (CSMA), are not suitable over unidirectional links, due to their dependence on feedback from the

receiver. Without the feedback from the receiver, the sender cannot decide whether packets have collided or not. In addition, Xu and Saadawi [17] have shown that contention-based approaches suffer from serious instability and unfairness issues in multi-hop MANETs. Schedule-based protocols, applying colouring theory to allocate time slots to each node such that the transmissions from these nodes are collision-free, are not suited to ad hoc networks with unidirectional links. This is because such approaches rely on handshakes among the neighbours, and only function correctly under the assumption that links are bidirectional.

Some contention-based protocols were proposed to improve the performance of conventional CSMA, by providing end-to-end feedback in the network or transport layer, but they are very complex in ad hoc networks and introduce unacceptable overhead and delay [5, 13–15]. Bao and Garcia-Luna-Aceves [1] proposed PANAMA, an algorithm which attempts to provide collision-free dynamic channel access scheduling algorithm. In PANAMA, each user generates its priority randomly and wins the contention in each time slot, if its priority is the highest among all contenders. However, it is impractical due to the following facts. First, it is assumed that each user already knows the set of its contenders, but it is difficult, if not impossible, to collect such information in mobile ad hoc networks due to the dynamic topologies and the existence of unidirectional links. Moreover, each user is assumed to know automatically the priorities of its contenders in each time slot. It cannot be implemented at all in practice, since gathering such information takes much longer than a time slot (8 ms in [1]). Even if one assumes that the aforementioned information can be collected at each time slot without any overhead, PANAMA fails to support throughput guarantee and cannot function well. When the link from the hidden terminal to the receiver is unidirectional, the hidden terminal cannot know the existence and priority value of the sender and may consider itself as having the highest priority, resulting in collisions. In addition, packets in a particular node may suffer extremely long delay when the network load is heavy, because the node may lose the contentions repeatedly.

Conventional topology-transparent scheduling algorithms [2, 3, 6, 8–10] can handle unidirectional links in mobile ad hoc networks. However, the sender does not know whether its packet can be successfully received by its neighbour(s) in a particular time slot, due to the lack of acknowledgements over unidirectional links. This implies that these algorithms are very inefficient, since each sender may have to transmit one packet repeatedly in one frame time.

In this work, we employ topology-transparent scheduling and erasure coding together to combat the nonexistence of feedback channels, implementing an efficient and reliable channel access algorithm in ad hoc networks with unidirectional links. The important features of our proposed algorithm are listed as follows:

- (1) Our algorithm is distributed, does not rely on detailed network connectivity information, and is thus adaptive to the network topology changes.

- (2) Our algorithm does not rely on the feedback from the receiver, and thus can handle unidirectional links in ad hoc networks.
- (3) Our algorithm can be applied over bidirectional links as well as unidirectional links.
- (4) Our algorithm achieves the same guaranteed throughput for both unicast and broadcast traffics.

We study the performance of our proposed algorithm analytically, and achieve the maximum guaranteed throughput of both unicast and broadcast traffics. The analytical and simulation results show that our proposed algorithm outperforms other existing algorithms over unidirectional links and achieves the same guaranteed throughput as those of other existing topology-transparent scheduling algorithms over bidirectional links.

2 System Model

2.1 Network Model

A mobile ad hoc network with unidirectional links can be represented by a directed graph $G(V, E)$, where V is the set of network nodes ($|V| = N$) and E is the set of directional links between nodes. If $(v, u) \in E$, u is an interfering neighbour of v . Note that $(v, u) \in E$ does not necessarily mean $(u, v) \in E$ in networks with unidirectional links. We define the degree of a node v , $D(v)$, as the number of interfering neighbours of v . The maximum degree D_{\max} is defined as $\max_{v \in V} d(v)$, and is assumed to be much smaller than N . In practice, the value of D_{\max} can be estimated according to the network density and heterogeneous interference ranges in the networks. We introduce a method to estimate the value of D_{\max} in the following section. Due to space limitations, the effect of inaccurate estimation of D_{\max} on the network throughput is left for future work. Hereafter, D_{\max} is assumed to remain constant, despite the fact that the network topology may change frequently [4].

Time is divided into frames, and each frame consists of equal-sized synchronized time slots. The synchronization can be achieved by using GPS or other commonly used approaches. For the transmissions over unidirectional links, acknowledgements are not available.

With the assumption that a reception failure is only resulted from transmission collisions, we can see that the transmission from Node u to Node v will be successful if and only if (1) Node v is not in the transmission mode and (2) other interfering neighbours of v are not in the transmission mode either.

2.2 Erasure Coding

According to the Singleton bound [11], we can use an $[n, k, d]$ maximum distance separable (MDS) code to protect k elements with $n-k$ redundant elements, if the minimum distance of the code, d , is set as $d = n - k + 1$. We apply Cauchy MDS

erasure code here [11]. Let $G_{k \times n} = (I_{k \times k} | C_{k \times (n-k)})$ be the generator matrix of used $[n, k, d]$ Cauchy code, where $I_{k \times k}$ is an identity matrix and $C_{k \times (n-k)}$ is a Cauchy matrix, respectively [9]. A vector \mathbf{x}_k consisting of k elements can be encoded to a vector \mathbf{y}_n consisting of n elements as follows:

$$\mathbf{y}_n = \mathbf{x}_k \mathbf{G}_{k \times n}. \quad (1)$$

The first k elements of the encoded vector \mathbf{y}_n are just the k original elements of \mathbf{x}_k , and the other $n - k$ elements of \mathbf{y}_n are encoded redundant elements.

For the decoder, given any k out of n elements of the vector \mathbf{y}_n received (denoted as \mathbf{y}_k), the original vector can be decoded successfully. Keeping the columns and the rows of the generator matrix $G_{k \times n}$ according to these k elements and deleting the other columns and rows, we thus get a $k \times k$ matrix $G'_{k \times k}$. Since the Cauchy code employed is an MDS code, $G'_{k \times k}$ is always invertible [11]. The detailed decoding is as follows:

$$\mathbf{x}_k = \mathbf{y}_k (\mathbf{G}'_{k \times k})^{-1}. \quad (2)$$

Note that even if less than k encoded elements are received, the original vector can be decoded partially. If the i -th element of the encoded vector \mathbf{y}_n , where $i = 1, 2, \dots, k$, is received successfully, the corresponding i -th element in the original vector \mathbf{x}_k can be decoded correctly, since it is equal to the i -th element of the encoded vector \mathbf{y}_n .

3 Proposed Algorithm

3.1 Frame Structure

In this paper, we consider a TDMA MANAT with unidirectional links, $G(V, E)$. We divide a frame into q subframes, and each subframe consists of p time slots. Assign each node v a unique polynomial of degree k over Galois Field $GF(p)$ (p is a prime or prime power), $f_v(x) = \sum_{i=0}^k a_i x^i \pmod{p}$, where $v \in V$, which is called as time slot assignment function (TSAF) [6]. Therefore, Node v transmits in the time slot $f_v(i)$ in Subframe i , where $i \in \{0, 1, 2, \dots, q-1\}$ [6]. Each node, thus, transmits q times in one frame time. The frame structure is shown in Fig. 1.

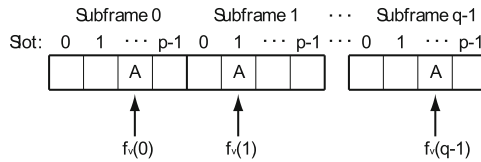


Fig. 1. The frame structure.

In order to assign a unique polynomial to each user, $p^{k+1} \geq N$ has to be satisfied. There are at most k conflicts between any two nodes during one frame if $q \leq p$ [6]. Each node has at most D_{\max} interfering neighbours. Therefore, the number of possible collisions of one node in one frame time is less than or equal to kD_{\max} . We set $q \geq kD_{\max} + 1$ to ensure that every node can have at least one collision-free time slot to transmit data to all neighbours successfully during one frame. This guarantee only depends on N and D_{\max} , despite the fact that network topology may change frequently. This is why we call it topology-transparent scheduling.

Each node encodes M queued packets in its buffer using a $[q, M, q - M + 1]$ Cauchy code and transmits the i -th encoded packet in Subframe $i - 1$, where $i = 1, 2, \dots, q$. We assume that there are always M data packets queued in the buffer at each node in every frame, for encoding and transmission. In order to ensure that all M packets are received correctly, we set $M = q - kD_{\max}$.

3.2 Estimation of the D_{\max}

D_{\max} is the most important design parameter of the proposed algorithm. The reliability and efficiency of the proposed algorithm rely on the accuracy of the estimation of D_{\max} . However, none of the previous work on topology-transparent scheduling elaborates on how to estimate the value of D_{\max} accurately, making such scheduling difficult to be implemented in practice. In this section, a method to estimate the value of D_{\max} , according to the network density and heterogeneous interference ranges in the networks, is introduced.

Suppose that an MANET with unidirectional links consists of n classes of nodes, C_i , where $i = 1, 2, \dots, n$. We assume that the nodes in each class are distributed as a two-dimensional Poisson point process with the density λ_i . The interference range of nodes in C_i is R_I^i . Let d_i be the number of interfering neighbours of a given node of Class C_i . Thus, the probability that there are y nodes interfering a given node is given as follows:

$$\Pr\left(\sum_{i=1}^n d_i = y\right) = \frac{\left[\pi \sum_{i=1}^n \lambda_i (R_I^i)^2\right]^y}{y!} e^{-\pi \sum_{i=1}^n \lambda_i (R_I^i)^2}. \quad (3)$$

Given λ_i and R_I^i , we choose D_{\max} as the smallest integer satisfying $\Pr\left(\sum_{i=1}^n d_i > D_{\max}\right) < \alpha$, where α is a given threshold. For example, when $n = 2$, $\lambda_1 = \lambda_2 = 2 \times 10^{-5} \text{ m}^{-2}$, $R_I^1 = 100 \text{ m}$, $R_I^2 = 200 \text{ m}$, and $\alpha = 0.01$, D_{\max} is estimated as $D_{\max} = 9$.

In practical, statistics and empirical data can be applied for the estimation of D_{\max} . Additionally, D_{\max} is always estimated pessimistically based on network parameters, in order to ensure that the actual number of interfering neighbours is not larger than the estimation.

3.3 Analysis of Proposed Algorithm

In the following, we analyze the guaranteed throughput of the proposed algorithm in the unicast scenario first, and then in the broadcast scenario. Note that $M = q - kD_{\max}$ collision-free slots are guaranteed within one frame time. Thus, all M packets can be received and decoded correctly within one frame time. We obtain the guaranteed throughput per node of the proposed algorithm as follows:

$$G = \frac{q - kD_{\max}}{pq}. \quad (4)$$

In order to achieve the optimal guaranteed throughput, we have Theorem 1 as follows.

Theorem 1: For given N and D_{\max} ,

- (1) Fixing p , the maximum guaranteed throughput is achieved when $q = p$.
- (2) When $N^{\frac{1}{k+1}} \geq 2kD_{\max}$, the maximum guaranteed throughput is achieved when $p = p_1$, where p_1 is the smallest prime or prime power not less than $N^{\frac{1}{k+1}}$; when $N^{\frac{1}{k+1}} < 2kD_{\max}$, the maximum guaranteed throughput is achieved when $p = p_2$, where $p_2 = \arg \max_{p \in \{p_3, p_4\}} G(p)$, p_3 is the largest prime or prime power less than $2kD_{\max}$, and p_4 is the smallest prime or prime power not less than $2kD_{\max}$.
- (3) The optimal value of k maximizing the guaranteed throughput (G) is less than or equal to $\lceil k_0 \rceil$, where k_0 is the root of $2kD_{\max} = N^{\frac{1}{k+1}}$.

Proof

- (1) Given p , we have: Noting that $q \leq p$, we conclude that the maximum guaranteed throughput is achieved when $q = p$.
- (2) In order to achieve the maximum guaranteed throughput, we have to solve the following equation:

$$\frac{\partial G}{\partial p} = \frac{\partial \frac{p - kD_{\max}}{p^2}}{\partial p} = 0. \quad (5)$$

Thus, $p = 2kD_{\max}$. Note that $p \geq \max(N^{\frac{1}{k+1}}, kD_{\max} + 1)$. If $N^{\frac{1}{k+1}} \geq 2kD_{\max}$, G decreases with increasing p , and thus the maximum value of G is obtained when $p = N^{\frac{1}{k+1}}$. If $N^{\frac{1}{k+1}} < 2kD_{\max}$, the maximum value of G is obtained when $p = 2kD_{\max}$. Recalling that p is a prime or prime power, we prove 2) of Theorem 1.

- (3) $2kD_{\max}$ increases and $N^{\frac{1}{k+1}}$ decreases with increasing k . If $k \geq \lceil k_0 \rceil$, $2kD_{\max} > N^{\frac{1}{k+1}}$. Thus, the maximum value of G is achieved when $p = 2kD_{\max}$, i.e.,

$$G_{\max} = \frac{kD_{\max}}{4k^2 D_{\max}^2} = \frac{1}{4kD_{\max}}, \quad (6)$$

which decreases with increasing k . For all $k > \lceil k_0 \rceil$, $G(k) < G(\lceil k_0 \rceil)$. This means that the optimal value of k maximizing the guaranteed throughput (G) is less than or equal to $\lceil k_0 \rceil$.

Thus, we proposed a topology-transparent scheduling algorithm with erasure coding over ULs, which achieves the maximum guaranteed throughput as follows.

- (1) For given N and D_{\max} , apply Theorem 1 to obtain the optimal k , p and q , where $q = p$.
- (2) Assign each node a unique degree- k TSAF randomly.
- (3) Calculate the TSLV of each node, according to the aforementioned method.
- (4) Each node encodes $M = q - kD_{\max}$ packets to q packets and transmits the i -th encoded packet at the selected slot in Subframe $i - 1$, where $i = 1, 2, \dots, q$.

3.4 Discussion

Considering broadcast traffic, at least $M = q - kD_{\max}$ collision-free time slots are guaranteed within one frame time for the transmission from a node to each of its neighbours. Therefore, M , out of q , packets can be received successfully and decoded by each of its neighbours within one frame time. Theorem 1 also holds for broadcast traffic. Thus, our algorithm is suitable for both unicast and broadcast traffics and achieves the same guaranteed throughput.

Our algorithm does not rely on any feedback channels. This implies that our algorithm works correctly over both unidirectional and bidirectional links. The proportion of unidirectional links does not effect the performance of the proposed algorithm.

To conclude, our algorithm is well suited over both unidirectional and bidirectional links, in both unicast and broadcast scenarios.

4 Performance Evaluation

In this section, we compare by simulations the proposed algorithm with the topology-transparent algorithm proposed in [2] (referred to as MGD) and the conventional TDMA fixed assignment scheme, both of which support guaranteed throughput over unidirectional links. We study the impact of different settings of N and D_{\max} on the maximum guaranteed throughput of our algorithm. Unlike the proposed algorithm and aforementioned algorithms, none of the contention-based protocols [5, 13, 14] and PANAMA [1] can support throughput and delay guarantees over the unidirectional links, and are therefore not included as comparisons.

4.1 Simulation Setup

We apply the Gauss-Markov mobility model, which is more realistic than the widely used Random Waypoint model. All nodes are distributed in a region of $1000 \text{ m} \times 1000 \text{ m}$, uniformly and randomly.

In order to model the existence of unidirectional links, half of N nodes are with higher transmission power, and the other half with lower transmission power. Let R_T^h and R_T^l be the transmission ranges, and R_I^h and R_I^l be the interference ranges of higher power nodes and lower power nodes, respectively. We set $r = \frac{R_T^h}{R_T^l} = \frac{R_I^h}{R_I^l} = 2$ in the simulation. In fact, our algorithm does not rely on any feedback and operation over unidirectional links such that the proportion of unidirectional links has no effect on the performance of the proposed algorithm. Thus, there are no differences in the operation and performance between the nodes with higher transmission power and lower transmission power, and the simulation results correspond to the average values of all N nodes.

We apply the optimal parameters (k and $p = q$) achieving the maximum guaranteed throughput, which are calculated according to Theorem 1. Each simulation lasts for 300 frames.

4.2 Simulation Results

1. Effect of N on Guaranteed Throughput

Given that $D_{\max} = 8$, and N is set with eight different values from 100 to 800, we study the performance of the proposed algorithm, in terms of maximum guaranteed throughput. Figure 2 shows that the proposed algorithm outperforms other algorithms, including MGD and the conventional TDMA. For the case of $N = 400$ and $D_{\max} = 8$, the guaranteed throughput of the proposed algorithm is almost six times better than that of MGD. The main reason of this superior performance is that we employ erasure coding and topology-transparent scheduling together to ensure that multiple packets rather than only one packet, as in MGD, are received and decoded successfully within a frame time, independently of the existence of the feedback channel over unidirectional links. Moreover, we can see that the performance of the proposed algorithm deteriorates with increasing N slowly, which implies that the performance of our algorithm is not very sensitive to the number of nodes in the network.

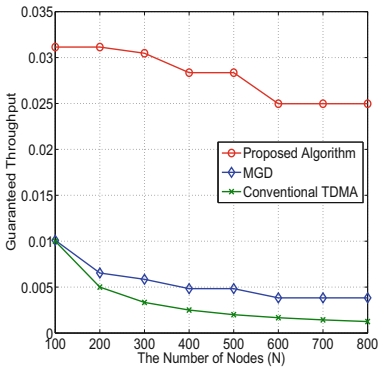


Fig. 2. The effect of N on the maximum guaranteed throughput.

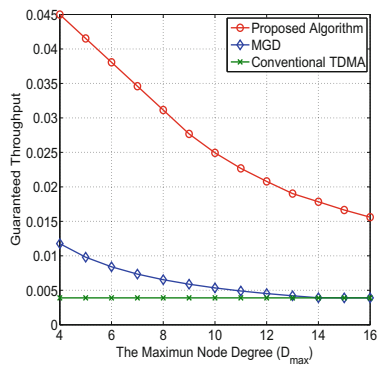


Fig. 3. The effect of D_{\max} on the maximum guaranteed throughput.

2. Effect of D_{\max} on Guaranteed Throughput

Given that $N = 256$, we study the performance of the algorithm with D_{\max} varying from six to 16. A larger D_{\max} implies a denser network and more possible collisions. As observed in Fig. 3, the proposed algorithm performs better than MGD and the conventional TDMA. The guaranteed throughput of the proposed algorithm is four times and three times better than that of MGD, for the cases of $(N = 256, D_{\max} = 4)$ and $(N = 256, D_{\max} = 16)$, respectively. Compared with Fig. 2, we can observe that D_{\max} has a much greater impact on the guaranteed throughput than N .

5 Conclusion

In this paper, we propose a way to employ topology-transparent scheduling and erasure coding together as an efficient and reliable transmission scheduling algorithm in mobile ad hoc networks with unidirectional links. Unlike other previous scheduling algorithm over unidirectional links, our algorithm does not rely on detailed network connectivity information and is adaptive to network topology changes. The proposed channel access algorithm does not rely on the existence of feedback channels, and can support guaranteed throughput for both unicast and broadcast traffics over both unidirectional and bidirectional links. We show that our algorithm performs best, compared with other algorithms supporting guaranteed throughput over unidirectional links.

Acknowledgement. This research is supported in part by the National Natural Science Foundation of China, under Grand No. 61501415.

References

1. Bao, L., Garcia-Luna-Aceves, J.J.: Channel access scheduling in ad hoc networks with unidirectional links. In: 5th ACM International Workshop on Discrete Algorithms and Methods for Mobile Computing and Communications (DIALM 2001), Rome, pp. 9–18 (2001)
2. Cai, Z., Lu, M., Georgiades, C.: Topology-transparent time division multiple access broadcast scheduling in multihop packet radio networks. *IEEE Trans. Veh. Technol.* **52**(4), 970–984 (2003)
3. Chalamatac, I., Farago, A.: Making transmission schedules immune to topology changes in multi-hop packet radio networks. *IEEE/ACM Trans. Netw.* **2**(2), 23–29 (1994)
4. Chou, A.M., Li, V.O.K.: Fair spatial TDMA channel access protocols for multihop radio networks. In: *IEEE INFOCOM 1991*, Bal Harbour, pp. 1064–1073 (1991)
5. Fujii, T., Takahashi, M., Bandai, M., Udagawa, T., Sasase, I.: An efficient MAC protocol in wireless ad hoc networks with heterogeneous power nodes. In: *IEEE WPMC 2002*, Honolulu, vol. 2, pp. 776–780 (2002)
6. Ju, J.H., Li, V.O.K.: An optimal topology-transparent scheduling method in multihop packet radio networks. *IEEE/ACM Trans. Netw.* **6**(3), 298–306 (1998)

7. Lin, C., Liu, B., Yang, H., Kao, C., Tsai, M.: Virtual-coordinate-based delivery-guaranteed routing protocol in wireless sensor networks with unidirectional links. In: IEEE INFOCOM 2008, Phoenix, pp. 351–355 (2008)
8. Liu, Y., Li, V.O.K., Leung, K.C., Zhang, L.: Distributed multi-channel topology-transparent broadcast scheduling in ad hoc networks. In: IEEE Wireless Communications and Networking Conference (IEEE WCNC 2014), Istanbul (2014)
9. Liu, Y., Li, V.O.K., Leung, K.C., Zhang, L.: Topology-transparent scheduling in mobile ad hoc networks with multiple packet reception capability. *IEEE Trans. Wireless Commun.* **13**(11), 5940–5953 (2014)
10. Liu, Y., Weng, L., Li, V.O.K., Xu, S.: Topology-transparent scheduling in mobile multihop ad hoc networks with directional antennas. In: IEEE Wireless Communications and Networking Conference (IEEE WCNC 2016), Doha (2016)
11. MacWilliams, F.J., Sloane, N.J.A.: *The Theory of Error-Correcting Codes*. North Holland Publishing Co., Amsterdam (1977)
12. Marina, M., Das, S.: Routing performance in the presence of unidirectional links in multihop wireless networks. In: ACM MOBIHOC 2002, Lausanne, pp. 12–23 (2002)
13. Poojary, N., Drishnamurthy, S.V., Dao, S.: Medium access control in a network of ad hoc mobile nodes with heterogeneous power capabilities. In: IEEE ICC 2001, Helsinki, vol. 3, pp. 872–877 (2001)
14. Wang, G., Turgut, D., Boloni, L., Ji, Y., Marinescu, D.C.: A MAC layer protocol for wireless networks with asymmetric links. *Ad Hoc Netw.* **6**(3), 424–440 (2008)
15. Weng, L., Liu, Y., Liu, L., Wang, Z.: Wireless link quality estimation and prediction: a survey. *J. Chin. Acad. Electron. Inf. Technol.* **11**(3), 239–244 (2016)
16. Wu, J.: Extended dominating-set-based routing in ad hoc wireless networks with unidirectional links. *IEEE Trans. Parallel Distrib. Syst.* **13**(9), 866–881 (2002)
17. Xu, S., Saadawi, T.: Does the IEEE 802.11 MAC protocol work well in multihop wireless ad hoc networks? *IEEE Commun. Mag.* **39**(6), 130–137 (2001)



Carrier Synchronizator in Nonbinary LDPC Coded Modulation Systems

Qiang Zhang, Zhong-yang Yu, and Baoming Bai^(✉)

State Key Laboratory of Integrated Service Networks, Xidian University,
Xi'an, China

bmbai@mail.xidian.edu.cn

Abstract. This paper proposes carrier synchronizator in a nonbinary LDPC and high-order QAM system in order to solve some relevant problems (e.g. Doppler shift, spectrum efficiency etc.) in the satellite communication. The carrier synchronizator is divided into two parts: frequency estimator and phase estimator. The frequency estimator has two steps: single pilot block-based coarse frequency estimation and multiple pilot block-based fine frequency estimation performed by an autocorrelation (AC) operation and a cross-correlation (CC) operation, respectively. Through frequency compensation, the following phase estimator is carried out by the classical maximum likelihood (ML) criterion. Simulation results show that, for a (225, 173) nonbinary LDPC code over GF(16) with a 16-QAM systems, the proposed carrier synchronizator can eliminate large Doppler shift in the presence of random phase offset with low complexity.

Keywords: Pilot-aided · Nonbinary LDPC · High-order QAM
Carrier synchronization

1 Introduction

In recent years, satellite communication has been forced to develop rapidly due to the ever-growing demands for the space TT&C and the deep-space exploration [1–3]. There exist large Doppler shift and limited spectrum resource in the above communication fields. Thus, it is absolutely necessary to design an appropriate carrier synchronization strategy applied into a new coded modulation system.

The so-called carrier synchronization is a key one of the synchronization techniques [4, 5]. According to whether using the pilot (known to both transmitter and receiver) or not, carrier synchronizator can be classified as data-aided (DA)-type synchronizator and non-data-aided (NDA)-type synchronizator [6, 7]. In the satellite communication, synchronization time (including its acquisition and track) required is extremely short, which means that the former is more preferred. With the help of the pilot, one can perform the carrier synchronization much more rapidly. Further, DA-type synchronizator can be divided into auto-correlation (AC) synchronizator and cross-correlation (CC) synchronizator, where the classical L&R [8] belongs to the former and has wide estimation range with low complexity, while the popular cross-correlation [9] owns high accuracy. Specifically, under the conditions of the same signal-to-ratio (SNR) and

pilot overhead, the AC synchronizator has larger estimation range and lower complexity, while the CC synchronizator achieves higher estimation accuracy. Thus, a joint AC and CC synchronizator is proposed.

Especially with the development of modern coding technique, more and more researchers try to combine both the carrier synchronization and channel codes (e.g. LDPC etc.) [10, 11]. However, their studies focus on binary LDPC-based carrier synchronization. In recent years, nonbinary LDPC coding technique has been widely concerned because of its numerous advantages, especially for the short code lengths [12, 13]. Further, the coding technique is more suitable for the combination of high-order QAM technique, obtaining higher spectrum efficiency.

Based on our previous work [14], a novel carrier synchronizator is proposed in a nonbinary LDPC and high-order QAM system. We consider making estimation of frequency offset by two steps i.e. coarse frequency offset estimation based on single pilot blocks and fine frequency offset estimation based on multiple disjoint pilot blocks. Then, ML-based phase offset estimation will be carried out. Simulation results show that the proposed synchronizator can achieve asymptotically optimal performance as pilot overhead increases.

The remaining sections of this paper are structured as follows: The system model is introduced in Sect. 2. The detailed descriptions of our proposed carrier synchronizator are presented in Sect. 3. Sections 4 and 5 give some relevant simulation results and conclusions, respectively.

2 System Model

Figure 1 depicts a system model used in this paper. First, a data sequence is sent into an encoder to obtain corresponding check bits. Then, the resulting codeword and a pilot sequence can make up of a specific frame structure shown in Fig. 2 with the use of a multiplexer (MUX), where it has N pilot blocks, each having L_i symbols ($i = 1, 2, \dots, N$) and $N - 1$ data blocks, each having M_i symbols ($i = 1, 2, \dots, N - 1$). Next, the multiplexed signals are converted into complex baseband signals by a modulator (MOD) corresponding to the nonbinary LDPC code. In the satellite communication, the modulated signals are disturbed by large Doppler shift f_d ($|f_d T| \leq 0.5$) and random phase offset θ ($\theta \in [-\pi, \pi]$ is constant per packet). Assume single carrier transmission in Gaussian noise (AWGN) channel with ideal symbol timing, the k -th received equivalent baseband signal can be expressed as

$$r(k) = s(k) \exp[j(2\pi f_d T k + \theta)] + n(k) \quad (1)$$

$$k = 1, 2, \dots, \sum_{i=1}^N L_i + \sum_{i=1}^{N-1} M_i$$

where T is the symbol duration, $s(k)$ is the normalized-energy modulation signal, $n(k) \sim \mathcal{CN}(0, N_0)$ is the circular symmetric complex Gaussian random variable, whose real and imaginary parts have variances $N_0/2$.

At receiver, the received pilot signals $\{r_p(k)\}$ from the demultiplexer (DEMUX) are first sent into the proposed carrier synchronizer (see Sect. 3 for details) to obtain corresponding estimates \hat{f}_d and $\hat{\theta}$. Then, the received data signals $\{r_d(k)\}$ are corrected by the above estimates through a compensator (COM). Again passing through a demodulator (DEMOD) and a nonbinary LDPC decoder, the original data information can be recovered.

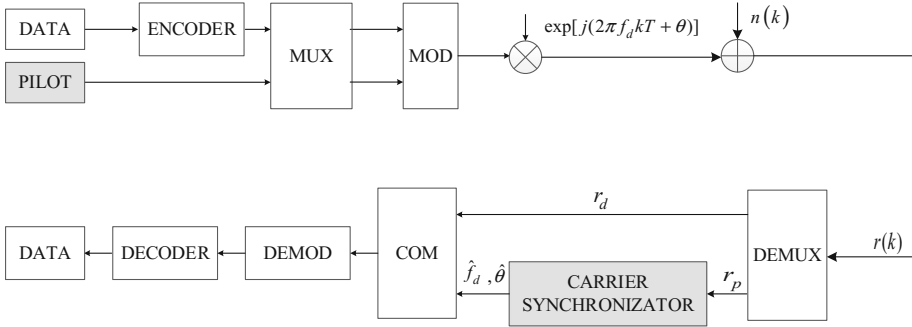


Fig. 1. System model

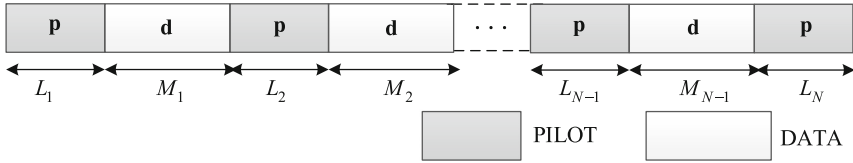


Fig. 2. Frame structure

3 Carrier Synchronizator

In this paper, the proposed carrier synchronizator is divided into two parts: one is a frequency estimator, and the other is a phase estimator. Further, the frequency estimator has two steps, i.e. coarse frequency estimation and fine frequency estimation performed by an auto-correlation (AC) operator and a cross-correlation (CC) operator respectively.

3.1 Coarse Frequency Estimation

In the coarse frequency estimation, we use the received signals corresponding to the first pilot block. First, a so-called removed-modulation operation is done by means of

$$\begin{aligned}
 z(k) &= r(k)s^*(k) \\
 &= \exp[j(2\pi f_d T k + \theta)] + v(k), k \in \kappa
 \end{aligned}
 \tag{2}$$

where $v(k) \triangleq n(k)s^*(k)$ is the noise signal, whose statistical characteristics are the same as $n(k)$. κ is the set of sampling instants corresponding to all the pilot signals, i.e. $\kappa = \{0, 1, \dots, L_1 - 1, L_1 + M_1, \dots, \sum_{i=1}^{N-1} (L_i + M_i), \dots, \sum_{i=1}^{N-1} (L_i + M_i) + 1, \dots, \sum_{i=1}^{N-1} (L_i + M_i) + L_N - 1\}$.

Next, a so-called autocorrelation operation is performed based on (2) with the form of

$$R_a(\alpha) = \frac{1}{L_1 - \alpha} \sum_{i=0}^{L_1-1-\alpha} z^*(i)z(i+\alpha) \quad (3)$$

where α is the effective delay length with an empirical range from 1 to $L_1/2$ [8], L_1 is the length of the first pilot block.

Then, taking argument of (3) can get a coarse frequency estimate with the form of

$$\hat{f}_d^c = \frac{1}{2\pi\alpha T} \arg\{R_a(\alpha)\}, |\hat{f}_d^c T| \leq \frac{1}{2\alpha}. \quad (4)$$

To estimate a larger frequency, letting the coefficient $\alpha = 1$ can yield

$$\hat{f}_d^{c1} = \frac{1}{2\pi T} \arg\{R_a(1)\}, |\hat{f}_d^{c1} T| \leq 0.5. \quad (5)$$

After frequency compensation, the classical L&R algorithm [8] is introduced to achieve a lower SNR threshold, resulting in another coarse frequency estimate

$$\hat{f}_d^{c2} = \frac{1}{\pi T(N_c + 1)} \arg\left\{ \sum_{\alpha_1=0}^{N_c-1} R_a(\alpha_1) \right\}, \quad (6)$$

$$|\hat{f}_d^{c2} T| \leq \frac{1}{N_c + 1}$$

where N_c is the smoothing noise coefficient with an empirical value of $L_1/2$, $R_a(\alpha_1)$ is the weighted summation term corresponding to all the compensated removed-modulation signals with the form of

$$R_a(\alpha_1) = \frac{1}{L_1 - \alpha_1} \sum_{i=0}^{L_1-1-\alpha_1} z_1^*(i)z_1(i+\alpha_1) \quad (7)$$

where $z_1(i) \triangleq z(i) \exp[-j(2\pi\hat{f}_d^{c1}Ti)]$ is also the removed-modulation signal corrected by the preliminary frequency estimate \hat{f}_d^{c1} .

It is found through simulations that, for a small pilot block, the coefficient $N_c \approx L_1/3$; and for a relatively large one, the coefficient $N_c \approx L_1/2$, which is the same as the L&R algorithm.

Based on the above discussions, the coarse frequency estimator can be formulated as follows:

Initialization: set the initial frequency estimate $\hat{f}_d^c = 0$, the sampling instant $k \in \{1, 2, \dots, L_1\}$.

- (a) obtain the removed-modulation signal $z(k)$ according to (2);
- (b) get the autocorrelation value $R_a(x)|_{x=1}$ via (3);
- (c) compute the coarse frequency estimate \hat{f}_d^{c1} by means of (5), and update \hat{f}_d^c as \hat{f}_d^{c1} ;
- (d) compensate $z(k)$ by \hat{f}_d^c and obtain the corrected one $z_1(k)$;
- (e) compute the other coarse frequency estimate \hat{f}_d^{c2} through (6), and update \hat{f}_d^c as $\hat{f}_d^{c1} + \hat{f}_d^{c2}$.

3.2 Fine Frequency Estimation

In the fine frequency estimation, we use the received signals corresponding to the multiple disjoint pilot blocks to obtain more precise frequency estimate.

With loss of generality, the equilibrium of all the pilot blocks is considered except the first pilot block, i.e. $L_i \equiv L$. A so-called cross-correlation operation is carried out as follows

$$R_c(i) = \sum_{k=0}^{L-1} z_2^*(k) z_2(k + D_i), \quad (8)$$

$$D_i = \sum_{j=1}^i (L_j + M_j), \quad i = 1, 2, \dots, N - 1$$

for each $R_c(i)$, we can obtain a fine frequency estimate (or say residual frequency estimate) via taking the argument of (8), i.e.

$$\hat{f}_d^{fi} = \frac{1}{2\pi T D_i} \arg\{R_1(i)\}. \quad (9)$$

So far, a final frequency estimate can be derived as combining (5), (6) and (9)

$$\hat{f}_d = \hat{f}_d^c + \hat{f}_d^f = \hat{f}_d^{c1} + \hat{f}_d^{c2} + \sum_{i=1}^{N-1} \hat{f}_d^{fi}. \quad (10)$$

Similarly, the fine frequency estimator can be summarized as follows:

Initialization: set $i = 0$, $\hat{f}_d^{i0} = 0$ and $k \in \kappa$.

- (a) compensate the removed-modulation signal $z(k)$ by \hat{f}_d^c ;
- (b) get the cross-correlation value $R_c(i)$ by (8);
- (c) if $i = N - 1$, stop and update the fine frequency estimate \hat{f}_d^f as $\sum_{i=1}^{N-1} \hat{f}_d^{fi}$, otherwise go to the next step;

- (d) let $i = i + 1$, compute the i -th fine frequency estimate value \hat{f}_d^i through (9) and go to the step b.

After the frequency estimation, the following phase estimation can be executed based on the maximum likelihood (ML) criterion, which is given in detail in [15].

3.3 Compensator

After the frequency estimation and the phase offset estimation, the estimates \hat{f}_d and $\hat{\theta}$ are obtained. The following compensator (COM) will apply the two estimates into the received data signals $\{r_d(k)\}$ i.e.

$$\tilde{r}_d(k) = r_d(k)\exp\left[-j\left(2\pi\hat{f}_d kT + \hat{\theta}\right)\right] \tag{11}$$

The summarized process of our proposed carrier synchronizator is shown in Fig. 3.

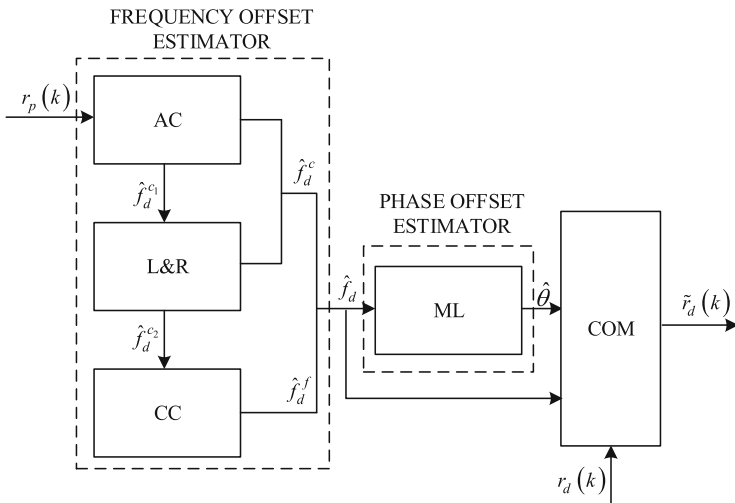


Fig. 3. The proposed carrier synchronizator

4 Simulation Results

In this section, we will evaluate both the estimation accuracy and bit-error-rate (BER) performance of the proposed carrier synchronizator.

Consider a (225,173) nonbinary LDPC code over GF(16) and 16-QAM system. Without loss of generality, we divide the coded modulation signals into two blocks: $M_1 = 113$ and $M_2 = 112$. The lengths of corresponding pilot blocks are L_1 , L_2 and L_3 ($L_2 = L_3$), respectively. Thus, the resulting pilot overhead can be defined as η with the form of

$$\begin{aligned}\eta &= \frac{L_1 + L_2 + L_3}{L_1 + L_2 + L_3 + M_1 + M_2} \times 100\% \\ &= \frac{L_1 + 2L_2}{L_1 + 2L_2 + 225} \times 100\%.\end{aligned}\quad (12)$$

We take three pilot block lengths for examples, followed by three corresponding pilot overheads listed in Table 1.

Table 1. The pilot lengths and corresponding pilot overheads.

L_1	L_2	L_3	η
20	3	3	10%
20	10	10	15%
27	15	15	20%

4.1 Analysis of Estimation Accuracy

In this part, we will analyze performance of both the frequency and phase offset estimation of the proposed carrier synchronizer, followed by corresponding Cramer-Rao bounds (CRBs).

Based on our previous work [14], the CRBs for frequency offset and phase offset can be expressed as respectively

$$\begin{aligned}\text{CRB}(f_d)^{-1} &= \frac{C}{6} \sum_{i=1}^N L_i(L_i - 1)(2L_i - 1) + C \sum_{i1=2}^N L_{i1} \sum_{i2=1}^{i1} (L_{i2} + M_{i2}) \cdot \\ &\quad \left[\sum_{i2=1}^{i1} (L_{i2} + M_{i2}) + L_{i1} - 1 \right]\end{aligned}\quad (13)$$

$$\text{CRB}(\theta)^{-1} = 2L_1 \times \frac{E_s}{N_0} \quad (14)$$

where the coefficient $C \triangleq 8\pi^2 T^2 E_s / N_0$. It is seen that for a DA synchronizer, both the CRBs will become lower with an increase of the SNR and/or the pilot block length.

Figure 4 shows frequency and phase offset estimation along with corresponding CRBs when $f_d T = 0.3$ and $\theta = \pi/2$. As shown in Fig. 4(a): if using 20% pilot overhead, the proposed synchronizer can achieve good accuracy extremely close to its CRB only at 3 dB. But if using fewer pilots overhead, the corresponding accuracy will deteriorate sharply. In Fig. 4(b), if using 20% pilot overhead, the proposed synchronizer can also achieve good accuracy very close to its CRB. Further, the achievable estimation accuracy of the proposed synchronizer depends on its BER performance.

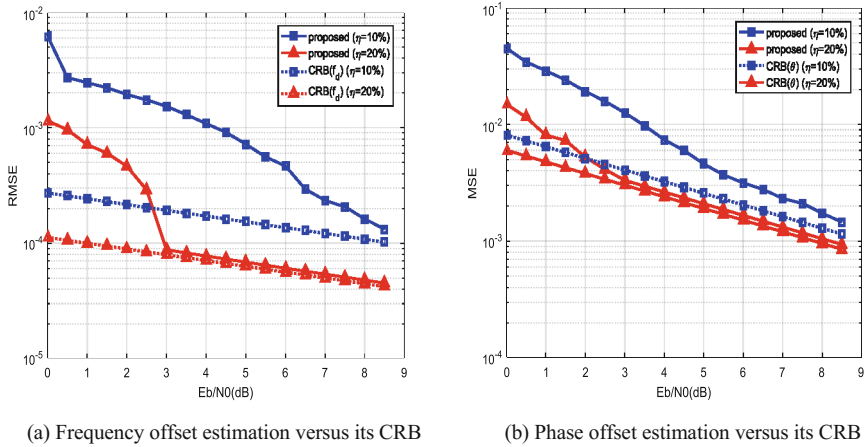


Fig. 4. Evaluation of the frequency and phase offset estimation along with the corresponding CRBs

4.2 Analysis of BER Performance

According to the above discussions, Fig. 5 shows BER performance of the proposed carrier synchronizer under the conditions of $f_d T = 0.3$ and $\theta = \pi/2$. It is seen that at a BER of 10^{-5} , the proposed carrier synchronizer using the 20% pilot overhead can obtain good performance which is 1.2 dB away from the ideal performance ($f_d = 0$ and $\theta = 0$); at a BER of 10^{-4} , the proposed carrier synchronizer using the 20% and 15% pilot overheads can achieve good performance (only 0.8 dB and 1.6 dB away from the ideal performance respectively). For less pilot overhead (e.g. 10%), the performance of our proposed carrier synchronizer will deteriorate sharply, which corresponds to the results of Fig. 4.

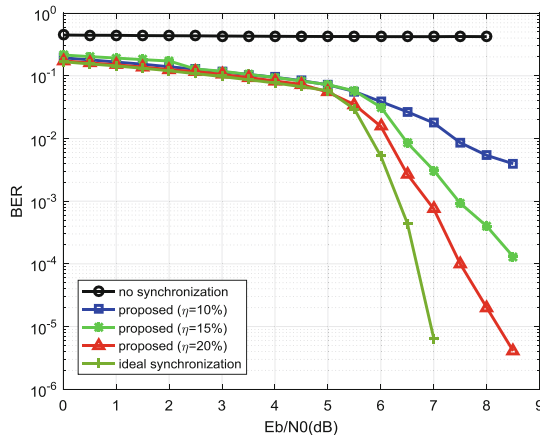


Fig. 5. Evaluation of BER performance of the proposed carrier synchronizer

5 Conclusions

Considering large Doppler shift, random phase offset and low spectrum efficiency in the satellite communication, we propose a carrier synchronizer in nonbinary LDPC and high-order QAM system. Based on the system, large Doppler shift can be eliminated by a single pilot block-aided joint AC and L&R algorithm and a multiple pilot block-aided CC algorithm. Also, random phase offset can be removed by using a single pilot block-aided ML algorithm. Simulation result shows that for a (225,173) nonbinary LDPC over GF(16) and 16-QAM system, our proposed carrier synchronizer can achieve good performance in both the RMSE/MSE and BER as the pilot overhead increases.

Acknowledgment. This work was supported in part by the National Natural Science Foundation of China, by the 973 Program of China under Grants 61372074 and 91438101 and 2012CB316103, by the Fundamental Research Funds for the Central Universities (JBG160103, XJS15019), and by the China Postdoctoral Science Foundation funded project (2015M580819).

References

1. Silva, J.S., et al.: Stereolithography-based antennas for satellite communications in Ka-Band. *Proc. IEEE* **105**(4), 655–667 (2017)
2. Joroughi, V., et al.: Generalized multicast multibeam precoding for satellite communications. *IEEE Trans. Wirel. Commun.* **16**(2), 952–966 (2017)
3. Meng, X., et al.: A DS-PAM UWB TT&C signal improvement method. In: 2016 IEEE 13th International Conference on Signal Processing, pp. 1157–1160 (2016)
4. Wang, W.-Q.: Carrier frequency synchronization in distributed wireless sensor networks. *IEEE Syst. J.* **9**(3), 703–713 (2015)
5. Zibar, D., et al.: Joint iterative carrier synchronization and signal detection employing expectation maximization. *J. Lightwave Technol.* **32**(8), 1608–1615 (2014)
6. Sun, J., Yu, Z., et al.: Simplified diagonal cross-correlation frequency estimation based on phase un-wrapping. In: 2015 10th International Conference on Communications and Networking in China (ChinaCom), Shanghai, pp. 739–744 (2015)
7. Moeneclaey, M., de Jonghe, G.: ML-oriented NDA carrier synchronization for general rotationally symmetric signal constellations. *IEEE Trans. Commun.* **42**(8), 2531–2533 (1994)
8. Luise, M., Reggiannini, R.: Carrier frequency recovery in all-digital modems for burst-mode transmissions. *IEEE Trans. Commun.* **43**(2), 1169–1178 (1995)
9. Godtmann, S., Hadaschik, N., Steinert, W., et al.: A concept for data-aided carrier frequency estimation at low signal-to-noise ratio. In: Proceeding of 2008 IEEE International Conference on Communications (ICC), Beijing, China, pp. 463–467 (2008)
10. Man, X., et al.: A novel code-aided carrier recovery algorithm for coded systems. *IEEE Commun. Lett.* **17**(2), 405–408 (2013)
11. Nele, N., Heidi, S., Moeneclaey, M.: Carrier phase tracking from turbo and LDPC coded signals affected by a frequency offset. *IEEE Commun. Lett.* **9**(10), 915–917 (2005)
12. Gallager, R.G.: Low-density parity-check codes. *IRE Trans. Inf. Theory* **8**(1), 21–28 (1962)

13. MacKay, D.J.C., Neal, R.M.: Near Shannon limit performance of low-density parity-check codes. *IEEE Electron Lett.* **33**(6), 457–458 (1997)
14. Yu, Z., Sun, J., Bai, B., et al.: A phase increment-based frequency estimator for general PSAM in burst communications. In: 2016 IEEE 83rd Vehicular Technology Conference (VTC Spring), Nanjing, pp. 1–5 (2016)
15. Wang, P.S., Lin, D.W.: On maximum-likelihood blind synchronization over WSSUS channels for OFDM systems. *IEEE Trans. Signal Process.* **63**(19), 5045–5059 (2015)



An Assessment Method of Pilot Situation Awareness in Manned/Unmanned-Aerial-Vehicles Team

Jun Chen ^(✉), Qilin Zhang, Xunjie Qiu, and Bo Hou

School of Electronics and Information,
Northwestern Polytechnical University, Xi'an 710129, China
junchen@nwpu.edu.cn

Abstract. In manned/unmanned-aerial-vehicles team, the situation awareness level of manned-aerial-vehicle (MAV) pilot affects the pilot's cognitive state. Evaluating the pilot's situation awareness level will enhance the cognitive and interactive capabilities of unmanned-aerial-vehicle (UAV) and MAV. This paper proposes an assessment method of pilot's situation awareness, which is based on attention resource allocation theory and conditional probability cognitive process. Using the presented method, the situation awareness level of pilot could be quantified and evaluated reasonably. Finally the paper simulated the model at different levels of autonomy (LOA) to demonstrate the rationality of the model.

Keywords: Manned/unmanned-aerial-vehicles team (MAV/UAVs team)
Situation awareness (SA) · MAV pilot · Human – robotics interaction

1 Introduction

Facing the increasingly complex battlefield environment in the future, making up for the lack of unmanned-aerial-vehicles (UAV) intelligence and fully use the role of the human intelligence at critical moments. Manned/unmanned-aerial-vehicles team as a new combat mode has been highly concerned by research institutions and scholars at home and abroad [1–3].

The process of Situation awareness (SA) includes perception of environmental elements, elements comprehension, and complete the projection of its future status [4] in a certain time and space.

The three processes of SA are indispensable, only after the becoming of projection information, the operator completed a SA process [5, 6].

2 MAV/UAVs Team Cooperative Combat System

In the process of MAV/UAVs team cooperative combat, in order to use pilot's wisdom and comprehensive judgment ability, at the same time maximize the UAV's independent combat capability. The function assignment between man and machine must be clarified. Specific structure as shown below.

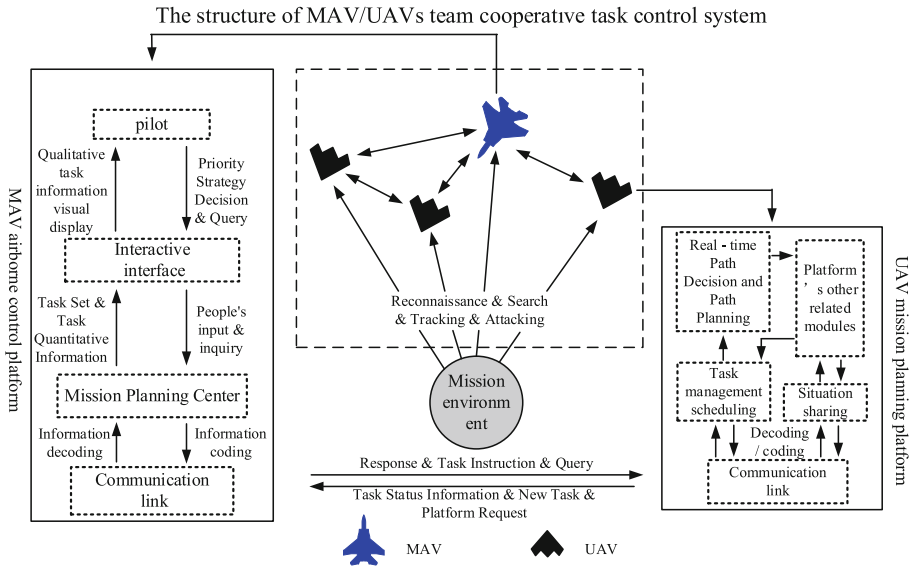


Fig. 1. The structure of MAV/UAVs team cooperative task control system

As shown in Fig. 1, manned-aerial-vehicles (MAV) as the leader of the team. It mainly acts as a manager and is responsible for the entire team of the supervision and control tasks. It also assign a task to UAV, query status, response to the request, and can directly control the UAV. UAV as a wing plane in the team, mainly as a managed or dominated role, to accept MAVs control commands, return status, tasks, threats and assistance requests and other information. In the air-and-space integration combat command system, the two together to complete the combat mission.

3 Pilot SA Assessment Model

3.1 The SA Assessment Model Based on Attention Resource Allocation

Operator's attention resource ratio

Typically, the pilot through the aircraft cockpit display interface to monitor n visual information, assuming n visual information obtained by the attention resources are as follows:

$$A = (A_1, A_2, \dots, A_i, \dots, A_n) \tag{1}$$

The information i obtained attention resource A_i is:

$$A_i = B_i V_i S_{ai} E_i^{-1} \tag{2}$$

B_i is occurrence probability of information i , V_i is related to information i , S_{ai} is the prominence of information. Indicates the impact of the display information on attention due to the difference in color, size, and character type. E_i^{-1} is the effort by the pilot eye movement or head to get information [7].

In the above formula, V_i is related to information i , which is determined by the following equation:

$$V_i = p_i \mu_i \tag{3}$$

p_i is potential cognitive state of information i , μ_i is important membership of information.

Fraction attention indicates the proportion of the displayed resources in all information. And the pilot assigned to the attention of each monitor resources need to meet the following equation:

$$\sum_{i=1}^n f_i = 1, f_i \geq 0 \tag{4}$$

In Eq. 4, f_i is the attention resource of the pilot obtained from the information displayed by the interface.

If the pilot is treated as an idealized monitor, in order to achieve the optimal allocation of resources, the pilots should allocate their own attention resources according to the importance of each interface, so attention resource ratio f_i can be derived from the following formula:

$$f_i = \frac{\mu_i}{\sum_{i=1}^n \mu_i}, i = (1, 2, \dots, n) \tag{5}$$

In the actual situation, the person’s attention distribution is random. Pilot uses the potential cognitive state p_i of information i indicating that the operator can correctly assess the importance of the display probability:

$$p = (p_1, p_2, \dots, p_i, \dots, p_n) \tag{6}$$

Combined Subjective Expected Utility Theory (SEU), The pilot’s attention resource ratio can be modified to the following equation:

$$f_i^* = \frac{p_i \mu_i}{\sum_{i=1}^n p_i \mu_i}, i = (1, 2, \dots, n) \tag{7}$$

f_i^* is modified attention resource ratio.

Introduced fuzzy entropy attention resource ratio

“Ambiguity” and “randomness” are two uncertainties in the human attention distribution mechanism. They can influence each other, but cannot replace each other. Thus, hybrid entropy [8] can be used to measure the impact of these two uncertainties. With the increase of mixed entropy, people’s desire to obtain information and anxiety caused by lack of information and other psychological activities will be strengthened, and it is helpful to attract people’s attention. This is consistent with the general knowledge of people. Thus, the mixed entropy can be defined by simulating the pilot’s mental cognitive process. Assuming that D is a fuzzy subset of the information utility set U , the mixed entropy can be defined as:

$$H_{tot}(D, P) = m(D, P) + H(P) \tag{8}$$

In Eq. 8, $m(D, P)$ is fuzzy entropy, $H(P)$ is probability entropy, $H_{avg}(D, P)$ is hybrid entropy, hybrid entropy and probability entropy can be obtained by the following formulas:

$$\begin{aligned}
 m(D, P) &= \sum_{i=1}^n p_i S(\mu_i) \\
 H(P) &= - \sum_{i=1}^n p_i \ln p_i
 \end{aligned}
 \tag{9}$$

In Eq. 9, $S(\mu_i)$ is the binary fuzzy entropy of μ_i :

$$S(\mu_i) = -\mu_i \ln \mu_i - (1 - \mu_i) \ln(1 - \mu_i) \tag{10}$$

According to Shannon’s information additive principle, the average hybrid entropy of n interfaces $H_{avg}(D, P)$ is:

$$H_{avg}(D, P) = \frac{1}{n} \sum_{i=1}^n H_{tot}(D, P) = \frac{1}{n} \sum_{i=1}^n p_i S(\mu_i) - p_i \ln p_i \tag{11}$$

The constraint condition that p_i needs to satisfy is:

$$p_i \geq 0, \sum_{i=1}^n p_i = 1 \tag{12}$$

In order to evaluate p_i , according to the maximum entropy theory [9], p_i should take the maximum value of $H_{avg}(D, P)$. By solving the extreme value of the Lagrangian function L under the constraint condition, p_i^* can be obtained to achieve the maximum probability of $H_{avg}(D, P)$:

$$L = \frac{1}{n} \sum_{i=1}^n (p_i S(\mu_i) - p_i \ln p_i) - \lambda \left(\sum_{i=1}^n p_i - 1 \right)$$

$$p_i^* = \frac{e^{S(\mu_i)}}{\sum_{i=1}^n e^{S(\mu_i)}} \quad (13)$$

On the basis of Eqs. (2), (3) and combining Eqs. (7), (13), the pilot's assigned resource allocation for information i is:

$$f_i^* = \frac{A_i}{\sum_{i=1}^n A_i} = \frac{B_i p_i^* \mu_i S_{ai} E_i^{-1}}{\sum_{i=1}^n B_i p_i^* \mu_i S_{ai} E_i^{-1}} \quad (14)$$

3.2 Cognitive Process Based on Conditional Probability

In this paper, according to Endsley's SA theory model, the cognition process of information displayed in the cockpit is defined as four parts: not perceived, perceived but not understood, understood but not predicted and can predict. Based on this, we defined the following events.

Definition 3.1: Event a_i is the behavior of the pilot to pay attention to the information component i at some point.

Definition 3.2: Event b_i is the behavior of the pilot to comprehend the information component i at some point.

Definition 3.3: Event c_i is the behavior of the pilot to project the information component i at some point.

The probability of occurrence of event a_i is given by the operator's attention resources rate, available from Eq. 14,

$$p(a_i) = f_i^* \quad (15)$$

The probability of comprehension the information on the basis of the perceive information i is:

$$p(b_i|a_i) = n_i \quad (16)$$

The probability of projecting the information on the basis of the comprehension information i is:

$$p(c_i|a_i b_i) = k_i \quad (17)$$

On the basis of the above definition and combine Endsley's SA theory model. Through the division of the cognitive state of the information component by the operator, using the conditional probability formula, we can get the following Table 1:

Table 1. Conditional probability of four kinds of SA state

SA state	Cognitive state	Conditional probability (P)
Not perceived	C_u	$1 - p(a_i) = 1 - f_i^*$
Perceived but not understood	C_d	$p(a_i)(1 - p(b_i a_i)) = f_i^*(1 - n_i)$
Understood but not predicted	C_c	$p(a_i b_i)(1 - p(c_i a_i b_i)) = f_i^* n_i (1 - k_i)$
Predict	C_p	$p(a_i b_i) p(c_i a_i b_i) = f_i^* n_i k_i$

We can obtain the expected value of the cognitive level of the information component i by Bayesian conditional probability formula.

$$\bar{p}_i = C_u(1 - f_i^*) + C_d(1 - n_i) + C_c f_i^* n_i (1 - k_i) + C_p f_i^* n_i k_i \tag{18}$$

The pilot’s awareness level \bar{SA} is obtained by accumulating the cognitive level expectation \bar{p}_i of each information.

$$\bar{SA} = \sum_{i=1}^n \bar{p}_i \tag{19}$$

4 Simulation and Result Analysis

In the simulation section, we select the fighter parameters, battlefield environment, decision results and task execution results as the information received by the operation. Calculate SA levels at different LOAs of MAV/UAVs team.

As shown in Table 2, the initial value of $B_i, E_i^{-1} S_{ai} \mu_i$ is given, Maximum probability P_i^* can be calculated by the Formula 13.

Table 2. The initial values of factors under different LOAs and information

Factors	LOA	Information			
		Fighter parameters	Battlefield environment	Decision results	Task execution result
Information probability B_i	Manual control	0.85	0.15	0	0
	Command control	0.5	0.4	0.1	0
	Consent management	0.3	0.3	0.4	0
	Exception management	0	0.2	0.4	0.4
	Completely independent	0	0	0	0

(continued)

Table 2. (continued)

Factors	LOA	Information			
		Fighter parameters	Battlefield environment	Decision results	Task execution result
Highlighting information S_{ai}	Manual control	0.5	0.5	0	0
	Command control	0.4	0.4	0.2	0
	Consent management	0.2	0.4	0.4	0
	Exception management	0	0.3	0.4	0.3
	Completely independent	0	0	0	0
Make efforts E_i^{-1}	Manual control	0.1	0.2	0	0
	Command control	0.1	0.5	0.4	0
	Consent management	0.1	0.4	0.4	0
	Exception management	0	0.2	0.4	0.4
	Completely independent	0	0	0	0
Fuzzy membership μ_i	Manual control	0.8	0.2	0	0
	Command control	0.4	0.4	0.2	0
	Consent management	0.2	0.4	0.4	0
	Exception management	0	0.2	0.4	0.4
	Completely independent	0	0	0	0
Maximum probability P_i^*	Manual control	0.27	0.4	0.16	0.17
	Command control	0.26	0.26	0.53	0.14
	Consent management	0.33	0.27	0.27	0.14
	Exception management	0.14	0.27	0.27	0.33
	Completely independent	0.2	0.2	0.2	0.2

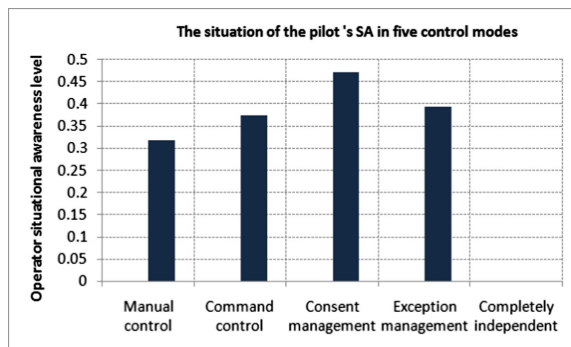
Table 3. Under different LOAs f_i^* , n_i , k_i and \bar{p}_i

	Manual control	Command control	Consent management	Exception management	Completely independent
f_1^*	0.918	0.185	0.032	0	0
f_2^*	0.082	0.74	0.416	0.047	0
f_3^*	0	0.075	0.552	0.5	0
f_4^*	0	0	0	0.453	0
n_1	0.3	0.3	0.4	0	0
n_2	0.3	0.4	0.5	0.4	0
n_3	0	0.2	0.5	0.5	0
n_4	0	0	0	0.4	0
k_1	0.2	0.2	0.4	0	0
k_2	0.2	0.3	0.5	0.3	0
k_3	0	0.1	0.5	0.4	0
k_4	0	0	0	0.3	0
\bar{p}_1	0.294	0.059	0.0128	0	0
\bar{p}_2	0.026	0.296	0.198	0.0178	0
\bar{p}_3	0	0.02	0.2622	0.205	0
\bar{p}_4	0	0	0	0.172	0
\bar{SA}	0.32	0.375	0.473	0.395	0

As shown in Table 3, f_i^* can be calculated by the Formula 14, n_i and k_i is given. Cognitive level expectation \bar{p}_i can be calculated by the Formula 18.

Finally, \bar{SA} at different LOAs can be calculated by the Formula 19.

It can be seen from Fig. 2, pilot's SA level at consent management mode is highest, followed by exception management mode. Manual control mode and command control mode is smaller and completely independent mode is minimum. Therefore, when the pilot needs to maintain a high level of SA, can switch to consent management mode or exception management mode.

**Fig. 2.** The situation of the pilot's SA in five control modes

5 Conclusion

In MAV/UAVs team, the situation awareness level of MAV pilot will affect the pilot's cognitive state. Evaluating the pilot's situation awareness level will enhance the cognitive and interactive capabilities of UAV and MAV. Attention resources are the key factors that constrain the operator to perceive, understand and predict the situation. This paper presents a situational awareness assessment method based on attention resource allocation and conditional probability cognitive process. Finally we simulated the model at different LOAs, proving the rationality of the model.

Acknowledgments. This work was sponsored by National Natural Science Foundation of China (61305133), Aeronautical Science Foundation of China (2016ZC53020) and the Fundamental Research Funds for the Central Universities (3102017jg02015).

References

1. Chen, Z.J., Zhang, R.L., Zhang, P., Zhang, R.: Flight control: challenges and opportunities. *J. Acta Automatica Sinica*. **39**(6), 703–710 (2013)
2. Chen, J., Zhang, X.W., Xu, J., Gao, X.G.: Human/unmanned-aerial-vehicle team collaborative decision-making with limited intervention. *J. Acta Aeronautica et Astronautica Sinica*. **36**(11), 3652–3665 (2015)
3. Liu, H.Q., Wei, X.Z., Fu, Z.W., Zhou, Z.L.: Cooperative task assignment of manned/unmanned aerial vehicle team in air combat. *J. Electron. Opt. Control* **20**(06), 16–19 (2013)
4. Endsley, M.R.: Toward a theory of situation awareness in dynamic systems. *J. Hum. factors* **37**(1), 32–64 (1995)
5. Liu, S., Wanyan, X.R.: Situational awareness model based on attention allocation. *J. Beijing Univ. Aeronaut. Astronaut.* **40**(8), 10 (2014)
6. Wanyan, X.R., Zhuang, D., Wei, H., et al.: Study on pilot attention allocation model based on fuzzy theory. *J. Comput. Math. Appl.* **62**(7), 2727–2735 (2010)
7. Wu, X., Wanyan, X.R.: Attention allocation modeling under multi-factor condition. *J. Beijing Univ. Aeronaut. Astronaut.* **39**(8), 1086–1090 (2013)
8. Zadeh, L.A.: Discussion: probability theory and fuzzy logic are complementary rather than competitive. *J. Technometrics*. **37**(3), 271–276 (1995)
9. Jaynes, E.T.: Clearing up mysteries the original goal. In: Skilling, J. (ed.) *Maximum Entropy and Bayesian Methods*. FTPH, vol. 36, pp. 1–27. Springer, Dordrecht (1989). https://doi.org/10.1007/978-94-015-7860-8_1



Minimum Interference Beam Selection for Millimeter Wave BeamSpace MIMO System

Dantao Li^{1,2}, Xiaohui Li^{1,2}(✉), Bin Zhou³, Yanbin Zhao⁴, and Danfeng Meng^{1,2}

¹ State Key Laboratory of Integrated Service Networks,
Xidian University Xi'an, Xi'an 710071, Shaanxi, China
xhli@mail.xidian.edu.cn

² Collaborative Innovation Center of Information Sensing and Understanding,
Xidian University Xi'an, Xi'an 710071, Shaanxi, China

³ AVIC Computing Technique Research Institute, Xi'an, Shaanxi, China

⁴ Geographic Information Center, Yangquan, Shanxi, China

Abstract. Millimeter Wave (mmWave) combined with massive multiple-input multiple-output (MIMO) can provide wider bandwidth and higher spectrum efficiency. It has been considered as a key technique for future 5G wireless communications. However, hardware costs and power consumption make traditional MIMO processing impractical in such systems, because a large number of radio frequency (RF) chains are needed. To solve this problem, the beamspace MIMO concept is proposed in mmWave multiuser MIMO (MU-MIMO) systems, which utilizes beam selection algorithm based on the sparsity of beamspace channel to reduce the required RF chains without obvious performance loss. The existing beam selection algorithms mainly select the beam with the strongest gain, but ignore the inter-beam interference and the complexity. Thus, a novel algorithm based on the minimum interference (MI) criterion is proposed. Specifically, the performance of the beams is measured by defining the beamspace signal-to-interference ratio (SIR). When choosing beams, not only the gain of beams but also the interference to other users is considered. The simulation results demonstrate that the proposed algorithm can substantially reduce the complexity while ensuring better system performance.

Keywords: Massive MIMO · mmWave communication systems
Low RF complexity · Beamspace MIMO · Beam selection

1 Introduction

With the rise of various intelligent terminals, mobile data traffic shows explosive growth trend. Thus, there is a higher requirement for future network capacity of mobile broadband communication systems (5th generation mobile communications, 5G) [1]. Most of the current communication systems mainly work in

low frequency band which range from 700 MHz to 2.6 GHz. The tension of spectrum resources poses an unprecedented challenge for mobile service providers. Fortunately, the mmWave has a large number of available unlicensed bands. Exploiting the rich spectrum resources of the mmWave enables to alleviate the pressure of the spectrum resources. However, the path loss of mmWave is more serious and the 60 GHz system has 22 dB additional free space loss compared with that of 5 GHz system [2]. Although the high path loss limits the mmWave communication distance, another unique advantage of the mmWave signal is that the wavelength is short and the antenna array occupies a small footprint, making it possible for the base station to install large-scale (usually tens to hundreds) antennas. Beamforming with massive MIMO and making full use of space-dimensional resources can cope with complex channel environment, enhance the quality of communication links and achieve high data rate transmission. In fact, the literature [3] shows that mmWave mobile broadband system could achieve gigabit per second data rate at distances up to 1 Km in an urban environment.

In traditional communication systems, the signal is usually processed at the baseband which can control its phase and amplitude. Full digital MIMO systems enjoy flexibility, adaptability, and performance optimality, however, with higher costs and power consumption, because that an RF unit is needed for each antenna. The large number of antennas anticipated in mmWave beamforming presents several challenges such as: high power consumption and the high cost of a large number of ADCs operating at very high sampling frequencies (possibly several GS/s to 100 GS/s) [4]. In order to take advantage of the mmWave, many researchers focus on mmWave systems designed to reduce the hardware complexity and power consumption of high-dimensional MIMO systems [5]. And beamspace MIMO system is one of the most promising approaches.

The beamspace MIMO is multiplexing data onto some fixed orthogonal spatial beams by fixed beamforming at the transmitter [6]. So the equivalent channel is low rank and sparse. With beam selection criteria, the RF chains needed is agree in the magnitude of the number of users, which will significantly reduce the hardware complexity, the digital signal processing complexity, and the power consumption [7]. Beamspace MIMO system uses spatial sparsibility to reduce RF complexity, but also requires a fast beam selection algorithm to choose optimal beams for users. The literature [6] proposed a beam selection scheme based on the criterion of magnitude maximization (MM), in which several beams with large magnitude are selected for each user. MM beam selection is simple but it only aims to maximize the power of each user without considering multiuser interferences. Another interference-aware (IA) beam selection algorithm first classifies all users into two user groups, the interference-users (IUs) and noninterference-users (NIUs). For NIUs, the beams with large power are selected, while the beams are selected based on the criterion of sum-rate maximization for IUs [8]. IA algorithm can obtain better performance, but it ignores inter-beam interference and iterative search for IUs with the large-scale matrix operation makes it more complicated.

In this paper, we propose an MI beam selection for mmWave beamspace MIMO system. Due to the criterions used in MM and IA beam selection exit the

problems of users sharing beam and inter-beam interference, MI criterion not only considers the beam gain for the users, but also considers the interference to other users. At the same time, the complexity of MI is low without iteration and large matrix operation. Simulation results verify that the proposed MI selection can achieve the performance of IA and is better than conventional MM selection. With the increase of the number of users, the proposed MI algorithm is better than the IA algorithm.

Notations: Lower-case and upper-case boldface letters denote a vector and a matrix. The $(\cdot)^T$, $(\cdot)^H$, $(\cdot)^{-1}$ and $tr(\cdot)$ denote the transpose, conjugate transpose, inverse and trace of matrix respectively. The $A(:, i)$, $A(j, :)$ is the i th column and j th row of the matrix A . $|\cdot|$ represents the amplitude of vector, and $Card(\cdot)$ denotes the cardinality of set. Finally, \mathbf{I}_N is an $N \times N$ identity matrix.

2 System Model and Assumption

2.1 Traditional MIMO System

Considering a single cell mmWave downlink MU-MIMO system as shown in Fig. 1, where the base station (BS) equips with an N_t dimensional uniform linear array (ULA) communicating with K single-antenna users. Then, the received signal at the i^{th} user is given by

$$y_i = \mathbf{h}_i \mathbf{w}_i x_i + \sum_{k=1, k \neq i}^K \mathbf{h}_i \mathbf{w}_k x_k + n_i \quad (1)$$

where $\mathbf{h}_i \in \mathbb{C}^{1 \times N_t}$ represents the channel vector of the i th user, $\mathbf{w}_i \in \mathbb{C}^{N_t \times 1}$ is a precoding vector for user i , and $n_i \sim CN(0, \delta^2)$ is additive white Gaussian noise (AWGN).

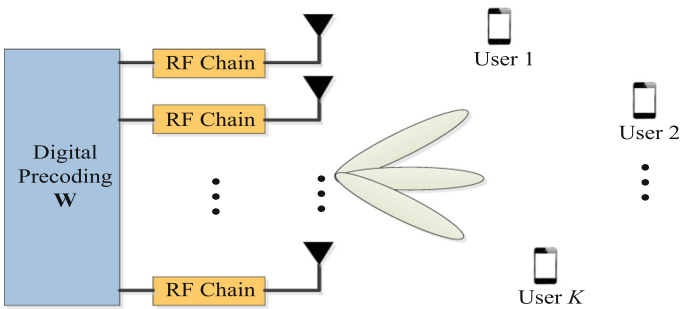


Fig. 1. Single cell millimeter wave downlink MU-MIMO system

If the received signal of K users is represented as a received vector, the $K \times 1$ received signal vector \mathbf{y} for all K users in the downlink can be expressed as

$$\mathbf{y} = \mathbf{H}\mathbf{W}\mathbf{x} + \mathbf{n} \quad (2)$$

where $\mathbf{H} = [\mathbf{h}^T_1, \mathbf{h}^T_2, \dots, \mathbf{h}^T_k]^T$ is the channel matrix, $\mathbf{W} = [\mathbf{w}_1, \mathbf{w}_2, \dots, \mathbf{w}_k]$ is the precoding matrix, \mathbf{x} of size $K \times 1$ is the sending signal vector for all K users with normalized power $\mathbf{E}\{\mathbf{x}\mathbf{x}^H\} = \mathbf{I}_K$. Due to the power constraint, the precoded signal $\mathbf{s} = \mathbf{W}\mathbf{x}$ satisfies $\mathbf{E}\{\mathbf{s}^H\mathbf{s}\} \leq P$, where P is the transmitted power.

Obviously it can be seen from Fig. 1 that the number of required RF chains for traditional MIMO systems is $N_{RF} = N_t$, which is usually large for mmWave massive MIMO systems and definitely a dramatic increase in cost and power consumption [9].

The high free space loss of mmWave limits the spatial scattering or spatial selectivity in mmWave communications, which leads us to adopt the extended Saleh-Valenzuela geometric channel model to describe the characteristics of mmWave channel [10]. Specifically, the channel \mathbf{h}_i from the BS to user- i can be modeled as

$$\mathbf{h}_i = \beta_{i,0}\mathbf{a}(\psi_{i,0}) + \sum_{l=1}^L \beta_{i,l}\mathbf{a}(\psi_{i,l}) \quad (3)$$

where $\beta_{i,0}\mathbf{a}(\psi_{i,0})$ is modeled for the LoS component and $\beta_{i,0}$ is the complex gain, $\beta_{i,l}\mathbf{a}(\psi_{i,l})$ for $1 \leq l \leq L$ is the l th non-line-of-sight (NLOS) component of the i th user, $\beta_{i,l}$ is the NLOS complex gain and L is the total number of NLOS path. The $N_t \times 1$ array response vector $\mathbf{a}(\psi_{i,l})$ for a ULA can be represented by

$$\begin{aligned} \mathbf{a}(\psi_{i,l}) &= \frac{1}{\sqrt{N_t}} \left[1 \ e^{-j2\pi\psi_{i,l}} \ \dots \ e^{-j2\pi(N_t-1)\psi_{i,l}} \right]^T \\ &= \frac{1}{\sqrt{N_t}} \left[1 \ e^{-j2\pi\frac{d}{\lambda}\sin(\theta_{i,l})} \ \dots \ e^{-j2\pi(N_t-1)\frac{d}{\lambda}\sin(\theta_{i,l})} \right]^T \end{aligned} \quad (4)$$

where $\psi_{i,l} = \frac{d}{\lambda}\sin(\theta_{i,l})$, λ is the signal wavelength, d is the antenna spacing satisfying $d = \lambda/2$, $\theta_{i,l} \in [-\frac{\pi}{2}, \frac{\pi}{2}]$ is the angle of departure of each cluster to the user- i , which is between the signal and the array antenna.

2.2 BeamSpace MIMO System

When the baseband RFs use fixed beamforming at the transmitter, the traditional MIMO spatial channel can be transformed into an equivalent beamspace channel. The system block diagram is shown in Fig. 2, where the fixed beamforming can be realized by discrete lens array (DLA) [11]. DLA behaves as a convex lens, directing the signals towards different points of the focal surface [12]. Specifically, such DLA plays the role of a beamforming matrix \mathbf{U} , which contains the array steering vectors of M orthogonal directions beam covering the entire space.

We assume that the number of generated beams is equal to the number of transmitting antenna $M = N_t$, which means the resolution of the beam is $\Delta\theta_0 = \frac{1}{N_t}$. Then, the system signal model of (2) can be expressed as

$$\mathbf{y} = \mathbf{H}\mathbf{U}\mathbf{W}\mathbf{x} + \mathbf{n} \quad (5)$$

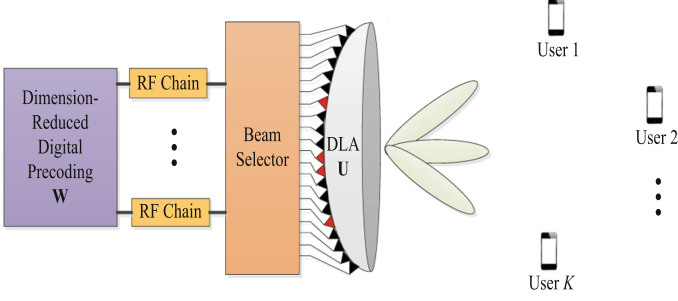


Fig. 2. Beam space MIMO system

where $\mathbf{U} \in N_t \times N_t$ is a beamforming matrix that can be expressed as

$$\begin{aligned} \mathbf{U} &= [\mathbf{a}(0), \mathbf{a}(\Delta\theta_0), \dots, \mathbf{a}((N_t - 1)\Delta\theta_0)] \\ &= \frac{1}{\sqrt{N_t}} \begin{Bmatrix} 1 & 1 & 1 & \dots & 1 \\ 1 & e^{-j2\pi \frac{1}{N_t}} & e^{-j2\pi \frac{2}{N_t}} & \dots & e^{-j2\pi \frac{N_t-1}{N_t}} \\ \vdots & \vdots & \vdots & \ddots & \vdots \\ 1 & e^{-j2\pi(N_t-1) \frac{1}{N_t}} & e^{-j2\pi(N_t-1) \frac{2}{N_t}} & \dots & e^{-j2\pi(N_t-1) \frac{N_t-1}{N_t}} \end{Bmatrix} \end{aligned} \quad (6)$$

Actually, \mathbf{U} is a normalized DFT (Discrete Fourier Transform, DFT) matrix from (6): $\mathbf{U}^H \mathbf{U} = \mathbf{U} \mathbf{U}^H = \mathbf{I}$. Let $\tilde{\mathbf{H}} = \mathbf{H} \mathbf{U} = [(\mathbf{h}_1 \mathbf{U})^T, (\mathbf{h}_2 \mathbf{U})^T, \dots, (\mathbf{h}_K \mathbf{U})^T]^T = [\tilde{\mathbf{h}}_1^T, \tilde{\mathbf{h}}_2^T, \dots, \tilde{\mathbf{h}}_K^T]^T$, the spatial domain matrix is changed to the beamspace channel matrix and the signal model of the beam domain can be expressed as

$$\mathbf{y} = \tilde{\mathbf{H}} \mathbf{W}_B \mathbf{x} + \mathbf{n} \quad (7)$$

where $\tilde{\mathbf{H}}$ is the beamspace channel matrix and \mathbf{W}_B is the precoding matrix of the beamspace.

The NLOS component L in (3) is much smaller due to the propagation characteristics of mmWave scattering. In addition, the high-resolution narrow beam has a strong spatial isolation, so the beamspace is sparse. Therefore $|\tilde{\mathbf{H}}(k, b)|^2$ reflects the channel energy distribution on these beams. Figure 3 gives an example of the energy distribution when the number of transmitting antenna N_t is 32 and user number K is 16. The energy distribution of conventional MIMO channel in the spatial domain is shown in the Fig. 3(a), from which we can see the energy distribution is very scattered. On the contrary, the beamspace MIMO energy distribution is relatively concentrated in Fig. 3(b).

Figure 3 obviously shows that the characteristics of the sparseness of the beamspace channel. The channel energy is mainly concentrated on some beams. So we can select only a small number of energy concentrated beams to serve users according to the sparse beamspace channel to reduce the dimension of MIMO system. After the beam selection, system model can be described as

$$\mathbf{y} \approx \tilde{\mathbf{H}}_s \mathbf{W}_s \mathbf{x} + \mathbf{n} \quad (8)$$

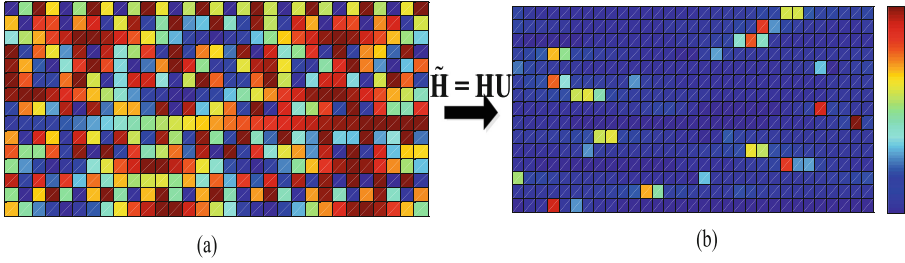


Fig. 3. Energy distribution: traditional MIMO in the spatial domain; (b) beamspace MIMO

where $\tilde{\mathbf{H}}_s = \tilde{\mathbf{H}}(:, \mathbf{B}_{select})$, \mathbf{B}_{select} is the selected beam set which contains the indices of selected beams. In order to guarantee the spatial multiplexing gain of K users, each user chooses 1 beam at least, $Card(\mathbf{B}_{select}) = N_{RF} = K$, and in the scenario of each user chooses 2 beams, $Card(\mathbf{B}_{select}) = N_{RF} = 2K$.

Then, the channel matrix dimension is reduced from $K \times N_t$ to $K \times Card(\mathbf{B}_{select})$. As the dimension-reduced digital precoding matrix, \mathbf{W}_s is much smaller than that of the traditional MIMO digital precoding matrix \mathbf{W} in (2). As a result, the sparseness can be used to achieve spatial multiplexing and reduce the number of RF chains from $O(N_t)$ to $O(K)$, which leads to low power consumption.

3 Beam Selection

3.1 Beam Selection Challenge

The two main problems existing in beam selection are users sharing beam and inter-beam interference, which will be explained as below.

The ideal situation is that there is no interference between the beams for each user, but the ideal state does not exist. Even if the number of N_t is very large and beam resolution is very high, multiple selections of the same beam for different users are not to be ignored. Now, the case that different users have different strongest beams is equivalent to select K different beams from total N_t beams. Therefore, the probability P that there exists users sharing the same strongest beam is $P = 1 - \frac{N_t!}{N_t^K (N_t - K)!}$ [7]. For a mmWave system with $N_t = 256$ and $K = 32$, $P \approx 87\%$. As shown in Fig. 4(a), the beam b_2 is the strongest gain beam of both U_1 and U_2 . It can be seen that ignores user sharing beam problem while selects the strongest beam for users, which will simultaneously select the sharing beam b_1 for U_1 and U_2 leading to the dimension-reduced beamspace channel matrix $\tilde{\mathbf{H}}_s$ rank-deficient. This means that some users cannot be served, resulting in an obvious performance loss. In order to avoid beam sharing, b_1 should be selected for U_1 and b_2 for U_2 .

Figure 4(b) shows the inter-beam interference scenario. It can be seen from the figure that the strongest beam for U_3 is b_1 and U_4 is b_2 . But there is serious interference between beam b_1 and beam b_2 . The better option is b_1 to provide

services for U_3 , b_3 for the user U_4 , which will greatly reduce the interference between the beams. Figure 4(b) indicates that the strongest gain beam is not the optimal beam and should not ignore the presence of interference.

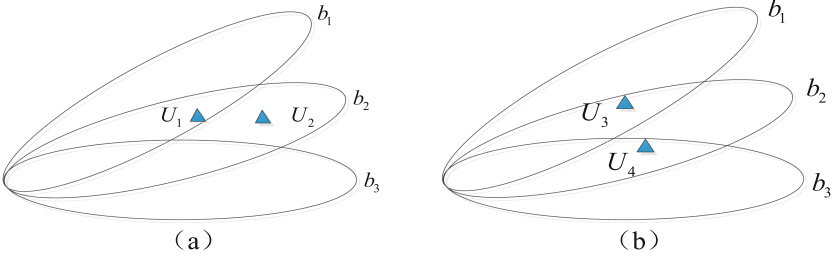


Fig. 4. User distribution scenario (a) users sharing beam; (b) inter-beam interference

3.2 Proposed MI Selection

For the above problems, this paper proposes a low complexity beam selection algorithm-MI beam selection. The two most basic criterias for beam selection are: (1) to serve the target user as much as possible; and (2) to minimize interference to other users. So the beamspace SIR B_{SIR} is defined to evaluate the beam performance selected.

$$B_{SIR}(k, b) = \frac{|\tilde{\mathbf{H}}(k, b)|^2}{\sum_{i \neq k}^K |\tilde{\mathbf{H}}(i, b)|^2} \quad (9)$$

where $|\tilde{\mathbf{H}}(k, b)|^2$ denotes the beam gain when the user k is served by beam b , $|\tilde{\mathbf{H}}(b, i)|^2$ is the interference of b to user i . $B_{SIR}(k, b)$ larger indicates that the beam gain is strong, on the other hand indicates that it has less interference to other users. Therefore, the first step of the beam selection is based on the channel state information and the beamforming matrix to obtain the beamspace channel matrix $\tilde{\mathbf{H}}$, and calculate the beamspace SIR B_{SIR} sorted by descending order. Choosing the maximum B_{SIR} means minimizing interference and solves the problem of inter-beam interference. Then, select the B_{SIR} first n (the number of beams per user needs) columns as an optional beam set. For the problem of shared beam between users, we classify all users into two user groups, shared beam users group (SUs) and non-shared users group (NSUs). The user k is defined as NUS if its largest $B_{SIR}(k, b)$ beam b is different from other users. For the NSUs, directly select the beam b of the largest $B_{SIR}(k, b)$ as the service beam. When a beam is the optimal beam shared by multiple users, the current beam can not be selected as the service beam. And the corresponding user needs to select the sub-optimal $B_{SIR}(k, b)$ beam b which is not selected by NSUs until all users have selected the beam. The MI beam selection algorithm is summarized in Algorithm 1.

Algorithm 1. Proposed MI beam selection algorithm

1. **Require** Beamspace channel matrix $\tilde{\mathbf{H}}$; Number of beams per user n
2. $\tilde{\mathbf{H}}_{abs} = \text{abs}(\tilde{\mathbf{H}})$
3. $\mathbf{S}_{clo}(b) = \text{sum}(\tilde{\mathbf{H}}_{abs}(:, b)), b = 1, 2, \dots, N_t$
4. **For** slot $k(1 \leq k \leq K)$
5. $\mathbf{B}_{SIR}(k, :) = \tilde{\mathbf{H}}_{abs}(k, :)/(\mathbf{S}_{clo}(:) - \tilde{\mathbf{H}}_{abs}(k, :))$
6. $[\text{value index}(k, :)] = \text{sort}(\mathbf{B}_{SIR}(k, :), \text{descend})$
7. **End for**
8. $\mathbf{NSUs} = \emptyset, \mathbf{SUs} = \emptyset, \mathbf{B}_{NSUs} = \emptyset, \mathbf{B}_{SUs} = \emptyset$
9. $\{b_1^*, \dots, b_{k-1}^*, b_k^*, b_{k+1}^*, \dots, b_{n*K}^*\} = \text{reshape}(\text{index}(:, 1:n), 1, n * K)$
10. **If** $b_k^* \notin \{b_1^*, \dots, b_{k-1}^*, b_{k+1}^*, \dots, b_{n*K}^*\}$ $k \in [1, n * K], b_k^* \in [1, N_t]$
11. $\mathbf{B}_{NSUs} = \{\mathbf{B}_{NSUs}, b_k^*\}$
12. **Else**
13. $\mathbf{SUs} = \{\mathbf{SUs}, k\}$
14. **End if**
15. **For** slot $i(1 \leq i \leq \text{Card}(\mathbf{SUs}))$
16. $j = 2$
17. **While** $(\text{index}(\mathbf{SUs}(i), j) \in \mathbf{B}_{NSUs})$
18. $j = j + 1$
19. **End While**
20. $\mathbf{B}_{SUs} = \{\mathbf{B}_{SUs}, \text{index}(\mathbf{SUs}(i), j)\}$
21. **End For**
22. $\mathbf{B}_{select} = \mathbf{B}_{SUs} \cup \mathbf{B}_{NSUs}$
23. **Return:** $\tilde{\mathbf{H}}_s = \tilde{\mathbf{H}}(:, \mathbf{B}_{select})$

Figure 5 shows the selected beams energy distribution by MI algorithm. It can be seen that each user selects the optimal beam as much as possible and the users of the shared beam select the suboptimal beam.

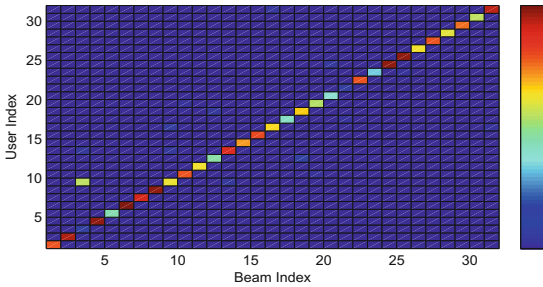


Fig. 5. The selected beams energy distribution by MI algorithm

4 Simulation Results

This section is dedicated to analyse the spectral and energy efficiency losses caused by the selection algorithm compared to the full digital system.

We use the Shannon capacity idealistic as the upper bound for the spectral efficiency [13]

$$R = \sum_{i=1}^K R_i = \sum_{i=1}^K \log_2(1 + SINR_i) \quad (10)$$

where $SINR_i$ is the signal-to-interference-and-noise ratio (SINR) for user i . With the power constraint, the classical digital zero-forcing (ZF) precoding matrix is given by

$$\mathbf{W} = \beta \mathbf{H}^H (\mathbf{H}\mathbf{H}^H)^{-1} \quad (11)$$

where $\beta = \sqrt{\frac{P}{\text{tr}(\mathbf{F}\mathbf{F}^H)}}$, $\mathbf{F} = \mathbf{H}^H (\mathbf{H}\mathbf{H}^H)^{-1}$. Then, the precoding vector \mathbf{w}_i for user i is defined as the i^{th} column of \mathbf{W} . From (1), $SINR_i$ is calculated as

$$SINR_i = \frac{|\mathbf{h}_i \mathbf{w}_i|^2}{\delta^2 + \sum_{k=1, k \neq i}^K |\mathbf{h}_i \mathbf{w}_k|^2} \quad (12)$$

The simulation parameters of the system are as shown in Table 1. Then, the MM algorithm, the IA algorithm and the proposed MI algorithm are simulated and analyzed. Meanwhile the full digital ZF precoding (the number of RF links is 256) is provided as the upper bound of the comparison.

Table 1. Simulation parameters

SNR	-10 dB–30 dB	Precoding	ZF
Antennas number N_t	256	User distribution	$[-\frac{\pi}{2}, \frac{\pi}{2}]$ uniform distribution
Users number K	2–70	NLoS components L	$\beta_{i,0} \sim CN(0, 1)$ $\beta_{i,l} \sim CN(0, 10^{-1})$

Figure 6 shows the spectrum efficiency comparison when user number $K = 32$. It can be seen from Fig. 6 that the performance of the proposed MI algorithm is close to the AI algorithm when the user selects 1 beam. Compared with MM algorithm, the performance of MI is about 30% higher at high SNR (SNR > 10 dB) region. Figure 6 also shows when 2 beams are selected by each user, the proposed MI algorithm is close to the full digital ZF precoding. At the same time, the performance of the MI algorithm with 1 beam per user is consistent with the performance of the MM algorithm with 2 beams per user. The

main reason for the poor performance of the MM algorithm is that it ignores the problems of users sharing beam and inter-beam interference. Although IA achieves better performance, iterative searching for IUs to maximize the achievable sum-rate leads to high computational complexity because of large-scale matrix operations including inverse [8].

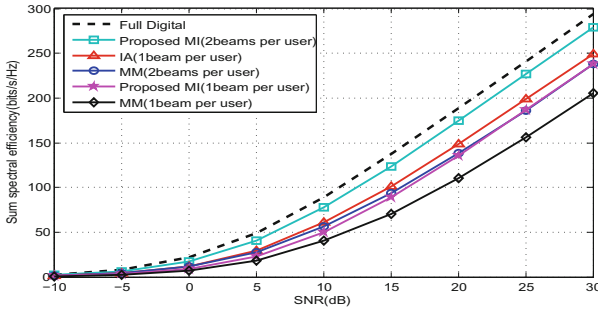


Fig. 6. Spectrum efficiency comparison when user number $K = 32$

Figure 7 further considers a $K = 64$ scenario where the MI algorithm and IA algorithm have almost the same performance when the user selects 1 beam in the low SNR environment. With the increase of SNR ($\text{SNR} > 15 \text{ dB}$), the performance of MI algorithm is obviously better than IA algorithm.

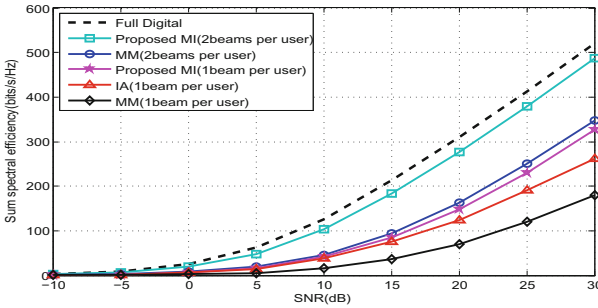


Fig. 7. Spectrum efficiency comparison when user number $K = 64$

Figure 8 illustrates the effect of the number of users K on the spectral efficiency in term of $\text{SNR} = 25 \text{ dB}$. When the number of users is small, the performance of the MI algorithm and IA algorithm is close to that of the MM algorithm performance of 2 beams per user. As the number of users ($K > 45$) increase, the performance of IA algorithm begins to decline and the proposed MI algorithm is better than the IA algorithm. This is mainly due to MI algorithm considering

the interference of the selected beam to other users, while MM and IA algorithm are based on the choice of the strongest beam.

The energy efficiency comparison is shown in Fig. 9 when SNR = 25 dB. The energy efficiency η is modeled as $\eta = \frac{R}{\rho + N_{RF}\rho_{RF}}$ (bps/Hz/W) [8], where R is spectral efficiency, ρ is the transmit power, $N_{RF}\rho_{RF}$ is the number of RF chains and energy consumed. This paper sets up the typical values $\rho = 32$ mw, $\rho_{RF} = 34.4$ mw. As expected in Fig. 9, the MI algorithm is superior to the MM algorithm for the case of 2 beams per user. For the case of 1 beam per user, with the increasing of users, MI algorithm is obviously better than the MM algorithm. When the user number satisfies $K > 42$, MI becomes the optimal algorithm.

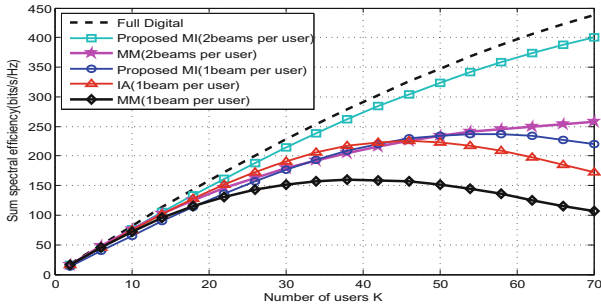


Fig. 8. Spectrum efficiency comparison when SNR = 25 dB

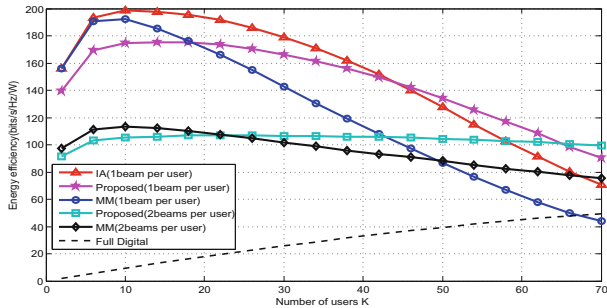


Fig. 9. Energy efficiency comparison when SNR = 25 dB

5 Conclusions

This paper introduces a low RF complexity beamspace MIMO system. Taking the potential multiuser interferences into consideration, we propose an MI beam selection algorithm. Finally, the simulation results verify that the proposed algorithm achieves the performance closing to full digital precoding when selecting 2 beams per user, and has better energy efficiency. It also has good performance when selecting one beam per user, especially in the condition of more users.

Acknowledgment. This work was supported by the State Major Science and Technique Project (MJ-2014-S-37), the National Natural Science Foundation of China (61201134), and the 111 Project (B08038).

References

1. Chen, S., et al.: Adaptive beamforming in TDD-based mobile communication systems: state of the art and 5G research directions. *IEEE Wirel. Commun.* **23**(6), 81–87 (2017)
2. Liu, P., Renzo, M.D., Springer, A.: Line-of-sight spatial modulation for indoor mmWave communication at 60 GHz. *IEEE Trans. Wirel. Commun.* **15**(11), 7373–7389 (2016)
3. Kim, Y., et al.: Feasibility of mobile cellular communications at millimeter wave frequency. In: *Global Communications Conference IEEE*, pp. 1–6 (2016)
4. Liu, J., Minn, H., Gatherer, A.: The death of 5G part 2: will analog be the death of massive MIMO? In: *IEEE ComSoc Technology News 2015* (2015)
5. Pu, W., et al.: Low Complexity hybrid beamforming based on orthogonal constraint and phase extraction. In: *IEEE Wireless Communications and Networking Conference IEEE*, pp. 1–5 (2017)
6. Wang, B., et al.: Spectrum and energy efficient beamspace MIMO-NOMA for millimeter-wave communications using lens antenna array. *IEEE J. Sel. Areas Commun.* **35**(10), 2370–2382 (2017)
7. Xue, Q., Fang, X., Wang, C.X.: Beamspace SU-MIMO for future millimeter wave wireless communications. *IEEE J. Sel. Areas Commun.* **35**(7), 1564–1575 (2017)
8. Gao, X., et al.: Near-optimal beam selection for beamspace MmWave massive MIMO systems. *IEEE Commun. Lett.* **20**(5), 1054–1057 (2016)
9. Han, S., et al.: Large-scale antenna systems with hybrid analog and digital beamforming for millimeter wave 5G. *IEEE Commun. Mag.* **53**(1), 186–194 (2015)
10. Amadori, P.V., Masouros, C.: Low RF-complexity millimeter-wave beamspace-MIMO systems by beam selection. *IEEE Trans. Commun.* **63**(6), 2212–2223 (2015)
11. Luo, F.L., Zhang, C.: *Millimeter-Wave MIMO Transceivers: Theory, Design and Implementation*. Wiley-IEEE Press, Hoboken (2016)
12. Brady, J., Hogan, J., Sayeed, A.: Multi-beam MIMO prototype for real-time multiuser communication at 28 GHz. *IEEE GLOBECOM Workshops IEEE*, pp. 1–6 (2016)
13. Han, Y., et al.: A joint SDMA and interference suppression multiuser transmission scheme for millimeter-wave massive MIMO systems. In: *Sixth International Conference on Wireless Communications and Signal Processing IEEE*, pp. 1–5 (2014)



An Efficient Algorithm for Constructing Underwater Sensor Barrier

Weiqliang Shen¹, Chuanlin Zhang^{1(✉)}, Min-Rong Chen², Jinglun Shi³,
and Guo-Qiang Zeng⁴

¹ College of Information Science and Technology, Jinan University,
Guangzhou 510632, China

weiqshen@gmail.com, tclzhang@jnu.edu.cn

² School of Computer, South China Normal University, Guangzhou 510631, China
mrongchen@126.com

³ School of Electronic and Information Engineering,
South China University of Technology, Guangzhou 510641, China
shijl@scut.edu.cn

⁴ National-Local Joint Engineering Laboratory of Digitalize Electrical Design
Technology, Wenzhou University, Wenzhou 325035, China
zeng.guoqiang5@gmail.com

Abstract. Most existing works on barrier coverage assume that sensors are deployed in a two-dimensional (2D) long thin belt region, where a barrier is a chain of sensors from one end of the region to the other end with overlapping sensing zones of adjacent sensors. However, 2D sensor barrier construction mechanism cannot be directly applied to three-dimensional (3D) sensor barrier construction problem, such as underwater sensor barrier construction, where sensors are finally distributed over a 3D space. In this paper, we investigate how to efficiently construct an underwater sensor barrier with minimum mobile sensors while reducing energy consumption. We first determine the minimum number of sensors needed for an underwater sensor barrier construction. Furthermore, we analyse the relationship between the initial locations of sensors and the optimal location of the underwater sensor barrier, based on which we derive the optimal final locations for all sensors. Finally, we propose an efficient algorithm to move sensors from their initial locations to final locations. Extensive simulations show that, compared with HungarianK approach, the proposed algorithm costs shorter running time and similar maximum movement distance of any one sensor.

Keywords: Underwater sensor barrier · Wireless sensor network
Deployment algorithm

1 Introduction

Wireless sensor networks (WSNs) have been widely used in many real life applications, such as battlefield surveillance, environmental monitoring and industrial

diagnostics [1]. As an critical issue in WSNs, barrier coverage is garnering more and more attention in recent years [2–5]. Different from area coverage, which aims at gathering the information occurring within the region of interest (ROI), barrier coverage concerns with constructing a barrier for intrusion detection, and has been widely employed in practical security applications. For example, international border surveillance and critical infrastructure protection.

Most existing works on barrier coverage assume that sensors are deployed in a 2D long thin belt region, where a barrier is a chain of sensors from one end of the region to the other end with overlapping sensing zones of adjacent sensors. Fan et al. [6] studied the coverage of a line interval with a set of wireless sensors with adjustable coverage ranges. Liu et al. [7] studied the strong barrier coverage of a randomly-deployed sensor network on a long irregular strip region. Wang et al. [2, 8] explored the effects of location errors on barrier coverage. Dobrev et al. [9] studied three optimization problems related to the movement of sensors to achieve weak barrier coverage. He et al. [10] presented a condition under which line-based deployment is suboptimal, and proposed a new deployment approach named curve-based deployment. Ban et al. [11] considered k-barrier coverage problem in 2D wireless sensor networks. Dewitt and Shi [12] incorporated energy harvesting into the 2D barrier coverage problem. Based on the 2D assumption, all sensors composing the barrier finally reside on a 2D plane. This assumption may be reasonable in a terrestrial wireless sensor network where the height of the network is usually negligible as compared to its length and width. However, 2D sensor barrier construction mechanism cannot be directly applied to 3D sensor barrier construction problem, such as underwater barrier construction, where sensors are finally distributed over a 3D space.

In the real life, a wide range of waterside critical infrastructures require the protection of underwater barrier, such as naval base, nuclear power plant and docks. How to protect them from illegal intrusion is an essential problem. A popular defense mechanism from intruders is deploying physical net, which is integrated with sensors as a barrier, along the surrounding waters of these infrastructures. For example, Marinet [13], a physical barrier, whose objective is to prevent swimmer, diver, frogman, floating explosive packages and other water based intruders from illegal intrusion. Despite the physical net barrier provides variety of functions satisfying common application to thwart illegal intruders, there are still some problems which it may not overcome so far. For example, the deployment of physical net barrier usually involves with artificial participation, this may not be a great efficient manner. Especially, when facing a vast and deep underwater space, it will cost a lot of resources whereas the construction progress of physical net is inefficient. Moreover, these physical net barriers may not satisfy the requirement of some special applications, such as submarine intrusion detection which aims to detect illegal submarine intrusion but hopes not to be discovered by the submarine that there are barriers.

To tackle aforementioned problems, constructing underwater sensor barrier (UWSB¹) with mobile sensors with capability of intrusion detection in 3D

¹ In this paper, we only consider strong underwater sensor barrier coverage. It will be shortly referred to as UWSB in the following.

underwater space, may be an adequate alternative choice. Compared to the barrier coverage in 2D plane, a barrier coverage in 3D space is not a chain of adjacent sensors any more. Instead, a barrier in 3D space should be a set of sensors with overlapping sensing zones of adjacent sensors that covers an entire (curly) surface that cuts across the space [14].

In this work, we aim to efficiently construct an underwater sensor barrier with minimum mobile sensors while reducing energy consumption. Inspired by [15], in which a Hungarian-based approach named HungarianK was proposed to solve UWSB construction problem, we focus on constructing an UWSB via assigning each sensor to desired final location (i.e., grid point²). Furthermore, we recognize that the computational complexity of the Hungarian-based method is at least $O(n^3)$, this may not be a good result in term of large-scale sensor network due to the severe constraint of limited computation capability of individual sensor node. In this case, we are looking forward to proposing another approach to reduce the computational complexity while minimizing the maximum movement distance of any one sensor so as to balance energy consumption of each sensor node. Considering the difference between 2D sensor barrier and 3D underwater sensor barrier, we first determine the minimum number of mobile sensors needed for an UWSB. Furthermore, we analyse the relationship between the initial locations of sensors and the optimal location of underwater sensor barrier, based on which we derive the optimal final location for each sensor. Finally, we propose an efficient algorithm to move sensors from their initial locations to final locations. Extensive simulations show that, compared with HungarianK approach proposed in [15], the proposed algorithm costs shorter running time and similar maximum movement distance of any one sensor.

The rest of the paper is organized as follows. In Sect. 2, we explain the network model, and define some important concepts. Next, in Sect. 3, we show how to efficiently construct an underwater sensor barrier with minimum mobile sensors while reducing energy consumption. Section 4 evaluates the performance of the proposed algorithm through extensive simulations, and finally, Sect. 5 concludes the paper.

2 Model Statement

We consider an underwater wireless sensor network consisting of sensors deployed in a large-scale 3D cuboid of size $l \times w \times h$, where l , w , and h denote the length, the width, and the height of the cuboid, respectively. Without loss of generality, we assume that the illegal objects move along the direction of cuboid length, as shown in Fig. 1, O_1 and O_2 denote object1 and object2, respectively. The following assumptions are made in this work.

- An object (or intruder) may cross the underwater sensor barrier via an crossing path starting at the left face and ending at the right face of the cuboid.

² In this paper, in order to make presentation clearer, we use final location instead of grid point.

- Each sensor has the following abilities: localize its own position, to move in all 3-dimensions underwater, communicate with other sensors, and detect intruders. For simplicity, we assume an ideal 0/1 sphere sensing model that an object within (outside) a sensor’s sensing sphere is detected by the sensor with probability one (zero).
- In the initial configuration, the locations of all sensors are uniformly and independently distributed in the cuboid. Such a random initial deployment is desirable in scenarios where prior knowledge of the region of interest is not available, and may be the result of certain deployment strategies [15].

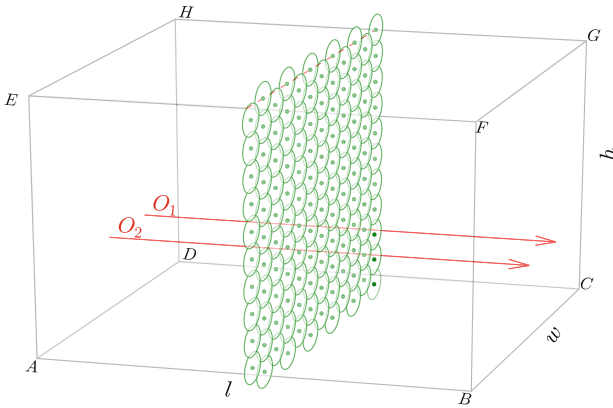


Fig. 1. Illustration of an underwater sensor barrier

In the following, we introduce some important definitions used in this work.

Definition 1 (Underwater sensor barrier [14]). *A set of sensors, with overlapping sensing zones of adjacent sensors, that cover an entire (curly) surface which cuts across the underwater space.*

Definition 2 (Crossing path). *A crossing path is a continuous moving trajectory with the start point at one face of the cuboid and the end point at the opposite face.*

Definition 3 (Initial location). *In the initial configuration, all sensors are uniformly and independently distributed in underwater space, the sensor’s location at this moment is referred to as initial location.*

Definition 4 (Final location). *The final location is the movement destination of sensor. An UWSB is constructed after all sensors arrive at their final locations.*

3 Constructing Underwater Sensor Barrier

According to aforementioned assumptions, initially, all sensors are uniformly and independently distributed in a cuboid. Our goal is to efficiently construct an underwater sensor barrier with minimum mobile sensors by moving them from their initial locations to optimal final locations. To construct an UWSB effectively and efficiently, we first derive the minimum number of required sensors, by which we can determine whether there are enough sensors to construct an UWSB. Then we implement UWSB construction via following three phases. (1) Find the optimal location of the UWSB. (2) Compute the optimal final locations of all sensors. (3) Propose an efficient algorithm to assign the sensors to their final locations.

3.1 The Minimum Number of Required Sensors

In the context of our work, it is a rectangle of size $w \times h$ after projecting the UWSB to the left face of the cuboid. Thus, the minimum number of required sensors equals to the minimum number of required circles with radius r to full cover a rectangle of size $w \times h$. In this case, the circle is the 2D projection of sensor’s sensing sphere, and the radius r is the sensing radius of the sensor.

Actually, in term of the minimum number of circles required for the complete area coverage problem, Kershner [16] had proved that the regular triangular tessellation is the optimal tessellation which results in a set of regular hexagons full cover a 2D plane without any overlap. These sensors finally locate at the center of each regular hexagon with circumradius r , which is the sensing radius of the sensor, as shown in Fig. 2. To obtain the minimum number of required sensors, Theorem 1 is given as follows:

Theorem 1. *The minimum number of required regular hexagons with circum-radius r to full cover a rectangle of size $w \times h$ is:*

$$\begin{aligned}
 f_s(w, h, r) = & \lceil \frac{h}{r \times \sqrt{3}} \rceil \times \lceil \frac{\lceil \frac{2 \times (w-r)}{3 \times r} \rceil + 1}{2} \rceil \\
 & + (\lceil \frac{h - \frac{r \times \sqrt{3}}{2}}{r \times \sqrt{3}} \rceil + 1) \times \lfloor \frac{\lceil \frac{2 \times (w-r)}{3 \times r} \rceil + 1}{2} \rfloor.
 \end{aligned}
 \tag{1}$$

Proof. Given a rectangle of size $l \times w$, in the length direction, we divide the rectangle into C columns, the first column width $a = r$, 2-th~ $(C - 1)$ -th column width $b = \frac{3 \times r}{2}$, and the last column width $\in (0, b]$, as shown in Fig. 2. So, the number of columns is:

$$f_c(w, r) = \lceil \frac{2 \times (w - r)}{3 \times r} \rceil + 1.
 \tag{2}$$

In the width direction, the number of rows of odd-number columns is:

$$f_o(h, r) = \lceil \frac{h}{r \times \sqrt{3}} \rceil.
 \tag{3}$$

The number of rows of even-number columns is:

$$f_e(h, r) = \lceil \frac{h - \frac{r \times \sqrt{3}}{2}}{r \times \sqrt{3}} \rceil + 1. \tag{4}$$

Combining Eqs. (2), (3), and (4), we have the minimum number of regular hexagons:

$$\begin{aligned} f_s(w, h, r) &= f_o(d, r) \times \lceil \frac{f_e(w, r)}{2} \rceil + f_e(h, r) \times \lfloor \frac{f_e(w, r)}{2} \rfloor \\ &= \lceil \frac{h}{r \times \sqrt{3}} \rceil \times \lceil \frac{\lceil \frac{2 \times (w-r)}{3 \times r} \rceil + 1}{2} \rceil \\ &\quad + (\lceil \frac{h - \frac{r \times \sqrt{3}}{2}}{r \times \sqrt{3}} \rceil + 1) \times \lfloor \frac{\lceil \frac{2 \times (w-r)}{3 \times r} \rceil + 1}{2} \rfloor. \end{aligned} \tag{5}$$

In this work, the projection of the UWSB is a rectangle of size $w \times h$, so the minimum number of required sensors is $f_s(w, h, r)$. Thus, if the number of deployed sensor $N \geq f_s(w, h, r)$, then at least one UWSB can be constructed. Otherwise, we cannot achieve our goal.

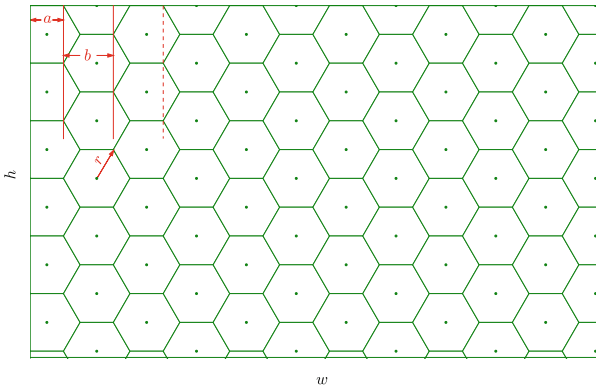


Fig. 2. Fully cover a rectangle of size $w \times h$ with minimum regular hexagons.

3.2 Find the Optimal Location of UWSB

We note that the optimal location of UWSB is similar to the optimal barrier location in [14], where an algorithm was devised to find the optimal sensor barrier location.

Supposing as in Fig. 3 that the plane X is parallel to the coast line to be protected, a set of mobile sensors dropped from an aircraft were floating on water surface. The sensors must move to some plane X , such that X minimizes the energy expended by any one sensor. In this case, we are assuming that the sensors

will only move in one direction to approach the X location. It is straightforward to show that X must be somewhere inside the set x -coordinates of the sensors, and as any two sensors move to meet one another, the total distance they travel is the distance between them. Thus, the sensors on either edge move the farthest, and half the distance between them minimizes the maximum distance any one sensor moves. So, to minimize the maximal distance traveled by any sensor, we can calculate the optimal X location as follows [14]:

$$X = (\max x_i + \min x_i)/2$$

For example, in Fig. 3, $\max x_i = 8, \min x_i = 2$. Thus, all the sensors should move to the line $X = (8 + 2)/2 = 5$ to minimize the movement distance of any one sensor. That means line $X = 5$ is the optimal location of the UWSB.

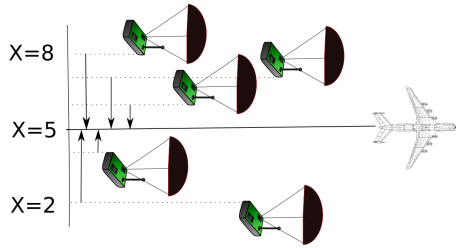


Fig. 3. The first phase: an air drop of sensors along a straight line resulting in scattered placement along that line. The figure is taken from [14].

3.3 Compute the Optimal Final Locations of All Sensors

Since an UWSB is actually a flat surface parallel to the left face of cuboid, the optimal final locations of all sensors are the central points of regular hexagon, as shown in Fig. 2. Thus, for each central point of regular hexagon, the x -coordinate equals to that of optimal location of UWSB, we can derive y, z -coordinates of each central points as follows:

We first get the y -coordinate of each column via Eq. (6),

$$f_y(w, r, i) = \begin{cases} \frac{r}{2}, & i = 0 \\ \frac{r}{2} + \frac{i \times r}{2}, & 1 \leq i < N_{sp} - 1 \\ \frac{r}{2} + \frac{i \times r}{2}, & i = N_{sp} - 1 \ \& \ \frac{r}{2} + \frac{(N_{sp}-1) \times r}{2} < w \\ w, & i = N_{sp} - 1 \ \& \ \frac{r}{2} + \frac{(N_{sp}-1) \times r}{2} \geq w. \end{cases} \quad (6)$$

then we get the z -coordinate of each point column by column. For odd-number columns, h is the cuboid height, r is the sensing radius, R_j denotes the j -th row, and $0 \leq j < \lceil \frac{h}{r \times \sqrt{3}} \rceil$, we have

$$f_z(w, r, R_j) = h - \frac{r \times \sqrt{3}}{2} - R_j \times r \times \sqrt{3}. \quad (7)$$

For even-number columns, h is the cuboid height, r is sensor's sensing radius, R_j denote the j -th row, and $0 \leq j < \lceil \frac{h - \frac{r \times \sqrt{3}}{2}}{r \times \sqrt{3}} \rceil + 1$, we have

$$f_z(w, r, R_j) = h - R_j \times r \times \sqrt{3}. \quad (8)$$

Combining Eqs. (7) and (8), we have

$$f_z(w, r, R_j) = \begin{cases} h - \frac{r \times \sqrt{3}}{2} - R_j \times r \times \sqrt{3}, & \text{odd-number columns} \\ h - R_j \times r \times \sqrt{3}, & \text{even-number columns.} \end{cases} \quad (9)$$

Therefore, by combining the optimal location x of UWSB, we get the coordinates $(x, f_z(w, r, R_j), f_z(w, r, R_j))$ of optimal final locations of all sensors.

3.4 Movement Algorithm

After determining the optimal final locations of all sensors, an UWSB can be constructed by moving sensors from their initial locations to the final locations. Actually, this movement process is related to the Assignment Problem, which aim to create a one-to-one matching between sensors and final locations. A classic solution to the Assignment Problem is known as the Hungarian Method which can be computed in $O(n^3)$, where n is the number of sensors or final locations.

In [15], the authors proposed a Hungarian-based approach named HungarianK, which can be computed in $O(n^4)$, to solve the sensor assignment problem. However, it may not be a good choice in term of large-scale sensor network due to the severe constraints of limited computation capability of individual sensor node. In this case, we are looking forward to proposing another method to reduce the computational complexity while minimizing the maximum movement distance of any one sensor.

Since all sensors are uniformly and independently distributed in the cuboid, to make control of the maximum movement distance of any one sensor while reduce the computation time, we propose a **height-based match algorithm (HBMA)** to solve our problem. We assume that the cuboid locates at a 3D coordinate system where integer coordinates (x, y, z) represent the location information of a point in underwater space, N_i denotes the number of sensors in the i -th column, all sensors are sorted by x -coordinate in ascending order firstly, this sorted sensor list is denoted as L_{sort} . For each column of the UWSB, N_i sensors are popped out from L_{sort} and assigned to the i -th column, and each sensor will assign to its final location according its height (i.e., z -coordinate). The detail of HBMA is shown in Algorithm 1.

From the pseudo-code of Algorithm 1, we learn that the proposed algorithm consists two main loops. In the outer loop (line 05–line 20), UWSB is constructed column by column, and the outer loop terminates if the last column (i.e., the N_{column} -th column) of UWSB is constructed. Thus, the outer loop runs N_{column} times. In the inner loop, there are two sub-loop (i.e., line 12–line 14 and line 16–line 19) both terminate in $O(n)$. However, line 15 concerns with Quicksort

Algorithm 1. *HBMA*(L_{init})**Input:**

The initial locations L_{init} of all sensors.

Output:

The matched list L_{match} , such as $\{((x_0, y_0, z_0), (x'_0, y'_0, z'_0)), ((x_1, y_1, z_1), (x'_1, y'_1, z'_1)), \dots\}$. $((x_n, y_n, z_n), (x'_n, y'_n, z'_n))$ means that sensor at the location of (x_n, y_n, z_n) should move to the location of (x'_n, y'_n, z'_n) .

```

1:  $L_{sort} \leftarrow Quicksort(L_{init})$ ;
2: Compute the optimal final locations of all sensors, return the optimal final location list  $L_{fl}$ 
3:  $N_{column} \leftarrow f_c(w, r)$ ;
4:  $seq \leftarrow 0$ ;
5: for  $col = 0 \rightarrow N_{column} - 1$  do
6:   if  $(col + 1) \% 2 == 1$  then
7:      $N_{row} \leftarrow f_o(h, r)$ ;
8:   else
9:      $N_{row} \leftarrow f_e(h, r)$ ;
10:  end if
11:   $L_{temp} \leftarrow null$ 
12:  for  $row = 0 \rightarrow N_{row} - 1$  do
13:     $L_{temp} \leftarrow L_{sort}.pop()$ 
14:  end for
15:   $L_{temps} \leftarrow Quicksort(L_{temp})$ ;
16:  for  $row = 0 \rightarrow N_{row} - 1$  do
17:     $L_{match} \leftarrow (L_{temps}[row], L_{fl}[seq])$ ;
18:     $seq \leftarrow seq + 1$ ;
19:  end for
20: end for

```

algorithm whose computational complexity is $O(n \log(n))$ in average, and in the worst case, the computation complexity of Quicksort is $O(n^2)$. Therefore, the proposed algorithm can be computed in $O(n^2 \log(n))$ in average. Even in the worst case, the computation complexity of HBMA is just $O(n^3)$. Compared with the HungarianK approach proposed in [15], whose computational complexity is $O(n^4)$, the proposed algorithm has lower computational complexity.

4 Performance Evaluation

In this section, we evaluate the performance of the proposed algorithm through extensive simulations by using Python program language. We setup the simulation environment as follows:

1. The underwater space is modeled as a cuboid with length $l = 4000$ m, width $w = 3600$ m, and height $h = 2500$ m, respectively.
2. We use the minimum number of required sensors to construct an UWSB in the simulations. Sensors are uniformly and independently distributed in the cuboid.
3. We vary the sensing radius r_s of the sensor from 400 m to 200 m. From the Eq. (5), we learn that the shorter the sensing radius, the more the number

of required sensors. Thus, as the variation of sensing radius r_s , the minimum number of required sensors varies from 31 to 104.

4. All experiments are repeated by 100 runs.

The following performance metrics are used to evaluate the performance of the proposed algorithm.

- Running time: The lower Running time, the lower requirement of computation power and the less energy to be consumed for the sensor.
- Maximum movement distance of any one sensor: For each sensor, the movement distance indicates the straight-line distance between the initial location and the final location. Generally, the movement distance of a sensor is proportional to its energy consumption, and the longer the movement distance, the larger the energy consumption. Thus, in order to balance energy consumption, we hope to minimize the maximum movement distance of any one sensor.

In the simulations, we evaluate the performance of the proposed algorithm by constructing an UWSB with the minimum mobile sensors. The sensing radius r_s varies from 400 m to 200 m, accordingly, the minimum number of required sensors increases from 31 to 104. As shown in Fig. 4, the running time increases with the increasement of the number of sensors, and the proposed algorithm HBMA costs shorter running time than the HungarianK proposed in [15]. Figure 5 depicts the maximum movement distance of any one sensor increases with the increasement of the number of sensors, the proposed algorithm HBMA is comparable to the HungarianK in term of the maximum movement distance of any one sensor. Overall, compared with the HungarianK, the proposed algorithm costs shorter running time and similar maximum movement distance of any one sensor.

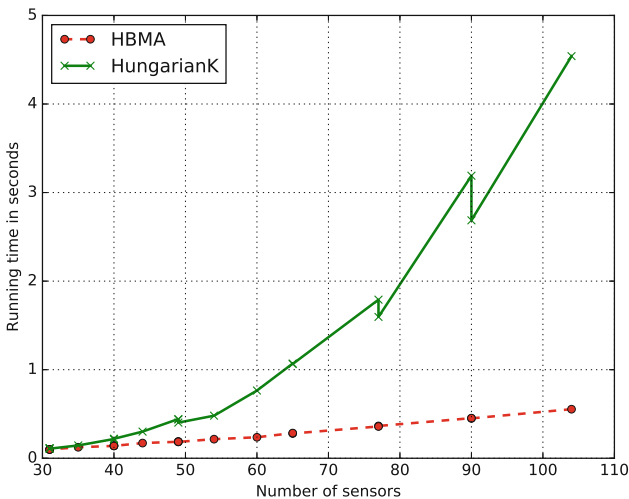


Fig. 4. Comparison of running time between the HungarianK and the proposed algorithm HBMA.

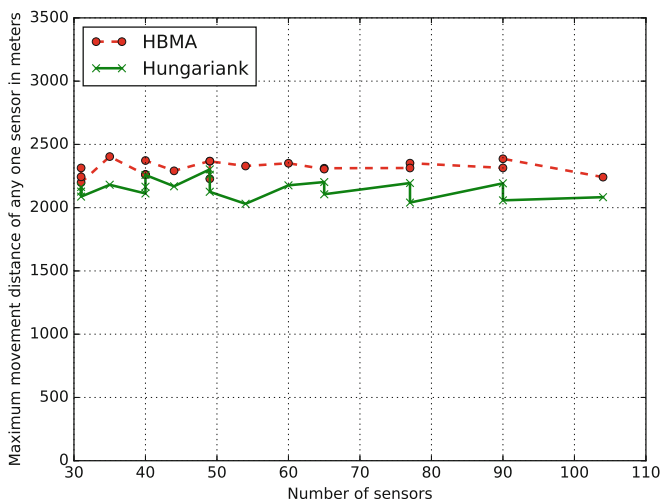


Fig. 5. Comparison of maximum movement distance of any one sensor between the HungarianK and the proposed algorithm HBMA.

5 Conclusion

In this work, to efficiently construct an UWSB with minimum mobile sensors while reducing energy consumption, we first analyse the relationship between the optimal location of UWSB and the initial positions of sensors, and determine the minimum number of mobile sensors needed for constructing an UWSB. Moreover, we derive the optimal final locations of all sensors, based on which we propose an efficient algorithm to move sensors from their initial locations to final locations. Extensive simulations show that, compared to the HungarianK approach, the proposed algorithm costs shorter running time and similar maximum movement distance of any one sensor.

Acknowledgements. The authors would like to thank the referees whose insightful comments have helped improve the presentation of this paper significantly. This work was supported in part by Major Omnibus Reform Project (Information and Computing Science) of China under Grant No. 82616611, National Science Foundation of China under Grant Nos. 61373158 and 61671213, Guangzhou Key Lab of Body Data Science under Grant No. 201605030011, and Zhejiang Provincial Natural Science Foundation of China under Grant Nos. LY16F030011 and LZ16E050002.

References

1. Wang, B.: Coverage problems in sensor networks: a survey. *ACM Comput. Surv. (CSUR)* **43**, 1–53 (2011)
2. Wang, Z., Chen, H., Cao, Q., Qi, H., Wang, Z., Wang, Q.: Achieving location error tolerant barrier coverage for wireless sensor networks. *Comput. Netw.* **112**, 314–328 (2017)

3. Silvestri, S., Goss, K.: MobiBar: an autonomous deployment algorithm for barrier coverage with mobile sensors. *Ad Hoc Netw.* **54**, 111–129 (2017)
4. Paul, B., Béla, B., Amites, S.: Barrier coverage. *Random Struct. Algorithms* **49**, 429–478 (2016)
5. Wu, F., Gui, Y., Wang, Z., Gao, X., Chen, G.: A survey on barrier coverage with sensors. *Front. Comput. Sci.* **10**, 968–984 (2016)
6. Fan, H., Li, M., Sun, X., Wan, P.J., Zhao, Y.: Barrier coverage by sensors with adjustable ranges. *ACM Trans. Sens. Netw. (TOSN)* **11**, 1–20 (2014)
7. Liu, B., Dousse, O., Wang, J., Saipulla, A.: Strong barrier coverage of wireless sensor networks. In: *Proceedings of the 9th ACM International Symposium on Mobile Ad Hoc Networking and Computing*, pp. 411–420 (2008)
8. Wang, Z., Chen, H., Cao, Q., Qi, H., Wang, Z.: Fault tolerant barrier coverage for wireless sensor networks. In: *INFOCOM, 2014 Proceedings IEEE*, pp. 1869–1877 (2014)
9. Dobrev, S., et al.: Weak coverage of a rectangular barrier. In: Fotakis, D., Pagourtzis, A., Paschos, V.T. (eds.) *CIAC 2017. LNCS*, vol. 10236, pp. 196–208. Springer, Cham (2017). https://doi.org/10.1007/978-3-319-57586-5_17
10. He, S., Gong, X., Zhang, J., Chen, J., Sun, Y.: Barrier coverage in wireless sensor networks: from lined-based to curve-based deployment. In: *2013 Proceedings of the IEEE, INFOCOM*, pp. 470–474 (2013)
11. Ban, D., Yang, W., Jiang, J., Wen, J., Dou, W.: Energy-efficient algorithms for k-barrier coverage in mobile sensor networks. *Int. J. Comput. Commun. Control* **5**, 616–624 (2016)
12. DeWitt, J., Shi, H.: Barrier coverage in energy harvesting sensor networks. *Ad Hoc Netw.* **56**, 72–83 (2017)
13. Marinet: Underwater Port Security System - Intrusion Detection Barrier. <http://www.rbttec.com/products/Maritime-Underwater-Security/marinetunderwatersecuritynet>
14. Barr, S.J., Wang, J., Liu, B.: An efficient method for constructing underwater sensor barriers. *JCM* **6**, 370–383 (2011)
15. Barr, S., Liu, B., Wang, J.: Barrier coverage for underwater sensor networks. In: *Military Communications Conference MILCOM*, pp. 429–478 (2008)
16. Kershner, R.: The number of circles covering a set. *Am. J. Math.* **61**, 665–671 (1939)



Distributed Coverage Hole Detection Algorithm Based on Čech Complex

Wang Yuchen¹, Lu Jialiang¹(✉), and Philippe Martins²

¹ SJTU-ParisTech, Elite Institute of Technology, Shanghai, China
lucassjtu@gmail.com, jialiang.lu@sjtu.edu.cn

² Institut Telecom, TELECOM ParisTech, LTCI, Paris, France
philippe.martins@telecom-paristech.fr

Abstract. Coverage problem is essential to Wireless Sensor Networks on energy efficient deployment and monitoring. In this paper, we propose a distributed Čech complex algorithm for coverage hole detection in WSNs. Based on our algorithm, each node takes only local information to build Čech sub-complex. Simulations on randomly deployed nodes show that the algorithm achieves a comparable accuracy and a much lower communication cost than a centralized Čech complex construction. Furthermore, it can be combined with distributed Rips complex algorithm to gain an even better performance.

Keywords: Coverage problem · Wireless Sensor Network
Čech complex · Distributed algorithm

1 Introduction

As the theoretical foundation of Internet of Things, Wireless Sensor Network (WSN) is a collection of nodes provided with wireless communication capability, limited computing ability, and sensors to detect physical signals in the environment in which they are deployed. However, the deployment of nodes is always either randomly or highly effected by other restrictions. Thus, it is important to study the coverage problem as fundamental issues in a WSN at the very beginning. In general, coverage problem of WSN reflects how well an area is monitored or tracked by sensors [1]. It plays an important role in many superior applications like energy saving, disaster recovering, load balancing and solving deployment problem. For example, researchers have developed an energy saving algorithm for wireless network based on detecting whether a coverage hole appears if certain nodes are shut down or weakened [2].

In the paper [3], Martins uses Čech complex to represent the coverage states of a node system and propose an algorithm to construct the Čech complex based on the coverage information of each node. In order to deal with its high complexity, a parallel version of this algorithm is already given as well [3]. However, the sensor nodes of WSN have also limited communication, computation powers and even unreliable physical links. Therefore, there is a need to process the

information gathered by the sensors locally and then send them back to a central processing unit [4], which means a distributed Čech complex algorithm that we are going to propose in the remainder of this paper is needed in practice.

2 Mathematic Preliminaries

2.1 Simplicial Homology

The homology of the simplicial complex gives us topology information, including connectivity and coverage, about the deployment of WSN nodes. Simplicial homology is a type of homology which results when the spaces being studied are restricted to simplicial complexes and sub-complexes.

Definition 2.1 (simplex): Given a set of vertices V and an integer k , a k -simplex is an unordered subset of $k + 1$ vertices $[v_0, v_1, v_k]$ where $v_i \in V$ and $v_i \neq v_j$ for all $i \neq j$ [6].

As represented in Fig. 1, a 0-simplex is a vertex, a 1-simplex is a segment of line, a 2-simplex is a filled triangle, a 3-simplex is a filled tetrahedron, etc.

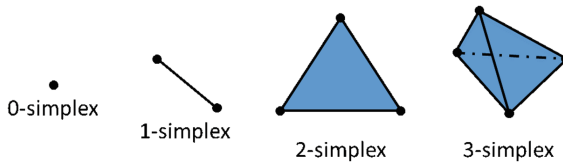


Fig. 1. Examples of simplices

Any subset of vertices included in the set of the $k + 1$ vertices of a k -simplex is a face of this k -simplex. Thus, a k -simplex has exactly $k + 1(k - 1)$ -faces, which are $(k - 1)$ -simplices [7].

Let X be a simplicial complex. For each $k \geq 0$, we define a vector space $C_k(X)$ whose basis is a set of oriented k -simplices of X . If k is greater than the highest dimension of X , let $C_k(X) = 0$. We define the boundary operator to be a linear map $\partial : C_k \rightarrow C_{k-1}$ as follows:

$$\partial[v_0, v_1, \dots, v_k] = \sum_{i=0}^k (-1)^i [v_0, v_1, \dots, v_{i-1}, v_{i+1}, \dots, v_k] \tag{1}$$

This formula suggests that the boundary of a simplex is the collection of its faces [6]. For example, the boundary of a segment is its two endpoints and a filled triangle is bounded by its three segments.

Consider two subspaces of $C_k(X)$: cycle-subspace and boundary-subspace, denoted as $Z_k(X)$ and $B_k(X)$ respectively. Let \ker be the kernel space and im be the image space. By definition, we have:

$$Z_k(X) = \ker(\partial : C_k \rightarrow C_{k-1}) \quad (2)$$

$$B_k(X) = \text{im}(\partial : C_{k+1} \rightarrow C_k) \quad (3)$$

$Z_k(X)$ includes cycles which are not boundaries while $B_k(X)$ includes only boundaries. A k -cycle u is said homologous with a k -cycle v if their difference is a k -boundary:

$[u] \equiv [v] \Leftrightarrow u - v \in B_k(X)$. A simple computation shows that $\partial \circ \partial = 0$. This result means that a boundary has no boundary. Thus, the k -homology of X is the quotient vector space:

$$H_k(X) = Z_k(X) \setminus B_k(X) \quad (4)$$

Definition 2.2 (Betti number): The k -th Betti number is the dimension of $H_k(X)$

$$\beta_k = \dim H_k = \dim Z_k - \dim B_k \quad (5)$$

This number has an important meaning for coverage problems. The k -th Betti number counts the number of k -dimensional holes in a simplicial complex. For example, the β_0 counts the number of connected components while β_1 counts the number of coverage holes, etc. [6].

2.2 Čech Complex

The definition of Čech complex is given by Martins in paper [3]:

Definition 2.3 (Čech complex): Given a collection of cover sets U , the Čech complex of U , denoted as $C(U)$, is the abstract simplicial complex whose k -simplices correspond to nonempty intersection of $k + 1$ distinct elements of U .

We choose $\epsilon(\omega)$ to be the cells coverage range R_{cov} , thus, the Čech complex will represent exactly the coverage states of our system. Graphically, each cell, which indicates a node and its coverage zone, is symbolized by a vertex. A covered space between cells corresponds to a triangle, tetrahedron, etc. filled with colors. A coverage hole between cells is represented by a non-filled triangle, rectangle, etc.

Figure 2 shows how we use Čech complex to symbolize all the coverage information of a network, while forsake all the other insignificant information like the size and position of each coverage zone. The construction of Čech complex needs the exact position and coverage range information of all nodes in WSN, which results in huge communication cost in practice.

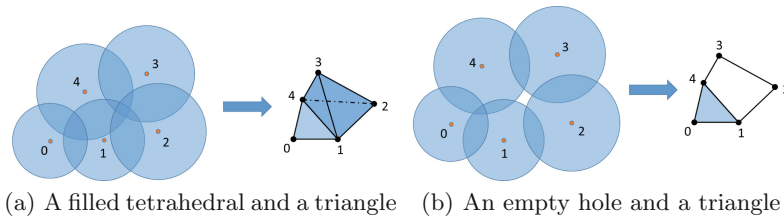


Fig. 2. Čech complex representation

2.3 Rips Complex

The definition of Rips complex is given by Martins in paper [3]:

Definition 2.4 (Rips complex): Given a metric space (M, d) , a finite set of points V on M and a fixed radius ε , the Rips complex of V , $R_\varepsilon(V)$, is an abstract simplicial complex whose k -simplices correspond to unordered $(k + 1)$ -tuples of point in V which are pairwise within distance ε of each other.

As an approximation of Čech complex, Rips uses only connectivity information, while coverage range is unknown to Rips complex [8]. Consequently, its accuracy and performance are decided by the ratio γ between communication range and coverage range. For $\gamma \leq \sqrt{3}$, Rips complex will not miss any coverage hole, while may detect fake one. For $\gamma \geq 2$, Rips complex will not detect any fake coverage holes, while may miss an existing one. For $\sqrt{3} < \gamma < 2$, Rips complex will not only miss an existing coverage hole, but also detect fake ones. The proof can be found in paper [9].

3 Distributed Čech Complex Algorithm

3.1 Basic Idea

The existing parallel Čech complex algorithm proposed in paper [3], divides assemble of all nodes in a WSN into several sub-domains according to their coordinates on one axe. Then, by constructing Čech sub-complexes and integral all the connection information of those sub-complex into a complete Čech complex, a global Čech complex is obtained. This algorithm is aiming at reducing the computation time to construct the full complex for a large network. Therefore, it is our task to bring forward a distributed version of the algorithm aiming at reducing communication cost and being applicable on real WSN nodes. Compared with geometry based distributed hole detection algorithms like the one in paper [10], our algorithm will not require the boundary information of the network. To start up, our test scenario will be judging whether there are coverage holes or not in a network.

The most basic distributed idea showing as Algorithm 1 is that we let every node collect the position information of all nodes within the communication

range R_{com} as their sub-domains. Then every node constructs their Čech sub-complexes on their own sub-domains. Finally, if any sub-domains finds coverage holes, there are coverage holes. Otherwise, there are not.

Unfortunately, in contrary with the centralized Čech complex constructed with acknowledge of all nodes, Čech sub-complexes have only parts of nodes, and thus may not only miss existing coverage hole, but also detect fake non-existing coverage hole. We will demonstrate it in the following section. Consequently, additional process is needed in order to obtain a better approximation to centralized one.

Algorithm 1. Basic distributed idea

```

 $S_0 = \emptyset$ ; {sub-domain of the node}
 $S_0 =$  all nodes within communication range;
 $C_0 =$  Construct Čech complex ( $S_0$ );
{ $C_0.Betti_1$  is the 1-th Betti number of  $C_0$ }
if  $C_0.Betti_1 > 0$  then
    There are  $C_0.Betti_1$  coverage holes
else
    There are no coverage holes
end if

```

3.2 Algorithm Design

Preliminaries

Proposition 1: *When range ratio $\gamma \geq 2$, which means communication range is at least 2 times greater than coverage range, all the nodes connecting with node v_0 can directly communicate with v_0 .*

The demonstration of Proposition 1 is obvious and it is the foundation of the following discussion and demonstration. We will thus consider $\gamma \geq 2$ as default from now on.

Triangular Hole Detection

Proposition 2: *When range ratio $\gamma \geq 2$, a triangular coverage hole will definitely be detected by all the nodes on its boundary who construct the Čech sub-complex of all nodes within their communication range.*

Demonstration: As a consequence of Proposition 1, for a triangular coverage hole shown in Fig. 3a, any of its boundary coverage zones must be directly connected with the other two. For Algorithm 1, this indicates that the other two boundary nodes are in its sub-domain for sure. So, the triangular coverage hole will definitely be detected by distributed Čech algorithm run by node A, B or C because they construct local Čech complexes which provide exactly the topology of their sub-domains.

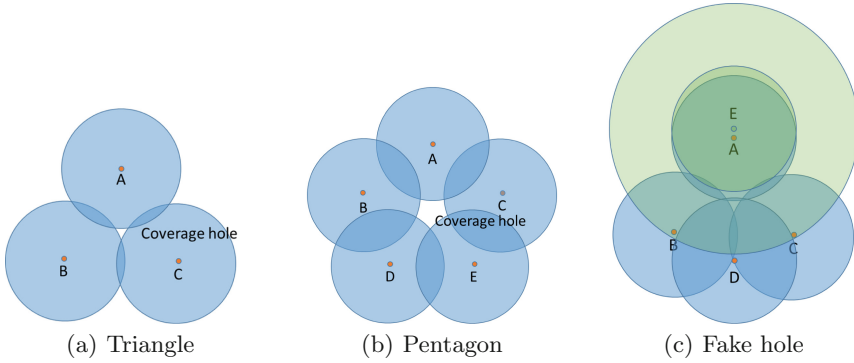


Fig. 3. Coverage holes

Non-Triangular Hole Detection

For the same reason, if we want to guarantee the detection of holes with more edges, we can let nodes collect multi-hop neighbor nodes information in order to ensure the awareness of vertexes which are not directly connected with it.

Proposition 3: *With n -hop neighbor node information, for all the:*

$$k \leq 2n + 1, k \in N \tag{6}$$

coverage holes with k edges can be guaranteed to be detected by at least one node.

Demonstration: Figure 3b shows an pentagonal example, the node A is guaranteed to see node B and C since they are within its communication range ($\gamma \geq 2$), while it cannot see node D or E. For the same reason, the node B is guaranteed to see node D. Therefore, if every node has 2-hop neighbor nodes information, node A is also guaranteed to see node D through node B and see node E through node C. Symmetrically, all the nodes on the boundary of a pentagonal coverage hole can now see each other. Čech complex of sub-domains with n -hop neighbor node information will thus never miss coverage holes with less than $2n + 1$ edges.

Fake Hole Exclusion

However, a triangular coverage hole could be covered by a fourth node D and remains no longer a hole like the one shown in Fig. 3c. Furthermore, this fourth node D may not be visible to a fifth node E which can see node A, B and C. Consequently, node E may detect fake coverage holes. In the case above, we can call node D a missing one to node E. This kind of fake coverage holes is actually not only limited in triangular case, but also in any non-triangular cases.

Proposition 4: *A fake coverage hole found by a node in its Čech sub-complex of all nodes in their sub-domain can be excluded by additional 1-hop neighbor nodes information and re-construct the Čech sub-complex.*

Demonstration: It is obvious that the missing one must be certainly connected with all the nodes on the boundary of the fake coverage hole in order to cover the whole fake area. For example, in Fig. 3c, node D must be connected to node A, B and C to cover the whole fake hole.

According to the Propositions 3 and 4, we can ameliorate Algorithm 1 to Algorithm 2 mainly in 2 step: the construction of sub-domain with n-hop neighbor nodes information and the verification of coverage holes. However, this algorithm cannot guarantee to exclude all fake cases. There is an exceedingly infrequent case where the suspected missing nodes we enlarge into the sub-domain form new fake coverage holes. We can identify the coverage hole to fix that, which takes a lot of extra cost. Nevertheless, Algorithm 2 already performs marvelously on detecting no fake hole in practice.

Algorithm 2. Distributed Čech complex algorithm

```

 $S_0 = \emptyset$ ; {sub-domain of the node}
 $S_{0+} =$  n-hop neighbor nodes;
{guarantee to find holes with at most  $2n+1$  edges}
 $C_0 =$  construct Čech complex ( $S_0$ );
{ $C_0.Betti_1$  is the 1-th Betti number of  $C_0$ }
if  $C_0.Betti_1 > 0$  then
   $S_1 =$  (1-hop neighbor nodes of  $S_0$ )- $S_0$ 
  for all  $n_i \in S_1$  do
    if  $n_i$  connect to at least 3  $n_j \in S_0$  then
       $S_{0+} = n_i$ 
    end if
  end for
   $C_1 =$  construct Čech complex ( $S_0$ );
  if  $C_1.Betti_1 > 0$  then
    There are  $C_1.Betti_1$  coverage holes
  else
    There are no coverage holes
  end if
else
  There are no coverage holes
end if

```

The Algorithm 2 is a distributed Čech complex algorithm that has the same complexity for constructing a Čech complex, but has significantly decreased the execution time and communication cost by reducing the number of nodes in it. Now that we obtain a guaranteed detection on triangular holes, with negligible chance to detect fake holes.

3.3 Combination with Rips Complex Algorithm

In paper [9], an important corollary about the range ratio γ and the Rips complex is proven:

Corollary 4.1: *When $\gamma \geq 2$, if there is a hole in Rips complex $R_{R_{com}}(V)$, there must be a hole actually.*

On the one hand, the distributed Rips complex algorithm proposed in paper [9] reaches a good approximation of centralized one with a high accuracy (over 99%) with no fake detection and can detect almost all the non-triangular coverage holes (>99%) [9]. On the other hand, with only direct neighbor nodes information for all nodes and 2-hop neighbor node information for nodes who detected coverage holes, our distributed Čech complex algorithm is guaranteed to detect all triangular coverage holes. In additional, distributed Rips complex acquires only connectivity information based on communication range, which is already included in the demand of our distributed Čech complex algorithm. Thus, we believe that combining the two distributed algorithms is valuable. For range ratio $\gamma \geq 2$, we can obtain exactly the accuracy of distributed Rips complex algorithm for detecting only non-triangular coverage holes.

4 Simulation and Performance

4.1 Simulation Settings

In order to prove the feasibility to combine our algorithm with the distributed Rips algorithm, we use almost the same simulation setting with what is presented in paper [5]. WSN nodes are randomly deployed in a $100\text{m} \times 100\text{m}$ square flat zone as target field according to a Poisson Point Process (PPP) with intensity λ selected from 0.002 to 0.0095 with interval of 0.0005. There are not fence sensors located along the edges of the square. The coverage range of all nodes is fixed to 10 m and the communication range is fixed to 20 m. Figures 4, 5 and 6 give different networks distribution examples under low, middle and high intensity. All the simulations are repeated 1000 times. The distributed Čech complex algorithm runs on different thread in simulation.

Two crucial values are recorded during each simulation. Firstly, the miss rate represents the percentage for distributed Čech complex algorithm to make wrong decision, the lower the better. Secondly, the communication cost is estimated under simple flooding protocol with message cache, which means nodes will not

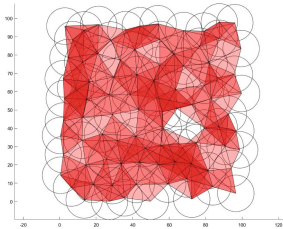


Fig. 4. $\lambda = 0.009$

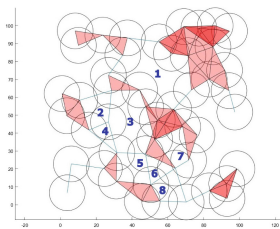


Fig. 5. $\lambda = 0.005$

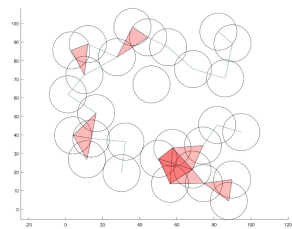


Fig. 6. $\lambda = 0.0025$

retransmit the same message twice. The unit of communication cost is defined as sending one location message to a direct neighbour node. Finally, we compare the communication cost of distributed and centralized algorithm as a ratio. This relative indice shows better the improvement in communication cost.

4.2 Random Deployment Results

Figure 7 shows the results of miss rate and Fig. 8 shows communication cost in accordance with intensity for random PPP deployment. We can have a clear view that for middle and high intensity (>0.005), 2-hop is practically enough to reach a high accuracy (over 99%). This is because that coverage holes with more edges have lower probability to appear as the intensity grows. For low intensity (<0.005), 3-hop has perceptible improvement over 2-hop and remains a high accuracy (over 98%).

On the other hand, Fig. 9 shows the cost ratios between distributed and centralized Čech algorithm. We can see that the communication cost ratio decreases as the intensity increases and converge at around 10% for 2-hop and 30% for 3-hop even under a number of node relatively low (<100). We can thus conclude that an acceptable trade off between accuracy and communication cost is realized. For all the intensity, we manually process a sample survey checking all the

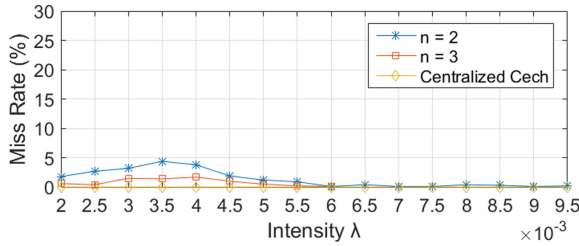


Fig. 7. Miss rate for random deployment

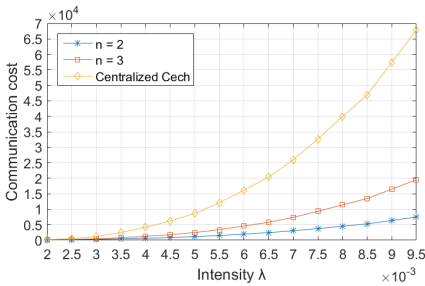


Fig. 8. Communication cost

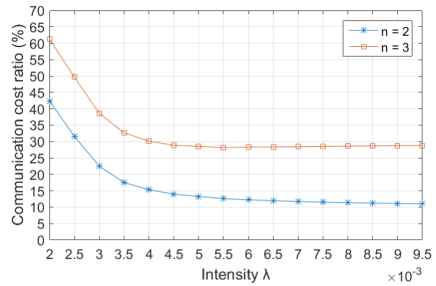


Fig. 9. Communication cost ratio

missing coverage holes and no missing triangular coverage hole is found. Besides, there are three fake coverage holes detected. They all share the same reason that we explained in Sect. 3.

5 Conclusion and Future Work

In this paper, we bring forward a distributed Čech complex algorithm for low cost WSN nodes with communication range at least two times larger than sensing range, which has for now two following usages. On the one hand, it can be used simultaneously with distributed Rips complex algorithm to obtain a detection on all coverage hole with an accuracy over 99%. On the other hand, it can be used independently to obtain an accuracy over 98% or even more with much lower communication cost comparing with centralized Čech complex algorithm and acquires no boundary information comparing with other geometry based algorithms. With adjustable number of hop, larger the network is, easier it becomes for us to find the compromise between accuracy and cost of both communication and computing.

Based on what we have already achieved, there are some perspectives we can proceed in the future. First and foremost, we can identify coverage holes found by separated nodes according to their boundary nodes. Current version of distributed Čech algorithm only takes into account the information on Betti numbers. A complete Čech complex construction from sub-Čech complex can be achieved as well, but a more light-weight representation should be considered. Then, besides the information on Betti numbers, distributed algorithm which can construct a complete Čech complex from sub-Čech complex is also possible. In the end, the hardware experiment of the distributed Čech complex algorithm on real WSN testbeds like IoT-Lab is already on our schedule.

Acknowledgements. This research was supported by 863 under grant No. 2015AA015802, NSF of China under grant No. U1401253 and No. 61373155.

References

1. Huang, C., Tseng, Y., Lo, L.: The coverage problem in three-dimensional wireless sensor networks. *J. Interconnection Netw.* **08**(03), 3182–3186 (2015). vol. 5
2. Le, N.K., Martins, P., Decreusefond, L., et al.: Simplicial homology based energy saving algorithms for wireless networks. In: *IEEE International Conference on Communication Workshop*. IEEE (2015)
3. Martins, P.: *Homologie simpliciale applique aux rseaux sans fil*. Doctorat Paris-Tech, 2013-ENST-00xx (2013)
4. Roosta, T., Mishra, S.M., Ghazizadeh, A.: Robust estimation and detection in ad hoc and sensor networks. *Ecology* **87**(2), 372–381 (2006)
5. Yan, F., Vergne, A., Martins, P., Decreusefond, L.: Homology-based distributed coverage hole detection in wireless sensor networks. *IEEE/ACM Trans. Netw.* **23**(6), 1705–1718 (2015)

6. Le, N.K., Martins, P., Decreusefond, L., et al.: Construction of the generalized Čech complex Complex. In: IEEE Vehicular Technology Conference, pp. 501–510 (2015)
7. Vergne, A., Decreusefond, L., Martins, P.: Simplicial homology for future cellular networks. *IEEE Trans. Mob. Comput.* **14**(8), 1712–1725 (2013)
8. Yan, F., Martins, P., Decreusefond, L.: Accuracy of homology based approaches for coverage hole detection in wireless sensor networks. In: IEEE International Conference on Communications, pp. 497–502 (2012)
9. Yan, F., Martins, P., Decreusefond, L.: Connectivity-based distributed coverage hole detection in wireless sensor networks. In: IEEE Global Telecommunications Conference, pp. 1–6 (2011)
10. Ma, H.C., Sahoo, P.K., Chen, Y.W.: Computational geometry based distributed coverage hole detection protocol for the wireless sensor networks. *J. Netw. Comput. Appl.* **34**(5), 1743–1756 (2011)



An Energy-aware Routing Protocol Based on Network Coding for Wireless Sensor Networks

Panpan Cui, Song Xiao^(✉), and Lei Li

State Key Laboratory of Integrated Service Networks, Xidian University,
No. 2, South Taibai Street, Xi'an 710071, China
xiaosong@mail.xidian.edu.cn

Abstract. In this paper, an energy-aware routing protocol based on network coding (NCEAR) is presented for wireless sensor networks which the energy is constrained. First, considering the rate matching problem of data flows, NCEAR adopts the distributed network coding to calculate the transmission cost of nodes, which reduces the energy consumption. In addition, NCEAR is capable of predicting the congestion degree of nodes through the energy consumption speed, thus balancing the network traffic. What's more, in order to reduce the probability of link failure and the number of routing maintenance, the protocol takes nodes with the minimum residual energy into consideration and sets the minimum threshold. The simulation results show that compared with other protocols, NCEAR can effectively reduce energy consumption of the transmission, balance the network energy and traffic, prolong the network lifetime and improve the throughput.

Keywords: Energy-aware · Network coding · Wireless sensor networks

1 Introduction

Wireless Sensor Networks (WSN)[1] is a combination of sensor, embedded computing and wireless network communication, which is exploited in several applications such as military defense, industry and agriculture, urban management, etc. With the increase in the amount of information and service diversification, energy-efficiently transmission has become very important for WSN which the energy is constrained. Therefore, research on optimizing the routing protocol in WSN to save energy consumption and extend the network lifetime is of great significance.

Traditional wireless sensor networks protocols such as AODV [2], DSR [3] with minimum hops or expectation transmission times for routing criterion which don't consider the node energy. Network coding was first proposed by Ahlswede et al. [4] which allowed intermediate nodes to integrate multiple packets into one packet for transmission. It has been shown to be able to achieve sufficiently

favorable performance in obtaining high throughput and reducing the transmission energy consumption [5–7]. However, these protocols often gain a limited performance improvement in balancing the network traffic with the increasing of data flows. Considering the above limitations, we propose an energy-aware routing mechanism based on network coding, which can make routing decisions with the awareness of both coding opportunity and energy of nodes.

2 Coding-aware Condition

In [8], the author proposed a distributed coding-aware routing mechanism (DCAR), which could concurrently discover the available paths and potential coding opportunities. DCAR can detect coding opportunities on the entire path to achieve high throughput, thus eliminating the “two-hop” coding limitation in COPE. So in this paper, we adopt the coding conditions given in DCAR.

Let a denotes a node and $N(\mathbf{a})$ denotes the set of one-hop neighbors of node a . Let $a \in F$ denotes a is along the flow F . Let $U(\mathbf{a}, F)$ and $D(\mathbf{a}, F)$ indicate the set of all upstream nodes of node a in flow F and the set of all downstream nodes respectively. If two flows F_1 and F_2 intersect at a node c , packets of them can be encoded for transmission at node c , if and only if the following coding conditions are met:

- (1) There exists $d_1 \in D(\mathbf{c}, F_1)$ such that $d_1 \in N(s_2)$, $s_2 \in U(\mathbf{c}, F_1)$, or $d_1 \in U(\mathbf{c}, F_2)$
- (2) There exists $d_2 \in D(\mathbf{c}, F_2)$ such that $d_1 \in N(s_1)$, $s_1 \in U(\mathbf{c}, F_1)$, or $d_2 \in U(\mathbf{c}, F_1)$.

3 Routing Strategy

3.1 Routing Metric

Coding cost. With network coding in data transmission of wireless sensor network, if a new flow can be encoded with existing flows, it requires no additional cost in “free-ride” by existing flows. However, a new data flow does not always fully carry on other existing flows due to the mismatch transmission rate in actual network. Therefore, we combine the network coding with the transmission rate of data flows to decide the coding cost function of nodes.

Consider a link $n_i \rightarrow n_j$, the coding cost of node n_j is denoted by cost (j).

$$\text{cost}(j) = \begin{cases} 0 & n_j \text{ with coding, } R_{req} \leq R \\ \frac{R_{req}-R}{R_{req}} & n_j \text{ with coding, } R_{req} > R \\ 1 & n_j \text{ without coding} \end{cases}, \quad (1)$$

where R is the matching rate, i.e. the transmission rate of the existing flow, R_{req} is the request transmission rate of the new flow.

Node congestion degree. Adopting the coding-aware, we can select the node with coding opportunities as the next-hop node to improve the network throughput. However this will lead to a large amount of data flows converge to the coding node, and the energy of this node is consumption very quickly. To avoid the network link failure caused by the energy depletion, we predict the congestion degree in the next-hop node according to the speed of energy consumption.

Each node updates its congestion degree after a sampling period T . The congestion degree of node is denoted by $v(t)$.

$$v(t) = \frac{E_{res}(t-1) - E_{res}(t)}{T \cdot E_{initial}}. \quad (2)$$

where $E_{initial}$ donates the initial energy of nodes, $E_{res}(t)$ expresses the residual energy of nodes after t cycles. $v(t)$ formulates the energy consumption speed of nodes at the t cycle, which represents the current congestion degree. The larger value of $v(t)$ shows the more data flows go through the node within period T , which indicates the more serious congestion. Therefore the congestion degree of nodes is considered in route selection to balance the traffic of the whole network.

Path transmission cost. Consider a path $L : s \rightarrow n_1 \rightarrow n_2 \rightarrow n_i \rightarrow n_j \cdots \rightarrow n_k \rightarrow d$. The cost function $C(L)$ is defined as the sum cost of all links on this path.

$$C(L) = \sum_{i=1}^k C(\text{Link}_{ij}) \quad (3)$$

$$C(\text{Link}_{ij}) = \alpha \text{cost}(j) + \beta v_j, \alpha + \beta = 1,$$

where Link_{ij} indicating the condition that node n_i selects n_j as the next-hop by considering the coding opportunities and congestion degree of n_j , and $C(\text{Link}_{ij})$ is the cost of Link_{ij} , and are tuning factors which can be adjusted adaptively according to current network state.

Routing metric function. Apart from the transmission cost, balancing the network residual energy is important when selecting a transmission path. We donate as the normalized minimum residual energy of nodes on the path.

$$\varepsilon = \frac{E_{min}}{E_{initial}}. \quad (4)$$

Based on above analysis, we propose a novel energy-aware routing metric $M(L)$.

$$M(L) = \frac{C(L)}{\text{Max } \varepsilon}, \quad (5)$$

where $C(L)$ is the path transmission cost, Max is the maximum of minimum residual energy of nodes. The optimal path can be obtained by searching the minimum $M(L)$. Then an optimal route will be selected which can not only keep the transmission cost at a low level but also protect the node with low energy, thus balancing the energy and traffic as well as extending the lifetime of network.

3.2 Routing Process

Packet format. Considering the node coding opportunities, congestion degree and the residual energy in route selection, we modify the RREQ as shown in Fig. 1. In addition to the basic routing information such as source ID, destination ID and routing ID, RREQ also increases the routing request rate (R_{req}), coding cost, node congestion (v), minimum residual energy (\mathcal{E}), and so on.

s_id	d_id	r_id	R_{req}	Coding cost	v	\mathcal{E}
------	------	------	-----------	-------------	-----	---------------

Fig. 1. RREQ packets format.

Route discovery. By using route discovery process we obtain the optimal path of data transmission in wireless sensor networks, and more details about this route discovery process can be referred to [7]. It's worth noting that during this period, the RREQ packet is updated by the transmission cost of path and the minimum residual energy of nodes, and then the new routing metric $M(L)_{new}$ is calculated and compared with previous $M(L)_{original}$ by the following formula. Finally the smaller one will be saved, and this intermediate node continue to broadcast to the next node.

$$M(L) = \begin{cases} M(L)_{new}, & M(L)_{new} \leq M(L)_{original} \\ M(L)_{original}, & M(L)_{new} > M(L)_{original} \end{cases}. \quad (6)$$

Route maintenance. When the energy of node is unable to meet the transmission energy, the routing link will be failure. So we set the threshold of the minimum residual energy ε_h . If the residual energy of node is lower than ε_h , the local routing maintenance will be triggered. Then this node exchange information with its neighbors to find a new link instead and thus preventing routing interrupt.

4 Experimental Results and Analysis

In this section, we conduct simulations to evaluate the performance of NCEAR using MATLAB compared with AODV [2], COPE [5] and ERPNC [7]. The simulation area size is set to 300 m with 30 static nodes placed randomly, and all nodes connected by wireless link. Each node is initially set to 50 J and the communication radius is set to 30 m. The link bandwidth is set to 2 Mbit/s. The period T of predicting congestion degree of nodes is set to 5 s, and the minimum residual energy threshold is set to 5 J. The number of flows in network is varied from 2 to 20. Simulation results are taken from an average of 20 experiments.

Figure 2(a) shows the network throughput situation of four protocols. At the beginning, the performance of network throughput of four protocols are roughly the same. With the number of data flows increasing, the advantage of COPE, ERPNC and NCEAR begin to emerge which can utilize network coding opportunities to increase the network throughput. ERPNC and NCEAR can further improve performance by using the distributed network coding to perceive potential coding opportunities compared with COPE which utilize passive encoding. The performance of NCEAR is better than ERPNC with considering the coding opportunities and congestion degree in selecting the next-hop node.

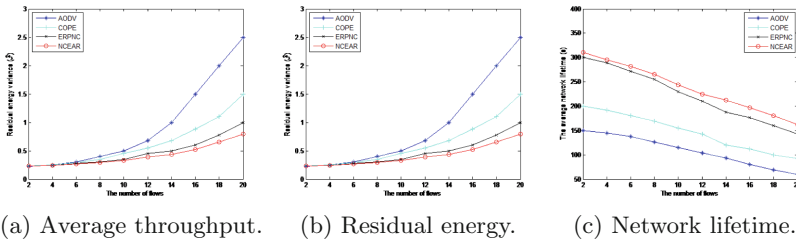


Fig. 2. Experimental results

Figure 2(b) shows the residual energy variance of nodes for four protocols. With the increase of data flows, these protocols become unbalanced gradually in network remaining energy. The performance of NCEAR and ERPNC is more balanced than AODV and COPE with considering the residual energy of nodes. NCEAR is capable of considering the congestion degree as well as the minimal residual energy of nodes in the path, which is superior to ERPNC and has further balanced the energy consumption of network.

Figure 2(c) depicts the network lifetime of four protocols. It can be seen that the lifetime of network will decrease as the increase of data flows. The network lifetime of NCEAR is longest with considering the coding opportunities and balancing the energy and traffic of network.

5 Conclusion

In this paper, an energy-aware routing protocol based on network coding (NCEAR) is proposed for the data transmission, which incorporates potential coding opportunities and congestion degree of node into route selection. It can reduce the energy consumption and balance the network traffic. In addition, the routing metric of NCEAR considers the node with minimum residual energy in the transmission path and sets the threshold of minimum residual energy in routing maintenance, thus effectively avoiding the link failure and reducing the number of routing maintenance caused by energy shortage. Simulation results demonstrate that the protocol achieves favorable performance in increasing the

network throughput, prolonging the network lifetime and balancing the energy and traffic of network. resents its corresponding label, and ϕ donates the kernel function.

Acknowledgments. This work was supported by NSFC (No. 61372069), “111” project (No. B08038) and the Fundamental Research Funds for the Central Universities.

References

1. Akyildiz, I.F., Su, W., Sankarasubramaniam, Y., et al.: Wireless sensor networks: a survey. *Comput. Netw. Int. J. Comput. Telecommun. Netw.* **38**(4), 393–422 (2002)
2. Perkins, C., Belding-Royer, E., Das, S.: Ad hoc on-demand distance vector (AODV) Routing. RFC Editor (2003)
3. Johnson, D.B.: The dynamic source routing protocol for mobile ad hoc networks (2007). [draft-ietf-manet-dsr-09.txt](#)
4. Ahlswede, R., Cai, N., Li, S.Y.R., et al.: Network information flow. *IEEE Trans. Inf. Theory* **46**(4), 1204–1216 (2000)
5. Wang, H., Xie, H., Qiu, L., et al.: COPE: traffic engineering in dynamic networks. In: *Conference on Applications, Technologies, Architectures, and Protocols for Computer Communications*, pp. 99–110. ACM (2006)
6. Gu, Y., Han, H., Li, X., et al.: Network coding-aware routing protocol in wireless mesh networks. *J. Tsinghua Univ. (Nat. Sci. Ed.)* **20**(1), 40–49 (2015)
7. Zhenzhao, W., Zhijie, C., Wenling, X.: Energy aware routing strategy based on network coding for ad hoc networks. *J. Comput. Sci.* **43**(7), 106–110 (2016)
8. Le, J., Lui, J.C.S., Chiu, D.M.: DCAR: distributed coding-aware routing in wireless networks. *IEEE Trans. Mob. Comput.* **9**(4), 596–608 (2010)



Detecting Hierarchical and Overlapping Community Structures in Social Networks Using a One-Stage Memetic Algorithm

Chun-Cheng Lin¹, Der-Jiunn Deng^{2(✉)}, Jung-Chao Wu¹,
and Liang-Yi Lu¹

¹ Department of Industrial Engineering and Management,
National Chiao Tung University, Hsinchu 300, Taiwan
cclin321@nctu.edu.tw, wu7419658@gmail.com

² Department of Computer Science and Information Engineering,
National Changhua University of Education, Changhua 500, Taiwan
djdeng@cc.ncue.edu.tw

Abstract. Detection of hierarchical and overlapping community structures for social networks is crucial in social network analysis. Previous strategies were focused on a two-stage strategy for separately detecting hierarchical and overlapping community structures. This paper develops a one-stage memetic algorithm for concurrently detecting hierarchical and overlapping community structures in social networks, where quality evaluation functions, community capacity, and hierarchical levels are taken into account to increase the solution quality. This algorithm includes a local search scheme to improve the solution searching ability. Through simulation, this algorithm shows pleasing quality.

Keywords: Hierarchical and overlapping community structure
Social network · Memetic algorithm

1 Introduction

Since the members with similar backgrounds and interests in social networks have frequent interactions with each other, they constitute a community. A social network with multiple communities is a community structure. Generally, the community structures of social networks to be investigated popularly are *overlapping community structures* and *hierarchical community structures*. Previous methods on detecting overlapping and hierarchical community structures were based on a two-stage strategy [1]. However, most previous works did not consider a one-stage strategy for this problem. Therefore, this work proposes a one-stage memetic algorithm (MA) for detecting overlapping and hierarchical community structures in social networks, while constraints of community size and hierarchical levels are considered. To design a one-stage method, this work proposes a novel optimization function of maximizing the quality of jointly overlapping and hierarchical community structures, in which the quality of overlapping community structures is based on the density function of links in each community (called the D value) [2]; and the quality of hierarchical community

structures is based on the EQ value proposed in [1]. Since the concerned community detection problem has been shown to be NP-hard [3], this work proposes a novel memetic algorithm (MA) for the problem, which is a genetic algorithm (GA) incorporated with local search scheme.

2 Literature Review

In detecting hierarchical community structures, Chen et al. [5] computed a similarity matrix that computes similarity of all adjacent vertices, and then merged vertices to form a hierarchical community structure according to the similarity matrix. Then, they applied the community density D [2] as the threshold value of determining the community structure at each hierarchical level. Shen et al. [1] proposed a so-called EAGLE algorithm to detect overlapping and hierarchical community structures, which first finds all maximal cliques in the input social network and lets them be overlapping communities; and then computes similarity of each pair of communities, and merge the communities with higher similarity to form a binary hierarchical structure. To obtain a good-quality community structure, they propose an EQ value to evaluate quality of overlapping community structure at each hierarchical level. They found the level with the community with the largest EQ value among all hierarchical levels, and let the level as the number of levels of the hierarchical structure.

3 The Concerned Problem

Consider to represent a social network topology as a graph G . The notations used for representing the input graph are summarized as follows. $G = (V, E)$: The social network is represented as graph G in which $V = \{v_1, v_2, \dots, v_n\}$ and $E = \{e_1, e_2, \dots, e_m\}$ represent set of vertices and edges, respectively, in which v_i represents a vertex; e_i represents an edge. The number of vertices in graph G is n ; and the number of edges in graph G is m .

The notations of the output of the problem are summarized as follows. Number of hierarchical levels of the hierarchical community structure of graph G is h . $H = \{H^1, H^2, \dots, H^h\}$ represent the output overlapping and hierarchical community structure of graph G . $H^k = \{C_1^k, C_2^k, \dots\}$ represent set of communities at the k -th hierarchical level, in which C_i^k denotes the i -th community at the k -th hierarchical level. This work allows $C_i^k \cap C_j^k \neq \emptyset$. $|C_i^k| = n_i^k$ denotes the number of vertices in the i -th community C_i^k at the k -th hierarchical level.

With the above notations, the concerned problem is described in detail as follows. Given the graph topology G , the problem is to detect $H = \{H^1, H^2, \dots, H^h\}$ where $H^k = \{C_1^k, C_2^k, \dots\}$ for graph G with the objectives: Maximize the D value and the EQ value i . Subject to the following constraints: $n_i^k \geq n_{threshold}$, $\forall k \in \{1, 2, \dots, h\}$, $\forall i \in \{1, 2, \dots, |H^k|\}$ where $n_{threshold}$ is a given lower bound of size of each community i at each hierarchical level k . $h_{threshold} \geq h$ where $h_{threshold}$ is a given upper bound of number of levels of the hierarchical community structure.

4 The Proposed MA

The proposed MA is detailed in Algorithm 1, whose main components are explained in detail as follows.

Solution Encoding and Population Initialization. This work is referred to the work [3] based on adjacency of links, which is more convenient to detect overlapping edges and vertices. In Algorithm 1, a population of η chromosomes are initialized randomly.

Algorithm 1 THE PROPOSED MA

- 1: Initialize the initial population P_0 and evaluate fitness of each chromosome in the population
 - 2: Let the generation number k be 0
 - 3: **while** k is less than the maximal generation number κ **do**
 - 4: Conduct binary tournament selection to select $p_c \cdot \eta$ chromosomes
 - 5: Conduct one-point crossover on each pair of the $p_c \cdot \eta$ selected chromosomes to generate the offspring population Q_k
 - 6: Conduct local search on the offspring population Q_k
 - 7: Conduct mutation with mutation rate p_m on the offspring population Q_k
 - 8: Conduct local search on the offspring population Q_k
 - 9: Evaluate fitness of each chromosome in the offspring population Q_k
 - 10: Replace the worst chromosomes in the current population P_k by the offspring population Q_k
 - 11: Iteration number $k \leftarrow k + 1$
 - 12: **end while**
 - 13: Output the community structure corresponding to the chromosome with the best fitness
-

Fitness Evaluation. The concerned problem is to maximize both the D value and the EQ value. Therefore, after the overlapping and hierarchical community structure is decoded in the last subsection in which D and EQ_{max} values can be obtained, the fitness value corresponded to the chromosome instance is evaluated as the following weighted sum of D and EQ values:

$$Fitness = \lambda D + (1 - \lambda)EQ_{max} \quad (1)$$

where λ is a weight falling within the range [0,1].

GA Operators. The conventional GA operators include parent selection, crossover, and mutation. The parent selection operator is the binary tournament selection. The crossover operator is one-point crossover. A mutation operator randomly selects a chromosome from the offspring population, then randomly selects a gene g_i from the chromosome, and then mutates gene g_i within the feasible range of g_i , which includes all possible adjacent edges of edge e_i .

Local Search. A local search is to randomly select a chromosome, then randomly select a gene from this chromosome based on roulette wheel selection, and then mutate the gene within its feasible range. The roulette wheel selection selects a gene based on the selection probability of each gene proportional to the number of feasible values.

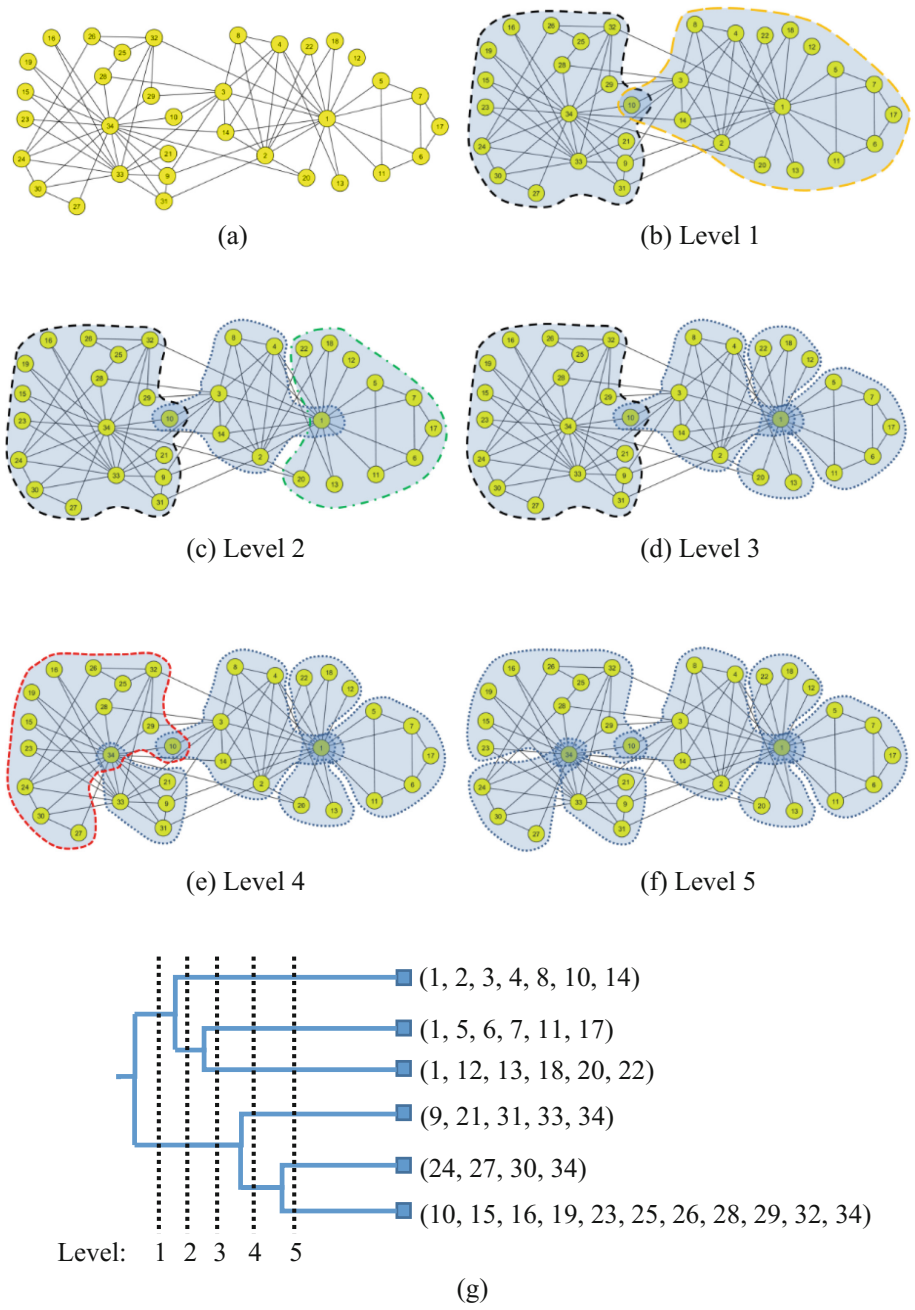


Fig. 1. The overlapping and hierarchical community structure of the network for Zachary's karate club detected by the proposed method. (a) The network structure. (b)–(f) Overlapping community structures at each hierarchical level. (g) The hierarchical tree corresponding to the overlapping and hierarchical community structure.

5 Experimental Results

The experiment is conducted on a karate club network (Fig. 1, with 34 vertices and 78 edges) [6]. After lots of experimental trials, the setting of experimental parameters in the proposed MA is given as follows: $n_{threshold} = 4$; $h_{threshold} = 4$; number of iterations = 2000; weight λ in the fitness function = 0.3; number of chromosomes $\eta = 20$; crossover rate $p_c = 0.5$; mutation rate $p_m = 0.01$; number of local search at each iteration $l_{round} = 20$; number of genes in a chromosome by local search $l_{num} = 2$.

This subsection compares the convergence performance of the proposed MA and the original GA on this social network instances in Fig. 2. It is obvious from Fig. 2 that the proposed MA have better performance in convergence in this instance.

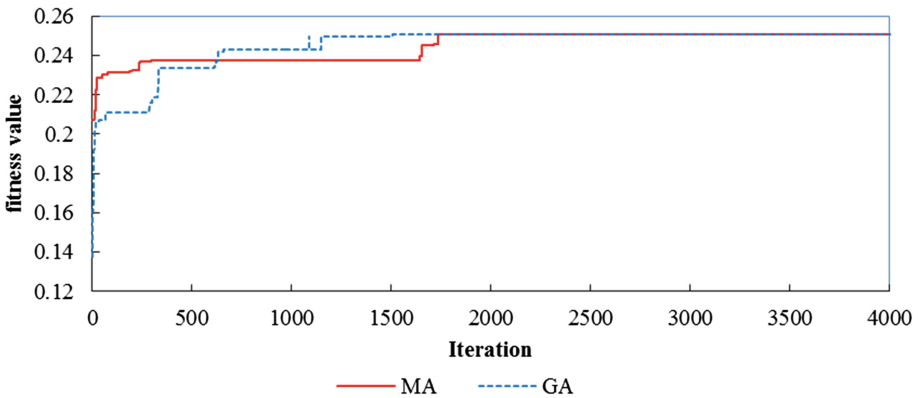


Fig. 2. Convergence comparison of the proposed MA and the original GA.

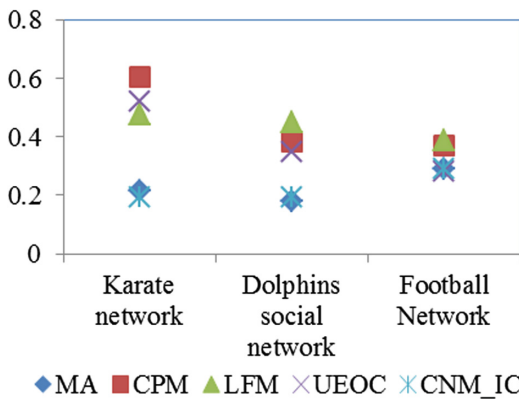


Fig. 3. Performance of the proposed MA and the other approaches for AC value (noting that a smaller AC value is better).

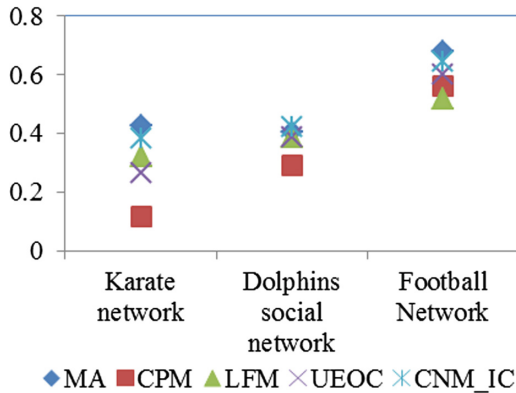


Fig. 4. Performance of the proposed MA and the other approaches for EQ value (noting that a larger EQ value is better).

Generally, the community structure cannot be realized from the network topology. Hence, some criteria are required to evaluate the performance of the results generated by different approaches. This section adopts two evaluation indices commonly. The first index is the average conductance function (AC) [4]. If the AC value is smaller, the community structure has a better quality. The second index is the EQ value. If the EQ value is greater, the quality of the overlapping community structure is better.

The two evaluation indices of the experimental results of the proposed MA and four previous approaches for three well-known network instances are compared in Figs. 3 and 4, in which the EQ value of the proposed MA is EQ_{max} . From Fig. 3, the proposed MA has better AC values than CPM, LFM, and UEOC in all network instances. From Fig. 4, the proposed MA has better EQ values than the other four approaches in three network instances.

6 Conclusion

This work has proposed a one-stage MA for detecting overlapping and hierarchical community structures in social networks which considers the constraints of community size and hierarchical level, both of which were not considered in previous works. The proposed MA includes a local search scheme to maximize two objectives D and EQ_{max} . Experimental results on three real social network instances show that the proposed MA performs better than the previous approaches.

References

1. Shen, H., Cheng, X., Cai, K., Hu, M.B.: Detect overlapping and hierarchical community structure in networks. *Phys. A Stat. Mech. Appl.* **388**(8), 1706–1712 (2009)
2. Ahn, Y.Y., Bagrow, J.P., Lehmann, S.: Link communities reveal multiscale complexity in networks. *Nature* **466**(7307), 761–764 (2010)

3. Cai, Y., Shi, C., Dong, Y., Ke, Q., Wu, B.: A novel genetic algorithm for overlapping community detection. In: Tang, J., King, I., Chen, L., Wang, J. (eds.) ADMA 2011. LNCS (LNAI), vol. 7120, pp. 97–108. Springer, Heidelberg (2011). https://doi.org/10.1007/978-3-642-25853-4_8
4. Leskovec, J., Lang, K.J., Mahoney, M.: Empirical comparison of algorithms for network community detection. In: Proceedings of the 19th International World Wide Web Conference (WWW 2010), pp. 631–640 (2010)
5. Chen, J., Saad, Y.: Dense subgraph extraction with application to community detection. *IEEE Trans. Knowl. Data Eng.* **24**(7), 1216–1230 (2012)
6. Zachary, W.W.: An information flow model for conflict and fission in small groups. *J. Anthropol. Res.* **33**(4), 452–473 (1977)



Optimal ZF Precoder Under per Antenna Power with Conjugate Beamforming for MU Massive MIMO Systems

James Kweku Nkrumah Nyarko^(✉) and Christian Anjo Mbom

School of Electronics and Information Engineering,
Northwestern Polytechnical University, Xi'an, People's Republic of China
kwekujames80@yahoo.com

Abstract. In this paper, we deliberate on multiuser massive multiple-input multiple-output (MU-MIMO) system in designing optimal zero forcing (ZF) precoder under per antenna power constraint. MU massive MIMO with non-square matrix is restrained by the large channel matrix dimension, conjugate beamforming maximization approach is developed to align the channel matrix for the optimal ZF precoder. We further introduced complex lattice reduction (CLR) to transform the lattice bases of the channel matrix and shorten the basis vector, thus meliorates the orthogonality of the conjugate beamforming. Simulation results show LR-based optimal ZF precoder outperforms other precoding schemas. The LR-based optimal ZF precoder improved the beamforming for the base station (BS) to focus on the users, thus improving spatial multiplexing gain and diversity order. As BS antennas and users turn large, the sum rate over the subchannels depends on the dominance of users (that is BS antennas to user antennas ratio) for the channel gain. Thus performance of the LR-based precoder schema under per antenna power can help save power in practical massive MIMO implementation.

Keywords: MU massive MIMO · Zero forcing (ZF) precoder
Conjugate beamforming · Lattice reduction (LR) · Per antenna power

1 Introduction

Multiuser massive MIMO system is an emerging technology, the system have spatial multiplexing and diversity gains as distinct pair of channel vectors turn orthogonal as number of antennas increase [1, 2]. However, the overall performance of MU massive MIMO requires efficient multi-user interference (MUI) elimination, hence transmit precoding is a strategy to study. Linear precoder such as zero forcing (ZF) can search domains of MU MIMO transmission over entire nullspace (nulling the space is a conventional method for interference elimination) of other users [3, 4]. In this paper, ZF precoder is designed to search domain of MU MIMO transmission over entire null of other users with block

diagonalization (BD). In [3,5] studied (BD) transmissions, as each user is set to the entire null space of other adjacent users, thus parallels the user subchannels, this however does not involve optimization over the subchannels. Therefore sum rate of optimal ZF precoder with BD is maximized under two conditions: firstly by transmitting on the right eigenchannel (set of parallel non-interfering subchannels) and secondly by power allocations on each non-interfering subchannel through optimization [6–8]. In [5,9] studied square and non square channel matrices respectively under sum power constraint. In this paper, we consider a system with large non-square channel matrix where the BS antennas M are more than the combined user antennas K and users N (i.e. $M \geq NK$), we analyze the user selection with the precoder with conjugate beamform vector in the downlink. Furthermore we extend this work to investigate the non-square matrix under per antenna power constraint. Per antenna power constraint (diagonal operations) is a novel power allocations approach for achieving massive MIMO performance. In [10], the sum rate with BD under per-antenna power constraint is suggested to be less than sum power constraint, to resolve this sum rate limitations, we propose a solution that bounds (orthogonal) the lattice size of the transmit beamforming vectors [11] under per-antenna power constraint. Lattice reduction (LR) using the complex Lenstra, Lenstra and Lovasz (CLLL) algorithm is efficient [3] in transforming the bases of the channel matrix, thus meliorating the orthogonality of basis vectors. In practice, per antenna power allocation is very critical as power to power amplifiers (PA) can serve each antenna effectively as compared to the sum power allocation where power is arbitrarily distributed to the antennas. Thus sum rate of MU massive MIMO systems for under per-antenna power constraint is a great contribution to power saving.

The paper is outlined as: Sect. 2 Designs the System Model, Sect. 3 describes the optimal ZF Precoder Design. Section 4 provides the numerical Analysis and discussions. Section 5 draws the conclusion of the paper.

2 System Model

We consider a single cell downlink MU massive MIMO system with base station (BS) equipped with M -array antennas and N users, with each user equipped with K ($K \geq 1$) antennas. The n th user received signal is modeled as $\mathbf{y}_n = \mathbf{H}_n \mathbf{x} + \mathbf{z}_n$, where $\mathbf{H}_n \in \mathbb{C}^{K \times M}$ is channel matrix and is full row rank and $\mathbf{z}_n \in \mathbb{C}^{K \times 1}$ is the (i.i.d) complex Gaussian noise vector. The statistical information of the transmitted vector $\mathbf{x} \in \mathbb{C}^{M \times 1}$ is defined as

$$\mathbf{x} = \sum_{n=1}^N \mathbf{T}_n \mathbf{s}_n \quad (1)$$

$$\mathbb{E} [(\mathbf{x}\mathbf{x}^H)]_{ii} = \left[\sum_{n=1}^N \text{tr}(\mathbf{T}_n \mathbf{T}_n^H) \right]_{ii} \leq p_i \quad \forall_i = 1, \dots, M \quad (2)$$

where $\mathbf{T}_n \in \mathbb{C}^{M \times K}$ and $\mathbf{s}_n \in \mathbb{C}^{K \times 1}$ denote the precoder matrix and transmit data vector respectively, $\mathbb{E}[(\mathbf{s}_n \mathbf{s}_n^H)] = \mathbf{I}_K$ and p_i is power of i th transmit antenna. The n th user received signal \mathbf{y}_n is expanded (1) as

$$\mathbf{y}_n = \mathbf{H}_n \mathbf{T}_n \mathbf{s}_n + \underbrace{\sum_{\substack{j=1 \\ j \neq n}}^N \mathbf{H}_n \mathbf{T}_j \mathbf{s}_j}_{\text{interference}} + \mathbf{z}_n \quad (3)$$

with the underlined term as the interference plus noise. As the transmitted signal, noise and interference signals are uncorrelated, we adopt a model to remove the interference in the next section.

3 Optimal ZF Precoder Design

Let assume the transmitter have perfect CSI, then estimation of n th user effective channel $\mathbf{H}_n \mathbf{T}_n$ is achieved by precoding the pilots of \mathbf{T}_n . The n th user (3) downlink MUI is mitigated by ZF condition enforced as

$$\mathbf{H}_n \mathbf{T}_j = 0 \quad \text{for } j \neq n \quad (4)$$

where (4) perfectly zeros the interference component in (3). The columns of $\mathbf{H}_n \mathbf{T}_n$ corresponding to singular values equal to the zero interference. Therefore invoking condition (4) into (3) is given by

$$\mathbf{y}_n = \mathbf{H}_n \mathbf{T}_n \mathbf{s}_n + \mathbf{z}_n \quad (5)$$

As MUI is annihilated, a practical multiuser ZF is achieved. Condition (4) forces \mathbf{T}_n to be located in the nullspace of $\bar{\mathbf{H}}_n = (\mathbf{H}_1^H, \mathbf{H}_2^H, \mathbf{H}_{n-1}^H, \mathbf{H}_{n+1}^H, \dots, \mathbf{H}_N^H)^H$ from reception by n th user due transmission from other users. Block diagonalization thus decomposes the MIMO channel into multiple parallel sub-channels, the singular value decomposition (SVD) is performed [12] as

$$\bar{\mathbf{H}}_n = \mathbf{U}_n \boldsymbol{\Sigma}_n \mathbf{V}_n^H \quad (6)$$

where \mathbf{U}_n and \mathbf{V}_n are $(N-1)K \times (N-1)K$ and $(M \times M)$ unitary matrices respectively, $\boldsymbol{\Sigma}_n$ is $(N-1)K \times M$ component of diagonal matrix consisting of the ordered singular values. Since $\text{rank}(\bar{\mathbf{H}}_n) = (N-1)K$, then columns of $\bar{\mathbf{H}}_n$ are constructed in \mathbf{V}_n for the precoder \mathbf{T}_n , we set $\hat{\mathbf{V}}_n \in \mathbb{C}^{M \times m}$ for $m = M - (N-1)K$ [5] and is conditioned as $\hat{\mathbf{V}}_n^H \hat{\mathbf{V}}_n = \mathbf{I}_m$ satisfying orthogonality. The precoder aggregation matrix is $\mathbf{T}_n = \hat{\mathbf{V}}_n \hat{\mathbf{V}}_n$, where $\hat{\mathbf{V}}_n \in \mathbb{C}^{m \times K}$ denotes arbitrary matrix of the power constraint, optimization over $\hat{\mathbf{V}}_n$ assumes computation of diagonal elements. Plugging (6) into (5), estimated signal n th user is expressed as

$$\hat{\mathbf{s}}_n = \mathbf{U}_n^H \mathbf{y}_n = \mathbf{U}_n^H \mathbf{U}_n \boldsymbol{\Sigma}_n \mathbf{V}_n^H \hat{\mathbf{V}}_n \hat{\mathbf{V}}_n \mathbf{s}_n + \tilde{\mathbf{z}}_n \quad (7)$$

with $\tilde{\mathbf{z}}_n = \mathbf{U}_n^H \mathbf{z}_n$ as the additive Gaussian noise and $\mathbf{U}_n \boldsymbol{\Sigma}_n \mathbf{V}_n^H \hat{\mathbf{V}}_n \hat{\mathbf{V}}_n \mathbf{U}_n^H$ is the parallelized non-interfering SU-MIMO channels. The precoder rotation

$\mathbf{T}_n = \bar{\mathbf{V}}_n \hat{\mathbf{V}}_n$ for the transmitted power¹ must be properly align with the sub-channels. Optimization over $\hat{\mathbf{V}}_n$ with SVD-ZF (7) often assumes water-filling to align the power to the parallelized eigenchannels.

3.1 Optimal ZF Precoder Optimization

To construct the precoder rotations $\mathbf{T}_n = \bar{\mathbf{V}}_n \hat{\mathbf{V}}_n$, we set $\hat{\mathbf{V}}_n$ as $\hat{\mathbf{V}}_n \hat{\mathbf{V}}_n^H = \Theta_n$ ($m \times m$) positive semi-definite matrix of the precoder power. The sum rate maximization problem under per antenna power constraint is formulated as

$$\begin{aligned} & \underset{\Theta_n}{\text{maximize}} \quad C_n(\mathbf{P}_n) = \sum_{n=1}^N \log \det(\mathbf{I} + \mathbf{B}\mathbf{P}_n) \\ & \text{subject to} \quad \left[\sum_{n=1}^N \text{tr} \left| \bar{\mathbf{V}}_n \Theta_n \bar{\mathbf{V}}_n^H \right| \right]_{ii} \leq p_i \quad \forall i = 1, \dots, M \\ & \quad \quad \quad \Theta_n \succeq 0 \quad n = 1, \dots, N \\ & \quad \quad \quad \text{rank}(\Theta_n) \leq K \end{aligned} \quad (8)$$

where $\mathbf{P}_n = \left| \mathbf{U}_n \Sigma_n \mathbf{V}_n \bar{\mathbf{V}}_n \Theta_n \bar{\mathbf{V}}_n^H \mathbf{V}_n^H \Sigma_n^H \mathbf{U}_n^H \right|$ and \mathbf{B} is any arbitrary matrix. The per antenna power constraint (8) gives the sum rate maximization over the diagonal entries of Θ_n . Considering the objective of this study in $M \geq NK$ (non-square) regime, the domain search for optimization (8) limits the span of diagonal $[\cdot]_{ii}$ in choosing Θ_n entries. Thus optimal precoder ($\bar{\mathbf{V}}_n \hat{\mathbf{V}}_n$) can not achieved best optimal solution, as dimensions of $\bar{\mathbf{V}}_n \in \mathbb{C}^{M \times m}$ is large or equal to the precoder \mathbf{T}_n [5] resulting in deficiency. This dimension restrained is easily optimized with square matrix ($M = NK$) under sum power constraint [9]. To solve this problem under per antenna power constraint, we propose conjugate beamforming approach to resize the matrix dimension. We define channel matrix as $\mathbf{X}_n = \Sigma_n \mathbf{V}_n \bar{\mathbf{V}}_n \in \mathbb{C}^{(N-1)K \times m}$ and conjugate transmit beamform matrix $\mathbf{W}_n \in \mathbb{C}^{M \times (N-1)K}$ that enforces the per antenna power constraint as

$$\mathbf{W}_n = \bar{\mathbf{V}}_n \mathbf{X}_n^\dagger \quad (9)$$

where $\mathbf{X}_n^\dagger = \mathbf{X}_n^H (\mathbf{X}_n \mathbf{X}_n^H)^{-1}$ is the Moore-Penrose inverse of \mathbf{X}_n and $\bar{\mathbf{V}}_n$ in \mathbf{V}_n (6) is for designing the precoder power. Capitalizing on $\mathbf{P}_n = \Sigma_n \mathbf{V}_n \bar{\mathbf{V}}_n \Theta_n \bar{\mathbf{V}}_n^H \mathbf{V}_n^H \Sigma_n^H$, the \mathbf{U}_n matrix is dropped in the sequel, we recompute $\Theta_n = (\Sigma_n \mathbf{V}_n \bar{\mathbf{V}}_n)^\dagger \mathbf{P}_n (\bar{\mathbf{V}}_n^H \mathbf{V}_n^H \Sigma_n^H)^\dagger = (\mathbf{X}_n^\dagger) \mathbf{P}_n (\mathbf{X}_n^\dagger)^H$. Now plugging Θ_n into (9), we rewrite (8) for optimal SVD-ZF with conjugate beamforming (BF) as

¹ For $\mathbf{T}_n = \left[\bar{\mathbf{V}}_1 \hat{\mathbf{V}}_1, \bar{\mathbf{V}}_2 \hat{\mathbf{V}}_2, \dots, \bar{\mathbf{V}}_N \hat{\mathbf{V}}_N \right]$ as the transmit power constraint (2) is formulated in $\text{tr} \left(\bar{\mathbf{V}}_n \hat{\mathbf{V}}_n \hat{\mathbf{V}}_n^H \bar{\mathbf{V}}_n^H \right)$ for the power constraint.

$$\begin{aligned}
 & \underset{\mathbf{P}_n}{\text{maximize}} \quad C_n(\mathbf{P}_n) = \sum_{n=1}^N \log \det(\mathbf{I} + \mathbf{B}\mathbf{P}_n) \\
 & \text{subject to} \quad \sum_{n=1}^N \text{tr} \left| \mathbf{W}_n \mathbf{P}_n \mathbf{W}_n^H \right|_{ii} \leq p_i \quad \forall_i = 1, \dots, M \\
 & \quad \quad \quad \mathbf{P}_n \succeq 0, \mathbf{W}_n \succeq 0 \\
 & \quad \quad \quad \text{rank}(\mathbf{W}_n) = \text{rank}(\mathbf{P}_n) \leq K
 \end{aligned} \tag{10}$$

thence optimal solution always has $\text{rank}(\mathbf{P}_n) \geq 1$ for $K \geq 1$ with the user antenna that allows the transmitted power to target user antenna. As $\mathbf{W}_n \succeq 0$ satisfies $\sum_{i=1}^M |\mathbf{W}_n|_{ii} \succeq 0$ for $p_i \geq 0$, the beamform is thus aligned with the channel matrix. The conjugate beamforming matrix (\mathbf{W}_n) is suboptimal when the channel matrix (\mathbf{X}_n) is orthogonal for the sum rate maximization.

Optimal SVD-ZF with conjugate beamforming (BF) Relaxation. To resolve the inequality constraint (10) for the fixed point p_i contained in the undetermined $|\mathbf{P}_n|_{ii}$, we let eigenvector of \mathbf{P}_n be $\mathbf{p}_n = (k, 1)$ for $1 \leq k \leq K$ and beamform vector $\mathbf{w}_n = (w_{1,k}, \dots, w_{M,k})$ with entry basis (i, k) form the Hermitian matrix $\mathbf{W}_n = (w_{i,k})$ as the k -dimensional volume of the parallelepiped form the basis vectors over the M antennas. By Shur's inequality [12], beamform coefficient is given as $\mathbf{W}_n = |\mathbf{w}_n|^2 \leq (\mathbf{w}_n^H \mathbf{w}_n)$, thus bounds of sum rate $C_n(\mathbf{P}_n)$ is reflection of linear inequality constraint (10) as

$$\sum_{n=1}^N \left[\mathbf{p}_n |\mathbf{w}_n|^2 \right]_{ii} \leq p_i \quad \forall_i = 1, \dots, M \tag{11}$$

where $\left[\mathbf{p}_n |\mathbf{w}_n|^2 \right]_{ii}$ is obtained from $\text{tr} \left| \mathbf{W}_n \mathbf{P}_n \mathbf{W}_n^H \right|_{ii}$ for the i th transmit antenna. Generally, the relaxation of constraint $(\mathbf{w}_n^H \mathbf{w}_n)$ [7] is rank-one or standard basis $|\mathbf{w}_n|^2 = \mathbf{W}_n = 1$, hence beamforming has unit norm vector. Since (10) is convex constraint, the optimal solution has $\text{rank}(\mathbf{p}_n) \geq 1$ as $k \geq 1$, is achieved with water-filling. However, the relaxation constraint is not tight if $1 < k \leq \text{rank}(\mathbf{W}_n)$, as the users (user antennas) grow large, the basis of conjugate beamform \mathbf{W}_n consisting of long \mathbf{w}_n vectors allow combination off diagonal elements to appear in the diagonal \mathbf{P}_n . This lacks the objective of orthogonality to the user channels. Massive MIMO matrix dimension constrained is studied in [11] for the complexity of user dimension (NK) with the channel matrix \mathbf{X}_n and $\bar{\mathbf{V}}_n$ precoding power constraints. In the next subsection evaluates the tightness of \mathbf{W}_n by reducing the basis \mathbf{w}_n consisting of short vectors, i.e. dimension span in vector space of the channel bases is to eliminate vectors that are linear combinations of others vectors.

Optimal SVD-ZF with Lattice Reduction based conjugate BF. The BS transmits to the users using lattice reduction based conjugate beamforming. The conjugate beamform matrix \mathbf{W}_n (9) is written in complex lattice form as

$$\begin{aligned} \mathbf{W}_n^* &= \bar{\mathbf{V}}_n^u \check{\mathbf{X}}_n^\dagger \\ &= \{ \kappa_1^u \check{\mathbf{x}}_1 + \dots + \kappa_n^u \check{\mathbf{x}}_n : \kappa_n^u \in \mathbb{Z} + j\mathbb{Z} \text{ for } n \in N \} \end{aligned} \quad (12)$$

with $\bar{\mathbf{V}}_n^u \in \mathbb{C}^{M \times m}$ as a unimodular transformation matrix² satisfying $\det |\bar{\mathbf{V}}_n^u| = 1$ and maintains the channel signal power during LR process. The (CLR) algorithm uses the Gram-Schmidt Orthogonalization (GSO) to transform $(\check{\mathbf{X}}_n^*)$ in order to bound the orthogonality defect³. The GSO is initiated by setting $(\check{\mathbf{X}}_n^*)^\dagger = (x_{i,k}^*)$ for $1 < k \leq K$ and $1 \leq i \leq M$, thus orthonormal basis for the i th BS antenna and k th user antenna is given [13] as

$$x_{i,k}^* = x_{i,k} - \sum_{i=1}^{k-1} \kappa_{i,k}^u x_{i,k}^* \text{ for } 1 \leq i < k \leq M \quad (13)$$

where $\kappa_{i,k}^u = \frac{\langle x_{i,k}, x_{i,k}^* \rangle}{\|x_{i,k}^*\|^2}$ is the GSO coefficient for the linear combination for any $k \in (1, n)$. As the reduction $|x_{1,k}|, \dots, |x_{k-1,k}|$ approach zero, the vector $\check{\mathbf{x}}_n$ is more orthogonal in the subspace span $\check{\mathbf{x}}_1, \dots, \check{\mathbf{x}}_{n-1}$ linearly independent vectors, hence $\kappa_{i,k}^u = 0$. The lattice basis is size reduced if $|\kappa_{i,k}^u| \leq 1/2$ [11], then

$$|x_{i,k}^*| = \frac{1}{2} |x_{i,i}^*| \text{ for } 1 \leq i < k \leq M \quad (14)$$

where the reduced basis ensures off-diagonal elements of the channel vectors are almost half the diagonal elements. The general size-reduced basis using Lovasz condition [13] is achieved by subtracting a suitable linear combination $(\rho - |\kappa_{k-1,k}^u|^2)$ for the consecutive basis $x_{k,k}^*$ and $x_{k-1,k-1}^*$, is given as

$$\|x_{k,k}^*\|^2 + \|\kappa_{k-1,k}^u x_{k-1,k-1}^*\|^2 \geq \rho \|x_{k-1,k-1}^*\|^2, 2 \leq k \leq M \quad (15)$$

where the reduction basis $\rho = \frac{3}{4}$ is standard value ($\frac{1}{4} < \rho < 1$) in achieving a better performance in (14). Thence the new shorter basis $x_{k,k}^* + \kappa_{k-1,k}^u x_{k-1,k-1}^*$ is transformation of $x_{k,k}^*$ onto the orthogonal vector space, similarly $x_{k-1,k-1}^*$ is component of $x_{k-1,k-1}^*$ beam vector basis. Thus $\check{\mathbf{x}}_n^*$ is near orthogonal and shorter projection of $\check{\mathbf{x}}_n$, then reduced vector $\mathbf{w}_n^* = \kappa_n^u \check{\mathbf{x}}_n^*$ of conjugate beamform $\mathbf{W}_n^* = \bar{\mathbf{V}}_n^u (\check{\mathbf{X}}_n^*)^\dagger$, the new basis $(\check{\mathbf{X}}_n^*)^\dagger$ for a given \mathbf{W}_n^* is near orthogonal and

² The basis vectors are multiplied by square vector and determinant of ± 1 , the elements are complex integer entries κ_n^u .

³ The orthogonality defect is used to measure the orthogonality basis vectors, formed by all the inner products as $\frac{\prod_{i=1}^n \|\check{\mathbf{x}}_i\|}{\|\check{\mathbf{X}}_n^\dagger\|^2}$.

shorter as compared with previous beamforming \mathbf{W}_n (9). The implementation of the CLLL algorithm requires QR decomposition on $\mathbf{W}_n^* = \mathbf{Q}_n^* \mathbf{R}_n^*$, where $\mathbf{Q}_n^* = \bar{\mathbf{V}}_n^u$ is $M \times m$ matrix and $\mathbf{R}_n^* = \left(\check{\mathbf{X}}_n^*\right)^\dagger$ is the $m \times (N-1)K$ upper triangular matrix, then followed by the iteration over polynomial time as

Algorithm 1

1. Initialize the GSO for $x_{1,k}, \dots, x_{i,k}$, calculate $x_{1,k}^*, \dots, x_{i,k}^*$ and coefficients κ_n^u
 2. Form size reduction for the pairs $x_{k,k}$ and $x_{k-1,k-1}$ and update $\kappa_{k-1,k}^u$
 3. Use Lovasz condition for the pair $x_{k,k}^*$ and $x_{k-1,k-1}^*$ and update $\kappa_{k-1,k}^u$
 4. Else go to step 2.
-

The CLLL algorithm swaps pair $x_{k,k}$ and $x_{k-1,k-1}$ for $x_{k,k}^*$ and $x_{k-1,k-1}^*$ as the size-reduction steps proceed. Applying the transformation for the conjugate beamform (12) and (10), the optimal precoder achieves the maximum sum rate as $C_n^* = \max_{\check{\mathbf{X}}_n^\dagger \in \mathbf{W}_n^*} C_n(\mathbf{P}_n)$ with reduced basis of the transformed beamforming.

Proposition 1. *Considering $(M \geq NK)$ with constant user antennas $1 < k \leq K$ for all N users, then (15) depends on user selection $(N-1)K$, assuming $M \rightarrow \infty$, $N \rightarrow \infty$, then $0 < k \leq \frac{M}{N} < \infty$ is constant with k values. Thus the singular values of $\mathbf{X}_n \mathbf{X}_n^H \in \mathbb{C}^{(N-1)K \times (N-1)K}$ converge to constant value $k \rightarrow \infty$, hence given as*

$$M \geq (N-1)K \tag{16}$$

for $(M-N+1)$ varies as $M \geq N$, thus objective function under per antenna power constraint is optimal (waterfilling) in achieving maximum sum rate for large $M \rightarrow \infty$, $N \rightarrow \infty$ in $M \geq NK$ regime.

4 Numerical Analysis and Discussions

In this section, numerical analysis and discussions are provided to validate performance of per-antenna power constraint for MU massive MIMO. The theoretical tightness of the study is validated with Monte Carlo simulations of 10000 realization. The precoder is constructed from the $\bar{\mathbf{V}}_n$ ($M \times m$) for $m = M - (N-1)K$ and the LR standard basis is $\rho = \frac{3}{4}$. The figures compare schemas such as direct SVD-ZF-BF (10), SVD-ZF-BF with conjugate BF matrix with inner product $|\mathbf{w}_n|^2 = [\mathbf{W}_n] = 1$ (11) and the LR-based SVD-ZF-BF, all the schemas are analyzed under per antenna power constraint.

Figure 1, shows the sum rate with SNR for all the schemas. LR-based SVD-ZF-BF achieves higher sum rate as users (N) selection increases, this validate tightness through orthogonal channel for the distinct pairs $x_{k,k}$ and $x_{k-1,k-1}$ and also the direct SVD-ZF-BF improve with user selections whilst SVD-ZF-BF with BF = $[\mathbf{W}_n] = 1$ shows worse performance, this is due to the rank one assumption of \mathbf{W}_n (unit norm vector) which constrained the beamforming diagonalization

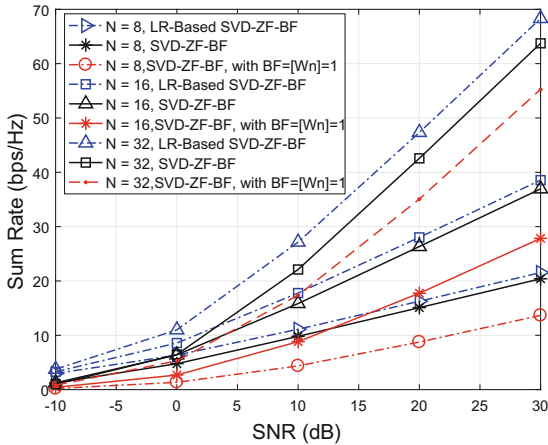


Fig. 1. Sum rate with SNR (dB) values, for M antennas = 128 and K antennas = 2.

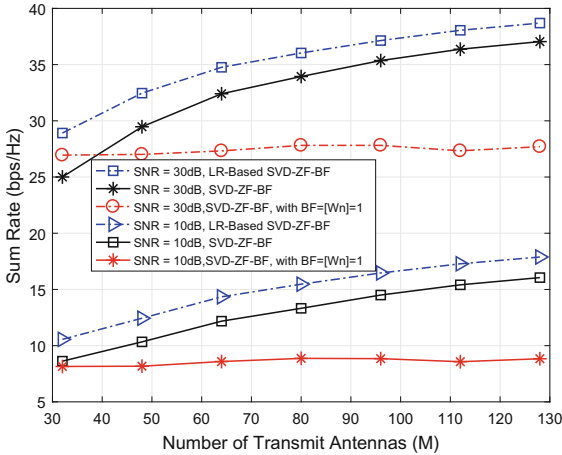


Fig. 2. Sum rate versus BS (M) antennas, for N users = 16 and K antennas = 2.

as user selections increases. The overall sum rate of our LR-based SVD-ZF-BF schema improved the performance than in [5, 10].

The sum rate versus transmit antennas M is presented in Fig. 2. Clearly sum rate increase with M for LR-based SVD-ZF-BF and direct LR-based SVD-ZF-BF, that argues an increase in channel gain for the subchannels as $M \geq NK$, the rate gain in LR-based SVD-ZF-BF is due to elimination of vectors which are linear combinations of others vectors. However as M turns large, the sum rate becomes stable suggesting limited gain due to the spread over the large $\mathbf{H}_n \mathbf{T}_n$ [5]. Subsequently sum rate of SVD-ZF-BF with $\mathbf{BF} = [\mathbf{W}_n] = 1$ schema is constant regardless of channel randomness, thus the $\mathbf{BF} = [\mathbf{W}_n] = 1$ restricts the diagonalize singular vectors of beamforming.

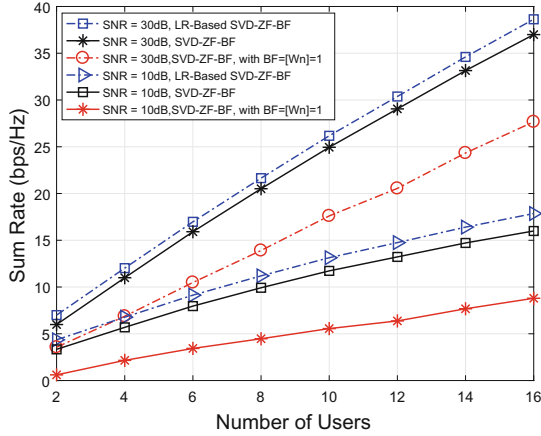


Fig. 3. Sum rate versus Users N , for M antennas = 128 and K antennas = 2.

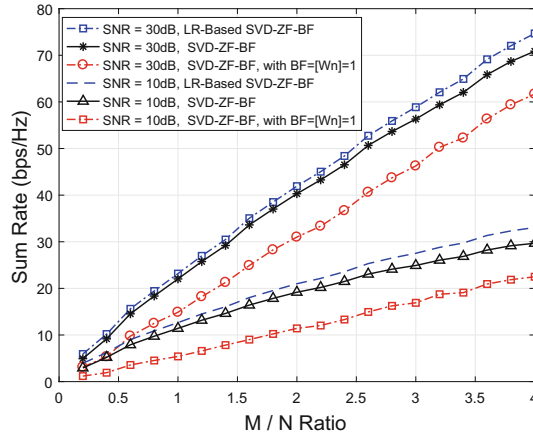


Fig. 4. Sum rate with the $0 < k \leq \frac{M}{N} < \infty$, the ratio k is equivalent user antennas.

Figure 3 plots the sum rate against the number of users N , i.e. selection of the SU-MIMO channels. The number of users increase with SNR gain hence increase sum rate in all schemas. Our LR-based SVD-ZF-BF shows high gain in the equivalent selection of SU-MIMO channels with the orthogonal bases justifying our argument that $1 < NK \leq \text{rank}(\mathbf{W}_n)$ is not tight for relaxation (less orthogonal), as $\text{BF} = [\mathbf{W}_n] = 1$ suffers from the assumption.

Figure 4 presents the sum rate compared with the ratio $k \leq \frac{M}{N} < \infty$ (as $1 \leq k \leq K$) for multiplexing gain and diversity order, hence sum rate increases with user antennas k for all schemas. As $M = (N - 1)K$ grows larger, the sum rate due to (16) turns to dominance of $M - N + 1$ channels. Thus increase in optimal power by the schemas for eigenchannel ($M \geq NK$). Then Fig. 3 is consistence

with Fig. 4 justifying Proposition 1. Moreover increase in transmit antennas M results in increase multiplexing gain $\Sigma_{\mathbf{n}}$ as in $(N-1)K$ and compensate increase in the optimal power allocation in our LR-based SVD-ZF-BF.

5 Conclusion

We present optimal ZF precoder with conjugate beamforming under per antenna power constraints with MU massive MIMO system. An optimal SVD-ZF precoder is designed for the per antenna power. The conjugate beamforming maximization efficiently aligned the channel matrix for constrained MU massive MIMO matrix dimension. Furthermore, conjugate beamforming with lattice reduction transform the lattice basis of the channel matrix. Optimal ZF precoder with LR-based SVD guaranteed higher sum rate (multiplexing gain and diversity order) in meliorating the orthogonality of the distinct vector basis as compared with other precoding schemas. This theoretical analysis fulfills practical issues for optimal ZF precoder with per antenna power in MU massive MIMO systems.

References

1. Rusek, F., Person, D., Lau, B.K., Larsson, E.G., Marzetta, T.L.: Scaling up MIMO: opportunities and challenges with very large arrays. *IEEE Sig. Proc. Mag.* **30**, 40–60 (2013)
2. Ngo, H.Q., Larsson, E.G., Marzetta, T.L.: Energy and spectral efficiency of very large MU MIMO systems. *IEEE Trans. Commun.* **61**(4), 1436–1449 (2013)
3. Zu, K., Lamare, R.C.: Low - complexity lattice reduction-aided regularized block diagonalization for MU-MIMO system. *IEEE Commun. Lett.* **16**(6), 925–928 (2012)
4. Serbetli, S., Yener, A.: Transceiver optimization for multiuser MIMO systems. *IEEE Trans. Sig. Process.* **52**(1), 214–226 (2004)
5. Yao, R., Nan, H., Xu, J., Li, G.: Optimal BD-ZF precoder for multi-user MIMO downlink transmission. *Electron. Lett.* **51**(14), 1121–1123 (2015)
6. Luo, Z.Q., Yu, W.: An introduction to convex optimization for communications and signal processing. *IEEE J. Sel. Areas Commun.* **24**(8), 1426–1438 (2006)
7. Boyd, S., Vandenberghe, L.: *Convex Optimization*. Cambridge University Press, Cambridge (2004)
8. Perez-Cruz, F., Rodrigues, M.R.D., Verdu, S.: MIMO Guassian channel with arbitrary inputs: optimal precoding and power allocation. *IEEE Trans. Inf. Theory* **56**(3), 1070–1083 (2010)
9. Kaviani, S., Krzymien, W.A.: On the optimality of multiuser ZF precoding in MIMO broadcast channels. In: *IEEE VTC Spring* (2009)
10. Vu, M.: MISO capacity with per-antenna power constraint. *IEEE Trans. Commun.* **59**(5), 1268–1274 (2011)
11. Zu, K., Song, B., Haardt, M., Lamare R.C.: Flexible coordinated beamforming with lattice reduction for MU massive MIMO systems. In: *IEEE EUSIPCO* (2014)
12. Lutkepohl, H.: *Handbook of Matrices*. Wiley, Hoboken (1996)
13. Bremner, M.R.: *Lattice Basis Reduction: An Introduction to the LLL Algorithm and Its Applications*. Taylor & Francis Group, London (2012)



Butterfly-Flow-Graph Based MAP Decoding Algorithm for Channel Quality Information in 3GPP-LTE

Qi Li^(✉), He Wang, Yunchuan Yang, Bin Yu, and Chengjun Sun

Samsung Research Institute China - Beijing (SRC-B),
Sun Palace Building, Chaoyang District, Beijing, China
{q1016.li, h0809.wang, yc0301.yang, bin82.yu, chengjun.sun}@samsung.com

Abstract. Channel quality information (CQI) is an essential element of uplink control signaling in Long Term Evolution (LTE) system. According to 3GPP standard, a linear block code based on Reed-Muller (RM) code has been employed for the CQI transmission for error control. In this paper, a low complexity *maximum a posteriori probability* (MAP) decoding algorithm for CQI decoding is described, which is performed by re-ordering the likelihood values of the received signal and all mapped codewords, and then calculating the probability of 0 and 1 of every transmitted information bit based on a butterfly-flow-graph (BFG). Compared to the standard MAP decoding algorithm, the proposed algorithm can reduce the addition calculation by 35.71% to 72.82% when the number of CQI bit is changing from 4 to 11, and the bit error rate (BER) performance is without degradation.

Keywords: 3GPP-LTE · CQI · MAP decoding

1 Introduction

In Long Term Evolution (LTE) system, channel quality information (CQI) is very crucial in evolved Node B (eNodeB) to decide the corresponding modulation and coding scheme [1]. According to the 3GPP standard [2], a $(32, k)$ linear block code based on Reed-Muller (RM) code is used for channel coding of CQI. Through fast and efficient decoding algorithm, receiver can retrieve the CQI report with low bit error rate (BER) and low latency [3].

In [4], a decoding algorithm with fast-Hadamard-transform (FHT) for CQI is proposed, which utilizes *maximum likelihood* (ML) algorithm based on the correlation between the Hadamard matrix and RM code. Rather than ML decoding algorithm, which can minimize the block error rate (BLER), the *maximum a posteriori probability* (MAP) decoding algorithm is one kind of decoding method which can not only minimize the BER, but also provide the corresponding soft information at the output of decoder [5–8]. However, due to the realization complexity, MAP decoding algorithm is not widely used for block codes [10, 11].

In this paper, we propose to use a butterfly-flow-graph (BFG) scheme for CQI decoding. The BFG scheme is derived from the fast-fourier-transform (FFT), which can greatly reduce the calculation complexity. Based on the BFG scheme, the proposed algorithm can reduce the addition calculation by 35.71% to 72.82% when the number of CQI bit is changing from 4 to 11, and the BER is without degradation compared with the standard MAP algorithm.

The rest of this paper is organized as follows. In Sect. 2, the introduction of linear block code and CQI encoder is described. In Sect. 3, the BFG based MAP decoding algorithm for CQI is proposed. Simulation result and complexity analysis are presented in Sect. 4. Finally, conclusions are drawn in Sect. 5.

2 Linear Block Code and CQI Encoder

2.1 Linear Block Code

Linear block code is a subclass of block code. For an (n, k) binary linear block code, the generator matrix \mathbf{G} is a $k \times n$ matrix with the elements from $GF(2)$, and the rows of which are a basis of the code. Denote the information sequence as $\mathbf{u} = [u_0 u_1 \dots u_{k-1}]$, the corresponding code can be obtained by

$$\mathbf{c} = \mathbf{u} \cdot \mathbf{G}. \quad (1)$$

where $\mathbf{c} = [c_0 c_1 \dots c_{n-1}]$, and the calculation is performed based on modulo-2 operation [6].

2.2 The Encoder of CQI

As mentioned in Sect. 2.1, let's assume the bit number of CQI is k , and then the CQI is encoded using a $(32, k)$ linear block code, where $k \leq 11$. The codewords of the $(32, k)$ block code are a linear combination of 11 basis sequences as defined in Table 1. Based on the 11 basis sequences, we can construct the generator matrix by $\mathbf{G} = [\mathbf{G}_0^T, \mathbf{G}_1^T, \dots, \mathbf{G}_{10}^T]^T$, where T is the transpose operation.

It can be seen that \mathbf{G}_0 is an all-one sequence, and \mathbf{G}_1 to \mathbf{G}_5 are the rows of a matrix with all possible 5-tuples as columns, which are also the interleaved first order RM generating sequences. \mathbf{G}_6 to \mathbf{G}_{10} are five mask sequences. According to Eq. (1), the encoded CQI block is denoted by $\mathbf{c} = [c_0 c_1 \dots c_{n-1}]$, where $n = 32$ and

$$c_j = \sum_{i=0}^{k-1} (u_i \cdot G_{i,j}) \quad \text{mod} 2. \quad (2)$$

where $j = 0, 1, \dots, 31$ and $G_{i,j}$ is the j -th element of sequence \mathbf{G}_i .

Table 1. 11 basis sequences of (32, k) block code

\mathbf{G}_0	1	1	1	1	1	1	1	1	1	1	1	1	1	1	1	1	1	1	1	1	1	1	1	1	1	1	1	1	1	1	1	1	1				
\mathbf{G}_1	1	1	0	0	1	1	0	0	1	0	0	1	0	1	1	0	1	0	0	1	0	1	1	0	1	1	0	1	0	0	1	0	0	1	0		
\mathbf{G}_2	0	1	0	1	1	0	1	0	0	1	1	1	0	0	0	1	0	0	0	1	0	0	1	1	0	1	1	1	1	1	1	0	0	0	0		
\mathbf{G}_3	0	0	1	1	1	0	0	1	1	1	0	0	1	1	0	0	0	1	1	0	0	1	0	0	1	1	0	1	1	0	1	1	0	1	1	0	
\mathbf{G}_4	0	0	0	0	0	1	1	1	1	1	0	0	0	0	1	1	1	1	1	1	0	0	0	1	1	1	0	0	0	1	1	1	0	0	1	1	0
\mathbf{G}_5	0	0	0	0	0	0	0	0	0	0	1	1	1	1	1	1	1	1	1	1	0	0	0	0	0	0	1	1	1	1	1	1	1	1	1	0	
\mathbf{G}_6	0	0	1	0	0	1	1	0	0	1	1	1	0	0	0	1	1	0	1	1	1	0	0	0	1	1	0	0	1	1	0	0	1	1	1	0	0
\mathbf{G}_7	0	0	0	0	1	1	0	1	1	0	1	0	1	1	1	1	0	0	1	0	0	0	1	0	1	1	0	1	0	1	0	1	0	1	1	0	0
\mathbf{G}_8	0	0	1	1	0	1	1	1	0	0	0	1	1	0	0	0	0	1	0	0	0	0	1	0	0	0	0	1	1	1	0	1	1	1	1	1	0
\mathbf{G}_9	0	1	1	0	0	0	1	0	1	1	1	0	1	1	0	1	1	0	0	0	0	1	0	1	1	0	1	1	0	1	1	0	0	1	0	0	0
\mathbf{G}_{10}	1	1	1	1	1	1	1	1	1	1	1	1	1	1	1	0	0	0	0	1	1	1	1	0	1	1	1	1	0	1	0	0	0	0	0	1	0

3 Decoding Algorithm for CQI

MAP decoding algorithm can provide the best BER performance as well as the soft decoding output. Denote the received vector as $\mathbf{r} = [r_0 r_1 \dots r_{n-1}]$, the rule of MAP decoding can be written as following:

$$\hat{u}_i = \arg \max_{u_i \in GF(2)} P(u_i | \mathbf{r}) \quad (3)$$

For the soft decoding output, we introduce the *log likelihood ratio* (LLR) for the i -th information bit

$$L_i = \ln \frac{P(u_i = 0 | \mathbf{r})}{P(u_i = 1 | \mathbf{r})} \quad (4)$$

By applying the rule of Bayes and following the principle of MAP decoding, we can rewrite the LLR as

$$\begin{aligned} L_i &= \ln \frac{f(u_i=0, \mathbf{r})}{f(u_i=1, \mathbf{r})} \\ &= \ln \frac{\sum_{\mathbf{c} \in \mathcal{C}\{u_i=0\}} f(\mathbf{c}, \mathbf{r})}{\sum_{\mathbf{c} \in \mathcal{C}\{u_i=1\}} f(\mathbf{c}, \mathbf{r})} \\ &= \ln \frac{\sum_{\mathbf{c} \in \mathcal{C}\{u_i=0\}} P(\mathbf{c}) f(\mathbf{r} | \mathbf{c})}{\sum_{\mathbf{c} \in \mathcal{C}\{u_i=1\}} P(\mathbf{c}) f(\mathbf{r} | \mathbf{c})} \end{aligned} \quad (5)$$

If memoryless channels and BPSK modulation ($0 \rightarrow +1, 1 \rightarrow -1$) are considered, and it is assumed that all codewords are equally probable (i.e., no *a priori* probability available), denote the corresponding mapped vector of the encoded codeword as $\mathbf{s} = [s_0 s_1 \dots s_{n-1}]$. We can have

$$L_i = \ln \frac{\sum_{\mathbf{c} \in \mathcal{C}\{u_i=0\}} f(\mathbf{r} | \mathbf{s}(\mathbf{c}))}{\sum_{\mathbf{c} \in \mathcal{C}\{u_i=1\}} f(\mathbf{r} | \mathbf{s}(\mathbf{c}))} \quad (6)$$

In additive white Gaussian noise (AWGN) channel, we can obtain

$$\begin{aligned}
 L_i &= \ln \frac{\sum_{\mathbf{c} \in \mathcal{C}\{u_i=0\}} \exp\{-\frac{1}{2\sigma^2} \|\mathbf{r} - \mathbf{s}(\mathbf{c})\|^2\}}{\sum_{\mathbf{c} \in \mathcal{C}\{u_i=1\}} \exp\{-\frac{1}{2\sigma^2} \|\mathbf{r} - \mathbf{s}(\mathbf{c})\|^2\}} \\
 &= \ln \frac{\sum_{\mathbf{c} \in \mathcal{C}\{u_i=0\}} \exp\{\frac{1}{\sigma^2} \langle \mathbf{r}, \mathbf{s}(\mathbf{c}) \rangle\}}{\sum_{\mathbf{c} \in \mathcal{C}\{u_i=1\}} \exp\{\frac{1}{\sigma^2} \langle \mathbf{r}, \mathbf{s}(\mathbf{c}) \rangle\}}
 \end{aligned} \tag{7}$$

where σ^2 is the noise variance and $\langle \cdot, \cdot \rangle$ denotes the inner product.

As we know, for the $(32, k)$ block code, the number of the codewords with the i -th information bit being 1 (or 0) is 2^{k-1} . The addition calculation in Eq. (7) will up to be $k(2^k - 2)$. Based on FFT, we can use a butterfly flow graph to reduce the calculation complexity [9]. The procedures are given in the following:

Step-1: For the $(32, k)$ block code, we denote all possible information sequence as $\mathbf{u}_0 = [00 \dots 0]$, $\mathbf{u}_1 = [00 \dots 1]$, \dots , $\mathbf{u}_{2^k-1} = [11 \dots 1]$, and the corresponding codewords are denoted as $\mathbf{c}_0, \mathbf{c}_1, \dots, \mathbf{c}_{2^k-1}$. After ± 1 mapping, the mapped symbol sets are expressed as $\mathbf{s}_0, \mathbf{s}_1, \dots, \mathbf{s}_{2^k-1}$.

Step-2: Define

$$\lambda_i = \exp\{\frac{1}{\sigma^2} \langle \mathbf{r}, \mathbf{s}_i \rangle\} \tag{8}$$

where $i = 0, 1, \dots, 2^k - 1$, and λ_i represents the likelihood value of the received sequence \mathbf{r} and the mapped i -th codeword \mathbf{s}_i .

Step-3: Re-order the generated λ_i : let $\mathbf{z}_i = [\lambda_i, \lambda_{2^k-1-i}]^T, i = 0, 1, \dots, 2^{k-1} - 1$, and introduce a $2^k \times 1$ sized vector $\mathbf{z} = [\mathbf{z}_0^T, \mathbf{z}_1^T, \dots, \mathbf{z}_{2^k-1}^T]^T$.

Step-4: Proceed on the BFG-based transform, we can obtain a $2k \times 1$ sized vector \mathbf{y} as

$$\mathbf{y} = [y_0, y_1, \dots, y_{2k-1}] = BFG(\mathbf{z}) \tag{9}$$

For simplicity, we take $k = 4$ for example, where $\boldsymbol{\lambda} = [\lambda_0, \lambda_1, \dots, \lambda_{15}]$, $\mathbf{z} = [\mathbf{z}_0^T, \mathbf{z}_1^T, \dots, \mathbf{z}_7^T]^T$, and \mathbf{y} is a 8×1 sized vector. The BFG-based transform can be shown in Fig. 1, from which it is obtained that:

$$\begin{aligned}
 y_0 &= \sum_{\mathbf{c} \in \mathcal{C}\{u_0=0\}} \exp\{\frac{1}{\sigma^2} \langle \mathbf{r}, \mathbf{s}(\mathbf{c}) \rangle\} \\
 y_1 &= \sum_{\mathbf{c} \in \mathcal{C}\{u_0=1\}} \exp\{\frac{1}{\sigma^2} \langle \mathbf{r}, \mathbf{s}(\mathbf{c}) \rangle\} \\
 y_2 &= \sum_{\mathbf{c} \in \mathcal{C}\{u_3=0\}} \exp\{\frac{1}{\sigma^2} \langle \mathbf{r}, \mathbf{s}(\mathbf{c}) \rangle\} \\
 y_3 &= \sum_{\mathbf{c} \in \mathcal{C}\{u_3=1\}} \exp\{\frac{1}{\sigma^2} \langle \mathbf{r}, \mathbf{s}(\mathbf{c}) \rangle\} \\
 y_4 &= \sum_{\mathbf{c} \in \mathcal{C}\{u_2=0\}} \exp\{\frac{1}{\sigma^2} \langle \mathbf{r}, \mathbf{s}(\mathbf{c}) \rangle\} \\
 y_5 &= \sum_{\mathbf{c} \in \mathcal{C}\{u_2=1\}} \exp\{\frac{1}{\sigma^2} \langle \mathbf{r}, \mathbf{s}(\mathbf{c}) \rangle\} \\
 y_6 &= \sum_{\mathbf{c} \in \mathcal{C}\{u_1=0\}} \exp\{\frac{1}{\sigma^2} \langle \mathbf{r}, \mathbf{s}(\mathbf{c}) \rangle\} \\
 y_7 &= \sum_{\mathbf{c} \in \mathcal{C}\{u_1=1\}} \exp\{\frac{1}{\sigma^2} \langle \mathbf{r}, \mathbf{s}(\mathbf{c}) \rangle\}
 \end{aligned} \tag{10}$$

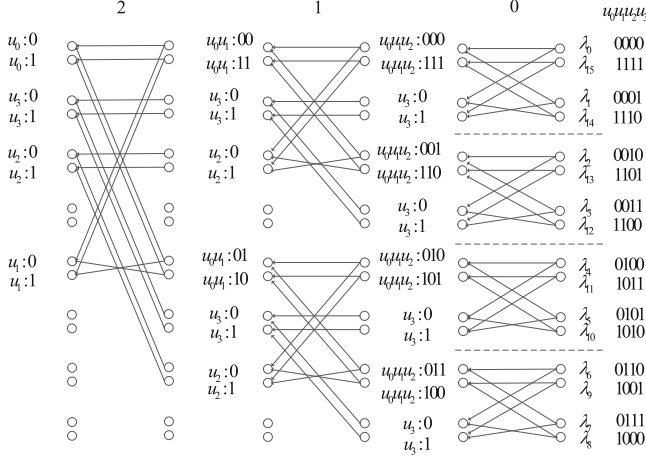


Fig. 1. The BFG-based transform of (32, 4) CQI decoder.

The BFG-based MAP decoding algorithm can be summarized as follows.

- (a) Define $\mathbf{Q}_0 = \begin{bmatrix} 1 & 0 \\ 0 & 1 \end{bmatrix}$, $\mathbf{Q}'_0 = \begin{bmatrix} 0 & 1 \\ 1 & 0 \end{bmatrix}$, we can obtain \mathbf{Q}_l by $\mathbf{Q}_l = \begin{bmatrix} \mathbf{Q}_{l-1} & \mathbf{Q}_{l-1} \\ \mathbf{Q}'_{l-1} & \mathbf{Q}'_{l-1} \end{bmatrix}$ and $\mathbf{Q}'_l = \begin{bmatrix} \mathbf{Q}'_{l-1} & \mathbf{Q}'_{l-1} \\ \mathbf{Q}_{l-1} & \mathbf{Q}_{l-1} \end{bmatrix}$ recursively, $l = 1, 2, \dots, k-1$.
- (b) In order to obtain the $2k \times 1$ sized vector \mathbf{y} , denote $\mathbf{x}_i = [y_{2i}, y_{2i+1}]^T$ firstly, $i = 0, 1, \dots, k-1$. We can get

$$\mathbf{x}_i = \begin{cases} \mathbf{Q}_{k-1,0} \cdot \mathbf{z}, & i = 0 \\ \mathbf{Q}_{k-1,2^i} \cdot \mathbf{z}, & i = 1, 2, \dots, k-1 \end{cases} \quad (11)$$

where $\mathbf{Q}_{k-1,i}$ denotes the i -th and $i+1$ -th row of \mathbf{Q}_{k-1} .

Based on $\mathbf{x}_i = [y_{2i}, y_{2i+1}]^T$, we can construct the $2k \times 1$ sized vector \mathbf{y} correspondingly, where $\mathbf{y} = [\mathbf{x}_1^T, \mathbf{x}_2^T, \dots, \mathbf{x}_{k-1}^T]^T$. Besides, with \mathbf{Q}_0 and \mathbf{Q}'_0 , the BFG-based transform can be represented as shown in Fig. 2.

Step-5: From Eq. (7) and the definition of vector \mathbf{y} , we can calculate the decoded LLR by

$$L_i = \begin{cases} \ln \frac{y_0}{y_1}, & i = 0 \\ \ln \frac{y_{2(k-i)}}{y_{2(k-i)+1}}, & i = 1, 2, \dots, k-1 \end{cases} \quad (12)$$

Step-6: Based on the decoded LLR, we can obtain the corresponding hard decision by

$$\hat{u}_i = \begin{cases} 0, & L_i > 0 \\ 1, & L_i < 0 \end{cases} \quad (13)$$

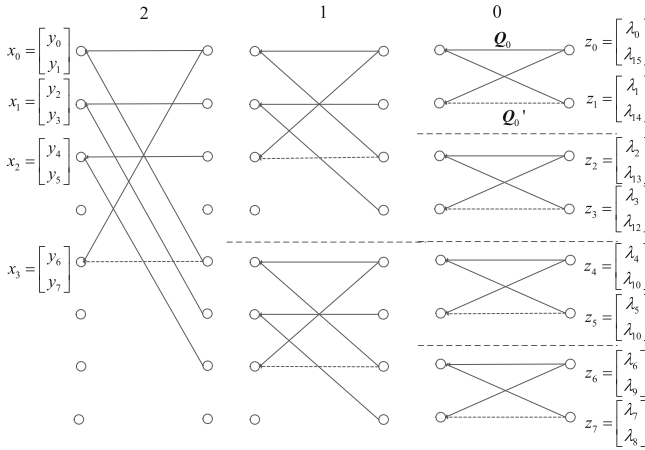


Fig. 2. Another representation of the BFG-based transform

4 Numerical Results

4.1 Performance Simulation

The simulation results are given in this section, where the simulation is carried out on AWGN channel with different signal-to-noise ratio (SNR), and the information bit number $k = 11$. The BER performance of standard MAP decoding algorithm and BFG-based MAP decoding algorithm are provided in Fig. 3. We can observe that the proposed BFG-based MAP decoding algorithm can obtain exactly the same BER performance as the standard MAP decoding algorithm.

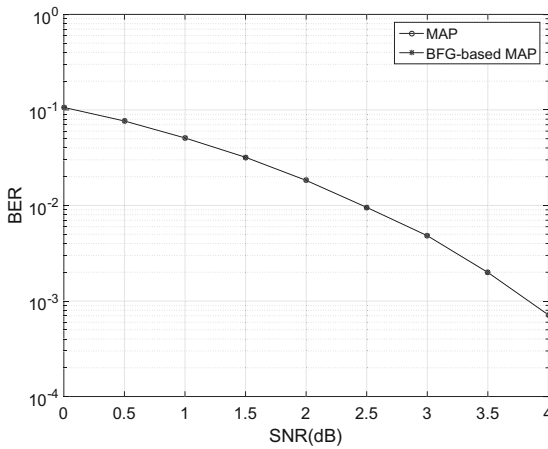


Fig. 3. The BER performance of the standard MAP decoding and BFG-based MAP decoding

4.2 Complexity Analysis

The addition calculation complexity of the standard MAP decoding algorithm and BFG-based MAP decoding algorithm with different information bit number k are shown in Fig. 4, and the relative complexity reduction is shown in Fig. 5. From the figure, it is known that, with the proposed BFG-based MAP decoding algorithm, the addition calculation complexity can be reduced by 35.71% when $k = 4$ and 72.82% when $k = 11$ accordingly. As a result, with the proposed BFG-based MAP decoding algorithm, the addition calculation complexity can be efficiently reduced.

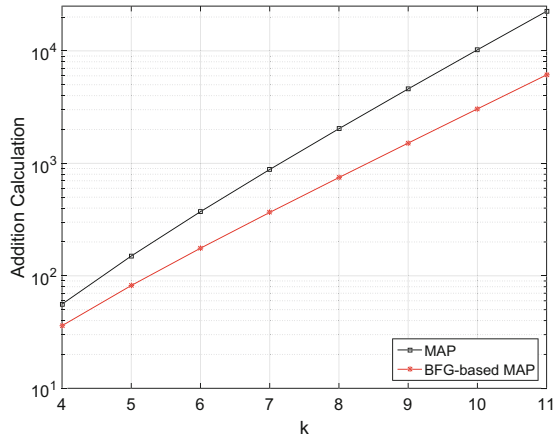


Fig. 4. The addition calculation complexity of the standard MAP decoding and BFG-based MAP decoding

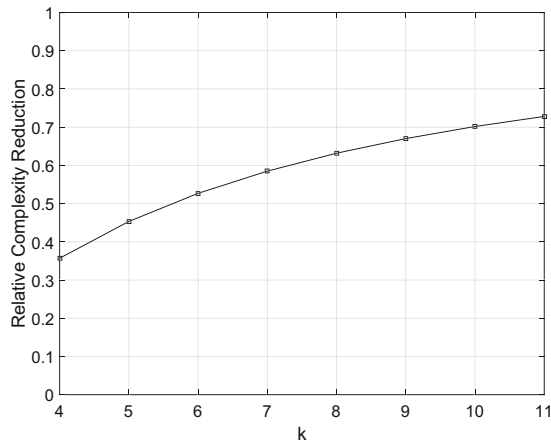


Fig. 5. The relative complexity reduction of BFG-based MAP decoding compared to the standard MAP decoding

5 Conclusion

In this paper, a BFG-based MAP decoding algorithm for CQI in 3GPP-LTE is described. From the simulation result, it is seen that compared to the standard MAP decoding algorithm, the propose algorithm can greatly reduce the complexity while the BER performance is without degradation. As a result, with the proposed algorithm, the receiver can retrieve the CQI report fast and efficiently.

References

1. Ramli, H.A.M., Sukor, M.A.: Performance analysis on automated and average channel quality information (CQI) reporting algorithm in LTE-A. In: 2016 International Conference on Computer and Communication Engineering (2016)
2. 3GPP: TS36.212, 3rd Generation Partnership Project; Technical Specification Group Radio Access Network; Evolved Universal Terrestrial Radio Access (E-UTRA); Multiplexing and channel coding (Release 12) (2015)
3. Moreira, J.C., Farrell, P.G.: Essentials of Error-control Coding. Wiley, New York (2006)
4. Li, M., Han, D., Ma, S.: Decoding algorithm with fast Hadamard transform for channel quality indication (CQI) in 3GPP-LTE, In: 2010 International Conference on Computer Application and System Modeling (2010)
5. Wolf, J.K.: Efficient maximum likelihood decoding of linear block codes using a trellis. *IEEE Trans. Inf. Theory* **24**, 76–80 (1978)
6. Lin, S., Costello, D.J.: Error Control Coding. Pearson Education Inc., London (2004)
7. MacKay, D.J.C.: Information Theory, Inference, and Learning Algorithms. Cambridge University Press, Cambridge (2003)
8. Ashikhmin, A., Litsyn, S.: Simple MAP decoding of first-order Reed-Muller and Hamming codes. *IEEE Trans. Inf. Theory* **50**(8), 1812–1818 (2004)
9. Li, Q., Yin, L.G., Lu, J.H.: Low rate coding and decoding scheme based on LDPC-BCH graph. *J. Tsinghua Univ. (Sci. Technol.)* **53**(11), 1515–1520 (2013)
10. Feng, W., Wang, Y., Ge, N., Lu, J., Zhang, J.: Virtual MIMO in multi-cell distributed antenna systems: coordinated transmissions with large-scale CSIT. *IEEE J. Select. Areas Commun.* **31**(10), 2067–2081 (2013)
11. Feng, W., Wang, Y., Lin, D., Ge, N., Lu, J., Li, S.: When mmWave communications meet network densification: a scalable interference coordination perspective. *IEEE J. Select. Areas Commun.* **35**(7), 1459–1471 (2017)



Group-Based Layered Scheduling of ADMM Decoding for LDPC Codes

Xing-Long Zhang^(✉), Meng Niu, Luo-Hui Su, and Ke-Pu Song

AVIC Xi'an Flight Automatic Control Research Institute, Xi'an 710065, China
zxilong@163.com

Abstract. For low-density parity-check (LDPC) codes decoding by alternating direction method of multipliers (ADMM), the layered scheduling sequentially updates the messages of check nodes one by one. Though the layered scheduling can speed up the convergence rates, it may limit the throughput when implementing the ADMM decoder with multi-core systems due to its serial style. To circumvent this problem, a group-based layered scheduling is proposed by updating a group of check node messages at one time. Extensive simulation results for the proposed scheme over two typical LDPC codes with the ADMM penalized decoding algorithm are provided.

Keywords: ADMM decoding · LDPC codes · Message scheduling
Convergence rate

1 Introduction

It is well known that the decoding of low-density parity-check (LDPC) codes can be formalized by an optimization problem and solved by linear programming (LP) [1]. However, the computational complexity of LP decoding is high when using the classical LP solvers such as the simplex and the interior point method. Recently, an efficient LP decoding method for LDPC codes based on the alternating direction method of multipliers (ADMM) is proposed [2]. Simulations show that both the error rate performances and the computational complexity of the ADMM decoding are comparable with that of the classical belief propagation (BP) decoding [3, 4].

The Euclidean projection operation is the most complex part in the ADMM decoding [5]. To reduce the decoding complexity, Zhang and Siegel proposed a two-step method to simplify the operation [3]. Firstly, the hyperplane in the check polytope contains the projection results is determined. Then a simple optimization problem is solved to find the exact projection points. Later, the Euclidean projection is reduced by using a linear projection algorithm onto simplex which is effective when the dimension of the input is high [6]. Recently, Jiao et al. proposed a look-up table (LUT) based method to simplify the Euclidean projections [7]. In addition to simplify the Euclidean projection itself, the complexity of the ADMM decoding can also be reduced by saving the number of Euclidean projections [8].

Another way to reduce the complexity is to accelerate the convergence rate of the ADMM decoding by using message scheduling [9, 10]. In [9], the layered scheduling for the ADMM decoding parallel to that of the BP decoding is proposed. Simulation

results in [9] show that the decoding time of the ADMM decoding can be reduced significantly by combining the layered scheduling and the method proposed in [8]. A problem for the layered scheduling is its fully serial structure which may prevent it from being implemented with parallel architectures. In this paper, we propose a partial parallel scheduling method for ADMM decoding, named group-based layered scheduling. Simulation results for two typical LDPC codes with different parallel degrees are provided.

2 Preliminaries

Suppose an LDPC code C with information length K and block length N . The parity-check matrix \mathbf{H} of C has M rows and N columns. The variable nodes in the Tanner graph of \mathbf{H} are indexed by $\mathcal{I} = \{1, 2, \dots, N\}$, and the check nodes are indexed by $\mathcal{J} = \{1, 2, \dots, M\}$. Let the degree of i -th variable node v_i be d_i and the degree of j -th check node c_j be d_j . Let $\mathcal{N}(i) = \{j \in \mathcal{J} : H_{ji} = 1\}$ be the index set of neighbors of v_i . Similarly, let $\mathcal{M}(j) = \{i \in \mathcal{I} : H_{ji} = 1\}$ be the index set of neighbors of c_j . Let \mathbf{x} be an LDPC codeword of length N and \mathbf{r} be the received vector when transmitting \mathbf{x} . The LP decoding of LDPC codes can be formulated as

$$\begin{aligned} & \min \quad \boldsymbol{\gamma}^T \mathbf{x} \\ \text{s.t. } & \mathbf{T}_j \mathbf{x} = \mathbf{z}_j, \mathbf{z}_j \in \mathbb{P}\mathbb{P}_{d_j}, \forall j \in \mathcal{J} \end{aligned} \tag{1}$$

where $\boldsymbol{\gamma} \in \mathbb{R}^N$ is the vector of log-likelihood ratios (LLRs) and the i th component of $\boldsymbol{\gamma}$ is defined as

$$\gamma_i = \log \left(\frac{\Pr(r_i|0)}{\Pr(r_i|1)} \right), \tag{2}$$

the $d_j \times N$ binary matrix \mathbf{T}_j selects out the d_j components of \mathbf{x} that participate in the j -th check node, $\mathbf{z}_j \in \mathbb{R}^{d_j}$ are ‘‘replica’’ variables, and the check polytope $\mathbb{P}\mathbb{P}_{d_j}$ is the convex hull of all binary vectors of length d_j with an even number of 1s [3]. The augmented Lagrangian of LP problem (1) with scaled dual variables is [3]

$$L_\rho(\mathbf{x}, \mathbf{z}, \mathbf{y}) = \boldsymbol{\gamma}^T \mathbf{x} + \frac{\rho}{2} \sum_{j \in \mathcal{J}} \|\mathbf{T}_j \mathbf{x} - \mathbf{z}_j + \mathbf{y}_j\|_2^2 - \frac{\rho}{2} \sum_{j \in \mathcal{J}} \|\mathbf{y}_j\|_2^2, \tag{3}$$

where $\mathbf{y}_j \in \mathbb{R}^{d_j}$ is the scaled dual variable and $\rho > 0$ is the penalty parameter. Based on (3), the $(k + 1)$ -th iteration of ADMM decoding is described as follows

$$\mathbf{x}^{k+1} := \operatorname{argmin}_{\mathbf{x}} \left(\boldsymbol{\gamma}^T \mathbf{x} + \frac{\rho}{2} \sum_{j \in \mathcal{J}} \left\| \mathbf{T}_j \mathbf{x} - \mathbf{z}_j^k + \mathbf{y}_j^k \right\|_2^2 \right), \tag{4}$$

$$\mathbf{z}_j^{k+1} := \Pi_{\mathbb{P}\mathbb{P}_{d_j}} \left(\mathbf{T}_j \mathbf{x}^{k+1} + \mathbf{y}_j^k \right), \tag{5}$$

$$\mathbf{y}_j^{k+1} := \mathbf{y}_j^k + \mathbf{T}_j \mathbf{x}^{k+1} - \mathbf{z}_j^{k+1}, \quad (6)$$

where $\Pi_{\mathbb{P}\mathbb{P}_{d_j}}(\mathbf{u})$ is the Euclidean projection of vector \mathbf{u} onto $\mathbb{P}\mathbb{P}_{d_j}$. The minimization of (4) can be calculated in component-wise as follows [2]

$$x_i = \Pi_{[0,1]} \left(\frac{1}{d_i} \left(\sum_{j \in N_v(i)} \left(z_j^{(i)} - y_j^{(i)} \right) \right) - \frac{1}{\rho} \gamma_i \right) \quad (7)$$

where $\Pi_{[0,1]}(\cdot)$ denotes the projection onto the interval $[0, 1]$, and the superscript (i) denotes the entries in \mathbf{z}_j and \mathbf{y}_j that correspond to the variable node i . The over-relaxed ADMM decoder can be implemented by replacing $\mathbf{P}_j \mathbf{x}^{k+1}$ in the \mathbf{z} - and \mathbf{y} -updates in (5) and (6) with

$$\theta \mathbf{P}_j \mathbf{x}^{k+1} + (1 - \theta) \mathbf{z}_j^k \quad (8)$$

where θ is an over-relaxation parameter and we choose $\theta = 1.9$ in our simulations as in [2].

It has been observed that the performance of ADMM decoder is worse than the BP decoding in the waterfall region. To address this problem, a penalty term is added to the objective function of (1) to penalize pseudocodewords. Two frequently used penalty terms are l_1 and l_2 penalty functions [4]. For more information about penalty functions, please refer to [11, 12]. In our simulations, the ADMM penalized decoder with l_1 penalty function is used.

3 Group-Based Layered Scheduling Algorithm

In the original ADMM decoding, the flooding scheduling simultaneously updates all the variable-to-check messages followed by all the check-to-variable messages. The advantage of the flooding scheduling is its fully parallel structure. While for the layered scheduling, the message corresponds to the check nodes are updated sequentially. For the j -th check node, the layered scheduling updates the variable-to-check messages associated with c_j firstly and then update the messages from c_j to its neighbor variable nodes. After that, the layered scheduling deals with the $(j + 1)$ -th check node. The layered scheduling converges faster than the flooding scheduling. But the serial message updates may hinder it from being implemented in parallel. In the following, we propose a group-based layered scheduling which shares the advantages of the flooding scheduling and the layered scheduling.

Assuming the M check nodes are divided into G groups, and each group contains $M/G = M_G$ check nodes. Let g be the index of the check-node groups. The group-based layered scheduling algorithm is described in Algorithm 1. Three remarks about Algorithm 1 need to be clarified:

- (1) When the ADMM penalized decoding is used, line 8 in Algorithm 1 should be calculated based on (12) in [4] for l_1 penalty function and (14) in [4] for l_2 penalty function;
- (2) For the over-relaxed ADMM, calculating z_j in line 12 of Algorithm 1 should be based on (5) and (8);
- (3) We do not use the traditional stopping condition for the ADMM framework such as the stopping condition in [2]. In Algorithm 1, we use the structural property of LDPC codes to terminate the iterative decoding. In particular, we test whether the hard decision bits satisfy all the parity checks in line 20. This is known as the early termination (ET) scheme in the literature. Simulations show that ADMM decoding with the ET scheme converges faster than the stopping condition in [2]. Therefore, we use the ET scheme throughout our simulations in the next section.

Algorithm 1: The group-based layered scheduling algorithm

```

1:  Kernel 1: Initialization
2:  Calculate  $\boldsymbol{\gamma}$  based on (2);
3:   $\mathbf{z}_j \leftarrow \mathbf{0.5}$ ,  $\mathbf{y}_j \leftarrow \mathbf{0}$ .
4:  For  $Iter$  from 1 to  $iter\_max$  do
5:    For  $g$  from 1 to  $G$  do
6:      Kernel 2: variable node update
7:      For all check nodes  $c_j$  with  $(g-1)M_G + 1 \leq j \leq gM_G$  do
8:        Calculate  $x_s$  for all  $s \in \mathcal{M}(j)$  based on (7)
9:      End for
10:     Kernel 3: check node update
11:     For all check nodes  $c_j$  with  $(g-1)M_G + 1 \leq j \leq gM_G$  do
12:       Calculate  $\mathbf{z}_j$  based on (5)
13:       Calculate  $\mathbf{y}_j$  based on (6)
14:     End for
15:   End for
16:   Kernel 4: Hard decisions from soft values
17:   For all variable nodes  $v_i$  with  $1 \leq i \leq N$  do
18:     If  $(x_i > 0.5)$   $\hat{x}_i=1$ ; else  $\hat{x}_i=0$ .
19:   End for
20:   If  $(\mathbf{H}\hat{\mathbf{x}}^T=\mathbf{0})$  break;
21: End for

```

In general, the flooding scheduling is used in each group of check nodes in Algorithm 1. However, for different groups of check nodes, we use the layered scheduling. Therefore, when $G = 1$, Algorithm 1 is indeed the flooding scheduling method; when $G = M$, Algorithm 1 is the layered scheduling method in [9].

In the following, we give a simple discussion on the parallelism of Algorithm 1 with different group size M_G . The “**For**” loop in line 5 of Algorithm 1 cannot expanded in parallel since there exists data dependent in the loop. In particular, the update of kernel 2 and kernel 3 at $g = t + 1$ needs the information obtained at $g = t$. When $M_G = 1$ or $G = M$, the number of check nodes in line 7 and 11 is only one since

$(g - 1)M_G + 1 \leq j \leq gM_G$ becomes $g \leq j \leq g$. In such a case, there is no parallelism can be utilized. When $M_G > 1$ or $G < M$, the “**For**” loop in kernel 2 and kernel 3 of Algorithm 1 can be expanded with a factor of M_G . Thus the degree of parallelism is M_G for kernel 2 and kernel 3 in the group-based layered scheduling. In addition, the hard decisions of kernel 4 in Algorithm 1 can also be implemented in parallel since the degree of parallelism for $\mathbf{H}\hat{\mathbf{x}}^T = \mathbf{0}$ in line 20 is M .

4 Simulation Results

In this section, we illustrate the frame error rate (FER) performances and the convergence rates of the proposed group-based layered scheduling for two LDPC codes C_1 and C_2 , where C_1 is the Margulis ($N = 2640$, $M = 1320$) regular LDPC code with rate 0.5 [13] and C_2 is the IEEE 802.16e ($N = 576$, $M = 288$) irregular LDPC code with rate 0.5 [14]. All the simulations are performed over additive white Gaussian noise (AWGN) channels with binary phase shift key (BPSK) modulation. The simulation environment we used is Intel Core i5 CPU, 4.0 GB memory and Visual C++ 6.0 software development tool. The l_1 penalty function $f(x) = -\eta|x - 0.5|$ is used in our simulations. The parameters ρ and η are selected by simulations. For C_1 , we choose $\rho = 3.0$ and $\eta = 0.8$. For C_2 , $\rho = 4.0$ and $\eta = 0.8$ are used.

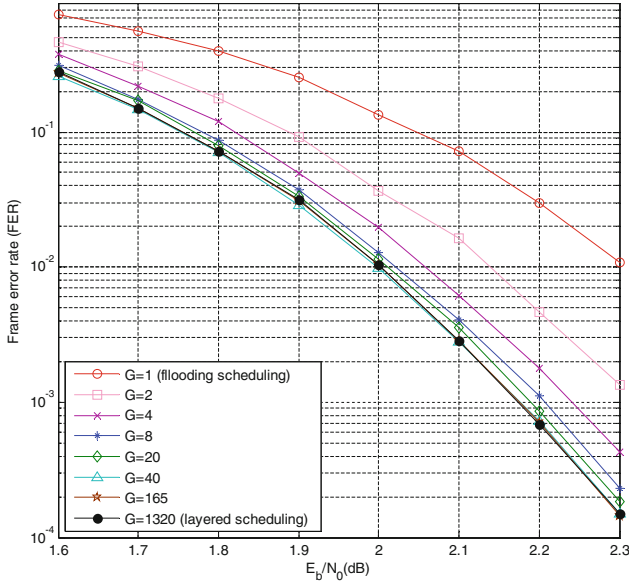


Fig. 1. FER performances for the ADMM penalized decoding with the proposed group-based layered scheduling for C_1 using different group sizes.

Figure 1 shows the FER performances of the ADMM penalized decoding with the proposed group-based layered scheduling for C_1 using $G = 1$ (flooding scheduling), 2, 4, 8, 20, 40, 165, and 1320 (layered scheduling). The maximum number of iterations is set to 20. It can be observed that the layered scheduling performs much better than the flooding scheduling and the larger the value of G , the better the FER performances. We can also see that there is no significant difference of the FER performances for $G = 40$, 165, and 1320. This means that a degree of parallelism with 33 can be obtained without performance degradation when compared to the layered scheduling with $G = 1320$.

Figure 2 depicts the average number of iterations for C_1 using the proposed method with different group sizes. It can be seen that the average number of iterations decreases as the group size increases. Moreover, as for the FER performances, the average number of iterations for $G = 40$, 165, and 1320 are almost the same. Therefore, there is almost no loss for both the FER performances and the average number of iterations when the degree of parallelism increased from 1 to 33.

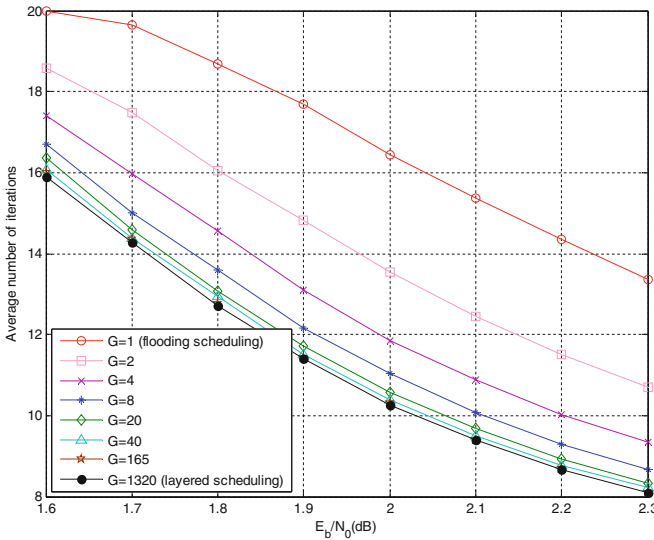


Fig. 2. Average number of iterations for the ADMM penalized decoding with the proposed group-based layered scheduling for C_1 using different group sizes, and at most 20 iterations.

Similarly, Figs. 3 and 4 show the FER performances and the average number of iterations, respectively, for the ADMM penalized decoding with the proposed group-based layered scheduling for C_2 using different group sizes. Similar observations can be obtained as for C_1 .

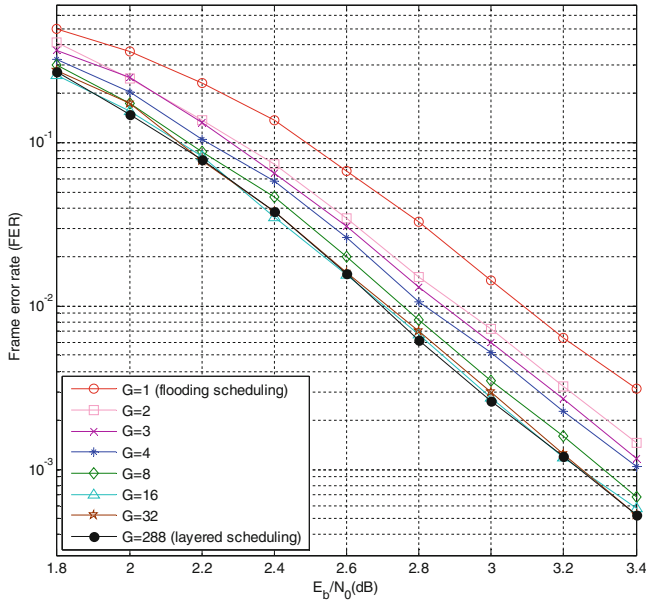


Fig. 3. FER performances for the ADMM penalized decoding with the proposed group-based layered scheduling for C_2 using different group sizes.

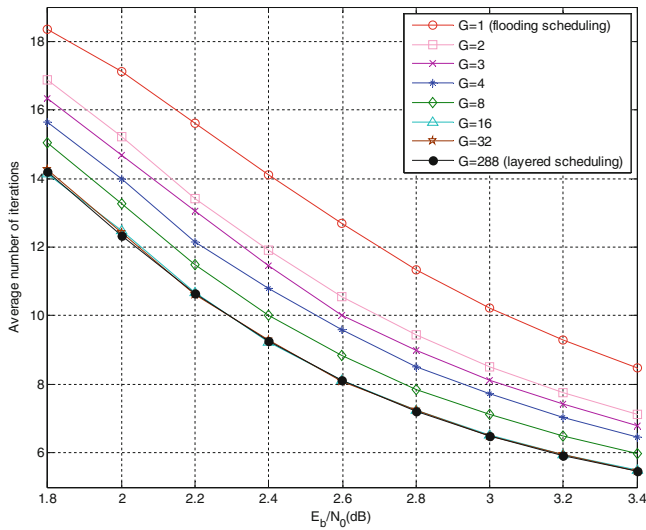


Fig. 4. Average number of iterations for the ADMM penalized decoding with the proposed group-based layered scheduling for C_2 using different group sizes, and at most 20 iterations.

5 Conclusion

In conclusion, a group-based layered scheduling for the ADMM decoding of LDPC codes is proposed. It shares the advantage of the flooding scheduling with fully parallelism and the advantage of the layered scheduling with fast convergence rates. Simulation results show that the proposed method can lift the degree of parallelism to some extent without performance degradation and convergence rate loss when compared to the layered scheduling which is totally serial.

References

1. Feldman, J., Wainwright, M.J., Karger, D.R.: Using linear programming to decode binary linear codes. *IEEE Trans. Inf. Theory* **51**, 954–972 (2005)
2. Barman, S., Liu, X., Draper, S.C., Recht, B.: Decomposition methods for large scale LP decoding. *IEEE Trans. Inf. Theory* **59**, 7870–7886 (2013)
3. Zhang, X., Siegel, P.H.: Efficient iterative LP decoding of LDPC codes with alternating direction method of multipliers. In: 2013 IEEE International Symposium on Information Theory, pp. 1501–1505. IEEE Press, New York (2013)
4. Liu, X., Draper, S.C.: The ADMM penalized decoder for LDPC codes. *IEEE Trans. Inf. Theory* **62**, 2966–2984 (2016)
5. Debbabi, I., Khouja, N., Tlili, F., Gal, B.L., Jegou, C.: Multicore implementation of LDPC decoders based on ADMM algorithm. In: 2016 IEEE International Conference on Acoustics, Speech and Signal Processing, pp. 971–975. IEEE Press, New York (2016)
6. Zhang, G., Heusdens, R., Kleijn, W.B.: Large scale LP decoding with low complexity. *IEEE Commun. Lett.* **17**, 2152–2155 (2013)
7. Jiao, X., Mu, J., He, Y., Chen, C.: Efficient ADMM decoding of LDPC codes using look-up tables. *IEEE Trans. Commun.* **65**, 1425–1437 (2017)
8. Wei, H., Jiao, X., Mu, J.: Reduced-complexity linear programming decoding based on ADMM for LDPC codes. *IEEE Commun. Lett.* **19**, 909–912 (2015)
9. Debbabi, I., Gal, B.L., Khouja, N., Tlili, F., Jegou, C.: Fast converging ADMM penalized algorithm for LDPC decoding. *IEEE Commun. Lett.* **20**, 644–647 (2016)
10. Jiao, X., Mu, J., Wei, H.: Reduced complexity node-wise scheduling of ADMM decoding for LDPC codes. *IEEE Commun. Lett.* **21**, 472–475 (2017)
11. Jiao, X., Wei, H., Mu, J., Chen, C.: Improved ADMM penalized decoder for irregular low-density parity-check codes. *IEEE Commun. Lett.* **19**, 913–916 (2015)
12. Wang, B., Mu, J., Jiao, X., Wang, Z.: Improved penalty functions of ADMM penalized decoder for LDPC codes. *IEEE Commun. Lett.* **21**, 234–237 (2017)
13. MacKay, D.J.C.: Encyclopedia of sparse graph codes. <http://www.inference.phy.cam.ac.uk/mackay/codes/data.html>
14. LDPC coding for OFDMA PHY: IEEE standard C802.16e-05/0066r3 (2005)



LUT-Based Efficient Impulse Shaping for Direct Synthesizing Digital Communication Signals at Arbitrary Symbol Rate

Ziyao Liu¹(✉), Zhijie Wang², Jun Wang², Di Huang¹,
and Nangen Zhang¹

¹ School of Information and Electronics,
Beijing Institute of Technology, Beijing, China
liuziyaochn@163.com, huangdibit@163.com,
zhangnangen@sina.com

² Institute of Telecommunication Satellite,
China Academy of Space Technology, Beijing, China
1554264456@qq.com, bitwj@163.com

Abstract. In this paper, we present a LUT-based efficient impulse shaping for direct synthesis of digital communication signal at arbitrary symbol rate. Compared with general approaches where sampling clock changes according to the symbol rate thus signal quality degrade as result of a complex analog hardware structure, or involving a fractional interpolation which consumes considerable computational resource, this new approach allows FPGA to synthesis variable high data rate signal with high quality directly at a fixed sampling rate which simplify the hardware structure and saves computational resource consumption. With some little modifications, the presented scheme could be easily adapted to 8PSK, 16QAM and other arbitrary amplitude-phase-modulation constellations. A hardware prototype has been built to verify the presented algorithms. In particular, we have achieved 4.8 Gbps parallel impulse shaping which supports input symbol rate ranging from 100 Ksps to 600 Msps.

Keywords: LUT-based · Impulse shaping · Direct synthesis
Variable symbol rate

1 Introduction

Producing digital communication signals such as the BPSK, QPSK, 8PSK or 16QAM signals at variable symbol rate is one of the fundamental functions provided by the state-of-the-art Vector Signal Generators (VSG) or Arbitrary Waveform Generators (AWG). For example, the famous KeySight™ (formerly known as Agilent) VSG E8267D is capable of generating QPSK signals with the symbol rate ranging from 100 Ksps to 50 Msps (when using basic kit) [1]. The more advanced Zodiac™ Cortex High Data Receiver XXL (when used as a simulator) may generate digital communication waveforms with various constellation patterns at the symbol rate of 1 Ksps–600 Msps [2]. Besides its application to advanced testing equipment, real-time synthesis of variable rate communication signals is also one of the enabling techniques for various Software Defined Radio (SDR) systems [3, 4].

To further elaborate on the challenges and solutions for variable symbol rate signal generation, let us examine the conceptual diagram of a simplest BPSK transmitter in Fig. 1. As illustrated in the figure, before modulating the Local Oscillator (LO), the baseband Non-Return-to-Zero (NRZ) signal is generated by passing the information carrying pulse-train through a pulse shaping filter, which usually has a Squared Root Raised Cosine (SRRC) function as its unit impulse response, to eliminate both out-of-band power leakage and Inter-Symbol Interferences (ISI) [5]. On most SDR platforms, pulse shaping operation is carried out in the digital domain by interpolating a symbol-rate binary pulse train with a digital SRRC Low-Pass Filter. The interpolation rate is often an integral to avoid fractional rate resampling. Due to the constraint of integral interpolation rate, a following quadrature (I/Q) modulator becomes a prevailing choice [6, 7].

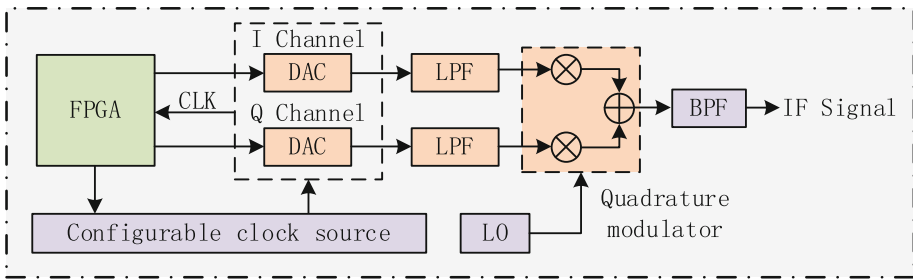


Fig. 1. Conceptual diagram of a simplest BPSK transmitter with integral rate sampling

As can be seen in the figure, the Field Programmable Gate Array (FPGA) and the double-channel DACs are driven by a reconfigurable clock f_{clk} , which satisfies $f_{\text{clk}} = k \cdot R_s$, where R_s is the symbol rate, and k is a positive integral. When the transmitter needs to work on a new symbol rate, it may simply change f_{clk} . As f_{clk} is independent of the RF or IF center frequency f_c , the topology of Fig. 1 allows for great flexibility to support variable symbol rate [8].

However, as modulation is accomplished in the analog domain in Fig. 1, the quality of the IF or RF output will inevitably suffer from the amplitude imbalance between the I/Q channels, as well as the non-orthogonality of the \cos & \sin LO pair. A more integrated, “Direct Synthesizing” transmitter solves this problem by modulating the digital LO waveforms directly inside the FPGA, and then generate IF or RF output by a single-channel DAC, as can be seen in Fig. 2. Direct synthesis complies with the general SDR principle of “placing the DAC or ADC as close to the RF front-end as possible”. Besides improved output quality, it also saves cost, volume and power consumption as it cancels a DAC channel, a stand-alone analog modulator and a reconfigurable clock source.

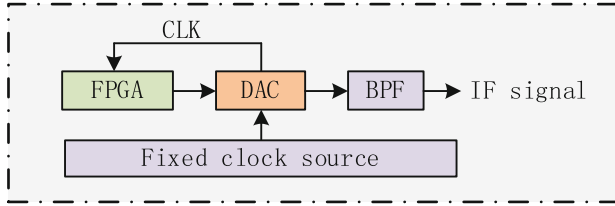


Fig. 2. Hardware diagram of the “Direct Synthesizing” transmitter

The challenge of direct synthesis when applied to variable symbol rate signal generation is, the FPGA and DAC’s driving clock has now to be determined by the output frequency f_c , and usually it is no longer an integral multiple of the symbol rate R_s , hence fractional resampling becomes a requisite in this case which is shown in Fig. 3.

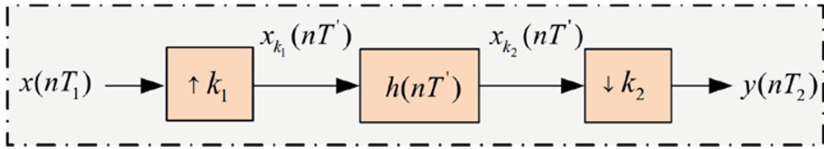


Fig. 3. A common structure of fractional resampling

Suppose $f_{\text{clk}}/R_s = k_1/k_2$, fractionally resampling a symbol stream at the rate of R_s into a digital baseband waveform at the sampling of f_{clk} means first interpolating by k_1 times with the pulse shaping filter, and then decimating the output by k_2 times. The computational overhead incurred by this process soon becomes formidable as R_s or f_c increases. Even worse, the “decimate after interpolate” method cannot give us a unified implementation framework as the interpolation and decimation rate, namely k_1 and k_2 , vary with R_s .

The motivation of this paper is to develop an efficient pulse shaping algorithm that makes direct synthesis practical for variable rate signal generation. As a low-complexity alternative to the on-line interpolating & decimating computation, a Look-Up-Table (LUT) based fractional resampling scheme is presented, which almost only relies on reading the content out from the proper address in a pre-defined memory space. We demonstrate the effectiveness of our pulse-shaping algorithm by directly synthesizing a 100 Ksps–600 Msps SRRC pulse-shaping QPSK signal at an IF center frequency of $f_c = 1.2$ GHz, using a DAC (MD622H) working at 4.8 GHz and a FPGA (Xilinx XC7VX690T) with clock rate 150 MHz ($\times 32$ parallel channels). It is observed the transmitter only takes 12% of the logic, computational and storage of the targeted FPGA. The output signal is examined by a vector signal analyzer. Both the spectrum and the Error-Vector-Magnitude (EVM) results are provided. With some minor modifications, our scheme can also be applied to other more complex constellations such as QPSK, 8PSK or 16QAM or other pulse-shaping functions than SRRC waveforms.

The remainder of the paper is organized as follow. We first describe a diagram of the “Direct Synthesizing” transmitter and illustrate the model of the LUT-based impulse shaping in Sect. 2.1. We dedicate Sect. 2.2 to the derivation of the relationship between LUT address updating and impulse shaping at variable symbol rate, based on Direct Digital Synthesis (DDS) and then present the algorithm in detail (Sect. 2.3). Next, we investigate the computational complexity of the proposed algorithm and introduce our hardware experiment platform in Sect. 3. The test result, such as spectrum and EVM, obtained by hardware test are also given in the last section (Sect. 3), followed by conclusion.

2 Proposed Scheme

2.1 Direct-Synthesizing Transmitter

As can be seen in the topology of “Direct Synthesizing” transmitter shown in Fig. 4, the parallel digital up conversion and Oserdes & FIFO is based on a conventional parallel DDS structure, which is out of this paper’s scope. In the sequel we focus on is the parallel impulse shaping module whose schematic diagram is illustrated in Fig. 5. Besides, as shown in Fig. 4, Data stream (a PN sequence) provided by Data source module in a parallel way will be constellation-mapped in accordance to the modulation type thus with little modification of mapping pattern, this “Direct Synthesizing” transmitter could be applied to arbitrary amplitude-phase-modulation constellations, such as BPSK, QPSK, or 16QAM.

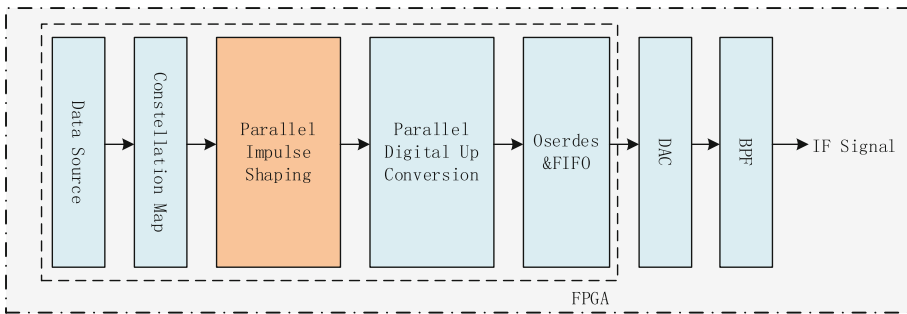


Fig. 4. Topology of “Direct Synthesizing” transmitter

As shown in Fig. 5, the schematic diagram is one channel of parallel impulse shaping module which simulate a convolution process involving 6 symbols (from Data ROM) and coefficients (from LU1 to LUT6) in the same amount. The reason why we assign 6 to the number of symbols involved in the convolution process will be explained in the next part. Therefore, our problem boils down to find the proper address of Data ROM and LUTs to obtain the proper data and coefficients.

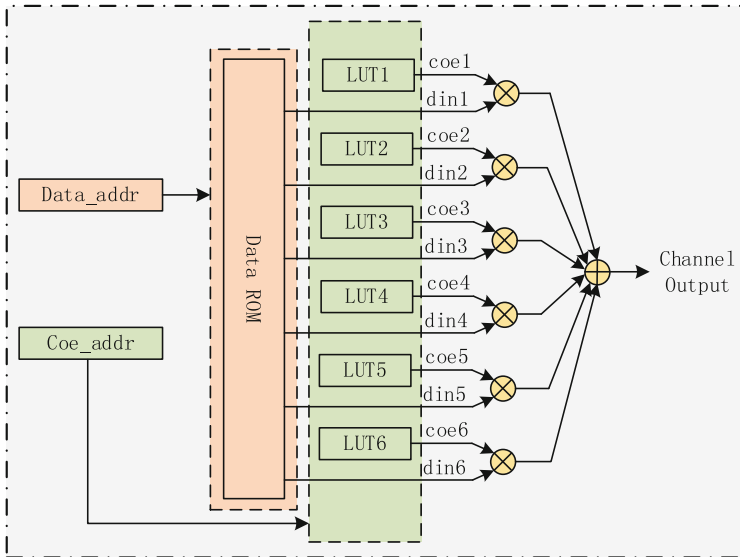


Fig. 5. Schematic diagram of the impulse shaping in one channel

2.2 Relationship Between LUT Address Updating and Impulse Shaping

In order to find the proper address of Data ROM and LUTs, we propose an algorithm updating the address on the basis of DDS theory. It is well known that classic DDS technique is capable of generating arbitrary-frequency sinusoid wave at a fixed sampling rate, given the frequency of the generated sinusoid is below $1/3$ or $1/4$ of the sampling rate. The structure of a classic DDS is shown in Fig. 6.

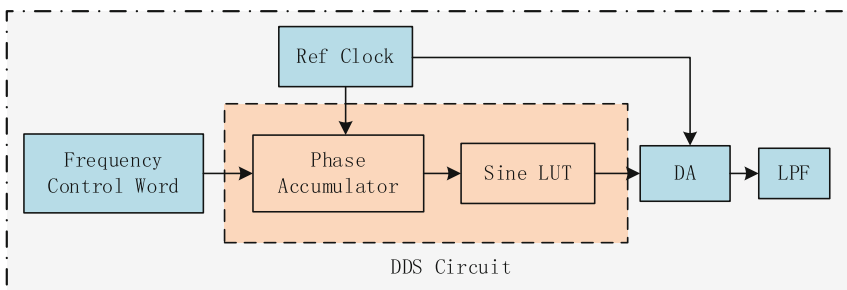


Fig. 6. A common DDS structure

As Fig. 6 shows, the sum of the Frequency Control Word (FCW) and phase data at last clock will be output from Phase Accumulator as look-up-table address to next part thus waveform could be generated from Sine LUT continuous output.

Considering the generation of digital I/Q baseband waveforms often relies on a pulse-shaping filter, or an interpolator when the output sampling frequency is integral multiples, i.e. $F_s = N * R_s$, where $N \in N^+$. But when $F_s \neq N * R_s$, as in the common case, producing baseband waveforms is often regarded as difficult. As in this case, a fractional resampling has to be adapted, and more particularly, if $F_s/R_s = k_1/k_2$, then a k_1 times interpolation will be followed by a k_2 times decimation to implement a k_1/k_2 resampling which bring about unaffordable computational consumption.

Therefore, we assume that if we can store the result of impulse shaping in a LUT and output it in a regular manner, specifically, based on DDS theory, unaffordable real-time computational resource consumption could be avoidable. Let us examine a SRCC (Square Root Raised Cosine) waveform which shown in Fig. 7.

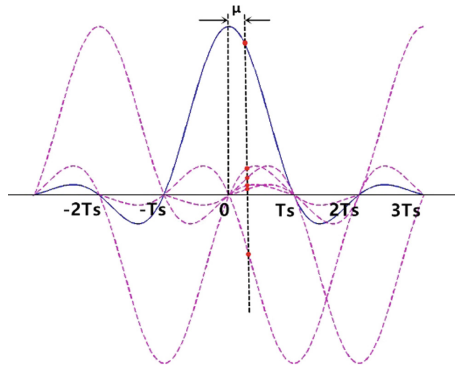


Fig. 7. A SRCC (Square Root Raised Cosine) waveform

It is well known that direct synthesis is on the basis of outputting the pre-stored approximate value of result, which can be expressed as a formula below.

$$y(kT_i) = y[(m_k + \mu_k)T_s] = \sum_{i=I_1}^{I_2} x[(m_k - i)T_s]h_I[(\mu_k + i)T_s] \tag{1}$$

$$\approx \sum_{i=I_1}^{I_2} x[(m_k - i)T_s]h_I[iT_s] \tag{2}$$

The difference of Eqs. 1 and 2 is the $h_I(t)$, assume the error of them is

$$\mu = (\mu_k + i)T_s - iT_s = \mu_k T_s \tag{3}$$

where $\mu \in [0, 1]$ thus $\mu = \mu_k T_s \leq T_s$. Since T_s is depend on the sampling rate, we can optimizing the interpolation performance by improving it. The initial value $k = 0$; If the current $\mu > 1$, then

$$k = k + 1 \tag{4}$$

$$\mu = \text{mod} [\mu, 1] \quad (5)$$

So if we discretize the waveform in $t \in (0, T_s)$ at a resolution of $T_s/1024$, then a 32×1024 -depth (the number of channel is 32) LUT is capable of covering any possible value of μ , at a resolution $T_s/1024$, which is in general sufficient in most practical contexts.

Meanwhile, when we fix the waveform of impulse shaping filter, the number of symbol involving in one clock is determined. Take the waveform of Fig. 7 for instance, the blue curve is the waveform of impulse shaping filter in time domain which has 6 x-intercept, we can observe that pulse shaping result of any point at $t \in (0, T_s)$ is determined by 6 symbol, as the red point of intersection illustrated in Fig. 7, which can be formulated to Eq. 4. This means that every impulse shaping process only need 6 symbols and 6 corresponding coefficients which explain the problem proposed in Part 2.1.

$$y(k) = \sum_{k=-2}^3 x(k)h(t - nT'_s) \quad (6)$$

Therefore, we pre-store the result of pulse shaping at very high resolution in LUTs, and take it out according to the symbol rate on the basis of DDS theory, a continuous waveform of impulse shaping could be obtained. A parallel impulse shaping scheme based on our algorithm is given in Fig. 8.

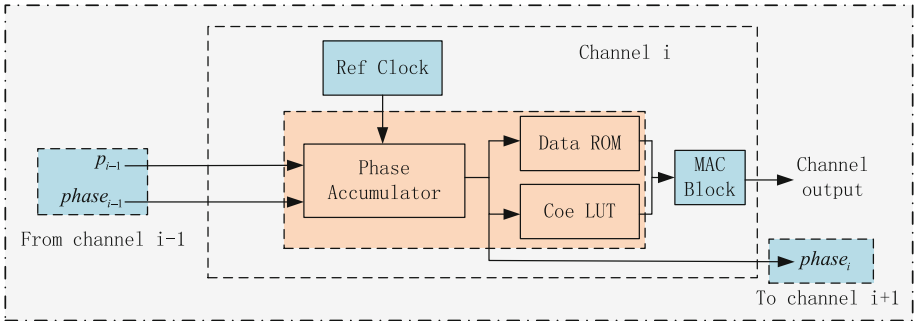


Fig. 8. A parallel impulse shaping scheme based on our algorithm

Besides, since the pulse shaping is based on a LUT process, unaffordable real-time computational resource consumption could be avoidable. This benefit will be observed in detail in Part 3.

2.3 Implementation Steps of LUT-Based Efficient Impulse Shaping

Through the discussion above, implementation steps of LUT-based efficient impulse shaping can be summarized as follows for example.

1. Store PN sequence generated by PN sequence generator in parallel structure into a FIFO. Update the FIFO according to the requirement proposed by address-updating module and output 8bit data into a register with a RFD (ready for data) signal.
2. Generate S LUT storing the coefficient and divide them into T ROM, the depth of ROM is 2^n . In general, consider the influence of side-lobe and computing quantity, $S = T = 6$, $n = 10$.
3. Parallel process the wideband signal that divide it into M channel. If the symbol rate is R_s , working clock is F_1 , sampling clock is F_s , then $M = F_s/F_1$, and the symbol control word of each channel can be expressed as

$$P_i = \left\lfloor i * R_s * \frac{M}{F_s} * 2^{32} \right\rfloor \quad (7)$$

Where 2^{32} is the normalization, and $\lfloor \rfloor$ is defined as rounding operation.

4. Update the phase of each channel to obtain the address of ROM to get the data and coefficient for convolution operation. The updating process is defined as below

$$Phase_i = 2 * 2^{32} \quad (8)$$

$$Phase_i = Phase_{i-1} + P_{i-1}, i = 2, 3, 4, \dots, M \quad (9)$$

Where $Phase_1$ is the phase of 1st channel, $Phase_i$ is the phase of i^{th} channel and it is expressed in 32bit. Denote the data address as Data_addr, coefficient address as Coe_addr, then Data_addr is equal to the highest 4 bit of $Phase_i$ and Coe_addr is equal to the highest n bit of the lowest 32bit of $Phase_i$.

5. According to the address we have obtained from last step, get the data and coefficient and make convolution operation of each channel.
6. Update the phase of the 1st channel as below

$$Phase_1 = Phase_1 + P_{32} \quad (10)$$

7. After $Phase_1$ have updated, generate a RFD signal and go back to the first step.

3 Implementation, Results and Discussion

A LUT-based efficient impulse shaping for direct synthesis of digital communication signal at arbitrary symbol rate is implemented using the algorithm mentioned above. The hardware platform on which the presented algorithm is tested is given below in Fig. 9. At the bottom of the figure is a Compact PCI Express (CPCIE) interface which allows the platform to be connected along a CPCIE bus, and become a part of a host computer. Since the on-board DAC is working at 4.8 GHz, it has to accept digital waveform data from the FPGA through 32 parallel channels at the rate of 150 MHz each. Quantization width of SRRC filter is 32, roll-off factor is 0.35, thus a group of filter coefficients whose

width = 32, depth = 6144 can be produced in advance by MATLAB, and then stored into 6 LUT with width = 32 and depth = 1024. Input symbol rate has been tested from 100 Ksps to 600 Msps, and the IF center frequency is fixed at 1.2 GHz. Without loss of generality the modulation type is chosen as 8PSK in our test.

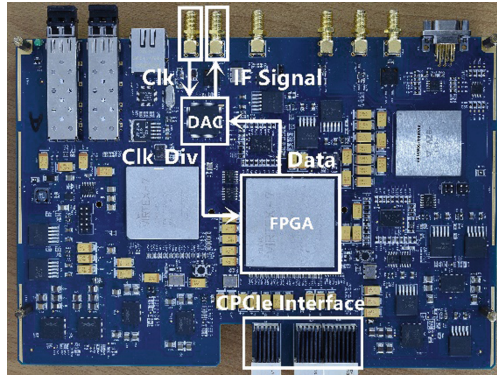


Fig. 9. Photograph of testing platform

As indicated in Fig. 9, DAC uses its internal clock divider using an exterior clock (“Clk”) to provide a fixed working clock (“Clk_Div”) to FPGA. FPGA sends the data (“Data”) generated by our algorithm to DAC which transforms it to an IF analog signal (“IF Signal”).

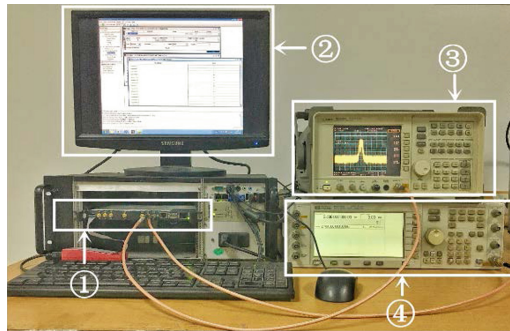


Fig. 10. Photograph of the testing system

The photograph of our testing system is shown in Fig. 10, and for the detailed models of the key components please refer to Table 1. As shown in the figure, the hardware platform (the PCB board) is inserted into an industrial PC through CPCIE bus. The PC provides power for the ADC + FPGA board, and also runs a GUI to facilitate real-time status monitoring and data analysis. The signal generator (HP E4433B) produces external clock for the testing system, and the IF output is fed to the spectrum analyzer (Agilent 8563EC).

Table 1. Critical components of the hardware system

Identifier	Component	Model number
1	DAC	Euvis MD622H
	FPGA	Xilinx XC7VX690T
2	Software interface	Xilinx Chipscope Pro
3	Spectrum analyzer	Agilent 8563EC
4	Signal generator	HP E4433B

Table 2. LUT-based impulse shaping consumption (Targeted FPGA model: Xilinx XC7VX690T)

Resource type	Used	Available	Utilization
Slice	9308	607200	12%
BlockRam18E	384	2060	18.6%
DSP48E1s	384	2800	13%

In Table 2 we summarize the resource consumption of the presented LUT-based impulse shaping algorithm for the targeted FPGA model Xilinx XC7VX690T. In particular, we are concerned about three different kinds of resources, namely the logic resource (slices), the storage resource (Block RAM 18E) and the computational resource (DSP48E1s). For all these three different categories of resources, we are glad to find the presented algorithm occupies less than 20% of the total available amount inside the FPGA, which suggests it may strike as a highly cost-efficient choice in practice.

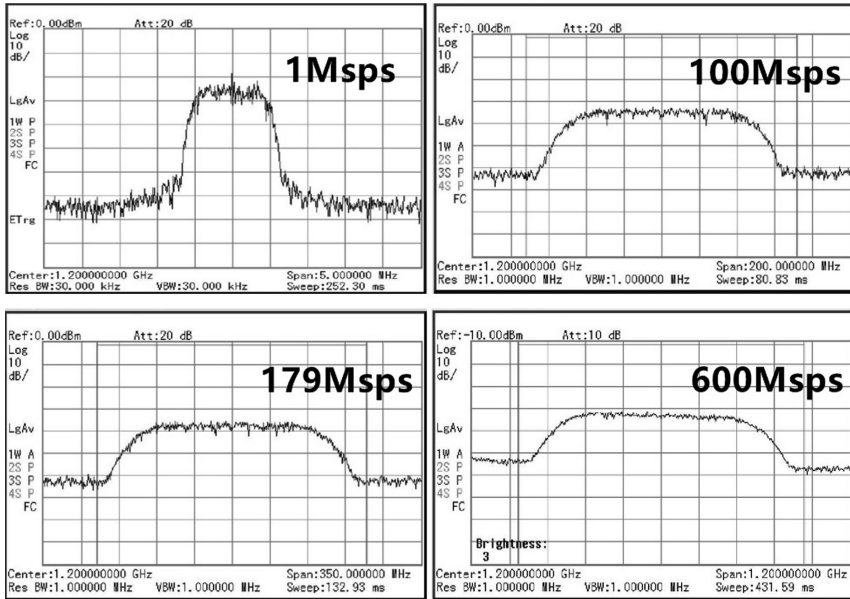


Fig. 11. Frequency spectrum of IF signal at different symbol rate

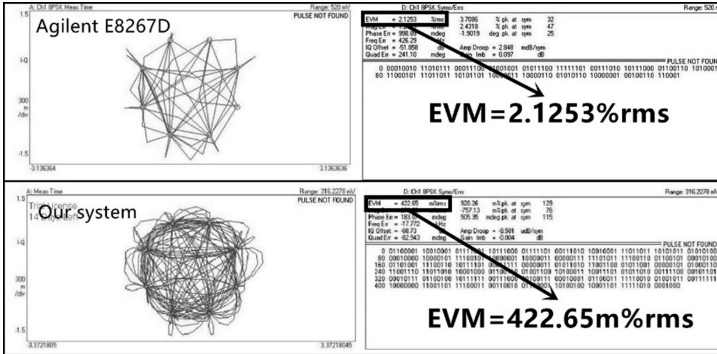


Fig. 12. Constellation, frequency spectrum and EVM of an 8PSK signal at 5 Msps symbol rate tested by Agilent 89600 Vector Signal Analyzer

In Fig. 11 we present the result obtained on the spectrum analyzer, when the IF output is generated for symbol rate 1 Msps, 100 Msps, 179 Msps and the maximum 600 Msps. Note that we choose 179 Msps deliberately to show the presented algorithm may work perfectly for the case where the sampling rate of the DAC (4.8 GHz) is not an integral multiple of the symbol rate (179 Msps). It is observed, the corresponding bandwidth is approximately, 1.4 MHz, 140 MHz, 252 MHz and 820 MHz, respectively, due to the 0.35 roll-off factor of the adopted SRRC baseband pulse. It should be noted when the output signal bandwidth is above 500 MHz, the far-end of the IF output spectrum is a little bit attenuated. The reason for this phenomenon is the DAC has a low-pass “Sinc” output characteristic [9]. Using digital pre-emphasis, it is feasible to compensate for the non-uniform output characteristic of the DAC inside the FPGA. This work is now underway (Fig. 12).

From a digital modulation point of view, the IF signal quality is usually evaluated by the Error Magnitude Vector [10], which characterize the deviation of the signal under-test with respect to a standard, error-free constellation. EVM could be measured by a Vector Signal Analyzer, and in our test, we use KeySight™ 89600 VSA software running on an E8563E. KeySight™ Vector Signal Generator E8267D is used as a performance benchmark, i.e. we compare the EVM of the IF signal generated by our presented algorithm and hardware with that of E8267D. Without loss of generality, the

Table 3. EVM of other higher symbol rate signal

Symbol rate	Error-Vector-Magnitude (EVM)
100 Msps	3.0470% rms
200 Msps	3.7903% rms
250 Msps	4.2828% rms
350 Msps	5.1685% rms
500 Msps	6.2878% rms
550 Msps	6.9851% rms
600 Msps	7.9340% rms

symbol rate is chosen as 5 Msps, which falls in both the available range of E8267D (10 Ksps–50 Msps) and our system (100 Ksps–600 Msps). It is found the EVM of our system is 0.422%, and is significantly better than that of E8267D, which is 2.12%. For other higher symbol rate, the EVM of the presented system is listed by Table 3.

4 Conclusion

The communication signal generation at arbitrary symbol rate is one of the most difficult problems on SDR platform. To solve this problem, we propose an efficient impulse shaping algorithm based on a low-complexity hardware system. Through test data compared with the counterpart of KeySight™ Vector Signal Generator E8267D, it is demonstrated that our experimental results are in consistence with the theoretical derivation. In particular, we have achieved 4.8 Gsps modulation with symbol rate ranging from 100 Ksps to 600 Msps. Moreover, with some little modifications, the scheme we proposed could be easily adapted to 8PSK, 16QAM and other arbitrary amplitude-phase-modulation constellations, or other baseband pulse-shaping functions in high speed modem.

Acknowledgement. This work is supported by National Natural Science Foundation of China under contract No. 61471360.

References

1. KeySight Technologies: Agilent E8267D PSG User Manual (2012)
2. ZODIAC AEROSPACE, Cortex HDR XXL-High Data Rate Receiver User Manual (2016)
3. Peiqing, C.: Digital Signal Processing Tutorial. Tsinghua University Press, Beijing (2007). pp. 182–188
4. Gongli, Z.: All Digital Receivers Theory and Techniques. Science Press, Beijing (2005). pp. 86–106
5. Tseng, B.D.: Directly realization of the structure for FIR and IIR filters. In: 23th Asilomar Conference on Signals, Systems and Computers, pp. 233–235 (1989)
6. Xiao, Z., Su, L., et al.: Fractional sampling rate transformation for wideband all digital receivers. *Tsinghua Univ. (Sci. Tech.)* **50**(10), 1643–1645 (2010)
7. Yang, J., Cui, S., Liu, C.: A joint implementation for bit synchronization and filtering in high-speed digital receivers, CN101789858A (2010)
8. Li, K.: Design and implementation of a variable data rate signal generator. In: The Eleventh Satellite Communication Conference (2015)
9. Vandebussche, J., Van Der Plas, G., Gielen, G., et al.: Behavioral model of reusable DA converters. *IEEE Trans. Circ. Syst. Analog Digital Sig. Process.* **46**(10), 1323–1326 (1999)
10. Mckinley, M.D., Remley, K.A., Myslinski, M., et al.: EVM calculation for broadband modulated signals, pp. 45–52 (2004)



An Adaptive Step-Size Prediction Joint OMP Algorithm for Beam Tracking in Millimeter Wave Systems

Xu Yang¹, Xiaohui Li¹(✉), Bin Zhou², Yanbin Zhao³, and Ruiyang Yuan¹

¹ State Key Laboratory of Integrated Service Networks,
Xidian University, Xi'an 710071, Shaanxi, China
xhli@mail.xidian.edu.cn

² AVIC Computing Technique Research Institute, Xi'an, Shaanxi, China

³ Geographic Information Center, Yangquan, Shanxi, China

Abstract. For the millimeter wave (mmWave) time-varying system, beamforming poses a formidable challenge for huge power overhead. In this paper, an adaptive step-size prediction joint orthogonal matching pursuit (OMP) algorithm (ASP-OMP), is proposed for beam tracking. With the direction of arrival (DOA) information obtained by OMP algorithm, kalman filter is used to predict the beamforming vector during N time slots to avoid huge sampling loss. In addition, we propose to determine the prediction step-size with outlier identification and eliminate the beam tracking error through data fusion based on Bayesian estimation. The simulation results demonstrate that the proposed algorithm can converge quickly and have a good performance for mmWave beam tracking.

Keywords: Millimeter wave time-varying system · OMP algorithm
Beam tracking · Outlier identification · Bayesian estimation

1 Introduction

In the 5th Generation mobile communication (5G) technology standard, 60 GHz millimeter wave wireless communication technology has become a research hotspot. Millimeter wave multi-input multi-output (MIMO) systems can provide throughput for future communication systems to meet the expected requirements of mobile data [1,2]. Aiming at reducing the huge path loss in millimeter wave communication, beamforming technology is introduced in the IEEE 802.11ad standard [3], which can improve the range and quality of the communication by directionally enhancing signal and control the signal propagation direction.

In order to conduct adaptive beamforming, channel estimation is required generally for that optimal singular value decomposition (SVD) beamforming. Due to the beam training overhead, the compressive sensing (CS) theory is

adopted for the channel estimation [4]. [5] proposed a novel compressed SNR- and-channel estimation algorithm, which can significantly improve the estimation performance over the scheme in IEEE 802.11ad with reducing the pilot overhead of beam tracking. While these compression-based channel estimation algorithms further reduce the overhead, it is still a huge challenge for multiple estimations in the 60 GHz millimeter wave time-varying system.

The general solution is to use the uplink information to carry out DOA estimation, indicating the direction of the user. The current research aims to reduce the overhead and improve the estimation accuracy. The algorithm proposed in [6] suggests that DOA can be determined by beam scanning and the fast beam tracking can be realized through wide beam training and narrow beam alignment with the layered codebook and the antenna pattern [7–9]. However, this algorithm can only enable one data stream and face the outdated risks. Aiming at further improving spectral efficiency, [10] proposed to adopt the OMP algorithm to estimate the AoAs and AoDs of multi-paths, which can be used to construct the beamforming vector. Although this method can provide high estimation accuracy and support multi-stream transmission, it has to face with the unavoidable problem of high iteration complexity and sampling loss with the OMP algorithm.

In this paper, the ASP-OMP algorithm is proposed to achieve the fast beam tracking with the partial information of channel, which can meet the channel time-varying characteristic. Compared to the previous works, the complexity and validity of the proposed algorithm are both considered. Moreover, to carry out beam tracking in time-varying channel, kalman filter is used to predict the beamforming vector. For keeping the tracking accuracy of OMP algorithm and reducing the tracking complexity and power loss, this paper sets the error threshold through the outlier identification method, which can adaptively determine the prediction step-size to achieve fast beam alignment. In addition, it is Bayesian estimation that is used to eliminate the effect of outliers on the tracking accuracy. The theoretical analysis and simulation results demonstrate that the proposed algorithm can provide a close performance to the existing algorithms with low complexity.

The remainder of paper is organized as follows. We first provide the preliminary background and present the system model and problem formulation in Sect. 2 and summarize the proposed tracking algorithm based on adaptive stride prediction with kalman filter in Sect. 3. Section 4 presents simulation results. Conclusions are presented in Sect. 5.

2 System Model

We consider a single user massive MIMO mmWave time-varying system, where a base station (BS) is equipped with N_t antennas and a mobile station (MS) is equipped with N_r antennas. For the initial beam alignment, a beamforming scheme based on OMP algorithm is considered in [10]. The system model is as illustrated in Fig. 1. In order to simplify the model, it is assumed that the

transmitter uses an antenna array for beamforming and the receiver uses an omnidirectional antenna. The downlink beamforming in 60 GHz millimeter wave system is considered in this paper with the BS tracking the MS. The transmit signal is expressed as \mathbf{s} and the receive signal can be expressed as:

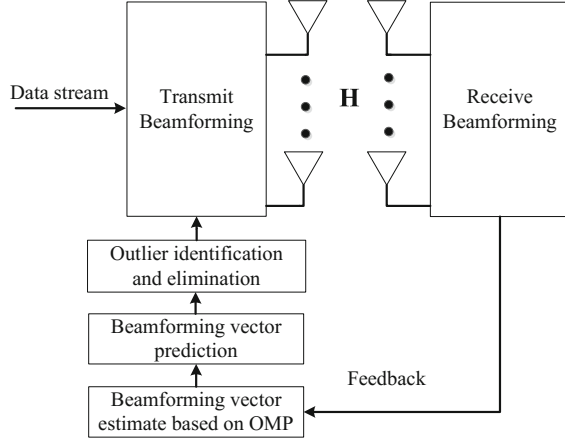


Fig. 1. System model

$$\mathbf{y} = \mathbf{h}\mathbf{w}\mathbf{s} + \mathbf{n} \quad (1)$$

where \mathbf{w} is the beamforming vector with the constraint $\|\mathbf{w}\| = 1$. The additive white Gaussian noise \mathbf{n} is assumed to be i.i.d complex Gaussian with unit variance, i.e. $\mathbf{n} \sim CN(0, 1)$. Due to the high path loss characteristics of millimeter wave signals, millimeter wave channels are expected to exhibit limited spatial scattering. Millimeter wave channel \mathbf{h} can be expressed as:

$$\mathbf{h} = \sqrt{\frac{1}{L}} \sum_{l=1}^L \alpha_l a_r(\theta_l) a_t^H(\phi_l) \quad (2)$$

where L denotes the number of transmission path, α_l represents the complex gain of the l_{th} path. θ_l and ϕ_l denote the AoA and AoD of the l_{th} path, respectively. $a_r(\theta_l)$ and $a_t(\phi_l)$ represent the receiver and transmitter array vector, respectively.

Millimeter wave beam tracking is to determine the millimeter wave beam direction between the BS and the MS to minimize energy loss and maximize received signal to noise ratio (SNR). The number of transmitted data stream is L_s . And the SNR of the i_{th} data stream can be calculated by:

$$SNR_i = \frac{1}{\sigma_n^2 [(\|\mathbf{h}\mathbf{w}\|^2 + \sigma_n^2 \mathbf{I}_{L_s})^{-1}]_i} - 1 \quad (3)$$

It is well known that the optimal beamforming matrix \mathbf{w} maximizing SNR_i is determined by the SVD of the channel matrix \mathbf{h} . It is Assumed that the SVD of \mathbf{h} bear the form below:

$$\mathbf{h} = \mathbf{U}\Lambda\mathbf{V}^H \quad (4)$$

where $\mathbf{U} = [\alpha_r(\phi_1), \alpha_r(\phi_2), \dots, \alpha_r(\phi_L)]$ denotes a unitary matrix with the size of $N_r \times L$, Λ is a $L \times L$ diagonal matrix. $\mathbf{V} = [\alpha_t(\theta_1), \alpha_t(\theta_2), \dots, \alpha_t(\theta_L)]$ denotes a $N_t \times L$ unitary matrix. Each array propagation vector in \mathbf{V} can be expressed as:

$$\alpha_t(\theta_k) = \frac{1}{\sqrt{N_t}} \left[1, e^{j\frac{2\pi}{\lambda}d_t \sin \theta_k}, \dots, e^{j\frac{2\pi}{\lambda}(N_t-1)d_t \sin \theta_k} \right] \quad (5)$$

where d_t is the antenna element spacing for the TX antenna array, and λ is the wavelength at the carrier frequency.

In order to track the channel change and reduce the energy loss, the adaptive beamforming vector can be calculated by:

$$\begin{aligned} \mathbf{w}_{opt}(i) &= \arg \max_{\mathbf{w}} SNR_i \\ &= \arg \min_{\mathbf{w}} \sigma_n^2 [(\|\mathbf{h}\mathbf{w}\|^2 + \sigma_n^2 \mathbf{I}_{L_s})^{-1}]_i \\ &= \arg \max_{\mathbf{w}} \|\mathbf{h}\mathbf{w}_i\|^2 \end{aligned} \quad (6)$$

When $\mathbf{w}_{opt} = \mathbf{V}_i$, $\|\mathbf{h}\mathbf{w}_i\|^2$ reaches the maximal value theoretically and it equals to Λ^2 . Thus, \mathbf{w}_{opt} can be derived as:

$$\begin{aligned} \mathbf{w}_{opt}(i) &= \arg \max_{\mathbf{w} \in \mathbf{V}_i} \|\mathbf{h}\mathbf{w}\|^2 \\ &= \arg \max_{\alpha_t(\theta_k)} \|\mathbf{h}\alpha_t(\theta_k)\|^2 \end{aligned} \quad (7)$$

The millimeter-wave beam tracking problem is transformed into the problem of determining the millimeter-wave transmitter array vector.

3 Beam Tracking Algorithm

According to the analysis above, it can be seen that the beam tracking only need to predict beamforming vector maximizing SNR. We can consider that the change of the DOA in the polar coordinates is in a linear state and we can introduce the kalman filter method for beam tracking.

Beamforming vector can be calculated through Eq. (5) with the DOA information obtained by OMP algorithm. The detailed steps of the OMP algorithm is given in [10]. The beamforming complexity based on the OMP algorithm is $O(N_t^3)$ for one iteration. To avoid a large number of matrix calculation involved in the beam tracking process with OMP algorithm, this paper proposes to predict the beamforming vector of the time $n + N$ by that of the time n . Thus, the beamforming complexity of the proposed method is $O(N_t^3/N)$ and the sampling times are reduced by N times.

Adaptive step-size prediction joint OMP algorithm: In order to reduce the complexity of the beam tracking with small tracking error, the adaptive step-size prediction joint OMP tracking algorithm is summarized as follows. The beam direction is kept constant within the prediction step, which reduces the complexity of beam tracking. For detail, the ASP-OMP algorithm can be concluded in three steps.

Step 1: Initialize DOA estimation $\{\theta_l\}$ based OMP algorithm and construct the beamforming vector \mathbf{w} according to the Eq. (5);

Step 2: Adaptive step-size prediction based on multi-step kalman filter. The heuristic algorithm is used to determine the predicted step-size, that is, by comparing the prediction error with the threshold δ , the prediction step-size is determined to achieve fast millimeter beam alignment.

Step 3: Outliers elimination based on Bayesian estimation. Through the fusion of the predicted beamforming vector and the measured beamforming vector, the effects of excessive prediction errors and measured errors are eliminated.

Prediction error threshold determination: The error threshold δ can be set up through outlier identification, the derivation is as follows.

Kalman filter measurement residuals is calculated as:

$$\mathbf{e}_n = Z_n - \mathbf{H}\mathbf{w}_{n|n-N} \quad (8)$$

where $\mathbf{w}_{n|n-N}$ is a $N_t \times 1$ dimensional vector, representing the predicted beamforming vector. Z_n denotes a vector with the size of $N_t \times 1$, which represents the measured value, \mathbf{H} is the observation matrix with the size of $N_t \times N_t$. \mathbf{e}_n obeys the Gauss random distribution with mean value of 0, its covariance is expressed as:

$$\begin{aligned} & E(\mathbf{e}_n \cdot \mathbf{e}_n^T) \\ &= E\left\{ (Z_n - \mathbf{H}\mathbf{w}_{n|n-N}) (Z_n - \mathbf{H}\mathbf{w}_{n|n-N})^T \right\} \\ &= E\left\{ |\mathbf{H}\mathbf{w}_n + \mathbf{g}_n - \mathbf{H}\mathbf{w}_{n|n-N}|^2 \right\} \\ &= \mathbf{H}\mathbf{P}_{n|n-N}\mathbf{H}^T + R \end{aligned} \quad (9)$$

where \mathbf{g}_n is a $N_t \times 1$ dimensional vector, which represents the observation noise vector, and R donates the variance of the observation noise. The outlier in adaptive step-size prediction process is discriminated according to the Eq. (9):

$$\|\mathbf{e}_{n+N}\| \leq r \cdot \left\| \sqrt{\text{diag}_i(\mathbf{H}\mathbf{P}_{n+N|n}\mathbf{H}^T + R)} \right\| \quad (10)$$

where r is the outlier identification coefficient. $\text{diag}_i(\cdot)$ denotes the vector composed of the diagonal elements about beamforming vector in the matrix.

If Eq. (10) is satisfied, then Z_n is the normal observation value. Otherwise, it is assumed that Z_n is the outlier. The value of r is determined by the actual channel. The error threshold can be set according to the method of the outlier identification.

Algorithm 1. ASP-OMP algorithm for beam tracking

-
1. Initialize the prediction step-size $N = 1$;
 2. The possible azimuth set is established by discrete sampling: $\{\theta_K\}$;
 3. Initialize DOA estimation based OMP algorithm : $\{\theta_l\}$;
 4. Given $\mathbf{F}, \mathbf{H}, \mathbf{Q}, \mathbf{R}, \mathbf{P}_0$;
 5. Construct the beamforming vector according to the Eq. (5): \mathbf{w} ;
 6. **If** $e_N \leq \delta$ then
 7. Update prediction step-size: $N = N + 1$;
 8. **Else**
 9. Update prediction step-size: $N = 1$;
 10. **End**
 11. **For** $i \leq N$
 12. $\mathbf{w}_{n+i|n} = \mathbf{F}^{\lfloor N/2 \rfloor} \mathbf{w}_n$;
 13. **End**
 14. Outlier elimination and update the prediction value $\mathbf{w}_{n+N|n}$;
 15. Update the measured residuals: $e_{n+N} = \|\mathbf{Z}_{n+N} - \mathbf{H}\mathbf{w}_{n+N|n}\|$;
 16. Calculate kalman gain: $K_{n+N} = \frac{\mathbf{P}_{n+N|n} \cdot \mathbf{H}^T}{\mathbf{H} \cdot \mathbf{P}_{n+N|n} \cdot \mathbf{H}^T + \mathbf{R}_n}$;
 17. State correction: $\mathbf{w}_{n+N} = \mathbf{w}_{n+N|n} + K_{n+N} \cdot e_{n+N}$;
 18. Correct error covariance: $\mathbf{P}_{n+N} = (\mathbf{I} - K_{n+N} \cdot \mathbf{H}) \cdot \mathbf{P}_{n+N|n}$;
 19. The azimuth set is established by discrete sampling: $\{\theta_{3l}\}$;
 20. Construct the beamforming vector matrix Ψ_θ ;
 21. DOA estimation based OMP algorithm: $\{\theta_l\} = \arg \min \|y - \Psi_\theta \hat{x}\|, \hat{x} = (\Psi_\theta^T \Psi_\theta)^{-1} \Psi_\theta^T y$;
 22. Go to 5;
-

$$\delta = r \cdot \left\| \sqrt{\text{diag}_i (\mathbf{H}\mathbf{P}_{n+N|n}\mathbf{H}^T + \mathbf{R})} \right\| \quad (11)$$

Error judgment is based on beamforming vector obtained through OMP algorithm in BS. By comparing the prediction error and the threshold, the prediction step-size is determined adaptively.

Outlier elimination based on Bayesian estimation: Since that the parameters of the beam tracking algorithm are Gauss normal distribution, the predicted beamforming vector $\mathbf{w}_{n|n-N}$ and the measured vector Z_n , which are recorded as x_1, x_2 , can be fused based on Bayesian estimation to predict the new beamforming vector to eliminate the influence of the excessive prediction errors and measured errors.

$$P(\mu|x_1, x_2) = \frac{P(\mu; x_1, x_2)}{P(x_1, x_2)} \quad (12)$$

where $\mu \sim N(\mu_0, \sigma_0^2)$ and $x_k \sim N(\mu, \sigma_k^2), k = 1, 2$. For the adaptive step-size prediction beam tracking algorithm proposed in this paper, the parameters satisfy that $\mu_0 = \frac{1}{2} \sum_{k=1}^2 x_k, \sigma_0^2 = \frac{1}{2} \sum_{k=1}^2 \sigma_k^2$ and $\sigma_k^2 = \begin{cases} \mathbf{P}_{n|n-N}, & k = 1 \\ \mathbf{P}_n, & k = 2 \end{cases}$. We assume that $\alpha = \frac{1}{P(x_1, x_2)}$, which is independent of the μ . Equation (11) can be rewritten as:

$$\begin{aligned} P(\mu|x_1, x_2) &= \alpha \frac{1}{\sqrt{2\pi}\sigma_0} \exp\left\{-\frac{1}{2}\left(\frac{\mu-\mu_0}{\sigma_0}\right)^2\right\} \prod_{k=1}^2 \frac{1}{\sqrt{2\pi}\sigma_k} \exp\left\{-\frac{1}{2}\left(\frac{x_k-\mu}{\sigma_k}\right)^2\right\} \\ &= \alpha \frac{1}{\sqrt{2\pi}\sigma_0} \prod_{k=1}^2 \frac{1}{\sqrt{2\pi}\sigma_k} \exp\left\{-\frac{1}{2}\left(\frac{\mu-\mu_0}{\sigma_0}\right)^2 - \frac{1}{2}\sum_{k=1}^2 \left(\frac{x_k-\mu}{\sigma_k}\right)^2\right\} \end{aligned} \quad (13)$$

The exponential part in (12) is a quadratic function of μ , so Eq. (12) can be rewritten as follows in the assumption that $(\mu|x_1, x_2) \sim N(\mu_n, \sigma_n^2)$.

$$P(\mu|x_1, x_2) = \frac{1}{\sqrt{2\pi}\sigma_n} \exp\left\{-\frac{1}{2}\left(\frac{\mu-\mu_n}{\sigma_n}\right)^2\right\} \quad (14)$$

Equation (15) can be obtained in comparison of Eqs. (12) and (13):

$$\begin{cases} \sum_{k=1}^2 \frac{\mu^2}{\sigma_k^2} + \frac{\mu^2}{\sigma_0^2} = \frac{\mu^2}{\sigma_n^2} \\ \sum_{k=1}^2 \frac{\mu x_k}{\sigma_k} + \frac{\mu \mu_0}{\sigma_0} = \frac{\mu \mu_n}{\sigma_n} \end{cases} \quad (15)$$

The solution of the Eq. (15) is shown as:

$$\begin{cases} \sigma_n = \frac{1}{\sqrt{\sum_{k=1}^2 \frac{1}{\sigma_k^2} + \frac{1}{\sigma_0^2}}} \\ \mu_n = \frac{\sum_{k=1}^2 \frac{x_k}{\sigma_k} + \frac{\mu_0}{\sigma_0}}{\sqrt{\sum_{k=1}^2 \frac{1}{\sigma_k^2} + \frac{1}{\sigma_0^2}}} \end{cases} \quad (16)$$

The Bayesian estimation of μ can be calculated as:

$$\begin{aligned} \hat{\mu} &= \int_{\Omega} \mu \frac{1}{\sqrt{2\pi}\sigma_n} \exp\left\{-\frac{1}{2}\left(\frac{\mu-\mu_n}{\sigma_n}\right)^2\right\} d\mu \\ &= \mu_N = \frac{\sum_{k=1}^2 \frac{x_k + \frac{\mu_0}{\sigma_0}}{\sigma_k + \frac{\mu_0}{\sigma_0}}}{\sqrt{\sum_{k=1}^2 \frac{1}{\sigma_k^2} + \frac{1}{\sigma_0^2}}} \end{aligned} \tag{17}$$

The predicted beamforming vector after eliminating outliers can be calculated as:

$$\mathbf{w}_{n|n-N} = \hat{\mu} \tag{18}$$

With the outlier recognition and elimination, we can set up reasonable prediction step-size and eliminate the influence of the outlier in the beam tracking process at the same time, solving the problem of the large prediction error caused by the various types of sudden errors and avoiding the tracking divergence.

4 Simulation Results

Here we give some performance comparison with the simulation results of several beam tracking algorithms, the simulation compared the proposed beam tracking algorithm with that in [7, 10] in the millimeter wave channel. The tracking performance of several algorithms is compared for 30 consecutive beam tracking cycles in the case of $N_t = 32$ and $N_r = 32$, user’s speed is 5 m/s and the initial distance between BS and MS is 50 m.

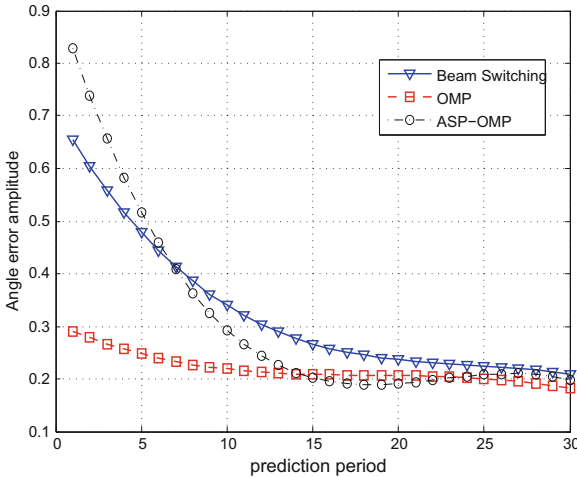


Fig. 2. Beam tracking angle error amplitude

To verify the effectiveness of the beam tracking algorithm proposed in this paper, Fig. 2 shows the average error amplitude curve of the DOA based on several beam tracking algorithms. When the tracking time is short, it can obviously be seen from the curve that the tracking error of the algorithm proposed is slightly higher than that based on OMP algorithm proposed in [10] and is almost the same as that proposed in [7], which is based on beam switching algorithm with the wide beam training and the narrow beam alignment. As time goes on, the tracking performance of the ASP-OMP algorithm gradually approaches the OMP algorithm and is better than the beam switching algorithm. The tracking error of all three beam tracking algorithms is within the acceptable range.

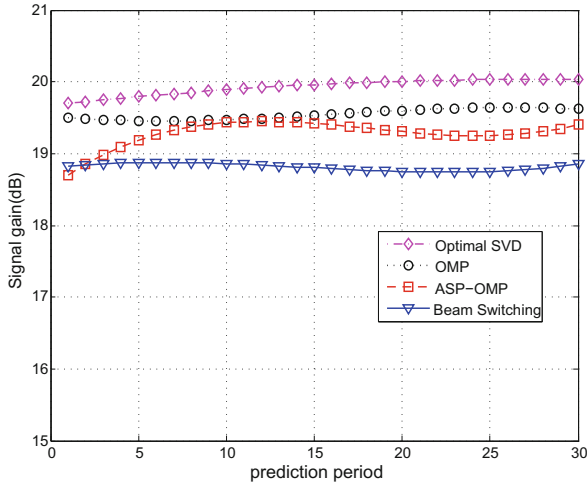


Fig. 3. Received signal gain of different beam tracking algorithms

Figure 3 shows the receiver gain curve for the beam tracking algorithm based on adaptive step-size prediction with Kalman filter. It obviously can be seen that the performance of the proposed ASP-OMP algorithm is close to that of the OMP algorithm in the literature [10], which is better than that of the [7] based on beam switching algorithm. Compared with the beamforming method based on the optimal SVD, the receiver gain of the proposed method is reduced by about 0.6 dB. The complexity of the proposed ASP-OMP algorithm is greatly reduced with little effect on the communication.

Figure 4 shows the spectral frequency of different beam tracking methods under different transmission streams. It obviously can be seen that the spectral frequency of the proposed ASP-OMP algorithm is close to that of the OMP algorithm in both single and multiple streams. Due to the absence of the channel estimation, the proposed ASP-OMP algorithm and the OMP algorithm in [10] cannot provide a high spectral frequency as same as the optimal SVD beamforming method. This performance gap between the optimal SVD beamforming

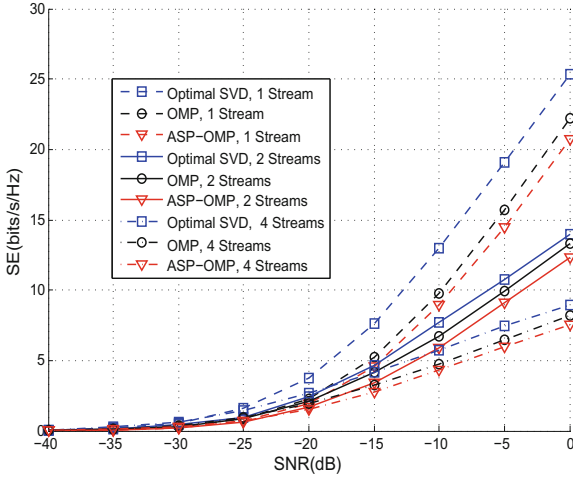


Fig. 4. Spectral frequency of different beam tracking algorithms

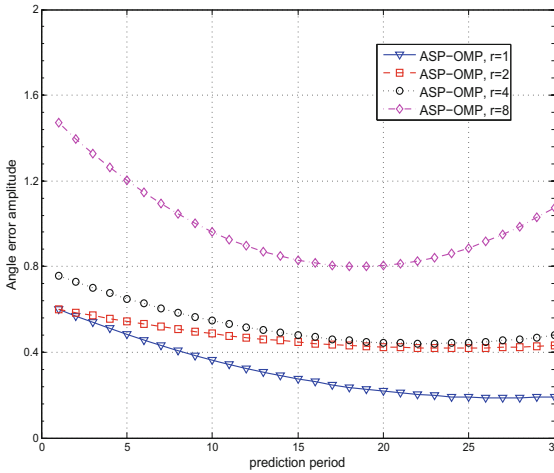


Fig. 5. Beam tracking angle error amplitude under different outlier identification coefficients

method and the proposed ASP-OMP algorithm will become increasingly large as the number of the transmission stream increases, which is a inevitable result of the decline in complexity.

Figure 5 shows the receiver gain curves under different outlier identification coefficients. When $r = 1$, which means that the threshold is low, the tracking error is small with the small prediction step-size. The tracking error gradually converges to the same value in case of that $r = 2$ and $r = 4$, which means that r should be in the range of 2 to 4 to predict the relatively accurate beamforming

vector. The curve gradually diverges due to the existence of outliers when $r = 8$. In this case, The outlier identification method is out of action due to that the error threshold is too large. Obviously, the selection of the outlier identification coefficient has a severe effect on the beam tracking accuracy.

All in all, the results point out that the proposed ASP-OMP algorithm can be adapted to the change of the channel and has a close tracking performance to the existing beam tracking algorithm with the algorithm complexity decreasing.

5 Conclusions

In this paper, an adaptive beam tracking algorithm is proposed for the mobile millimeter wave communication system. For the complexity of downlink beam tracking and the requirement of the coherent communication, the proposed ASP-OMP algorithm uses the kalman filter to carry out the adaptive step-size prediction and beam tracking with the DOA information obtained by OMP algorithm. By setting the error threshold with the outlier identification, the prediction step-size is determined adaptively.

The optimal beam is kept constant within the prediction step, which reduces the complexity of beam tracking. In practice, it only needs to predict the optimal beamforming vector in advance before the communication link suffers from significant fading. The beam tracking method proposed in this paper can be adapted to the change of the channel and the mobility of the users, which reduces the complexity of the traditional beam tracking algorithm and helps to reduce the path loss of millimeter wave communication. Finally, the theoretical analysis and simulation results demonstrate that the proposed algorithm has no apparent performance loss with the complexity being significantly reduced.

Acknowledgment. This work was supported by the State Major Science and Technique Project (MJ-2014-S-37), National Natural Science Foundation of China (61201134) and 111 Project (B08038).

References

1. Zhu, D., Choi, J., Heath, R.W.: Auxiliary beam pair enabled aod and aoa estimation in closed-loop large-scale mmwave mimo system. *IEEE Trans. Wirel. Commun.* **16**, 4770–4785 (2017)
2. Pu, W., Li, X., Lin, Y., et al.: Low complexity hybrid beamforming based on orthogonal constraint and phase extraction. In: *Wireless Communications and Networking Conference (WCNC)*, pp. 1–5 (2017)
3. Yaman, Y., Spasojevic, P.: Reducing the LOS ray beamforming setup time for IEEE 802.11 ad and IEEE 802.15. 3c. In: *Military Communications Conference (MILCOM)* (2016)
4. Han, Y., Lee, J.: Asymmetric channel estimation for multi-user millimeter wave communications. In: *International Conference on Information and Communication Technology Convergence (ICTC)*, pp. 4–6 (2016)

5. Bo, G., Changming, Z., Depeng, J., et al.: Compressed SNR-and-channel estimation for beam tracking in 60-GHz WLAN. *Chin. Commun.* **12**(6), 46–58 (2015)
6. Wang, Y., Shi, Z., Zeng, K., et al.: Two layers of beam alignment for millimeter-wave communications. In: 2016 Third International Conference on Digital Information Processing, Data Mining, and Wireless Communications (DIPDMWC), pp. 262–267 (2016)
7. Xiao, Z., Xia, P., Xia, X.G.: Codebook design for millimeter-wave channel estimation with hybrid precoding structure. *IEEE Trans. Wirel. Commun.* **16**(1), 141–153 (2017)
8. Gao, K., Cai, M., Nie, D., et al.: Beampattern-based tracking for millimeter wave communication systems. In: Global Communications Conference (GLOBECOM), pp. 1–6 (2016)
9. Thejaswi, P.S.C., Bynam, K., Nair, J.P., et al.: Low-complexity direction estimation techniques for fast beamforming training in millimeter wave multiantenna systems. In: IEEE International Conference on Communications (ICC), pp. 1–6 (2016)
10. Xiaohui, L., Meimei, M., Yingchao, L., et al.: Low complexity asymptotically unitary algorithm for hybrid beamforming in mmWave communication systems. *J. Chin. Univ. Posts Telecommun.* **24**(1), 18–25 (2017)



Priority-Based Multi-carrier Access Schemes for Safety Message Transmission in Vehicular Networks

Huichao Wang, Longjiang Li, Fan Wu^(✉), Ke Zhang,
and Supeng Leng

School of Communication and Information Engineering,
University of Electronic Science and Technology of China, Chengdu, China
201521010518@std.uestc.edu.cn,
{longjiangli, wufan, zhangke, spleng}@uestc.edu.cn

Abstract. With the explosive growth of vehicles, current vehicular networks, based on CSMA/CA, are unable to guarantee the low latency and high reliability for safety message transmission under heavy traffic condition. In this paper, we propose a Priority-based Multi-carrier Random Access with Carrier Switching (PMRA/CS) scheme, which is designed for OFDMA-based vehicular networks to support massive concurrent access of large number of vehicles. Compared to CSMA/CA, PMRA/CS utilizes a special short detecting frame to resolve the alarm message collision with less cost. Moreover, the scheme provides more opportunities for vehicles to access the channel in one period by allowing the loser of one sub-carrier to switch to another idle one and continue to access contention. Use of vehicle priority assignment makes the proposed strategy more applicable to realistic scenarios. Furthermore, we provide some theoretical analysis of the proposed scheme combined with derived formula derivation. Simulation results are provided to demonstrate the improvements of message sending success rate and average delay reduction of our proposed scheme.

Keywords: PMRA/CS · Concurrent access · Conflict resolution
Vehicle priority

1 Introduction

As a promising approach to bring real-time traffic condition and vehicle driving information in a large area to the users, vehicular networks attract considerable interest recently. By providing efficient communication between vehicles and road side infrastructure, vehicular networks are helpful in decreasing traffic and improving the driving experience. Furthermore, with the aid of accurate and reliable information in vehicular networks to prevent accident, road safety can be further enhanced. However, the strict latency requirement in traffic warning message dissemination and the high mobility of vehicles make the design of efficient transmission schemes in vehicular networks a challenge [1].

To reduce data transmission delay and boost the reliability of safety-critical messages sent by vehicles, it is essential to design an efficient way to allocate channel resource. In [2], IEEE 802.11p/WAVE (Wireless Access in the Vehicular Environment), supporting high-speed mobile communication, is used to provide vehicle services. However, WAVE cannot support the absolute priorities of different types of messages to access the resource. Besides, the hidden terminal and high latency problem in high-density traffic flow remain unsolved [3–5]. In the last few years, a variety of researches suggest that the advanced communication systems, such as long-term evolution (LTE) 4G or 5G technology using orthogonal frequency division multiple access (OFDMA) could replace WAVE networks [6]. Hidden terminal problem was avoided through the allocation of resources. The authors in [7] show that LTE-V is feasible in vehicular scenarios. In [8], a multiple access mechanism of OFDMA was compared with the CSMA/CA in IEEE 802.11p and the results showed a higher delivery rate and lower delivery delay of OFDMA in high-load conditions. Use of OFDMA for alert message was discussed in [9]. It improved reliability and resource use efficiency, while this solution had a drawback of an increase in delivery delay. In summary, previous works mainly focused on delay-insensitive scenarios leaving the message transmission with strict delay constraints scarcely considered. Additionally, message loss problem caused by conflicts in heavy density traffic is totally ignored.

In this paper, we mainly focus on dynamic resource allocation and sub-carrier competition mechanism for safety-related messages in vehicular networks. An OFDMA-based access method with vehicle priorities is proposed. We achieved in our scheme a high sending success rate and low average delay in high-density networks. Specifically, the main contents and contributions of this paper are as follows.

Firstly, we propose the concept of vehicle priority. Vehicles access the channel in different ways according to their priorities. Therefore, special public vehicles with high-priority, such as police vans, ambulances, fire engines and engineering rescue vehicles could access first using the assigned resource. Other ordinary vehicles access sub-carriers in competition.

Secondly, an efficient channel utilization access scheme, named PMRA/CS is proposed. PMRA/CS uses a short detecting frame to resolve collisions of emergency warning messages. Reduction of alarm message loss improves traffic safety and reliability level.

Thirdly, in the course of channel sense, vehicles can not only confirm success of access, but also recognize the idle sub-carriers to further reuse. Specifically, if a vehicle fails to access on one sub-carrier, it would switch to another idle one and continues to contend for channel access. Since the PMRA/CS scheme provides more opportunities for vehicles to access the channel in one period, the efficiency of special reuse will be improved, especially for the massive vehicles scenario.

The remainder of this paper is structured as follows: Sect. 2 describes the system model. Next, Sect. 3 presents the channel allocation scheme and details of the PMRA/CS competitive strategy. Thereafter, we compare simulation results with CSMA/CA mechanism in Sect. 4. Finally, conclusions are summarized in Sect. 5.

2 System Model

Figure 1(a) shows the OFDMA-based vehicular networks communication system. In the system, a base station locates on the side of a bidirectional two-lane highway, providing communication services to vehicles and controlling resource allocation. Base stations allocate bandwidth to traffic safety service separately, avoiding interference with the normal messages [10]. A number of vehicles moving in different directions access vehicular wireless networks. Considering the practical situation, we divide vehicles into two groups according to their traffic modes. One group is the vehicles that involve public safety such as ambulances. The system should guarantee these special vehicles with high-priority to access the vehicular networks even when the channel resource is in shortage. The other group is ordinary vehicles with lower priority. Different groups will adopt certain access methods under the control of the base station.

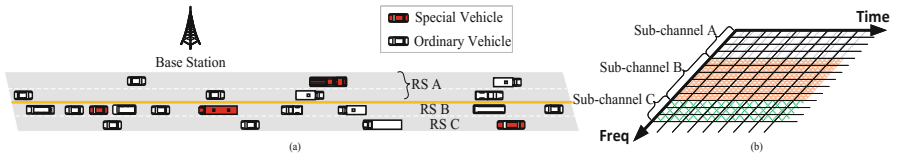


Fig. 1. (a) The scenario shows four road sections in two directions and different traffic flows. (b) Sub-channel resource allocation based on road sections.

We assign separated resource to vehicles in opposite directions to reduce collisions. Also, traffic flows can be different for each road section (RS). Dynamic resource allocation according to traffic flows can make channel resource to be utilized more efficiently [11]. In OFDMA-based system, sub-channels are assigned to each section in accordance with direction and vehicle flows. Then, vehicles use the sub-channel belonging to their section to send safety-critical messages.

In this paper, vehicles receive the signal of all bands, which means that they can collect all occupied sub-carriers and free sub-carriers. Assume N sub-carriers are to support K_o ordinary vehicles and K_s special vehicles. Vehicles of the same type have a fixed probability to generate critical safety message. Let p_o and p_s represent the alarm probability of ordinary and special vehicles, respectively.

3 Sub-channel Resource Allocation and Sub-carrier Contention Strategy

This section describes a distributed-centralized combination structure that contains a roadside system controlling resource allocation and vehicles using PMRA/CS strategy to access sub-carriers.

3.1 Resource Allocation Arrangement

In vehicular environment, in order to guarantee high reliability and low latency for the safety messages delivery, the roadside system as the control center should fulfill two requirements as follows.

Firstly, roadside system dynamically allocates sub-channel resource based on the driving direction and vehicle density. The roadside system receives traffic information from sensors or vehicle beacon messages. According to the traffic information, the roadside system adjusts the number of sub-carrier to different road sections to achieve resource dynamical equilibrium. In addition, the dynamic partition of resource also decreases channel interference and suppresses the hidden terminal problem.

Secondly, the roadside system only assists vehicles to contend for sub-carriers rather than allocating sub-carriers to the vehicles. The reason is that the procedure of allocation will introduce high latency, which will increase safety risks. Thus, vehicles need to access sub-carrier in a competitive way.

The carrier access scheme is related to vehicle priority. When a vehicle enters the coverage of a new cell, it will send a message regarding its priority to the roadside system. The roadside system chalks up the priority level and provides the appropriate access strategies. There are two ways for vehicles to use sub-carrier resource: fixed allocation and competition. Special vehicles have right to access the channel first without competition. In general, the number of high priority vehicles is less than the number of sub-carriers. Thus, the roadside system would allocate a certain sub-carrier named exclusive sub-carrier directly to each special vehicle. When special vehicles need to alarm, they send safety-critical messages using their private exclusive sub-carriers rapidly. On the other hand, ordinary vehicles have a large number. Channel resource may not be enough when lots of vehicles need to send messages simultaneously. The roadside system informs the ordinary vehicles information about the directly available sub-carriers, exclusive sub-carriers and the competitive approach. In CSMA/CA, an ordinary vehicle can just choose directly available sub-carriers. The exclusive sub-carriers are likely to be wasted. Therefore, it is important to design an efficient access scheme to reuse the wasted resources.

3.2 PMRA/CS in Wireless Vehicular Networks

Except for wasted resources, message collision is another main factor to degrade the performance of vehicle networks. Under the emergency state, ACK messages and continuous retransmission are not allowed. Hence, message collision directly contributes to alarm message loss. Although CSMA/CA mechanism already satisfies the requirement of collision avoidance and enhances the channel access performance, it is still possible for safety messages to be collided because of message delay. Assume that the vehicle system is identical and stable, and message delay T_m can be regarded as a fixed value. Obviously, T_m is shorter than the entire transmission cycle T . However, it still will affect the message transmission success rate.

In this paper, a transmission cycle consists of contention period (CP) and data period (DP). Figure 2(a) and (b) illustrate the competitive process using CSMA/CA and PMRA/CS schemes. In Fig. 2(a) vehicle A has already generated a message at t_1 ,

and other vehicles don't receive its message until $t_1 + T_m$. When the back-off time of vehicle B is over at t_2 , it will also start to send a message. Such message conflicts cannot be avoided by CSMA/CA, while PMRA/CS scheme using detecting frame and carrier-sense solves the message conflict perfectly.

The contention period of PMRA/CS is distributed into random back-off, detecting frame and carrier-sense stages. In random back-off period, to reduce collisions, PMRA/CS uses a random back-off process. Unlike CSMA/CA mechanism, PMRA/CS has a collision avoidance control which prevents the collisions from message delay T_m . To simplify the model, the maximum back-off time is set as long as the message delay T_m . After random back-off period, the system goes into detecting frame period. Vehicles broadcast a detecting frame instead of an alarm message. When nodes send messages, they are unable to accept messages at the same time. It means that vehicles are unaware if detecting frame collisions occur. The duration of detecting frame is set as T_m in accordance with the maximum difference between maximum and minimum back-off time. Otherwise, vehicles with longer back-off time may miss the detecting frame of the other vehicles in carrier-sense period. In carrier-sense period, carrier-sense is the key step in CP, because vehicles can confirm whether they can successfully access the sub-carriers and prepare for second competition in this period. At the beginning of this period, vehicles stop sending the detecting frame and listen for the frames from others. If the selected channel is idle, it means the vehicle is the only one in this sub-carrier or it has the shorter back-off time than all other competitors. Thus, the vehicle could send alarm message using the sub-carrier. Before sending messages, the successful vehicles still need to wait T_m to avoid conflicts between their alarm messages and detecting frames of other vehicles. Failed competitors will receive detecting frame signal from others immediately. They will give up the chosen sub-carriers and the intercept signal of all bands to find free sub-carriers. At $2T_m$, failed access vehicles could reuse free sub-carriers by re-competition.

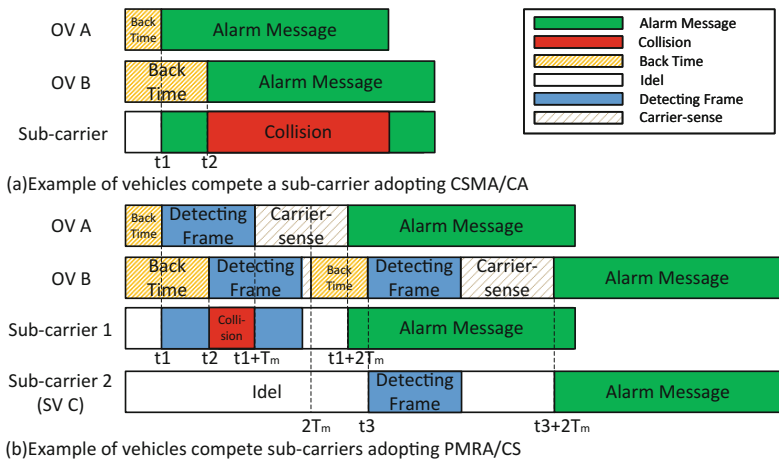


Fig. 2. Collision scenarios in sub-carrier competition

As shown in Fig. 2(b) vehicle A and B choose sub-channel 1 first. Utilizing PMRA/CS, Vehicle A successfully accesses the sub-carrier 1 and sends an alarm message, while B gives up this sub-carrier and senses again for free sub-carriers. Then, B starts a new round of competition, and accesses the sub-carrier 2 which belongs to special vehicle C, but not used in this transmission cycle. Thus, it can be seen that PMRA/CS reduces message loss, and idle sub-carrier is fully utilized in a transmission cycle.

Contention period of PMRA/CS quickly and efficiently determines the only user in each sub-carrier. When the carrier-sense period is over, access vehicles start to send messages. If the remaining time of CP permits, PMRA/CS allows failed vehicles to compete for idle sub-carriers again. The advantages of PMRA/CS are reducing alarm message loss and improving the channel utilization rate in every cycle period.

3.3 Analysis on Sending Success Rate and Sending Delay

Compared with the traditional CSMA/CA method, PMRA/CS takes resource reuse and delay time T_m into account. The carrier utilization is improved significantly and the message loss caused by delay is avoided. The improvements are critical for emergency scene.

Assume that x vehicles compete in one sub-carrier. Each vehicle selects a certain back-off time. We order their back-off time from the smallest to the largest: $[T_1, T_2, \dots, T_x]$. Suppose there is no same back-off time, so that the vehicle with the smallest back-off time always gets the channel resource in PMRA/CS. However, in CSMA/CA, channel conflict occurs if $T_2 < T_1 + T_m$. The vehicle with back-off time T_2 will send the message because it doesn't receive any signal when its back-off time is over. In the sending process, wireless nodes cannot sense the channel. The vehicles cannot realize the conflicts until the end of the transmission. The warning information would be lost owing to collision. It also brings a serious wastage of channel slots.

At first, without considering vehicle priority, we assume that total of K vehicles with alarm probability p per cycle. N sub-carriers are allocated to these vehicles. In one cycle, P_m is the probability that m vehicles need to send an alert.

$$P_m = C_K^m p^m (1 - p)^{K-m} \tag{1}$$

Let $D(m, N, l)$ denote the possible combinations that m vehicles randomly compete N sub-carriers and eventually l sub-carriers are used in one competition.

$$D(m, N, l) = \begin{cases} 1 & l = N = 0, \text{ or } l = m = 0 \\ C_N^l \left(l^m - \sum_{i=0}^{l-1} D(m, l, i) \right) & N \geq l > 0, m \geq l \\ 0 & \text{elsewhere} \end{cases} \tag{2}$$

When repeating PMRA/CS competitive strategy, the average sending success rate becomes to $P_{\text{PMRA/CS-2}}$ in one cycle.

$$P_{\text{PMRA/CS-2}} = \frac{\sum_{m=0}^K \left(P_m \cdot \sum_{l=0}^{\min(m,N)} \left(l \cdot \frac{D(m,N,l)}{N^m} + \sum_{i=0}^{\min(m-l,N-l)} i \cdot \frac{D(m-l,N-l,i)}{(N-l)^{m-l}} \right) \right)}{Kp} \quad (3)$$

Simply make sure the sum time of contention period and data period is no more than a cycle time T and the PMRA/CS system supports contention counts as many as possible. The sending success rate will improve with the increase of competition count.

In terms of transmission delay, it includes a random back-off time, sending detecting frame and waiting time. When s vehicles compete in one sub-carrier, the average value of the minimum back-off time T_{\min} :

$$T_{\min} = T_m \int_{t=0}^1 t(1-t)^{s-1} dt = \frac{T_m}{s+1} \quad (4)$$

Let $\bar{T}_{\text{PMRA/CS}}$ be the average delay which is based on the unit of T_m .

$$\bar{T}_{\text{PMRA/CS}} = \frac{\sum_{m=0}^K \left(P_m \cdot \sum_{l=0}^{\min(m,N)} \left(l \cdot \frac{D(m,N,l)}{N^m} \cdot \sum_{s=0}^{m-l+1} \frac{(2s+3)T_m}{s+1} K(m,l,s) \right) \right)}{KpP_{\text{PMRA/CS}}} \quad (5)$$

$K(m,l,s)$ is the probability of s vehicles in one channel when m vehicles choose a total of l sub-carriers.

$$K(m,l,s) = \begin{cases} 1 & m = s = 0, \text{ or } l = s = 0 \\ \frac{C_m^s \cdot D(m-s, l-1, l-1)}{D(m,l)} & m \geq s > 0, m \geq l > 0, m \geq s + l - 1 \\ 0 & \text{elsewhere} \end{cases} \quad (6)$$

In CSMA/CA, let us assume the back-off time is a random time in $(0, iT_m]$. If s vehicles compete in one sub-channel, $P_c(s,i)$ means the conflict-free rate of this channel and $T_c(s,i)$ is the average delay of the message.

$$P_c(s,i) = \begin{cases} 1 & s = 1 \\ \frac{(i-1)^s}{i^s} & s > 1, i > 1 \\ 0 & \text{elsewhere} \end{cases} \quad (7)$$

$$T_c(s,i) = \begin{cases} \frac{iT_m}{2} & s = 1 \\ \frac{(i-1)T_m}{s+1} & s > 1, i > 1 \\ 0 & \text{elsewhere} \end{cases} \quad (8)$$

The average sending success rate and delay are computed as in Eqs. (9) and (10).

$$P_{\text{CSMA/CA}} = \frac{\sum_{m=0}^K P_m \cdot \sum_{l=0}^{\min(m,N)} \left(l \cdot \frac{D(m,N,l)}{N^m} \cdot \sum_{s=0}^{m-l+1} P_c(s,i) K(m,l,s) \right)}{Kp} \quad (9)$$

$$\bar{T}_{CSMA/CA} = \frac{\sum_{m=0}^K P_m \cdot \sum_{l=0}^{\min(m,N)} \left(l \cdot \frac{D(m,N,l)}{N^m} \cdot \sum_{s=0}^{m-l+1} P_c(s,i) T_c(s,i) K(m,l,s) \right)}{KpP_{CSMA/CA}} \quad (10)$$

The success probability of PMRA/CS is significantly higher than that of CSMA/CA. However, the average delay time in CP is longer than in PMRA/CS because sending short detecting frame and carrier-sense time needs at least $2T_m$. In addition, repeating competitive strategy also increases the delay. In other words, PMRA/CS sacrifices sending delay for success rate in transmission. The message delay time is so short that it has a minimal impact on the vehicular system. Nevertheless, the improvement of message sending success rate is significant. Therefore, PMRA/CS can provide safety and reliability in theory for improving the performance of the vehicular networks.

4 Simulation

In this section, we compare the performance of multi-carrier CSMA/CA and PMRA/CS using MATLAB.

To better explain research achievement, we did a simulation to compare four strategies: N_PMRA/CS, P_PMRA/CS, N_CSMA/CA and P_CSMA/CA. N means to consider the vehicle priority. Special vehicles will have exclusive sub-carriers, and ordinary vehicles use competitive strategies to access. P indicates that all vehicles compete all sub-carriers. We will verify the proposed algorithm using the parameters in Table 1. If vehicles which need to alarm fail to access the channel in the first cycle, they will try to retransmission at most two times. In other words, every alarm message has three opportunities to be sent. Once failed three times in a row, alarm messages will be discarded.

Table 1. Simulation parameters

Parameter	Value
Duration of contention period	$5 T_m$
Maximum message retransmission count	2
Competition count in PMRA/CS	2
Total simulation cycle number	10000
Number of special vehicle (K_s)	2
Message sending probability of special vehicle (p_s)	0.6
Message sending probability of ordinary vehicle (p_o)	0.3

Figure 3(a) shows the success rate of sending messages using four strategies mentioned above with a different total number of vehicles or channel resource. N_PMRA/CS and P_PMRA/CS are always superior to others. Even the vehicles surge,

N-PMRA/CS and P-PMRA/CS still maintain a success rate of ninety percent. When channel resource is in severe shortage, dedicating sub-carriers for special vehicles causes performance degradation. If accessible sub-carriers are relatively plentiful, this approach is very unlikely to have any effect on sending success rate. Although exclusive channels may impact the whole system, it is reasonable and practical. In a word, PMRA/CS greatly improves the success rate of sending messages compared to CSMA/CA.

The average transmission count of four strategies is shown in Fig. 3(b). The average number becomes higher with vehicle number increasing or sub-carrier number decreasing. It can be seen that PMRA/CS cannot stay ahead of the other two CSMA/CA strategies, particularly when the ratio of vehicle number to resource number is great. The primary cause of this phenomenon is the collision due to message delay T_m . In PMRA/CS, message loss only happens when a vehicle failed the competition for channel 3 times in a row. But beyond that the channel collision will directly raise data packet loss in CSMA/CA. Message dropping makes the demand for retransmission decrease, and it brings a high rate of packet loss.

From the results in Fig. 3, it can be seen that PMRA/CS has a higher success rate of sending messages. For the transmission time, PMRA/CS functions well for six sub-channels, while performing poorly in four sub-channels when the vehicle number is large. To better explain the relationship between sending success rate and average sending time, we will give one specific example with more detailed information.

We choose experiment of twelve ordinary vehicles and two special vehicles as an example. In the simulation, the transmission time of each alarm message is counted. The simulation result is shown in Fig. 4. PMRA/CS for four sub-carriers has a relatively high proportion of two or three times transmissions, while the failure rate is high in CSMA/CA. However, when computing an average transmission time, a failure message will be excluded. This is the reason that CSMA/CA method is sometimes better than PMRA/CS in respect of average transmission time.

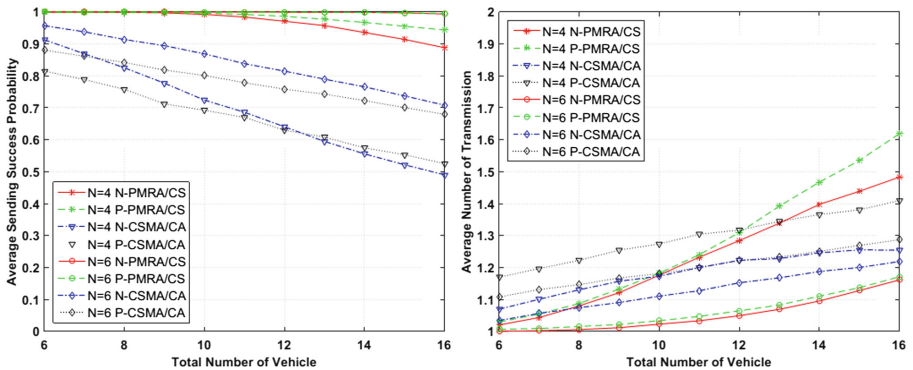


Fig. 3. (a) The average sending success rate. (b) The average number of transmission.

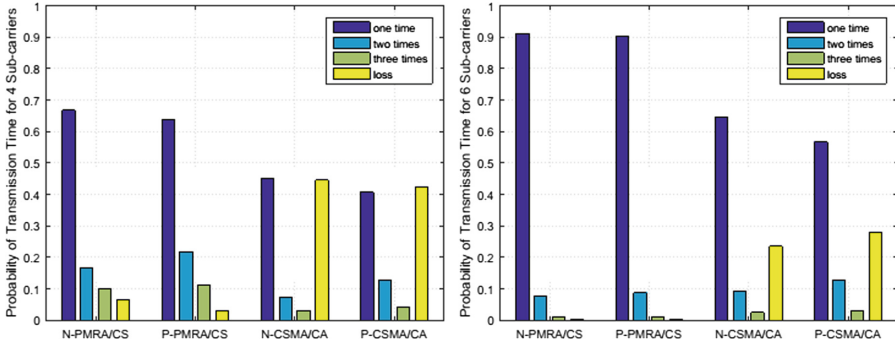


Fig. 4. (a) Probability of transmission time for 4 sub-carriers. (b) Probability of transmission time for 6 sub-carriers.

5 Conclusion

In this paper, we proposed a vehicular priority-based channel allocation and sub-carrier access scheme for LTE-V networks. Vehicle priority changes the original vehicle alarm model, thus making full use of the channel resource. Then, the PMRA/CS scheme modifies the traditional contention access in wireless communication systems by adding detecting frame and carrier-sense stages to reuse idle resource and avoid message collision. Compared with multi-channel CSMA/CA mechanism, the message loss decreases and resource utilization rate rises. Theoretical analysis and simulation results prove the proposed method to be effective with respect to increasing sending success rate and reducing the average transmission time in heavy traffic. The achievements in this paper can improve future vehicular communication systems in the aspects of safety and reliability.

Acknowledgments. This work is supported by the National Natural Science Foundation of China under Grant No. 61374189, the Fundamental Research Funds for the Central Universities, China No. ZYGX2016J001 and the National Natural Science Foundation of China under Grant No. 61273235.

References

1. Chen, S., Hu, J., Shi, Y.: LTE-V: a TD-LTE-based V2X solution for future vehicular network. *IEEE Internet Things J.* **3**(6), 997–1005 (2016)
2. Zafar, B.A., Ouni, S., Boulila, N.: Communication delay guarantee for IEEE 802.11p/wave vehicle networks with RSU control. In: 2016 IEEE 13th International Conference on Networking, Sensing, and Control, pp. 1–7. IEEE Press, Mexico City (2016)
3. Wang, S., Yang, B., Gu, F.: A novel reliable broadcast protocol for VANET's safety applications. In: 2016 6th International Conference on Electronics Information and Emergency Communication, pp. 282–286. IEEE Press, Beijing (2016)
4. Shen, Z., Zhang, X., Zhang, M.: Self-sorting based MAC protocol for high-density vehicular Ad Hoc networks. *IEEE Access* **PP**(99), 1 (2017)

5. Mao, Y., Yan, F., Shen, L.: Multi-round elimination contention-based multi-channel MAC scheme for vehicular Ad-Hoc networks. *IET Commun.* **11**(3), 421–427 (2017)
6. Bazzi, A., Masini, B.M., Zanella, A.: On the use of OFDMA for next generation vehicular Ad-Hoc networks. In: 2013 IEEE 24th International Symposium on Personal Indoor and Mobile Radio Communications, pp. 2223–2228. IEEE Press, London (2013)
7. Li, W., Ma, X., Wu, J.: Analytical model and performance evaluation of long-term evolution for vehicle safety services. *IEEE Trans. Veh. Technol.* **66**(3), 1926–1939 (2017)
8. Guo, Y., Yang, Q., Kwak, K.S.: Quality-oriented rate control and resource allocation in time-varying OFDMA networks. *IEEE Trans. Veh. Technol.* **66**(3), 2324–2338 (2017)
9. Bazzi, A., Masini, B.M., Zabini, F.: On the exploitation of OFDMA properties for an efficient alert message flooding in VANETs. In: 2013 IEEE International Conference on Communications, pp. 5094–5098. IEEE Press, Budapest (2013)
10. Chour, H., Nasser, Y., Artail, H.: VANET aided D2D discovery: delay analysis and performance. *IEEE Trans. Veh. Technol.* **PP**(99), 1 (2017)
11. Li, G., Yang, Z., Chen, S.: A traffic flow-based and dynamic grouping-enabled resource allocation algorithm for LTE-D2D vehicular networks. In: 2016 IEEE/CIC International Conference on Communications in China, pp. 1–6. IEEE Press, Chengdu (2016)



V2V Resource Allocation Schemes for Non-safety Service in Cellular Vehicular Networks

Lei Jiang, Fan Wu^(✉), Ke Zhang, and Lixiang Ma

University of Electronic Science and Technology of China, Chengdu 611731, China
201621010507@std.uestc.edu.cn, {wufan,zhangke,lixiangma}@uestc.edu.cn

Abstract. Vehicle-to-vehicle (V2V) communication has been widely considered as a promising approach for delivering messages between vehicles. However, the highly dynamic topology caused by vehicle mobility makes V2V communication unreliable, especially in the case where the SINR at the receiver below a given threshold. To address the problem, we propose a resource allocation scheme for transmission non-safety messages in cellular vehicular networks. In this scheme, the instability of vehicular network topology has been taken into account. Furthermore, to make the SINR at the receiver under given constraints, distance prediction as well as extra resource allocation is adopted in the design of the scheme. Simulation results demonstrate that the proposed scheme greatly improves the wireless resource utilization.

Keywords: V2V communication · Resource allocation
Non-safety service · Topology prediction

1 Introduction

Due to the advantages of wide coverage, fast transmission rate and low transmission delay, cellular vehicular networks are considered as one of promising approaches for ITS (intelligent transportation system) [1–3]. The resource allocation for V2V communication is one of the key technologies for CVN (Cellular Vehicular Networks) and has been studied extensively. In [4], a distributed spectrum allocation and mode selection scheme for overlay D2D network is proposed. In [5], the authors design a centralized resource allocation scheme for D2D underlay communication based on the hypergraph theory. In [6], the research on resource sharing and power control with QoS provisioning in D2D underlying cellular networks is studied. In [7], the authors studied a enhanced autonomous resource selection for LTE-based V2V communication. In [8], a resource allocation scheme is designed to maximize the ergodic capacity of V2I (vehicle to infrastructure) connections while ensuring reliability guarantee for each V2V link. In [9–11], some distributed V2V resource selection schemes are studied.

In addition to safety application, the non-safety service is also one of the significant application in CVN. Compared with safety application, the non-safety

service values the volume of transmitted data more than transition delay. To transmit large volume of data within limited bandwidth, the non-safety service needs a longer communication time. Unfortunately, as studied in [12], the dynamic topology makes it pretty difficult to keep continuous data transmission in vehicle network environment.

In this paper, we propose a resource allocation scheme for transmission non-safety messages in cellular vehicular networks. In this scheme, the instability of vehicular network topology has been taken into account. Furthermore, to make the SINR at the receiver under given constraints, distance prediction as well as extra resource allocation is adopted in the design of the scheme.

The rest of the paper is organised as follows. In Sect. 2, the system model is established. In Sect. 3, we analysis the key part of this resource allocation issue. In Sect. 4, our resource allocation scheme is proposed. Then simulation results is presented in Sect. 5. Finally, Sect. 6 concludes this paper.

2 System Model

In this paper, we consider an unidirectional road covered by cellular system. In this system, several cells make up a group, called a cellular set. To communicate in V2V model, every vehicle has to find its partner with some discovery strategy, and we call this two vehicles as a V2V-pair. In V2V-pair i , we use R_i and T_i to denote the receiver and transmitter, respectively. In Fig. 1, there are three cells making up a cellular set and two V2V-pairs communicating in this cellular set.

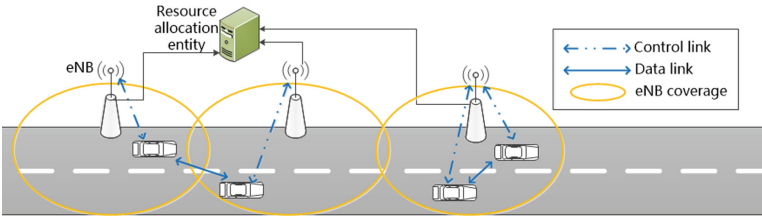


Fig. 1. The architecture of cellular system

The channels used for V2V-pairs communication are divided into two parts: control channels and data channels. In a cellular set, the data channels is managed centrally by an allocation entity (referred as Entity), and eNBs are responsible for the management of control channels separately. In each ΔT period, potential V2V-pairs transmit connection setup request to eNB on the control channels. After calculation, Entity transmits the result to every eNB and then eNB will notify potential V2V-pairs to communicate on the allocated data channels in this period. In a cellular set, to improve the resource utilization, different V2V-pairs can reuse the same data channel if all of them can tolerate the co-channel interference from each other.

Based on the geographical information of all potential V2V-pairs in this cellular set, the Entity can calculate the distance between R_i and T_j , which is denoted as d_{ij} .

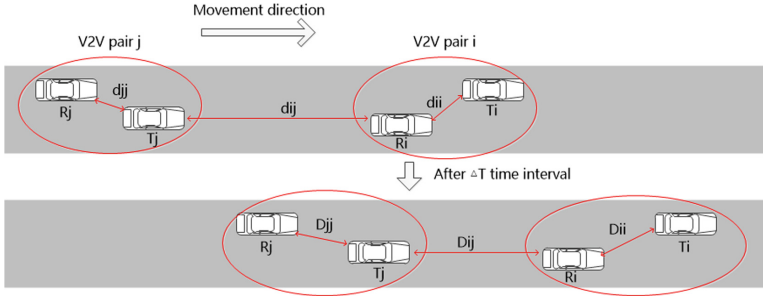


Fig. 2. Distance between vehicles

In Fig. 2, there are two potential V2V-pairs i and j . Let Θ_i denote the set of V2V-pairs which reuse the data channels of V2V-pair i , h_{ij} denote the channel between V2V-pairs i and j and α denote the path loss exponent. We set all of the v-UEs' transmit power to be P . So, the $SINR$ of V2V-pair i can be expressed as

$$\gamma_i = \frac{P d_{ii}^{-\alpha} H_{ii}}{\sum_{j \in \Theta_i} P d_{ij}^{-\alpha} H_{ij} + N_0} \tag{1}$$

where $H_{ij} = |h_{ij}|^2$ and N_0 is the noise power.

For V2V-pair i , a successful communication requires $\gamma_i \geq \gamma_{th}$ where γ_{th} is the threshold for V2V communication.

3 Problem Formulation

The key issue is, how to allocate the fewest channels while satisfying the $SINR$ requirement for all of the V2V-pairs in a cellular set. As shown in Fig. 2, d_{ii} may become bigger and d_{ij} may become smaller, and these changes will lead $SINR$ to be worse according to (1). If we don't take this into consideration, the $SINR$ may not satisfy the threshold and this V2V communication will be failed. In order to complete their communication, the v-UEs of this V2V-pair will shift to use the cellular network and this makes resource consumption increased. In order to minimize the resource consumption, the robustness of the interference analysis must be required. In mathematics, we use k to denote the number of the potential V2V-pairs, n to denote the number of the resources for V2V communication and assume that $n \geq k$ is always true. $a_{n,k}$ is the resource allocation. If $a_{n,k} = 1$, it indicates that V2V-pair k uses the resource n and on the contrary, $a_{n,k} = 0$. To describe the dynamic topology, we use $D_{ij}(t)$ to

denote the random variable of distance between V2V-pairs in the ΔT period, and the planning can be written as

$$\begin{aligned}
 & \text{P1: } \min \sum_{n \in N} (1 - \prod_{k \in K} (1 - a_{n,k})) \\
 \text{s.t. } & \text{C1: } \gamma_k = \frac{PD_{kk}^{-\alpha}(t)H_{kk}}{\sum_{n \in N} (a_{n,k} \times \sum_{j \in K, j \neq k} (PD_{jk}^{-\alpha}(t)H_{jk}a_{j,k})) + N_0} \geq \gamma_{th}, \forall k \in K \\
 & \text{C2: } a_{n,k} \in \{0, 1\}, \forall n \in N, k \in K; \text{ C3: } \sum_{n \in N} a_{n,k} \in \{0, 1\}, \forall k \in K \\
 & \text{C4: } \sum_{k \in K} a_{n,k} \in \{0, 1\}, \forall n \in N; \text{ C5: } 0 \leq t \leq \Delta T
 \end{aligned} \tag{2}$$

In the rest of the paper, $D_{ij}(t)$ will be replaced with D_{ij} for simplification.

In more detail, D_{ij} is related to the velocity random variables of two vehicles. According to the conclusion of [13], the velocity of vehicle follows Gaussian distribution, that is, if V is the random variable of a vehicle velocity, then V satisfies

$$V \sim N(\mu, \sigma^2) \tag{3}$$

where μ stands for the mean value of V and σ is the standard deviation.

In order to get velocity information, V2V-pair i will send it to eNB. We use v_{Ri} and v_{Ti} to denote the mean velocity of receiver and transmitter in V2V-pair i , respectively. Also, σ_{Ri} and σ_{Ti} are denoted as the standard deviation of receiver and transmitter.

However, it is a NPC problem to solve this resource allocation planning according to the conclusion of [14], so we have to find some other polynomial ways to get the approximate result.

4 V2V Resource Allocation Scheme FDV

In this section, we firstly design a Free Distance scheme for static D2D resource allocation. Then we discuss how to predict the distance between vehicles in V2V network. And finally, our V2V resource allocation scheme FDV (Free Distance scheme for Vehicular network) is proposed based on the above discussion.

4.1 Free Distance Scheme

In Free Distance scheme, there are two key parameters [15]:

1. d_s : The strong interference distance. If the distance between two V2V-pairs is less than d_s , the co-channel interference around them will be very big. So we won't allocate the same resource to two V2V-pairs i and j if $d_{i,j} \leq d_s$.

According to the d_s , we can separate Θ_i into two parts: strong interference set Θ_{is} and weak interference set Θ_{iw} :

$$\Theta_{is} = \{j \mid j \in \Theta_i \text{ and } d_{ij} \leq d_s\}; \Theta_{iw} = \{j \mid j \in \Theta_i \text{ and } d_{ij} > d_s\} \quad (4)$$

In this way, V2V-pairs only suffers from weak interference.

2. TID_i : The number of the weak interference that V2V-pair i can tolerate. Let's set the biggest weak interference around V2V-pair i to be I_{i0} , that is, the maximum value in Θ_{iw} , and TID_i can be calculated by the following formula:

$$TID_i = \left(\frac{Pd_{ii}^{-\alpha}}{\gamma_{th}} - N_0 \right) / I_{i0} \quad (5)$$

We can see that, in order to simplify the problem, TID_i treat all of the weak interference as the biggest one, and this leads to some redundancy. For increasing the utilization rate of resources, we propose a new parameter based on the original scheme, that is d_{free} (free distance).

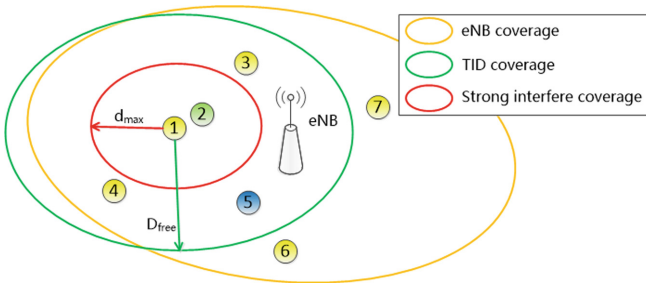


Fig. 3. Free distance demonstration

Since the path loss exponent α is usually within the range of [3, 4], $d_{ij}^{-\alpha}$ will be exponentially decreased with the linear growth of d_{ij} . When d_{ij} reaches a value, the co-channel interference between V2V-pairs i and j will be quite small. For this reason, we regulate that when $d_{ij} > d_{free}$, V2V-pairs i and j can reuse a same resource without considering any other conditions to fill the redundancy.

In Fig. 3, we use one point to denote a V2V-pair, and assume $TID_1 = 2$. For V2V-pair 1, V2V-pair 2 is within its strong interference coverage, so V2V-pair 2 can't reuse the resource with V2V-pair 1, and V2V-pair 3 and 4 can use the same resource of V2V-pair 1 because they satisfy the TID scheme. But V2V-pair 5 must be allocated with another resource for $TID_1 = 2$. V2V-pair 6 and 7 can also reuse the resource of V2V-pair 1, because the distance between them is bigger than d_{free} , so they can reuse the resource without any else consideration. Although we only discuss the scheme from the from the perspective of V2V-pair 1, the rule is suitable for all of the V2V-pairs in this cellular set. We call this enhanced scheme as Free Distance scheme.

4.2 Distance Prediction

In Sect. 2, we have proposed that the dynamic topology of V2V network is a trouble for resource allocation. However, the motion law of vehicles provides the possibility to predict the distance between them.

We assume that vehicle a is in front of vehicle b geographically, and let V_a and V_b denote the velocity random variables of these vehicles in ΔT period respectively. At the start of the period, D_{ab} is equal to d_{ab} , and at the end of the period,

$$D_{ab} = (V_a - V_b) \times \Delta T + d_{ab} \tag{6}$$

Because of the Gaussian distribution of vehicle velocity, D_{ab} follows Gaussian distribution, too.

$$D_{ab} \sim N((v_a - v_b) \times \Delta T + d_{ab}, (\sigma_a^2 + \sigma_b^2) \times \Delta T^2) \tag{7}$$

For V2V-pairs, the expressions are pretty much the same. And for simplification, we assume transmitter is always in front of the receiver.

$$D_{ii} = (V_{Ti} - V_{Ri}) \times \Delta T + d_{ii} \tag{8}$$

$$D_{ij} = (V_{Ri} - V_{Tj}) \times \Delta T + d_{ij}, (i \neq j) \tag{9}$$

where we assume that V2V-pairs i is in front of V2V-pairs j .

To guarantee the reception power, we must restrict D_{ii} smaller than a certain distance \hat{d}_{ii} with a probability p , that is

$$P(D_{ii} \leq \hat{d}_{ii}) > p \tag{10}$$

and \hat{d}_{ii} can be calculated by the following formula:

$$\hat{d}_{ii} = d_{ii} + (\Theta^{-1}(p) \times \sqrt{\sigma_{Ti}^2 + \sigma_{Ri}^2} + (v_{Ti} - v_{Ri})) \times \Delta T \tag{11}$$

where $\Theta^{-1}(p)$ is the inverse function of the probability distribution function for standard Gaussian distribution.

Similarly, we limit D_{ij} within \hat{d}_{ij} to control the co-channel interference:

$$P(D_{ij} \geq \hat{d}_{ij}) \geq p, (i \neq j) \tag{12}$$

$$\hat{d}_{ij} = d_{ij} + (\Theta^{-1}(1 - P) \times \sqrt{\sigma_{Ri}^2 + \sigma_{Tj}^2} + (v_{Ri} - v_{Tj})) \times \Delta T, (i \neq j) \tag{13}$$

We call \hat{d}_{ii} and \hat{d}_{ij} as prediction distance. After getting the prediction distance, we use them to run Free Distance Scheme instead of the static d_{ij} . In this way, we can guarantee that $SINR$ will meet the threshold in ΔT period with a probability p .

Algorithm 1. FDV scheme

Input: The matrix of interval distance between vehicles, $d_{n,n}$;**Output:** The vector of the allocated resource number, $ResNum_n$; $\hat{d}_{ij} = \text{Distance Prediction algorithm}(d_{n,n})$ $ResNum_n = \text{Static Free Distance algorithm}(\hat{d}_{ij})$ **return** $ResNum_n$;

Algorithm 2. Distance Prediction scheme

Input: The matrix of interval distance between vehicles, $d_{n,n}$;**Output:** The matrix of predicted interval distance between vehicles, $\hat{d}_{n,n}$;**for all** $i = 1 : n$ **do****for all** $j = 1 : n$ **do** $\text{predict } \hat{d}_{ij} \text{ based on } d_{ij}$ **end for****end for****return** $\hat{d}_{n,n}$;

Algorithm 3. Free Distance scheme

Input: The matrix of interval distance between vehicles, $d_{n,n}$;**Output:** The vector of the allocated resource number, $ResNum_n$; $\text{initialize } ResNum_n \text{ to be } 0$ $ResNumIndex = 0$ **while** $ResNum_n$ contains 0 **do** $i = \text{the first index of } ResNum_n \text{ where } ResNum_i = 0$ $ResNumIndex = ResNumIndex + 1$ $\text{Allocate } ResNumIndex \text{ to } i$ **for all** j where $ResNum_j = 0$ **do****if** $\text{Satisfy the interference constraint after allocating } ResNumIndex \text{ to } j$
then $\text{Allocated } ResNumIndex \text{ to } j$ **end if****end for****end while****return** $ResNum_n$;

4.3 Free Distance V2V Resource Allocation Scheme

With the previous discussion, now, we can propose our V2V resource allocation scheme based on free distance and distance prediction, and referred as FDV. It's described in Algorithm 1, and FDV internally invokes the Distance Prediction scheme and Free Distance scheme. In our scheme FDV, the most complex part is Static Free Distance algorithm, and its complexity is $O(n^2)$, so the complexity of FDV is $O(n^2)$, it's a polynomial time algorithm.

5 Simulation Results

In this section, we simulate our proposed FDV scheme that is combined with Free Distance scheme and distance prediction, and compare it with other two schemes. One of the reference scheme is the TID scheme with distance prediction, which is referred as TID-V2V scheme in the following part. And another reference scheme is the Free Distance scheme without distance prediction, which is referred as Static Free Distance scheme. In the simulation, there are two kinds of vehicles, that is small vehicles and big vehicles, uniformly distributed on the one direction road. And the simulation run time is 10000. The parameters are listed in the Table 1.

Table 1. Simulation parameters

Simulation parameter	Value	Simulation parameter	Value
Number of V2V-pairs	100	Cell radius	1000 m
Cell number in a cellular set	3	Path loss factor α	3
Maximum V2V link	50 m	Strong interference distance	50 m
SINR threshold	10 dB	Noise power	-118 dBm
V2V transmission power	0 dBm	Period ΔT	3 s
Small vehicle proportion	70%	Big vehicle proportion	30%
Small vehicle average velocity	25 m/s	Big vehicle average velocity	20 m/s
Small vehicle velocity standard deviation	1.5 m/s ²	Distance prediction probability	99.7%
Big vehicle velocity standard deviation	2.7 m/s ²		

In Fig. 4, the CDF (cumulative distribution function) of SINR for three schemes are presented. We can see that threshold of V2V communication is noted where $x = 10$ dB, and our proposed FDV scheme and TID-V2V scheme both satisfy this line. But the Static Free Distance scheme can't ensure that all of the V2V-pairs will get the SINR bigger than 10 dB, there are about 5% of the V2V-pairs failing in the V2V communication. The cause of failure is that Static Free Distance scheme doesn't predict the dynamic change of topology, so it can't adapt to the dynamic V2V network.

In Fig. 5, the CDF of used resources number for three schemes are presented. We can find out that Free Distance Scheme has two function curves. The solid one stands for the allocated resources number of Static Free Distance scheme, but some V2V-pairs will fail in V2V communication because of the strong co-channel interference, in order to complete the communication, they will turn to using cellular resources just like c-UEs. So the dotted curve stands for the total resources used by V2V-pairs. As shown in Fig. 5, FDV scheme allocates more resources than Static Free Distance scheme, because FDV scheme will add some redundancy to adapt to the dynamic topology, but FDV scheme will use less resources in total. In addition, TID-V2V scheme uses much more resources than other two schemes, it's not efficient.

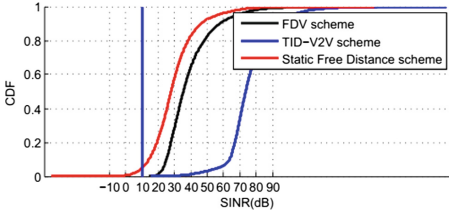


Fig. 4. Comparison of the SINR for three schemes, $d_{free} = 300$ m

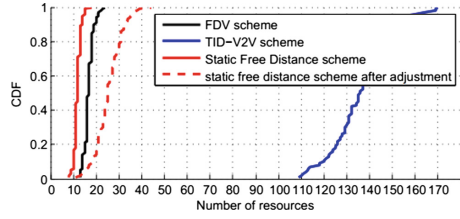


Fig. 5. Comparison of the used resources number for three schemes, $d_{free} = 300$ m

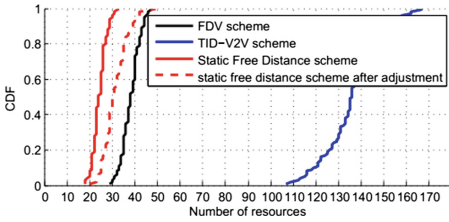


Fig. 6. Comparison of the used resources number for three schemes, $d_{free} = 1000$ m

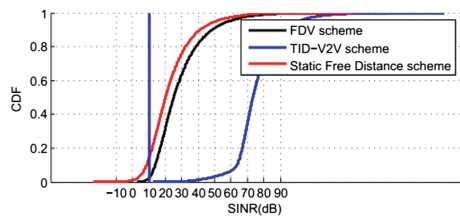


Fig. 7. Comparison of the SINR for three schemes, $d_{free} = 100$ m

In Fig. 6, d_{free} is set to be 1000 m. We can see that the allocated resource number of FDV scheme is bigger than Static Free Distance scheme. Because of the enlargement of d_{free} , Free Distance scheme can't make full use of the redundancy caused by TID, so the Static Free Distance scheme have more opportunity to satisfy the threshold with the remainder redundancy.

In Fig. 7, d_{free} is set to be 100 m, and the failure probabilities of FDV and Static Free Distance scheme are both increased compared with Fig. 4. For the decrement of d_{free} , more V2V-pairs can reuse a same resource without consideration. So it is much more difficult to control the co-channel interference.

6 Conclusion

In this paper, we study resource allocation scheme for long time V2V communication in cellular network. We first defined a cellular set system model, which can reduce the handover of data channel substantially. Then, We introduced the free distance constraint to improve the TID scheme. After that, we devised a distance prediction solution to solve the dynamic topology problem in V2V network. The simulation results remonstrated that the performance of the FDV scheme is superior to both TID scheme and Static Free Distance scheme.

Acknowledgements. This work is supported by the National Natural Science Foundation of China under Grant No. 61374189 and the Fundamental Research Funds for the Central Universities, China No. ZYGX2016J001.

References

1. Seo, H., Lee, K.D., Yasukawa, S., et al.: LTE evolution for vehicle-to-everything services. *IEEE Commun. Mag.* **54**(6), 22–28 (2016)
2. Kuruvatti, N.P., Klein, A., Ji. L., et al.: Robustness of location based D2D resource allocation against positioning errors. In: 2015 IEEE 81st Vehicular Technology Conference (VTC Spring), pp. 1–6 (2015)
3. Lin, X., Ratasuk, R., Ghosh, A.: Network-assisted device-to-device scheduling in LTE. In: 2015 IEEE 81st Vehicular Technology Conference (VTC Spring), pp. 1–5 (2015)
4. Cho, B., Koufos, K., Jantti, R.: Spectrum allocation and mode selection for overlay D2D using carrier sensing threshold. In: 2014 9th International Conference on Cognitive Radio Oriented Wireless Networks and Communications (CROWNCOM), pp. 26–31. IEEE (2014)
5. Zhang, H., Song, L., Han, Z.: Radio resource allocation for device-to-device underlay communication using hypergraph theory. *IEEE Trans. Wirel. Commun.* **15**(7), 4852–4861 (2016)
6. Huang, X., Wu, F., Leng, S., et al.: Resource sharing and power control with QoS provisioning in device-to-device underlying cellular networks. In: 2016 IEEE/CIC International Conference on Communications in China (ICCC), pp. 1–6. IEEE (2016)
7. Zhang, X., Shang, Y., Li, X., et al.: Research on overlay D2D resource scheduling algorithms for V2V broadcast service. In: 2016 IEEE 84th Vehicular Technology Conference (VTC-Fall), pp. 1–5. IEEE (2016)
8. Liang, L., Li, G., Xu, W.: Resource allocation for D2D-enabled vehicular communications. *IEEE Access* **PP**(99), 1 (2017)
9. Garai, M., Sliti, M., Boudriga, N.: Access and resource reservation in vehicular visible light communication networks. In: 2016 18th International Conference on Transparent Optical Networks (ICTON), pp. 1–6. IEEE (2016)
10. Yang, J., Pelletier, B., Champagne, B.: Enhanced autonomous resource selection for LTE-based V2V communication. In: 2016 IEEE Vehicular Networking Conference (VNC), pp. 1–6 (2016)
11. Ashraf, M.I., Bennis, M., Perfecto, C., et al.: Dynamic proximity-aware resource allocation in vehicle-to-vehicle (V2V) communications. *arXiv preprint [arXiv:1609.03717](https://arxiv.org/abs/1609.03717)* (2016)
12. Sun, L., Shan, H., Huang, A., et al.: Channel allocation for adaptive video streaming in vehicular networks. *IEEE Trans. Veh. Technol.* **66**(1), 734–747 (2017)
13. Xu, C.: Distribution of vehicle free flow speeds based on Gaussian mixture model. *J. Highw. Transp. Res. Dev.* **29**(8), 132–136 (2012)
14. Safdar, G.A., Ur-Rehman, M., Muhammad, M., et al.: Interference mitigation in D2D communication underlying LTE-A network. *IEEE Access* **4**, 7967–7987 (2016)
15. Xu, Y., Liu, Y., Li, D.: Resource management for interference mitigation in device-to-device communication. *IET Commun.* **9**(9), 1199–1207 (2015)



Adaptive Slot Assignment for TDMA Based Dynamic Airborne Ad Hoc Networks

Yueyan Qian^{1,2}, Mingwu Yao^{1(✉)}, and Liang Zhang^{1,2}

¹ State Key Laboratory on ISN, School of Telecommunications Engineering,
Xidian University, Xi'an 710071, China

d689571@126.com, mwyao@xidian.edu.cn,
mcliangwlmqz1@163.com

² Science and Technology on Communication Networks Key Laboratory,
Shijiazhuang, China

Abstract. The time division multiple access (TDMA) is thought a better choice for mobile ad hoc networks, especially for sparse and dynamic airborne wireless networks, and its efficiency largely depends on the slot scheduling method. Fully taking the dynamic characteristics of the 3-dimensional airborne network into account, we proposed an adaptive slot assignment TDMA (ASA-TDMA) scheme. It allows for changeable traffic load of the nodes due to the network topology dynamics in sparse airborne ad hoc networks. Slot allocation is performed not only when nodes request for time slots to access, but also when real-time load level changes. The sharing algorithm realizes concurrent transmissions to achieve high slot utilization. Furthermore, our scheme can flexibly adjust the schedule strategy to deal with network emergencies such as node failures. Simulations are provided to validate the performance our approach, and the results show its advantages over some known methods.

Keywords: Ad hoc · Slot assignment · Time division multiple access (TDMA)
3D airborne networks

1 Introduction

TDMA scheduling scheme is an important issue in medium access control (MAC) protocols for ad hoc networks. Since the conflicts caused by simultaneous transmissions would degrade the network performance, collision-avoidance strategy should be considered. In reservation-based TDMA protocols, like DTRA mechanism [1], node pairs with communication demands would make reservations on channel resource. Usually it takes three stages to complete a transmission: neighbor discovery, reservation and confirmation, and data transmission. SDVCS mechanism [2], a modification of DTRA, uses a frame structure where reservation and data transmission stage are partitioned into several parts which are set alternately. The potential conflicting slots would be declared between a node pair in the reservation stage, thus SDVCS shows better performance in throughput compared with DTRA. In TMRR mechanism [3], active nodes compete for slots, in which nodes would transmit beacon, and nodes with data to transmit would ask for slots reservation in the beacon period (BP) and the

data transmission period (DTP) in the way of Carrier Sensing Multiple Access (CSMA) for a multi-hop transmission in order to achieve low delay. If there are no enough slots to assign, the reservation would be performed in the resource reservation period (RP). Reservation-based schemes described above are demand-driven, so some node pairs would suffer starvation because of time slots exhaustion in some cases. Contrastingly, in contention-based mechanisms, no predefined schedule is required, and each node will compete for channel access when it needs to transmit, and naturally is not entitled to any guarantee of success [4]. The resulted packet loss and large access delay may be a serious problem to real-time applications [5]. These schemes are not suitable for networks requiring a certain level of reliability and delay. The benefits of using TDMA protocols include equal access to the channel for all vehicular nodes, efficient channel utilization without collisions, high reliability of communications, deterministic access time even with a high traffic load, and QoS for real-time applications [6]. Some efficient TDMA protocols are specifically designed, such as one for cooperative relaying (CRTDMA) [7], and the P-TDMA [8].

In P-TDMA, a frame is segmented into three epochs: Claim, Response and Info, and each part is further segmented into N slots equal to the number of nodes. Active members send request-to-send (RTS) in the Claim stage without collisions. In the Response stage, the response packets (RSP) are sent out containing the active neighbors ID heard in the previous stage. Learning the active nodes within two hops by the above two stages makes simultaneous collision-free transmissions feasible in the Info stage. However, a large proportion of a frame is used to exchange RTS and RSP, resulting in P-TDMA's low efficiency. Because the stages are structured alternately, inconsecutive epoch for transmission leads to bad performance in delay.

Motivated by reducing delay and improving packet reception rate, we propose an ASA-TDMA scheme for sparse and dynamic airborne wireless networks. In the assumed scenario, nodes are of 100 km in distances more or less in the air, and the maneuvers of the flying vehicles will stochastically form links between nodes via directional antenna, and the link is prone to disconnect frequently. As the nodes are flying in a high speed, the network is seen high dynamics, and the time slot assignment should not be predetermined. Instead, it should change due to the scale of each cluster and the network topology. Thus, an adaptable time slot assignment scheme is needed. Collision-free concurrent transmissions are achieved by performing a time slot sharing algorithm. Additionally, timely node lost detection is included to handle the emergencies, which guarantees the minimal wastes. Simulation shows our scheme provides superior performance than P-TDMA and fixed TDMA in respect of delay and packet reception rate.

The rest of the paper is organized as follows. Section 2 gives an overview and then key procedures of ASA-TDMA. Simulation results and performance comparison of ASA-TDMA scheme with existing works are analyzed in Sect. 3. Section 4 concludes our work.

2 The ASA-TDMA Scheme

The network comprises of a dozen of high speed airborne vehicles, e.g., a flock of Unmanned Aerial Vehicles (UAVs) flying in one formation. Basically, these nodes are bearing to one same destination but have some freedom to choose their own routes or

trajectories during working in a 3-dimensional (3D) space. A communication link is possible to be formed during the flying when two nodes are within each other's radio transmission range. Several neighboring nodes will form one cluster, and a cluster head is selected to control the communication and networking in a TDMA mode. To cope with the high dynamics in the whole flying process, during which communication links are prone to be disconnected and re-formed, clusters should be able to divide or merge. Our TDMA scheme is featured in its adaptive time slot assignment as well as suitability to this dynamic topology change.

2.1 Frame Structures

The length of an ASA-TDMA frame is denoted by l_{frame} and a frame is divided into T_{slot} slots. In this paper, we choose the two parameters to be 250 ms and 10 respectively. The first slot of each frame is exclusively occupied by the cluster head for broadcasting slot assignment and cluster management information. Each idle slot is further divided into $M_{mini} = 5$ mini-slots. Mini-slot in any idle slot is randomly chosen by nodes to send Access Request (AR) to join the network. The last slot of each frame is always reserved for this purpose.

2.2 Overview of ASA-TDMA

The implementation of wireless airborne networks requires QoS guarantee of the MAC protocols. In this new ASA-TDMA scheme, an effective time slots allocation scheme is introduced to mainly improve ETE delay and packet reception rate performance. Table 1 gives the parameters that help describing the protocol.

Table 1. Parameters

Parameters for ASA-TDMA	
N^i	The identifier of mobile node i
CLU^i	The cluster formed on the basis of the head node N^i
RT	The relaying node table carried by AR, records intermediate nodes along the path
sT	Slot assignment table, recording slot assignment information and is broadcast by head
rT	Forwarding node record table, created by source nodes in a cluster and contained in AR, to be appended by the nodes along the path to the cluster head
TR	Contains traffic load amount of each member, maintained by head
sraT	Reassigned slots record, is created by the head, recording reassigned slots according to actual work load of all nodes in the cluster
tx_cnt	Records the amount of transmission of each source node in the current TDMA frame, maintained and refreshed by the head, flushed when reassignment is done

The proposed MAC protocol has five states. In Cluster Access state, node sets a timer and listens for Beacon (Beacons will be firstly forwarded by members in their slots before other types of data are transmitted). It will send an AR if it hears a Beacon

before timer expires or simply becomes a head. In the Work state of a head, head is responsible for allocating time slots, handling access requests, and managing the cluster. In the Work state of a common node, packets in the queue are scheduled to be sent in the assigned slots. The Send_AR state indicates the node is sending AR. All nodes can send AR to request accessing to a new cluster if the condition satisfies. As shown in Fig. 1, N^7 of CLU^7 hears several Beacons with higher priority from N^1 directly or via N^{10} , it sends AR to request accessing, then, N^3 and N^8 listen for Beacons and request to access. Clusters merge in this way, which is in one hand more efficient to manage nodes in a centralized way by reducing network overhead, and in the other hand reasonable for adjacent clusters to converge into one. When two clusters are flying close enough it is necessary to combine to avoid transmission interference, to efficiently utilize the time resource and to facilitate information sharing. Wait-response state is a transient stage after Send-AR state, in this state the node is waiting for cluster access grant and slot allocation information.

2.3 Key Procedures of ASA-TDMA

With an overview of ASA-TDMA in mind, the key steps that differentiate our work from other current works are presented in detail in the following.

- Adaptable slot assignment to fit for the changes of the cluster size
- Dynamically-performed load-based slot reassignment strategy
- Efficient slot sharing mechanism for collision-free concurrent transmissions
- Improvement in slot resource utilization by virtue of timely node state detection and slot resource retrieval

2.3.1 Cluster Establishment

A cluster is defined as a node group where the head manages common nodes, gathers sensing data (SD) and delivers them to a ground station. Each node is configured as a backup of the head. The formation of clusters is intrinsically determined by the change of the distances between nodes over time. This complex dynamic network behavior incurs some difficulties and challenges in the protocol design.

Cluster priority is the same as cluster head priority. We assume each node to be pre-assigned an priority.

In Cluster Access state, a node listens for Beacons. This state is essential in determining whether a node joins an existed cluster as a common member or becomes a head of a new cluster. We depict a diagram of this state to explain all the complicated cases, as Fig. 2 shows.

Cluster head would perform initial slot assignment when an AR arrives. rT in the AR will be evaluated at first, which is appended along the path by its intermediate nodes. If the number of residual idle slots is enough to assign to the new member and its intermediate hops, then the head assigns the resource directly without retrieving. Or else, the required number of slots recorded in $sraT$ would be retrieved (see the traffic based slot reassignment below). Here, we assume that nodes request accessing always have higher priority than nodes that have already been recently assigned slots but with the demand for more transmission chance.

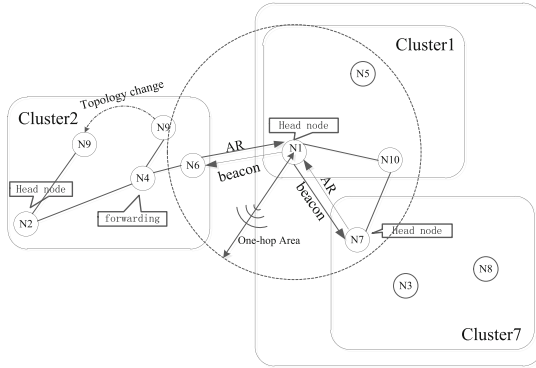


Fig. 1. Scenario1

2.3.2 Traffic Load Based Slot Reassignment

As stated in Sect. 1, the mismatch between resource and demand which leads to waste and starvation in resource needs to be addressed. Since our scheme aims at improving the resource utilization, a traffic load based slot reassignment scheme is proposed to address this issue. As described in Sect. 2.3.1, initial slot assignment is performed in the Cluster Access stage, each of the requesting node as well as intermediate hops is assigned only one slot. However, in consideration of resource utilization, residual idle slots would be reassigned, with which the slot allocation scheme becomes more sound and flexible.

Reassignment begins at the start of each TDMA frame. Cluster head refreshes TR based on piggybacking traffic load information from each member, and reassignment is performed according to TR by the head node. For example, as depicted in Fig. 1, head N^2 manages CLU^2 which accommodates N^4 , N^6 and N^9 , N^4 serves as intermediate hop in path $\langle N^2-N^4-N^6 \rangle$ and $\langle N^2-N^4-N^9 \rangle$, if the condition that equal rate of traffic flow from the upper layer of each node is assumed, N^4 bears more traffic due to its role in forwarding. Nodes with heavier traffic load, like N^4 , are granted higher priority and hence should be assigned more slots in reassignment process. Once a packet is received by N^2 , the value in field “tx_num” of the packet will be extracted. This value is the number of packets that are transmitted by a certain node. However, packets with more recent information may come earlier than ones with obsolete statistics and thus the statistic may be overridden. For instance, in Fig. 1, N^9 sends pkt67, containing the current transmission count value10, to N^2 via N^4 at time t1, so pkt67 waits in a very long queue at N^4 to be forwarded. Since network topology dynamically changes, N^9 may become a one-hop neighbor of head N^2 , so it sends pkt71 in the next transmission slot of N^9 directly to N^2 . In this case pkt71 contains the current transmission count value14 at time t2 without participation of any forwarding nodes, therefore pkt71 with newer “tx_num” information arrives at N^2 earlier than pkt67. Thereby, it’s incorrect to refresh tx_cnt only based on the packets’ arrival time, because the newly arrived packet may suffer delay but with a small packet identifier. In anyway, “tx_num” information contained in a packet with a smaller packet identifier should be ignored.

In our scheme, each packet is given a sequence number to identify its sending order from the source. In this way, though a packet suffers from heavy delay in wireless network, its sending order is the sole criteria according to which the tx_cnt refresh decision is made. In the example above, $pkt67$ cannot override the statistic recorded by the head, since $pkt71$ has already submitted a more reliable data.

This method is capable of adaptively modifying slot assignment strategy. The adaptive feature of our scheme is beneficial to improving the network performance.

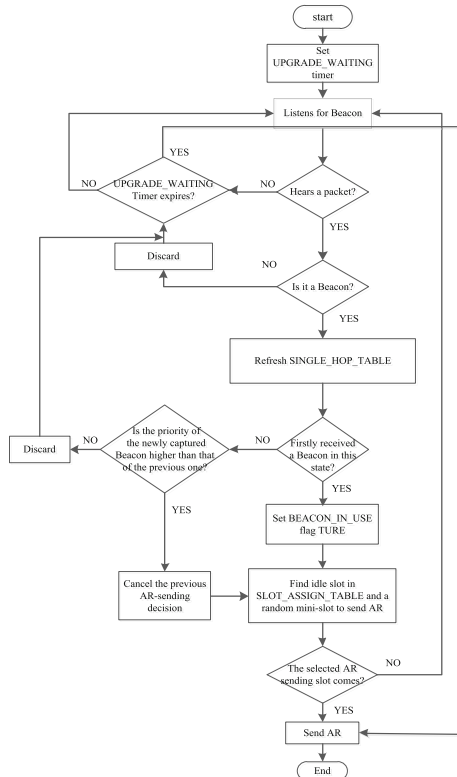


Fig. 2. Cluster access state diagrams

2.3.3 Slot Sharing for Collision-Free Concurrent Transmissions

Conflict-free transmission and adjustable resource scheduling strategy based on the real-time traffic load of nodes is described above. We go a step further to exploit a method that implements concurrent transmissions for the purpose of higher slot utilization efficiency.

As each node keeps a record of its neighbors within two hops, it is allowed to reuse the time slots assigned to any nodes in the same cluster 3-hops away. In this way, the concurrent transmissions are boosted to improve spatial reuse. If all members make the slot sharing decision locally, regardless of other's potential attempts to acquire the

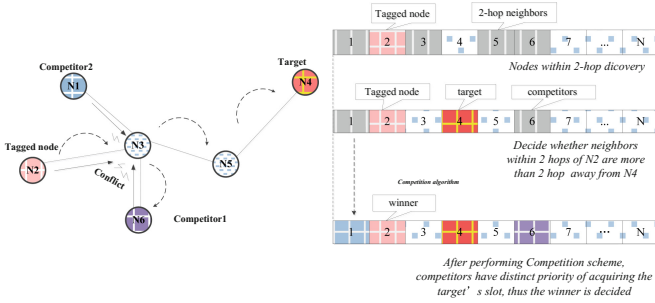


Fig. 3. Competition for shared slot

same slots, however, collisions may occur. For instance, in Fig. 3, N^1 , N^2 and N^6 consider sharing slot with N^4 is conflict-free. Actually, if slot sharing among N^1 , N^2 , N^6 and N^4 are all approved, conflicts caused by simultaneous transmissions may occur.

To avoid such collisions, with the help of the broadcast network topology messages, we introduce a slot sharing competition mechanism. In Fig. 3, the winner in one competition cycle comes from N^1 , N^2 and N^6 by performing the competition algorithm. The algorithm is described as follows:

Let Id_x denote the id number of node N^x , target (time slots of which competitors compete for) Id_n , S_m is the set records competitors of N^m .

Obtain:

$$argmin_{Id_k} |Id_k - Id_n| \tag{1}$$

$$Id_k \in S_m \cup Id_m, Id_k \neq Id_n \tag{2}$$

If there exists p, and p satisfies

$$|Id_p - Id_n| = \min |Id_k - Id_n| \tag{3}$$

$$winner = Id_p \tag{4}$$

Else if there exist p and q, and satisfy

$$|Id_p - Id_n| = |Id_q - Id_n| = \min |Id_k - Id_n|; \tag{5}$$

$$winner = \min\{Id_p, Id_q\} \tag{6}$$

As each node in S_m knows the winner in this competition cycle, the winner is alternately chosen from the residual nodes in S_m in subsequent competition cycles, which guarantees the fairness among competitors.

2.3.4 Node Lost Detection and Slot Resource Retrieval

Node lost has significant influence on network performance. Two-way judgment on “lost” is made by the head or the member node.

A member node is considered lost if it has not been heard by the head for continuous LOST_COUNT TDMA frames. A member in a cluster without hearing Beacons for continuous LOST_COUNT frames consider itself to be lost, and it reenters the Cluster Access state.

Since the node gets lost, all the slots related to it should be retrieved, including the slots assigned to its intermediate hops in the path from it to the head. Resource retrieval is a key procedure in resource utilization improvement and the detailed algorithm for slot retrieval is described in Algorithm 1. According to the descriptions of the scheme in above sections, a node is assigned slots in several circumstances: (1) when its access request is permitted; (2) it is an intermediate node of another node whose access request is permitted; (3) idle slots reassignment is performed based on the traffic load; (4) it wins the slot sharing competition.

Algorithm 1 Slot Retrieving Algorithm

```

Procedure Slot_retrieve ( $N^i$ ) //ID number of the lost node
Begin
  1: <sT traversal>
  2: Retrieve the particular slot assigned to  $N^i$  in initial slot
     assignment;
  3: if intermediate hops exist between  $N^x$  and head then
  4: Decrease the number of slots possessed by intermediate
     hops by 1;
  5: end if
  6: if  $N^i$  has child  $N^x$  then
  7: Child node  $N^x$  is sentenced to lost;
  8: Perform recursion Slot_retrieve( $N^x$ );
  9: end if
  10: Retrieve slots marked “assigned” which are used to
     forward other nodes’ traffic;
  11: Retrieve slots won in shared slot competition;
  12: <rT traversal>
  13: if  $N^i$  has been assigned slots in reassignment then
  14: Retrieve these slots;
  15: end if
  16: end

```

3 Simulation Evaluations

In this section, we provide simulation results of the proposed protocol, which is implemented in OPNet. Mobile nodes are configured moving in air with 3-dimensional trajectory, with their attitudes change over time. The data rate of transceivers is set to be

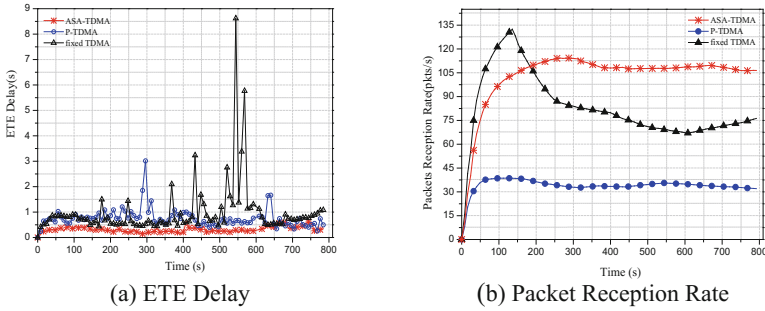


Fig. 4. Simulation results A

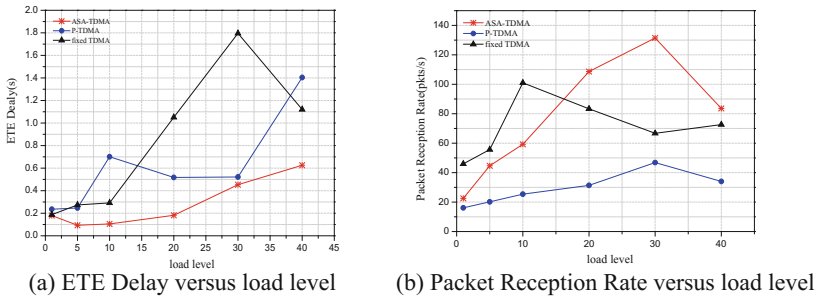


Fig. 5. Simulation results B

2 Mbps, and antenna pattern is ideal with a 70-degree-wide main lobe. We ran simulations for 800 s and compared the performance of ASA-TDMA with that of P-TDMA and fixed TDMA. Figure 4(a) shows the delay curves over the simulation time. Our scheme outperforms the other two as the figure shows. The feedback traffic load amount information to the head is vital in TDMA scheduling, which implies that nodes with heavy load can request more slots. Both the waste of unavailable slots of lost nodes, and the lack in transmission chances of nodes with heavy load can be the reason of the high delay in fixed TDMA scheme. Under multi-hop circumstances, because the phases of neighbor discovery, response and data transmission are structured alternately, inconsecutive epoch for data transmission leads to bad performance in P-TDMA. Figure 4(b) depicts packet reception rate curves over the simulation time. Overall, the proposed scheme outperforms others. In the early stage, fixed TDMA, benefiting from omitting the process of requesting slots and the grant information delivery, shows good performance. As the network complexity growing with time advancing, the fixed scheme can neither keep up with the dynamic slot demands, nor cope with the lost case flexibly, and the insufficient utilization of time slots resources is consequently inevitable.

ASA-TDMA is capable of handling complex network behavior and it shows superiority in pursuing high slot utilization. Though P-TDMA scheme is provided with collision-free concurrent transmissions, bad performance is unavoidable owing to the high overhead. The scheme achieves collision-free transmissions at the cost of high expense. Little specific resource is needed in our scheme, on the contrary, neighbor discovery and nodes access information exchange is done in an explicit and piggy-backing way by a good packet design.

In most realistic scenarios, networks show bad performance or simply crash under high load level. Thus, a protocol with high-load-adaptability property is urgently needed. We performed further simulations to verify the performance under different load levels and high-load-adaptability of ASA-TDMA scheme. As shown in Fig. 5(a), the delay increase as load level grows, and ASA-TDMA always gives the lowest ETE delay compared with others. Our scheme gives the best even under high load level, as the figure depicts: ASA-TDMA achieves approximately 55.44% decrease compared with P-TDMA, and 44.15% decrease compared with fixed TDMA under the level 40. Figure 5(b) shows packets reception rate versus load level. It is observed that the ASA-TDMA outperforms P-TDMA under all load levels, and gives higher performance under high load level than Fixed TDMA. This demonstrates the superiority of ASA-TDMA in adaptability under high load level circumstance. ASA-TDMA achieves 145.68% increase compared with P-TDMA, and 15.06% increase compared with fixed TDMA under the level 40.

4 Conclusion

In this paper, we propose a new TDMA-based scheme for dynamic airborne ad hoc networks, i.e. ASA-TDMA. It achieves high efficiency by assigning time slots not only when there are demands for accessing, but also periodically at the beginning of each TDMA frame based on real-time traffic load of all members. By virtue of the slot sharing scheme, ASA-TDMA achieves collision-free concurrent transmissions to realize higher slot utilization. Furthermore, ASA-TDMA can flexibly change previous slot schedule to cope with lost or failure of nodes. Simulation results in 3-D scenario show that the ASA-TDMA has lower delay and higher packet reception rate compared with P-TDMA and fixed TDMA, and the high-load-adaptability of our proposed scheme is also verified. The deeper insights of the self-adaptive protocol, and its improvements to suitable for more dynamic characteristics, e.g., fast flying nodes with beamforming antenna, are left to our future works.

Acknowledgements. This work is supported by the National Natural Science Foundation of China under Grant 61671353, and partly by the 111 Project (B08038) of MOE, China, and the Foundation of Science and Technology on Communication Networks Laboratory.

References

1. Zhang, Z.: DTRA: directional transmission and reception algorithms in WLANs with directional antennas for QoS support. *IEEE Netw.* **19**(3), 27–32 (2005)

2. Tu, Y., Zhang, Y., Zhang, H.: A novel MAC protocol for wireless ad hoc networks with directional antennas. In: 2013 15th IEEE International Conference on Communication Technology, pp. 494–499. IEEE Press, Guilin (2013)
3. Cha, J.R., et al.: TDMA-based multi-hop resource reservation protocol for real-time applications in tactical mobile ad hoc network. In: 2010 Military Communications Conference, MILCOM 2010, pp. 1936–1941. IEEE Press (2010)
4. Felemban, E., Lee, C.-G., Ekici, E.: MMSPEED: multipath Multi-SPEED protocol for QoS guarantee of reliability and timeliness in wireless sensor networks. *IEEE Trans. Mob. Comput.* **5**(6), 738–754 (2006)
5. Ye, F., Yim, R., Zhang, J., Roy, S.: Congestion control to achieve optimal broadcast efficiency in VANETs. In: 2010 IEEE International Conference on Communications, pp. 1–5. IEEE Press, South Africa (2010)
6. Hadded, M., et al.: TDMA-based MAC protocols for vehicular ad hoc networks: a survey, qualitative analysis, and open research issues. *IEEE Commun. Surv. Tutorials* **17**(4), 2461–2492 (2015)
7. Lee, J.K., Noh, H.J., Lim, J.: TDMA-based cooperative MAC protocol for multi-hop relaying networks. *IEEE Commun. Lett.* **18**(3), 435–438 (2014)
8. Gexin, P., Shengli, X., Caiyun, C.: A collision-avoid dynamic slots assignment algorithm based on fixed TDMA. *China Inf. Secur.* **11**, 115–120 (2005)



On Low-Pass Phase Noise Mitigation in OFDM System for mmWave Communications

Xiaoming Chen¹✉, Wei Fan², and Anxue Zhang¹

¹ School of Electronic and Information Engineering, Xi'an Jiaotong University,
Xi'an, China

{xiaoming.chen, anxuezhang}@mail.xjtu.edu.cn

² Department of Electronic Systems, Aalborg University, Aalborg, Denmark
wfa@es.aau.dk

Abstract. A phase noise (PN) mitigation scheme was proposed for orthogonal frequency division multiplexing (OFDM) in a previous work. The proposed scheme does not require detailed knowledge of PN statistics and can effectively compensate the PN with sufficient number of unknowns. In this paper, we analyze the performance of PN estimation/mitigation using the proposed scheme. It is shown that increasing the number of unknowns reduces the modeling error, yet increases the additive noise. Hence, increasing the number of unknowns increases the computational complexity and can even degrade the estimation performance. It is also shown that the PN spectral shape of the phase-locked-loop (PLL) based oscillator also affects the PN mitigation and that a larger PN may not necessarily degrade the performance of the OFDM system with PN mitigation. Simulations with realistic millimeter-wave (mmWave) PN and channel models are conducted to verify these findings.

Keywords: Phase noise mitigation · mmWave communications
OFDM systems

1 Introduction

The orthogonal frequency division multiplexing (OFDM) technique [1] (that has been adopted in many modern communication systems) is recently chosen to be the main waveform for 5G communications below 40 GHz and is currently considered as a strong waveform candidate for 5G communications above 40 GHz, according to the 3GPP 5G standardization [2]. In this work, we focus on OFDM systems at millimeter-wave (mmWave) frequencies [3–5].

Like other multicarrier waveforms, the OFDM system is sensitive to oscillator phase noises (PNs). PN impairments on OFDM systems have been studied intensively in the literature, e.g., [6–17]. A PN suppression scheme was proposed in [7]. The scheme suppresses the PN effect via the minimum mean square error

(MMSE) equalization with prior knowledge of additive white Gaussian noise (AWGN) and PN statistics. The authors in [8] proposed an intercarrier interference (ICI) self-cancellation scheme by modulating one symbol to two adjacent subcarriers with opposite weights. This scheme can effectively cancel the PN effect at the cost of reducing the OFDM spectral efficiency by half. An ICI correction algorithm (by estimating discrete spectral components of the PN) was proposed in [9]. The algorithm was further developed in [10] by linear interpolating between adjacent OFDM symbols, resulting in enhanced system performance at the cost of increased complexity and one extra OFDM symbol delay. Both ICI correction algorithms require iteratively processing. A non-iterative PN mitigation method (based on maximum likelihood estimation) was proposed in [11]. The method was improved by exploiting the spectral geometry of the PN [12]. Another non-iterative PN mitigation scheme with lower complexity was proposed in [13]. Joint compensation of PN and IQ imbalance was tackled in [14]. Joint estimation of PN and carrier frequency offset (CFO) was studied in [14, 15]. Joint mitigation of PN, CFO, and sampling frequency offset (SFO) was investigated in [17].

The PN mitigation scheme proposed in [17] does not require detailed knowledge of PN statistics. It estimates the PN (within each OFDM symbol) at certain time or spectral anchors (unknowns), and approximate the PN by linear interpolation between time anchors or discrete Fourier transform of spectral anchors. Nevertheless, a thorough performance analysis of the scheme is missing. Therefore, in this work, we analyze the performance of the scheme. It is shown that increasing the number of anchors reduces the modeling error, yet increases the additive noise in PN estimation.

The Wiener PN of a free-running oscillator is the most popular PN model in the literature [6, 7, 9–17], whereas the PN of a phase-locked-loop (PLL) based oscillator (referred to as PLL PN hereafter) is used in [9] as well. The spectrum of Wiener PN has a constant decay of 20 dB/decade, whereas spectrums of PLL PNs can have different shapes, depending on the levels of different noise sources (cf. Sect. 2). Another contribution of this work is that we show that the PN's spectral shape also affects the performance of the PN mitigation scheme and that, by having suitable subcarrier spacing and anchor number, a larger PN may even result in better performance with the PN mitigation scheme (provided that most of its energy is concentrated at low offset frequencies).

Notations: Throughout this paper, $*$, T , H , and \dagger denote complex conjugate, transpose, Hermitian, and Moore-Penrose pseudoinverse, respectively. Lower case bold letter (\mathbf{x}) and upper case bold letter (\mathbf{X}) represent column vector and matrix, respectively. \mathbf{I} is the identity matrix. $\|\mathbf{x}\|$ is the Euclidean norm of \mathbf{x} . $\text{diag}(\mathbf{x})$ denotes a diagonal matrix whose diagonal elements are given by \mathbf{x} .

2 System Model

In order to focus on PN impairments, we assume perfect time-synchronization and quasi-static multipath channel (with a channel length of L). The PN impaired signal at the receiver at the n th time sample can be expressed as

$$y(n) = \exp(j\phi(n)) \sum_{l=0}^{L-1} h_l x(n-l) + w(n) \tag{1}$$

where x represents the transmitted OFDM signal including cyclic prefix (CP), h_l ($l = 0, \dots, L-1$) is the l th tap of the channel impulse response (CIR), w denotes the AWGN, and ϕ denotes the PN.

The Wiener PN is the most popular PN model in the literature [6, 7, 9–17]. It is given as

$$\phi(n+1) = \phi(n) + \eta(n) \tag{2}$$

where η is a zero-mean Gaussian random variable with variance of $4\pi f_{3\text{dB}}/f_s$ with f_s denoting the sampling frequency and $f_{3\text{dB}}$ representing the 3-dB bandwidth of the PN. As can be seen, the Wiener PN can be characterized by a single parameter, i.e., its 3-dB bandwidth $f_{3\text{dB}} = \pi\varsigma f_s^2$, where ς is a parameter that reflects the quality of the oscillator [18]. Nevertheless, the value of $f_{3\text{dB}}$ (instead of ς) is usually given in the literature.

Due to its simplicity, the Wiener PN model (2) is widely used in the literature. However, PLL-based oscillators are ubiquitously used in practical mmWave transceivers. As a result, we resort to the PLL PN in this paper.

The PLL PN consists of three main noise sources, i.e., noises from the reference oscillator θ_{ref} , the phase-frequency detector and the loop filter θ_{LP} , and the voltage controlled oscillator (VCO) θ_{VCO} , as shown in Fig. 1. The Laplace transform of the PN of the PLL-based oscillator is given as [19]

$$\theta_{\text{out}}(s) = \frac{N_D K_{\text{VCO}} Z(s) [K_D \theta_{\text{ref}}(s) + \theta_{\text{LP}}(s)] + s N_D \theta_{\text{VCO}}(s)}{s N_D + K_D K_{\text{VCO}} Z(s)} \tag{3}$$

where K_D denotes the gain of the phase-frequency detector, K_{VCO} represents the sensitivity of the VCO, $Z(s)$ represents the loop filter, and $1/N_D$ is the frequency divider. The detailed modeling parameters are listed in Table 4-2 of [19].

As can be seen from (3), θ_{ref} and θ_{LP} dominate at low (offset) frequencies, and θ_{VCO} dominates at high frequencies. By adjusting their levels, different spectral shapes of PN can be obtained. Figure 2 shows power spectral densities (PSDs) of

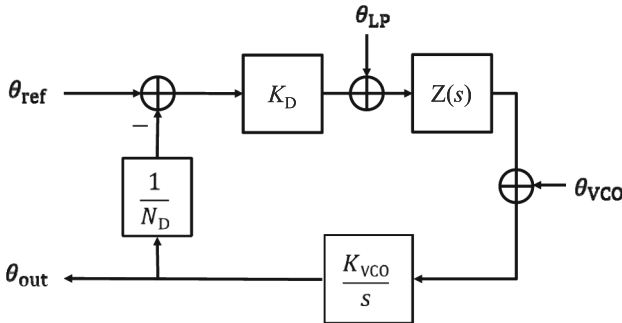


Fig. 1. Phase noise model of PLL-based oscillator.

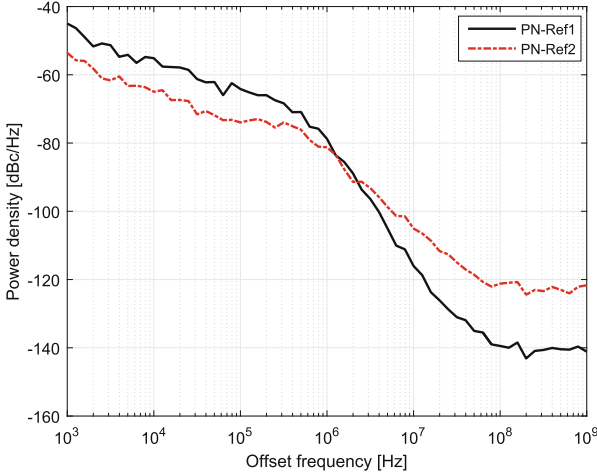


Fig. 2. PSDs of two PLL PNs. (Color figure online)

two PLL PNs at 82 GHz. The red curve (PN-Ref2) is obtained by choosing the high PN mode (see Table 4-2 of [19]). The black curve (PN-Ref1) is obtained by increasing the power of θ_{LP} by 10 dB and reducing the power of θ_{VCO} by 18 dB. The two PLL PNs are used to show the spectral shape effect on PN mitigation in Sect. 5.

3 PN Mitigation Scheme

Let $\mathbf{y} = [y(0) \ y(1) \ \dots \ y(N - 1)]^T$ be the received time-domain OFDM symbol (after CP removal), where N is the number of subcarriers. The PN is mitigated by $\Phi\mathbf{y}$, where

$$\Phi = \text{diag} \left\{ \left[\exp(-j\hat{\phi}(0)) \ \dots \ \exp(-j\hat{\phi}(N - 1)) \right]^T \right\} \tag{4}$$

with $\hat{\phi}$ denoting the estimate of ϕ . Hence the task of PN mitigation is essentially PN estimation.

Let \mathbf{H}_p be an $N_p \times N_p$ diagonal matrix consisting of the channel transfer functions (CTFs) at the N_p pilot subcarriers ($N_p \leq N$), \mathbf{s}_p be a vector consisting of the N_p subcarriers, \mathbf{D} be an $N_p \times N$ submatrix of the $N \times N$ discrete Fourier transform (DFT) matrix \mathbf{F} (whose elements are given by $\exp(-j2\pi nk/N)/\sqrt{N}$, ($k, n = 0, \dots, N - 1$) corresponding to the N_p pilot subcarriers, and $\tilde{\mathbf{w}}$ be an $N \times 1$ vector consisting of the time-domain AWGNs. Left multiplying (1) by $\mathbf{D}\Phi$, one obtains

$$\mathbf{D}\Phi\mathbf{y} = \mathbf{H}_p\mathbf{s}_p + \mathbf{D}\Phi\tilde{\mathbf{w}}. \tag{5}$$

Let $\mathbf{Y} = \text{diag}(\mathbf{y})$ and \mathbf{T} be an $N \times q$ transformation matrix, such that $\mathbf{\Phi} \approx \text{diag}(\mathbf{T}\boldsymbol{\alpha})$, where $\boldsymbol{\alpha}$ consists of q unknowns or anchors ($q \leq N_p$), and is given as

$$\boldsymbol{\alpha} = (\mathbf{D}\mathbf{Y}\mathbf{T})^\dagger \mathbf{H}_p \mathbf{s}_p + (\mathbf{D}\mathbf{Y}\mathbf{T})^\dagger \tilde{\mathbf{w}}. \quad (6)$$

The first term in the right hand side (RHS) of (6) is the least-square (LS) estimator of $\boldsymbol{\alpha}$ [15], whereas the second term in the RHS of (6) is additive noise.

The physical meaning of $\boldsymbol{\alpha}$ depends on the type of the transformation matrix. If \mathbf{T} is a linear interpolation matrix [16], the elements in $\boldsymbol{\alpha}$ are estimates of the inverse carrier PN $\exp(-j\phi)$ at the q anchors (time samples). These anchors are usually evenly distributed in the time-domain OFDM symbol.

Since the PN spectrum is concentrated at low frequencies [9], \mathbf{T} can be a $N \times q$ submatrix of \mathbf{F} , corresponding to the q lowest spectral components. In this case, the elements in $\boldsymbol{\alpha}$ are the spectral components of $\exp(-j\phi)$.

The computational complexity of the PN mitigation scheme mainly depends on the pseudoinverse of an $N_p \times q$ matrix in (6), whose complexity increases linearly with N_p , yet cubically with q [20]. In the next section, we analyze the performance of the PN mitigation/estimation with respect to (w.r.t.) q .

4 Performance Analysis

For the convenience of analysis, we study the performance of the PN mitigation/estimation in the preamble (where $N_p = N$). (As shown in Sect. 5, the findings hold for the payload as well.)

The LS estimator of the PN, i.e., the first term in the RHS of (6), contains modeling error $\mathbf{\Phi} - \text{diag}(\mathbf{T}\boldsymbol{\alpha})$. Assuming perfect estimation of $\boldsymbol{\alpha}$ (by setting the second term in the RHS of (6), i.e., the additive noise, to zero), it is self-evident that the modeling error reduces to zero as q increases to N .

Now we examine the effect of the additive noise in (6) w.r.t. q . Let $\check{\mathbf{w}} = \mathbf{F}\mathbf{\Phi}\tilde{\mathbf{w}}$. Since $\mathbf{F}\mathbf{\Phi}$ is unitary matrix, $\check{\mathbf{w}}$ and $\tilde{\mathbf{w}}$ have the same statistics. Thus, the additive noise in (6) can be equivalently written as

$$\mathbf{z} = (\mathbf{F}\mathbf{Y}\mathbf{T})^\dagger \check{\mathbf{w}} = (\mathbf{T})^\dagger (\mathbf{Y})^{-1} (\mathbf{F})^H \tilde{\mathbf{w}}. \quad (7)$$

For simplicity, we assume that \mathbf{T} is the DFT transformation matrix. The power of the additive noise is given as

$$\begin{aligned} \mathbb{E}[\mathbf{z}^H \mathbf{z}] &= \sigma_w^2 \mathbb{E} \left\{ \text{Tr} \left[(\mathbf{T})^\dagger (\mathbf{Y})^{-1} \left((\mathbf{Y})^{-1} \right)^* \left((\mathbf{T})^\dagger \right)^H \right] \right\} \\ &= \sigma_w^2 \mathbb{E} \left\{ \text{Tr} \left[\left(\mathbf{T}\mathbf{T}^H \right)^\dagger (\mathbf{Y})^{-1} \left((\mathbf{Y})^{-1} \right)^* \right] \right\} \\ &= \sigma_w^2 \frac{q}{N} \mathbb{E} \left\{ \text{Tr} \left[(\mathbf{Y})^{-1} \left((\mathbf{Y})^{-1} \right)^* \right] \right\}. \end{aligned} \quad (8)$$

Using Jensen's inequality, it is easy to show that (8) is lower bounded by $\frac{q}{N} \frac{\sigma_w^2}{\sigma_h^2 \sigma_s^2 + \sigma_w^2} = \frac{q}{N} \frac{1}{\gamma_0 + 1}$, where σ_h^2 , σ_s^2 , and σ_w^2 are the variances of the CIR, subcarrier symbol, and AWGN, respectively, and $\gamma_0 = \sigma_h^2 \sigma_s^2 / \sigma_w^2$ is the signal-to-noise-ratio (SNR). As can be seen from (8) that increasing q will increase the power

of the additive noise in (6) for fixed N and SNR. This is because that there are more anchors to estimate as q increases. All in all, for PN estimation, increasing q reduces the modeling error, yet increases the additive noises.

The PN mitigation scheme (cf. Sect. 3) is in essence a low-pass filter, which removes the PN at low (offset) frequencies. This is obvious when the DFT transformation is used, which only estimate (and remove) the q lowest spectral components. The impulse response of the linear interpolation is a triangular function, which is a convolution of two identical rectangular functions. Hence, the frequency response of the linear interpolation is the multiplication of two identical Sinc function, implying that it is also a low-pass filter. The cutoff frequency (f_{cut}) of the PN mitigation scheme approximately equals the inverse of the temporal spacing of the anchors, T/q , where T denotes the OFDM symbol duration. Thus, f_{cut} is approximately given as

$$f_{\text{cut}} \approx q/T = qf_{\text{sub}} \quad (9)$$

where f_{sub} denotes subcarrier spacing. Therefore, it is the spectral power above f_{cut} that dominates the residual PN after PN mitigation.

5 Simulations

In this section, we verify the findings of the previous section by simulations.

Figure 3 shows an example of the PN and its estimates using the PN estimation scheme with linear interpolation and DFT transformation, respectively, for an OFDM system (in an ideal channel) with $N = 512$, $N_p = 32$, $q = 7$, and sampling frequency of $f_s = 250$ MHz. The PLL PN, PN-Ref2 (cf. Fig. 2), is used.

In order to demonstrate the effect q on PN estimation, we calculating the average MSE of the estimated PNs over 500 symbols. Figure 4 shows the MSE performance of the PN estimation as a function of q . Figure 4a corresponds to the preamble case, while Fig. 4b corresponds to the payload case with $N_p = 32$ scattered pilots. As can be seen, PN estimations with linear interpolation and DFT transformation has similar performances. It is also shown that MSE performances improve as q increases when $q < 15$, yet degrade as q increases when $q > 15$. This is because, when q is small, the modeling error dominates, however, as q becomes large, the additive noise begins to dominate, as shown in the previous section.

Now we investigate the PN's spectral shape effect on the PN mitigation. Since the PN estimations with linear interpolation and the DFT transformation have similar performance, we focus on the PN mitigation with linear interpolation hereafter.

The two PLL PNs, i.e., PN-Ref1 and PN-Ref2 (see Fig. 2), are used for simulations. The PN-Ref1 has higher spectral power at low (offset) frequencies and lower spectral power at high frequencies, as compared to the PN-Ref2. The PSD curves of the two PNs cross each other at 1–2 MHz frequencies. It can be seen from (9) that f_{cut} can be adjusted by varying the number of anchors and/or the subcarrier spacing.

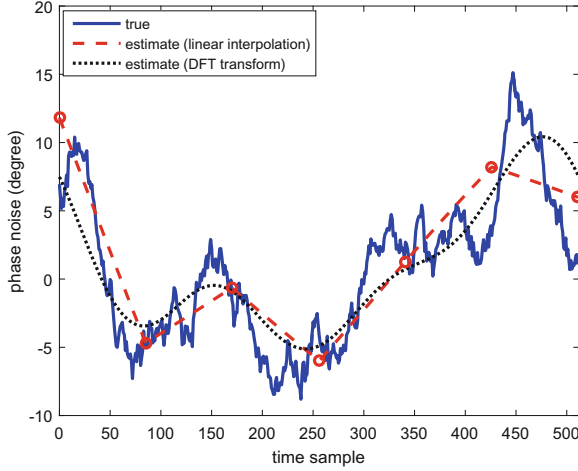


Fig. 3. Example of PN and its estimates using linear interpolation and DFT transformation within one OFDM symbol.

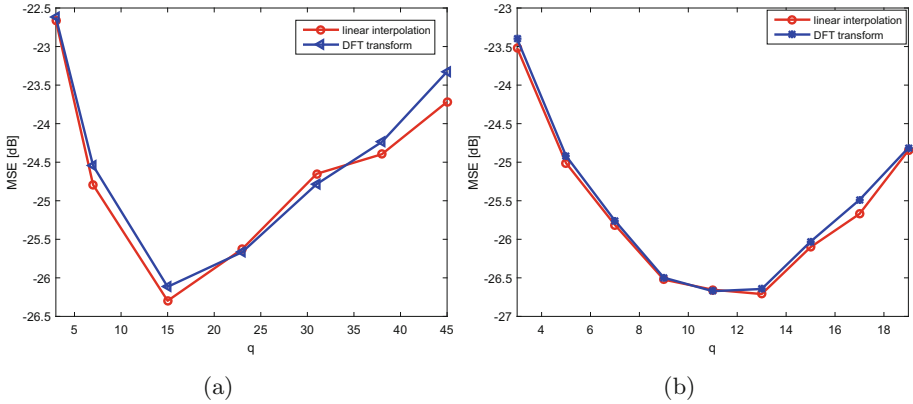


Fig. 4. MSE performances of the PN estimation using linear interpolation and DFT transformation: (a) $N_p = N$; (b) $N_p = 32$.

We assume an OFDM system with $N = 512$ and $N_p = 32$. The QuaDRiGa channel model [21] (a geometry-based stochastic channel model) is used for emulating the mmWave channel at 82 GHz. In order to see the spectral shape effects of the two PNs, we conduct two sets of simulations. One with $q = 3$ and $f_{\text{sub}} = 240$ kHz, so that $f_{\text{cut}} = 0.72$ MHz is smaller than the crossing frequency of the two PNs. The other with $q = 7$ and $f_{\text{sub}} = 480$ kHz, so that $f_{\text{cut}} = 3.36$ MHz is larger than the crossing frequency of the two PNs.

Figure 5 shows the bit-error-rate (BER) performance of the OFDM system with 16-QAM, $q = 3$, and $f_{\text{sub}} = 240$ kHz. As a reference, the BER performance with common phase error (CPE) correction [7] is also presented as a reference.

Figure 5a corresponds to PN-Ref1, whereas Fig. 5b corresponds to the PN-Ref2. As can be seen by comparing the BERs without PN correction, PN-Ref1 degrades the OFDM system (without PN mitigation) more than PN-Ref2 does. This is because its energy (over the whole frequency) is larger than that of PN-Ref2. Since $f_{\text{cut}} = 0.72$ MHz is smaller than the crossing frequency of the two PNs (i.e., PN-Ref1 has more residual energy than PN-Ref2 does after the PN mitigation), the PN-Ref1 degrades the OFDM system (with PN mitigation) more severely than PN-Ref2 does.

Figure 6 shows the BER performance of the OFDM system with 64-QAM, $q = 7$, and $f_{\text{sub}} = 480$ kHz. Figure 6a corresponds to PN-Ref1, whereas Fig. 6b

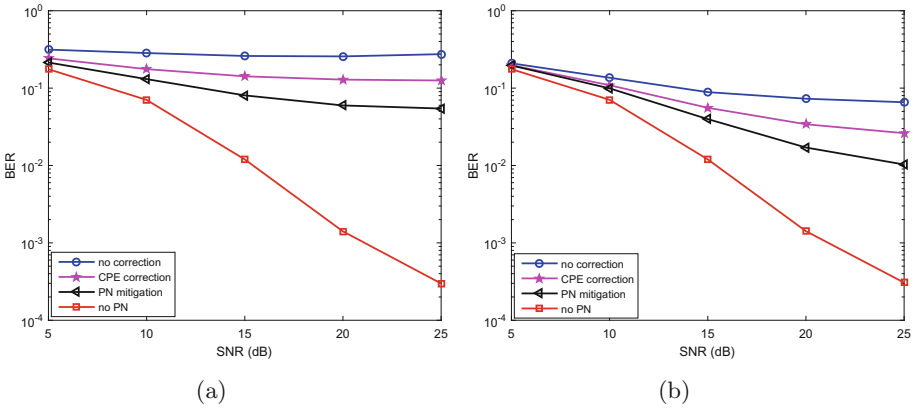


Fig. 5. BER performances of OFDM system (with 16-QAM, $f_{\text{sub}} = 240$ kHz, $q = 3$) without PN correction, with CPE correction, with PN mitigations, and without PN in mmWave multipath fading channel: (a) PN-Ref1; (b) PN-Ref2.

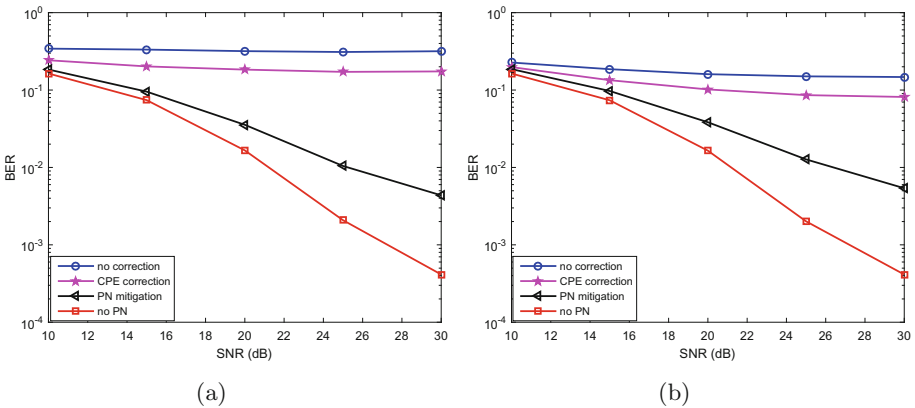


Fig. 6. BER performances of OFDM system (with 64-QAM, $f_{\text{sub}} = 480$ kHz, $q = 7$) without PN correction, with CPE correction, with PN mitigations, and without PN in mmWave multipath fading channel: (a) PN-Ref1; (b) PN-Ref2.

corresponds to PN-Ref2. As can be seen even though PN-Ref1 has larger energy than PN-Ref2, with the phase noise mitigation, the BER performance of the OFDM system in the presence of PN-Ref1 is (slightly) better than that in the presence of PN-Ref2. This is because $f_{\text{cut}} = 3.36$ MHz is larger than the crossing frequency of the two phase noises, and, after removing the phase noise below f_{cut} (using the phase noise mitigation), the residual PN-Ref1 is smaller than that of PN-Ref2. Comparing Figs. 5 and 6, it is safe to conclude that the spectral shape of the phase noise also affects the performance of phase noise mitigation. A larger phase noise may not necessarily degrade the performance of the OFDM system (with PN mitigation) more than a smaller PN does. It depends on the spectral shape and the cutoff frequency of the phase noise mitigation scheme.

6 Conclusion

In this paper, we studied the performance of a PN mitigation scheme for mmWave OFDM systems with realistic PN and channel models. It was shown that increasing the number of anchors reduces the modeling error, yet increases the additive noise, and therefore, may not necessarily improve the performance of PN estimation. It was also shown that the spectral shape of the PN also affects the PN mitigation, and that it is the PN's power above the cutoff frequency of the PN mitigation scheme that dominates the residual PN impairment.

References

1. Bingham, J.A.C.: Multicarrier modulation for data transmission, an idea whose time has come. *IEEE Comm. Mag.* **28**, 5–14 (1990)
2. 3GPP. <http://www.3gpp.org/>
3. Fan, W., Carton, I., Nielsen, J.Ø., Olesen, K., Pedersen, G.F.: Measured wideband characteristics of indoor channels at centimetric and millimetric bands. *EURASIP J. Wirel. Commun. Netw.* **2016**, 58 (2016)
4. Guan, K., Li, G., Kuerner, T., Molisch, A.F., Peng, B., He, R., Hui, B., Kim, J.H., Zhong, Z.: On millimeter wave and THz mobile radio channel for smart rail mobility. *IEEE Trans. Veh. Technol.* **66**, 5658–5674 (2017)
5. Ai, B., Guan, K., He, R., Li, J., Li, G., He, D., Zhong, Z.: On indoor millimeter wave massive MIMO channels: measurement and simulation. *IEEE J. Sel. Areas Commun.* **35**, 1678–1690 (2017)
6. Armada, A.G.: Understanding the effects of phase noise in orthogonal frequency division multiplexing (OFDM). *IEEE Trans. Broadcast.* **47**, 153–159 (2001)
7. Wu, S., Bar-Ness, Y.: OFDM system in the presence of phase noise: consequences and solutions. *IEEE Trans. Commun.* **52**, 1988–1996 (2004)
8. Zhang, J., Rohling, H., Zhang, P.: Analysis of ICI cancellation scheme in OFDM systems with phase noise. *IEEE Trans. Broadcast.* **50**, 97–106 (2004)
9. Petrovic, D., Rave, W., Fettweis, G.: Effects of phase noise on OFDM systems with and without PLL: characterization and compensation. *IEEE Trans. Commun.* **55**, 1607–1616 (2007)

10. Tchamov, N.N., Rinne, J., Hazmi, A., Valkama, M., Syrjala, V., Renfors, M.: Enhanced algorithm for digital mitigation of ICI due to phase noise in OFDM receivers. *IEEE Wirel. Commun. Lett.* **2**, 6–9 (2013)
11. Rabiei, P., Namgoong, W., Al-Dhahir, N.: A non-iterative technique for phase noise ICI mitigation in packet-based OFDM systems. *IEEE Trans. Sig. Process.* **58**, 5945–5950 (2010)
12. Mathecken, P., Riihonen, T., Werner, S., Wichman, R.: Phase noise estimation in OFDM: utilizing its associated spectral geometry. *IEEE Trans. Sig. Process.* **64**, 1999–2012 (2016)
13. Chen, X.: OFDM based multi-node transmission in the presence of phase noises for small cell backhaul. *IEEE Commun. Lett.* **21**, 1207–1210 (2017)
14. Zou, Q., Tarighat, A., Sayed, A.H.: Joint compensation of IQ imbalance and phase noises in OFDM wireless systems. *IEEE Trans. Commun.* **57**, 404–414 (2009)
15. Lin, D.D., Pacheco, R., Lim, T.J., Hatzinakos, D.: Joint estimation of channel response, frequency offset, phase noise in OFDM. *IEEE Trans. Sig. Process.* **54**, 3542–3554 (2006)
16. Salim, O.H., Nasir, A.A., Mehrpouyan, H., Xiang, W., Durrani, S., Kennedy, R.A.: Channel, phase noise, and frequency offset in OFDM systems: joint estimation, data detection, and hybrid cramer-rao lower bound. *IEEE Trans. Commun.* **62**, 3311–3324 (2014)
17. Chen, X., Wolfgang, A.: Phase noise mitigation in OFDM-based backhaul in the presence of channel estimation and synchronization errors. In: *IEEE 83rd Vehicular Technology Conference*, pp. 1–5. IEEE Press, New York (2016)
18. Demir, A., Mehrotra, A., Roychowdhury, J.: Phase noise in oscillators: a unifying theory and numerical methods for characterisation. *IEEE Trans. Circ. Syst.* **1**(47), 655–674 (2000)
19. Zetterberg, P., Wolfgang, A., Westlund, A.: Initial multi-node and antenna transmitter and receiver architectures and schemes. *mmMAGIC Deliverable D5.1* (2016)
20. Bürgisser, P., Clausen, M., Shokrollahi, A.: *Algebraic Complexity Theory*. Springer, Heidelberg (1997). <https://doi.org/10.1007/978-3-662-03338-8>
21. Jaeckel, S., Raschkowski, L., Börner, K., Thiele, L.: QuaDRiGa: a 3-D multi-cell channel model with time evolution for enabling virtual field trials. *IEEE Trans. Antennas Propag.* **62**, 3242–3256 (2014)

Network and Information Security



Secure Algorithm via Hybrid Relaying Scheme and Resource Allocation for OFDM Networks

Xianwen Zhou, Pinyi Ren^(✉), and Qinghe Du

School of Electronic and Information Engineering, Xi'an Jiaotong University,
Xi'an 710049, China

zhou19910225@stu.xjtu.edu.cn, {pyren,duqinghe}@mail.xjtu.edu.cn

Abstract. Due to its high spectrum efficiency, strong ability to resist multipath fading, OFDM networks is widely applied in various wireless communication systems. However, physical layer security is also an important problem in OFDM networks. By using relay nodes, the secrecy outage probability can be reduced since relay nodes could increase freedoms of optimization for the cooperative OFDM networks. By optimizing multiple variables, which includes adaptive hybrid relaying scheme, relay selection, and resource allocation, we propose the secure algorithm which aims at minimizing the secrecy outage probability of multiuser in cooperative OFDM networks. To achieve this goal, we establish an optimization problem including multiple optimization variables. Then, we convert the optimization problem into a graph theory problem. Simulation results show that the secure algorithm can significantly reduce the secrecy outage probability of multiuser in cooperative OFDM networks.

Keywords: Physical layer security · Hybrid relaying scheme
Resource allocation · Cooperative OFDM networks

1 Introduction

Due to its high spectrum efficiency, strong ability to resist multipath fading, the Orthogonal Frequency Division Multiplexing (Orthogonal Frequency Division Multiplexing, OFDM) technology is widely applied in various wireless communication systems. Because people pay more and more attention to information security, physical layer security also becomes a critical issue in OFDM networks. In [1], Shannon pointed out that complete secret communication can be realized by means of “one word one secret” when the wiretap channel and the legitimate channel are not differential channels. Then, a degraded wiretap channel was proposed in the discrete memoryless channel by Wyner in [2] which considers a more general situation. However, when legitimate receiver’s channel state information is worse than the eavesdropper’s channel state information, secrecy rate is zero. To overcome this problem, in [3–8], the author uses cooperative relay communication technology to strengthen secure communication of legal receivers.

Due to the relay technology advantages in the physical layer security, in [9–12], the author found that the cooperative OFDM networks could achieve the maximal secrecy throughput by resource allocation. However, sometimes secrecy throughput is inappropriate in some scenes which hopes secrecy outage probability of multiuser in cooperative OFDM networks is low. Furthermore, secrecy performance is poor when a single relay protocol is used. To address the problem, in [13–16], some adaptive hybrid relaying scheme is proposed.

To address the problems of above, we consider a scenario consisting of a base station, multiple relay nodes, multiple users, and a passive eavesdropper. And in this paper, we define secrecy outage probability of multiuser as performance indicator in cooperative OFDM network which considers user's scheduling fairness, and a adaptive hybrid relaying scheme which switches between Amplify-and-Forward protocol (AF) and Decode-and-Forward protocol (DF) for multiple relays is proposed.

In this paper, our goal is to reduce the secrecy outage probability of multiuser in cooperative OFDM networks by optimizing multiple variables, which includes adaptive hybrid relaying scheme, relay selection, resource allocation. Here, the relaying scheme includes Decode-and-Forward protocol (DF) and Amplify-and-Forward protocol (AF). To order to achieve the above goal, we establish a multi-variable optimization problem. Then, we convert the optimization problem into a graph theory problem. Lastly, numerical results illustrate that the proposed algorithm have better secrecy outage probability performance.

The rest of this paper is organized as follows. Section 2 introduces the system model. Section 3 focuses on the optimization for secrecy outage probability of multiuser in cooperative OFDM networks. Section 4 shows the numerical results. Finally, Sect. 5 offers conclusions.

2 System Model

As illustrated in Fig. 1, In this paper, we consider a cooperative OFDM network which consists of a base station (S), K relays (R), a passive eavesdropper (Eve) and N users ($d(1), \dots, d(N)$), the OFDM network has M available subcarriers ($N \leq M$). Each node has a single antenna, and operates in half-duplex mode. We call s-d pairs between base station and multiple users under different subcarrier. Due to channel fading, let's assume that there are no direct transmission links between S and $d(n)$ or Eve. We define the channel coefficient on subcarrier m from S to R, from R to $d(n)$ and from R to Eve as h_{sr}^m , $h_{rd(n)}^m$ and h_{re}^m , respectively. We assume that N_0 is the Gaussian noise variance, and channels are subjected to quasi-static flat fading. Finally, we assume that each node knows the full channel state information (CSI).

The cooperative relay transmission between each user pair is divided into two slots. In the process of cooperative transmission, the first transmission time-slot and second transmission time-slot use the same subcarrier by resource allocation. To improve performance of secrecy outage probability, a adaptive hybrid relaying

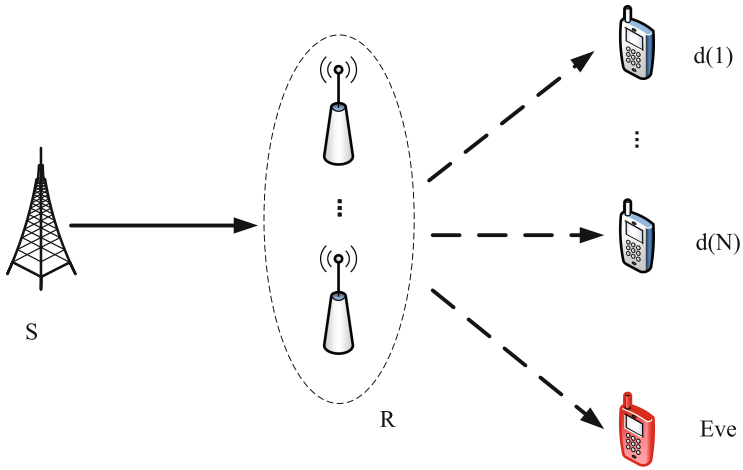


Fig. 1. System model.

scheme which switches between AF and DF for the relays is proposed. In such an adaptive hybrid relaying scheme, a relay could choose between AF and DF according to its own decoding ability.

3 Optimization Problem Description and Optimal Solution

3.1 Optimization Problem Description

The problem which we will solve is that in a multiple relays and multiuser cooperative OFDM network, how we jointly select its relaying transmission scheme, relay selection and resource allocation to minimize the secrecy outage probability of multiuser. To order to build the optimization problem effectively, the binary integral variables $\rho_n^i(r, m)$ represent a user's joint selection strategy. Concretely speaking, $\rho_n^i(r, m) = 1$ means that the n th user selects the r relay and the i relaying transmission scheme, and the first transmission time-slot and second transmission time-slot use the same subcarrier m . Finally, the variables $R_n^i(r, m)$ represent the secrecy rate which the n th user can obtain under the strategy of $\rho_n^i(r, m)$.

In such an adaptive hybrid relaying scheme, a relay could choose between AF and DF according to its own decoding ability. when the decoding ability of the relay node is strong, the DF relay protocol is used. Otherwise, the AF relay protocol is used instead. We show the achievable secrecy rate of using DF or AF protocol as follows.

(1) Amplify-and-Forward Relay Mode (AFM): When the relaying nodes are very far from the base station, the relays's decoding ability may become low. The AF relaying scheme may obtain a greater secrecy rate for users. In the

cooperative transmission process, the base station sends the information to the selected relay r on subcarrier m in the first time-slot. Then, the relay node r amplifies its received signals and sends them to the user n on subcarrier m in the second time-slot. The secrecy rate of AF relaying scheme can be expressed as follows,

$$R_n^1(r,m) = \frac{1}{2} \left\{ \begin{array}{l} \log_2 \left(1 + \frac{\gamma_0^2 |h_{sr}^m|^2 |h_{rd(n)}^m|^2}{\gamma_0 |h_{sr}^m|^2 + \gamma_0 |h_{rd(n)}^m|^2 + 1} \right) \\ -\log_2 \left(1 + \frac{\gamma_0^2 |h_{sr}^m|^2 |h_{re}^m|^2}{\gamma_0 |h_{sr}^m|^2 + \gamma_0 |h_{re}^m|^2 + 1} \right) \end{array} \right\}^+ \tag{1}$$

where $\{\cdot\}^+$ is defined as $\{\cdot\}^+ = \max(\cdot, 0)$ and $\gamma_0 = \frac{P_S}{N_0} = \frac{P_R}{N_0} = \text{SNR}$.

(2) Decode-and-Forward Relay Mode (DFM): When the relaying nodes are very close to the base station, the relays’s decoding ability may become high, The DF relaying scheme may obtain a greater secrecy rate for users. Similar to the AF relay protocol, when relay nodes use DF relay protocol, the base station sends the information to the selected relay r on subcarrier m in the first time-slot. Then, the relay decodes the received signal and forwards the decoded signal to the destination user n on subcarrier m in the second time-slot. The secrecy rate of DF relaying scheme can be expressed as follows,

$$R_n^2(r,m) = \frac{1}{2} \left\{ \begin{array}{l} \min \left\{ \log_2 \left(1 + \gamma_0 |h_{sr}^m|^2 \right), \right. \\ \left. \log_2 \left(\frac{1 + \gamma_0 |h_{rd(n)}^m|^2}{1 + \gamma_0 |h_{re}^m|^2} \right) \right\} \end{array} \right\}^+ \tag{2}$$

where $\{\cdot\}^+$ is defined as $\{\cdot\}^+ = \max(\cdot, 0)$ and $\gamma_0 = \frac{P_S}{N_0} = \frac{P_R}{N_0} = \text{SNR}$.

In this article, we want to reduce the secrecy outage probability of multiuser. An interruption occurs to a user pair when its secrecy rate is smaller than the secrecy outage threshold R . We define 0–1 binary variable to represent the secrecy outage of multiuser. The expression of secrecy interruption of user pair can be expressed as follows,

$$I_n^i(r,m) = \begin{cases} 0, & \rho_n^i(r,m) R_n^i(r,m) \geq R \\ 1, & \rho_n^i(r,m) R_n^i(r,m) < R \end{cases} \tag{3}$$

Next, we could obtain the secrecy outage probability of multiuser F as follows,

$$F = \frac{1}{N} \sum_{n=1}^N \sum_{i=1}^Q \sum_{r=0}^K \sum_{m=1}^M I_n^i(r,m) \tag{4}$$

which Q means different relaying scheme. Concretely speaking, $Q=1$ means that the user uses AF relaying scheme, and $Q=2$ means that the user uses DF relaying scheme.

To avoid interference among multiuser, A subcarrier can only be assigned to one user for transmitting information. The specific restrictions are expressed as follows,

$$\sum_{n=1}^N \sum_{i=1}^Q \sum_{r=0}^K \rho_n^i(r,m) \leq 1, m=1,2,\dots,M \tag{5}$$

Each user can only select a relay forwarding strategy for each information transmission and the user works on the same subcarrier in the first and second transmission time-slot. The specific restrictions are represented as follows:

$$\sum_{i=1}^Q \sum_{r=0}^K \sum_{m=1}^M \rho_n^i(r, m) \leq 1, n=1, 2, \dots, N \quad (6)$$

In summary, the optimization problem of minimizing the secrecy outage probability of multiuser in cooperative OFDM networks could be represented as follows,

$$\begin{aligned} \min_{\rho_n^i(r, m)} & \frac{1}{N} \sum_{n=1}^N \sum_{i=1}^Q \sum_{r=0}^K \sum_{m=1}^M I_n^i(r, m) a \\ \text{s.t.} & \begin{cases} \sum_{n=1}^N \sum_{i=1}^Q \sum_{r=0}^K \rho_n^i(r, m) \leq 1, m=1, 2, \dots, M \\ \sum_{i=1}^Q \sum_{r=0}^K \sum_{m=1}^M \rho_n^i(r, m) \leq 1, n=1, 2, \dots, N \\ \rho_n^i(r, m) \in \{0, 1\} \end{cases} \end{aligned} \quad (7)$$

In order to minimize the secrecy outage probability of multiple users in cooperation OFDM network, each user can not simply decide which relay node, relaying scheme, subcarrier to select according to user's own secrecy rate, but should be to find a optimal strategy which could minimize the secrecy outage probability of multiuser in whole cooperative OFDM network.

3.2 Optimal Solution

We find that the above established optimization problem is an integer programming problem through analysis. There are four optimization variables which includes relay nodes, relay forwarding strategy, user selection and available subcarrier. Decision sets include a total of 2^{NQKM} decision choice. Therefore, if we use the exhaustive search to solve the optimal solution, the time complexity of the solution is 2^{NQKM} . In order to reduce the computational complexity, we must find an efficient algorithm to solve the above optimization problem. In the following optimization solution, we find that the Hungarian algorithm could effectively solve the above integer programming problem. Through analysis, we could find that each user could only select one relay and one subcarrier in first and second time-slot. This characteristic implies that the optimization problem could indeed be transformed into a integer programming problem.

As illustrated in Fig. 2, in order to use graph theory to solve the optimization problem, we must construct a bipartite graph $G = (V \cup U, E)$. Firstly, we use set $V = \{(s, d(n)) | 1 \leq n \leq N\}$ to represent all possible user pairs, and set $U = \{(i, r, m) | 1 \leq i \leq Q, 0 \leq r \leq K, 1 \leq m \leq M\}$ to represent user's all possible joint strategies. The strategy $u \in U$ shows that a user selects relay protocol i , relay node r and transmits on subcarrier m during the first and second time-slots. If the user pair $v \in V$ has a greater secrecy rate than the secrecy outage threshold R under the strategy $u \in U$. We use one edge $e \in E$ to connected

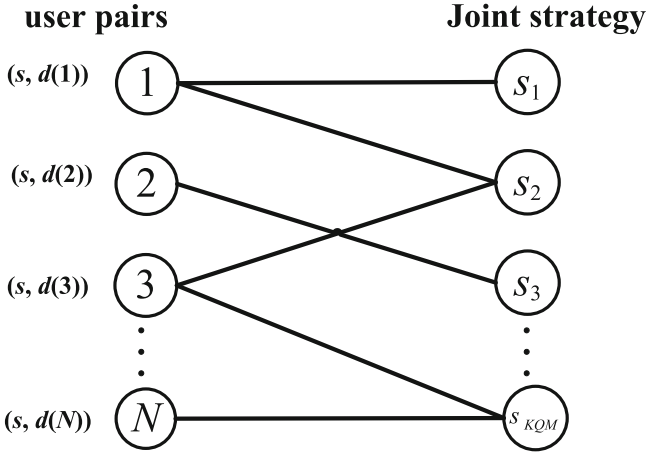


Fig. 2. The constructed bipartite graph.

vertex v with u . The set of all edges in graph G is E . When we have completed the abstract construction of the bipartite graph $G = (V \cup U, E)$. Then, the original optimization problem can be transformed into graph theory and solved equivalently by Hungarian algorithm.

The key of the proposed optimal solution is the equivalent transformation from parametric programming to the max-matching problem. When the bipartite graph G is constructed, the Hungary algorithm could effectively solve the above integer programming problem for G [17, 18]. The optimization solution is expressed as Algorithm 1.

Algorithm 1. Find the optimal relaying scheme and resource allocation

- 1: First, we should construct the bipartite graph G .
 - 2: Then, we use the Hungarian algorithm to obtain a max-matching T .
 - 3: The $|T|$ is maximum number of users without occurring secrecy interruption. Therefore, the minimal secrecy outage probability of multiuser in the cooperative OFDM network is $1 - |T|/N$.
-

4 Numerical Results

In the end, the numerical results are given to demonstrate the performance of the proposed algorithm which hopes to minimize secrecy outage probability of multiuser in the cooperative OFDM network. The simulation parameters are given as follows. We fix base station at point $(0, 0)$, relay nodes, multi-users, and the passive eavesdroppers are randomly distributed in a two-dimensional 1×1 rectangular plane. The simulation mainly considers small scale fading. The number of users are $N = 20$ and there are $M = 20$ available subcarriers in the

cooperative OFDM network. The numerical simulation is performed over 1000 independent Rayleigh channel realizations totally.

Figure 3 gives the secrecy outage probability of multiuser under different SNR conditions. And in this simulation, we set up the number of relay nodes $K = 6$, secrecy outage threshold $R = 1$ bit/s/Hz. From the simulation result of Fig. 3, it can be seen that the proposed joint algorithm can achieve a lower secrecy outage probability of multiuser under different SNR conditions compared to AF or DF relay protocol. Figure 3 also shows that under different SNR conditions, the best transmission mode is hybrid relay protocol. The relay nodes can automatically switch according to according to its own decoding ability, so the proposed algorithm compared to the AF or DF relaying protocol has a lower the performance of secrecy outage probability.

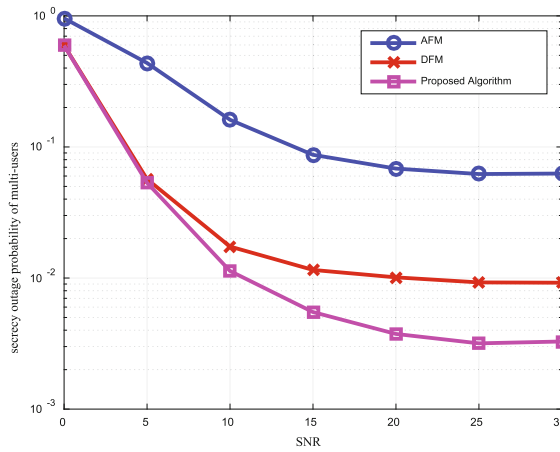


Fig. 3. Secrecy outage probability of multi-users under different SNR.

Figure 4 gives the secrecy outage probability of multiuser under different secrecy outage threshold R , And in this simulation, we set up the number of relay nodes $K = 6$, $SNR = 5$ dB. From the simulation result of Fig. 4, it can be seen that the proposed algorithm has better secrecy outage probability performance than AFM or DFM, and secrecy outage probability increases with the increasing of secrecy outage threshold R .

Figure 5 gives the secrecy outage probability of multiuser under different number of relay nodes, And in this simulation, we set up $SNR = 10$ dB, secrecy outage threshold $R = 1$ bit/s/Hz. From the simulation result of Fig. 5, it can be seen that the proposed algorithm has better secrecy outage probability performance than AFM or DFM, and secrecy outage probability decreases with the increasing of number of relay nodes. This is because, with the increasing of number of relay nodes, the channel state condition between base station and user is better, so secrecy outage probability of multiuser is lower with the increasing of number of relay nodes.

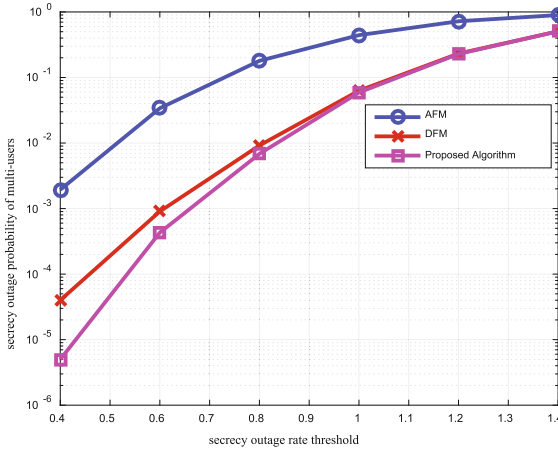


Fig. 4. Secrecy outage probability of multi-users under different secrecy outage threshold.

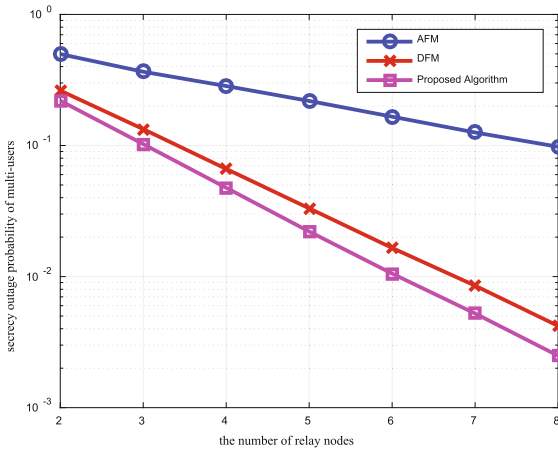


Fig. 5. Secrecy outage probability of multi-users under different number of relay nodes.

5 Conclusions

In this paper, we propose a secure algorithm towards minimizing the secrecy outage probability of multiuser in cooperative OFDM network. Firstly, To order to achieve the above goal, we establish a multi-variable optimization problem. Then, we convert the optimization problem into a graph theory problem. Lastly, numerical results illustrate that the proposed algorithm has a lower secrecy outage probability.

References

1. Shannon, C.E.: Communication theory of secrecy systems. *Bell Syst. Tech. J.* **28**(4), 656–715 (1949)
2. Wyner, A.D.: The wire-tap channel. *Bell Syst. Tech. J.* **54**(8), 1355–1387 (1975)
3. Li, J., Petropulu, A.P., Weber, S.: Optimal cooperative relaying schemes for improving wireless physical layer security. *IEEE Trans. Sig. Process.* **59**(10), 4985–4997 (2011)
4. Yang, Y., Li, Q., Ma, W.K., Ge, J.: Cooperative secure beamforming for AF relay networks with multiple eavesdroppers. *IEEE Sig. Process. Lett.* **20**(1), 35–38 (2013)
5. Dong, L., Han, Z., Petropulu, A.P., Poor, H.V.: Improving wireless physical layer security via cooperating relays. *IEEE Trans. Sig. Process.* **58**(3), 1875–1888 (2010)
6. Goeckel, D., Vasudevan, S., Towsley, D., Adams, S.: Artificial noise generation from cooperative relays for everlasting secrecy in two-hop wireless networks. *IEEE J. Sel. Areas Commun.* **29**(10), 2067–2076 (2011)
7. Gamal, H.E., Lai, L.: The relay-eavesdropper channel: cooperation for secrecy. In: *IEEE International Symposium on Information Theory*, pp. 931–935 (2012)
8. Mo, J., Tao, M., Liu, Y.: Relay placement for physical layer security: a secure connection perspective. *IEEE Commun. Lett.* **16**(6), 878–881 (2012)
9. Cai, C., Cai, Y., Wang, R., Yang, W.: Resource allocation for physical layer security in cooperative OFDM networks. In: *IEEE International Conference on Wireless Communications Signal Processing*, pp. 1–5 (2015)
10. Jeong, C., Kim, I.M.: Optimal power allocation for secure multicarrier relay systems. *IEEE Trans. Sig. Process.* **59**(11), 5428–5442 (2011)
11. Ng, D.W.K., Lo, E.S., Schober, R.: Secure resource allocation and scheduling for OFDMA decode-and-forward relay networks. *IEEE Trans. Wirel. Commun.* **10**(10), 3528–3540 (2011)
12. Cai, C., Cai, Y., Yang, W.: Subcarrier allocation for physical-layer security in cooperative OFDMA networks. *IEICE Trans. Commun.* **94**(12), 3387–3390 (2011)
13. Divya, T., Gurralla, K.K., Das, S.: Performance analysis of hybrid decode-amplify-forward (HDAF) relaying for improving security in cooperative wireless network. In: *Communication Technologies*, pp. 682–687 (2015)
14. Chen, H., Liu, J., Zhai, C., Zheng, L.: Performance analysis of SNR-based hybrid decode-amplify-forward cooperative diversity networks over rayleigh fading channels. In: *Wireless Communications and Networking Conference*, pp. 1–6 (2010)
15. Duong, T.Q., Zepernick, H.: Hybrid decode-amplify-forward cooperative communications with multiple relays. *IEEE Trans. Sig. Process.* 273–278 (2009)
16. Duong, T.Q., Zepernick, H.J.: On the performance gain of hybrid decode-amplify-forward cooperative communications. *EURASIP J. Wirel. Commun. Netw.* **2009**, 1–10 (2009)
17. Chen, H., Ren, P., Sun, L., Du, Q.: A joint optimization of transmission mode selection and resource allocation for cognitive relay networks. In: *2013 IEEE International Conference on Communications (ICC)*, pp. 2852–2856 (2013)
18. Koide, T., Kubo, H., Watanabe, H.: A study on the tie-set graph theory and network flow optimization problems. *Int. J. Circ. Theory Appl.* **32**(6), 447–470 (2004)



Dynamic Group Behavior Analysis and Its Application in Network Abnormal Behavior Detection

Yan Tong^{1(✉)}, Jian Zhang¹, Wei Chen¹, Mingdi Xu², and Tao Qin³

¹ System Research Department, Wuhan Digital Engineering Institute,
718 Luoyu Road, Hongshan District, Wuhan, China
tongyan.cherish@139.com, richardxx@126.com,
772382203@qq.com

² System Software Department, Wuhan Digital Engineering Institute,
718 Luoyu Road, Hongshan District, Wuhan, China
mingdixu@163.com

³ School of Electronic and Information Engineering, Xi'an Jiaotong University,
28 Xianning West Road, Xi'an, Shaanxi, China
qin.tao@mail.xjtu.edu.cn

Abstract. Focus on the difficulty of large-scale network traffic monitoring and analysis, this paper proposed the concepts of Group Behavior Flow model to aggregate traffic packets and perform abnormal behavior detection. Based on the flow model the pivotal traffic metrics can be extracted while the number of flow records are reduced significantly. Secondly, we employ the graph model to capture the traffic feature distribution between different group users. And optical flow analysis methods are proposed to extract the dynamic behavior changing features between different groups and achieve the goal of abnormal behavior detection. The experimental results based on actual traffic traces show that the methods proposed in this paper can capture the traffic features effectually in the current 10 Gbps network environment, and achieve the goal of abnormal behavior detection and abnormal source location, which is very important for traffic management.

Keywords: Group user model · Dynamic behavior · Optical flow analysis
Abnormal detection

1 Introduction

It is an important task that how to capture and analysis abnormal network traffic in order to maintain network under control, but it is more and more difficult to capture and analysis the abnormal traffic with the increase of number of users and bandwidth of backbone networks [1]. How to deal with the massive traffic data and detect the abnormal behavior effectively is an urgent problem to be solved.

Analysis the statistical traffic characteristics (such as the total number of packets per unit time, bytes, etc.) can not satisfied the need for traffic monitoring in large scale networks, many abnormal behavior detection methods based on suddenly change are ineffective [2-4]. In order to overcome this difficulty, CISCO proposed the conception

of Netflow [5], based on the Netflow framework many detailed features can be extracted from the raw traffic, but with the rapid growth of network traffic, even a medium-size enterprise LAN can generate about millions Netflow records per minute, which bring great difficulties for mining network traffic characteristics effectively. To solve those challenges, Kim and Reddy [6] proposed a method to describe network traffic characteristics based on image, which can monitor network traffic characteristics effectively, abnormal detection methods suit for large scale networks are also proposed. In order to further reduce the difficulty to monitor large-scale network traffic, Lakhina proposed the concept of ODFlow in [7], which divides the network into different domains with AS (Autonomous System), all packets through the border routers will be aggregated for different ODFlow records according to the source AS and destination AS. However, this method is only suitable for detecting abnormal behavior in autonomous domains and can't be applied to large-scale enterprise LAN.

To solve the above problems, this paper proposed the concepts of Group Behavior Flow Model to describe the network traffic characteristics, group users can be defined by different network address-prefix, such as using 24-bit address-prefix to aggregate network IP address, which can generate different scale network group users. The packets which have the same source group and destination group are aggregated into a group behavior flow within a certain statistical interval. The distribution of network traffic on different logical links consisted by different groups can be described by a graph, and different elements of the graph describe the characteristics of communication relationship between different group behaviors. The proposed methods can detect abnormal behaviors based on the dynamic change of the feature distributions between adjacent time. The experimental results based on actual traffic traces show that the methods proposed in this paper can capture the traffic features effectually in the current 10 Gbps network environment, and achieve the goal of abnormal behavior detection and abnormal source location.

2 The Concept of Group Behavior

The results of the literature [8] show that more than 98% of IP addresses are no more than 1 km in physical distance for the same C network segment. The survey results about the IP address distribution based on the campus network of Xi'an Jiao Tong University show that the IP address in the same C network segment is distributed in the same dormitory building, that is to say the physical distance is very close. Also the students from the same school are often in the same dormitory, which shows the network users in the same C network segment have the same network requirements, which also provide a reasonable explanation for splitting users in to the group flow model according to the C network segment.

Figure 1 presents the definition of group behavior flow, according to the monitoring location the network are divided into two parts, the internal monitoring network and external network, the internal monitoring network is the network need to be monitored, which is the campus network of Xi'an Jiao Tong University, the external network is the external Internet which composed by the monitoring network communicate with. The network topology can be described by the logical links formed between groups, then

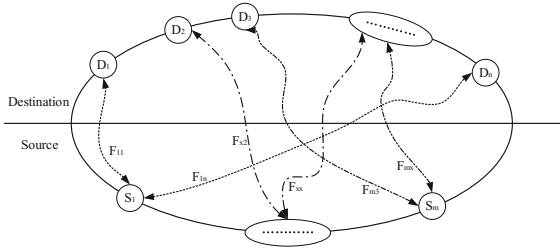


Fig. 1. Group behavior flow

the monitoring of network abnormal behaviors can be implemented according to the network traffic distribution on the logical topology. The paper only focuses on the communication between internal network and external network, and the change of the interaction behavior between the internal users and external network.

The variable d represents the destination group, s shows the source group, F means the network flow between groups, and such as F_{11} indicates the network flow from source group s_1 to destination d_1 . We can describe the network logical topology using the below matrix according to the definition of group behavior flow.

Region	d_1	d_2	$d_{..}$	d_n
s_1	F_{11}	F_{12}	$F_{1..}$	F_{1n}
s_2	F_{21}	F_{22}	$F_{2..}$	F_{2n}
$s_{..}$	$..$	$..$	$..$	$..$
s_m	F_{m1}	F_{m2}	F_{m3}	F_{mn}

The above matrix uniquely defines the interaction behavior between internal and external network. As time goes on, the change of the element of the above matrix can reflect the changes of the network traffic distribution. The paper will use this change to achieve network traffic monitoring.

3 Algorithm Framework of Network Traffic Feature Extraction

According to the above definition of group behavior flow, the processing framework of this paper is described as Fig. 2.

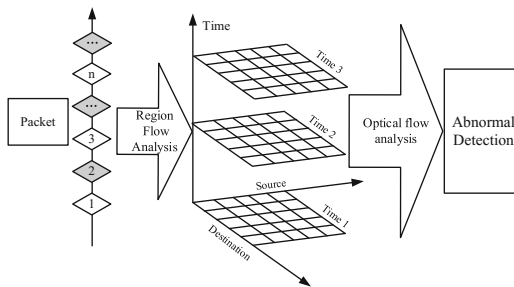


Fig. 2. The algorithm framework based on group behavior flow

Figure 2 is the algorithm framework of network traffic monitoring based on group behavior flow. First of all, according to the definition of network group flow, we regard the network packet sequence as group behavior flow, and then form the distribution matrix which can describe network traffic characteristics. As time goes on, it can form the traffic characteristics graph for different time, the behavior monitoring of dynamic network and extraction of behavior features can be implemented using the method of optical flow analysis which can analyze the dynamic change characteristics of network traffic among the groups with the change of time.

4 Description of Group Network Behavior Feature

4.1 Description of Group Network Behavior

Network traffic is generated by users, and this paper will describe network behavior by the dynamic characteristics of network traffic statistics. Supposing the sampling time is the variable t , $Byte_{ij}(t)$ means the total amount of data transmitted between the source region S_i and the destination region d_j , and the definition of data distribution function as shown as formula (1)

$$\begin{cases} p(s_i, d_j, t) = \frac{Byte_{ij}(t)}{\sum_{ij} Byte_{ij}(t)} \\ \Delta p(s_i, d_j) = \Delta p(s_i, d_j, t) - \Delta p(s_i, d_j, t - 1) \end{cases} \quad (1)$$

The distribution function is uniquely defined the distribution of the logical links which formed by the communication relationship among different groups at time t , the distribution can reflect the characteristics of users behavior in a certain time point, when the network is running normally, the distribution has certain stability, namely the changes of network data in the logical link are very small, or is approximately stable, this paper summarizes the change of distribution as follows:

- (1) The stability of group behavior: the situation can describe the most common habitual behavior in the network, namely the network user behaviors are relatively stable in a short time interval, and the behavior changes gently, and the case is described as follows:

$$\begin{cases} p(s_i, d_j, t - 1) \neq 0 \\ p(s_i, d_j, t) \neq 0 \\ \Delta p(s_i, d_j) \approx 0 \end{cases} \quad (2)$$

- (2) The change of network group behavior, the abrupt change of network behavior is the main information source of network abnormal behavior monitoring, it can be described as formula (3).

$$\begin{cases} p(s_i, d_j, t - 1) \neq 0 \\ p(s_i, d_j, t) \neq 0 \\ \Delta p(s_i, d_j) \neq 0 \end{cases} \quad (3)$$

- (3) The disappearance of network group behavior, which represents the disappearance of network behavior among a particular group, and it describes as formula (4).

$$\begin{cases} p(s_i, d_j, t - 1) \neq 0 \\ p(s_i, d_j, t) = 0 \end{cases} \quad (4)$$

- (4) The birth of network group behavior, which represents the birth of network behaviors among specific groups, and it describes as formula (5).

$$\begin{cases} p(s_i, d_j, t - 1) = 0 \\ p(s_i, d_j, t) \neq 0 \end{cases} \quad (5)$$

The above four cases describe the changes of network behavior on different logical links, case 1 describes the stability of network behavior statistically, and it is the main feature of network behavior. The other three cases describe difference changes of network behavior. Case 2 describes the changes of transmission between network groups, which shows the abrupt change of data transmission between groups. Case 3 and case 4 describe the migration of network behavior among different groups. Those three cases are the key characteristics which should be extracted for abnormal behavior detection.

4.2 Network Abnormal Behavior Detection

The occurrence of network abnormal behavior will lead to changes of network traffic patterns, the distribution characteristics of groups which include hackers and victims will change in a certain degree. When there are massive attacks (such as DDOS attacks and worm attacks), the network traffic will have significant changes on the logical link. Furthermore, the behaviors among different groups include victims are will express a certain synergy, this paper uses two parameters to measure those large-scale network abnormal behaviors.

We define the similarity between network group behaviors to measure the synergy among network group behaviors. The behavior similarity between group s_i and group s_j is defined as formula (6).

$$r(S_{ij}) = \frac{\sum_{k=1}^n w_{ijk} (p(s_i, d_k) + p(s_j, d_k))}{\sum_{k=1}^n p(s_i, d_k) + \sum_{k=1}^n p(s_j, d_k)} \quad (6)$$

The weight coefficient w_{ijk} means $p(s_i, d_k)$ and $p(s_j, d_k)$ are not null at the same time. It to say if there is communication relationship between the source group s_i and

the destination group d_k , then the value of w_{ijk} is 1, otherwise 0. If the similarity between groups is bigger than the threshold, then we can conclude that there is a synergistic phenomenon between network group behavior, and can further analyze the reasons for the phenomenon.

We define the maximum value of network group behavior change as the abnormal degree of network group behavior, which can be used to described the changes of network group behavior on logical links, to describe whether there are large-scale network abnormal behaviors on logical links, such as massive network attacks (DDOS and DOS attacks)

$$c(s_i) = \max_j (|\Delta p(s_i, d_j)|) \quad (7)$$

5 Experimental Results

5.1 Network Traffic Acquisition

The network traffic used in the paper collects from the ingress router of the backbone network of Northwest network center of education network, and the bandwidth is 10 Gbps. Northwest network center of education network is the access point of CERNET for the educational institutions in Northwest provinces, and also the access point for some commercial organizations. There are about 3 million hosts are access to internet through it. The monitored network includes nearly 80 C network segments, the monitoring hosts about 10 thousand, and the web traffic about 8 Gbpm, and the network traffic used in the experiment lasted about 10 h.

5.2 Network Traffic Analysis

According to the definition of network group flow, firstly the network IP addresses should be solved by 24-bit network address prefix, which can form different network user groups, and then form different network links according to the communication between groups, and use the distribution of network traffic on the logical links to describe the characteristics of network group behavior.

We extract a sampling time randomly, the distribution of network traffic on different logical links is shown as Fig. 3, from the figure we can see that the amount of variation of data flow between different groups, and a small number of region flow carries most of network data, there are only account for about 1/10000 of the total traffic in some region flow, which is the phenomenon of heavy tail of network traffic.

Optical flow analysis is widely used in the feature extraction in images [9], the difference between adjacent frames of moving images can reflect the change characteristics of images, which can be used to detect the moving object and extract features. In this paper, we use the distribution which is formed by network traffic in different time to describe the characteristics of network behavior, and the difference between adjacent distribution graphs can describe the dynamic characteristics of network behavior. We take two adjacent frames randomly, and the differences of them are

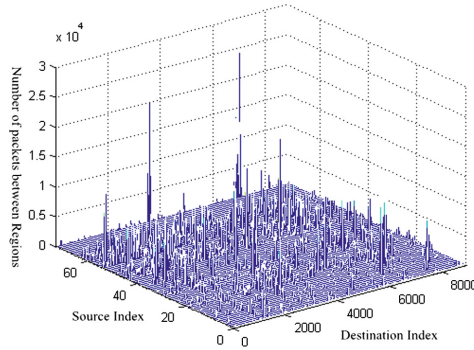


Fig. 3. The distribution of network traffic on the region links

shown as Fig. 4. From Fig. 4, we can see that the network behaviors described by distribution are approximately stable on most logical links of groups, and the dynamic changes are close to zero. But there are a few larger changes of network behavior in a small number of networks, which express the increase and decrease of communication volume among the network groups dramatically. According to the characteristics, we can locate the logical links which have violently changes of network behaviors and network groups, and lay the foundation for the control of network abnormal behavior.

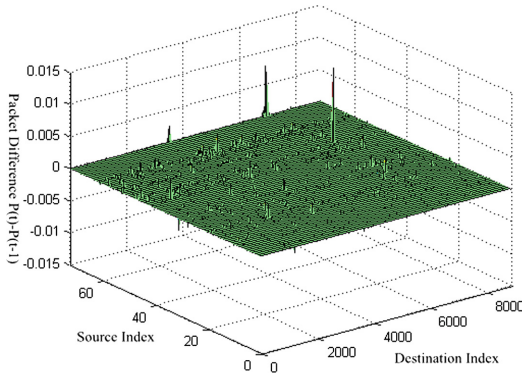


Fig. 4. The difference between adjacent frames of network distribution graph

From the Fig. 4, we can see that there are three peak positions about the difference between adjacent distributions, which describes the changes of network behavior on three logical links are obviously, according to analysis, we can also find that the changes account for 23.6% of the total data changes, the three logical links are (s_{50}, d_{7145}) , (s_{73}, d_{6899}) and (s_{73}, d_{6938}) respectively. The changes of network behavior on the three-logical links lead to the overall changes of network behavior, which is very important information to study network abnormal behaviors. In addition, from Fig. 4, we can also see that the changes in the amount of data are mainly concentrated on the

indexes of three groups, s_{50} , s_{64} and s_{73} , the variability of behavior of the users in the three source groups accounts for 48.2% of the total variability of behavior. The three source groups fluctuate intensely for network behavior, and they are the focus groups which we should monitor.

5.3 Network Abnormal Behavior Detection

According to the change characteristics of the network behavior on the logical link described above, the paper calculates the similarity of network behaviors among network source groups, and the results are shown as Fig. 5.

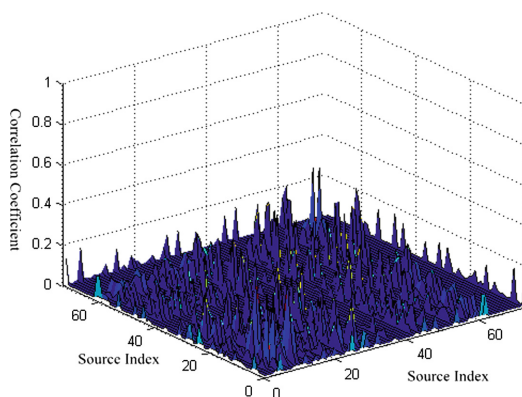


Fig. 5. The similarity of network behavior among source region

From Fig. 5, we can see that the similarity of network behavior among network source group is very low generally. That is to say, the similarity of network behavior among network source group is very small, namely there is no large-scale network collaboration behavior in the network. But if it appears the network collaboration behavior of different groups in network, namely there are the same behavior characteristics in different groups, the hosts in the network groups may be controlled by hackers, who are detecting the network or some other destructive activities for network.

The change degree of the group behavior to measure the changes of network abnormal behavior is shown as Fig. 6. From the figure we can see that the vast majority of network group behavior between adjacent frames is table, but we can also see that there is a group which changes dramatically, denoted by an asterisk. According to the change we can conclude that there are massive network abnormal behavior in the source groups of index numbers 73 and 50. According to analysis, we find that there are DOS attacks on the two logical links at the time. There are a large number of UDP packets on the two logical links flowing to 80 ports, which seriously occupy the network bandwidth.

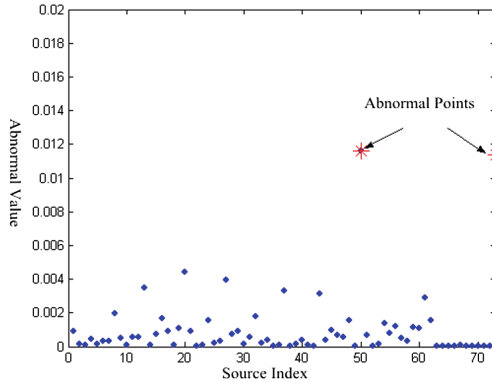


Fig. 6. The change degree of region behavior

6 Summary

As it is very difficult to monitor large-scale network traffic, we proposed the conception of network group behavior flow. From the results of experiment, we can see that the network group behavior flow can describe the characteristics of network traffic effectively, although the method of group flow aggregation can reduce the fine-grained characteristics of some network traffic, the conception of group flow can describe the characteristics of large-scale network flow effectively. The optical flow analysis proposed in the paper can describe the dynamic changes of network group accurately and detect the fluctuation groups of network behavior in real time, and lay the foundation for the control of network abnormal behavior.

Acknowledgments. The research presented in this paper is supported in part by the Natural Science Foundation of China (61502438, 61672026), Natural Science Foundation of Shaanxi Province (2016JM6040), and Chinese Defense Advance Research Program (B0820132036).

References

1. Baldi, M., Baralis, E., Risso, F.: Data mining techniques for effective and scalable traffic analysis. In: IEEE International Symposium on Integrated Network Management, 15–19 May 2005, pp. 105–118 (2005)
2. Zhou, A., Guang, C., Guo, X.: High-speed network traffic measurement methods. *J. Softw.* **25**(1), 135–153 (2014)
3. Zhang, B., Yang, J., Wu, J.: Survey and analysis on the internet traffic model. *J. Softw.* **22**(01), 115–131 (2011)
4. Wang, J., Rossell, D., Cassandras, C.G., et al.: Network anomaly detection: a survey and comparative analysis of stochastic and deterministic methods. In: Proceedings of the 52nd IEEE Conference on Decision and Control, Florence, Italy (2013)
5. CISCO NetFlow: Cisco systems, Inc. (2004). http://www.cisco.com/en/US/products/ps6601/products_white_paper09186a00800a3db9.shtml

6. Kim, S.S., Reddy, A.L.N.: A study of analyzing network traffic as images in real-time. In: 24th Annual Joint Conference of the IEEE Computer and Communications Societies, 13–17 March 2005, vol. 3, pp. 2056–2067 (2005)
7. Lakhina, A., Papagiannaki, K., Crovella, M., et al.: Structural analysis of network traffic flows. In: Proceedings of the Joint International Conference on Measurement and Modeling Of Computer Systems, pp. 61–72 (2004)
8. Freedman, M.J., Vutukuru, M., Feamster, N., et al.: Geographic locality of IP prefixes. In: Proceedings of the ACM Internet Measurement Conference Berkeley, CA, pp. 153–158, October 2005
9. Wang, X., Zhang, G.: Research on moving object detection method based on optical flow. *J. Comput. Eng. Appl.* **40**(1), 43–46 (2004)



A Simplifying Logic Approach for Gate Level Information Flow Tracking

Yu Tai, Wei Hu^(✉), Dejun Mu, Baolei Mao, Lantian Guo, and Maoyuan Qin

School of Automation, Northwestern Polytechnical University, Xi'an, China
taiyu@mail.nwpu.edu.cn, weihu@nwpu.edu.cn

Abstract. With the increase of design scale and complexity, security vulnerabilities residing in hardware designs become hard to detect. Existing functional testing and verification methods cannot guarantee test and verification coverage in design phase. Fortunately, gate level information flow tracking (GLIFT) has been proposed to enforce bit-tight information flow security from the gate level to detect security vulnerabilities and prevent information leakage effectively. However, there is a significant limitation that the inherent high complexity of GLIFT logic causes significant overheads in static verification and physical implementation. In order to address the limitation, we propose a simplified GLIFT method that incorporates more detailed optimization logic routes to reduce its complexity and allow don't care to simplify original GLIFT logic. Experimental results have demonstrated that the simplified GLIFT method can reduce the design overhead in several gates by sacrificing a fraction of GLIFT precision.

Keywords: Hardware security · Gate level information flow tracking
Security lattice · Don't care · Optimization

1 Introduction

Existing functional verification methods cannot ensure testing and verification coverage or detect design flaws, security vulnerabilities, malicious code and other security vulnerabilities. Guaranteeing hardware security is a big challenge for designers due to the increasing size of circuit design and unpredictable supply chain. For example, an implementation flaw in Qualcomm's TrustZone is used to break Android's full disk encryption [1]. However, there is a fact that the traditional hardware design flows focus on function verification and provide limited security verification. It is almost inevitable that these designs will have design vulnerabilities and security flaws. Recent researches revealed that security vulnerabilities in hardware devices are more than designers might previously have thought [2]. There is a relatively high estimated rate of design flaws in millions of lines of hardware description language (HDL) code [10].

There are two information security policies non-interference [7] and Bell and LaPadula [3], which are frequently used to isolate data in the systems. While

these common security policies are very strong and strict, which they all require that trusted information should be never affected by untrusted and secret information should never leak to a public domain.

As a technique for enforcing information policies, information flow tracking (IFT) that has been proven to be effective in detecting security vulnerabilities and preventing attacks through side channels in the end-to-end designs, can be used to apply the principle of hardware designs to the specification of their security requirements. IFT is a frequently used method to analyze the security of a system [5,19]. IFT provides an effective approach for preventing unintended interaction between different components in a system. It is useful for deploying information flow security and enforcing its security properties at various levels of the entire system, including compiler/programming language [14], operating system [11,17], instruction set architecture [15] and hardware level [16,20]. However, the coarse-grained design rules are generally used in these previous IFT methods, which lead to higher design complexity [13,19], the huge number of additional overhead [11,20] or overly conservative propagation policies [4,18].

To fully account for information flow security, gate level information flow tracking (GLIFT), which uses fine granularity labels and propagation policies, has been proposed to precisely measure how information flows through Boolean gates in hardware system [16]. It captures and monitors all logical flows in a unified manner that enables the verification of important security properties related to confidentiality, integrity, and logical side channels. Recent work has shown that GLIFT can be used to investigate the precision and complexity tradeoffs of GLIFT through logic synthesis optimizations [8], guarantee information flow security in embedded systems [12], and detect hardware Trojans that violate information flow security properties related to confidentiality and integrity [9].

The original GLIFT logic method generates information flow tracking logic through direct GLIFT library mapping, which can be confronted with high overheads in terms of design complexity and verification performance. In this paper, we propose a new simplified method that use don't care to search out some optimized routes to generate the most simplified GLIFT logic. Specifically, this paper makes the following contributions:

1. Proposing an approach to search out the most simplified logic routes for gate level information flow tracking;
2. Providing this simplified GLIFT logic method to implement reduced GLIFT logic and optimized design;
3. Presenting optimized and comparative analysis using primitive gates with don't care to evaluate area and delay.

The reminder of this paper is organized as follows. Section 2, we briefly cover the background in security lattices and GLIFT. In Sect. 3, we discuss how to carry out the label propagation and mapping. We propose the simplified method to optimize GLIFT logic in Sect. 4. Section 5 presents experimental results using don't care optimizations. We conclude the paper in Sect. 6.

2 Background

We explain background work in this section that enable a better understanding of our research. We focus on various background literatures including security lattice model, gate level information flow tracking and two-level information flow tracking.

2.1 Security Lattice Model

The lattice model was first proposed for describing information flow policy by Denning [6]. An information flow policy can be modeled as a finite security lattice $L = \{SC, \sqsubseteq\}$, where SC is the set of security classes indicating different security levels of data objects and \sqsubseteq defines the partial order on these security classes.

The symbols in the lattice represent security classes i.e., $SC = \{\text{Unclassified}, \text{Confidential}\}$. Defined function $L: x \rightarrow SC$ to represent safety data object x belongs to the security class. The arrow indicates the direction of information flows that reflect security policy and the partial order defined by the security lattice. Let U, C, S and T denote Unclassified, Confidential, Secret and Top Secret respectively. For better understanding, Let $U, C,$ and S denote Unclassified, Confidential and Secret respectively in the three-level linear security lattice. So security class set is simplified to $SC = \{U, C, S\}$. Security class set can be simplified to $SC = \{U, C, S, T\}$ in the four-level linear security lattice.

2.2 Gate Level Information Flow Tracking

Gate level information flow tracking (GLIFT) is established for monitoring the flow of information that models digital information flows using bit level labels at the Boolean level [16]. GLIFT provides a model for understanding how data propagates through a design. In GLIFT, data are typically assigned a label to characterize their trustworthiness or security level, such as untrusted/trusted, low/high or unclassified/confidential/secret. It adopts fine-grained labels to implement strict and precise analysis at Boolean level, which this label is propagated through the system under pre-defined policies to prevent unintended information flows. Each binary data bit is associated with a tag called taint label (security label). When the data involve in computing in the hardware system, the taint label also will be propagated in this hardware circuit. The information included in the data is called to be tainted when its taint is logic true '1' and untainted when its taint is logic false '0'. Taint is propagated from the input to the output of the hardware design if and only if the value of any tainted input has an influence on the output.

2.3 Two-Level Information Flow Tracking

Binary security properties can be verified on a two-level information flow tracking model. The information flow security property enforced by the corresponding security lattice states that **HIGH** information should never flow to a **LOW** portion.

Two-level information flow tracking model targets a two-level security lattice $LOW \sqsubseteq HIGH$. Under such a lattice, all signals in the hardware design will be classified as either LOW or $HIGH$. Then, a two-level information flow model will be used to understand the flow of $HIGH$ information. Consider a two-input AND (AND-2) gate and let input A be LOW while input B be $HIGH$. The information flow model should precisely track when the $HIGH$ information in B could flow to the output O . Table 1 illustrates such a model.

Table 1. A partial two-level information flow model for AND-2

A	B	O
(LOW, 0)	(HIGH, 0)	(LOW, 0)
(LOW, 0)	(HIGH, 1)	(LOW, 0)
(LOW, 1)	(HIGH, 0)	(HIGH, 0)
(LOW, 1)	(HIGH, 1)	(HIGH, 1)

According to the notion of information flow, the $HIGH$ information in B flows to O if and only if B has an effect on the output. In the first two rows of Table 1, the LOW input dominates the output and thus there is no $HIGH$ information flow.

Table 2. A partial two-level information flow model for OR-2

A	B	O
(LOW, 0)	(HIGH, 0)	(HIGH, 0)
(LOW, 0)	(HIGH, 1)	(HIGH, 1)
(LOW, 1)	(HIGH, 0)	(LOW, 1)
(LOW, 1)	(HIGH, 1)	(LOW, 1)

Similarly, consider a two-input OR (OR-2) gate and let input A be LOW while input B be $HIGH$, the partial results for OR-2 can be shown in Table 2. Information of a higher security level cannot flow to the output when an input of lower security level dominates the output. The difference is that the model allows a finer classification of security labels, which is desirable when reasoning about the security between multiple parties.

3 Label Policy and Mapping

In this section, we provide an approach for information flow tracking. A fundamental problem in this process is to define label propagation policies and map label encoding for GLIFT library.

3.1 Label Propagation Policy

The two-level IFT model provides a precise measurement of if there is a flow. Take a two-input AND (AND-2) gate for example. Let A , B and O be its inputs and output respectively. Use At , Bt and O_t to denote their security labels under two-level IFT. The label propagation policy for AND-2 under two-level IFT can be formalized as (1).

$$O_t = A \cdot B_t + B \cdot A_t + A_t \cdot B_t \tag{1}$$

Equation (1) indicates that when A is logical 1 and B is HIGH, the output will be HIGH; when B is logical 1 and A is HIGH, the output will also be HIGH; Or when both A and B are HIGH, the output will doubtlessly be HIGH. It cares about if there is any HIGH information flow from either A or B to the output.

As mentioned, the two-level IFT model precisely indicates if there is a flow. When there is no flow, the security label should be all zeros. The subtle case is when there are HIGH inputs. The label propagation policy should track the HIGH information flow from each of these inputs to the output. Figure 1 describes such a label propagation policy for AND-2 gate and OR-2 gate, which track the information flow from both inputs to the output.

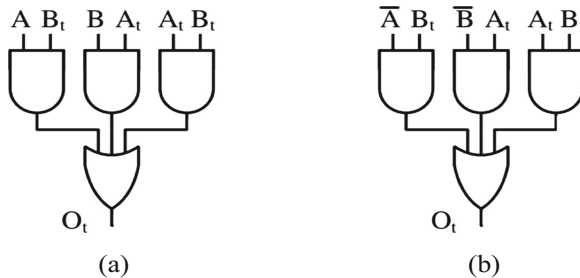


Fig. 1. (a) Label propagation policy for AND-2 gate; (b) Label propagation policy for OR-2 gate

From Fig. 1(a), A and B are the original inputs of AND; A_t and B_t are the two-level security labels; We define O_t as an output variable, which reflects the two-level security label for the output. The OR-2 gate is the dual of AND-2 according to Demorgan’s law. Thus, its label propagation policy can be derived by inverting the original inputs A and B . Using the same notation as AND-2, it can be seen from Fig. 1(b).

3.2 Label Mapping

To track the propagation of information flows, we need to set up the single bit security label for two-level IFT or binary security label for multi-level IFT (three-level or four-level) to a one-hot encoding. In this way, each bit in the security

label only tracks the propagation of one bit. For a better understanding, the two-level IFT method targets a two level security label. Thus, we have the taint labels $At[w] \in \{0, 1\}$, where $0 \leq w \leq 3$. The multi-level IFT method allows a finer classification of security labels. If each individual bit in A takes a different label, we have the taint labels $At[w] \in \{00, 01, 10, 11\}$. Using a binary encoding, two bits will be enough for encoding the taint labels.

4 Simplified Model

4.1 Logic Optimization with Don't Care

As a common optimization method for logic synthesis in integrated circuit design, don't care computation can be used to optimize GLIFT logic, where the different routes in the logic network may affect the way in which signal flows through hardware design. Consider two-level linear security lattice (such as Unclassified and Confidential). If don't care is not considered, AND-2 GLIFT logic is described as first row in Table 3. In the scheme as Fig. 2, we can study the various routes for don't care to achieve an optimized GLIFT logic. After the above don't care is considered, AND-2 GLIFT logic can be simplified as Table 3 at simplified nodes in different logic synthesis.

#	A	At	B	Bt	Orig_Ot	Simp_Ot	#
0	0	0	0	0	0	0	
1	0	0	0	1	0	→ -	1
2	0	0	1	0	0	0	
3	0	0	1	1	0	→ -	2
4	0	1	0	0	0	→ -	3
5	0	1	0	1	1	1	
6	0	1	1	0	1	1	
7	0	1	1	1	1	1	
8	1	0	0	0	0	0	
9	1	0	0	1	1	1	
A	1	0	1	0	0	0	
B	1	0	1	1	1	1	
C	1	1	0	0	0	→ -	4
D	1	1	0	1	1	1	
E	1	1	1	0	1	1	
F	1	1	1	1	1	1	

Fig. 2. Optimized logic using don't care

Logic synthesis has an effect on the complexity and precision of the GLIFT logic in two ways. On one hand, logic synthesis can reduce design redundancy to be frequently used for logic optimization. By comparison, the GLIFT logic equations are shown in Fig. 3, we see that logic synthesis can possibly make the GLIFT logic more simplified. On the other hand, this will typically make the resulting GLIFT logic less precise.

4.2 Logic Library Mapping

For the above approach, we can derive different simplified versions of GLIFT logic for the AND-2, which has 4 different minterms between the most and least precise GLIFT logic. This yields a total of 16 possible combinations for the simplified logic with don't care on each route. This reveals how many versions of GLIFT logic can be derived, which shows in Fig. 3 using AND-2 as an example. From Fig. 3, in the second optimized route, we have the most precise GLIFT logic for AND-2 At the top level, where A, B and O are the inputs and output of AND-2; At, Bt and Ot are their security labels respectively. By setting any possible combinations of the inputs with don't-care as Fig. 3, we can obtain three simplified versions of GLIFT logic as shown at the different nodes in this route. When the four observing zeros are all don't cares, we reach the most simplified GLIFT logic for AND-2, shown at the last node. In this way, we reduce the complexity to achieve a simplified version GLIFT logic through a tractable route with don't care. Now that we can create a simplified GLIFT library, we can map logic primitives to each alternative version of its GLIFT logic in order to obtain simplified logic, i.e. equations and reduce the overhead, i.e. area and delay. It can be seen that the area, delay and equations from precise version to simplified one of AND-2 GLIFT logic from Table 3.

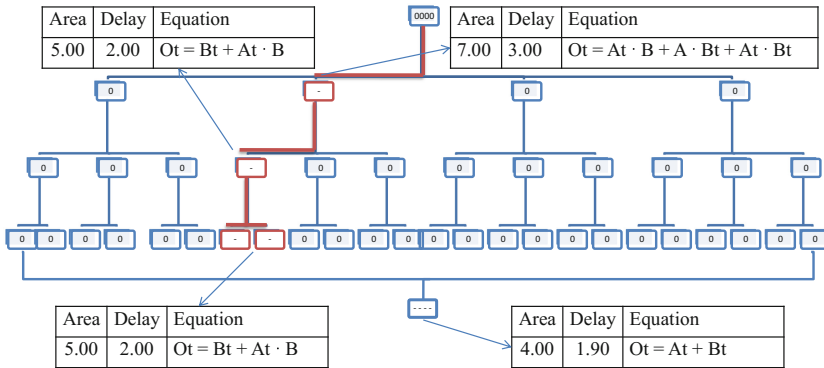


Fig. 3. Simplified tracking logic model

Table 3. Area, delay and equation with don't care for AND-2

#	A	B	Area	Delay	Equation
1			7.00	3.00	$Ot = At \cdot B + A \cdot Bt + At \cdot Bt$
2	-		5.00	2.00	$Ot = Bt + At \cdot B$
3		-	5.00	2.00	$Ot = At + A \cdot Bt$
4	-	-	4.00	1.90	$Ot = At + Bt$

5 Experimental Results

This section presents our experimental results. It shows how GLIFT logic can be simplified while introducing don't care, and demonstrates that the most precise and simplified GLIFT logic can result in overheads as an example of AND-3. Area and delay need to be taken into consideration in GLIFT logic design for information flow tracking. ABC is used as the synthesis tool. The resyn2 synthesis script in ABC is used to optimize the GLIFT logic circuits that can provide a good tradeoff between area and delay. The ABC mcnclib library does not provide units for area and delay results.

We carried out experiments on several N input AND gate (AND-N) to obtain area and delay results of the different GLIFT logic. In our experiments, the GLIFT logic is generated using the method discussed in the Sect. 4. Table 4 shows some statistics of the original and simplified GLIFT logic area in our experiments including the different AND-N gates. Figure 4 shows some original and simplified delay reports of GLIFT logic in these gates. From Table 4 and Fig. 4, we can discover that GLIFT logic represented in the simplified method gives significantly smaller area and delay. As an example, the GLIFT logic for AND-4 described using the original GLIFT reports an area/delay of 24.00/4.60, while that represented using the simplified one reports a result of 8.00/2.30; there are significant reduction in area and delay.

Subsequently, we carried out experiments to obtain area and delay reports of AND-3 for GLIFT logic circuits represented the schemes in Sect. 4. GLIFT logic formalization for AND-3 results are also generated using the schemes to verify optimized GLIFT logic. Table 5 shows some statistics of the area,

Table 4. Original and simplified GLIFT logic area for AND-N

AND-N	AND-2	AND-3	AND-4	AND-5	AND-6	AND-7	AND-8
Area_orig	7.00	11.00	24.00	123.00	176.00	489.00	1082.00
Area_simp	4.00	6.00	8.00	8.00	9.00	11.00	12.00

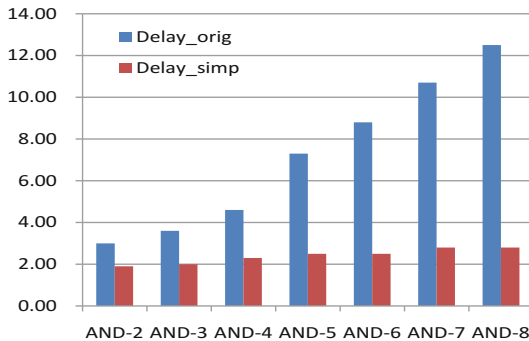


Fig. 4. Original and simplified GLIFT logic delay for AND-N

delay and equations of these logics in our experiments. It can be seen that the area/delay/equation of $6.00/2.00/Ot = At + Bt + Ct$ are the most optimized results when all three variables are introduced as don't cares.

Table 5. Area, delay and equation with don't care for AND-3

#	A	B	C	Area	Delay	Equation
1	-			9.00	3.20	$Ot = At \cdot B \cdot C + Bt \cdot C + B \cdot Ct + Bt \cdot Ct$
2		-		9.00	3.20	$Ot = At \cdot C + A \cdot Bt \cdot C + A \cdot Ct + At \cdot Ct$
3			-	9.00	3.20	$Ot = At \cdot B + A \cdot Bt + A \cdot B \cdot Ct + At \cdot Bt$
4	-	-		6.00	2.60	$Ot = At \cdot C + Bt \cdot C + Ct$
5	-		-	6.00	2.60	$Ot = At \cdot B + Bt + B \cdot Ct$
6		-	-	6.00	2.60	$Ot = At + A \cdot Bt + A \cdot Ct$
7	-	-	-	6.00	2.00	$Ot = At + Bt + Ct$
8				11.00	3.60	$Ot = At \cdot B \cdot C + A \cdot Bt \cdot C + A \cdot B \cdot Ct + At \cdot Bt \cdot C$ $+ At \cdot B \cdot Ct + A \cdot Bt \cdot Ct + At \cdot Bt \cdot Ct$

6 Conclusion

The GLIFT method can effectively monitor and measure all logical information flows at gate level to detect security vulnerabilities and prevent leakage of sensitive information in hardware designs. This paper presents the method of optimized GLIFT logic that search out some simplified routes to decrease logic complexity using don't care in design logic synthesis. The experimental results show that the method can effectively reduce the area and delay of original GLIFT logic.

Acknowledgments. This research was financially supported by the National Natural Science Foundation of China under Grant 61303224 and Grant 61672433, the National Cryptography Development Fund under Grant MMJJ20170210.

References

1. Extracting qualcomms keymaster keys - breaking android full disk encryption (2016). <http://bits-please.blogspot.com/2016/06/extractingqualcomms-keymaster-keys.html>
2. Becker, G.T., Regazzoni, F., Paar, C., Burleson, W.P.: Stealthy dopant-level hardware trojans. In: Bertoni, G., Coron, J.-S. (eds.) CHES 2013. LNCS, vol. 8086, pp. 197–214. Springer, Heidelberg (2013). https://doi.org/10.1007/978-3-642-40349-1_12
3. Bell, D.E., LaPadula, L.J.: Secure computer systems: mathematical foundations. Technical report, DTIC Document (1973)

4. Dalton, M., Kannan, H., Kozyrakis, C.: Raksha: a flexible information flow architecture for software security. In: ACM SIGARCH Computer Architecture News, vol. 35, pp. 482–493. ACM (2007)
5. Denning, D.E.: A lattice model of secure information flow. *Commun. ACM* **19**(5), 236–243 (1976)
6. Denning, D.E.: *Cryptography and Data Security*. Addison-Wesley Longman Publishing Co., Inc., Boston (1982)
7. Goguen, J.A., Meseguer, J.: Security policies and security models. In: IEEE Symposium on Security and Privacy, vol. 11, p. 77 (1982)
8. Hu, W., Becker, A., Ardeshiricham, A., Tai, Y., Ienne, P., Mu, D., Kastner, R.: Imprecise security: quality and complexity tradeoffs for hardware information flow tracking. In: Proceedings of the 35th International Conference on Computer-Aided Design, p. 95. ACM (2016)
9. Hu, W., Mao, B., Oberg, J., Kastner, R.: Detecting hardware trojans with gate-level information-flow tracking. *Computer* **49**(8), 44–52 (2016)
10. Keating, M.: *The Simple Art of SoC Design: Closing the Gap Between RTL and ESL*. Springer Science & Business Media, Heidelberg (2011). <https://doi.org/10.1007/978-1-4419-8586-6>
11. Krohn, M., Yip, A., Brodsky, M., Cliffer, N., Kaashoek, M.F., Kohler, E., Morris, R.: Information flow control for standard OS abstractions. In: ACM SIGOPS Operating Systems Review, vol. 41, pp. 321–334. ACM (2007)
12. Mu, D., Hu, W., Mao, B., Ma, B.: A bottom-up approach to verifiable embedded system information flow security. *IET Inf. Secur.* **8**(1), 12–17 (2014)
13. Pottier, F., Simonet, V.: Information flow inference for ML. *ACM Trans. Program. Lang. Syst. (TOPLAS)* **25**(1), 117–158 (2003)
14. Sabelfeld, A., Myers, A.C.: Language-based information-flow security. *IEEE J. Sel. Areas Commun.* **21**(1), 5–19 (2003)
15. Suh, G.E., Lee, J.W., Zhang, D., Devadas, S.L: Secure program execution via dynamic information flow tracking. In: ACM Sigplan Notices, vol. 39, pp. 85–96. ACM (2004)
16. Tiwari, M., Wassel, H.M., Mazloom, B., Mysore, S., Chong, F.T., Sherwood, T.: Complete information flow tracking from the gates up. In: ACM Sigplan Notices, vol. 44, pp. 109–120. ACM (2009)
17. Vandeboogart, S., Efstathopoulos, P., Kohler, E., Krohn, M., Frey, C., Ziegler, D., Kaashoek, F., Morris, R., Mazières, D.: Labels and event processes in the asbestos operating system. *ACM Trans. Comput. Syst. (TOCS)* **25**(4), 11 (2007)
18. Venkataramani, G., Doudalis, I., Solihin, Y., Prvulovic, M.: Flexitaint: a programmable accelerator for dynamic taint propagation. In: 2008 IEEE 14th International Symposium on High Performance Computer Architecture, pp. 173–184. IEEE (2008)
19. Volpano, D., Irvine, C., Smith, G.: A sound type system for secure flow analysis. *J. Comput. Secur.* **4**(2–3), 167–187 (1996)
20. Zhang, D., Wang, Y., Suh, G.E., Myers, A.C.: A hardware design language for timing-sensitive information-flow security. In: The Twentieth International Conference on Architectural Support for Programming Languages and Operating Systems, ASPLOS 2015, pp. 503–516, New York, NY, USA (2015)



A Cloud-Based Distance Bounding Protocol for RFID Conforming to EPC-C1 G2 Standards

Zhenjiang Dong^{1,3(✉)}, Xinluo Wang², Miao Lei², Wei Wang³, and Hui Li²

¹ Shanghai Jiao Tong University, Shanghai, China

² Beijing University of Posts and Telecommunications,
Beijing 100876, People's Republic of China

{2013212985,lihui11}@bupt.edu.cn, sinper1005@163.com

³ ZTE Cloud Computing and IT Research Institute,
Nanjing, People's Republic of China

{dong.zhenjiang,wang.wei8}@zte.com.cn

Abstract. The development and maturation of cloud computing provides a new idea for deploying RFID systems. A Cloud-based RFID system becomes a new promising architecture. It can be offered as a service of cloud computing to individuals and organizations. However, the cloud-based RFID systems are confronted with more special security and privacy threats, especially the untrustworthy cloud provider and insecure backward communications. Unfortunately, most current RFID authentication schemes fail to meet the special security and privacy requirements of cloud-based RFID, i.e. to provide anonymity and confidentiality against the cloud and build secure backend channels. In this paper, we propose a secure distance bounding protocol for a RFID system, which is cloud-based RFID mutual authentication protocol compatible with the mature EPC-C1 G2 standards. It can effectively resist various threats in cloud environment comparing with other cloud-based RFID authentication protocol and reduce the success probability of a Mafia attack and make it lower than the optimal situation $(1/2)^n$ in academic circles.

Keywords: RFID · Authentication · Distance bounding
Cloud computing

1 Introduction

Radio Frequency Identification (RFID) is a wireless communication technology in which readers can automatically identify tags attached to objects and transfer data through radio signals without a mechanical or optical contact. Due to its ability for automatic identification and low cost, RFID systems are pervasively deployed in both military and civilian fields.

A traditional RFID system consists of three parts: a backend server, readers and tags. In this architecture, a reader relays messages from tags to a backend server and the backend server helps the reader to verify tags according to the database the server maintains. Readers and tags use a radio channel for communication which is commonly assumed to be insecure. While the private connection (wired or wireless) between a reader and the backend server is always assumed to be secure.

However, there exist some limitations in the deployment of traditional RFID systems. Firstly, establishing the entire RFID system would take high costs and therefore does not meet the small and medium-sized enterprises economic benefits, which greatly hinders the market promotion of RFID systems. Secondly, we need to erect a dedicated server and cables for a traditional RFID system, which is not suitable for a trans-regional enterprise.

Cloud-based RFID is a new promising architecture. It is composed of tags, readers, and a serving cloud to store and process data instead of the traditional backend server. Comparing with traditional RFID architecture, the cloud-based one has advantages in many aspects. Global deployment of the Internet and mobile networks make it available to access a cloud service almost everywhere. Therefore, the pervasive RFID service would be accessible using fixed or mobile readers over the Internet whenever and wherever needed. Moreover, users commitments for investment and operations are minimized, and costs are in direct relation to usage and demand.

Meanwhile, the cloud-based RFID systems are confronted with more special security and privacy threats, especially in two aspects:

Firstly, cloud-based RFID authentication schemes are required to secure backend communications besides protections of the frontend security. In the cloud-based RFID, readers access the public cloud through open Internet connections, which cannot be asserted as secure [1].

Secondly, cloud-based RFID authentication schemes are required to prevent tags from privacy-revealing to the untrustworthy cloud. In the cloud-based RFID, the cloud provider is not trusted by the reader holders; therefore, it needs provide tags with confidentiality of data storage and anonymity of access [1].

Contribution: In this paper, we introduce a novel cloud-based RFID authentication protocol. It is the first EPC C1 G2 standards compliant cloud-based RFID authentication protocol, which achieves mutual authentication between tags and readers, and scalability with $O(1)$ computational complexity of verifying a tag. It is proved to be resistant to various attacks like impersonating attack, terrorist attack, desynchronizing attack and tracking attack. Meanwhile, its able to reduce the probability of a Mafia attack less than the optimal $(1/2)^n$.

Organization: Sect. 2 gives the current state of the art and explain the necessity of our work. The proposed protocol is presented in Sect. 3, followed by security analyses and comparisons with another representative cloud-based RFID authentication scheme in Sect. 4. At last, we conclude the article in Sect. 5.

2 Background

2.1 Existing Attacks and Related Work on RFID Security Schemes

This subsection will introduce some attacks, they still exist in RFID scheme and threaten RFID's security and privacy.

As [2] said, An impersonation attack is an attack in which an adversary successfully assumes the identity of one of the legitimate parties in a system or in a communications protocol. In RFID scheme, this attack can make impersonated adversary be regarded as a real tag or a authority reader to corrupt the RFID security.

As for the Mafia Fraud, according to the paper [3], an adversary can use the pre-ask or post-ask strategy to achieve this attack, and the former is more effective. That is, before attacking the reader, the adversary sends predicted challenges C'_j s to the tag and gets the responses R'_j s from the tag. Then the adversary executes the rapid bit exchange with the reader and receives the challenges C_j s. In half of all cases, the adversary has guessed the right challenge bit, that is $C'_j = C_j$, so the adversary sends the correct response with probability of 1. Otherwise, if $C'_j \neq C_j$, the adversary can reply with a guessed bit and its probability of being correct is 1/2. If just considering the rapid bit exchange, the adversary therefore has a 3/4 probability of replying correctly for each challenge bit and hence $(3/4)^n$ for the n-round rapid bit exchange.

The Terrorist Fraud is an attack where an adversary defeats a distance bounding protocol with a man-in-the-middle between the reader and a dishonest tag located outside of the neighborhood, such that the latter actively helps the adversary to maximize her attack success probability, without giving to him any advantage for future attacks. The definition of the Terrorist Attack means the dishonest tag cannot give the adversary the secrets or the information with which the adversary can determine the secrets.

In Tracking Attack, attackers usually disguise as one or more real readers and send authentication messages to each tags. So the attacker can get and analyze the response messages from tags and track the movements of each tag.

The Desynchronizing Attack is based on the protection of Tracking Attack. In order to prevent the tag from returning the same message and being tracked, the RFID system requires synchronizing the label and the backend database and refresh the authentication key from time to time. After refreshed, both the tag and reader will save the new key for the next authentication process, so after synchronization, the message returned by tag is different from previous one. Therefore, if attacker interrupts the update process, the label will not be able to update the key, when the next scan, the label using the key and the reader is not the same, the reader will prohibit the label authentication request, thus deleting the label.

In 1987, Desmedt et al. [4] introduced the Mafia Fraud and Terrorist Frauds that can defeat all the RFID authentication protocols. In these attacks, an adversary can successfully pass the authentication by simply relaying the signals between reader and tag without dealing with the authentication cryptography.

To resist these frauds, one idea is to measure the round trip time of exchanged messages between the reader and tag.

In 1993, Brands and Chaum [5] proposed the first distance-bounding protocol with this idea to prevent Mafia Fraud while leaving the Terrorist Attack as an open issue.

In 2005, Hancke and Kuhn [6] published a new distance bounding protocol which become a key reference later.

In 2013, Xie et al. [1] provide a new RFID authentication architecture focused on solving the security and privacy challenges about the cloud-based RFID. It is the first research considered this new architecture and we will discuss it in next subsection.

In 2014, protocols [7–9] which use the round trip time method have been proposed to resist against Mafia and Terrorist attacks. And they agree that the maximum resistance to mafia frauds is $(1/2)^n$, which is the probability of a naive adversary who answers randomly to the -verifiers challenges during the rapid bit exchange phase.

2.2 When RFID Meets Cloud Computing

As the development of cloud computing. The cloud-based RFID architecture has attracted more attentions. However, new architecture brings new problems about security and privacy. In the cloud-based RFID, reader holders do not totally trust the cloud provider. They need to keep data plain-text from exposing to the cloud while using the computing and storage resources of the cloud, and even to maintain anonymity of tags from cloud in the process of authentication. Existing traditional RFID authentication protocols are obviously inapplicable to cloud-based applications.

Besides, to the best of my knowledge, up to now not many researches have fully considered the security challenges in cloud environment. The research in [1] is the one considered that, while the other cloud-based RFID schemes [10–13] did not. However, the protocol in [1] still cannot resist Tracking Attack, Mafia Attack [4] and Terrorist Attack [4]. Take the Tracking Attack as an example: after truncating the last message in the protocol, an adversary can track the tag by eavesdropping the first message $H(R||T||S)$ next time the protocol executed. Furthermore, the reader in this scheme needs to search the cloud constantly which may increase network delay and result in low efficiency. Besides, the scheme is designed based on hash functions, difficult to be compatible with the prevailing EPC Class 1 Generation 2 standards.

2.3 EPC RFID Standard

In order to foster and publicize RFID technology, standardization is certainly important to allow interoperability at large scale. As one of the most viable standard providers, EPCglobal Inc is focusing on the area of logistical supply chain and try to enhance the transparency and traceability of supply chain.

And Being compatible with ISO – another biggest RFID standard provider can ensure the EPC standard’s compatibility. The latest RFID standard ratified by EPCglobal is named UHF Class 1 Gen 2 Standard version 2.0.0 (EPC-C1 G2 RFID for short) [14]. Three properties of a G2 RFID tag are briefly listed as follows:

- G2 RFID tag is passive, meaning that its power is triggered by the readers.
- G2 RFID tag communicates with readers in UHF band (800–960 MHz) and its communication range is from 2 m to 10 m.
- G2 RFID tag only supports on-chip Pseudo-Random Number Generator (PRNG) and Cyclic-redundancy check (CRC).

In recent years, several protocols [15–18] are compatible with the EPC-C1 G2 standards have been proposed. However, most of them are vulnerable to Tracking Attack and Desynchronizing Attack [19–22]. And this paper [20] points out that the two kinds of attacks are both based on the linear attributes of CRC functions.

3 Proposal

Since the EPC-C1 G2 standards stipulates that G2 RFID tag only supports PRNG and CRC function as well as other lightweight operations such as XOR and concatenation, A cloud-based RFID authentication protocol is designed to conform to the EPC-C1 G2 standards.

3.1 Notations and Attack Model

Notations in the protocol are listed in Table 1.

Table 1. Notations

Symbol	Meaning
K_1	Authentication keys shared between a reader and a tag
<i>Info</i>	Any data relevant to a session about the tag
$E()$	A symmetric encryption function in the reader
$D()$	A symmetric decryption function in the reader
K_2	The private key of $E()$ and $D()$
$PRNG()$	A secure one-way pseudo-random number generator function
ID/PRN	A random number generated by $PRNG()$
N_R	A random number generated by a reader
N_T	A random number generated by a tag
	The concatenation operation

To facilitate the subsequent analysis, a reasonable attack model about system security in this paper is shown as follows:

- The frontend communication is unsafe. A reader and a tag use a radio channel for communication on which an attacker can easily eavesdrop, tamper, delete and replay the messages.
- In backward channel, readers and the cloud will communicate through VPN connections. As [1] said, since the VPN agency can offer a reader a random virtual IP address in each login, the malicious can not link the same reader from different access sessions based on the source IP address in IP packets. So in network layer, we think the VPN can protect the readers' anonymity and we do not consider an adversary to intercept, block, and resend TCP/IP packets in this layer.
- The cloud provider is not trusted and may be malicious or vulnerable. Therefore, the protocol needs to provide anonymous access and confidentiality for a tag.
- Before the authentication step, there exists a procedure that the tags are securely enrolled in this RFID system. So the RFID reader can share the authentication key K_1 with each enrolled tags, and the tags' original information $(ID_i, E_{K_2}(Info_{origin}))$ will be stored in the cloud server.

3.2 Description of Our Protocol

The architecture of our protocol is depicted in Fig. 1. On the backward channel, similar to [1], mobile or fixed readers anonymously access the cloud through wireless or wired VPN connections, and an encrypted PRN table which is similar to the Encrypted Hashed Table in [1] is constructed. The index is a random number generated by PRNG() function, and the record indexed by the random number is the $E_{K_2}(info)$, it is a cipher text using a reader-defined encryption algorithm with a reader-managed key K_2 . So all of the data in cloud are encrypted by reader-self to prevent tags secrets from revealing to the cloud. While on the frontend communication, a distance bounding technology is utilized between a reader and a tag for distance detection to resist Mafia attacks.

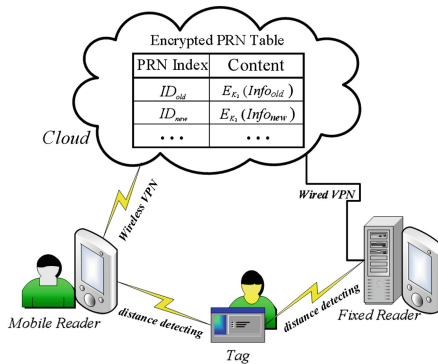


Fig. 1. A security architecture for cloud-based RFID authentication

As illustrated in Fig. 2, the proposed cloud-based RFID authentication protocol can be logically split into three stages: the distance-bounding stage, the mutual authentication stage and the data-updating stage.

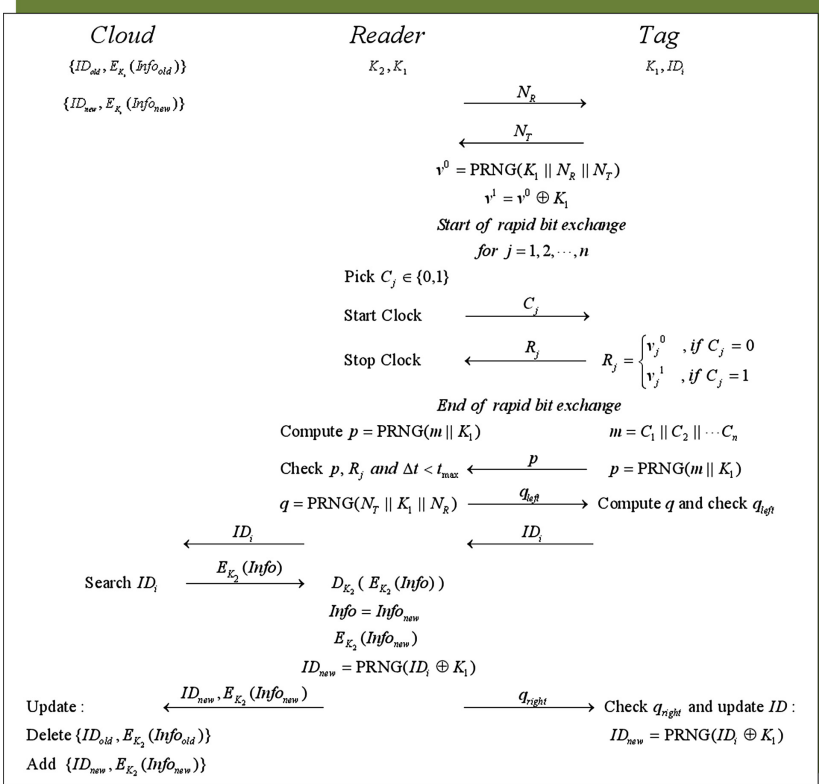


Fig. 2. The proposed protocol

Distance-Bounding. The reader and the tag first generate a random number N_R, N_T respectively and send to each other. Then they both calculate $v^0 = PRNG(K_1 || N_R || N_T)$ and $v^1 = v^0 \oplus K_1$ to prepare for rapid bit exchange. During each round of the n-round rapid bit exchange, the reader chooses a random timing bit C_j to challenge the tag and the tag immediately responds R_j on receiving C_j . R_j is jointly determined by j, v^0, v^1 and C_j . That is, if $C_j = 0$, the value of R_j is taken from the j-th bit of v^0 , else, it is from v^1 . The timing of each round starts when the reader sends C_j and stops on receiving R_j . After the rapid bit exchange, the reader checks R_j and Δt .

Mutual Authentication. Both the reader and the tag take bits C_j s and concatenate them to an m , and then compute $p = PRNG(m || K_1)$. Then the tag

sends p . Upon receiving p , the reader checks its correctness and rejects the tag if false. Else, the reader calculates $q = PRNG(N_T || K_1 || N_R)$ and sends its left half part q_{left} to the tag. The tag also computes q , and then checks the receiving q_{left} . If it fails, the tag terminates the protocol; else, it continues.

Data-Updating. The tag sends data to the reader, and the reader forwards it to the cloud. Then the cloud looks up the corresponding record (current record) using this pseudo-random number index, and returns the cipher texts of the tag to the reader. The reader will then decrypt, data process, encrypt into cipher texts, and update $ID_{new} = PRNG(ID_i \oplus K_1)$. At last, the reader sends back the new record to the cloud and notify the tag to update ID with the right half part q_{right} . After receiving the new record, the cloud keeps the current record, deletes other old records and adds the new record. Simultaneously, if q_{right} is correct, the tag then computes $PRNG(ID_i \oplus K_1)$ as the new index ID_{new} .

4 Security Analysis

The following part will analyze and evaluate how our protocol performs against these attacks.

Anonymity and Confidentiality Against the Cloud. Since all the records in the cloud are encrypted by readers with a symmetric algorithm E_{K_2} and only these readers possess the key K_2 , so the confidentiality is achieved. Using pseudo random number indexes not only can accelerate the searching speed and achieved scalability, which is conducive to support large-scale applications, but can also guarantee an anonymous access for a tag. In addition, as said in the assumption in attack model, we ensure that the VPN technology on the backward channel can ensure the security of communication between readers and the cloud.

Impersonation Attack Resistance. The protocol supports distance detection and more importantly, mutual authentication between a reader and a tag, therefore the authenticity of both parties is achieved.

Mafia Attack Resistance. As shown in background, the Mafia Fraud can be achieved by pre-ask or postask strategy. If consider the rapid bit exchange only, the adversary therefore has a $3/4$ probability of replying correctly for each challenge bit and hence $(3/4)^n$ for the n -round rapid bit exchange. However, as a matter of fact, in the mutual authentication phase the presence of p could provide the reader with the list of challenges received by the genuine tag and adds a line of defense to a mafia attacker. The premise of generating p is to obtain all the random challenge bits. Therefore, the security of p relies on the security of function $PRNG()$. According to the EPC Class 1 Generation 2 standards, the pseudo-random function $PRNG()$ is a one-way function similar to a hash function, i.e. it is nearly impossible (a probability less than 0.025% [14]) to deduce

the seed parameter in parentheses using the pseudo random number generated by this function, namely $m||K_1$. When the length of p is 1, the probability that the adversary guesses correctly shall be $(1/2)^l$. Hence, the maximum success probability of a mafia attack is $(3/4)^n \times (1/2)^l$, the actual probability depends on the length of $PRNG()$, but if the length l is long enough, the probability is less than $(1/2)^n$ which is the maximum resistance to Mafia Fraud in academic circles [7–9] while $(3/4)^n$ in most cases.

Terrorist Attack Resistance. In our protocol, the dishonest tag cannot provide the registers v^0 and v^1 to the adversary since the adversary can determine the key $K_1 = v^0 \oplus v^1$. So tags cannot help the attacker without any leakage on the long term key K_1 . Therefore, the protocol is resistant to Terrorist Fraud.

Desynchronizing Attack Resistance. Consider the attack in [20], an adversary intercepts or manipulates the last message q_{right} the reader sends to the tag. In fact, the tag will not update ID either way due to check failure. When the tag communicates with the reader next time, the cloud can still retrieve a record of the tag.

Tracking Attack Resistance. Assuming that an attacker obtains the index ID after eavesdropping on the exchanges between a reader and a tag, when attacker eavesdrops next time, it cannot track the tag for the ID has been updated. Supposing that the attacker counterfeits a reader to cheat the tag, because the tag needs to check q_{left} before it transmits ID , the attacker would ultimately be unable to provide q_{left} and cannot get ID .

Table 2 shows a comparison between our protocol and [1]. In terms of performance, the computation complexity for the cloud to verify a tag are both $O(1)$. In our protocol, the tag only needs to execute PRNG functions while it needs to execute 4 Hash functions in [1], which is not supported by the EPC-C1 G2 standards.

Table 2. Comparison of cloud-based authentication protocols

Protocol	Complexity to verify a tag	Mafia	Terrorist	tracking	EPC-C1 G2 compliant
Xie [1]	$O(1)$	No	No	No	No
Our protocol	$O(1)$	Yes	Yes	Yes	Yes

In summary, our protocol can provide anonymity and confidentiality protection for a tag against the cloud and effectively resist impersonating reader attacks, impersonating tag attacks, Mafia attacks, Terrorist attacks, desynchronizing attacks and tracking attacks. Compared with the protocol in literature [1],

it keeps the high efficiency of verifying a tag for the cloud, further strengthens the security of a cloud-base RFID system, and makes the system be compatible with current mature EPC-C1 G2 standards.

5 Conclusions

In this paper, two main security challenges of a cloud-based RFID system have been considered, i.e. the untrustworthy cloud provider and the insecure backward communication. Most current RFID authentication protocols did not fully consider the above security challenges and therefore inapplicable to cloud-based applications. Besides, they are not compatible with the prevailing EPC Class 1 Generation 2 standards. Moreover, many RFID authentication protocols are threatened by Mafia Frauds and Terrorist Frauds. A distance bounding protocol, as a possible measure, is not yet efficient enough to resist. Motivated by the above, the first EPC-C1 G2 standards compliant cloud-based RFID authentication protocol has been purposed, which can preserve tags users privacy from leaking to the cloud and defend against various attacks. Besides, we improved the distance-bounding technology and it can effectively reduce the success probability of a Mafia attack.

Future works include that we keep on improving the distance-bounding technology, design a more lightweight authentication protocol in accordance with the EPC-C1 G2 standards and solve the problem of insecure communications between the cloud and readers in cloud-based RFID.

Acknowledgments. This work was supported by ZTE Corporation and University Joint Research Project.


References

1. Xie, W., Xie, L., Zhang, C., et al.: Cloud-based RFID authentication. In: IEEE International Conference on RFID 2013, pp. 168–175 (2013)
2. Van Tilborg, H.C.A., Jajodia, S. (eds.): Encyclopedia of Cryptography and Security. Springer Science & Business Media, Heidelberg (2014)
3. Avoine, G., Bingol, M.A., Kardas, S., Lauradoux, C., Martin, B.: A framework for analyzing RFID distance bounding protocols. *J. Comput. Secur.* **19**(2), 289–317 (2009)
4. Desmedt, Y., Goutier, C., Bengio, S.: Special uses and abuses of the fiat-shamir passport protocol (extended abstract). In: Pomerance, C. (ed.) CRYPTO 1987. LNCS, vol. 293, pp. 21–39. Springer, Heidelberg (1988). https://doi.org/10.1007/3-540-48184-2_3
5. Brands, S., Chaum, D.: Distance-bounding protocols. In: Helleseth, T. (ed.) EURO-CRYPT 1993. LNCS, vol. 765, pp. 344–359. Springer, Heidelberg (1994). https://doi.org/10.1007/3-540-48285-7_30
6. Hancke, G.P., Kuhn, M.G.: An RFID distance bounding protocol. In: 2005 SECURECOMM (2005)

7. Gambs, S., Onete, C., Robert, J.M.: Prover anonymous and deniable distance-bounding authentication. In: Proceedings of the 9th ACM Symposium on Information, Computer and Communications Security, AsiaCCS 2014, pp. 501–506 (2014)
8. Trujillo-Rasua, R., Martin, B., Avoine, G.: Distance-bounding facing both mafia and distance frauds. *IEEE Trans. Wireless Commun.* **13**(10), 5690–5698 (2014)
9. Jeon, I.-S., Yoon, E.-J.: An ultra-lightweight RFID distance bounding protocol. *Int. J. Math. Anal.* **8**(46), 2265–2275 (2014)
10. Kiraz, M.S., Bingl, M.A., Karda, S., et al.: Anonymous RFID authentication for cloud services. *Int. J. Inf. Secur. Sci.* **1**(2), 32–42 (2012)
11. Karda, S., Celik, S., Bingl, M.A., et al.: A new security and privacy framework for RFID in cloud computing. In: 2013 IEEE 5th International Conference on Cloud Computing Technology and Science, vol. 1, pp. 171–176. IEEE (2013)
12. Jobe, S., Venifa Mini, G., Celin, J.J.A.: Efficient RFID authentication in cloud computing. *Int. J. Sci. Eng. Technol. Res. (IJSETR)* **2**(4), 954–958 (2013)
13. Chen, S.-M., Wu, M.-E., Sun, H.-M., et al.: CRFID: an RFID system with a cloud database as a back-end server. *Future Gener. Comput. Syst.* **30**, 155–161 (2014)
14. UHF Class 1 Gen 2 Standard v. 2.0.0 [S], GS1/EPCglobal (2013)
15. Chien, H., Chen, C.: Mutual authentication protocol for RFID conforming to EPC Class 1 Generation 2 standards. *Comput. Stand. Interfaces* **29**, 254–259 (2007)
16. Chen, C.-L., Huang, Y.-C., Shih, T.-F.: A novel mutual authentication scheme for RFID conforming EPCglobal Class 1 Generation 2 standards. *Inf. Technol. Control* **41**(3), 220–228 (2012)
17. Pang, L., Li, H., He, L., Alramadhan, A., et al.: Secure and efficient lightweight RFID authentication protocol based on fast tag indexing. *Int. J. Commun. Syst.* **27**, 3244–3254 (2014)
18. Gao, L., Ma, M., Shu, Y., Wei, Y.: An ultra-lightweight RFID authentication protocol with CRC and permutation. *J. Netw. Comput. Appl.* **41**, 37–46 (2014)
19. Han, D., Kwon, D.: Vulnerability of an RFID authentication protocol conforming to EPC Class 1 Generation 2 standards. *Comput. Stand. Interfaces* **31**, 648–652 (2009)
20. Safkhani, M., Bagheri, N.: For an EPC-C1G2 RFID compliant Protocol, CRC with Concatenation: No; PRNG with Concatenation: Yes. *Cryptology ePrint Archive, Report 2013/490* (2013)
21. Akg, M., Caglayan, M.U.: On the security of recently proposed RFID protocols. *IACR Cryptology ePrint Archive, 2013/820* (2013)
22. Zahra, S.B., Mahdi, R.A., Aref, M.R.: Formal cryptanalysis of a CRC-based RFID authentication protocol. In: 2014 22nd Iranian Conference on Electrical Engineering (ICEE), Shahid Beheshti University, pp. 1642–1647 (2014)



Research on the Monitoring Method of the Road Communication Network Quality Based on Vehicle Borne Internet of Things

Baihua Ji¹, Xiao Liu¹, Tenghui Ke¹(✉) , Rongjie Kuang¹, Zibin Gao², and Daoce Wang³

¹ China Unicom, Shenzhen Branch, Shenzhen 518000, China
keth@chinaunicom.cn

² Pennsylvania State University, 137 Dewsbury Heights,
State College, PA 16803, USA

³ University of Electronic Science and Technology of China,
Qingshuihe Campus, Chengdu 611731, China

Abstract. This article proposes a monitoring method of the road communication network quality based on vehicle borne IoT (Internet of Things) by extracting and analyzing the MR (Measurement Report) data from the bus in the vehicle borne IoT to monitor the wireless network quality on key highways and to efficiently and accurately locate and detect the network errors. This method has proven to be accurate and meets the practical demands. It can further enhance the accuracy and timeliness of network evaluation and its impact in tremendous on increasing the stability of the quality of Mobile Telecommunication Networks.

Keywords: Vehicle · Internet of Things · Monitor method
Mobile network · Measurement report

1 Introduction

Mobile Communication Networks are the important Internet carrier to realize vehicle borne IoT. The vehicle borne IoT is a cutting-edge technology, which involves installing the communicating terminal on vehicles and connecting the vehicles on the Internet to establish wireless communication among driving vehicles in order to substantially elevate the security and efficiency of future transportation system. With the increased speed and carrying capability of the 4G internet, the vehicle-loaded Internet will become an important component of future intelligent transportation system. Meanwhile, the quality of the Mobile Communication Networks needs to be highlighted [1]. The traditional method involves monitoring the road network via DT (Drive Test), that is measuring the

performance of the wireless network by driving along the highway, which is inefficient and at a high cost [2–4]. It is realistic now to monitor the wireless network quality along the highways accurately and efficiently with the bus connected to the IoT.

The Measurement Report, abbreviated as MR, is the chief gauge of the quality of the wireless network environment, sent via mobile phones to the Internet system, which includes the information of base station detected, reception level and quality. This article proposes a new method to evaluate the quality of the road mobile network based on vehicle borne IoT to realize the accurate locating of the mobile users along the highway, assisting the monitoring on the road network quality to optimize the targeted area and increasing the efficiency of supervision on network quality.

2 Method to Monitor the Wireless Network Quality Based on Vehicle Borne IoT

2.1 Object of Supervision and Control

The vehicles are consistently connected to the vehicle borne IoT, therefore MR data can be extracted and analyzed via the number and type of the communication terminal installed on the bus known. For example, there are more than 3200 buses installed with communication terminal available in Shenzhen Bus Group with a broad monitoring area covering all the arterial roads and highways (Fig. 1).

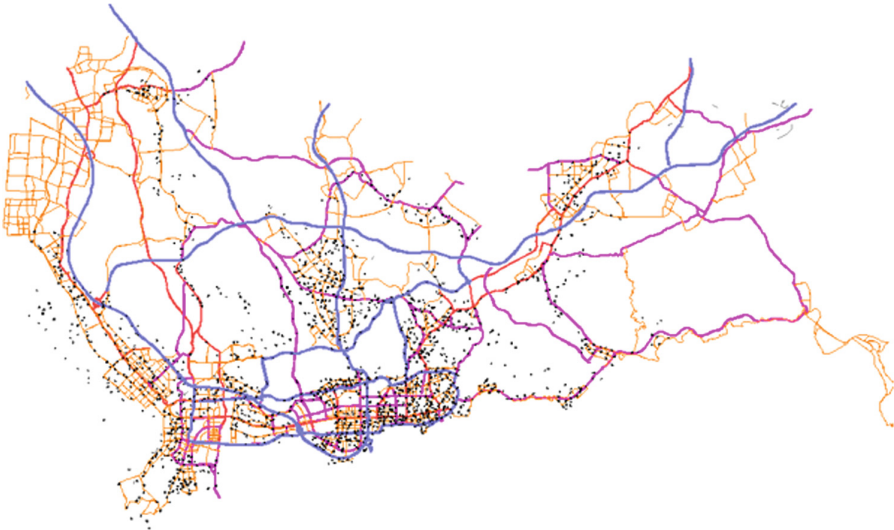


Fig. 1. The route map of the buses in the vehicle borne IoT in Shenzhen

2.2 The Multiple-user Base Station Switching Chain Algorithm

The difficulty of conducting road network detection based on the MR data extracted from multiple users lies in how to decide the base station switching chain on the targeted road. This article proposes a new sequencing method to realize the sorting of base station switching chain and data analysis.

This sequencing method contains three components, including the segmentation and arrangement of MR, cross banding, and the calibration of the standard switching chain. The flow chart of this sequencing algorithm is as follows:

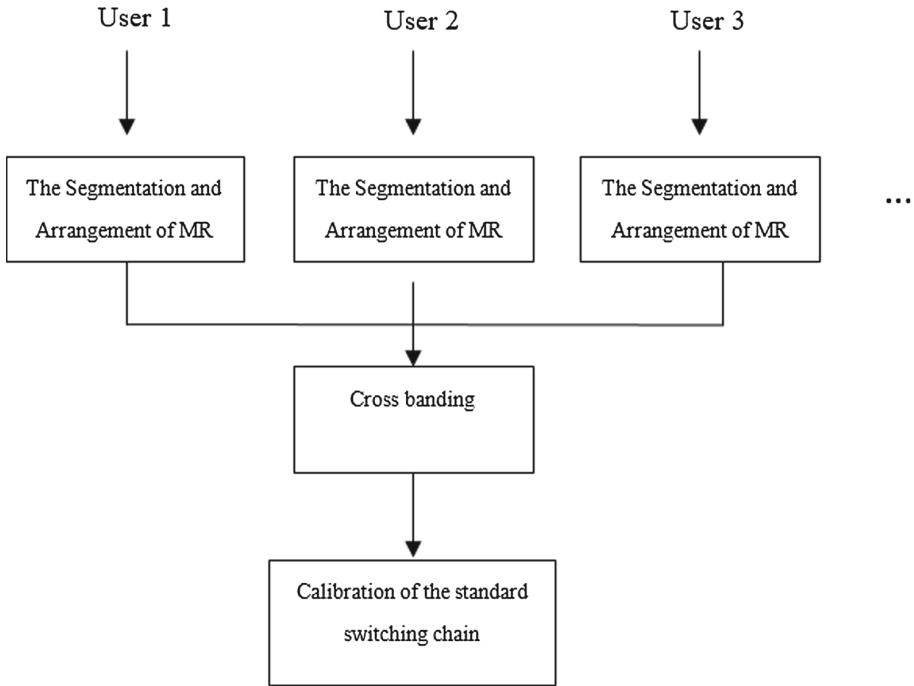


Fig. 2. The flow chart of base station switching chain algorithm

- (1) The segmentation and arrangement of MR data: The aim is to segment the MR data into multiple-sectioned return switching chain, including the go sequence and return sequence to identify the direction the bus is going.
- (2) Cross banding: Integrate the dispersion sequence of the multiple return trips conducted by multiple users into one sequence.
- (3) The Calibration of Standard Switching Chain: Update and calibrate the standard switching chain when the circuit is changed or a new Internet station is established (Fig. 2).

2.3 An Accurate Position-marking Method Based on RTT

To realize the accurate locating of the bus on the road, taking the WCDMA system as an example, the Measurement Report contains RTT fields to log the

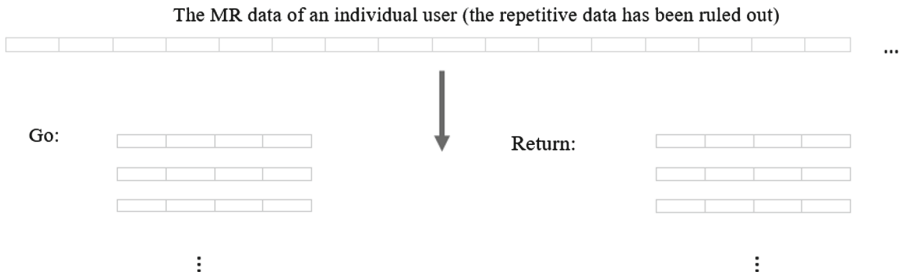


Fig. 3. The segmentation of the MR data

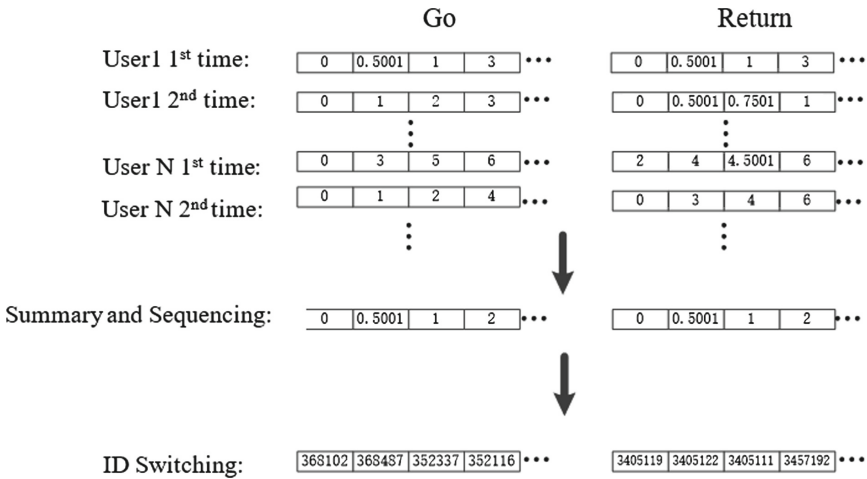


Fig. 4. The cross banding of MR data

time consumed by the signal in a return trip from the terminal to the base station. The linear distance between the terminal and the base station when it is sending the measurement report to the base station can be calculated based on RTT. According to the exact definition of MR fields in the 3GPP protocol, the calculation is as follows [5]

$$dist = \frac{3 \times 10^8}{3.84 \times 10^6} \times \frac{1}{2} \times \left[\frac{rtt}{16} + 876 - RxTxTime \right] \quad (1)$$

In the formula above, 3×10^8 is the speed of radio wave, 3.84×10^6 is the chip rate in WCDMA, $dist$ is the distance between the user and the base station in reality (Figs. 3 and 4).

It is noted that this formula can only be applied in the WCDMA system as the parameters and protocols vary from one system to another, as the result, the formulas used are various. In the case of GSM and FDD-LTE system, the

core principles of the two are the same, but the parameter in equivalence with RTT is named TA (Timing Advance), and the formulas used are different.

In step 1, the longitude and latitude are known, we can therefore calculate *dist*, and draw a circle with the base station as the center and *dist* as radius. There are at least two intersection points on the highway. As the specific sections covered by the base stations are already documented in the MR, with the azimuthal angle of the aerials, we can then measure the equivalent point of MR.

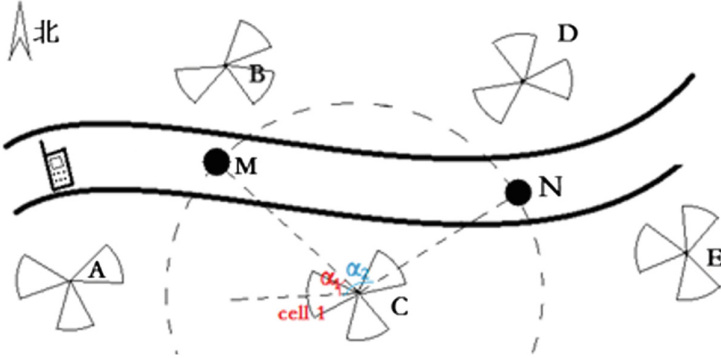


Fig. 5. The accurate locating of users on the targeted highway

As is shown in Fig. 5, cell 1 collects the users MR in the current spot, and then calculates *dist* and the longitude and latitude of the base station to locate two points M and N. The azimuthal angle of CM and CN between the aerials are α_1 and α_2 , $\alpha_1 < \alpha_2$. It can be deduced that M is the equivalent point of the user. Given the longitude and latitude, M can be color marked indicating the intensity of the signal. If there are more than one MR equating to the same point, an average can be drawn.

$$\frac{E_c}{I_{o_{total}}} = Avg\left(\frac{E_c}{I_o}\right) \tag{2}$$

2.4 Filling the Blank Area on the Road Map by Spreading the Point

As the reporting cycle of MR is fixed, there appear to be blank areas on the highway. Further spreading of the data is required to ensure the completion of monitoring data of the whole highway.

$$V_{i+1} = \frac{(V - V_i) \times (r - \frac{1}{2})}{r} + V_i \tag{3}$$



Fig. 6. The cartography of the road network quality (Color figure online)

In the formula above, V is the numerical value of the spread point, V_i is the i -th point to the spread point, and r is the number of spread points of the target.

In Fig. 6, A and B are acquired by the method illustrated above. A represents low signal intensity marked by the color red and B represents high signal intensity marked by the color green. There is a blank belt between A and B . To fill the gap, based on formula 3, we take $r = 5$, A and B as datum points, calculating the signal intensity of the five points a, b, c, d and e between A and B and then marking on the map to render a fluent flow between A and B .

In addition, if there appears to be an inconsistency or breakdown of the base stations covering a large area, as the result, the MR sent from users mobile phones will not be received. As a consequence, there will be a large blank area on the map. Therefore, based on the large blank area on the monitoring map, it can be deduced that there is a breakdown or inconsistency of the base station. This method has realized the monitoring of network breakdown to ensure the quick locating of the fault locations and the area affected.

3 Application Result and Analysis

Taking the WCDMA system as an example, when this method was adopted to evaluate the quality of the network along the roads in Shenzhen, the result is as follows. The result from this method and that of the DT evaluation test are compared in the following table. The error rate is kept within $\pm 10\%$ to ensure that the evaluation result is valid (Table 1).

Table 1. The comparison of the results of the two network quality evaluation methods

Shennan avenue	The new method	Traditional DT test	Relative error
Total sampling points	1764	1695	4.1%
Coverage sampling points RSCP>-85 dbm	1685	1627	3.6%
Coverage rate	95.52%	96.04%	0.5%
Bad quality sampling points $E_c/I_o < -12$ dB	45	40	-
Bad quality rate	2.55%	2.37%	7.6%
Consistent bad quality sampling points	4	4	0.0%
The quality during ping-pong handover	-9.6	-10.1	5.0%
Frequency of serving cell alteration	814	806	1.0%
Frequency of ping-pong handover	115	110	4.5%

4 Conclusion

This article presents a method to evaluate the quality of road communication network based on vehicle borne IoT by extracting and analyzing the MR data from the bus connected to the vehicle borne IoT to realize the accurate locating of



Fig. 7. Marked road map

the bus and to conduct quality supervision and control over the wireless network along the key roads, efficiently and accurately locating and detecting Internet errors. This method can also be applied to LTE and other network systems. The advantages of this method are as follows: (1) Accurate locating of the quality of the road networks; (2) More accurate and effective evaluation data; (3) Lower cost of road test; (4) MR data can be obtained with available facilities without large-scale investment (Fig. 7).

In conclusion, the new method proposed in this article can realize the real-time and whole-network backstage monitoring of the Mobile Telecommunication Network along the highways in aim to ensure the real-time feedback and location. It can be applied universally and has huge promotional value.

Acknowledgments. This work was support by the Open Fund of Key Laboratory of Urban Land Resources Monitoring and Simulation, Ministry of Land and Resources No. KF-2016-02-030.

References

1. Liu, X., Yuan, K., Mo, L., et al.: Research and application of a daily monitoring method of WCDMA network quality along arterial highways. In: IEEE, International Conference on Electronics Information and Emergency Communication, pp. 70–73. IEEE (2014)
2. Dou, Z., Lei, X.: WCDMA System Principle and Wireless Network Optimization. Tsinghua University Press (2009)
3. ZTE Corporation: UniPOS NetMAX-U ServerV12.4 User Manual
4. Heine, G., Horrer, M.: GSM Networks: Protocols, Terminology, and Implementation. Artech House, Inc. (1999)
5. 3GPP TS 25.331: Radio Resource Control (RRC)



A Negotiation-Based Collision Avoidance Scheme for Autonomous Mobile Robots

Zhaoxuan Chen, Pin Lv^(✉), Siyu Pan, and Jia Xu

School of Computer, Electronics and Information, Guangxi University,
Nanning, China
lvpin@gxu.edu.cn

Abstract. Autonomous mobile robots become increasingly more popular in many fields to execute tasks instead of human beings. When multiple autonomous mobile robots coexist in an area and move autonomously, how to avoid collision among them is a critical issue. In this paper, a distributed negotiation-based collision avoidance scheme is proposed. With this scheme, mobile robots negotiate with each other when they are about to collide. Based on the negotiation, the robots make the most appropriate decision to avoid collision, and move forward to their own destinations with the least cost. The effectiveness and the efficiency of the proposed scheme are proved by extensive simulations.

Keywords: Autonomous mobile robot · Collision avoidance
Negotiation

1 Introduction

Autonomous mobile robots, which are currently undergoing a period of rapid development, have been employed in many fields to undertake tasks instead of humans. For instance, in a warehouse of Amazon, hundreds of autonomous mobile robots are busy in carrying goods. Once online orders are generated, these robots fetch the goods listed in the order from a mass of shelves. Moreover, an increasing number of factories, hypermarkets, logistics companies begin to use mobile robots to fulfil tasks such as sorting, transporting, placing objects, and so on. With the help of autonomous mobile robots, workloads for human employees have been alleviated greatly, and working efficiency has been improved dramatically.

When multiple robots coexist in an area and move autonomously, how to avoid collision among them is a critical problem. If the problem is solved in a centralized way, a central controller is needed in the system. The controller collects current positions and moving states of all mobile robots, and computes moving paths for every robot. However, single-point failure is an inherent problem of the centralized scheme. Moreover, the centralized scheme is not flexible enough, because its scalability is limited by the number of mobile robots. When the number of robots is large, the computation becomes time-consuming, which

is not suitable for real-time control for robots. Hence, a distributed mechanism is preferred in practical scenarios.

In this paper, a negotiation-based collision avoidance algorithm for autonomous mobile robots is proposed. The algorithm operates in a distributed manner. Each mobile robot senses its surrounding environment, and negotiates with related robots when a collision is about to happen. They exchange their urgency degrees or the optional moving directions. Based on the negotiation, a robot decides whether to give way to the other robot. The concessive robot also selects a new moving direction. In order to measure the moving efficiency of robots, a metric called actual time to theoretical time ratio (ATR) is utilized. Extensive simulations are conducted to verify the effectiveness and the efficiency of our proposed algorithm.

Many previous work focus on path planning [1–3] or group communication protocols [4, 5] for mobile robots. To the best of our knowledge, we are the first to put forward a distributed negotiation-based collision avoidance algorithm for autonomous mobile robots. Our contributions are summarized as follows:

- (1) A new metric, which is actual time to theoretical time ratio (ATR), is defined to measure the moving efficiency of mobile robots.
- (2) A concessive robot decision algorithm is put forth. The algorithm is based on the urgency degrees or the number of optional moving directions.
- (3) A moving direction selection strategy for concessive robot is proposed. The new moving direction is selected based on the shortest distance.
- (4) A simulator is developed to evaluate the performance of the collision avoidance scheme. Both effectiveness and efficiency of the scheme are verified.

The remainder of the paper is organized as follows. Related work is summarized in Sect. 2. The system model and the problem is described in Sect. 3. The negotiation-based collision avoidance algorithm for autonomous mobile robots is elaborated in Sect. 4. The results of extensive simulations are shown and analyzed in Sect. 5. Finally, the paper is concluded in Sect. 6.

2 Related Work

Path planning and navigation has been a research hotspot in the field of mobile robots for many years. Surveys are given in [1, 6]. A number of previous works focus on planning a path for a mobile robot to avoid static obstacles [2, 7] or moving obstacles [3]. In [8], a method of collision avoidance based on rules and communication proposes, which combines the local environmental model with the dynamic scene. But it just be appropriate for two robots, and can not deal with the situation that two robots have the same priority. With the development of artificial intelligence, some researchers begin to solve the problem based on computer vision [9]. A real implementation is reported in [10].

Since method in [2] is centralized, distributed solutions are proposed in [3, 7, 11]. In [3, 11], collisions of mobile robots are avoided by adjusting the speeds of the robots. These methods are not fit for the scenario that the speed cannot be

adjusted arbitrarily. In [7], a virtual repulsion-like force is introduced. The force between two mobile robots is determined by the distance between them. Hence, a mobile robot decides its moving direction according to the distance between it and other robots. However, this solution cannot minimize the moving time cost of the robots.

In [4], an efficient group communication protocol for mobile robots is designed. Furthermore, the authors of [4] present a mobility-aware ad hoc routing protocols for mobile robot teams in [5].

In this paper, we design a distributed negotiation-based collision avoidance mechanism. When two mobile robots are about to collide, one of them gives way to the other one based on the negotiation, and the moving time cost is minimized. This scheme has not been put forward in previous work. In this paper, mobile robots negotiate with each other using short distance communication technologies, such as WiFi, Bluetooth, ZigBee, etc. Once a wireless link is set up between a pair of mobile robots, they can transmit information mutually. Routing protocols are not necessary in our scenario.

3 System Model and Problem Description

3.1 System Model

The scenario considered in this paper is that a group of autonomous mobile robots are distributed randomly in a two-dimension (2D) rectangular area, as demonstrated in Fig. 1(a). The number of the robots is m , and the robot group can be represented by an m -dimension vector $\langle R_1, R_2, \dots, R_m \rangle$. The area is divided into $X \times Y$ grids of the same size. Each grid can only accommodate one robot. Thus, the position of a robot can be indicated by the coordinates of the grid in which the robot locates. Specifically, the location of the i -th robot is $L(R_i) = (x_i, y_i)$, where $1 \leq i \leq m$, $1 \leq x_i \leq X$, $1 \leq y_i \leq Y$, and $i, x_i, y_i \in \mathbb{N}$. Suppose each robot knows its position at any time via a certain positioning technology.

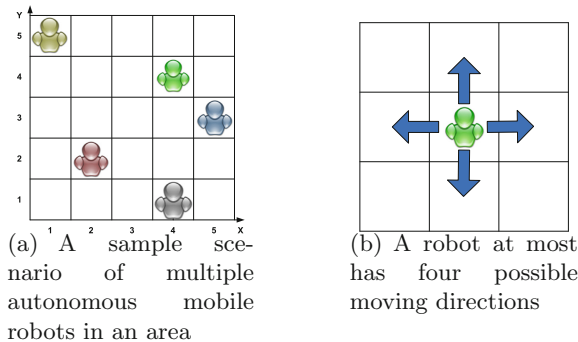


Fig. 1. System model

The goal of each robot is to move from its initial location to a predetermined destination. The initial location of robot R_i is denoted as $L(R_i)_{start} = (x_i^{(s)}, y_i^{(s)})$, and its destination is $L(R_i)_{des} = (x_i^{(d)}, y_i^{(d)})$. It is assumed that each robot can only move towards four directions, i.e., forward, back, left, and right, as shown in Fig. 1(b). Therefore, the distance between two locations for robots is measured as the Manhattan distance. The distance between the starting point of R_i and its destination is $D(L(R_i)_{start}, L(R_i)_{des})$, which is computed as:

$$D(L(R_i)_{start}, L(R_i)_{des}) = |x_i^{(d)} - x_i^{(s)}| + |y_i^{(d)} - y_i^{(s)}| \tag{1}$$

The moving speed of R_i is represented by $S(R_i)$. In this paper, all mobile robots are supposed to move at the same speed. The time that a robot can move from one grid into a neighboring grid is viewed as a time slot. In other words, the distance that a robot can move in a time slot is 1. Thus, the theoretical moving time of R_i from beginning to arrival is denoted as $T(R_i)$, which is computed by:

$$T(R_i) = \frac{D(L(R_i)_{start}, L(R_i)_{des})}{S(R_i)} \tag{2}$$

As demonstrated in Fig. 2, there are two cases that lead to potential collisions between two mobile robots. In Case 1, two robots will move to the same grid in the next time slot. In Case 2, the current position of a robot is the expected position of the other robot, and vice versa. In order to avoid collision, each robot needs to have the ability of sensing and communication. The sensing ability can be achieved by equipping robots with sonar ranging sensors, and the communication ability can be attained through short-range wireless communication technologies, such as WiFi, ZigBee, Bluetooth, etc. Once a robot perceives a potential collision, it avoids the collision through negotiating with the other robot. According to Case 1, the minimal sensing range and the minimal communication range of a robot are both set to 2.

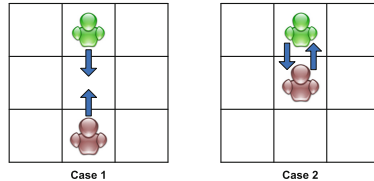


Fig. 2. Two cases of potential collision between two mobile robots

Since a robot may make a detour or stay to avoid collision during the move, its actual moving time, expressed by $A(R_i)$, is no less than the theoretical moving time between the starting point and the destination:

$$A(R_i) \geq T(R_i) \tag{3}$$

3.2 Problem Description

Given starting positions and predetermined destinations of all mobile robots, the total moving time of all robots, recorded as \mathbb{T} , is:

$$\mathbb{T} = \sum_{i=1}^m T(R_i) \quad (4)$$

The total time of all robots actually move, denoted as \mathbb{A} , is calculated by:

$$\mathbb{A} = \sum_{i=1}^m A(R_i) \quad (5)$$

According to inequality (3), the following relationship holds:

$$\mathbb{A} \geq \mathbb{T} \quad (6)$$

In order to improve moving efficiency of all robots, \mathbb{A} should be minimized. Since the starting positions and the destinations of all robots are randomly chosen, the absolute value of \mathbb{A} cannot reflect real moving efficiency. For the sake of fair comparison, actual time to theoretical time ratio (ATR) is put forward as a new metric:

$$ATR = \frac{\mathbb{A}}{\mathbb{T}} \quad (7)$$

Consequently, the objective of the problem is formalized to minimize ATR as follows:

$$\text{minimize } \frac{\mathbb{A}}{\mathbb{T}} \quad (8)$$

s.t. Eqs. (1), (2), (4) and (5).

4 Negotiation-Based Collision Avoidance Scheme

When two robots come into a situation that they will collide in the next time slot as shown in Fig. 2, one of them should change its planned moving direction to avoid the potential collision. Since no centralized controller exists in the system and decisions are made in a distributed manner, three questions are raised. The first question is that which robot should make a concession and alter its planned moving direction. The second question is that, when a robot has to change its moving direction, how to select a new direction for the robot. The last one question, when the number of robots is more than two, how to deal with the collision among them. In this section, all these issues are settled.

4.1 Decision on Concessive Robot

Due to lack of centralized controller, two robots with potential collision should coordinate their moving directions by themselves. Hence, a negotiation-based scheme is designed. With this scheme, two robots establish a wireless link

between them, and exchange necessary information. Based on the exchanged information, both robots make a consistent decision that which one keeps its planned route unchanged, while the other one changes its moving direction. In terms of whether robots have different urgency degrees, how to reach an agreement between two robots is discussed in the following two cases.

Case 1: Robots have different urgency degrees. In a practical scenario, robots that fulfil various tasks may have different urgency degrees. Under this circumstances, two robots exchange their urgency degrees, and the robot with lower urgency degree should make a concession. In this way, the robot with higher urgency degree keeps its route unchanged without making a detour, thus it can arrive its destination as soon as possible. Since the robot with lower urgency degree has to yield, it inevitably leads to longer moving time than its expectation. In order to minimize the metric of ATR, how to select the next step is discussed in Sect. 4.2. If two robots are with the same urgency degree, which one to make a concession is determined as explained in Case 2.

Case 2: Robots have the identical urgency degree. If all robots have the identical urgency degree, a new criterion is needed. The number of optional moving directions is utilized as the new criterion. A robot at most has four optional moving directions. If one or more possible moving directions are blocked by other robots or obstacles, or the robot just locates at the boundary of the region, the number of optional moving direction decreases. As depicted in Fig. 3, the robot R_1 has two optional moving directions (marked by stars), while R_2 has three (marked by circles). After exchanging the number of optional moving directions, the robot with more options changes its planned route, because it has more choices.

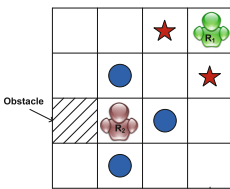


Fig. 3. Examples of the number of optional moving directions

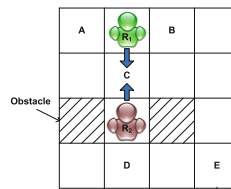


Fig. 4. An examples of decision on concessive robot when robots have the identical urgency degree

An example is demonstrated in Fig. 4. Robots R_1 and R_2 both plans to move into the same grid (marked by C) in the next time slot, and there is a potential collision. Thus, they need to negotiate, and their optional moving direction numbers are exchanged. Robot R_1 has three options (i.e., A, B, and C), while R_2 has two (C and D). As a result, R_1 has to make a concession, and

changes its planned moving direction. To give way to R_2 , R_1 can move into A or B in the next time slot.

If two robots have the same number of next-step options, a winner between them is selected randomly based on a certain distributed algorithm. For instance, each robot generates a random number to compare. It can be appointed that the robot with larger (or smaller) number makes a concession.

4.2 Decision on Moving Direction

Once a robot is determined to alter its moving direction based on the negotiation, it should decide where to move in the next time slot. In order to reduce the cost incurred by the detour, the robot selects the position that has the shortest distance to its destination among all the options. Take Fig. 4 for example again. Suppose E is the destination of R_1 . R_1 selects B as its next position, because the distance between B and E is shorter than the distance between A and E.

If all its optional moving directions are blocked, the robot stays at the current position in the next time slot, and its actual moving time still increases by 1.

4.3 More Discussions

In the case that more than two robots are about to collide, the solution is similar. Each robot broadcasts its urgency or the number of optional moving directions to other relevant robots. If they have different urgency degrees, the robot with higher urgency has higher priority to select moving direction. If relevant robots have the same urgency degree, the robot with less optional moving directions has higher priority to move.

In some particular cases, the priority of two mobile robots are alternated after a negotiation, and they may move between one location and next location. In order to break such deadlock, each robot should record the locations that it has passed. If it finds itself enters a loop, another strategy should be used for breaking out. Due to page limitation, the detailed solution will be described in the extended version of this paper.

5 Performance Evaluation

5.1 Simulation Setup

In order to evaluate effectiveness and performance of the proposed scheme, a simulator is developed using Java programming language. In the simulator, multiple mobile robots are distributed in a 2D region. The starting positions and destinations of all robots are generated randomly following a uniform distribution. Once a simulation starts, each robot moves a distance of 1 in a time slot. The robots move along one dimension (e.g., along X axis) first, then move along the other dimension.

Our proposed concessive robot selection is based on negotiation. For comparison, a random selection strategy is also used in simulations. The recommended

new moving direction of the concessive robot is selected based on shortest route. A random selection strategy is also employed for comparison. The four schemes implemented in the simulations are listed in Table 1. Our proposed scheme is abbreviated as NS, the other three are NR, RS, and RR, respectively.

Table 1. Four schemes are implemented in the simulations

Scheme abbreviation	Concessive robot selection	Moving direction selection
NS	Negotiation	Shortest
NR	Negotiation	Random
RS	Random	Shortest
RR	Random	Random

Simulations are conducted to evaluate performance under following two cases, respectively.

Case 1: Robots have different urgency degrees. In this case, three different urgency degrees are set, i.e., low, medium, and high. Each robot is randomly assigned a urgency degree from the three levels. The size of the area is 100×100 , and the number of robots is set to 100.

Case 2: Robots have the identical urgency degree. In this case, all robots have equal urgency degree. The size of the area is 100×100 . The number of robots is set to 200. Fixed obstacles are distributed in the area following a uniform distribution. The proportion of fixed obstacles varies from 0.01 to 0.03. In another settings, the proportion of fixed obstacles is 0.01, and the number of mobile robots varies from 100 to 300.

A simulation under one setting repeats ten times, and the average results are shown in the following.

5.2 Simulation Results

Case 1: Robots have different urgency degrees. When the number of robots is 100, ATR of robots with different urgency levels are displayed in Fig. 5. With the NS scheme, robots with high urgency degree have the lowest ATR, which means high-urgency robots arrive at their destinations consuming less time. Due to concession made by low-urgency robots, they need to spend more time to move. The results are in accordance with expectation. With other three schemes, it cannot ensure that the robots with high urgency consume the least time.

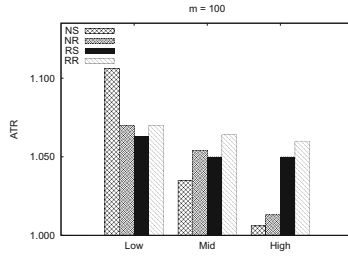


Fig. 5. Performance with different urgency degrees when $m = 100$

Case 2: Robots have the identical urgency degree. As indicated in Fig. 6, performances of the four schemes with varied fixed obstacle are compared. The NS scheme has the lowest ATR, which outperforms other three schemes. The ATR of RS is a little higher than NS, which implies that it is significant to choose a new moving direction for the concessive robot based on the shortest distance. The ATR values of both NS and RS increase slowly with the increase of fixed obstacle proportion, while the ATRs of NR and RR have higher growth rate. As expected, the scheme of RR has the highest ATR.

When the proportion of fixed obstacles is 0.01, and the number of mobile robots varies from 100 to 300, the performances of the four schemes are shown in Fig. 7. With the increase of robot number, ATRs of all schemes grow. However, the NS scheme always has the lowest ATR, and RR has the highest ATR. It can be concluded that the negotiation-based concessive robot selection and the shortest distance-based moving direction selection strategies are effective and efficient.

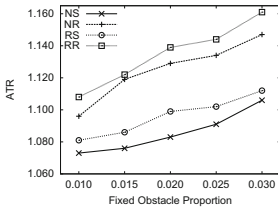


Fig. 6. Performance with varied fixed obstacle proportions

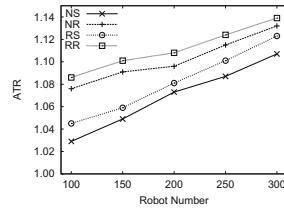


Fig. 7. Performance with varied mobile robot densities

6 Conclusion

In order to avoid collision when multiple autonomous mobile robots coexist in an area, a negotiation-based scheme was put forward in this paper. With the scheme, a robot that should make a concession was selected, and the direction it should move forward was also decided. Extensive simulations proved the effectiveness of the scheme. Implementation of this scheme on a real test is subject to future research.

Acknowledgment. The work is supported in part by the National Natural Science Foundation of China (NSFC) under Grant Nos. 61402513 and 61402494, Guangxi Natural Science Foundation under Grant Nos. 2015GXNSFBA139243 and 2016GXNSFBA380182, and the Scientific Research Foundation of Guangxi University under Grant Nos. XGZ150322 and XGZ141182. The authors would like to thank these sponsors for their generous support.

References

1. Sariff, N., Buniyamin, N.: An overview of autonomous mobile robot path planning algorithms. In: Proceedings of the 4th Student Conference on Research and Development, pp. 183–188. IEEE (2006)
2. Pandey, A., Sonkar, R.K., Pandey, K.K., Parhi, D.R.: Path planning navigation of mobile robot with obstacles avoidance using fuzzy logic controller. In: Proceedings of the IEEE 8th International Conference on Intelligent Systems and Control (ISCO), pp. 39–41. IEEE (2014)
3. Li, Q., Zhou, Z., Wang, S., Yin, Y.: Path planning in environment with moving obstacles for mobile robot. In: Proceedings of the 31st Chinese Control Conference (CCC), pp. 5019–5024. IEEE (2012)
4. Das, S.M., Hu, Y.C., Lee, C.S.G., Lu, Y.H.: An efficient group communication protocol for mobile robots. In: Proceedings of the IEEE International Conference on Robotics and Automation, pp. 87–92. IEEE (2005)
5. Das, S.M., Hu, Y.C., Lee, C.S.G., Lu, Y.H.: Mobility-aware ad hoc routing protocols for networking mobile robot teams. *J. Commun. Netw.* **9**(3), 296–311 (2007)
6. Shaikh, M.H., Kosuri, K., Ansari, N.A., Khan, M.J.: The state-of-the-art intelligent navigational system for monitoring in mobile autonomous robot. In: Proceedings of the International Conference of Information and Communication Technology (ICoICT), pp. 405–409. IEEE (2013)
7. Rezaee, H., Abdollahi, F.: A decentralized cooperative control scheme with obstacle avoidance for a team of mobile robots. *IEEE Trans. Ind. Electron.* **61**(1), 347–354 (2013)
8. Asama, H., Abdollahi, F.: Collision avoidance among multiple mobile robots based on rules and communications. In: International Workshop on Intelligent Robots and System, pp. 1215–1220. IEEE (1991)
9. Ziaei, Z., Oftadeh, R., Mattila, J.: Vision-based path coordination for multiple mobile robots with four steering wheels using an overhead camera. In: Proceedings of the IEEE International Conference on Advanced Intelligent Mechatronics (AIM), pp. 261–268. IEEE (2015)
10. Su, K.L., Shiau, S.V., Guo, J.H., Liao, Y.L.: Implement a path planning method for mobile robots on the unknown environment. In: Proceedings of the Fourth International Conference on Genetic and Evolutionary Computing (ICGEC), pp. 445–448. IEEE (2010)
11. Zheng, J., Yu, H., Liang, W., Zeng, P.: Distributed and optimal algorithm to coordinate the motion of multiple mobile robots. In: Proceedings of the 7th World Congress on Intelligent Control and Automation (WCICA), pp. 3027–3032. IEEE (2008)



Intelligent Access Scheme for Internet of Things Supported by 5G Wireless Network

Yingshuan Song¹(✉), Heli Zhang¹, Xi Li¹, Chunsheng Zhu²,
and Hong Ji¹

¹ Key Laboratory of Universal Wireless Communication, Ministry of Education,
Beijing University of Posts and Telecommunications,
Beijing 100876, People's Republic of China

{songchunming, zhangheli, lixi, jihong}@bupt.edu.cn

² Department of Electrical and Computer Engineering,
The University of British Columbia, Vancouver, BC, Canada
chunsheng.tom.zhu@gmail.com

Abstract. In future Internet of things (IoT) network, some of the prime objectives or demands that need to be addressed are massive data, increased devices, decreased delay and reduced energy cost. To meet these demands, drastic improvements need to be made. This paper integrates 5G network with IoT scenario and presents a massive IoT device access scheme. In our small cell-IoT network, IoT devices share the resource block (RB) with small cell devices in an overlay way. Under this context, we formulate the access problem with the objectives of minimizing network overall energy cost and maximizing the number of accessed IoT devices. By utilizing data mining tool, the massive data generated by the small cell network and IoT devices is highly utilized and IoT devices can access to the available RBs with higher intelligence. In addition, under the support of K-means algorithm, IoT devices are classified into different clusters. We further propose a cluster access method, with which, each cluster is allocated appropriate RB. All the devices within the same cluster share the same RB in a sequence while considering RB's vacant time. Simulation results show that our solution leads to a satisfactory outcome.

Keywords: Intelligent access scheme · 5G small cell · IoT · K-means

1 Introduction

In last decades, Internet of Things (IoT) attracted a lot of attention and a large variety of connectivity technologies gradually emerged. Traditional technologies such as WiFi are only able to support short range IoT devices while modern tools including LoRa are designed for wide area coverage. Since IoT has potential facilitation to economy growth, future smart personal life and industry, it will continue to evolve. As predicted, by 2020, the number of IoT devices will be over 50 billion [1] and the total data generated by IoT devices will exceed 4.4 zettabytes [2]. Under this context, how to bear the enormous amounts of devices and data is a big challenge.

The previous works mainly try to combine IoT with 5G related key technologies or try to find better ways to allocate resources to improve the network performance. In [3]

Software Defined Network technologies are jointly introduced to IoT architectures. The authors in [4] focus on the realization of innovative architectures for the Cloud-IoT, From this vision, IoT system can be enhanced by the Cloud environment feature. And in [5], Mobile Edge Computing is considered as a promising technology for its advantage of offering cloud-computing capabilities and an information technology service environment at the edge of the mobile network, close to mobile subscribers. Different from the papers above, author of paper [6] introduce the current status of industrial IoT development and the technical architecture and key elements of IoT to perform device management. And work of [7] considers resource allocation in heterogeneous networks, while the authors in [8] concern on design solution to uplink spectrum sharing with Narrow Band Internet of Things (NB-IoT) technology. The authors in [9] propose and evaluate an intelligent container-based resource management platform for the IoT, where the utilization of these IoT resources is increased while the generated network traffic is analyzed. In [10], smart resource management is proposed in IoT by leveraging Radio-Frequency Identification, Near Field Communication, Wireless Sensor Network, and universal mobile accessibility advanced technologies, a use case is described to prove the efficiency of the scheme. Authors in [11] combine information-centric approach with IoT resources, and also use virtualization technology to aggregate resources. Under this context, resource provisioning and management for users across IoT can be designed and implemented automatically.

In this paper, we focus on the small cell-IoT scenario and formulate the massive IoT devices access problem with the objectives to minimize network overall energy cost and maximize the number of accessed IoT devices. We come up with a novel approach that endow cellular network the ability of bearing massive IoT devices' access. By using K -means algorithm in our scheme, we provide a way to classify IoT devices with better similarity to one cluster. And a novel access sequence method is designed for each IoT device cluster, considering each RB's vacant time length.

The remainder of this paper is organized as follows. In Sect. 2, we introduce the system model. The design of the intelligent access algorithm for Internet of Things supported by 5G wireless network is represent in Sect. 3. In Sect. 4, we evaluate the performance of the proposed algorithm. Finally a conclusion is given in Sect. 5.

2 System Model

Here, the network scenario of future 5G small cell-IoT is described. Based on which, the network model and communication model are introduced. Finally, we formulate the IoT device access problem that studied in this paper.

2.1 Network Model

In this paper, we study the 5G small cell-IoT network involved by a group of small cell base stations (SBSs) denoted by $\mathbb{H} = \{1, 2, \dots, K\}$ and a set of IoT devices $\mathbb{U} = \{1, 2, \dots, U\}$, as illustrated in Fig. 1. IoT devices access to SBSs to acquire wireless service. Let the $a_{u,k}$ be the access indicator between SBS k and IoT device u . If device u can be allowed to access to SBS k , then $a_{u,k} = 1$, otherwise $a_{u,k} = 0$.

We assume IoT and SBS devices share resource blocks (RBs) in an overlay mode, so that IoT devices can only use the RBs when they are not occupied by SBS devices. Denote RBs by set $\mathbb{H} = \{(1, 1), (1, 2), \dots, (i, j), \dots, (I, J)\}$, where $i \in \{1, 2, \dots, I\}$ is corresponding to time slot of RBs and $j \in \{1, 2, \dots, J\}$ is equalized to frequency band of RB. Each RB has a status $\{h_{i,j}, t_i, \sigma_j^2\}$, where $h_{i,j}$ is the channel state information, t_i is the vacant time and σ_j^2 denotes the interference on the RB. For each IoT device, since delay is the key element when completing a data transmission task, we assume they have a access requirement state $\{l_u, T_u, p_u\}$, where l_u, T_u and p_u mean the size of data in one data transmission task, the total delay that one device can tolerate and the transmission power of device u .

In addition, in our network model only one macro base station exists, which can collect the overall network state information, and the IoT devices and SBSs transmit their local states periodically to the macro base station. Furthermore, macro base station is responsible to implement the proposed scheme and compute the access relationship between IoT devices and SBSs.

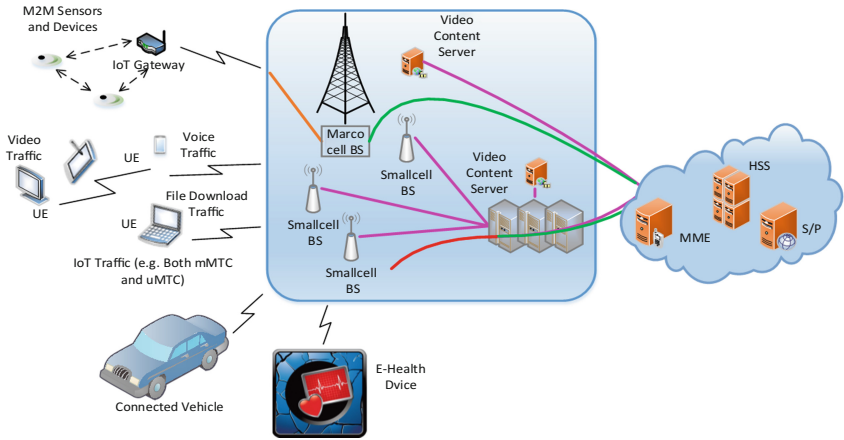


Fig. 1. Future 5G internet of things network

2.2 Communication Model

In this paper, we intend to consider uplink transmission access for IoT devices, then the communication model can be denoted as the following:

$$\gamma_u = a_{u,k} B_{u,k} \log(1 + h_{i,j}^{u,k} p_{u,k} (\sigma_{j,k}^2)^{-1}) \quad (1)$$

where $B_{u,k}$ denotes the bandwidth of the RB that is allocated to device u by SBS k , $p_{u,k}$ is the transmission power for device u .

2.3 Energy Consumption Model

Since energy consumption is attracting researchers' attention in IoT study, we consider this parameter in our scheme. The energy consumed in our model includes two parts as shown in the following.

$$E_{u,k} = E_{u,k}^t + E_{u,k}^w = p_{u,k}t_{u,k} + \lambda_{u,k}w_{u,k} \quad (2)$$

where $E_{u,k}^t$ is the transmission energy consumed when device u transmit data to SBS k . $E_{u,k}^w$ is the waiting energy which is utilized for RB monitor or singling information exchange before device u can access to SBS k . $\lambda_{u,k}$ is the power to evaluate the waiting power and $w_{u,k}$ means the waiting time. While $t_{u,k}$ denotes the transmission delay for device u and it is calculated with this function:

$$t_{u,k} = \frac{l_{u,k}}{B_{u,k} \log(1 + p_{u,k}(\sigma_{k,j}^2)^{-1})} \quad (3)$$

2.4 Problem Formulation

In our study, one of the objectives is to maximize the number of IoT devices that can be allowed to access to the SBS, which is shown by the following function,

$$\max N = \sum_{k=1}^K \sum_{u=1}^U a_{u,k} \quad (4)$$

Energy is another important parameter that should be considered in the IoT devices selection. In our consideration, we intend to minimize the network overall energy cost,

$$\min C = \sum_{k=1}^K \sum_{u=1}^U C_{u,k} \quad (5)$$

where $C_{u,k}$ means the energy consumed by transmitting per unit data and calculated with the following function:

$$\begin{aligned} C_{u,k} &= a_{u,k}E_{u,k}^t/l_{u,k} \\ &= a_{u,k}p_{u,k}t_{u,k}/l_{u,k} \\ &= a_{u,k}p_{u,k}/\gamma_{u,k} \end{aligned} \quad (6)$$

Since the vacant time scale for SBS's RB resource is limited, the total transmission time for all devices accessed to SBS k should be no larger than a threshold. So that we have the following constraint:

$$\sum_{j=1}^J a_{u,k} d_{u,k} \leq TD_k \quad \forall k \in \mathcal{T} \quad (7)$$

where TD_k denotes the available access time scale of SBS k . Under this limitation, only parts of the devices can be finally chosen to complete their data transmission.

To each IoT devices, delay is an important factor for data transmission, then the inequation below should be followed,

$$t_{u,k} \leq T_u \quad (8)$$

The foregoing analysis can be regarded as an integer-programming problem.

3 Algorithm Design

In this section, we intend to propose an algorithm for the problem mentioned above.

3.1 Problem Analysis

In the future 5G small cell-IoT scenario, large amount of devices and data exist, while the resources are limited. Moreover, each IoT devices has its own QoS requirements, so that the device fairness also needs to be taken into account.

In order to solve the proposed problem in a higher efficiency, we intend to utilize data mining tools. Since large amounts of network data such as the information of the RBs and devices can be generated, utilizing data mining can help digging these data and design intelligent solutions for our access problem. In addition, by collecting and analyzing network data, architectural and functional flexibilities can be achieved.

Considering the network scenario, we propose the scheme for IoT devices' access, which is called intelligent and massive access for 5G IoT devices (IMAIID). This scheme consists of three steps. Firstly, the access requirement information of all IoT devices is collected by SBSs. One cluster algorithm, K -means, is applied to study these data and construct IoT device clusters. Secondly, by analyzing RBs' state information and the clusters' characteristics, SBSs and IoT device clusters are matched in an appropriate way, where the network energy cost is considered. Finally, for data transmission, IoT devices are arranged in a better sequence while considering the vacant time of RBs. In the following, the three steps are described in detail.

3.2 IoT Cluster Construction

K -means [12] as a well-known and popular clustering approach is also an efficient iterative clustering method. It is intended for scenarios wherein all variables are of the quantitative type. This algorithm can effectively partitions the N -dimensional data into K sets. The detail of K -means clustering algorithm is shown in Algorithm 1.

Algorithm 1: The K-means Clustering Algorithm

Input: D (data item sets), K (number of required clusters), $t=0$ is the iteration time.

1. **Initial centroids selection:** select K data-items from D as initial centroids;
2. **Cluster construction:** $t = t + 1$. Allot each data item to its closest centroid and then K clusters are constructed. The new clusters are $D' = D_{k'}$, $k' \in \{1, 2, \dots, K\}$;
3. **New means determination:** Compute new means for each cluster according to new means determination rule;
4. Repeat step 2 and 3;
5. **Stop rule:** Stop until convergence criteria is achieved.

Output: $D_{k'} \in D$, $k' \in \{1, 2, \dots, K\}$.

In Algorithm 3, according to the result of power divided by the length of the packet, we sort the IoT devices and partition the sorted IoT devices into K equal sets and choose the ones with middle value in each sets as the initial centroids. At last, we can get the final grouping result with Algorithm 1.

3.3 IoT Device Cluster Access

After classifying IoT devices into different clusters, the next work is to design the cluster access scheme. Within our access algorithm, RB state information is regarded as the important element to match different device clusters with SBSs. And the detail of IoT device cluster access algorithm is shown in Algorithm 2.

Algorithm 2: Energy Efficient Access for IoT Device Cluster

Input: K clusters, SBS set k , RB status $\{h_{i,j}, t_i, \sigma_j^2\}$; data transmission requirement state of each IoT device $\{l_u, T_u, p_u\}$;

1. Compute the energy-data ratio $C_{s,k} = \sum_{u=1}^{C_s} p_{u,k} / \gamma_{u,k}$ for each cluster s when accessing to SBS k , and finally get the ratio set $\{C_{s,k}\}$;
2. Select the SBS k' providing minimum energy-data ratio to the IoT device cluster s as the access SBS;
3. Remove the selected SBS from SBS set, $k = k - s$;
4. Repeat 2-3 until all the clusters are allocated appropriate SBS;

Output: Access Matrix $A = \{a_{u,k}\}$.

Firstly, network information is collected by the macro base station. Then the energy-data ratio set $\{C_{s,k}, k \in \mathbb{N}\}$ for each cluster s is figured out according to function (6). Within each set, select the SBS offering minimum energy-data ratio as the serving SBS for cluster s . This rule intends to decrease the network energy consumption. Steps 2–3 is repeated until all clusters find the appropriate SBS to access, then the access matrix A can be output finally.

3.4 Data Transmission Sequence Determination

Since the available RB is limited, IoT devices have to share the same RB for data transmission. Under this circumstance, IoT devices should be ordered and send data in a sequence. For this purpose, we propose a transmission delay minimization method to determine the transmission sequence for IoT device clusters, where the SBS could serve as many devices as they can. However, when delay-tolerant parameter is not appropriate for IoT device, these devices will be abandoned directly.

The steps of transmission delay minimization method can be obtained clearly from the Algorithm 3, with which we can get the final transmitting queue, shown below.

4 Simulation Result

In this section, the performance of the algorithm is simulated and verified by MATLAB, and a specific simulation scenario is designed to acquire more appropriate evaluation results in this paper. In this scenario, the number of base stations is fixed to 5, and the number of devices is set from 1 to 500. The power and delay tolerant value of devices both follow normal distribution. And the specific parameters in the simulation are summarized and shown in Table 1.

Algorithm 3: Data Transmission Sequence Determination

Input: K clusters, SBS set k , RB status $\{h_{i,j}, t_i, \sigma_j^2\}$; data transmission requirement state of each IoT device $\{u, T_u, p_u\}$, Cluster user set $U_{s,k} = \{u_i\}$, accessed user set $U_{s,k} = \{\Phi\}$ and iteration time $p=0$;

1. Each IoT devices sends its delay tolerant T_u to accessed SBS.
2. Sort IoT devices within set $U_{s,k}$ in an incremental order according to their delay tolerant T_u .
3. Set $p = p + 1$, $U_{s,k} = U_{s,k} - \{u_p\}$, $U'_{s,k} = U'_{s,k} + \{u_p\}$.
4. SBS calculates the overall delay tolerant $T'_{u,k}$ for devices intending to send data, where $T_{u,k}$ is derived by:

$$T_{u,k} = \sum_{u=1}^{U'_{s,k}} t_{u,k}, \quad u \in U'_{s,k}$$

5. **If** $T_{u,k} \leq TD_k$ and $T_{u,k} \leq T_u$
 This IoT device is served by SBS k ;
Else
 Abandon this IoT device $U'_{s,k} = U'_{s,k} - \{u_p\}$ and continue to check other devices;
6. **End if**
7. Repeat 2-6 until all users in the cluster have been removed, i.e. $U_{s,k} = \{\Phi\}$

Output: $U'_{s,k}$

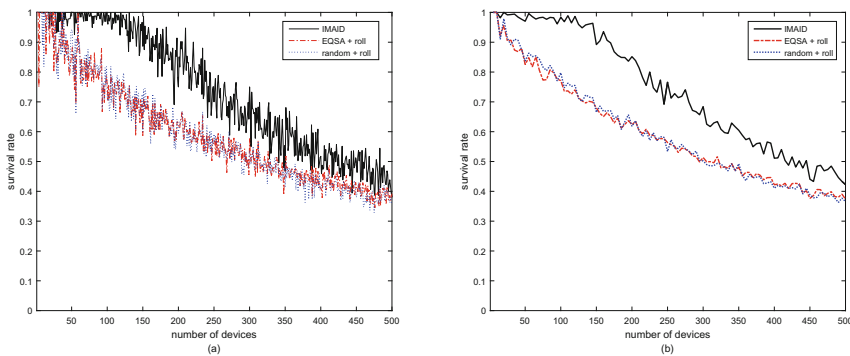
Table 1. Simulation parameters

Parameters	Value
Power-average	30 mW
Power-variance	15
Delay-tolerant-average	20 ms
Delay-tolerant-variance	20
Packet-size	10–30 Byte
Idle-time of base station	30–50 ms

Since our algorithm is divided into clustering and intra-cluster sorting parts, so that each of the resource allocation scheme also includes device clustering and intra-cluster sorting parts. Here we use two comparison schemes. One scheme employs the energy-centered and QoS-aware services selection algorithm (EQSA) as the clustering method and roll polling algorithm as the intra-group sorting algorithm. The other scheme uses a random clustering method and the roll polling algorithm as the intra-clustering algorithm. In the following illustration of the simulation diagram, we use IMAID, EQSA + roll, and random + roll to represent the three schemes respectively. And the performance of IMAID is evaluated through the following aspects.

A. Device Survivability

Device survivability is one of the most important metrics that can be used to measure the performance of a scheme. Considering the number of base stations is constant and the number of devices is flexible in our scenario, we choose the survival rate but not the number of the survival devices as the simulated performance.

**Fig. 2.** Survival rate of the devices versus the number of devices

The survival rate with varying number of devices is shown in Fig. 2(a). Comparing the three curves, we can learn that IMAID scheme could provide higher device survivability in the same situations compared with the other two schemes. It is also shown in Fig. 2(a) that with the number of devices increasing, the survival rate gradually decreases in a slow speed. That is because that the number of base stations is constant,

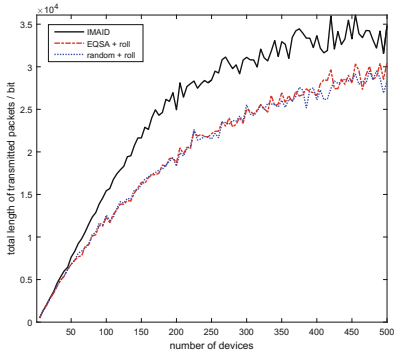


Fig. 3. Survival rate of the devices versus the number of devices (Color figure online)

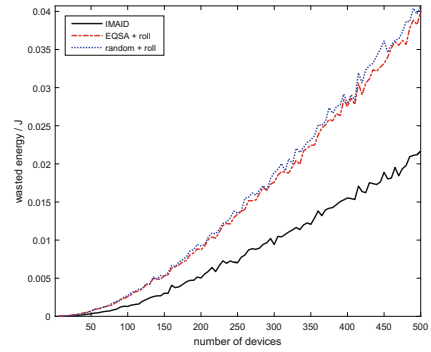


Fig. 4. Wasted energy versus the number of devices (Color figure online)

which means all available resources have an upper bound. The more devices there are, the more significant the competition is, and the lower the survival rate is. It is notable that the performance curves are not stable, but with a fluctuation in Fig. 2(a). This is due to the idle time and channel quality parameter of each base station are both generated by independent random distribution, which is used to reflect the time-varying nature of these parameters. Figure 2(a) clearly shows that our resource allocation scheme has an advantage in guaranteeing device survivability.

To avoid the impact of curves severe fluctuation on performance analysis, we have processed the simulation result minutely by time-averaging before generating the simulation curves, under the premise that without affecting the analysis accuracy. The processed result is shown in Fig. 2(b) and from these modified curves, we can get all the conclusions that has been got from Fig. 2(a), proving this processed solution maintain the accuracy of the simulation result successfully. And we have carried out a similar treatment to the figures with excessive fluctuation in the after analysis.

B. Total Length of the Transmitted Packets

Total length of transmitted packets is the sum of the packets that are transmitted successfully, which can be used to measure the total throughput in the period of time. Total length of transmitted packets versus the number of devices is shown in Fig. 3.

Figure 3 shows all the three curves increase linearly with the number of devices at first, but when the number of devices increases to about 200, the growth rate becomes slow, and when it comes to about 400, the total length of the transmitted packets becomes stable relatively. The reason is that when the number of devices is small, the resources are enough to serve all so that the total length of transmitted packets will increase linearly with the increase of the number of devices. However, when there are too more devices in a cell, the resources gradually becomes limited and the growth rate of the total length of transmitted packets becomes slow and until becomes stable.

Comparing these three curves, it is obvious that there is a high degree of similarity between the red curve and the blue curve. And the black curve is higher than the other two when the number of devices is the same, which means that our proposed IMAID scheme can provide a higher throughput.

C. Wasted Energy

The wasted energy simulated is the sum of the wasted energy of all devices. In this paper, wasted energy of each device is defined as the product of its power and waiting time and a scale factor which is set to 0.05. The wasted energy will be reduced to a reasonable minimum value by employing appropriate scheme. Wasted energy of the devices versus the number of devices is shown in Fig. 4.

The simulation result shows obviously that the wasted energy is positively related to the number of devices whichever scheme being executed in a cell. The growth rate of the red curve and the blue curve is almost the same, and the energy consumption of them is similar. However, using IMAID scheme can reduce the energy consumption to about half of the other two, and this can greatly extend the battery life.

5 Conclusion

To meet these demands of massive data and device support, delay decrement and energy cost reduction for future Internet of things network, we propose an intelligent access scheme named IMAID. Within this scheme, 5G wireless network integrated with IoT scenario is investigated, where IoT devices share the resource block (RB) with small cell devices in an overlay way. We also formulate the access problem with the objectives of minimizing network overall energy cost and maximizing the number of accessed IoT devices. At last, various simulation results are done to show the advantage of our solution.

Acknowledgments. This paper is sponsored by the National Natural Science Foundation of China for the Youth (61501047) and Fundamental Research Funds for the Central Universities of China (2017RC04), and the National Science and Technology Major Project of the Ministry of Science and Technology of China (2016ZX03001017).

References

1. Ericsson, L.: More than 50 billion connected devices. White Pap. **14**, 124 (2011)
2. <http://www.zdnet.com/topic/the-power-of-iot-and-big-data/>, September 2016
3. Bizanis, N., Kuipers, F.A.: SDN and virtualization solutions for the internet of things: a survey. *IEEE Access* **4**, 5591–5606 (2016)
4. Call: FP7-ICT-2013-EU-Japan Type: STREP: Cloud-of-things-(clout) project, April (2015). <http://clout-project.eu>
5. Frankston, B.: Mobile-edge computing versus the internet?: Looking beyond the literal meaning of MEC. *IEEE Consum. Electron. Mag.* **5**(4), 75–76 (2016)
6. Sheng, Z., Mahapatra, C., Zhu, C., Leung, V.C.M.: Recent advances in industrial wireless sensor networks toward efficient management in IoT. *IEEE Access* **3**, 622–637 (2015)
7. Xie, F., Yu, F.R., Ji, H.: Dynamic resource allocation for heterogeneous services in cognitive radio networks with imperfect channel sensing. *IEEE Trans. Veh. Technol.* **61**(2), 770–780 (2012)

8. Mo, Y., Do, M.-T., Goursaudc, C., Gorce, J.-M.: Optimization of the predefined number of replications in a ultra narrow band based IoT network. In: 2016 Wireless Days (WD), pp. 1–6 (2016)
9. Renner, T., Meldau, M., Kliem, A.: Towards container-based resource management for the internet of things. In: Proceedings International Conference on Software Networking (ICSN), pp. 1–5 (2016)
10. He, J.S., Atabekov, A., Haddad, H.M.: Internet-of-things based smart resource management system: a case study intelligent chair system. In: 25th International Conference on Computer Communication and Networks (ICCCN), pp. 1–6 (2016)
11. Truong, H.-L., Narendra, N.: Sinc-an information-centric approach for end-to-end IoT cloud resource provisioning. In: 2016 International Conference on Cloud Computing Research and Innovations, pp. 1–8 (2016)
12. Khan, S.S., Amir, A.: Cluster center initialization algorithm for K -means clustering. Pattern Recogn. Lett. **25**(11), 1293–1302 (2004)



Fast Group Paging Algorithm for Large-Scale MTC Systems

Si Huang¹, Xiaohui Li¹(✉), Bin Zhou², Yanbin Zhao³, and Ruiyang Yuan¹

¹ State Key Laboratory of Integrated Service Networks,
Xidian University, Xi'an 710071, Shaanxi, China
xhli@mail.xidian.edu.cn

² AVIC Computing Technique Research Institute, Xi'an, Shaanxi, China

³ Geographic Information Center, Yangquan City, Shanxi, China

Abstract. Group paging (GP) is an effective way to solve the serious congestion problem. Congestion problem usually is caused by lots of machine-type communication (MTC) devices communicating at the same time. A certain number of MTC devices in each time slot is been activated, and the number of MTC devices can achieve the maximum of resource utilization. First of all, the total number of MTC devices in each time slot should be calculated according to the different new arrivals in each time slot. By making the resources utilization maximum, the optimal number of total MTC devices can be obtained, from which the optimal number of arriving MTC devices in each time slot will be get. To estimate the total number of MTC devices for traffic scattering GP, a Fast Group Paging Algorithm (FGPA) is proposed, which aims to improve the performance of GP under the condition of massive MTC devices. FGPA is an iterative algorithm that converges fast and has low arithmetic complexity. The corresponding simulation results demonstrate that the proposed FGPA requires less number of iterations under the condition of the same estimation results of total number of MTC devices compared with the existing iterative algorithm.

Keywords: Machine-type communication · Group paging
Low-complexity iteration method · Severe congestion

1 Introduction

Machine-type communication has significant influence on the next generation networks, which involves lots of MTC devices to support different type of services. The future MTC cellular networks have main features, for example, low-power, low-cost, and high coverage. In order to meet these characteristics, the system design has some new challenges [1]. As the number of MTC devices has increased dramatically and MTC simultaneously access [2] the network, which may cause serious collisions and intolerable delays, and thus affect the performance of the network. In order to solve this problem, many methods of

congestion control [3] have been studied. Specifically, the main reason for the emergence of congestion is, because many MTC devices contend for the same RA resource simultaneously [4].

Paging [4], a push based method, sending a paging message over the network to the MTC device which is considered by aiming at its individual ID. However, if the paging mechanism is applied to a scenario that has large-scale MTC device, which may cause a significant reduction in paging efficiency. In order to solve this problem, the concept of group paging (GP) is presented. In group paging (GP), MTC devices grouped into groups in terms of different metrics, and each group identified by a unique, ID (GID) [5]. So that all MTC devices belonging to the same group can paging through a paging message, which greatly reduce the number of paging messages and the paging time.

The GP method in MTC systems was used in [6], where improves the performances by doing paging operations scattered in different time slots. However, the total number of MTC devices in which is estimated by ordinary iteration algorithm. And this kind of estimation method requires a large number of iterative operations, which seriously affecting the performance of the algorithm, so the algorithm needs to be improved.

Therefore, we propose a Fast GP Algorithm (FGPA) in this paper to estimate the total number of MTC devices, which greatly improves the performance of GP. In order to more accurately estimate the total number of MTC equipment in every slot, FGPA algorithm proposed converges fast and has low arithmetic complexity. And then the number of MTC devices successfully accessed in each time slot can be calculated based on the total number of MTC devices in each slot. Finally, calculate the utilization of resources according to the MTC device number of successful access to the network.

The remainder in this paper is organized as follows. In Sect. 2, system model used in our study is introduced and the analysis of our proposition for Fast GP Algorithm are detailed in Sect. 3. The performance results including the estimation accuracy and comparison of iterations number between the proposed FGPA and ordinary iteration algorithm are investigated in Sect. 4. Finally, in the Sect. 5, summarizing the conclusions for this paper.

2 System Model

In this section, through the analysis of numerous inference and calculation under different conditions, we introduce an improved scheme that reduces the complexity of the ordinary iterative algorithm. Firstly, we introduce the system model, and then present the improved algorithm that estimating the total number of MTC devices.

In our study, we consider a group of M MTC devices which share a common GID uniformly distributed in a cell, so one paging message can notify the M MTC devices to communicate with the MTC server. It is assumed that the eNB reserves R RA resources defined as RA Opportunities (RAOs) for the contention access [7]. In this paper, we assume that the number of resources is equal to the number of preambles.

When the number of new arrivals at each RA slot is same, in each situation there will be an optimal number of total MTC devices in every slot that maximizes resource utilization rate. All M MTC devices will start the RACH procedure [8], and scattering the paging operation of the MTC devices over a GP interval after receiving the paging message, instead of transmitting their access attempts at the same RA slot immediately.

The performance of group paging during a group paging interval of I_{\max} RA slots is studied. The utilization of RAOs which is denoted as U is the ratio of the average number of successfully accessed RAOs to the total number of reserved RAOs and U is given by

$$U = \frac{\sum_{i=1}^{I_{\max}} \sum_{n=1}^{N_{PT_{\max}}} M_{i,S}[n]}{I_{\max}R} \tag{1}$$

where $M_{i,S}[n]$ is the number of MTC devices which transmit their n_{th} preamble at the i_{th} RA slot and successfully complete the RA procedure. From the Eq. (2), we can come to a conclusion that in order to improve the resource utilization rate in certain parameters of the situation, we should maximize the value of $M_{i,S}[n]$.

Equation (2) can be written as follows [9]:

$$M_i = M_1 \sum_{n=1}^{N_{PT_{\max}}-1} \beta_m e^{-\frac{M_i}{R}} p_k \tag{2}$$

where $\beta_m = \sum_{t=1}^{N_{PT_{\max}}-m} (-1)^m \sum_{k_1=1}^t \dots \sum_{k_m=k_{m-1}+1}^{t+m-1} p_{k_1} \dots p_{k_m}$ [4]. According to the exponential function e^x can be approximated by Eq. (4). And then applying Eq. (3) to Eq. (2), we can obtain Eq. (4)

$$e^x \approx 1 + x + \frac{x^2}{2!} \tag{3}$$

$$\begin{aligned} & \left(\sum_{m=0}^{N_{PT_{\max}}-1} m^2 \beta_m \right) \times M_i^2 - 2 \left(\frac{R^2}{M_1} + R \sum_{m=0}^{N_{PT_{\max}}-1} m \beta_m \right) \times M_i \\ & + 2R^2 \sum_{m=0}^{N_{PT_{\max}}-1} \beta_m = 0 \end{aligned} \tag{4}$$

Due to Eq. (4) is a second order equation for M_i , which can be solved by using ordinary iteration operation. However, the estimation of M_i under ordinary iteration operation has very high complexity, so we put forward a new iteration method to improve the performance of estimation of M_i with low complexity.

3 The Fast Group Paging Algorithm

In view of the ordinary iteration method has a higher complexity and has the large number of iterations. So here we can consider using Newton iteration method instead of the ordinary iteration method, which is an approximate

method of solving the equation for real number domain and complex domain. Generally speaking, the iterative method is a recursive process that with the old values of variables replace by the new value. So the accuracy of the estimated value is very important which will influence the successful number of MTC devices.

Newton iteration method is to find the equation of the root by taking some leading terms of Taylor series belong to the function. Newton iterative method is one of the important methods for equation root, whose biggest advantage is square convergence in near simple root of equation $f(x) = 0$, so Newton iterative method is used to solve the equation, which is called Fast Group Paging Algorithm (FGPA) in this paper.

First of all, we need to construct a function according to Eq. (2) and make the value of function is equal to zero

$$f(M_i) = M_i - M_1 \sum_{m=0}^{N_{PT_{\max}}-1} \beta_m e^{-\frac{mM_i}{R}} = 0 \tag{5}$$

To solve this equation we can use the Newton Iteration Estimation Algorithm which is square convergence, and we can get the derivative of $f(M_i)$

$$f'(M_i) = 1 + \frac{m}{R} M_1 \sum_{m=0}^{N_{PT_{\max}}-1} \beta_m e^{-\frac{mM_i}{R}} \tag{6}$$

which is the further improvement of the approximated value of M_i .

Then, the initial guess of the total number of MTC devices M_{ig} is assumed that the value calculated by Eq. (4) which is a quadratic equation of one unknown.

$$M_{ig} = [-b \pm \sqrt{(b^2 - 4ac)}] / 2a \tag{7}$$

where

$$a = \left(\sum_{m=0}^{N_{PT_{\max}}-1} m^2 \beta_m \right) \tag{8}$$

$$b = -2 \left(\frac{R^2}{M_1} + R \sum_{m=0}^{N_{PT_{\max}}-1} m \beta_m \right) \tag{9}$$

$$c = 2R^2 \sum_{m=0}^{N_{PT_{\max}}-1} \beta_m \tag{10}$$

In step 2, first a general iteration is used, which will make the guess value much closer to the real solution of the equation.

$$M_{in} = M_1 \sum_{m=0}^{N_{PT_{\max}}-1} \beta_m e^{-\frac{mM_{ic}}{R}} \tag{11}$$

In the next step, according to Newton Iteration algorithm and repeating Newton Iteration operation until $|M_{in} - M_{ic}| < \delta$, which will obtain the estimation value of M_i . where δ is the tolerate error, and $\delta = 0.001$ is supposed in this paper. We can get

$$M_{ic} = M_{in} \tag{12}$$

$$M_i = M_{ic} - \frac{f(M_{ic})}{f'(M_{ic})} \tag{13}$$

Finally, the current number of MTC devices is obtained by M_{ic} . The FGPA is as follows Algorithm 1.

Algorithm 1. FGPA for the approximated value of M_i

1. Set the first guess value of M_{ig} ;
 2. $M_{ic} = M_{ig}$, and calculate the new number of MTC devices $M_{in} = M_1 \sum_{m=0}^{N_{PTmax}-1} \beta_m e^{-\frac{mM_{ic}}{R}}$;
 3. Repeat operation: $M_{ic} = M_{in}$
 $M_i = M_{ic} - \frac{f(M_{ic})}{f'(M_{ic})}$
 Until $|M_{in} - M_{ic}| < \delta$;
 4. Update the existing value $M_{ic} = M_{in}$.
-

Estimating the value by the FGPA is still accurate, and the algorithm is much simpler and has less number of iterations. After obtaining the total number of MTC devices, the optimal value of new arrival MTC number will be got by taking resource utilization into consideration according to Eq. (2). In other words, the number of new arrival MTC is the activated MTC number in every slot, and the optimal value can be obtained by simulation results.

For example, Fig. 1 shows the relationship between MTC number of new arrivals and the corresponding resource utilization rate when $R = 42$ and $R = 54$, from which we can obtain the optimal number of MTC new arrivals. The new arrivals number is the value that makes the resource utilization rate maximum, and we should activate the number of MTC devices in every slot. From the figure we can get the number of new arrivals should be 15 and 20 when $R = 42$ and $R = 54$, respectively.

4 Simulation Results Analysis

First of all, we will verify the estimation accuracy of proposed algorithm is very high by simulating the total number of MTC devices and the successful number

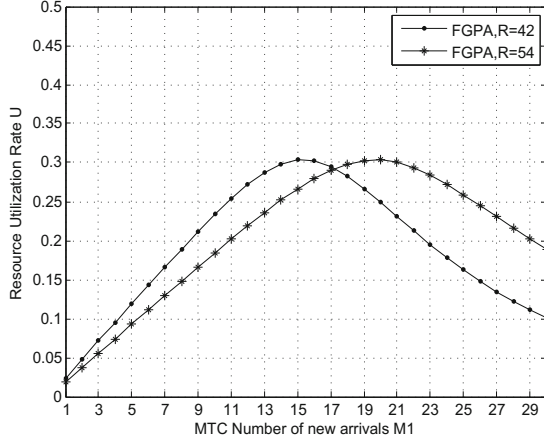


Fig. 1. The relationship between MTC number of new arrivals and the corresponding resource utilization rate when $R = 42$ and $R = 54$.

of MTC devices under certain parameters circumstance. After the true value of MTC devices number is obtained, we compare the performance of the proposed algorithm with the ordinary iteration algorithm in the FI-TSFGP. The basic parameters summarized in Table 1 are used in the simulation.

Table 1. Simulation parameters

Notions	Description	Values
M	Number of devices (each cell)	10–5000
R	Total number of preambles (per slot)	42 or 54
$N_{PT_{\max}}$	Maximum preamble transmissions	5
W_{BO}	Back-off window Size	$BI+1$
W_{RAR}	Size of RAR window	5
$T_{RA_{REP}}$	Interval (consecutive RA slot)	5
p_n	Preamble detection probability	$1 - e^{-n}$
N_{ACK}	Maximum number of ack (an RAR window)	$W_{RAR} * N_{RAR}$

Figures 2 and 3 illustrate the true and the approximate values of the total number of MTC and the number of successful MTC, respectively. Besides the proposed FGPA method and the true value, these figures include the results for ordinary iteration algorithm which is used in the FI-TSFGP for the sake of comparison. Moreover, different values of M_1 were considered. From these figures, we clearly see that the proposed FGPA gives a good estimation of both the total number and successful MTC devices number.

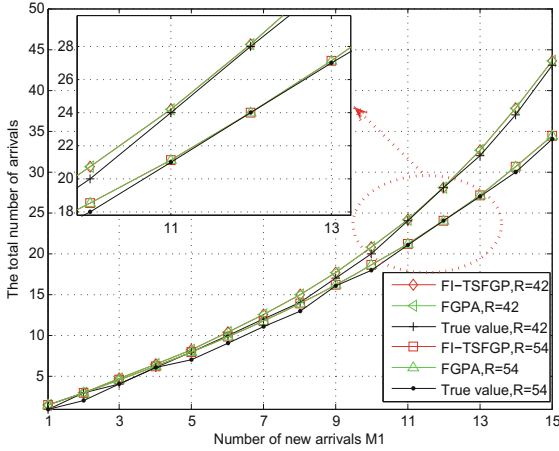


Fig. 2. Number of iterations with different number of new arrivals

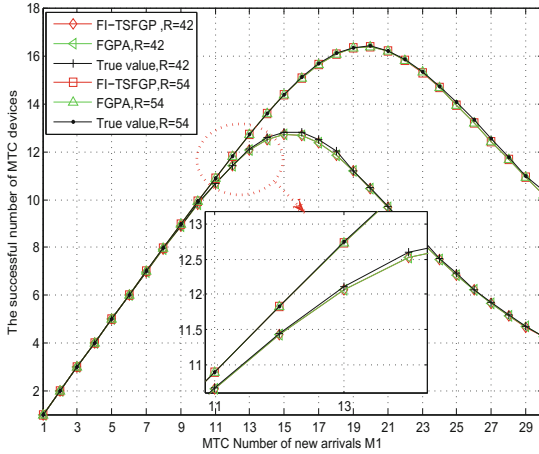


Fig. 3. The number of successful MTC devices as function of the number of new arrivals M_1 for different number of preambles

Then, the performance metrics of the iterations number is investigated, which is defined as how many times of iteration will achieve an accurately estimate of MTC devices. The performance of the proposed FGPA for group paging is evaluated by computer simulation. Figure 4 illustrates the number of iterations with different number of new arrivals. In Fig. 4, the number of new arrivals is set from 1 to 20. In generally, from the figure which is under the condition of $R = 42$ and $R = 45$, it is found that the proposed FGPA has much lower number of iterations than the ordinary iteration algorithm. From this figure, we can learn that though the proposed FGPA has a little more iteration number

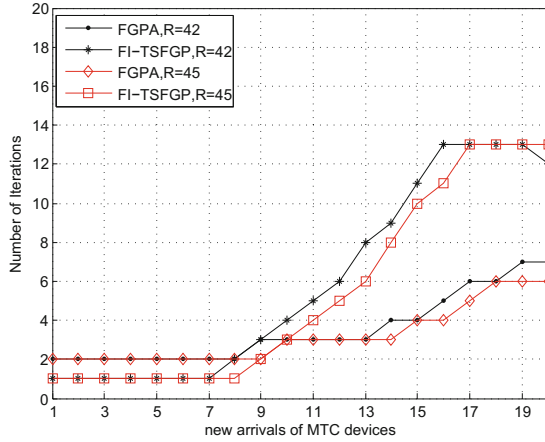


Fig. 4. Number of iterations with different number of new arrivals

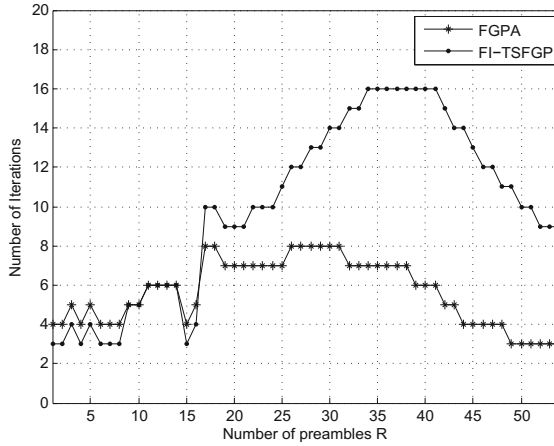


Fig. 5. Number of iterations with different number of preambles R

when new arrival number is small, the number of iterations is relatively less when new arrival number becomes bigger which will improve the performance of the algorithm. So if we want to achieve the required accuracy, the iteration number of the proposed FGPA will be much lower than the ordinary iteration algorithm.

The relationship between the number of iterations and the number of preambles R is illustrated in Fig. 5, from which we can find that the proposed FGPA is better in terms of complexity than the ordinary iteration algorithm in the FI-TSFGP. From the figure we can learn that the improved performance is not significant and could be worse when the number of preambles R is small, but the proposed FGPA has much fewer iteration times compared with the ordinary iteration algorithm in the FI-TSFGP when the number of preambles R becomes bigger. This is attributable to improvement obtained by the new iterative operation.

From the analysis of this paper, we can learn that the proposed FGPA is simple, fast and has low computational complexity. The main contribution of this paper is to estimate the total number of MTC devices by using an iterative algorithm that converges fast and has low arithmetic complexity instead of the ordinary iterative algorithm. After obtaining the total number of MTC devices M_i , the optimal value of new arrival MTC number will be got, which is the activated MTC number in every slot.

5 Conclusions

In this paper we think about reducing the collision probability. Firstly, we need to obtain the total number of MTC devices M_i in every slot when the MTC number of new arrivals follows uniform distribution. Then the optimal value of new arrivals making the resource utilization rate maximum will be got, and the number of new arrivals is the activated MTC number in every slot, and the optimal value can be obtained by simulating the relationship between MTC number of new arrivals and the corresponding resource utilization rate.

In order to obtain the total number of MTC devices M_i , we have proposed FGPA for large scale MTC systems instead of the ordinary iteration algorithm. The estimation accuracy of proposed algorithm is the same as ordinary iteration algorithm. What's more, the proposed FGPA outperforms ordinary iteration algorithm for GP mechanism, in terms of the complexity of the algorithm under the same condition compared with ordinary iteration algorithm. Furthermore, the algorithm proposed is simple, converging fast and has low computational complexity, which is the main contribution of this paper. The corresponding simulation results demonstrate that the proposed iteration algorithm FGPA requires less number of iterations under the condition of the same estimation results of total number of MTC devices.

Acknowledgment. This work was supported by the State Major Science and Technique Project (MJ-2014-S-37), National Natural Science Foundation of China (61201134) and 111 Project (B08038).


References

1. Ali, A., Hamouda, W.: Cell search evaluation: a step towards the next generation LTE-MTC systems. In: 2016 IEEE Wireless Communications and Networking Conference (WCNC), pp. 1–6. IEEE (2016)
2. Ali, M.S., Hossain, E., Kim, D.I.: LTE/LTE-a random access for massive machine-type communications in smart cities. arXiv preprint [arXiv:1608.03042](https://arxiv.org/abs/1608.03042) (2016)
3. Chang, C.W., Lin, Y.H., Ren, Y., et al.: Congestion control for machine-type communications in LTE-a networks. In: 2016 IEEE Global Communications Conference (GLOBECOM), pp. 1–6. IEEE (2016)
4. Cheng, M.Y., Lin, G.Y., Wei, H.Y., et al.: Overload control for machine-type-communications in LTE-advanced system. IEEE Commun. Mag. **50**(6), 38–45 (2012). 34(5), pp. 1086–1102

5. Chang, C.T., Yang, S.R.: Modeling LTE group paging mechanism for machine-type communications. In: 2015 International Wireless Communications and Mobile Computing Conference (IWCMC), pp. 1295–1300. IEEE (2015)
6. Arouk, O., Ksentini, A., Taleb, T.: Group paging optimization for machine-type-communications. In: 2015 IEEE International Conference on Communications (ICC), pp. 6500–6505. IEEE (2015)
7. 3GPP R2-104870. Pull Based RAN overload control, August 2010
8. Hasan, M., Hossain, E., Niyato, D.: Random access for machine-to-machine communication in LTE-advanced networks: issues and approaches. *IEEE Commun. Mag.* **51**(6), 86–93 (2013)
9. Arouk, O., Ksentini, A., Taleb, T.: Group paging-based energy saving for massive MTC accesses in LTE and beyond networks. *IEEE J. Sel. Areas Commun.* **34**, 1086–1102 (2016)
10. Wei, C.H., Cheng, R.G., Tsao, S.L.: Performance analysis of group paging for machine-type communications in LTE networks. *IEEE Trans. Veh. Technol.* **62**(7), 3371–3382 (2013)



A Honeyfarm Data Control Mechanism and Forensic Study

Wei Yin^(✉) , Hongjian Zhou, and Chunlei Yang

North China Institute of Computing Technology, Beijing, China
yinweihappy168@yahoo.com

Abstract. Honeyfarm is a model to deploy honeypots for global network attack monitoring, correlation and forensic analysis. Data control is a fundamental problem in the honeyfarm to protect the Internet from being attacked by compromised honeypots in the honeyfarm, while providing a controlled environment for worm behaviour study. However, this problem is not well addressed in a limited number of existing implementations. This paper presents a honeyfarm system and focuses on the design of a data control mechanism based on Intrusion detection and Data redirection (DOID). Comprehensive experiments including attack event tracing, worm behaviour study and forensic analysis display that DOID is a good tool for attack monitoring and forensic analysis.

Keywords: Honeyfarm · Data control · Forensic analysis

1 Introduction

Honeypot, representing as a vulnerable system, attracts hackers to probe, explore and attack. A single honeypot or multiple independently deployed honeypots can only provide a limited local view of network attacks, and global network attack monitoring, correlation and trend prediction is not available. Also, attack monitoring and analysis is non-trivial and maintenance of honeypots in various locations introduces high cost. This motivates the honeyfarm architecture, as shown in Fig. 1(a). It puts all honeypots into a resource pool located in one single area. A redirector is installed on each monitored production network, which redirects attack traffic to the corresponding honeypot in the resource pool. Therefore, only one security personnel, instead of one personal per location, is required at the central location to manage all honeypots.

However, there are only a limited number of honeyfarm prototypes in the literature. As far as we know, two most famous honeyfarm prototypes are Collapsar [1] and Potemkin [2]. Collapsar realises the traditional honeyfarm vision as well as the reverse honeyfarm vision. In the reverse honeyfarm, honeypots act as vulnerable clients, e.g. a web browser, exploited by malicious servers, e.g. a

The work is supported by the NSFC project 61702542 and the China Postdoctoral Science Foundation project 2016M603017.

web server. Potemkin aims to improve honeyfarm scalability by memory sharing of VM (Virtual Machine) honeypots on a guest operating system. On one hand, a honeyfarm contains thousands of honeypots so it should not be utilised to launch attacks against other hosts on the Internet after being compromised. Therefore, attack traffic should be at least blocked. Or even better, to give hackers a certain degree of freedom so that attack actions can be contained and monitored within the honeyfarm. This can lead to a better understanding of hackers' actions and worm propagation behaviours. On the other hand, hackers may download toolkits from the Internet to conduct subsequent actions or the compromised host may need to receive commands from a master on the Internet. Therefore, these behaviours cannot be blocked or contained. Consequently, hackers' behaviours in a honeyfarm need to be fine-grained controlled. However, in both realisations, the containment problem is not well addressed, or not even mentioned. Simply blocking all outbound connections may not work efficiently [3], because a hacker may download and install software on a compromised system. Blocking such non-attack connections may not be appropriate for studying the hacker's behaviours. Restricting outbound traffic rate and the number of outgoing connections [3] cannot stop all outgoing attacks and the risk for hackers to attack other hosts still exists. Therefore, a proper containment mechanism is essential for the honeyfarm architecture. In this paper, we propose a data control mechanism, in which the intrusion detection system (IDS) and the reverse firewall are introduced. The IDS is used to recognise attack traffic and redirects the attack traffic to an emulated target to study hacker's further behaviours. Non-attack traffic is not restricted, hence toolkits downloaded by hackers can be captured. Outgoing traffic will be further checked by the reverse firewall and DDoS attacks are filtered to avoid the liability issue.

The paper achieves the following contributions.

First, this paper is a real implementation of the honeyfarm concept. One advantage of our mechanism is that attack traffic is not simply blocked, but redirected to an emulated target in order to capture hacker's subsequent behaviours. Another advantage is that non-attack traffic can be recognised and forwarded to the Internet. Therefore attackers' non-attack activities, e.g. communicating with C&C (Command & Control) server and downloading toolkits, can be monitored as well.

Second, we deployed the honeyfarm on the Internet to monitor a number of production networks. A large number of attack statistics are recorded, gathered and analysed. It is proved that our implemented honeyfarm is an effective tool for attack event tracing [4], worm behaviour study [5] and forensic analysis [6].

The rest of the paper is organised as follows. Section 2 discusses the DOID data control mechanism. The experimental setup and results with the deployed DOID architecture is discussed in Sect. 3. The related work is presented in Sect. 4. The paper concludes in Sect. 5.

2 Data Control Mechanism

In this section, we present the DOID containment architecture and the defined policies for processing incoming and outgoing packets by the DOID gateway.

2.1 Containment Architecture

In the traditional honeyfarm architecture as shown in Fig. 1(a), redirectors in production networks transfer attack traffic to the honeyfarm gateway which redistributes the traffic to the corresponding honeypot in the resource pool. Responding packets are forwarded by the gateway to the redirectors and no other functionality is performed by the gateway in the traditional honeyfarm. When an attacker breaks a system, he may launch attacks to hosts on the Internet and initiate non-attack traffic to download toolkits. Therefore, outgoing traffic should be differentiated and controlled respectively to mitigate risks as well as providing freedom for the attacker to behave normally. In addition, worm behaviours should be contained and monitored in the honeyfarm so that their feature can be studied and understood. In our design as shown in Fig. 1(b), the DOID gateway has four components in order to achieve a good data control purpose: (1) Containment: implementing policies, e.g. dropping and forwarding, on incoming and outgoing traffic; (2) ARP responder: the gateway configured on the honeypot does not exist in the resource pool so that the DOID gateway should respond to the ARP request for the configured network gateway; (3) Monitoring: listening for configuration requests and making changes to DOID gateway configurations; (4) Virtual machine (VM) manager: managing VM honeypots.

Two external components are required to assist data control. One is intrusion detection system (IDS) that differentiates attack and non-attack traffic. The other is a reverse firewall, which functions as a firewall, but it implements policies on outbound traffic instead of inbound traffic so that it prevents the outside world from being attacked by honeypots in the honeyfarm. IDS is utilised for both inbound and outbound traffic checking. The inbound traffic will be checked by the IDS before forwarding to honeypots in the honeyfarm and the payload of known attacks can be modified to fail attacks so that hackers are encouraged to try various methods to penetrate the system, which enhances the security value of honeypots. The outbound traffic will be processed by multiple DOID gateway components and examined by IDS. Only non-attack traffic is forwarded to the Internet and attack traffic is redirected to the honeypots in the resource pool. After IDS, the non-attack traffic will be further checked by the reverse firewall for clearing DDoS attack.

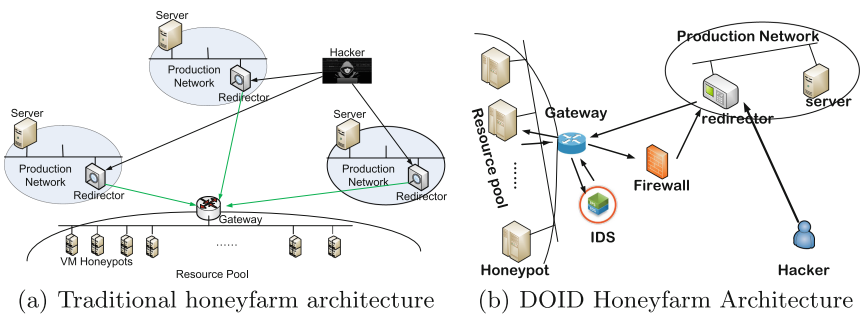


Fig. 1. Honeyfarm architectures

2.2 Containment Policy

The containment component implements strategies on incoming and outgoing traffic.

Inbound Traffic Strategies. Incoming traffic are forwarded by redirectors. They are packets from attack sources or responding packets of outgoing non-attack traffic. Since packets are encapsulated by the redirector and forwarded to the DOID gateway, they are decapsulated by the DOID gateway and the packet payload is checked by the IDS. The attack payload will be modified if the DOID gateway is configured to modify known attack payload. Otherwise, the packet is forwarded to the corresponding honeypot directly.

Packet Filtering Policy. The goal of the packet filtering policy is to prevent the honeyfarm from the Denial of Service (DoS) attack. The honeyfarm gateway generates a honeypot for each packet with a unique destination address. The redirector can be misused to deliver a large number of packets with different destination addresses to the honeyfarm gateway. Due to limited hardware resource in the honeyfarm, a bulk of requests cause exhaustion of hardware resource. To solve this issue, the honeyfarm gateway maintains a white list that lists all monitored IP addresses in production networks. When outgoing non-attack packets are forwarded, the destination addresses are recorded in another list named non-attack address list. All packets, of which the destination address does not belong to the white list or the source address does not belong to the non-attack address list, are filtered and no honeypot is generated. Consequently, the DoS attack is avoided under such a condition.

Packet Distribution Policy. For packets of which the destination address belongs to the white list or the source address belongs to the non-attack address list, they are distributed to the corresponding honeypot.

Packet Modification Policy. The value of a honeypot can be maximised by encouraging hackers to try zero-day exploits. This is done by enabling the DOID gateway to modify known attack payloads to fail an attack.

Outbound Traffic Strategies. Outbound packets include ARP requests, packets responding to the attack source, outgoing non-attack and attack packets initiated from honeypots.

Packet responding Policy. When the DOID gateway receives an ARP request, it uses its MAC address as the response to allow honeypots to send packets to it for forwarding.

Packet Encapsulation Policy. In order to monitor attackers' behaviours, including downloading toolkits and browsing websites, their outgoing non-attack traffic is forwarded instead of being blocked. Responding packets to the attack source are also forwarded. However, reverse firewall checking is done before forwarding to mitigate DDoS attacks from the Honeyfarm to the Internet. Finally these

packets are encapsulated and forwarded to the redirector which decapsulates and forwards them to the Internet. They are not forwarded by the honeyfarm gateway to the attack source directly to avoid the inconsistency problem because the network gateway on the redirector's production network may use NAT.

Packet Redirection Policy. After compromised, the honeypot may be used as a drawboard to attack other hosts on the Internet. Therefore, the honeyfarm could be an incubator for malicious software and an accelerator for network worms. The IDS is utilised to recognise outgoing attacks and they are redirected to honeypots in the honeyfarm, preventing Internet hosts from being attacked from compromised honeypots in the honeyfarm. In this way, subsequent attack behaviours can be monitored as well.

Packet Drop Policy. Horizontal port scanning generates a bulk of packets targeted at different destinations. This causes overuse of honeypot resource. To solve this problem, we use a scan filter to limit the number of outbound scanning packets from a given honeypot in the honeyfarm. Also, we maintain a list of honeypots that are generated directly or indirectly by each attack source. If the number of generated honeypots exceeds a certain amount, it stops generating honeypots and subsequent packets will be dropped.

3 Experiments with DOID Honeyfarm

In this section, we discuss the experiment environment setup and the evaluation results including attack event tracing, worm behaviour study and forensic analysis. We also conduct performance evaluation of the system.

3.1 Experiment Environment

The resource pool is built in Beijing and a redirector is installed in 9 cities respectively. The traffic that is redirected from a particular city is forwarded to a certain honeypot in the honeyfarm, which has different types of system vulnerabilities. Table 1 shows the configuration of these honeypots. The monitoring starts from 1st Feb 2017 to 20th July 2017.

3.2 Aggregate Statistics

We capture the number of incoming attacks targeted at these honeypots in the resource pool, the number of outgoing attacks and non-attacks initiated from the resource pool. Due to the variety of running operating systems, open services and exposed vulnerabilities, the number of received attacks is not evenly distributed over these honeypots. We find that honeypots representing Shanghai, Guangzhou and Xi'an attract most attacks. Among 1101 attack attempts, 752 attempts are targeted at these three honeypots. This is because they expose more vulnerabilities than other honeypots. Most attacks are carried out between 9 am and 6 pm. This may indicate that most hackers are professionals and make

Table 1. Honeypot configuration for various cities

City	Honeypot configuration	
	Operating system	Running service
Shanghai (SH)	Ubuntu metasploitable2 [7]	FTP, SSH, TELNET, SMTP, HTTP, RPC, NETBIOS-SSN, MICROSOFT-DS
Guangzhou (GZ)	Unpatched Win XP SP3	MSRPC, NETBIOS-SSN, MICROSOFT-DS
Xi'an (XA)	Unpatched Win server 2003	FTP, HTTP, RPC, NETBIOS-SSN
Zhengzhou (ZZ)	Patched Ubuntu metasploitable2	SSH, FTP
Chengdu (CD)	Patched Win XP SP3	MSRPC
Nanjing (NJ)	Redhat 7.0 with apache web service (version 1.3 with mod-cgi feature). Bash not patched	HTTP
Wuhan (WH)	Win 7. Patched without fixing the MS15-067 vulnerability	RDP (Remote Desktop Protocol)
Changsha (CS)	Unpatched Win server 2008, running a web app with a SQL injection vulnerability	FTP, IIS, MySQL
Kunming (KM)	Patched Win 10	No service

a living on it. Using compromised honeypots as drawboards, hackers launch a number of attacks to the outside world. They also establish non-attack connections to the outside world to download files through FTP or use ICMP echo requests to probe hosts on the Internet. From the aggregate statistics, we find that the more vulnerabilities a honeypot has, the more attacks it attracts, and the more likely it is used as the drawboard to compromise the outside world. The captured outgoing non-attacks and attacks indicate that differentiating outgoing traffic types is essential for the data control architecture in the honeyfarm. On one hand, outgoing non-attack connections cannot be blocked so that hackers' toolkit download actions can be captured. On the other hand, outgoing attacks should be redirected to the emulated target in the honeyfarm so that the liability problem is avoided as well as hackers' subsequent behaviours can be monitored. This confirms that our design is appropriate for these scenarios.

For 134 outgoing attacks, we also monitor the target geographic distribution. Most of the outgoing attacks are targeted at intra-network hosts. This means most of the time hackers use the compromised honeypot as the entry point to explore and penetrate hosts in the inner network. Therefore most hackers are interested in data residing in the network where the redirector is located. We also find that famous Japan companies including Sony and Nikon, and European multi-national corporations, e.g., Benz and Siemens, become the drawboard

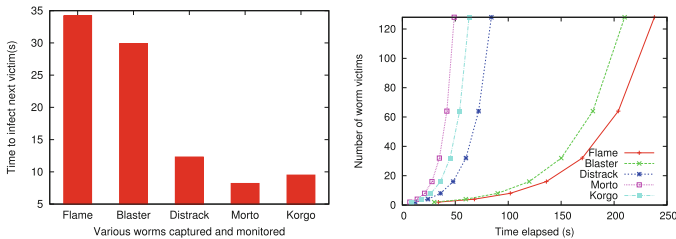
targets. This means the motivation of most hackers could probably be stealing commercial secrets from those companies and they sell commercial documents to their competitors for a living.

According to the statistic analysis, we totally captured 948 different attacking sources. They belong to 59 different countries. Over half of the source addresses are from China. Most of these addresses are from prefixes of 123.233/16, 27.224/16 and 27.115/16. Japan ranks the second, followed by the US and Europe. Although statistics show attacks are from these addresses, it does not mean attacks are actually from those areas, because technologies such as VPNs and the Tor technology [8] make the source tracing very difficult.

3.3 Worm Propagation Analysis

In the design of the DOID architecture, attack behaviours are contained and monitored so that it can be utilised to capture, contain and study worm propagation behaviours. Simply blocking attack traffic fails to give worms freedom to propagate. Allowing worms to propagate to the Internet causes the liability issue and worm behaviours cannot be monitored. Over five-month monitoring, our farm system captured a number of worms including Flame, Morto and Blaster. We studied the propagation speed of various worms. Figure 2(a) illustrates the time taken for each worm to infect the next victim after it first time infects a honeypot in the farm. We find that the infection speed for Morto is the fastest. It takes 7s to infect the next honeypot. The speed for Flame and Blaster is comparatively slow, around 30 s. Morto propagates itself through weak password in the remote desktop protocol (RDP) and its goal is to gain remote desktop access authority. In our farm, the password for RDP is null. No wonder the Morto worm propagates so fast. Flame propagates itself through network shared files and its goal is to gather information through screen-shots, keystroke and network traffic record. Blaster propagates itself by an RPC (Remote Procedure Call) vulnerability. Therefore, vulnerability scanning and exploitation takes longer time.

In our data control mechanism for the farm, we configured that an attack source can generate at most 128 honeypots. So we give worms a certain degree of freedom to infect other honeypots. The intrusion detection system recognises different types of worms and corresponding vulnerable honeypots are generated in order to study the behaviours of each worm type. Figure 2(b) shows the time



(a) Time to infect next victim (b) Worm propagation activity

Fig. 2. Statistics of worm propagation

line of propagation for each worm monitored. We find that worm propagates exponentially. The *Morto* worm is the first one finishing infecting 128 honeypots. It takes around 50 s. The *Flame* and *Blaster* worms are slower.

3.4 Forensic Analysis

Over five-month deployment period, we captured more than 1000 attacks. Here, we present the forensic details about the first successful exploit event to the Nanjing, Wuhan and Changsha honeypots.

Shellshock Exploit. We installed Redhat operating system (Enterprise version 7.0) on the Nanjing honeypot. The Apache web server (version 1.3) is running on top of the operating system and the *mod-cgi* feature is enabled. The Bash version is 4.2. We run the *Sebek* client module on the operating system. Bash of which the version is before 4.3 has the shellshock vulnerability. The definition of “*var =() {::}; command*” defines a variable *var* as a function in Bash scripts, and the following “command will be executed when the Bash sentence is interpreted. So if the attacker assigns ‘*() {::}; command*’ to the ‘*HTTP_USER_AGENT*’ field in the HTTP request, the *HTTP_USER_AGENT* will be passed to Bash by the web server and then Bash executes the *command* followed by the function definition. In this case, the *HTTP_USER_AGENT* is no longer taken as a meaningless string and is likely to be exploited by hackers as a malicious input to the web server. Hence risk exists.

The honeypot was deployed in the honeyfarm at 1:10 pm on 2nd Feb 2017. It was compromised at 10:34 am on 4th Feb 2017. The attacker first connected to the honeypot and scanned the website for vulnerabilities such as SQL injection, XSS (cross site scripting). After finding no such vulnerabilities, the attacker fabricated a malicious HTTP request containing “*HTTP_USER_AGENT=() {::}; uname -a*” and tested whether our web server has the shellshock vulnerability. After confirming the existence of the vulnerability, the attacker used a HTTP request containing *HTTP_USER_AGENT=() {::}; /bin/bash -c “cd /tmp; wget http://123.*.*./download/shv4.tar.gz.tar; tar xzf shv5.tar.gz.tar; ./setup alice 6543”* to download the *shv5* rootkit and installed the ssh server. The ssh server was configured with password *alice*, and the server port is set to 6543. Then the attacker connected to the ssh server at port 6543. The connection between the honeypot and the attacker was encrypted. Traditional packet analyser, e.g., *tcpdump*, is unable to analyse encrypted data. However, the *Sebek* module can capture keystrokes, as it hijacks the *SYS_read()* function. Through analysis of the keystrokes, we found that the attacker downloaded a BSSH2 script from “<http://sshbruteforce.com>”. It is an ssh brute-force attacking tool. Using BSSH2, the attacker executed brute-force attack against IP addresses ranging from 122.96.0.1 to 122.96.255.255. The attacker then modified a number of binary files including *ps*, *ifconfig*, *netstat*, *top*, *ls*, *find* and *md5sum* by *shv5*. As a consequence, when the system user calls those programs, the output of these programs shield information about that the system has been compromised. For example, when we ran

the `netstat` command and we found that the ssh server which was running on the port 6543 was hidden. The MD5 hash values of modified files were stored in `.shmd5`. Therefore, when running the `md5sum` command, the modified `md5sum` program obtained the original MD5 value from the `.shmd5` file to avoid being detected.

MS15-067 Exploit. The Windows 7 operating system is installed on the Wuhan honeypot, which has the MS15-067 vulnerability. It is a critical remote code execution vulnerability in the remote desktop protocol (RDP). Through exploiting the vulnerability, attackers can execute codes with the administrator privilege. After compromising the system, attackers can perform various tasks including installing software, modifying user data and creating users.

The honeypot was deployed in the honeyfarm at 10:15 am on 5th Feb 2017 and first compromised at 3:50 pm on 6th Feb 2017. The attacker first established a TCP reverse shell and reversely connected to the attacker from the honeypot. Then the attacker listed all running processes on the honeypot and inserted its process into `explorer.exe` and hid its existence. Then the attacker shutdown anti-virus software and the firewall. A persistent connection was established and the system would reversely connect to the attacker's machine every 10 seconds after the system rebooted. The attacker searched `*.pdf`, `*.doc`, `*.jpg` files on the honeypot and downloaded some files. Then all files in the `C:\Windows\System32\config` directory are downloaded. After that, the attacker scanned the production network. Finally, the attacker deleted all system and application logs in the `C:\Windows\System32\winevt\Logs` directory.

4 Related Work

Honeyfarm is related with, but defers from the honeypot [9], honeynet [10] and distributed honeynet [11] architectures. Data control is a research issue in those architectures.

Gen I honeynet [3] presents two alternatives for data control. The first method is to deny all outbound connections. This ensures safety, but this approach cannot study worm and botnet behaviours, as their behaviours are restricted. The second approach allows a certain number of outbound connections and all subsequent connections are forbidden after the maximum number is reached. This method still has a risk to harm a certain number of hosts on the Internet.

Gen II and III honeynets [3] use rate limiting to reduce the outbound rate. They refuse attack traffic to go outside of the honeynet. Therefore, this method cannot study malware further behaviours [12]. Our mechanism redirects the attack traffic to the honeyfarm honeypots in order to capture subsequent activities, hence worm propagation and botnet behaviours can be well monitored.

He et al. [13] propose a data control mechanism to prevent hackers attacking websites on the Internet using a compromised honeypot. The first connection to the website is allowed, but the rate is limited in order to gain enough time to clone the same website in the honeyfarm. Subsequent access to the website

is directed to the honeyfarm. This architecture requires installing a honeypot and a corresponding adjacent honeyfarm in the monitored network, while our architecture only installs a redirector on the monitored network and a central honeyfarm for all monitored networks, which is lightweight.

The GQ architecture is proposed in [14] to control malware in the honeyfarm. In the architecture, the GQ gateway split the honeyfarm and the Internet. Policies are implemented at the gateway to control outgoing connections, which includes forwarding, rate-limiting, dropping, redirecting, reflecting and rewriting. However, due to paper length limitations, the detail about under which condition to apply each policy is not discussed.

Forensic analysis is a hot topic in the security area. Fahdi et al. [15] and Nassif et al. [16] respectively present a data clustering approach to speed up the forensic analysis process. Most recent forensic analysis focus on instant messaging applications [17–19] and malware [20] on mobile devices. Although mobile applications attract so much attention, exploitation of traditional desktop vulnerabilities is still an important issue as new vulnerabilities are discovered every day. Our paper presents a comprehensive forensic study on a new honeyfarm architecture and we find that: (1) It is essential for the honeyfarm gateway to differentiate attack and non-attack traffic to perform fine-grained data control. (2) Worms propagate exponentially. (3) Hackers break a system through one or multiple vulnerabilities and therefore mitigating vulnerabilities can prevent hackers from breaking in.

5 Conclusion

Honeyfarm, a conceptual idea for honeypot deployment, is a promising tool for global network attack monitoring, correlation, forensic analysis and trend prediction. In order to protect the Internet from being attacked by compromised honeypots in the honeyfarm as well as being able to capture attack behaviours for study, the traffic must be controlled effectively. We presented and implemented a honeyfarm system, DOID, for such a purpose. We deployed the system on the Internet and conducted comprehensive experiments including attack event tracing, worm behaviour capture and forensic analysis, which confirm DOID is a good tool in attack monitoring and forensic analysis. We also summarised observations based on these experiments.

References

1. Jiang, X., Xu, D., Wang, Y.-M.: Collapsar: AVM-based honeyfarm and reverse honeyfarm architecture for network attack capture and detention. *J. Parallel Distrib. Comput.* **66**, 1165–1180 (2006)
2. Vrable, M., Ma, J., Chen, J., Moore, D., Vandekieft, E., Snoeren, A.C., Voelker, G.M., Savage, S.: Scalability, fidelity, and containment in the potemkin virtual honeyfarm. In: *Proceedings of the ACM Symposium on Operating Systems Principles*. ACM, Brighton, October 2005

3. Spitzner, L.: Honeypots: Tracking Hackers, pp. 1–480. Addison Wesley, Boston (2002)
4. Burkhart, M., Schatzmann, D., Trammell, B., Boschi, E., Plattner, B.: The role of network trace anonymization under attack. *SIGCOMM Comput. Commun. Rev.* **40**(1), 5–11 (2010)
5. Jain, P., Sardana, A.: Defending against internet worms using honeyfarm. In: Proceedings of the CUBE International Information Technology Conference, CUBE 2012, Pune, India, pp. 795–800. ACM (2012)
6. Krishnan, S., Snow, K.Z., Monrose, F.: Trail of bytes: efficient support for forensic analysis. In: Proceedings of the 17th ACM CCS, Chicago, Illinois, USA, pp. 50–60. ACM (2010)
7. Metasploitable2. <https://community.rapid7.com/docs/DOC-1875>
8. Tor technology. <http://www.torproject.org/>
9. Kaur, R., Singh, M.: A survey on zero-day polymorphic worm detection techniques. *IEEE Commun. Surv. Tutor.* **16**(3), 1520–1549 (2014)
10. Abbasi, F.H., Harris, R.J.: Experiences with a generation III virtual honeynet. In: Proceedings of ATNAC, pp. 1–9 (2009)
11. Kumar, S., Singh, P., Sehgal, R., Bhatia, J.S.: Distributed honeynet system using Gen III virtual honeynet. *Int. J. Comput. Theory Eng.* **4**(4), 537–541 (2012)
12. Kim, I.S., Kim, M.H.: Agent-based honeynet framework for protecting servers in campus networks. *IET Inf. Secur.* **6**(3), 202–211 (2012)
13. He, X.-Y., Lam, K.-Y., Chung, S.-L., Chi, C.-H., Sun, J.-G.: Real-time emulation of intrusion victim in honeyfarm. In: Chi, C.-H., Lam, K.-Y. (eds.) *AWCC 2004*. LNCS, vol. 3309, pp. 143–154. Springer, Heidelberg (2004). https://doi.org/10.1007/978-3-540-30483-8_18
14. Kreibich, C., Weaver, N., Kanich, C., Cui, W., Paxson, V.: GQ: practical containment for measuring modern malware systems. In: Proceedings of the 2011 ACM SIGCOMM IMC, Toronto, Canada, pp. 397–412. ACM (2011)
15. Al Fahdi, M., Clarke, N.L., Li, F., Furnell, S.M.: A suspect-oriented intelligent and automated computer forensic analysis. *Digit. Invest.* **18**, 65–76 (2016)
16. da Cruz Nassif, L.F., Huschka, E.R.: Document clustering for forensic analysis: an approach for improving computer inspection. *IEEE Trans. Inf. Forensics Secur.* **8**(1), 46–54 (2013)
17. Ovens, K.M., Morison, G.: Forensic analysis of Kik messenger on iOS devices. *Digit. Invest.* **17**, 40–52 (2016)
18. Walnycky, D., Baggili, I., Marrington, A., Moore, J., Breitingner, F.: Network and device forensic analysis of android social-messaging applications. *Digit. Invest.* **14**, 77–84 (2015)
19. Anglano, C.: Forensic analysis of whatsapp messenger on android smartphones. *Digit. Invest.* **11**, 201–213 (2014)
20. Vrable, M., Ma, J., Chen, J., Moore, D., Vandekieft, E., Snoeren, A.C., Voelker, G.M., Savage, S.: A forensic analysis of android malware how is malware written and how it could be detected? In: Proceedings of IEEE 38th Annual International Computer, Software and Applications Conference (2014)



Environment-Related Information Security Evaluation for Intrusion Detection Systems

Ran Cheng^{1(✉)}, Yueming Lu¹, and Jiefu Gan²

¹ School of Information and Communication Engineering,
Beijing University of Posts and Communications,
Key Laboratory of Trustworthy Distributed Computing and Service (BUPT),
Ministry of Education, Beijing, China

{hscrws, ymlu}@bupt.edu.cn

² China Information Security Certification Center, Beijing, China
gjfsecure@163.com

Abstract. The features of actively detection of intrusion detection systems (IDSs) are crucial in cyberspace security evaluation. Most of existing evaluation models are insufficient for selecting proper IDS in varying situations since these methods only base on detection rate and false alarm ratio. The paper proposes an environment-related information security evaluation model for IDSs, and applies the model in a practical IDS evaluation process. Compared to existing ones, the proposed model considers two more factors: background traffic and workload, and thus can achieve a more objective and comprehensive evaluation result for IDSs.

Keywords: Intrusion detection system · Precision · Recall
Background traffic

1 Introduction

An increasing number of network security devices, including firewalls, intrusion detection systems (IDSs) and virtual private network (VPN) devices, etc. are implemented in widely distributed information systems nowadays. In particular, firewalls build protective barriers between internal networks and external networks; IDSs work behind the firewalls and detect potential attacks; VPNs allow encrypted information to transmit between internal networks and external networks, thus extend the range of internal networks [1]. These security devices work collaboratively for guaranteeing data to be integrate, confidential and usable.

In order to describe their relationship, ISS (Iterated Service Solution) proposed the PDR (Protection, Detection and Response) model for cyberspace security. PDR consists of protection, detection and response units. The protection unit, which is implemented by firewalls and VPNs, lags behind the

detection unit, and is not capable enough to defend against constantly changing attacks, thus causes endless system vulnerabilities. Therefore, it is not enough to keep network environments safe relying only on the protection unit. IDSs' actively detection compensates the time difference between protection and detection and builds a bridge between processes of protection and response. As the study of IDSs develops in depth, the requirements of evaluating IDSs are emerging.

Common Criteria (CC) provides a detailed set of evaluation metrics for information security products, which helps developers ensure security of their entire product development processes [2]. However, CC has two issues: 1. Evaluation results are limited to examine the documents in the scenario provided by developers; 2. evaluation time is too long.

Gan [3], and Li [4] established complete index trees for IDSs where methods including analytic hierarchy process (AHP), etc. are used to determine the weight of each index, leading to a comprehensive evaluation result. However, there are constraints among certain indices, which may lead to biased result when the result is the sum of weights.

Among those constrained indices, the performance index is the most important one when choosing an IDS since the correctness of its judgement is more measurable and more intuitive. Lincoln Laboratory of MIT conducted evaluation on performance index of IDSs back in 1998 [5]. NPV (Negative predict value), PPV (Positive predict value) and NPR (Negative Positive Ratio) metrics were extended from performance index. Those metrics are all rely solely on performance index, ignoring the different contribution of the sub-indices in performance index in the various environments of background traffic, which make them not comprehensive and objective enough under different circumstances.

Accordingly, in order to balance the constraints in the performance index, this paper proposes an environment-related evaluation model for IDSs. The model considers two supplement factors, background traffic and workload, and evaluates IDSs more comprehensively.

A comprehensive index system is still needed. According to international standard technical requirements and IDS evaluation methods, as well as the reliability requirements of IDS systems, this paper considers five quality properties including reliability, security, usability, function and performance. Upon these five properties, the paper proposes an evaluation index system for IDS devices according to their actively detection characteristics. The IDS evaluation index system is shown in Fig. 1.

Among the 5 principal indices and 12 sub-indices in Fig. 1, C_1-C_{10} are qualitative indices and the others are quantitative indices. To obtain the evaluation results, this paper uses fuzzy comprehensive evaluation (FCE) method for qualitative indices and implements the proposed model for the quantitative index, i.e., the performance index.

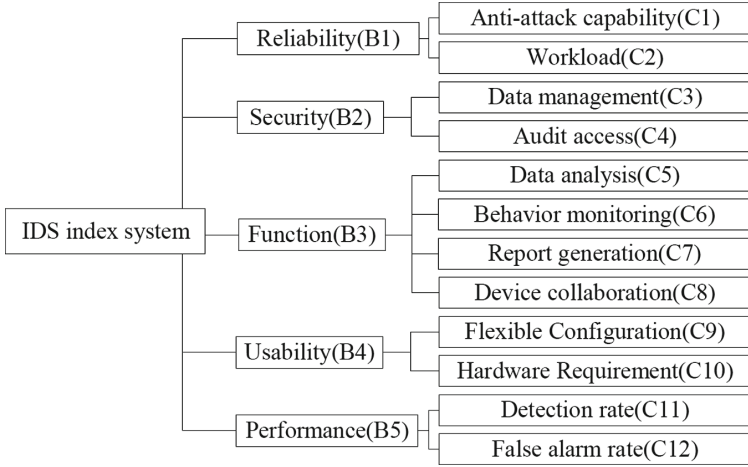


Fig. 1. IDS index system

2 Evaluation of IDS Performance

2.1 Performance Index

The most crucial factor of IDS performance evaluation is IDSs’ attack detection ability and IDSs only trigger alarms when operations are judged to be abnormal. Accordingly, we can treat the IDS as a binary-classifier, which provides four possible results.

As shown in Table 1, TP (True Positive) indicates the instances where the attack is successfully detected by the system; FN (False Negative) shows the instances where the attack is not detected by the system; FP (False Positive) represents the instances where a normal operation is falsely considered as an attack by the system and TN (True Negative) is the instances where the system successfully identifies the normal operation.

Table 1. Classification results

		Predicted instances	
		Attack	Normal
Actual instances	Attack	TP	FN
	Normal	FP	TN

Accordingly, we define FAR (False alarm ratio) and DR (detection rate) as:

$$FAR = \frac{FP}{TP + FP}. \tag{1}$$

$$DR = \frac{TP}{TP + FN}. \tag{2}$$

FAR is the ratio of non-attack operations among all the operations marked abnormal by systems. DR is the fraction of intrusion operations that are detected by systems. These two indices are mainly used to evaluate IDSs.

2.2 ROC Curve

When an IDS is set to different detection thresholds, with the same input signal, the relationship between its FAR and DR can be depicted by an ROC (Receiver Operating Characteristic) curve.

In Fig. 2, curve A is a typical intrusion detection ROC curve and line B is the result of a random input. The IDS with better performance corresponds to a curve closer to the upper left corner of the graph [6].

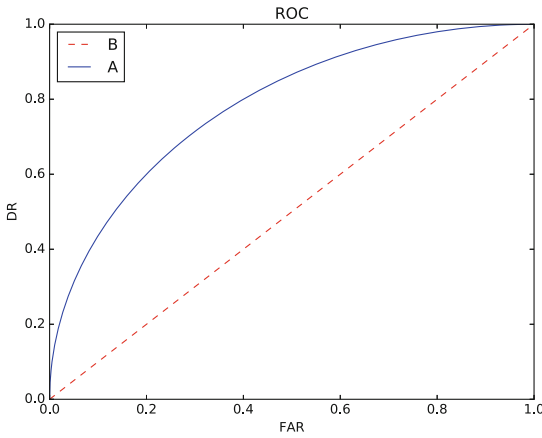


Fig. 2. Typical ROC curve

2.3 NPV and PPV Metric

This metric proposes another two metrics, i.e., NPV and PPV, which are defined from users' perspectives. PPV, also known as Bayesian detection rate, is the probability of real intrusions happening when IDSs trigger alarms. On the contrary, NPV is the probability of intrusions not happening when alarms are not triggered. However, in practice, PPV's value can be very small since the probability of the intrusion is usually low [7].

2.4 NPR Metric

NPR measures negative positive ratio [8]. The performance of an IDS can be evaluated by comparing actual NPR and predicted NPR, which is:

$$NPR = \frac{TN}{TP}. \quad (3)$$

If $NPR_P > NPR_a$, the IDS predicts more negative instances than the actual value, which means the IDS may miss attack operations and as a result DR is relatively low but FAR is high.

On the other hand, $NPR_P < NPR_a$ means FAR is relatively low but DR is high.

The NPR metric provides a new direction on evaluations of IDSs' performance, but leads to information missing at the same time.

3 An Environment-Related Performance Evaluation Model

3.1 Description of Model

In statistics, two indices, precision and recall, are used to evaluate the quality of classification results [9]. Precision is used to evaluate how accurate a system is and recall is used to evaluate how comprehensive a system is. These set of indices can be introduced into the evaluation of IDSs:

$$Precision = \frac{\text{number of detected attacks}}{\text{number of alarmed operations}} = \frac{TP}{TP + FP} = 1 - FAR. \quad (4)$$

$$Recall = \frac{\text{number of detected attacks}}{\text{number of attacks in input}} = \frac{TP}{TP + FN} = DR. \quad (5)$$

Precision and recall are negatively, non-linearly correlated. For example, if the system is very skeptical, and then judges most operations as attacks, its recall will be large but precision will be small. On the contrary, if the system judges few operations as attacks, its precision will be large and recall will be small. In order to integrate these two metrics into one single number, we introduce F1-score, widely used in statistical analysis, which computes the harmonic mean of precision and recall.

In practice, we consider the contribution of precision and recall in F1-score differently according to the workload of IDSs. For example, if the FAR of an IDS is too high, the credibility of the alarm decreases. Consequently, the IDS has to spend much time identifying useless information in order to get rid of false alarms, which not only costs much time but also increases workload, making system crash. Even having high DR cannot resolve this performance issue.

$$F1 - score = \frac{2 * Precision * Recall}{Precision + Recall}. \quad (6)$$

In order for the F1-Score to be large, both precision and recall must be large meaning small FAR and large DR.

Accordingly, we give different weights to precision and recall, and the resulted performance score can be represented as follows:

$$Score_{performance} = \frac{(1 + K) * (1 - FAR) * DR}{1 - FAR + DR}, \quad (7)$$

and

$$K = \frac{T}{L}, \quad (8)$$

where T is the log-transformed background traffic in network environments measured in required environments, and L is the normalized score of the IDS's workload, which is computed according to the number of packages caught per second and the number of cases handled per second of the IDS.

3.2 Validation of the Model

In an environment with controlled background traffic, we measured the performances of four identical open-source IDSs. In the experiment, A and B, C and D used two different matching algorithms respectively. Their detection thresholds stay the same. We configured the method of log recording on A and C in order to get them a better recording speed and thus a higher workload score. Now given A and B's DR = 0.946, FAR = 0.182, C and D's DR = 0.86, FAR = 0.067. The results of environment-related evaluation model are as shown in Table 2.

Table 2 and Fig. 3 show the performance score of four IDSs in different background traffic environments. As shown in Fig. 3, with background traffic increasing, the scores of A and B are decreasing. This tendency does not indicate worse performance under higher background traffic, but actually means that with higher background traffic, the size of data to be processed by IDSs is larger and thus the requirement for precision is higher. As a result, the score of precision makes more contribution to the overall performance score. On the contrary, the trend for C and D increases as background traffic increases. This is because their precision score is higher than recall score.

Table 2. Implementation results

Background traffic (Mbps)	1	10	50	100	500	1000
T	0	0.3333	0.5663	0.6667	0.8997	1
AL = 0.9	0.946	0.9076	0.8920	0.8869	0.8773	0.8740
BL = 0.6	0.946	0.8959	0.8792	0.8740	0.8649	0.8617
CL = 0.9	0.863	0.8809	0.8888	0.8915	0.8966	0.8985
DL = 0.6	0.863	0.8868	0.8956	0.8985	0.9037	0.9055

We can also conclude from Fig. 3 that the slope of the curve gets lower as L increases, indicating that the IDS with higher workload depends less on precision in environments of high background traffic.

There are crossing points of four curves, which means we are not able to directly judge the performance of an IDS even with its DR and FAR given. We have to select the appropriate IDS equipment according to the environment, and this is an information that NPV, PPV, NPR evaluation metrics are not able to provide.

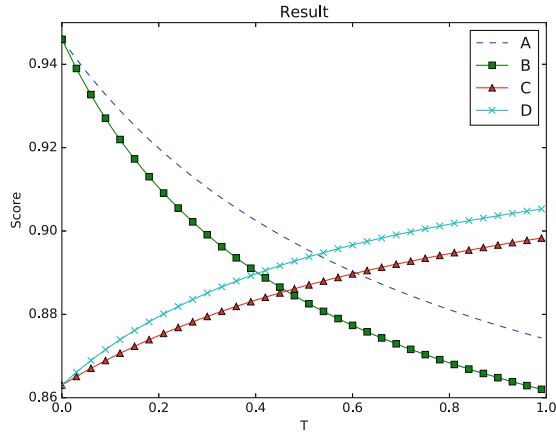


Fig. 3. Implementation results

4 Application of Evaluation Model

To give a real-world example of the effective evaluation of IDS using the environment-related performance evaluation model, we evaluate the information security level of a real-world IDS using the model with the help of the AHP and FCE.

4.1 Using the AHP to Obtain the Comparison Matrix

The AHP is about breaking a problem down and then aggregating the solution of all the sub-problems into a conclusion. A comparison matrix is built to represent the relationship between every two elements that share a common parent, and the weights of the elements will be obtained via matrix computation.

Five experts in IDS field were asked to grade the IDS's five principal indices and we use the scores to build the comparison matrix, in which each a_{ij} is an integer ranges from 1 to 9 or its reciprocal. The bigger the value, the more important index i compared to index j . The comparison matrix is showed in Table 3.

Table 3. Comparison matrix

	B1	B2	B3	B4	B5
B1	1	1/2	1/3	4	1/5
B2	2	1	1/2	5	1/4
B3	3	2	1	7	1/2
B4	1/4	1/5	1/7	1	1/8
B5	5	4	2	8	1

4.2 Matrix Consistency Test and Acquisition of Weight Vector

After finishing the comparison matrix, we test the matrix’s consistency. First, we calculate the square root of the product of each row in the matrix.

$$w_1^* = \sqrt[5]{1 * \frac{1}{2} * \frac{1}{3} * 4 * \frac{1}{5}} \approx 0.668. \tag{9}$$

$$w_2^* = \sqrt[5]{2 * 1 * \frac{1}{2} * 5 * \frac{1}{4}} \approx 1.046. \tag{10}$$

$$w_3^* = \sqrt[5]{3 * 2 * 1 * 7 * \frac{1}{7}} \approx 1.838. \tag{11}$$

$$w_4^* = \sqrt[5]{\frac{1}{4} * \frac{1}{5} * \frac{1}{7} * 1 * \frac{1}{8}} \approx 0.246. \tag{12}$$

$$w_5^* = \sqrt[5]{5 * 4 * 2 * 8 * 1} \approx 3.170. \tag{13}$$

We then normalize vector w and we get $W = [0.096, 0.150, 0.264, 0.035, 0.455]$.

Next, we calculate matrix’s maximum eigenvalue:

$$\lambda_{max} = \sum_{i=1}^5 \frac{5w_i}{BW_i} = 5.196. \tag{14}$$

Thus we can obtain consistency index $CI = \frac{5.196-5}{5-1} = 0.049$. According to the table of average random index (RI) in 1–9 scale, the RI of the 5th order matrix is $RI = 1.12$ [10]. Since $\frac{CI}{RI} < 1$, the comparison matrix pass the consistency test and the weights of five principal indices are $W = [0.096, 0.150, 0.264, 0.035, 0.455]$.

Similarly, we do the AHP computation for each sub-indices and the final weight vector for C_1-C_{10} is $w = [0.04, 0.056, 0.1, 0.05, 0.039, 0.065, 0.082, 0.078, 0.021, 0.014]$.

We use the proposed model to compute B_5 as whole so its sub-indices do not need weight assignment.

4.3 FCE of Qualitative Indices

C_1-C_{10} are all qualitative indices and thus difficulty to measure accurately. To achieve the comprehensive evaluation of the system, this paper uses FCE to evaluate qualitative indices [11].

FCE is based on membership function of fuzzy mathematics, i.e., the distribution function of each index on comment set. FCE then transform the qualitative indices into quantitative form according to comment set’s quantification result and thus we can achieve a comprehensive evaluation of a system restricted by various factors.

We set comment set as $V = \{excellent, good, fair, poor, very poor\}$ and the corresponding quantization values are $\{1, 0.75, 0.5, 0.25, 0\}$. We can obtain a

fuzzy membership matrix of C_1-C_{10} using Delphi method and it is showed in (15).

$$R = \begin{bmatrix} 0.5 & 0.3 & 0.2 & 0 & 0 \\ 0.2 & 0.6 & 0.2 & 0 & 0 \\ 0.3 & 0.3 & 0.2 & 0.2 & 0 \\ 0.1 & 0.2 & 0.4 & 0.3 & 0 \\ 0 & 0.1 & 0.5 & 0.3 & 0.1 \\ 0.2 & 0.2 & 0.5 & 0.1 & 0 \\ 0 & 0 & 0.3 & 0.4 & 0.3 \\ 0.3 & 0.3 & 0.3 & 0.1 & 0 \\ 0.5 & 0.4 & 0.1 & 0 & 0 \\ 0.3 & 0.4 & 0.2 & 0.1 & 0 \end{bmatrix}. \tag{15}$$

The five elements in each row of (15) show the fuzzy distribution of each index.

C_1-C_{10} 's comprehensive evaluation vector can thus be calculated as $B = w * R = [0.1173, 0.1399, 0.1641, 0.0952, 0.0285]$. The score after Quantification is 0.328.

4.4 Calculation of Quantitative Indices' Scores

Quantitative indices are sub-indices in B5, i.e., the performance index of IDS and their scores can be calculated using (7). The results are averaged under 10 different runs of the experiment. We have $L = 0.2*1 + 0.6*0.75 + 0.2*0.5 = 0.75$, $T = 0.57$, $DR = 0.946$, $FAR = 0.182$ and the performance score is 0.78.

We combine the results of qualitative and quantitative indices and the overall score of the IDS information system is $0.328 + 0.7800.455 = 0.6829$, 'good' according to comment set.

If the background traffic in the required environment is high, in the situation where $T = 0.9$, we will have score 0.767 after recalculation, which means the tested IDS has better security detection ability in the situation where background traffic is high.

5 Conclusion and Future Work

Detection rate and false alarm ratio are both important evaluation indices to evaluate the performance of IDSs. However, in different kinds of network environments, evaluation results, obtained only upon these two indices, are not comprehensive and objective enough. By adding two supplement factors, i.e., background traffic and workload to the models utilizing DR and FAR, this paper proposed an evaluation model, which provides a new way of selecting IDSs with optimized performance in environments with different background traffic.

There is still room to improve this model. For example, there are other ways of normalizing background traffic, which makes this evaluation a qualitative but

non-quantitative process. In the future, we will keep working to get a more optimized, comprehensive and objective model.

Note that it is not necessary that the proposed model be used with AHP and FCE as in this paper.

Acknowledgments. This work was supported by The Research of Key Technology and Application of Information Security Certification Project (No. 2016YFF0204001) of China Information Security Certification Center.

References

1. Stallings, W.: *Network Security Essentials: Applications and Standards*. Pearson Education India, Delhi (2007)
2. Herrmann, D.S.: *Using the Common Criteria for IT Security Evaluation*. CRC Press, Boca Raton (2002)
3. Gan, Z., He, J.: Study on multi-hierarchical fuzzy comprehensive evaluation of intrusion detection system. *Appl. Res. Comput.* **4**, 29 (2006)
4. Li, L., Xia, Z., Xiong, J.: Study on evaluation method of multilayer hybrid intrusion detection system. *Comput. Sci.* **42** (2015)
5. Lippmann, R., Fried, D., Graf, I., Haines, J., Kendall, K., McClung, D., Zissman, M.: Evaluating intrusion detection systems: the 1998 DARPA off-line intrusion detection evaluation. In: *Proceedings of the DARPA Information Survivability Conference and Exposition*, vol. 2, pp. 12–26. IEEE (2000)
6. Haines, J., Lippmann, R., Fried, D.: 1999 DARPA intrusion detection system evaluation: design and procedures. *DARPA Intrusion Detection Evaluation Design & Procedures* (2001)
7. Gu, G., Fogla, P., Dagon, D., Lee, W., Skorić, B.: Measuring intrusion detection capability: an information-theoretic approach. In: *Proceedings of the 2006 ACM Symposium on Information, Computer and Communications Security*, pp. 90–101. ACM (2006)
8. Aggarwal, P., Sharma, S.: A new metric for proficient performance evaluation of intrusion detection system. In: Herrero, Á., Baruque, B., Sedano, J., Quintián, H., Corchado, E. (eds.) *International Joint Conference. AISC*, vol. 369, pp. 321–331. Springer, Cham (2015). https://doi.org/10.1007/978-3-319-19713-5_28
9. Powers, D.: Evaluation: from precision, recall and F-measure to ROC, informedness, markedness and correlation. *J. Mach. Learn. Technol.* **2**, 2229–2239 (2011)
10. Saaty, L.: How to make a decision: the analytic hierarchy process. *Eur. J. Oper. Res.* **48**(1), 9–26 (1990)
11. Wang, X., Shi, Y., Huang, R.: Application of multi-layer fuzzy comprehensive evaluation method in debris flow assessment. *J. Catastrophology* **19**(2), 1–6 (2004)



A Novel Accurate Source Number Estimation Method Based on GBSA-MDL Algorithm

Taha Bouras^(✉) , Di He, Fei Wen, Peilin Liu, and Wenxian Yu

Shanghai Key Laboratory of Navigation and Location-Based Services,
Shanghai Jiao Tong University, Shanghai, People's Republic of China
tahabouras04@yahoo.com,
{dihe, wenfei, liupeilin, wxyu}@sjtu.edu.cn

Abstract. Several classical source number estimation methods have been proposed in the past based on information theoretic criteria such as minimum description length (MDL). However, in most known real applications there is a scenario in which the number of sensors goes to infinity at the same speed as the number of snapshots (general asymptotic case) which yields to a blind performance for the classical MDL and results in an inaccurate source number estimation. Accordingly, in this work, the Galaxy Based Search Algorithm (GBSA) is modified and applied with the MDL criteria in order to optimize and correct the detection of source number under such sample-starving case. Simulation results show that the proposed GBSA-MDL based method gives reliable results compared to several used source number estimation methods.

Keywords: Source number estimation methods
Minimum Description Length (MDL) · General asymptotic case
Optimization · Galaxy Based Search Algorithm (GBSA)

1 Introduction

In recent decades, direction-of-arrival (DOA) or angle-of-arrival (AOA) estimation of multiple sources using an array is a fundamental problem in modern signal processing and it has found wide applications in radar, sonar, communications, geophysics, tracking, localization [1–4] and indoor positioning such as the application of AOA-based positioning through the use of wireless local area network (WLAN) infrastructure [5]. However, compared with different DOA estimation methods, the subspace-based methods are the most commonly used due to their high resolution and simplicity of computational such as multiple signal classification (MUSIC) [6] and estimation of signal parameters via rotational invariance techniques (ESPRIT) [7]. Meanwhile, in order to separate between source subspace and noise subspace which are the compositions of the signal impinging the array elements on the receiver side, the subspace-based algorithms require the exact information of the source number which is usually unknown.

Several classical source number estimation methods have been proposed in the past which are based on information theoretic criteria like the Akaike information criterion (AIC) [8], Bayesian information criterion (BIC) [9], predictive description length

(PDL) [10], Gerschgorin disk estimator (GDE) [11], and Minimum Description Length (MDL) [12]. Compared to other source estimation methods like, the decomposition of eigenvalues, methods based on information criteria do not require any parameters in order to fitly estimating the source number from the blended signals which allow them to be easier and efficient methods. However, it has been shown in [13, 14] that the MDL criteria suffer from the very low SNR as well as the sampling rate.

In the other side, the interaction between intelligent software tools and nature yields to a something new called Meta-heuristic algorithms. They are simply algorithms who imitate the behavior of nature in order to find a precise solution to hardly optimized problems. These type of methods (also named as nontraditional optimization methods) are known with their robustness for solving complicated engineering problems such as Simulated Annealing (SA) [15], Genetic Algorithm (GA) [16], Invasive Weed Optimization (IWO) [17] and Particle Swarm Optimization (PSO) [18] - as framework based on swarm behavior. Newly, a novel optimization algorithm was invented called Galaxy Based Search Algorithm (GBSA) which mimics the spiral galaxies in the outer space and it has gained more attention in a wide variety optimization problems, such as the use of GBSA to optimize the Otsu's criterion for multilevel thresholding of gray-level images in [19], GBSA for principal components analysis in [20] and a method for tracking an object using modified GBSA (M-GBSA) has been used in [21].

After constructing a complex objective function, the main problem of the information-based methods is to find its correct extremum values based on information criteria aspect. Otherwise, in real applications, there is a case when the number of sensors will be larger or equal to the number of samples that is known as the asymptotic case and this affects the performance of the MDL and yields to a non-detection for the source number or inaccurate source enumeration [13]. According to that, in this work, GBSA is used to solve this non-uniform optimum problem in order to enhance the shortcoming performance of the MDL under the effects of such starving environments.

The following of the paper is organized as follows. In Sect. 2, we set the problem formulation and the classical minimum description length. In Sect. 3, the main idea and the procedure for the GBSA are introduced. The proposed GBSA-MDL is described in Sect. 4. In Sect. 5, we present the simulation results and in the last Sect. 6, we draw conclusions for our work.

2 Problem Formulation and Minimum Description Length

In DOA estimation, the typical signal model is;

$$X(t) = A(\theta) * S(t) + w(t) \quad (1)$$

Where, time is represented as t^{th} sample such that $t = 1, \dots, n$. $X(t) = [X_1(t) \dots X_m(t)] \in \mathbb{C}^{m \times 1}$ is the observed snapshot vector. $A(\theta) = [a(\theta_1) a(\theta_2) \dots a(\theta_d)] \in \mathbb{C}^{m \times d}$ is the steering matrix, where $a(\theta)$ is called steering vector and $\theta = [\theta_1, \theta_2, \dots, \theta_d]^T$ are the parameters of interest or true DOA's.

$S(t) = [S_1(t) \dots S_d(t)]^T \in \mathbb{C}^{d \times 1}$ is the d source vector and $w(t) = [w_1(t) \dots w_m(t)]^T \in \mathbb{C}^{m \times 1}$ is the noise vector. $(\cdot)^T$ represents the transpose operation, d is the unknown source number, m is the number of antennas at the receiver side and n is the number of snapshots. A fateful problem here is to estimate d from n finite set of observations before an efficient source separation by using the MDL criterion function based on the concept of the shortest description length for data done by Wax [12]. So for presumed sources, the MDL criterion is given as:

$$MDL(k) = n(m - k) \log \left(\frac{\frac{1}{m-k} \sum_{i=k+1}^m l_i}{\left(\prod_{i=k+1}^m l_i \right)^{1/m-k}} \right) + \frac{1}{2} k(2m - k) \log n \quad (2)$$

Where l_i is the i^{th} eigenvalue of the covariance R , with $i = 1, \dots, m$, and $l_1 \geq l_d \geq l_{d+1} \geq \dots \geq l_m$, such that $R = E[XX^T]$ and $E[\cdot]$ is the expectation function. As we have mentioned before, the classical MDL criterion function described in (2) can provide a reliable performance just in the case when n tends to infinity while m remains fixed. Otherwise, the used criteria will easily fail. As result, The main problem of our work is to use the GBSA as a rescue algorithm, more clearly after modifying the GBSA to be more suitable for our optimization problem in the general asymptotic case, it is then used to find the correct source number \hat{d} and this can be performed by minimizing the objective (fitness) function (2) with respect to k in different situations ($m = n$, $m < n$, and $m > n$).

$$\hat{d} = \arg_{k=0, \dots, \bar{m}-1} \min MDL(k) \quad (3)$$

Where \bar{m} is the upper limit of the source number. Generally, is fixed to $\min(m, n) - 1$.

3 GBSA

3.1 Origin of GBSA

Spiral galaxies are a certain kind of galaxy, which consists of a flat disk with a bulging center and surrounding spiral arms [20]. Figure 1 displays a Photograph for a spiral galaxy. As the galactic disk angular speed of turnover differs with distance from the galactic center, a radial arm (such as a spoke) would speedily become curved to tightly curved just after slight galactic rotations. According to that, the GBSA algorithm uses a spiral chaotic move in order to imitate this spiral arm. After each iteration, it will be more narrowly curved which allows reaching precisely to the optimum solution.

Recently, GBSA is becoming a breakthrough optimization method because of its simplicity of implementation as well as ability to swiftly converge to a convenient solution. It does not require any gradient information of the function to be optimized and uses only primitive mathematical operators. Also, GBSA is well suited to solve the non-linear, non-convex, continuous, discrete, integer variable type problems.



Fig. 1. An example of spiral galaxy

3.2 GBSA Procedure

A. Initialization

B. Spiral Chaotic Move

The spiral chaotic move is the procedure of the GBSA used to find the global optima. It follows the procedures shown in Fig. 2. When the initial solution SG is set randomly, the spiral chaotic move searches globally around the given solution in order to find the area where the peak point may locate and this is known as exploration. The initial solution SG is updated to SG_{next} and this happens continuously every time the updated solution is more superior to the current one. Since the multimodal problems suffer from the high existence of the local optimum, the GBSA algorithm uses a chaotic variable in order to avoid falling into the same solution and thus keep the chance of the variation in the solutions.

C. Local search

After exploring the searching area globally, the local search procedure would be activated to exploit the promising area where may the peak of the fitness function exists following the steps shown in Fig. 3.

4 The Proposed GBSA-MDL Source Estimation Method

The proposed GBSA-MDL is shown in Fig. 4. A major breakthrough in the new proposed algorithm takes advantage from the presumed source number of the MDL which relies on the dimension of GBSA, as a result ending up with an efficient source enumerator in the general asymptotic case.

First of all is to verify whether the number of sensors goes to infinity at the same speed as the number of snapshots, $m, n \rightarrow \infty$ and $m/n \rightarrow c \in (0, \infty)$, if the condition is not satisfied then the classical MDL is called in order to find the number of sources frugally. Hence, GBSA can be used to find the solution even that the above-mentioned condition is not satisfied, however using the classical MDL is more convenient to avoid time conception as well as computation complexity we can see that more clearly in the simulation section.

```

 $\theta \leftarrow -\pi$ 
While  $rep < MaxRep$ 
  Repeat for  $i = 1$  to  $L$ 
   $SN_{nexti} \leftarrow S_i + NextChaos() rcos(\theta_i)$ 
  Endrepeat
  If  $(f(S_{next}) \geq (f(S)))$  then
  Flag  $\leftarrow True$ 
  Goto Endprocedure
  Endif
  Repeat for  $i = 1$  to  $L$ 
   $SN_{nexti} \leftarrow S_i - NextChaos() rcos(\theta_i)$ 
  Endrepeat
  If  $(f(S_{next}) \geq (f(S)))$  then
  Flag  $\leftarrow True$ 
  Goto Endprocedure
  Endif
   $r \leftarrow r + \Delta r$ 
  Repeat for  $i = 1$  to  $L$ 
   $\theta_i \leftarrow \theta_i + \Delta \theta$ 
  Endrepeat
  Repeat for  $i = 1$  to  $L$ 
  If  $(\theta_i > \pi)$  then
   $\theta_i \leftarrow -\pi$ 
  Endif
  Endrepeat
   $rep \leftarrow rep + 1$ 
  Endwhile
Endprocedure

```

Fig. 2. The pseudo-code of “*spiral chaotic move*” procedure.

```

Repeat for  $i = 1$  to  $L$ 
 $\alpha \leftarrow 1$ 
 $k \leftarrow 0$ 
While  $k < kMax$ 
   $SL_i \leftarrow S_i - \alpha \cdot \Delta S \cdot NextChaos()$ 
   $SU_i \leftarrow S_i + \alpha \cdot \Delta S \cdot NextChaos()$ 
  If  $(f(SL_i) < f(S))$  and  $(f(SU_i) < f(S))$  then
  Goto Endprocedure
  Endif
  If  $(f(SU_i) > f(S))$  then
   $S_i \leftarrow SU_i$ 
   $SL_i \leftarrow S_i$ 
   $\alpha \leftarrow \alpha + 0.01 \times NextChaos()$ 
   $k \leftarrow k + 1$ 
  Else
   $(f(SL_i) > f(S))$  then
   $S_i \leftarrow SL_i$ 
   $SU_i \leftarrow S_i$ 
   $\alpha \leftarrow \alpha + 0.01 \times NextChaos()$ 
   $k \leftarrow k + 1$ 
  Else
   $\alpha \leftarrow \alpha + 0.05 \times NextChaos()$ 
   $k \leftarrow k + 1$ 
  Endif
  Endifwhile
   $SL_i \leftarrow S_i$ 
   $SU_i \leftarrow S_i$ 
  Endrepeat
   $SN_{next} \leftarrow S$ 
  Endprocedure

```

Fig. 3. The pseudo-code of “*local search*” procedure.

In the opposite side, when the general asymptotic case occurs, the classical MDL criteria will suffer from the multidimensionality, nonlinearity and complexity problems ending up with a blind estimation or maybe not detection at all.

However, in such sample-starving case, the rescue of the modified GBSA algorithm involves, it takes the following steps as shown in Fig. 4 in order to search for the optimum solution which is at the same time the number of sources needed:

- (1) Over the searching space, the generation of initial random solutions should be determined using the “Generate Initial Solution” component of the GBSA, the presumed source number will be set as the dim of the GBSA.
- (2) Evaluate the fitness of all agents using Eq. (3) which is determined by taking the data from all the elements of the array for n number of snapshots.
- (3) The solution that GBSA-MDL seeks is the locus of the agent corresponding to minimum fitness which in fact represents the source number estimation. So, after step two we apply the GBSA algorithm. The turn of “Spiral Chaotic Move” is activated in order to explore the study area and confines the space where the maximum solution might be included.

After the discovery of the likely area by the “Spiral Chaotic Move”, the Flag is set to true as shown in Fig. 4, next, the local search procedure starts to find locally new optimum solution better than its two immediate neighbors until it converges to the appropriate source number.

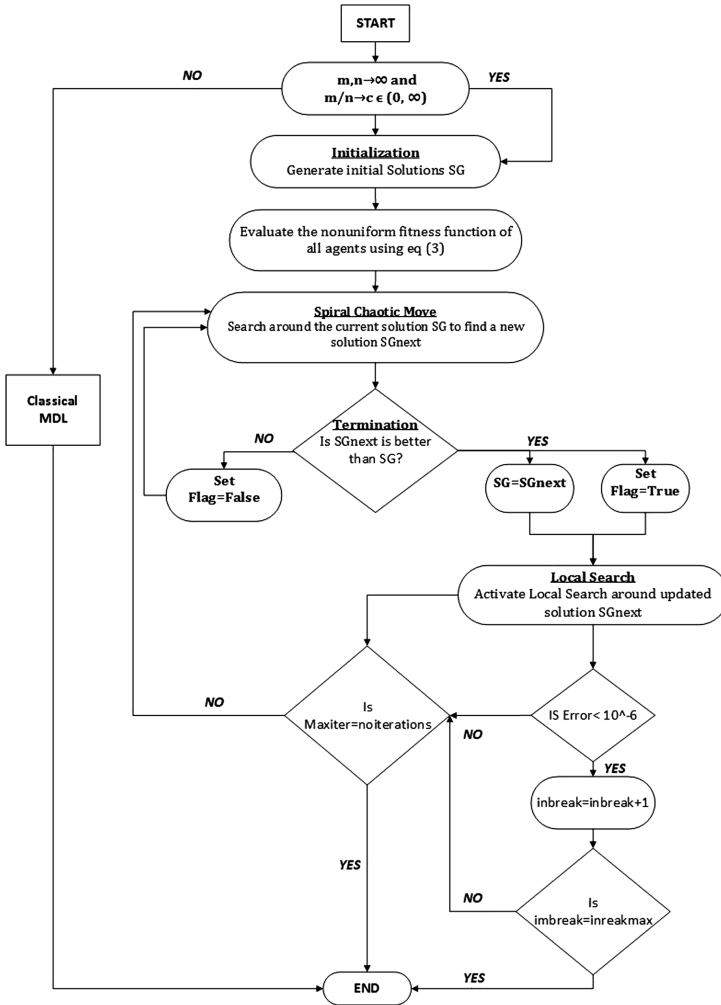


Fig. 4. Flowchart of the GBSA-MDL source estimation method

- (4) The GBSA-MDL terminates when it reaches the following stopping criteria Fig. 4.
- (a) The GBSA-MDL stops when the iteration counting of the GBSA overruns $Maxiter = 100$.
 - (b) The second stopping criterion examines whatever the difference error between two sequential solutions is less than the value of $1e-10$. If it is true then $inbreak = inbreak + 1$. Hence, when 'inbreak' exceeds a predetermined value our algorithm halts computations.
 - (c) The last stopping criterion is the number of trials and is set to be 100 in our simulations.

5 Simulation Results and Discussions

We consider a ULA of 30 sensors with half wavelength element separation impinged by three uncorrelated far-field narrow band Stationary Gaussian signals with angles [2.9°, 9.4°, 16.5°]. Figures 5, 6 and 7 show the performance of our proposed GBSA-MDL compared with some existing information criteria, called exponentially embedded families (EEF), RMT-AIC and corrected AIC (AIC_{c3}) in terms of probability of error detection versus SNR with ratio $m/n = 1/3, 1,$ and 3 respectively such that m represents the number of antennas at the receiver side and n is the number of snapshots. Meantime, all numerical results are computed for 300 independent trials such that parameters of the GBSA used during the optimization process are given in Table 1.

When the sample size n is smaller than the number of sensors m Fig. 5, the proposed method outperforms the two schemes EEF and AIC_{c3}. It is obvious that the GBSA-MDL provides a consistent estimation for source number compared to EEF which cannot provide any detection. Also, the GBSA-MDL performs better than the AIC_{c3} in terms of probability of error detection. In addition of that, we can observe that our algorithm can proceed an accurate source detection while the RMT-AIC be unstable even when the SNR goes to infinity.

When the number of samples increases and is equal to m , all methods can provide a detection as shown in Fig. 6. The proposed GBSA-MDL, EEF and AIC_{c3} criteria can correctly detect the source number, GBSA-MDL still performs better than EEF, and almost proceed the same as the AIC_{c3}. In addition of that, EEF and AIC_{c3} need a higher SNR in order to end up with an accurate detection. Meanwhile, RMT-AIC gives unreliable estimation even that the number of SNR is larger compared to GBSA-MDL.

Table 1. GBSA parameters used for optimization.

Spiral chaotic move		Local search		GBSA	
<i>Maxrep</i>	50	<i>Kmax</i>	50	<i>Iteration number</i>	60
<i>Drmax</i>	1	<i>Ls_sstep</i>	0.0001	<i>Dimension</i>	6
		<i>Ls_lstep</i>	0.05		
<i>Dtmax</i>	0.1	<i>Dsmax</i>	10	<i>Chaosvar</i>	0.19

As illustrated in Fig. 7, when n becomes much larger than m the gap between the proposed GBSA-MDL and the two criteria EEF and AIC_{c3} is reliable which implies that the performance of GBSA-MDL is always consistent while RMT-AIC criterion is still suffering for reaching zero probability of detection even that at sufficiently SNR.

In this part, we want to prove the performance of the proposed GBSA-MDL in terms of snapshots compared to the classical MDL by considering a ULA with the same number of sensors $m = 30$ received two far-field narrow bands Stationary Gaussian signals from two different angles [0.5°, 3.5°], SNR is set to be -5 dB.

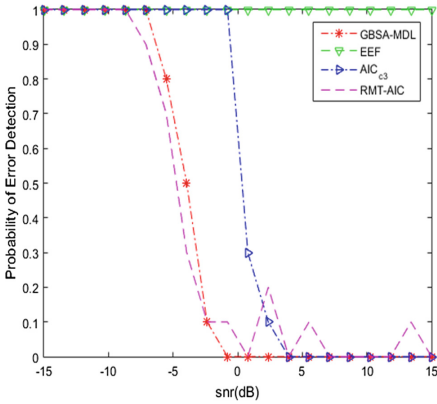


Fig. 5. Probability of error detection versus SNR with $m = 30$ and $n = 10$.

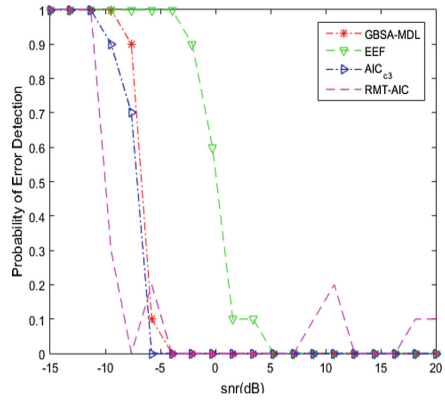


Fig. 6. Probability of error detection versus SNR with $m = 30$ and $n = 30$.

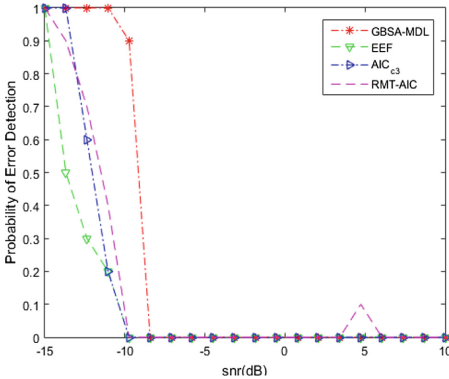


Fig. 7. Probability of error detection versus SNR with $m = 30$ and $n = 90$.

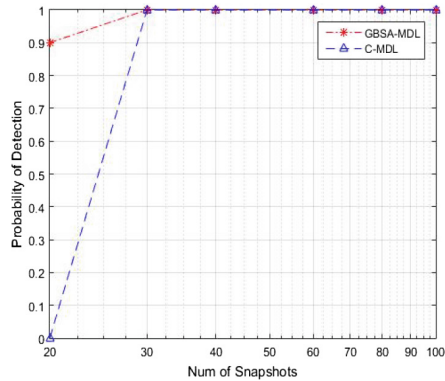


Fig. 8. Probability of detection versus number of snapshots. SNR = -5 db.

Figure 8 shows the probability of detection of source of interest with respect to the number of snapshots for the proposed GBSA-MDL and the Classical MDL. It is obvious from Fig. 8 that the GBSA-MDL outperforms the CMDL in terms of snapshots. When the number of snapshots is less than the number of sensors, $n < 30$, and the probability of correct detection for GBSA-MDL is almost one while CMDL suffers to reach the correct detection and this can improve the reliable detection of the GBSA-MDL in the general asymptotic case compared to the classical MDL. Meanwhile, the CMDL criterion needs around additional 30 snapshots in order to provide the same accuracy as GBSA-MDL.

6 Conclusion

In this work, a GBSA-MDL source number estimation method has been investigated by using the meta-heuristic GBSA Algorithm to improve the performance of the Classical MDL. Numerical results proved the usability of the GBSA-MDL for source enumerator in several environments. In addition to that, the comparison with the existing source enumerators (CMDL, EEF, RMT-AIC, AIC_{c3}) shows the capability and the robustness of the GBSA-MDL for providing an accurate estimation for source number in the general asymptotic case where the number of sensors tends to infinity at the same time as the number of snapshots whereas the other approaches fail in such starving environment.

Acknowledgment. This research work is supported by the Important National Science and Technology Specific Project of China under Grant No. 2016ZX03001022-006, the Shanghai Science and Technology Committee under Grant No. 16DZ1100402, and the National Natural Science Foundation of China under Grant No. 91438113.

References

1. Xie, W., Wen, F., Liu, J., Wan, Q.: Simultaneously source association, DOA and fading coefficients estimation for multipath signals. *IEEE Trans. Signal Process.* **65**(11), 2773–2786 (2017)
2. Wen, F., Wan, Q., Fan, R., Wei, H.: Improved MUSIC algorithm for multiple noncoherent subarrays. *IEEE Signal Process. Lett.* **21**(5), 527–530 (2014)
3. Wen, F., Xie, W., Chen, X., Liu, P.: DOA estimation for noncircular sources with multiple noncoherent subarrays. *IEEE Commun. Lett.* (2017). <https://doi.org/10.1109/lcomm.2017.2703649>
4. Xie, W., Wang, C., Wen, F., Liu, J., Wan, Q.: DOA and gain-phase errors estimation for noncircular sources with a central symmetric array. *IEEE Sens. J.* **17**(10), 3068–3078 (2017)
5. Wong, C., Klukas, R., Messier, G.: Using WLAN infrastructure for angle-of-arrival indoor user location. In: *Proceedings of the 68th Semi-Annual IEEE Vehicular Technology (VTC 2008)*, pp. 1–5, September 2008
6. Schmidt, R.O.: Multiple emitter location and signal parameter estimation. *IEEE Trans. Antenna Propag.* **34**(3), 276–280 (1986)
7. Roy, R., Kailath, T.: ESPRIT-estimation of signal parameters via rotational invariance techniques. *IEEE Trans. Signal Process.* **37**(7), 984–995 (1989)
8. Akaike, H.: A new look at the statistical model identification. *IEEE Trans. Autom. Control* **AC-19**(6), 716–723 (1974)
9. Schwarz, G.: Estimating the dimension of a model. *Ann. Stat.* **6**(1978), 461–464 (1987)
10. Valaee, S., Kabal, P.: An information theoretic approach to source enumeration in array signal processing. *IEEE Trans. Signal Process.* **52**(5), 1171–1178 (2004)
11. Wu, H.T.: Source number estimators using transformed Gerschgorin radii. *IEEE Trans. Signal Process.* **43**(6), 1325–1333 (1995)
12. Wax, M., Kailath, T.: Detection of signals by information theoretic criteria. *IEEE Trans. Acoust. Speech Signal Process.* **33**(2), 387–392 (1985)

13. Huang, L., So, H.C.: Source enumeration via MDL criterion based on linear shrinkage estimation of noise subspace covariance matrix. *IEEE Trans. Signal Process.* **61**, 4806–4821 (2013)
14. Huang, L., Long, T., Mao, E., So, H.C.: MMSE-based MDL method for accurate source number estimation. *IEEE Signal Process. Lett.* **16**, 798–801 (2009)
15. Kirkpatrick, S., Gelatt, C.D., Vecchi, M.P.: Optimization by simulated annealing. *Science* **220**, 671–680 (1983)
16. Goldberg, D.E.: *Genetic Algorithms in Search Optimization and Machine Learning*. Addison-Wesley, Boston (1989)
17. Mehrabian, A.R., Lucas, C.: A novel numerical optimization algorithm inspired from weed colonization. *Ecol. Inform.* **1**, 355–366 (2006)
18. Kennedy, J., Eberhart, E.C.: Particle swarm optimization. In: *IEEE International Conference on Neural Networks*, vol. 4, pp. 1942–1948 (1995)
19. Shah-Hosseini, H.: Otsu's criterion-based multilevel thresholding by a nature-inspired metaheuristic called galaxy-based search algorithm. In: *Third World Nature and Biologically Inspired Computing (NaBIC)* (2011). 2013 MECS
20. Shah-Hosseini, H.: Principal components analysis by the galaxy-based search algorithm: a novel metaheuristic for continuous, optimisation. *Int. J. Comput. Sci. Eng.* **6**(1/2), 132–140 (2011)
21. Sardari, F., Moghaddam, M.E.: An object tracking using modified galaxy based search algorithm. *Swarm Evol. Comput.* **30**, 27–38 (2016)

Communication QoS, Reliability and Modeling



A Green Load Balancing Algorithm for Dynamic Spatial-Temporal Traffic Distribution in HetNets

Jichen Jiang^(✉), Xi Li, and Hong Ji

Key Laboratory of Universal Wireless Communications, Ministry of Education,
Beijing University of Posts and Telecommunications,
Beijing, People's Republic of China
{jiangjichen,lixi,jihong}@bupt.edu.cn

Abstract. With the increasing users demands, the data traffic in the network reveal different characteristics in both spatial and temporal dimensions, bringing severe load imbalance problem. This may impact resource utilization, users experience and system energy efficiency, and then need further investigation. In this paper, we propose a distributed load-balancing algorithm considering this spatial-temporal variation in a two-tier heterogeneous network. Instead of illuminating the spatial-temporal influence, we make use of this characteristic while designing the algorithm, and accordingly switch ON/OFF small cell base stations (SBSs) for improving the energy efficiency. A load factor described with load variance is derived, based on which the problem is formulated as a non-linear integer programming that seeks to minimize a load function. Then a suboptimal solution is obtained by an effective heuristic algorithm. Simulation results show that our proposed algorithm balances the traffic load better and significantly reduces the total energy consumption, compared with conventional load-balancing scheme.

Keywords: Spatial-temporal variation · Load balance
Small cell ON/OFF

1 Introduction

With the development of mobile communication technology, the data traffic flow of wireless cellular network has grown rapidly in the past decade [1–4]. This growth not only increases the traffic load on wireless cellular network, but also reveals dynamic characteristics of data traffic in both temporal and spatial dimensions. This spatial-temporal variation of data traffic distribution may lead to load imbalance and impact the network performance in energy efficiency, users quality of service (QoS) requirements and resource utilization. So how to solve the load imbalance problem in different scenarios is worth studying.

There have been approaches proposed about traffic load balancing, such as complementary communication technologies, direct transfer, cell range expansion

(CRE), and so on [5–9]. These works have designed algorithms for the load-balancing problem in conventional scenario and achieved good results. However, existing works are mainly aimed at illuminating the influence caused by the variations. In fact, those variations could also be used to cope with the load imbalance problem.

Reference [5] provides a strategy to offload the mobile data traffic from cellular network to WiFi infrastructure for extra capacity and better network performance. This work also proposes a load-based SNR-threshold algorithm that controls the amount of WiFi offloading. Reference [6] analyzes the downlink and uplink transmission performance in two-tier heterogeneous network when micro BS employs CRE and derives an optimal CRE bias and optimal transmit power of SBSs to maximize transmission success probability and energy efficiency. An analytical framework is proposed in [7] which allows to analyze the trade-off between the energy consumption and the traffic offload of cognitive network and can be used for the energy efficient design and operation of cognitive small cell access points. In [8] a new separation architecture called Hyper-Cellular Network (HCN) is proposed, which is supposed to guarantee the coverage. Then two small cell sleeping schemes (random and repulsive schemes) are proposed in HCN. Numerical results show that these two schemes can keep the load of the network balanced and save a lot of energy. In [9] a dynamic pico on/off algorithm is proposed in which the traffic load coefficient is formulated as a function of bandwidth. By controlling this load coefficient under a fixed threshold, the traffic load can be seen as balanced and minimum pico base stations will be switched to active mode.

Although the above works provide many good insights on balancing traffic load and improving energy efficiency, these methods are not appropriate for some typical spatial-temporal variation scenario. For example, in a shopping mall area, there will be not much people early in the morning and these people would more likely to be in the supermarket underground. As time goes by, there will be more and more users arriving at the mall and by noon most of them choose to go upstairs having lunch. Due to this variation, the traffic load would be unbalanced on these two dimensions. Frequent handover from one SBS to another could cause a decline in throughput and result in user experience decreasing.

In this paper, we propose an algorithm of load balancing based on SBSs sleep mode in two-tier heterogeneous networks (HetNets), in which SBSs can decide automatically whether to switch on or off, using the spatial-temporal variation characteristics of data traffic distribution. This self-organized algorithm is able to adjust automatically as the traffic load changes. We use a load factor to measure the traffic load level which is formulated as the variance of traffic load. The goal of the algorithm is to minimize this load factor. We model this problem into a non-linear integer programming problem in which an optimal solution can not be obtained in linear time. So we reformulate the problem into a max-min optimization problem and find a method to solve it through genetic algorithm. Simulation results show that the proposed algorithm can balance the network traffic load efficiently and save the total energy consumption, compared with conventional load-balancing approach.

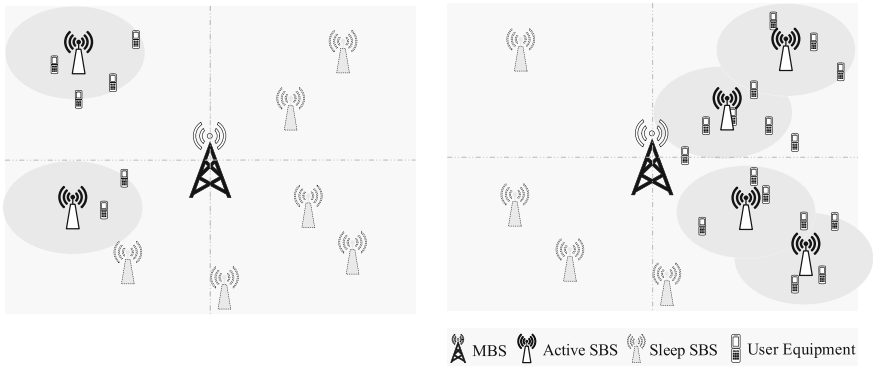
The rest of this paper is organized as follows. In Sect. 2, the system model is defined and the studied scenario is described. Section 3 presents the problem formulation and describes the proposed load-balancing algorithm, followed by simulation results and conclusion in Sects. 4 and 5, respectively.

2 System Model and Scenario

2.1 Network Scenario

We consider a two-tier HetNet, where several SBSs are randomly distributed in a macro base station (MBS) covered area, where users distributed in different location at different time. We illustrate the scenario as in Fig. 1. The upper left area is numbered as region 1, and remaining areas are clockwise marked as region 2, region 3 and region 4. At time t_1 , user equipments are mostly distributed in region 1 and region 4, so only the SBSs in these two regions are switched on while others are off, as Fig. 1(a) shows. And as time goes by, at time t_2 , some user equipments leave region 1 and region 4 and appear in region 2 and region 3, leading to the fact that SBSs in region 1 and region 4 are switched off meanwhile SBSs in region 2 and region 3 are switched on.

Without loss of generality, we assume that the arrival of users follows a Poisson Point Process (PPP), whose arrival rate at time t is λ . Orthogonal bandwidth is used by different layers to avoid the severe inter-layer interference, especially for protecting the signaling coverage [8]. System bandwidth is \mathcal{W} and the bandwidth of each subcarrier is B . In this paper, we only consider the scenario that the SBSs covered with one MBS. We denote the sets of SBSs and users by $\mathcal{J} = \{1, 2, \dots, J\}$ and $\mathcal{I} = \{1, 2, \dots, I\}$, respectively. The transmission power of SBS_j , $j \in \mathcal{J}$, is P_j , and h_{ij} is used to denote the channel gain between SBS_j and $user_i$. In order to realize the load balancing of the whole network, each SBS



(a) User equipments distribution at time t_1 (b) User equipments distribution at time t_2

Fig. 1. Illustration of the studied network at different time.

is set to have two operation modes, one is the active mode, and another is the sleep mode. To express the problem better, an indicator $\xi_{i,j}^w$ is used to describe the connection state between stations, users and bands. If $\xi_{i,j}^w = 1$, the $user_i$ is associated with the SBS_j and deployed on $band_w$; otherwise, $\xi_{i,j}^w = 0$.

2.2 Traffic Model

In this paper, we assume that a user equipment can only be served by one active SBS at one subcarrier frequency. Therefore, the received signal to interference and noise ratio (SINR) of $user_i$ from SBS_j is given by

$$SINR_{i,j}^w = \frac{\xi_{i,j}^w p_j |h_{ij}|^2}{\sigma^2 + \sum_{k \neq j} \zeta_k^w p_k |h_{ik}|^2} \quad (1)$$

where σ^2 is the thermal noise energy, and $|h_{ij}|^2$ is the channel gain from SBS_j to $user_i$, $j \in \mathcal{J}$, $i \in \mathcal{I}$. If $\zeta_k^w = 1$, it indicates that SBS_j is active and use $band_w$ to transmit signals. Further, according to Shannon Theory, the data rate of $user_i$ is given by

$$r_{i,j}^w = B \log_2(1 + SINR_{i,j}^w) \quad (2)$$

We use ρ_j to denote the ON/OFF state of SBSs, which is defined as follows:

$$\rho_j = \begin{cases} 1 & \text{SBS}_j \text{ is active} \\ 0 & \text{otherwise} \end{cases}$$

so we can obtain the number of active SBSs in the network from above. Accordingly, the average rate of whole network can be denoted as

$$\bar{r} = \frac{\sum_{i,j,w} r_{i,j}^w}{\sum_j \rho_j} \quad (3)$$

where $\sum_{i,j,w} r_{i,j}^w$ enlightens the sum of data rate brought by the users that associated with SBSs in the network.

3 Problem Formulation and Algorithm Design

3.1 Problem Formulation

Based on the network model, we consider a mechanism to balance the system load by controlling the SBSs' operation mode to active mode or sleep mode, which aims at keeping the load of whole network balanced around an average level while ensuring the QoS of users. In a period of time, the number of users may change and could distribute in different part of the area, so the SBSs of different location may have different operation mode. By switching some SBSs

of the network ON/OFF, the load of each SBS can be stabilized near the mean value, ensuring the load of the network to be balanced. In other words, if we keep the difference between the load of each SBS and the average load of the whole network as low as possible, then the network can be seen as a load-balanced system. The load deviation of SBS_j can be written in the following expression:

$$d_j = \sum_w \sum_i \xi_{i,j}^w r_{i,j}^w - \bar{r} \quad (4)$$

As to balance the load of the network, the load deviation of each SBS has to be as low as possible, that is, the load variance of the network has to be minimum. In this paper, we derive a load factor to describe the load variance, which is defined as:

$$\mathcal{L} = \sum_j d_j^2 \quad (5)$$

For the purpose of minimizing the load variance of the network, the optimal load-balancing problem can be formulated as the following:

$$\begin{aligned} & \min \mathcal{L} \\ \text{s.t.} \quad & \sum_w \sum_i \xi_{i,j}^w \leq 1, i \in \mathcal{I}, j \in \mathcal{J}, w \in \mathcal{W} \\ & P_j \leq P_{max}, i \in \mathcal{I} \\ & \xi_{i,j}^w \in \{0, 1\}, i \in \mathcal{I}, j \in \mathcal{J}, w \in \mathcal{W} \end{aligned} \quad (6)$$

where P_{max} is the maximum transmit power of SBS.

The goal of this work is to propose a load-balancing algorithm in which the traffic load of each SBS is balanced near a average value by switching the SBS to active or sleep. The optimization formulation is to minimize the traffic load variance as in Eq. (6). Note that (6) is a non-linear integer optimization programming problem which is not suitable to be solved by linear integer programming method. Fortunately, we notice that the formulation can be seen as a max-min optimization problem [10], then the problem can be re-formulated as:

$$\begin{aligned} & \max \sum z \\ \text{s.t.} \quad & z \leq d_j, i \in \mathcal{I}, j \in \mathcal{J}, w \in \mathcal{W} \\ & \sum_w \sum_i \xi_{i,j}^w \leq 1, i \in \mathcal{I}, j \in \mathcal{J}, w \in \mathcal{W} \\ & P_j \leq P_{max}, i \in \mathcal{I} \\ & \xi_{i,j}^w \in \{0, 1\}, i \in \mathcal{I}, j \in \mathcal{J}, w \in \mathcal{W} \end{aligned} \quad (7)$$

3.2 Load-Balancing Algorithm Design

Problem (7) is still difficult to get an optimal solution in linear time scale, thus, we propose a load-balancing algorithm through switching SBSs ON/OFF based on genetic algorithm (GA).

When there are users arriving at the area, the data traffic is also brought to the network, resulting in the traffic load change of SBSs. As this change happened, SBSs will check their operation modes and decide to change or not according to Eq. (6). If the total traffic load is increasing, then several SBSs should be switched active to share some load. On the contrary, when users depart from the area, the data traffic is also reducing, causing some SBSs have to be switched off. Therefore, different operation mode of SBSs will directly affect the traffic load distribution of the network, so our goal is to choose the appropriate $\xi_{i,j}^w$ for $user_i$ and SBS_j keeping the load function minimum.

Algorithm 1. Load-Balancing Algorithm through Switching SBSs ON/OFF via GA

```

1: Initialization:
   a)Users arrive and randomly distributed in the network
   b)Set the maximum number of iterations  $M$ , population size  $Z$  and encoding length
    $l$ ,  $p_c$ ,  $p_m$  and  $p_s$ 
   c)Initialize the population according to  $\mathcal{Z}$ ,  $l$ , set  $\min V = V_1$ 
2: for  $m = 1, 2, \dots, M$  do
3:   for each individual  $z$  in the population,  $z = 1, 2, \dots, Z$  do
4:     Calculate the objective function: the load variance  $V$  for each individual
5:   end for
6:   if  $p_1 < p_m$  then
7:     Calculate the mutation point
8:     if  $m_{point} = 1$  then
9:       change the value to 0
10:    else
11:      change the value to 1
12:    end if
13:  end if
14:  if  $p_2 < p_c$  then
15:    Calculate the crossover point and exchange the value of  $individual_z$  with
     $individual_{z+1}$ 
16:  end if
17:  Calculate  $\sum V$  and  $\frac{V_z}{\sum V}$ 
18:  if  $\frac{V_z}{\sum V} < p_s$  then
19:    Select this individual as a member of new population
20:  end if
21:  Update the population
22:  if  $Var_z < \min V$  then
23:     $\min V = Var_z$ 
24:  end if
25: end for
26: Output the  $\min V$ , best individual, and obtain the load-balancing policy according
    to the result

```

Because the problem is NP-hard which is difficult to obtain an optimal solution, so we derive a suboptimal solution through GA. GA updates a population

of solutions via genetic operators such as crossover, mutation and selection to achieve offsprings with better quality until some convergence criteria are met [11]. At each generation, a GA is capable of producing and maintaining a set of feasible solutions, maintaining a population of candidate solutions, and evaluating the quality of each candidate solution according to the objective fitness function. We view each combination of SBS operation modes as an individual of the population, that is, a combination of all the SBSs' binary-state mode value. The original population is set randomly. Equation (7) is the objective fitness function. Mutation probability p_m and crossover probability p_c is used to decide whether to perform mutation and crossover procedures for this individual or not. After the traffic load variance of each individual is calculated, the lower value will be selected, and the corresponding individual will be seen as a good individual and insert to the new population. After several times of iteration, the individuals in the population will tend to be consistent and the solution to our problem can be obtained. This load-balancing algorithm can be summarized as Algorithm 1.

4 Simulation Results

In this section, simulation results are present to show the performance of our proposed algorithm. We consider a scenario that several SBSs are covered by one MBS where those SBSs are deployed uniformly. The parameter used for the simulations are summarized in Table 1. Additionally, we compare the following algorithms for performance evaluating in the this simulation:

- Proposed algorithm: Control the operation mode of each SBS and calculate the traffic load of each SBS. Find the best operation modes combination and obtain the minimum variance of the load in the network.
- Conventional approach: SBSs don't have the capability to switch between sleep-active modes and don't apply the load-balancing scheme either, referred to hereinafter as "SBSs all-on".
- Classical Load-Balancing (LB) algorithm: The SBS with over-loaded traffic will select one potential target SBS with under-loaded traffic to offload, the

Table 1. Parameter

Parameter	Value
Carrier frequency	2 GHz
System bandwidth	10 MHz
Inter site distance of SBSs	40 m
Thermal noise	-174 dBm/Hz
Path loss model (d in km)	$140.7 + 37.6 \log_{10} d$
Maximum transmit power	30 dBm
Users distribution	3/4 in the hot spot

whole process of which is motivated by the settings of self-adjustment of specific system parameters in LTE, referred to hereinafter as “conventional algorithm”.

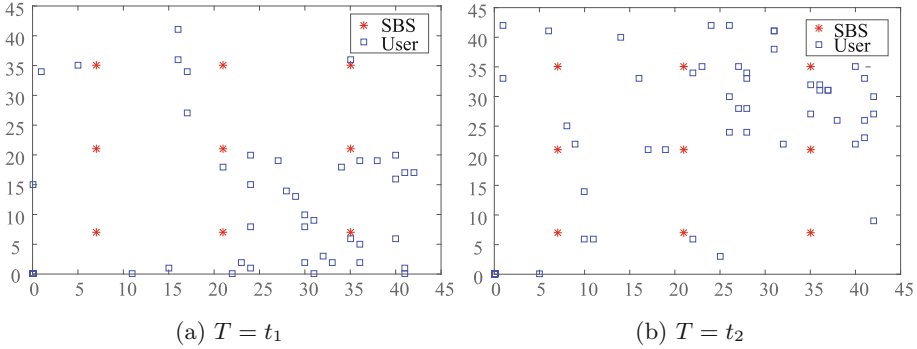


Fig. 2. Distribution of SBSs and users.

Figure 2 illustrates the scenario. The simulation starts with 20 users, randomly distributed in the area and as time goes by, more and more users arrive in and some of them will centrally distributed in one hot spot which is not a fixed location and will change as time varies. So not only the number of users in the network will change, but also the users’ spatial distribution. We assume that each 10 min a maximum of 10 users will join the network and there will be 3/4 of total users are distributed in one hot spot area while others are uniformly distributed in the remaining area within the coverage of MBS.

Figure 3 shows the traffic load variance in the aforementioned scenario about the above three algorithm as time varies from 10 min to 80 min, which indicates the balancing level of the network. To meet the QoS requirement of users, the data throughput offered by SBSs has to be up to 80% of the total data request, and the rest will be transferred to MBS. We can see from the result that although the number and distribution of users in the network is changing over the time, our proposed algorithm manages to stabilize the variance of traffic load and maintain at a lower value by switching SBSs to active or sleep modes, compared with the classical LB algorithm and “SBSs all-on” algorithm.

In Fig. 4, we show the total energy consumption of the network. In this simulation, we only consider the transmission power of the SBSs, for example, if SBS_j is in active mode, then the energy consumption is P_j , otherwise, the energy consumption is 0. As in the conventional LB algorithm, SBSs are always in active mode in which the total energy consumption stays the same while in our proposed algorithm, SBSs’ operation modes are different from each other since the number and distribution of users vary from time to time. So when some SBSs are switched to sleep mode, they actually save a large portion of energy, relative to the classical LB algorithm.

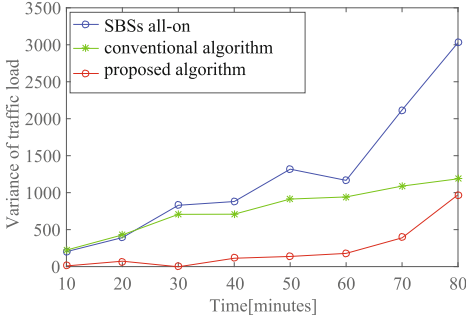


Fig. 3. Variance of traffic load per SBS as time varies.

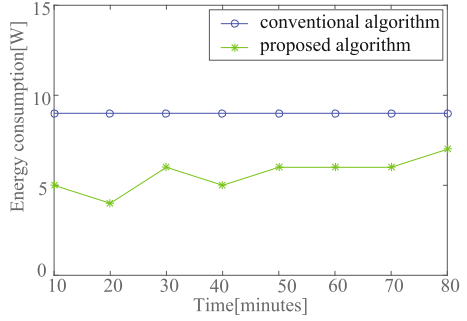
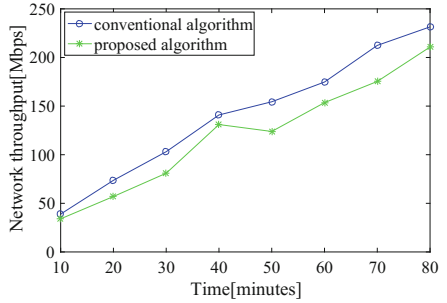
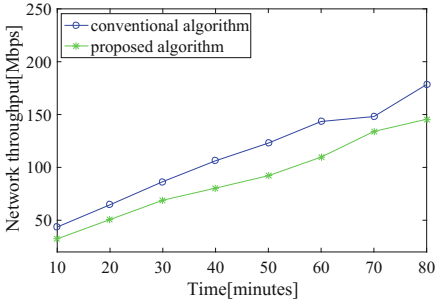


Fig. 4. Energy consumption of the network with respect to time.



(a) 10 users join the network/10 minutes (b) 20 users join the network/10 minutes

Fig. 5. Network throughput with respect to time.

Figure 5 shows the data traffic throughput of the network using our proposed algorithm and classical LB algorithm with different user’s arrival rate. We can see from the result that data throughput increases as time flows, for the reason that the number of users increases with time. The value is not much different between those two algorithms, even the classical LB algorithm is a litter larger. The main reason is that our proposed algorithm switches off some unnecessary SBSs while the classical LB algorithm is not, thus a few users have to associate with the MBS which can lower down the throughput slightly (only the data throughput of SBSs is measured in our simulation).

5 Conclusion

In a two-tier HetNet where the users distribution and data traffic are changing from time and geographical location, it may result in traffic load imbalance problem. We propose an energy-efficient load-balancing algorithm in which SBSs can automatically switch between active or sleep mode. In order to describe the load difference among each SBSs, a load factor is derived and modeled as a load

variance. Then, to improve the energy efficiency of the system, switching SBSs ON/OFF is considered. Since the problem is NP-hard and an optimal solution is difficult to obtain, we reformulate the problem to a max-min optimization problem and solve it with the proposed algorithm via GA. Simulation results show that the proposed algorithm is energy efficient and can obviously balance the traffic load in the network, compared with classical LB algorithm.

Acknowledgement. This paper is jointly sponsored by the National Natural Science Foundation of China (Grant No. 61671088) and the National Science and Technology Major Project of the Ministry of Science and Technology of China (Grant No. 2016 ZX03001017).

References

1. Chen, L., Yu, F.R., Ji, H., Rong, B., Li, X., Leung, V.C.M.: Green full-duplex self-backhaul and energy harvesting small cell networks with massive mimo. *IEEE J. Sel. Areas Commun.* **34**(12), 3709–3724 (2016)
2. Mehmeti, F., Spyropoulos, T.: Performance analysis of mobile data offloading in heterogeneous networks. *IEEE Trans. Mob. Comput.* **16**(2), 482–497 (2017)
3. CISCO: Cisco visual networking index: global mobile data traffic forecast update 2016–2021, February 2017. <http://www.cisco.com/c/en/us/solutions/collateral/service-provider/visual-networking-index-vni/mobile-white-paper-c11-520862.html>
4. Zhang, H., Chen, S., Li, X., Ji, H., Du, X.: Interference management for heterogeneous networks with spectral efficiency improvement. *IEEE Wirel. Commun.* **22**(2), 101–107 (2015)
5. Hagos, D.H., Kapitza, R.: Study on performance-centric offload strategies for LTE networks. In: 6th Joint IFIP Wireless and Mobile Networking Conference (WMNC), pp. 1–10, April 2013
6. Yang, K., Wang, P., Hong, X., Zhang, X.: Joint downlink and uplink network performance analysis with CRE in heterogeneous wireless network. In: 2015 IEEE 26th Annual International Symposium on Personal, Indoor, and Mobile Radio Communications (PIMRC), pp. 1659–1663, August 2015
7. Wildemeersch, M., Quek, T.Q.S., Slump, C.H., Rabbachin, A.: Cognitive small cell networks: energy efficiency and trade-offs. *IEEE Trans. Commun.* **61**(9), 4016–4029 (2013)
8. Zhang, S., Gong, J., Zhou, S., Niu, Z.: How many small cells can be turned off via vertical offloading under a separation architecture? *IEEE Trans. Wireless Commun.* **14**(10), 5440–5453 (2015)
9. Jin, Z., Pan, Z., Liu, N., Li, W., Wu, J., Deng, T.: Dynamic pico switch on/off algorithm for energy saving in heterogeneous networks. In: 2015 IEEE 81st Vehicular Technology Conference (VTC Spring), pp. 1–5, May 2015
10. Vlachos, C., Friderikos, V.: Optimal device-to-device cell association and load balancing. In: 2015 IEEE International Conference on Communications (ICC), pp. 5441–5447, June 2015
11. Keskinturk, T., Yildirim, M.B.: A genetic algorithm metaheuristic for bakery distribution vehicle routing problem with load balancing. In: 2011 International Symposium on Innovations in Intelligent Systems and Applications, pp. 287–291, June 2011



Research on the Construction of Radio Environment Map (REM) Based on Spatial Interpolation

Ran Zi^(✉), Jun Chang, Rong Zong, Ruonan Wang, and Guiwen Liao

Yunnan University, Kunming 650500, China
790354420@qq.com

Abstract. For the further performance improvement of Cognitive Radio systems, providing accurate or comprehensive information support to Cognitive Radio devices or networks, there is a use of “Radio Environment Map (REM)”, which presents multi-dimensional information of radio environments and scenarios. With the study of Spatial Interpolation, a method of constructing REM is proposed, and the performance of each algorithm is compared. Experiments show that the RMSM algorithm has advantages like high efficiency and low error, which can be used for the construction of REM.

Keywords: Radio Environment Map · Cognitive Radio · Spatial Interpolation

1 Introduction

Currently, promoting dynamic spectrum management (DSM) has become an international trend. Cognitive Radio (CR), breaking the traditional frequency distribution mechanism which was closed or protected, which enabling the dynamic sensing of spectrum environment by wireless devices or systems, making the spectrum access more efficient and flexible [1]. For the further performance improvement of Cognitive Radio systems, the technique “Radio Environment Map (REM)” appears.

Radio Environment Map (REM), proposed by Y.P. Zhao in 2005, is a comprehensive spatiotemporal database and an abstraction of real-world radio scenarios [2], which presents multi-dimensional information of radio environments. Now the concept of REM has been acknowledged by the international group “Wireless Innovation Forum” and referenced by several standard documents such as IEEE, ITU-R, ETSI [3]. The objective of the project FARAMIR (Flexible and Spectrum-Aware Radio Access through Measurements and Modelling in Cognitive Radio Systems), conducted by Framework Program 7 (FP7) in 2010, is to research and develop a complete REM prototype system for increasing the radio environmental and spectral awareness of future wireless systems, improving the capacity or innovation of radio resource optimization and radio management in European industry [4–7]. In recent years, many colleges or institutions have conducted the research on the techniques of spectrum management based on REM [8–12].

Spatial Interpolation is a method to evaluate the unknown point and fill the blank space by using the sample point [13], which is widely applied to Geographic

Information System (GIS), image processing, indoor positioning and so on. The techniques of Spatial Interpolation, which are commonly used, include Inverse Distance Weighting (IDW) [14, 15], Natural Neighbor [13], Spline Interpolation [16], and Kriging Interpolation [17]. In this paper, Spatial Interpolation algorithm are compared and used for analyzing the radio environment, and a method of constructing the REM based on Spatial Interpolation and Received Signal Strength (RSS) is proposed.

The rest of this paper is structured as follows. Section 2 explains the general model and classic method of Spatial Interpolation and the modified algorithm called RMSM. Section 3 provides the algorithm procedure and complexity analysis of RMSM, while Sect. 4 presents the experiment and comparison. Finally, Sect. 5 concludes the paper.

2 Spatial Interpolation

2.1 General Model and Classic Method

Spatial Similarity is the basic ideal of Spatial Interpolation, that is to say, in terms of an unknown point, the closer to the sample data point, the more similar to the sample point. As it is shown in Fig. 1, the general model of Spatial Interpolation can be depicted with the subsequent formula:

$$P(x_0, y_0) = \sum_{i=0}^N \omega_i(x_0, y_0) \cdot P(x_i, y_i) \tag{1}$$

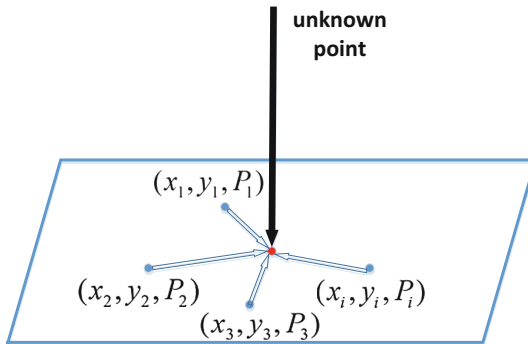


Fig. 1. Schematic diagram of Spatial Interpolation

Here, $P(x_0, y_0)$ is a certain estimated value of the location (x_0, y_0) , $P(x_i, y_i)$ is known value at the point (x_i, y_i) , and $\omega_i(x_0, y_0)$ is the weight assigned to the interpolation point (x_0, y_0) by the sample data point (x_i, y_i) .

IDW classic method, introduced by Shepard in 1968 [14], is a local method, in which interpolation value is influenced by all of the data. That is, the method regards the weights as the negative exponent of distances and uses all the available sample data (N) to perform the interpolation:

$$\left\{ \begin{array}{l} \omega_i(x_0, y_0) = \frac{1}{d_i^{d_{exp}}} \\ d_i = \sqrt{(x_i - x_0)^2 + (y_i - y_0)^2} \\ (i = 1, 2, \dots, N) \end{array} \right. \quad (2)$$

Here, d_i is the Euclidean distance between each sample data point and the interpolated point (x_0, y_0) and d_{exp} is the distance exponent. Simple and widely used as the method is, but the drawbacks like large amount of computation are obvious. The local method of Modified Shepard's Method (MSM), proposed by Renka [15], is the main enhancement compared to the IDW classic method. By defining the influence radius R , only the sample data points in a circle of it around the interpolation point are taken into consideration. Then the weights are modified by:

$$\omega_i(x_0, y_0) = \begin{cases} \left[\frac{(R-d_i)}{R-d_i} \right]^{d_{exp}}, & d_i \leq R \\ 0, & d_i > R \end{cases} \quad (3)$$

The optimal condition of this method is all the sample data point are distributed into square grid.

2.2 Revised Modified Shepard Method (RMSM)

Through the research on MSM, this paper presents a Revised Modified Shepard Method (RMSM) algorithm, which is improved as follows:

1. Optimizing the weights. The sample data points (x_i, y_i) are not always well-distributed in REM scenarios. For example, when sample data points are few or not uniformly distributed, the weights assigned to interpolation point fail to be reasonable. Hence, relative weights ω'_i are defined by:

$$\left\{ \begin{array}{l} \omega'_i = \frac{\omega_i}{\omega_0} \\ \omega_0 = \left[\frac{R - \min(d_i)}{R \times \min(d_i)} \right]^{d_{exp}} \\ (i = 1, 2, \dots, N) \end{array} \right. \quad (4)$$

where ω_i is still calculated by (3) and ω_0 is the weight assigned by the shortest point.

2. Flexibly using the local features. The aim of nodal function $Q(x, y)$ fitting by local data points, introduced in MSM method, was to optimize the weight of a certain point (x_i, y_i) using other neighbor point within the influence radius R . However, there are several limitations of MSM method to choose R in actual REM scenarios when sample data points are undesirably distributed (e.g. centralized on one point) such as few or no data points within the R . RMSM method solves this problem by selecting a certain number of neighbor points— N_q for nodal function fitting, while N_W for weights calculating to interpolate.

The nodal function $Q_k(x, y)$ of a sample point (x_k, y_k) in a two-dimensional surface could be various form (linear, quadratic etc.). Here, to fit the radio propagation, RMSM method chooses the quadratic form to $Q_k(x, y)$ fitting:

$$Q_k(x, y) = c_{k1}(x - x_k)^2 + c_{k2}(x - x_k)(y - y_k) + c_{k3}(y - y_k)^2 + c_{k4}(x - x_k) + c_{k5}(y - y_k) + P_k \tag{5}$$

coefficients $c_{k1}, c_{k2}, \dots, c_{k5}$ are performed by the principle of LMS (Least Mean Square) as:

$$\arg \min_{Q_k(x,y)} \left\{ \sum_{i=1}^{N_q} \omega'_j(x_k, y_k) [Q_k(x_j, y_j) - P(x_j, y_j)]^2 \right\} \tag{6}$$

$$\begin{matrix} (j = 1, 2, \dots, N_q \\ k = 1, 2, \dots, N_w) \end{matrix}$$

where $Q_k(x_j, y_j)$ denotes the output of the point (x_k, y_k) at one of its neighboring point (x_j, y_j) , while $\omega'_j(x_k, y_k)$ is the relative weight of (x_k, y_k) assigned by the point (x_j, y_j) , which is also calculated by (3) and (4), replacing the R/d_i with R_q/d_j or R_w/d_k in (7):

$$\begin{cases} R_q = \max(d_j), & j = 1, 2, \dots, N_q \\ R_w = \max(d_k), & k = 1, 2, \dots, N_w \\ 1 < N_q, N_w \leq N \end{cases} \tag{7}$$

Here, as it is vividly depicted in Fig. 2, d_j refers to the Euclidean Distance between a sample point (x_i, y_i) and one of its N_q neighboring point (x_j, y_j) , while d_k is the distance between the interpolation point (x_0, y_0) and one of its N_w neighboring point (x_k, y_k) . N_q and N_w could be equal or not because there is no relationship between them.

3. Efficiently neighbor searching. To find N_w neighboring points of interpolation point (x_0, y_0) and its N_q neighboring points for nodal function fitting, RMSM method makes the Near Neighbor (NN) searching twice by constructing the KD-Tree data structure. KD-Tree (k -Dimensional Tree) is a special binary tree, which is widely used for range searing [18]. Through the spatial division by hyperplanes, instead of time-consuming method that traverses all data point, KD-Tree conducts the NN searching only by backtracking of its sub-tree. After the searching, the RSS of N_w data points are optimized as

$$f_k = \frac{1}{N_q} \sum_{j=1}^{N_q} Q_k(x_j, y_j) \tag{8}$$

Finally, the interpolation value of the point (x_0, y_0) is calculated using

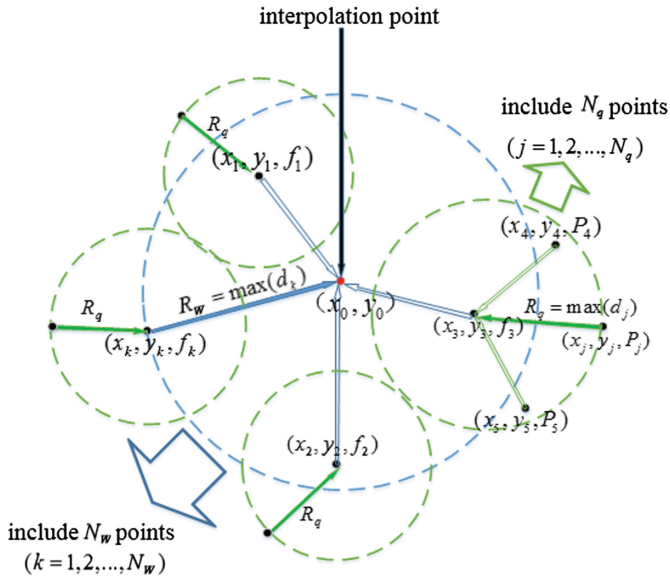


Fig. 2. Schematic diagram of RMSM algorithm

$$P(x_0, y_0) = \sum_{k=0}^{N_w} \omega'_i(x_0, y_0) \cdot f_k \quad (9)$$

$$(k = 1, 2, \dots, N_w)$$

In practice, it is difficult to get the best result of Spatial Interpolation—expanding the discrete data into surface data, but the substitutional way of interpolation gridding is always used. That is, defining the space as a grid are at a certain resolution (size of the grid), and interpolating for each grid point. The construction of Radio Environment Map (REM) is right a case of expanding the measurement data points into a RSS surface.

3 Algorithm Process and Complexity

3.1 Algorithm Process

1. Input

- ① RMSM algorithm related parameters:

$$N, d_{exp}, N_q, N_w$$

② Grid area related parameters:

$$\text{Number of grid points: } M = X_{points} \times Y_{points}$$

(X_{points}, Y_{points} denotes the number of grid point on X and Y coordinates axes)

2. Initialization

① Data points matrix *points*:

$$\text{double[,]points} = \text{new double}[N,3]$$

filled by the values as follows:

$$\mathbf{points} = \begin{bmatrix} x_1 & y_1 & P_1 \\ \vdots & \vdots & \vdots \\ x_N & y_N & P_N \end{bmatrix}_{N \times 3}$$

② Weights matrix ω' and outputs matrix of nodal function *q*:

$$\begin{aligned} \text{double[]w1} &= \text{new double}[Nq] \\ \text{double[]w2} &= \text{new double}[Nw] \\ \text{double[]q} &= \text{new double}[Nw] \end{aligned}$$

③ Grid points (all of the interpolations for the construction of REM) matrix *XY*:

$$\text{Double[,]XY} = \text{new Double}[xPoints, yPoints]$$

3. Constructing the two-dimensional KD-Tree in *points*

4. Starting with the first grid point ($m = 1$) and repeating the steps of ①–③ as follows:

① NN searching for N_w neighboring points and weights calculating by (4), hence

$$\omega' = [\omega'_1 \quad \dots \quad \omega'_{N_w}]$$

② NN searching again for N_q neighboring points and nodal function fitting by (6), filling the matrix *q*:

$$\mathbf{q} = [f_1 \ \cdots \ f_k \ \cdots \ f_{N_w}]^T$$

③ Calculating the interpolation value of present grid point by

$$result = \omega' \cdot \mathbf{q}$$

5. Until the last grid point ($m = M$) is calculated, the RMSM algorithm is ended up with M outputs for the REM construction.

3.2 Complexity Analysis

IDW Classic is a global method that uses all known points to interpolate, it requires $O(N)$ when N points are measured, and the complexity will reach $O(MN)$ for REM construction. While MSM and RMSM are local method (the number of local points $N' < N$ in most general case, which is depended on R and N_q/N_w choosing), use the NN searching, required $O(\log N)$, for local points. Both of them need $O(M \log N)$ complexity.

Undoubtedly, it is obviously improved of MSM and RMSM method, compared to IDW Classic, on computational efficiency and, the denser of the grid, the closer to continuous data surface the REM is, but the greater processing requirements needed.

4 Experiments and Analysis

4.1 Experimental Scenario

There are six routers placed in an $15\text{m} \times 20\text{m}$ indoor area (AP1–AP6 in Fig. 3), where some Non-Line-of-Sight propagation condition like walls or obstacles existed. Each router could transmit 2.4 GHz WIFI signal, and the RSS values are measured by cellphone.

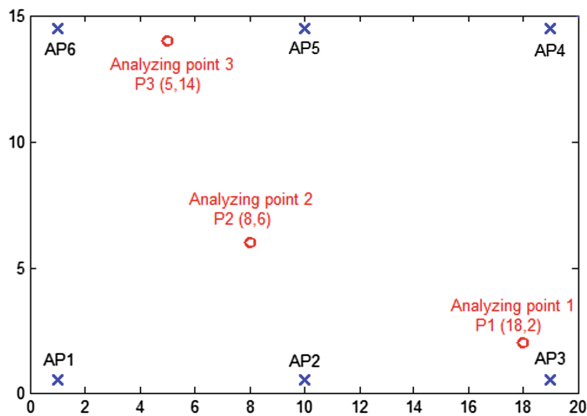


Fig. 3. Schematic diagram of experimental scenario

All the algorithms this paper mentioned are implemented by C# in Visual Studio 2010, and the related data are stored in SQL Server 2008. A total of six kind of scenarios (combinations of 6 routers) are tested, RSS (dBm) from 50 different positions are measured in each scenario. After that, choosing three points (analyzing point P1–P3 in Fig. 3) to calculate the interpolation value (performing calculation $3 \times 6 = 18$ times each analyzing point) using the algorithms above. Parameters setting as Table 1.

Table 1. Experimental parameters settings

Parameters	Values
Distance exponent d_{exp}	1
Number of sample points N	Exp.1: 30 Exp.2: 50
R (for MSM method)	6(m)
$Q(x, y)$	Quadratic
N_q	Exp.1: 18 Exp.2: 30
N_w	Exp.1: 24 Exp.2: 40

4.2 Performance Evaluation

Figure 4 presents the error bars of three methods mentioned above (IDW Classic, MSM, RMSM) in different sample points N . Specifically, the histograms denote the MAE (Mean Absolute Error) of each methods:

$$MAE = \frac{\sum_{i=1}^N |P_m - P_c|}{S} \tag{10}$$

where P_m, P_c refers respectively to RSS value of measurement and estimation, and S is experimental times ($S = 18$ in this section). The line-segments represent the standard deviation, which indicate the robustness of each methods by the length.

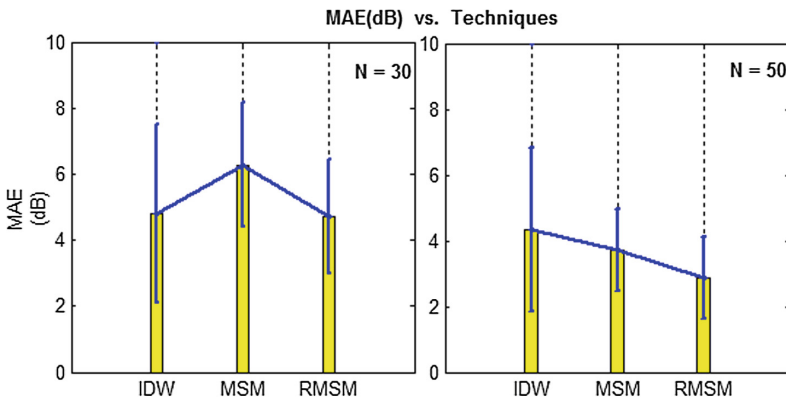


Fig. 4. Comparison of algorithms

Obviously, IDW Classic method refers the relatively high MAE and poor robustness due to the use of all sample points and its low computational efficiency, and the existence of certain measurement error is also a factor inevitably; MSM method shows the poorest MAE performance when sample data points are less (left sub-diagram in Fig. 4), though it gets the better robustness than IDW Classic method; By optimizing the weights and flexibly using the local feature, depicted in Fig. 4, RMSM method improves approximately half of the robustness (50.4%, 55.37% for $N = 30, N = 50$) compared to IDW classic, and keeps the relatively low MAE even in less sample points condition.

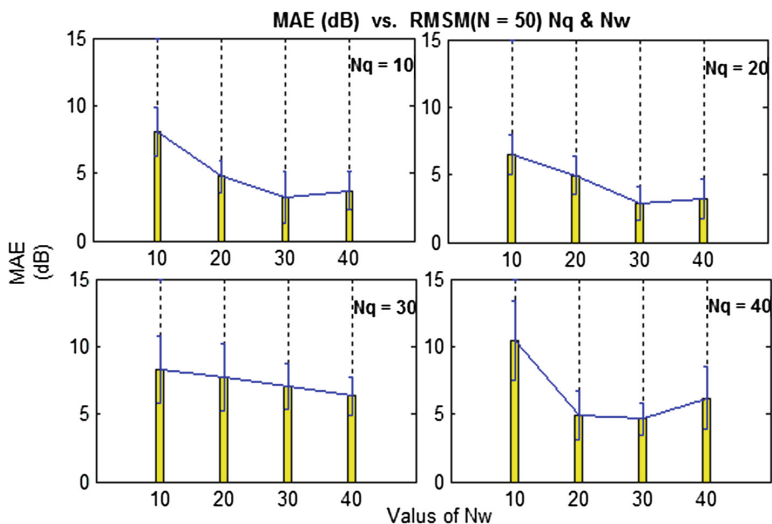


Fig. 5. Performance of RMSM in different values of N_q/N_w

Performance of RMSM itself in different values of N_q/N_w is depicted in Fig. 5. The choosing of these two values is depended on environment surrounding (obstacles, walls etc.), that is, larger N_q means smoothing of complex features. Best case is $N_q = 20, N_w = 30$, the MAE is about to 2.85 db in this condition (decreased by 1.96 db compared to IDW Classic), while the standard deviation is about 2.48 db, which indicate the desirable robustness.

4.3 Construction of Radio Environment Map (REM)

Based on the analysis above, this experiment uses the RMSM method for the construction of REM due to its favorable performance. The radio scenario is shown in Fig. 3 also, where six routers (AP1–AP6) work simultaneously. Setting parameters as $N_q = 20, N_w = 30$ in measured sample points $N = 50$. Figure 6 presents the REM at different grid points (M) choosing ($M = 1200$ in left sub-diagram, while $M = 30000$ in right one). It is easy to see that, the closer to the router, the larger RSS of the location is, which means the greater radio interference of the position.

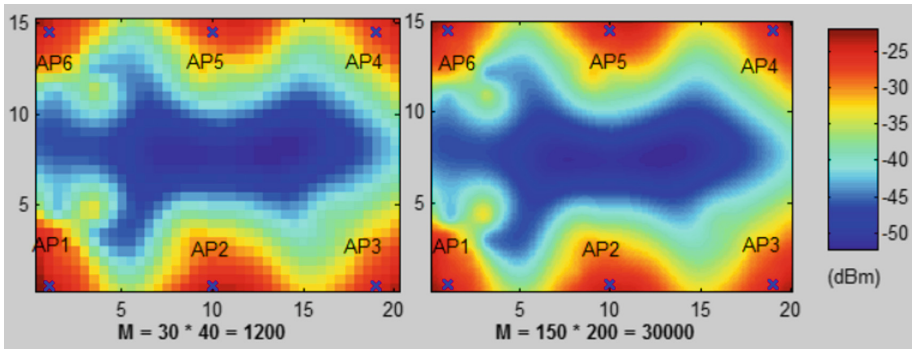


Fig. 6. Schematic diagram of REM

5 Conclusion and Future Work

Through the research on papers or deliverables of Cognitive Radio (CR), Radio Environment Map (REM) and the project FARAMIR, the construction of REM based on Spatial Interpolation is proposed in this paper called RMSM method, which shows the desirable performance in experiments. Future work will focus on environmentally-adaptive RMSM method with radio propagation model and the construction of RSS fingerprint database based on REM.

References

1. Huang, B., Li, J.C., Tan, H.F., Fang, J.: Cognitive Radio and Spectrum Management, pp. 2–4. Posts & Telecom Press, Beijing (2014)
2. Zhao, Y.P., Reed, J.: Network support: the environment map. In: Fette, B. (ed.) Cognitive Radio Technology, Chapter 11, pp. 337–339. Elsevier (2006)
3. Zhao, Y.P., Tan, K., Yao, Y.: Cognitive Software Defined Systems: Principles and Experiments, pp. 5–6. Tsinghua University Press, Beijing (2016)
4. Deliverable D2.4: Final System Architecture. EC FP7–248351 FARAMIR Project, pp. 8–10, December 2011
5. Deliverable D4.1: Final System Architecture. EC FP7-248351 FARAMIR Project, pp. 8–12, April 2011
6. Deliverable D4.3: Final System Architecture. EC FP7-248351 FARAMIR Project, pp. 7–15, February 2012
7. Deliverable D6.2: Final System Architecture. EC FP7-248351 FARAMIR Project, pp. 10–22, June 2011
8. Wang, L.: Research on Generation Technique of Radio Environment Map in WRAN, pp. 8–11. Chongqin University (2011)
9. Li, Y.: Handover Technology Research Based on Radio Environment Map of High-speed Railway, p. 2. (2013)
10. Li, W., Feng, Y., Xiong, N.: Research of spectrum sharing network based on radio environment map, vol. 40, no. 10, pp. 60–66 (2016)

11. Luo, Y., Gao, L., Huang, J.: Economics of Database-Assisted Spectrum Sharing. WN. Springer, Cham (2016). <https://doi.org/10.1007/978-3-319-43231-1>
12. Gao, Y., Zhou, W.H., Kuang, Z.: Realization and prospective of radio environment map. Shanghai Informatization, pp. 66–67 (2015)
13. Zhang, M.J.: Analysis & research of outdoor WiFi coverage intensity based on GIS technology, pp. 18–25 (2012)
14. Shepard, D.: A two dimensional interpolation function for irregularly spaced data. In: Proceedings of the 23rd National Conference of the Association for Computing Machinery. ACM, Princeton, NJ, pp. 517–524 (1968)
15. Renka, R.J.: Multivariate interpolation of large sets of scattered data. ACM Trans. Math. Softw. **14**(2), 139–148 (1988)
16. Cheng, L., Xu, X.L., Yang, Q., Chen, G.C.: Wireless signal strength propagation model based on cubic spline interpolation. J. Zhejiang Univ. (Eng. Sci.) **45**(9), 1521–1527 (2011)
17. Liu, Z.J., Guan, W.G., Hua, H.L.: Location fingerprint database construction algorithm based on Kriging spatial interpolation. Appl. Res. Comput. **33**(10), 3139–3142 (2016)
18. Bentley, J.L., Friedman, J.H.: Data structures for range searching. ACM Comput. Surv. **11**(4), 397–409 (1979)



Resource Allocation in OFDM-Based Cognitive Radios Under Proportional Rate Constraint

Hongzhi Wang, Yongfei Yan, and Mingyue Zhou^(✉)

College of Computer Science and Technology,
Changchun University of Technology, Changchun 130012, Jilin, China
{hzwang, zmyjlu}@ccut.edu.cn, buddy.yan11@gmail.com

Abstract. The objective of this paper is to optimize the power allocation to maximize the total rate of secondary users (SUs) under the SU total transmit power constraint and primary user (PU) interference temperature constraint, a proportional rate constraint is also used to assure that each SU can achieve fairness. The power allocation problem is not a convex optimization problem, which can be converted to a convex optimization problem without introducing auxiliary variables. To reduce the burden of information exchange and computational complexity, PU interference temperature constraint can be decoupled to an average interference constraint. The Lagrangian duality method is used to solve the optimal transmission power. Numerical results show that the proposed algorithm not only improves the rate fairness of each SU, but also guarantees the quality of service (QoS) of PU.

Keywords: Cognitive radio
Orthogonal frequency division multiplexing (OFDM)
Resource allocation · Proportional fairness · Spectrum sharing

1 Introduction

As the broadband wireless communications field continues to grow at a rapid rate, the emergence of new technologies, i.e., WiMAX [1] Bluetooth and LTE [2] lead to a rapidly escalating demand for radio spectrum resources. In [3], as a result of the static spectrum usage policy, some global authorized frequency bands are fixed which results in a lower spectral efficiency. Spectrum resources have been assigned to an existing wireless system which has a lot of idle time and space. The issue of spectrum scarcity has been exacerbated due to inefficient use of the fixed spectrum resources.

The grim spectrum utilization situation urgently requires a way of communication by opportunistic access the underutilized radio spectrum. This form of communication in dynamic spectrum access to the characteristics is cognitive radio. The concept of cognitive radio was first proposed by Joseph Mitola III in a seminar at KTH Royal Institute of Technology in Stockholm in 1998 and published in an article by Mitola and Gerald Q. Maguire, Jr. in 1999. To enhance the spectral utilization efficiency of wireless communication technology, it can detect spectrum holes and allows the unlicensed secondary user to access idle cognitive spectrum without affecting the communication quality of the primary user, to effectively reduce the waste of spectrum.

OFDM [5] divides transmission bandwidth into a series of non-overlapping orthogonal subcarriers, by assigning different sets of subcarriers to different users. OFDM not only enables efficient use of the limited spectrum resources, but also cuts back a variety of adverse environmental impact of the channel due to multipath fading. Thereby greatly improve system performance to meet the needs of different users. OFDM is regarded as an ideal alternative technology of realizing CR system which can highly improve the performance of cellular system by effectively utilizing the characteristic of multiuser diversity to distribute the sub-channel, bit and power.

According to the literatures on resource allocation in OFDM-based CR systems [6–11], it attracts more attentions by the development of CR technology in recent years. In [6], the resource allocation (RA) problem is formulated as a dynamic selection of spectrum patterns and power allocations that are better suited to the available spectrum range. However, the interference introduced by SUs is not mentioned. An optimal RA algorithm is proposed in [7], which ensures the rates of SUs are maintained in proportion to predefined target rates. However, the algorithm is designed for non-real-time applications. In [8], both optimal and suboptimal algorithms are developed to maximize the sum capacity of a CR network without consider the transmission power limitation. In [9], the authors want to maximize the sum capacity of the CR system while keeping proportional rate constraints satisfying to guarantee the fairness among SUs. In [10], a linear water-filling scheme is proposed. This algorithm maximizes the overall transmitted data rate of the CR system while keeping the interference introduced to the PU bands below a threshold. The fairness among users is ignored. The equal power allocation-proportional rate greedy (EPA-PRG) [11] algorithm is proposed to maximize the system throughput while keeping the fairness. The cooperative transmission technology isn't applied in this algorithm.

In this paper, we study the algorithm to optimize the total rate of SUs in OFDM-CR networks by considering the proportional fairness constraint under the underlay spectrum access method. Three sets of constraints are considered: interference power constraints to the PU, maximum transmission power constraints to the SU, the proportional rate constraint. The Lagrange decomposition algorithm and sub-gradient algorithm are used to solve the problem of power allocation. Simulation results show that the algorithm proposed in this paper improves the rate fairness of each SU effectively and it can keep the performance of the system.

2 System Model

We consider the underlay spectrum access method of an OFDM-based CR network. There are M CR user links which are distributed in an area that is away from the one primary user link. And the different CR users are allocated to the K subcarriers.

The transmit power of the cognitive user transmitter is deterministic, the sum of the transmit powers of the transmitter of user i on all subcarriers must be less than or equal to the total power of the transmitter of the cognitive user i

$$\sum_{k=1}^K p_k^i \leq p_{\max}^i \quad (1)$$

where p_{\max}^i denotes the maximum total transmit power (MTTP) of user i . p_k^i is the transmit power of user i on the subcarrier k .

Without affecting the communication quality of PU, the most important constraint is as follows that the interference power generated by all secondary user transmitter (SU-TX) on all subcarriers should not exceed the threshold which the PU can tolerate, i.e.,

$$\sum_{i=1}^M \sum_{k=1}^K p_k^i h_k^i \leq I^{MTI} \quad (2)$$

where I^{MTI} denotes maximum tolerated interference (MTI) at primary user receiver (PU-RX). h_k^i denotes the channel gain between the i th SU-TX to the PU-RX at the k th subcarrier.

Fairness is an important issue to be considered in the resource allocation of OFDM cognitive radio. The benefit of imposing a proportional fairness constraint is to assure that we can control the rate ratios among users, and generally ensure that each user is able to achieve a required data rate. The proportional rate constraints are expressed as

$$R_1 : R_2 : \dots : R_M = r_1 : r_2 : \dots : r_M \quad (3)$$

where r_M is a positive real number, r_1, r_2, \dots, r_M represents a predetermined proportionality constraint factor. R_M expresses the data rate of cognitive user M , when considering an ideal optimization scheme and using the Shannon rate formula [12], it can be expressed as

$$R_M = \sum_{k=1}^K \log \left(1 + \frac{p_k^i g_k^{ii}}{\sum_{j \neq i} p_k^j g_k^{ji} + I_k^{ps} + \sigma_k^i} \right) \quad (4)$$

where I_k^{ps} indicates the interference of PU to cognitive user M . σ_k^i denotes the background noise of the cognitive user on subcarrier K .

3 The Proposed Power Allocation Algorithm

Our objective is to maximize the total rate of SUs under the SU total transmit power constraint and PU interference temperature constraint. The proportional fairness is introduced into the frame that we can control the rate ratio among users.

The optimization problem for OFDM-CR power allocation can be expressed as

$$\begin{aligned}
 & \max \sum_{i=1}^M \sum_{k=1}^K \log \left(1 + \frac{p_k^i g_k^{ii}}{\sum_{j \neq i} p_k^j g_k^{ji} + I_k^{ps} + \sigma_k^i} \right) \\
 \text{s.t. } & C1 : \sum_{k=1}^K p_k^i \leq p_{\max}^i \tag{5} \\
 & C2 : \sum_{i=1}^M \sum_{k=1}^K p_k^i h_k^i \leq I_k^{MTI} \\
 & C3 : R_1 : R_2 : \dots : R_M = r_1 : r_2 : \dots : r_M
 \end{aligned}$$

The problem (5) is not convex optimization problem. We may rewrite the optimization problem as

$$\begin{aligned}
 & \min - \sum_{i=1}^M \sum_{k=1}^K \log \left(1 + \frac{p_k^i g_k^{ii}}{\sum_{j \neq i} p_k^j g_k^{ji} + I_k^{ps} + \sigma_k^i} \right) \\
 \text{s.t. } & C1 : \sum_{k=1}^K p_k^i - p_{\max}^i \leq 0 \tag{6} \\
 & C2 : \sum_{i=1}^M \sum_{k=1}^K p_k^i h_k^i - I_k^{MTI} \leq 0 \\
 & C3 : R_1 : R_2 : \dots : R_M = r_1 : r_2 : \dots : r_M
 \end{aligned}$$

From C2, the transmission power of each cognitive user in the network is coupled in the interference to the primary user during the resource sharing. To ensure the normal communication of the primary users, the channel gain h_k^i between the cognitive user and the primary user is indispensable, but it requires a large amount of information exchange. To reduce the system burden which is caused by the large amount of information exchange, constraint C2 can be divided into $K * M$ parts, the total interference is transformed into the interference for each cognitive user. Then the cognitive user does not need to exchange the information, the constraint C2 will change into

$$p_k^i h_k^i \leq \frac{I^{MTI}}{K * M} \tag{7}$$

Equation (7) shows that the channel gain h_k^i has been decoupled. If the transmission power of each cognitive user meets the requirements of Eq. (7), the primary user communication quality will be guaranteed.

Combining Eqs. (6) and (7), the power allocation problem becomes

$$\begin{aligned}
 & \min - \sum_{i=1}^M \sum_{k=1}^K \log \left(1 + \frac{p_k^i g_k^{ii}}{\sum_{j \neq i} p_k^j g_k^{ji} + I_k^{ps} + \sigma_k^i} \right) \\
 \text{s.t. } & C1 : \sum_{k=1}^K p_k^i - p_{\max}^i \leq 0 \\
 & C2' : p_k^i h_k^i - \frac{I_k^{MTI}}{K * M} \leq 0 \\
 & C3 : R_1 : R_2 : \dots : R_M = r_1 : r_2 : \dots : r_M
 \end{aligned} \tag{8}$$

where the constraints $C1$, $C2'$ are linear constraints. The convexity of the utility function is verified in the previous part. The optimization Eq. (8) is a standard convex problem that can be solved in a straightforward manner by using the Lagrange multiplier method [13]. Lagrangian basic idea converts inequality optimization problem to a weighted total objective function through a certain number of Lagrange multipliers, then use the extreme method to solve.

Combining with the Karush-Kuhn-Tucker (KKT) conditions [14], the paper constructs the Lagrangian function of the formula (8) by using the convex optimization theory and categorizes the same item on the right side of the equation, the function is simplified as

$$\begin{aligned}
 & L(\{\lambda_i\} \ \{\mu_n\} \ \{v_i\} \ \{p_k^i\}) \\
 & = \sum_{i=1}^M \left[\sum_{k=1}^K \left(-1 + v_i \frac{r_1}{r_i} \right) \log \left(1 + \frac{p_k^i g_k^{ii}}{\sum_{j \neq i} p_k^j g_k^{ji} + I_k^{ps} + \sigma_k^i} \right) \right. \\
 & \quad \left. + \sum_{k=1}^K \lambda_i p_k^i + \sum_{k=1}^K \sum_{n=1}^N \mu_n p_k^i h_k^i \right] - \sum_{i=1}^M \lambda_i p_{\max}^i - \sum_{n=1}^N \mu_n \frac{I^{MTI}}{K * M}
 \end{aligned} \tag{9}$$

where $\{\lambda_i\}$, $\{\mu_n\}$, $\{v_i\}$ are the Lagrangian coefficients of constraints $C1$, $C2'$, $C3$.

Using the Lagrangian dual decomposition method, the Eq. (9) is transformed into the minimum value problem of principal variables p_k^i and the dual optimization problem with the Lagrangian multiplier as the optimal variable, which as follows

$$\begin{aligned}
 & D(\{\lambda_i\} \ \{\mu_n\} \ \{v_i\}) \\
 & = \sum_{i=1}^M \min L_i(p_k^i, \lambda_i, \mu_n, v_i) = - \sum_{i=1}^M \lambda_i p_{\max}^i - \sum_{n=1}^N \mu_n \frac{I^{MTI}}{K * M}
 \end{aligned} \tag{10}$$

where

$$\begin{aligned}
 L_i(p_k^i, \lambda_i, \mu_n, v_i) &= \sum_{k=1}^K \left(-1 + v_i \frac{r_1}{r_i} \right) \log \left(1 + \frac{p_k^i g_k^{ii}}{\sum_{j \neq i} p_k^j g_k^{ji} + I_k^{ps} + \sigma_k^i} \right) + \sum_{k=1}^K \lambda_i p_k^i + \sum_{k=1}^K \sum_{n=1}^N \mu_n p_k^i h_k^i \\
 & \quad (11)
 \end{aligned}$$

Using to the KKT condition, the optimal power control solution of the cognitive user can be solved by the following equation

$$\frac{\partial L_i(p_i, \lambda_i, \mu_n, v_i)}{\partial p_k^i} = 0 \quad (12)$$

The optimal power solution can be obtained as

$$p_k^{i*} = \left[\frac{1 - v_i \frac{r_1}{r_i} - \frac{\sum_{j \neq i} p_k^j g_k^{ji} + I_k^{ps} + \sigma_k^i}{g_k^{ii}}}{\ln 2 \left(\lambda_i + \sum_{n=1}^N \mu_n h_k^i \right)} \right]^+ \quad (13)$$

where, $[X]^+ = \max\{0, X\}$ denotes a projection in a non-negative quadrant.

The Lagrange multipliers can be updated by sub-gradient search method [15] in a parallel way as follows

$$\lambda_i^{t+1} = \left[\lambda_i^t + a_1 \left(\sum_{k=1}^K p_k^i - p_{\max}^i \right) \right]^+ \quad (14)$$

$$\mu_n^{t+1} = \left[\mu_n^t + a_2 \left(p_k^i h_k^i - \frac{I^{MTI}}{K * M} \right) \right]^+ \quad (15)$$

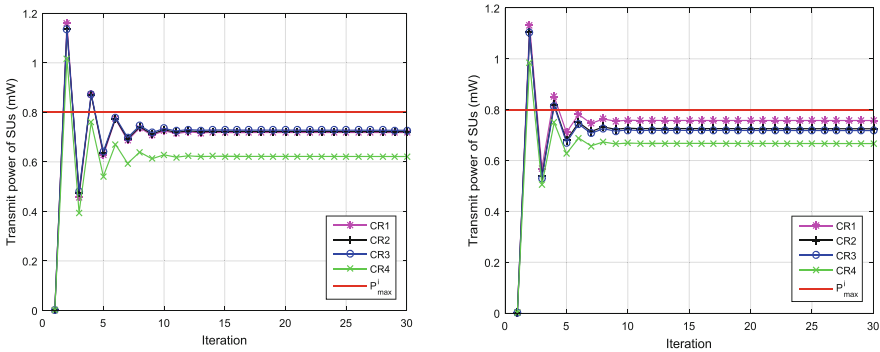
$$v_i^{t+1} = \left[v_i^t + a_3 \frac{r_1}{r_i} \log \left(1 + \frac{p_k^i g_k^{ii}}{\sum_{j \neq i} p_k^j g_k^{ji} + I_k^{ps} + \sigma_k^i} \right) \right]^+ \quad (16)$$

where t is the iteration number, a_1, a_2, a_3 denote the positive step sizes. By choosing the appropriate step size, the stability and convergence of the dual algorithm can be guaranteed. As the gradient method can converge to the dual optimal solution (λ^*, μ^*, v^*) , thus ensures the convergence of the optimal transmission power p_k^{i*} . Note that a_1, a_2, a_3 are sufficiently small, (λ^*, μ^*, v^*) can converge to the optimal point $(\lambda_i^*, \mu_n^*, v_i^*)$, when $t \rightarrow \infty$.

4 Simulations and Discussions

In this section, we present some numerical results to illustrate the performance of our proposed algorithms. We consider the OFDM system with 4 SU pairs ($M = 4$) and 1 PU pair, the number of available subcarriers for the CR network is 2 ($k = 2$). As Ref. [15], the nominal values of g_{ii} , g_{ij} , and h_i are randomly chosen from the intervals $[0.7, 1]$, $[0, 0.3]$, and $[0, 0.2]$. The maximum transmission power of each SU is $p_{\max}^i = 0.8 \text{ mW}$. The interference of PU to cognitive user M is $I_k^{ps} = 0.93 \text{ mW}$. The background noise power of every subcarrier is 0.003 mW .

Figure 1 depicts the transmit power for each user at two subcarriers. We determine the transmit power of each SU according to the maximum transmitting power of the SU i . It can be seen that the curves tend to be stable point near the 13th iteration and the total power of each cognitive user does not exceed the maximum total power specified.



(a) Transmit power for SUs at subcarrier 1 (b) Transmit power for SUs at subcarrier 2

Fig. 1. Transmit power of each cognitive user at two subcarriers

Figure 2 describes the relationship between the data rate and the number of iterations. It shows the curves of the total rate of each cognitive user. The purpose of this paper is to allocate resources to users based on proportional fairness and to bring all of these users to the similar data transmission rate. From Fig. 2, the data rate continuously improves in the initial stage, followed into a horizontal state by the fifth iteration. When $r_1:r_2:r_3:r_4 = 1:1:1:1$, it indicates that the cognitive user meets the minimum proportional rate requirement and the reachable rate between cognitive users is the same, all users at the same rate to achieve the most fairness.

Figure 3 shows the capacity distribution among cognitive users. It can be seen that the capacity of each cognitive user is uneven under non-proportional constraint, however, each cognitive user get the same capacity level to transmit when the rate ratio is 1:1:1:1, this reflects the fairness that each cognitive user gets the same opportunity to transmit under the premise of considering the proportional rate constraint of the cognitive user.

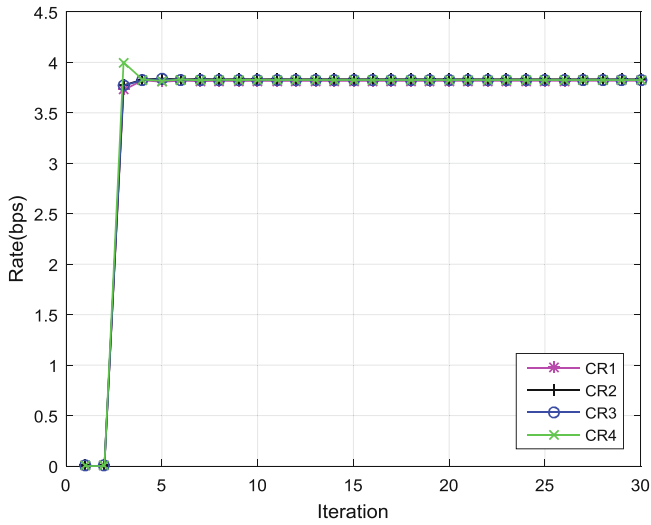


Fig. 2. The rate of each cognitive user.

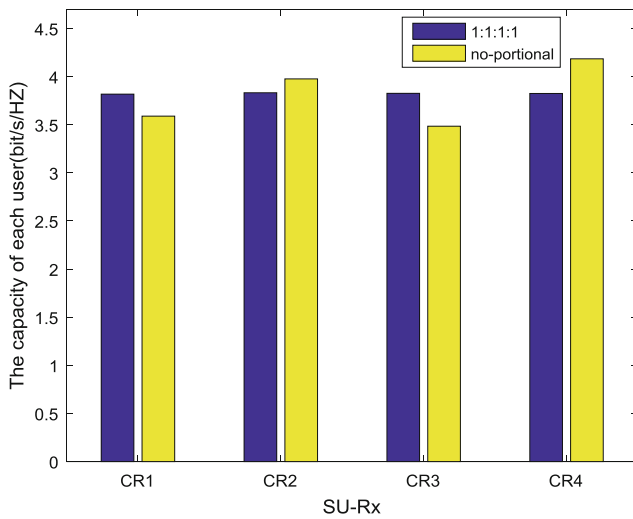


Fig. 3. The capacity distribution among cognitive users

Figure 4 describes the interference power at the PU receiver. With the increase of iterations, the interference power from SUs has increased dramatically at the beginning. When the transmission power reaches at Nash equilibrium point state, the interference power at PU receiver is stable.

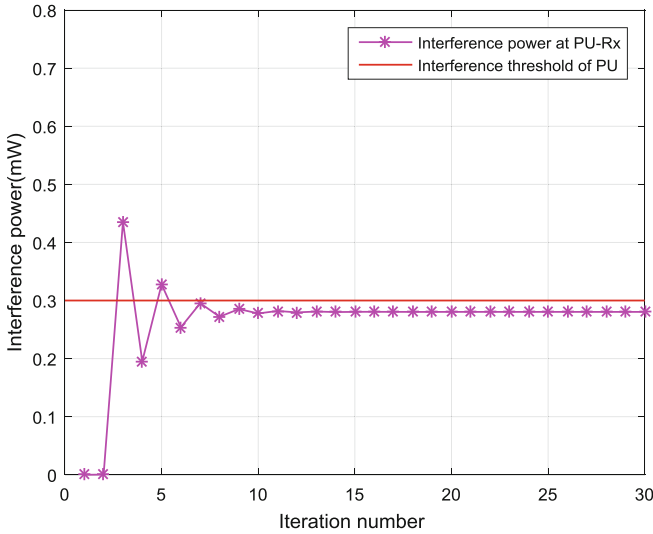


Fig. 4. The relationship of the interference power and the number of iterations.

5 Conclusion

In this paper, we have studied the problem of maximize the total channel rate of SUs and power allocation under the SU total transmit power constraint and PU interference temperature constraint in OFDM-based CR networks. Using the proportional fairness as the constraint, we can improve proportional fairness of resource allocation and achieve substantial transmitted data rate gain. We transform non-convex optimization objective function into convex form, and use the Lagrange decomposition method and sub-gradient method to derive the subcarrier allocation. It is shown by simulation results that the transmission power of SUs can quickly reach the optimal point and the data rate of each SU is almost equal, the interference introduced to the PU bands below interference power threshold, the computational complexity of this paper is relatively lower.

6 Acknowledgments

This work was supported by the National Natural Science Foundation of China under Grant No. 61501059, the Education Department of Jilin Province under Grant No. 2016343.

References

1. Aalamifar, F., Lampe, L.: Optimized WiMAX profile configuration for smart grid communications. In: IEEE Transactions on Smart Grid, pp. 1–10 (2016)
2. Ghaboosi, K., Vemulapalli, M.G., Oates, N.J.: Duplexing in long term evolution (LTE) cellular networks (2016)

3. Matheson, R.J.: Spectrum usage for the fixed services (2000)
4. Cai, K., Li, H., Mitola, J.: Exploiting spectral regrowth for channel identification. *IEEE Signal Process. Lett.* **21**, 1050–1053 (2014)
5. Falahati, A., Hosseini, E.: An iterative resource allocation algorithm for multi-user OFDM-CR system with low complexity. In: *International Symposium on Telecommunications*, pp. 725–728. IEEE (2014)
6. Lacatus, C., Akopian, D., Yaddanapudi, D., Shadaram, M.: Flexible spectrum and power allocation for OFDM unlicensed wireless systems. *IEEE Syst. J.* **3**, 254–264 (2009)
7. Zhang, Y., Leung, C.: Resource allocation for non-real-time services in OFDM-based cognitive radio systems. *IEEE Commun. Lett.* **13**, 16–18 (2009)
8. Bansal, G., Hossain, M., Bhargava, V.: Optimal and suboptimal power allocation schemes for OFDM-based cognitive radio systems. *IEEE Trans. Wirel. Commun.* **7**, 4710–4718 (2008)
9. Wang, S., Huang, F., Wang, C.: Adaptive proportional fairness resource allocation for OFDM-based cognitive radio networks. *Wirel. Netw.* **19**, 273–284 (2013)
10. Wu, J., Yang, L.X., Liu, X.: Subcarrier and power allocation in OFDM based cognitive radio systems. In: *Proceedings of the 2011 Fourth International Conference on Intelligent Computation Technology and Automation (ICICTA)*, Shenzhen, China (2011)
11. Lu, W.S., Ji, F., Yu, H.: A general resource allocation algorithm with fairness for SDMA/MISO/OFDMA systems. *IEEE Commun. Lett.* **15**, 1072–1074 (2011)
12. Al-Imari, M., Xiao, P., Imran, M.A.: Low complexity subcarrier and power allocation algorithm for uplink OFDMA systems. *EURASIP J. Wirel. Commun. Netw.* **2013**, 98 (2013)
13. Sidhu, G.A.S., Gao, F., Wang, W.: Resource allocation in relay-aided OFDM cognitive radio networks. *IEEE Trans. Veh. Technol.* **62**, 3700–3710 (2013)
14. Dreves, A., Facchinei, F., Kanzow, C.: On the solution of the KKT conditions of generalized Nash equilibrium problems. *SIAM J. Optim.* **21**, 1082–1108 (2011)
15. Yousefvand, M., Ansari, N., Khorsandi, S.: Maximizing network capacity of cognitive radio networks by capacity-aware spectrum allocation. *Wirel. Commun.* **14**, 5058–5067 (2012)



Capacity Analysis of Secondary User System in Cognitive MIMO Networks Based on NOMA

Han Liao^(✉)

Chongqing Key Lab of Mobile Communications Technology,
Chongqing University of Posts and Telecommunications,
Chongwen Road No. 2, Chongqing, China
LiaohanAmanda@outlook.com

Abstract. Nowadays, 5G puts forward a number of candidate multiple access technologies, among which the non-orthogonal multiple access (NOMA) is attracting more and more attention. Combining cognitive MIMO with NOMA is of great significance to improve the capacity for future mobile communication. Cognitive system includes two kinds of users, which are secondary users (SUs) and primary users (PUs), and the underlay spectrum sharing paradigm needs to consider the interference of the SUs system to the PUs system is below the predetermined threshold. And therefore, in order to reduce interference and improve capacity, we precode firstly at the transmitter. Then SUs were clustered according to the merits of the channel quality and performed power allocation for each cluster. During this process, the mean of the channel matrix's trace is used as the dynamic reception weight to enhance the system capacity. Meanwhile, taking the SUs' quality of service (QoS) and the requirement of successive interference cancellation (SIC) into account. The objective function is NP-hard problem, we need to transform it into system capacity for sub-cluster, and finally using Lagrange function, nonconvex KKT conditions and mathematical induction (MI) to solve the optimal power allocation coefficient, which is between zero and one. The simulation shows that this proposed scheme can improve the capacity obviously compared with the average power allocation.

Keywords: Non-orthogonal multiple access · Cognitive MIMO
Underlay paradigm · Power allocation · Lagrange function · KKT conditions

1 Introduction

The combination of cognitive radio technology and MIMO technology is called cognitive MIMO network, which can greatly improve mobile communication capacity because of MIMO spatial parallel transmission advantage. Facing with the upcoming 5G era, spectrum scarcity is still a serious problem. MIMO Cognitive, which have advantages of both the flexibility of cognitive and the spatial transmission of MIMO, may enhance the spectrum utilization and improve the system capacity, and therefore, it has a wide range of prospect for future mobile communications [1]. Looking back 1G to 4G, are using orthogonal multiple access technology, in 5G era, non-orthogonal

multiple access technology is increasingly concerned about the industry, which perhaps not only further enhance the spectral efficiency, but also is an effective approach to approaching the capacity domain of multi-user channels [2]. It can be seen from the literature [3] that the underlay scheme is widely used due to its simplicity and promising prospect. In underlay paradigm, the PUs and SUs exist and transmit messages at the same time, they occupy the same frequency to accomplish their own communication, but the SUs to the PUs' harmful interference may not affect the normal communication of PUs, otherwise SUs cannot work properly [4].

NOMA is a new type of multiple access technology that introduces interference at the transmitter and uses the SIC to eliminate the interference at the receiver [5]. Since this technology was put forward so far, more and more researchers study NOMA with MIMO, and their main purpose is to improve the system capacity, but there are little people study NOMA cognitive MIMO, but this method not only improve the system capacity greatly, but also frequency efficiency. In [6], the optimal solution is obtained by solving the maximum value of the quadratic equation, and it is obvious that the method is simple and can get the global optimal solution. However, this method can only solve only two users situation, so this literature does not have universality. The reference [7] only studies two users which meet the requirements of many users, and the document does not pre-code the transmission signal, so that the interference control cannot be carried out well. The reference [8] studied the downlink NOMA multi-user beamforming system, which divides multiple users into clusters with only two users in each cluster, there are only two users in each cluster, and the number of transmitting antenna of clusters and the base station are the same, otherwise, it is not suitable to meet the requirements of this method.

According to the literature [8], the number of sub-user clusters is redesigned, and the number of clusters are determined according to the number of effective antennas of the secondary subscriber base station. That is, if the SBS has two effective transmitting antennas, the secondary users are divided into two cluster. It is known from the literature [9] that the influence of the power allocation factor on the user with poor channel quality is much greater than that of the user with good channel quality. Therefore, when the power allocation is performed, the users with poor channel status are assigned more power, the allocation of less power. Compared to the traditional water-filling, this power allocation is more conducive to system performance.

Where $(\bullet)^H$ represents the conjugate transpose of the matrix or vector, and $tr(\bullet)$ represents matrix trace.

2 System Model

Considering a multi-user downlink communication network, the cognitive system adopts the underlay spectrum sharing mode. At this time, it is necessary to consider the interference constraint of the secondary user system to the primary user system. The secondary users receive the signals from the secondary base station (SBS), and the signals include the useful signals and the harmful signals, the PUs receive the interference signal from the SBS as well. The system model shown in Fig. 1. Assuming that SBS have N_t antennas, and there are N SUs in this system. In order to facilitate the

analysis, SUs are divided into N_t clusters, and there are K users in each cluster, so $\sum_{n=1}^{N_t} K = N$.

When performing power, water-filling is a common method to choose, but water filling power allocation algorithm must know the channel information, so the receiver needs current feedback channel information, which introduces some delay and additional overhead, and especially when the channel changes more slowly, the water-filling method is also easier to achieve, but when the channel conditions change faster, the method is difficult to achieve. In addition, the water-filling method needs to deal with the channel information, thus introducing a greater complexity. In this paper, for the sake of analysis, it is assumed that the power of each antenna accounted for the same proportion of the total power.

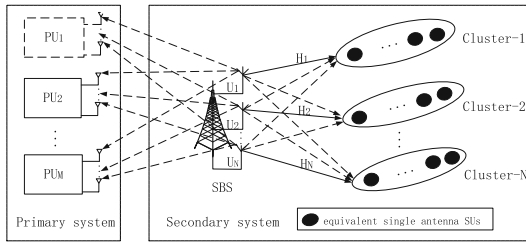


Fig. 1. System model

The signal sent by the sub user base station is expressed as

$$\mathbf{x} = [x_1, x_2, x_3, \dots, x_{N_t}] \in C^{N_t \times 1}$$

The vector \mathbf{x} represents the transmit information sequence from SBS

$$x_{n,k} = \sqrt{a_{n,k} P_t / N_t^{S_{n,k}}}$$

Then, the signals were sent to the n -th cluster can be expressed as

$$x_n = \sum_{k=1}^K x_{n,k} = \sum_{k=1}^K \sqrt{a_{n,k} P_t / N_t^{S_{n,k}}}$$

Where $x_{n,k}$ is the signals were sent to the k -th user of the n -th cluster, $a_{n,k}$ is the power allocation from the k -th user of the n -th cluster, and $s_{n,k}$ is the data information from the k -th user of the n -th cluster, and P_t represents the actual transmission power from SBS.

According to the system model, the SBS sends the information to the N users of N_t clusters. Meanwhile, the precoding is performed at the transmitter and the precoding matrix is $\mathbf{U} = \{\mathbf{u}_1^H, \mathbf{u}_2^H, \mathbf{u}_3^H, \dots, \mathbf{u}_{N_t}^H\} \in C^{N_t \times N_t}$. In this process, the primary user system will also receive interference from SBS. The received information at the the k -th user of the n -th cluster is

$$\begin{aligned}
 y_{n,k} &= \chi(\mathbf{h}_{n,k} \mathbf{U} \mathbf{x} + z_{n,k}) \\
 &= \chi \mathbf{h}_{n,k} \mathbf{u}_n^T x_n + \chi \mathbf{h}_{n,k} \sum_{i=1, i \neq n}^N \mathbf{u}_i^T x_i + \chi z_{n,k} \\
 &= \chi \mathbf{h}_{n,k} \mathbf{u}_n^T \sqrt{a_{n,k} \frac{P_t}{N_t}} s_{n,k} + \chi \mathbf{h}_{n,k} \mathbf{u}_n^T \sum_{j=1, j \neq k}^K \sqrt{a_{n,j} \frac{P_t}{N_t}} s_{n,j} + \chi \mathbf{h}_{n,k} \sum_{i=1, i \neq n}^N \mathbf{u}_i^T x_i + \chi z_{n,k}
 \end{aligned} \tag{1}$$

Because NOMA uses Successive interference cancellation (SIC) at the receiver, so concerning the nature of NOMA, the $y_{n,k}$ in (1) can be rewritten as:

$$\begin{aligned}
 y_{n,k} &= \underbrace{\chi \mathbf{h}_{n,k} \mathbf{u}_n^T \sqrt{a_{n,k} \frac{P_t}{N_t}} s_{n,k}}_{\text{desired signals}} + \underbrace{\chi \mathbf{h}_{n,k} \mathbf{u}_n^T \sum_{j=1}^{k-1} \sqrt{a_{n,j} \frac{P_t}{N_t}} s_{n,j}}_{\text{intra-cluster interference}} + \underbrace{\chi \mathbf{h}_{n,k} \sum_{i=1, i \neq n}^N \mathbf{u}_i^T x_i}_{\text{inter-cluster interference}} + \underbrace{\chi z_{n,k}}_{\text{channel noise}}
 \end{aligned} \tag{2}$$

Where χ the mean of the channel matrices' trace is used as the dynamic reception weight, that is $\chi = \frac{1}{K} \sum_{i=1}^K tr(h_{n,i} h_{n,i}^H)$, which means the weight of the received signal is in association with the mean of the channel trace. When channel station is better, the received signal is large, but when the channel station is relatively poor, the intensity of the received signal is relatively small. $z_{n,k}$ is the Gauss distribution noise signal whose mean value is zero and variance is σ^2 .

From the literature [8], we can see that the influence of power factor on users with poor channel quality is far greater than that of users with good channel quality, and therefore, considering the influence of power factor on the channel quality and made the overall performance of the system is further improved, we assign less power to the users with better channel quality, more power allocation with poor channel quality. Suppose in the n -th cluster, channel gains are sorted as $h_{n,1} > h_{n,2} > h_{n,3} > \dots > h_{n,K}$, and the corresponding power allocation factor is $a_{n,1} < a_{n,2} < a_{n,3} < \dots < a_{n,K}$.

We can get the signal-to-interference-and-noise-rate (SINR) from the formulation (2), which is

$$\begin{aligned} \text{SINR}_{n,k} &= \frac{|\chi \mathbf{h}_{n,k} \mathbf{u}_n^T|^2 a_{n,k} \frac{P_i}{N_i}}{|\chi \mathbf{h}_{n,k} \mathbf{u}_n^T|^2 \sum_{j=1}^{k-1} a_{n,j} \frac{P_i}{N_i} + \sum_{i=1, i \neq n}^N \sum_{j=1}^K |\chi \mathbf{h}_{n,k} \mathbf{u}_i^T|^2 a_{i,j} \frac{P_i}{N_i} + \chi z_{n,k}} \\ &= \frac{\chi |\mathbf{h}_{n,k} \mathbf{u}_n^T|^2 a_{n,k}}{\chi |\mathbf{h}_{n,k} \mathbf{u}_n^T|^2 \sum_{j=1}^{k-1} a_{n,j} + \chi \sum_{i=1, i \neq n}^N |\mathbf{h}_{n,k} \mathbf{u}_i^T|^2 + (\frac{1}{P_i/N_i}) z_{n,k}} \end{aligned} \tag{3}$$

Assuming $E[|s_{i,j}|^2] = 1, \forall i, j$, then the rate of the k -th users is

$$R_{n,k} = B \log_2 |1 + \text{SINR}_{n,k}| = B \log_2 \left| 1 + \frac{g_{n,k} a_{n,k}}{g_{n,k} \sum_{j=1}^{k-1} a_{n,j} + 1} \right| \tag{4}$$

Where B represents the bandwidth of each transmitted beam, and

$$g_{n,k} = \frac{|\chi \mathbf{h}_{n,k} \mathbf{u}_n|^2}{B(\sum_{i=1, i \neq n}^N |\chi \mathbf{h}_{n,k} \mathbf{u}_i|^2 + (\frac{1}{P_i/N_i}) \chi z_{n,k})} \tag{5}$$

Here, $g_{n,k}$ represent the normalized channel, the channel is able to simplify the calculation of the normalized objective, then type (3) can be written as follows

$$\text{SINR}_{n,k} = \frac{g_{n,k} a_{n,k}}{g_{n,k} \sum_{j=1}^{k-1} a_{n,j} + 1} \tag{6}$$

The capacity of the whole secondary user system is:

$$\hat{R}_{SBS-sus} = \sum_{n=1}^N \sum_{k=1}^K B \log_2 \left| 1 + \frac{g_{n,k} a_{n,k}}{g_{n,k} \sum_{j=1}^{k-1} a_{n,j} + 1} \right| \tag{7}$$

3 Problem Description and Solution

The PUs are equipped with two antennas, the SBS equipped with 2 antennas, and there are N SUs in total and each SU is equipped with one antenna, the entire SUs are divided into two large clusters, and each cluster has K SUs, that is, $N = 2K$.

3.1 Cognitive System

Because of the cognitive MIMO system based on NOMA underlay model, in this system, apart from the interference from SBS to PUs, we mainly consider the inter-cluster and intra-cluster interference of secondary users system. Other interference is not main interference, so for the sake of simplicity here, they are not being discussed.

In MIMO cognitive network, if researchers selected underlay spectrum sharing paradigm, then the interference between SBS and PUs need to be less than predefined threshold I_p , and if interference is larger than this threshold, then SUs can not to work properly [8], so in other words, the presence of secondary user is based on the premise that the normal communication of the primary user is not influenced at all. The number of PUs are modeled based on homogeneous poisson point processes (PPPs), denoted by ϕ_l with density of λ_l , $|m_l|^2$ is equivalent gain from SBS to PUs. In this case, SBS's actual maximum transmission power P_t can be described as follows

$$P_t = \min \left\{ \frac{I_p}{\max_{l \in \phi_l} |m_l|^2}, P_s \right\} = \min \left\{ \frac{I_p}{\max_{l \in \phi_l} (\hat{m}_l)^2 L(d_l)}, P_s \right\} \quad (8)$$

Where P_s is the maximum transmit power from SBS. \hat{m}_l is the channel gain of Rayleigh fading channel from SBS to PUs, and $L(d_l) = 1/(1 + d_l^\delta)$ is large-scale path loss where d_l is the distance between k -th PUs and SBS, and δ is path-loss coefficient.

This is a MIMO cognitive radio, and the transmit power of SBS takes into account the performance of the primary system and the SBS itself as well. Figure 2 can describe this relationship between them. From this figure, it is obvious that the transmission power of the SBS is maintained at its maximum transmission power P_s when the interference threshold reached a certain value.

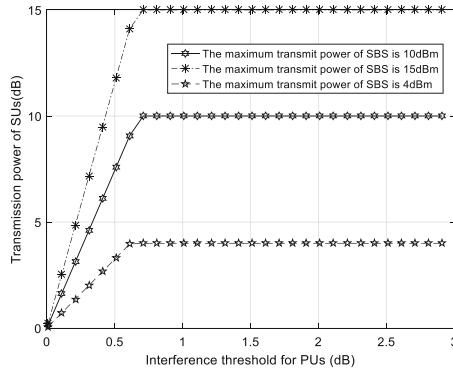


Fig. 2. The relationship between interference threshold (IT) transmit power of SBS

3.2 Precoding Selection

Nowadays, many literatures use zero-forcing (ZF) precoding method to precode the signal. The literature [8] adopt the zero-forcing precoding method, which is simple, and when there is only one user in each cluster, this method can eliminates inter-cluster

interference ideally when neglect system noise. However, in actual communication systems, the number of users in each group is larger than or equal to two, this approach is no longer simple anymore. And if we precode through minimum mean square error (MMSE), the bit error rate (BER) is lower, and MMSE is more realistic than ZF method. The precoding matrix of MMSE method is closely related to the channel, and the expression is: $\mathbf{U} = (\mathbf{H}^H \mathbf{H} + \sigma^2 \mathbf{I})^{-1} \mathbf{H}^H$. In the NOMA cognitive MIMO system, since the NOMA receiver uses the SIC to receive desired signals, the BER can be further reduced. Figure 3 is the comparison of BER.

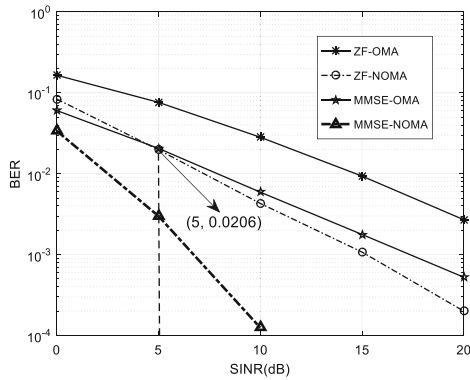


Fig. 3. The comparison of BER for different precoding methods

3.3 Clustering

Compared with conventional orthogonal multiple access (MA), non-orthogonal multiple access (NOMA) can enlarge the performance gap between them through applying user pairing [9]. Compared with conventional orthogonal multiple access (MA), non-orthogonal multiple access (NOMA) can enlarge the performance gap between them through applying user pairing [10]. In order to suppress interference and receive useful signals as much as possible, NOMA system typically cluster users. Clustering needs to consider the users in each cluster which have a neutralization between channel diversity and channel correlation [11]. Some researchers are simply distributed two clusters which the channel gain is strong and divided into one cluster while the channel gain is weak into another group, so that the group can merely guarantee the correlation between the channels without considering the difference between them fully [12]. Some researchers study signal antenna in NOMA system and cluster by head and tail [12]. We cluster SUs according to [11, 12] which consider a neutralization between channel diversity and channel correlation. The SUs channel gains are being sorted descendingly

firstly, which is $\mathbf{h}_1 > \mathbf{h}_2 > \mathbf{h}_3 > \dots > \mathbf{h}_{N-1} > \mathbf{h}_N$, and then perform clustering. There, we divide the SUs into two clusters, and discuss two situations which is the number of users in each cluster are odd or even, that is $n = \{1, 2\}$. The clustering is shown as follows.

When K is even, the channel gain distribution in the first cluster is

$$\mathbf{h}_{1,k} = \{\mathbf{h}_1, \mathbf{h}_3, \mathbf{h}_5, \dots, \mathbf{h}_{K-1}, \mathbf{h}_{K+2}, \mathbf{h}_{K+4}, \dots, \mathbf{h}_{N-2}, \mathbf{h}_N\};$$

And the channel gain distribution in the second cluster is

$$\mathbf{h}_{2,k} = \{\mathbf{h}_2, \mathbf{h}_4, \mathbf{h}_6, \dots, \mathbf{h}_K, \mathbf{h}_{K+1}, \mathbf{h}_{K+3}, \dots, \mathbf{h}_{N-3}, \mathbf{h}_{N-1}\}.$$

When K is odd, the channel gain distribution in the first cluster is

$$\mathbf{h}_{1,k} = \{\mathbf{h}_1, \mathbf{h}_3, \mathbf{h}_5, \dots, \mathbf{h}_K, \mathbf{h}_{K+3}, \mathbf{h}_{K+5}, \dots, \mathbf{h}_{N-2}, \mathbf{h}_N\};$$

And the channel gain distribution in the second cluster is

$$\mathbf{h}_{2,k} = \{\mathbf{h}_2, \mathbf{h}_4, \mathbf{h}_6, \dots, \mathbf{h}_{K+1}, \mathbf{h}_{K+2}, \mathbf{h}_{K+4}, \dots, \mathbf{h}_{N-3}, \mathbf{h}_{N-1}\}.$$

After clustering and precoding, the sum rate of the cluster is obtained:

$$\bar{R}_n = \sum_{k=1}^K B \log_2 \left| 1 + \frac{\bar{g}_{n,k} a_{n,k}}{\bar{g}_{n,k} \sum_{j=1}^{k-1} a_{n,j} + 1} \right| \tag{9}$$

The goal of this paper is to find the maximum of formula (9).

3.4 Power Allocation and Problem Solving

According to document [12], the power between each user needs to be satisfied when the serial interference cancellation of each subsystem is repeated:

$$\frac{P_t}{2} a_{n,k} \bar{g}_{n,k-1} - \frac{P_t}{2} \bar{g}_{n,k-1} \sum_{j=1}^{k-1} a_{n,j} \geq p_{tol}$$

Let $\frac{p_{tol}}{p_i/2} = \beta$, $\frac{R_0}{B} = \gamma$, and β, γ are constant. R_0 is the minimum rate of SUs need to meet the rate. When the secondary users' rate are greater than or equal to R_0 , then they can work properly, otherwise, they can not work normally. After the above analysis, according to the system model, we can get the optimization equation of the coefficient distribution:

$$\begin{aligned}
 \mathbf{Q} : & \quad \underset{\{a_{n,k}, \forall k=1,2,\dots,K\}}{\text{maximize}} && \sum_{k=1}^K B \log_2 \left| 1 + \frac{\bar{g}_{n,k} a_{n,k}}{\bar{g}_{n,k} \sum_{j=1}^{k-1} a_{n,j} + 1} \right| \\
 \text{S.t.} & && \\
 \mathbf{C1} : & \quad \sum_{k=1}^K a_{n,k} \leq 1, && n = \{1, 2\} \\
 \mathbf{C2} : & \quad \log_2 \left(1 + \frac{\bar{g}_{n,k} a_{n,k}}{\bar{g}_{n,k} \sum_{j=1}^{k-1} a_{n,j} + 1} \right) \geq \gamma, && n = \{1, 2\}, \forall k = 1, 2, \dots, K \\
 \mathbf{C3} : & \quad \left(a_{n,k} - \sum_{j=1}^{k-1} a_{n,j} \right) \bar{g}_{n,k-1} \geq \beta, && n = \{1, 2\}, \forall k = 2, \dots, K \\
 \mathbf{C4} : & \quad a_{n,k} \in [0, 1], && \forall n, k
 \end{aligned}$$

Here, constraint **C1** indicates that the power allocation coefficient is less than or equal to one; Constraint **C2** limits the rate of the secondary user, indicating that the rate of each user in the secondary user system satisfies greater than a certain value, thus ensuring the user service quality of the secondary user system; Constraint **C3** indicates that the minimum power difference between the SUs that has been decoded and the un-decoded is greater than p_{tol} ; Constraint **C4** represents the condition that the power distribution coefficient is to be satisfied.

A simplified analysis of constrained **C2** is performed as

$$\mathbf{C2} \Leftrightarrow \bar{g}_{n,k} a_{n,k} \geq (2^\gamma - 1) \left(\bar{g}_{n,k} \sum_{j=1}^{k-1} a_{n,j} + 1 \right)$$

Then the Lagrange function is available as

$$\begin{aligned}
 \mathbf{L}(a_{n,k}, \lambda, \eta, \zeta) = & \sum_{k=1}^K B \log_2 \left| 1 + \frac{\bar{g}_{n,k} a_{n,k}}{\bar{g}_{n,k} \sum_{j=1}^{k-1} a_{n,j} + 1} \right| + \lambda \left(1 - \sum_{k=1}^K a_{n,k} \right) \\
 & + \sum_{k=1}^K \eta_k \left(\bar{g}_{n,k} a_{n,k} - (2^\gamma - 1) \left(\bar{g}_{n,k} \sum_{j=1}^{k-1} a_{n,j} + 1 \right) \right) \\
 & + \sum_{k=2}^K \zeta_k \left(\left(a_{n,k} - \sum_{t=1}^{k-1} a_{n,t} \right) \bar{g}_{n,k-1} - \beta \right)
 \end{aligned}$$

According to KKT conditions available

$$\begin{aligned}
 \frac{\partial \mathbf{L}}{\partial a_{n,k}^*} = & \frac{B \bar{g}_{n,k}}{\bar{g}_{n,k} \sum_{j=1}^k a_{n,j} + 1} - \sum_{j=k+1}^K \frac{B a_{n,j} \bar{g}_{n,j}^2}{\left(\sum_{t=1}^j a_{n,t} \bar{g}_{n,j} + 1 \right) \left(\sum_{t'=1}^{j-1} a_{n,t'} \bar{g}_{n,j} + 1 \right)} - \lambda \\
 & + \eta_k \bar{g}_{n,k} - \sum_{j=k+1}^K (2^\gamma - 1) \eta_j \bar{g}_{n,j} + \zeta_k \bar{g}_{n,k-1} - \sum_{j=k+1}^K \zeta_j \bar{g}_{n,j} \leq 0, \\
 & 0 \leq a_{n,k}^* \leq 1, \forall k = 2, 3, \dots, K,
 \end{aligned} \tag{10}$$

$$\frac{\partial \mathbf{L}}{\partial \lambda^*} = 1 - \sum_{k=1}^K a_{n,k} \geq 0, \lambda^* \geq 0, \eta_k^* \geq 0, \forall k = 2, 3, \dots, K \quad (11)$$

$$\frac{\partial \mathbf{L}}{\partial \eta_k^*} = \bar{g}_{n,k} a_{n,k} - (2^\gamma - 1) \left(\bar{g}_{n,k} \sum_{j=1}^{k-1} a_{n,j} + 1 \right) \geq 0 \quad (12)$$

$$\frac{\partial \mathbf{L}}{\partial \zeta_k^*} = \left(a_{n,k} - \sum_{j=1}^{k-1} a_{n,j} \right) \bar{g}_{n,k-1} - \beta \geq 0, \zeta_k^* \geq 0, \forall k = 2, 3, \dots, K \quad (13)$$

The original problem is a non-convex NP-hard problem [13], so it is difficult to solve the optimal value. In this paper, the Lagrange function and the KKT condition are used to solve the above problems by combining mathematical induction method, and verify that the value of the solution meets the requirement.

Letting $O = \{\lambda\}$; $\Omega = \{\eta_1, \eta_2, \eta_3, \dots, \eta_K\}$; $\Theta = \{\zeta_1, \zeta_2, \zeta_3, \dots, \zeta_K\}$, since $K \geq 2$, so the set of optimal solution of Lagrange function $\mathbf{L}(a_{n,k}, \lambda, \eta, \zeta)$ may be assumed as $\Psi = \{\lambda, \eta_2/\zeta_2, \eta_3/\zeta_3, \eta_4/\zeta_4, \dots, \eta_K/\zeta_K\}$. Suppose that the minimum rate of the cognitive system is satisfied $\Psi = \{\lambda, \zeta_2, \zeta_3, \zeta_4, \dots, \zeta_K\}$ and $\zeta_1 = \eta_1 = \eta_2 = \eta_3 = \dots = \eta_K = 0$.

Then

$$\sum_{k=1}^K a_{n,k} = 1 \quad (14)$$

$$\left(a_{n,k} - \sum_{t=1}^{k-1} a_{n,t} \right) \bar{g}_{n,k-1} - \beta = 0, \forall k = 2, 3, 4 \quad (15)$$

$$\bar{g}_{n,k} a_{n,k} - (2^\gamma - 1) \left(\bar{g}_{n,k} \sum_{j=1}^{k-1} a_{n,j} + 1 \right) > 0, \forall k = 1, 2, 3, 4 \quad (16)$$

From the above formula (14)–(15), the power allocation coefficient can be solved when the number of users in each group is 2, 3, 4, as shown in Table 1.

By mathematical induction (MI), at this time, can get each cluster head power allocation coefficient:

$$a_{n,1} = \frac{1}{2^{K-1}} - \sum_{j=2}^K \frac{\beta}{\bar{g}_{n,j-1} 2^{j-1}}$$

The power allocation factor of the other $K - 1$ users in this cluster is:

$$a_{n,k} = \frac{1}{2^{(K-k+1)}} - \sum_{j=k}^K \frac{\beta}{\bar{g}_{n,j-1} 2^{(j-k+1)}} + \frac{\beta}{\bar{g}_{n,k-1}}, 2 \leq k \leq K.$$

Where $n = \{1, 2\}$.

Table 1. Power allocation coefficient of SUs

The number of users in each cluster	Power allocation coefficient
2	$a_{n,1} = \frac{1}{2} - \frac{\beta}{2\bar{g}_{n,1}}$ $a_{n,2} = \frac{1}{2} + \frac{\beta}{2\bar{g}_{n,1}}$
3	$a_{n,1} = \frac{1}{4} - \left(\frac{\beta}{2\bar{g}_{n,1}} + \frac{\beta}{4\bar{g}_{n,2}}\right)$ $a_{n,2} = \frac{1}{4} + \frac{\beta}{2\bar{g}_{n,1}} - \frac{\beta}{4\bar{g}_{n,2}}$ $a_{n,3} = \frac{1}{2} + \frac{\beta}{2\bar{g}_{n,2}}$
4	$a_{n,1} = \frac{1}{8} - \frac{\beta}{2\bar{g}_{n,1}} - \frac{\beta}{4\bar{g}_{n,2}} - \frac{\beta}{8\bar{g}_{n,3}}$ $a_{n,2} = \frac{1}{8} + \frac{\beta}{2\bar{g}_{n,1}} - \frac{\beta}{4\bar{g}_{n,2}} - \frac{\beta}{8\bar{g}_{n,3}}$ $a_{n,3} = \frac{1}{4} + \frac{\beta}{2\bar{g}_{n,2}} - \frac{\beta}{4\bar{g}_{n,3}}$ $a_{n,4} = \frac{1}{2} + \frac{\beta}{2\bar{g}_{n,3}}$

By the nature of the KKT conditions when $N = 8$ verify the situation, at this time, there are four secondary users in each cluster: $K = 4$. At this point, assuming $\Psi = \{\lambda, \zeta_2, \zeta_3, \zeta_4\}$, $\Theta = \{\zeta_2, \zeta_3, \zeta_4\}$ and setting formulation (10) is equal to zero, then the following relation can be obtained according to the geometric operations:

$$\frac{B\bar{g}_{n,k}}{\bar{g}_{n,k} \sum_{j=1}^k a_{n,j} + 1} - \sum_{j=k+1}^K \frac{Ba_{n,j} \bar{g}_{n,j}^2}{\left(\sum_{t=1}^j a_{n,t} \bar{g}_{n,j} + 1\right) \left(\sum_{t=1}^{j-1} a_{n,t} \bar{g}_{n,j} + 1\right)} - \lambda + \zeta_k \bar{g}_{n,k-1} - \sum_{j=k+1}^K \zeta_j \bar{g}_{n,j} = 0$$

$$\Leftrightarrow \frac{B\bar{g}_{n,4}}{\bar{g}_{n,4} \sum_{j=1}^4 a_{n,j} + 1} - \sum_{j=1}^3 \frac{Ba_{n,j}(\bar{g}_{n,j-1} - \bar{g}_{n,j})}{\left(\sum_{t=1}^j a_{n,t} \bar{g}_{n,j} + 1\right) \left(\sum_{t=1}^{j-1} a_{n,t} \bar{g}_{n,j} + 1\right)} - \lambda + \zeta_4 \bar{g}_{n,3} - \sum_{j=k}^3 \zeta_j \bar{g}_{n,j} = 0$$

Based on the nature of the equation, it can be solved:

$$\lambda = \frac{B\bar{g}_{n,4}}{\bar{g}_{n,4} \sum_{j=1}^4 a_{n,j} + 1} + \zeta_4 \bar{g}_{n,3}$$

$$\zeta_2 = \frac{Ba_{n,2}(\bar{g}_{n,1} - \bar{g}_{n,2})}{\bar{g}_{n,1} (a_{n,1} \bar{g}_{n,1} + 1) (a_{n,1} \bar{g}_{n,2} + 1)}$$

$$\zeta_k = \frac{Ba_{n,k}(\bar{g}_{n,k-1} - \bar{g}_{n,k})}{\bar{g}_{n,k} \left(\sum_{t=1}^{j-1} a_{n,t} \bar{g}_{n,j-1} + 1\right) \left(\sum_{t=1}^{j-1} a_{n,t} \bar{g}_{n,j} + 1\right)} + \zeta_{k-1} \bar{g}_{n,k-2}, \quad k = 3, 4$$

$$\zeta_1 = \eta_k = 0, \quad k = 1, 2, 3, 4$$

In the above formula, $\bar{g}_{n,k-1} > \bar{g}_{n,k}$, η_k, λ, ζ_k are larger than zero, so the solution satisfy KKT conditions. What's more, when the user system uses the average power distribution mode, $a_{n,k} = \frac{1}{K}$, then the system capacity is

$$\begin{aligned}
C_{apa} &= \tilde{R}_1 + \tilde{R}_2 \\
&= \sum_{k=1}^K B \log_2 \left(1 + \frac{\frac{1}{K} \bar{g}_{1,k}}{\bar{g}_{1,k} \sum_{j=1}^{k-1} \frac{1}{K} + 1} \right) + \sum_{k=1}^K B \log_2 \left(1 + \frac{\frac{1}{K} \bar{g}_{2,k}}{\bar{g}_{2,k} \sum_{j=1}^{k-1} \frac{1}{K} + 1} \right) \\
&= \sum_{k=1}^K B \log_2 \left(1 + \frac{K \bar{g}_{1,k}}{(k-1) \bar{g}_{1,k} + K} \right) + \sum_{k=1}^K B \log_2 \left(1 + \frac{K \bar{g}_{2,k}}{(k-1) \bar{g}_{2,k} + K} \right)
\end{aligned}$$

4 Simulation Results and Analysis

This section mainly verifies the capacity problem of the MIMO cognitive secondary users system based on NOMA. System parameters: the cognitive base station has two transmit antennas, the number of SUs in the cognitive system is greater than or equal to 4, which each user is configured with a single transceiver antenna. The authorization system has two main users and are configured with two transceiver antennas. The maximum power that can be sustained by each antenna of the cognitive base station is 50 dBm, and the power difference between the sub-users satisfying the NOMA condition is 10 dBm, and the system bandwidth is 1 MHz (Table 2).

Table 2. Simulation parameters

Parameters	Values
Maximum transmit power of base station P_s	47 dBm
Difference in power between SUs p_{tol}	10 dBm
System bandwidth	8 MHz
The distance between PU1 and SBS	50 m
The distance between PU2 and SBS	100 m
The antennas of SBS N_t	2
The effective antennas of SUs	1
The number of SUs	4, 6, 8
Interference threshold I_p	5 W
Gaussian white noise power σ^2	0.1 W
Path loss exponent δ	3

In the first experiment, the Monte Carlo simulation was used to compare the change in the capacity of the secondary user system under two different ways: the dynamic power allocation mode and the average power mode. It can be seen that the use of dynamic power distribution, when the number of secondary users increased, the system capacity will increase also, and it is worth noting that the number of SUs from four increased to six, the system capacity to improve more than the number of users from 6 increased to 8. However, in the average power allocation method, the more the secondary users, the lower the capacity. It can be seen that the dynamic power allocation method has more system capacity than the average power allocation method. As shown in Fig. 4.

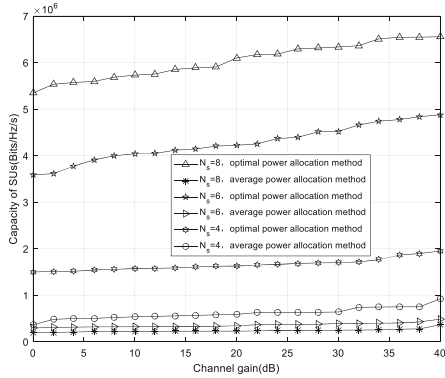


Fig. 4. The variation of secondary users’ number with channel gain

The second experiment compare the capacity changes of the cognitive system under different interference thresholds. When the IT is small, the user’s interference to PUs is small, relatively, and the system capacity of the SUs is larger. As shown in Fig. 5.

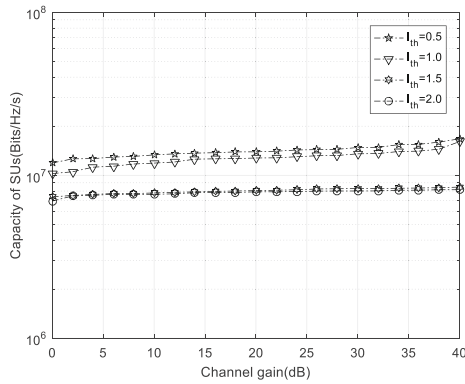


Fig. 5. Capacity comparison of cognitive system with PUs’ IT

5 Conclusion

With the further development of integrated circuits, NOMA technology is an important technology to increase the capacity of the system for the future mobile communication, which is based on the increase of the receiver’s complexity. In this paper, the problem of improving the capacity of secondary users system is studied by combining the cognitive MIMO and NOMA technology. The simulation results show that the proposed algorithm can improve the system capacity. The next step is to consider the new pre-coding method combined with other clustering and power allocation methods to further optimize the state of the NOMA cognitive MIMO secondary users system.

Acknowledgements. This work was supported by program for changjiang scholars and innovative research team in university (IRT1299) project of CSTC (cstc2013yykfA40010) and special fund of chongqing key laboratory (CSTC).

References

1. Akyildiz, I.F., Lee, W.Y., Vuran, M.C., Mohanty, S.: Next generation/dynamic spectrum access/cognitive radio wireless networks: a survey. *Comput. Netw.* **05**, 2127–2159 (2006)
2. Benjebbour, A., Saito, Y., Kishiyama, Y., Li, A.X., Harada, A., Nakamura, T.: Concept and practical considerations of non-orthogonal multiple access (NOMA) for future radio access. In: *Proceedings of the International Symposium on Intelligent Signal Processing and Communications Systems*, Naha, Japan, pp. 770–774. IEEE Press (2013)
3. Moualeu, J.M., Hamouda, W., Takaeira, F.: Cognitive coded cooperation in underlay spectrum-sharing networks under interference power constraints. *IEEE Trans. Veh. Technol.* **66**, 2099–2113 (2017)
4. Slimeni, F., Scheers, B., Nir, V.L., et al.: Learning multi-channel power allocation against smart jammer in cognitive radio networks. In: *International Conference on Military Communications and Information systems*, Brussels, Belgium pp. 1–7. IEEE Press (2016)
5. Li, A.X., Lan, Y., Chen, X.H., et al.: Non-orthogonal multiple access (NOMA) for future downlink radio access of 5G. *China Commun.* **12**, 28–37 (2015)
6. Zabetian, N., Baghani, M., Mohammadi, A.: Rate optimization in NOMA cognitive radio networks. In: *International Symposium on Telecommunications*, Tehran, Iran, pp. 62–65. IEEE Press (2016)
7. Ding, Z.G., Fan, P.Z., Poor, H.V.: Impact of user pairing on 5G non-orthogonal multiple-access downlink transmissions. *IEEE Trans. Veh. Technol.* **65**, 6010–6023 (2016)
8. Kim, B., Lim, S.M., Kim, H., et al.: Non-orthogonal multiple access in a downlink multiuser beamforming system. In: *IEEE Military Communications Conference*, San Diego, CA, USA, pp. 1278–1283. IEEE Press (2013)
9. Zeng, M., Tsiropoulos, G.I., Dobre, O.A., et al.: Power allocation for cognitive radio networks employing non-orthogonal multiple access. In: *IEEE Global Communications Conference*, Washington, DC, USA, pp. 1–5. IEEE Press (2016)
10. Liu, Z.X., Lei, L., Zhang, N.B., et al.: Joint beamforming and power optimization with iterative user clustering for MISO-NOMA systems. *IEEE Access* **99**, 1–11 (2017)
11. Kim, B., Chung, W., Lim, S., et al.: Uplink NOMA with multi-antenna. In: *IEEE Vehicular Technology Conference (VTC Spring)*, Glasgow, UK, pp. 1–5. IEEE Press (2015)
12. Ali, M.S., Tabassum, H., Hossain, E.: Dynamic user clustering and power allocation for uplink and downlink non-orthogonal multiple access (NOMA) systems. *IEEE Access* **04**, 6325–6343 (2016)
13. Boyd, S., Vandenberghe, L.: *Convex Optimization*. Cambridge University Press, Cambridge (2004)



A Novel Energy Aware Coded Opportunistic Routing for Social Cognitive Radio Networks

Shoubai Xiao¹, Renhao Lu², and Xiaoxiong Zhong^{2,3}(✉)

¹ Nanchang Institute of Science and Technology,
Nanchang 330108, People's Republic of China

² Guangxi Key Laboratory of Trusted Software,
Guilin University of Electronic Technology,
Guilin 541004, People's Republic of China

xixzhong@gmail.com

³ Graduate School at Shenzhen, Tsinghua University, Shenzhen 518055,
People's Republic of China

Abstract. As a huge numbers of heterogeneous devices will be connected in social cognitive radio networks (SCRNs), it needs more frequency spectrum. Moreover, dynamic spectrum availability and heterogeneous devices make it more difficult for routing design in SCRNs. Opportunistic routing (OR) can leverage the broadcast nature of wireless channels, and then can enhance network performance. In this work, we propose an energy aware coded OR (ECOR) in SCRNs, which jointly considers energy efficiency and social feature for designing coded OR. In the proposed OR, we exploit a new scheme for candidate selection and use network coding in data transmission between selected nodes in SCRNs. In addition, we propose a game-theoretic approach to decide forwarding candidate set which is based on auction mechanism. The simulation results demonstrate that the ECOR performs better compared with existing routing in SCRNs in terms of hop count and packet delivery ratio.

Keywords: Coded opportunistic routing · Social cognitive radio networks

1 Introduction

The cognitive radio (CR) [1] has been considered as a promising technology to improve spectrum usage in wireless networks. In CRNs, which exploit CR, it includes two types of users: primary users (PUs) and secondary users (SUs). The spectrum is used in an opportunistic manner, and thus, the spectrum for SUs is varying with locations and time, which is affected by the PU's behavior. The Social CRNs, on the other hand, is a branch of the CRNs where social relationships are established in an autonomous way among objects, things, and human and where social graphs are created. Thus, how to design routing scheme such that it can improve energy efficiency and transmission reliability for SCRNs, is an important issue.

Opportunistic routing (OR) [2], was introduced to enhance the routing performance in wireless networks, which can improve data transmission efficiency and reliability. In OR, the node broadcasts the packet to its neighbors, and then its neighbors will have

the chance to receive/hear it, hence, they can cooperate in packet forwarding. In SCRNs, because of dynamic spectrum access and heterogeneity in cognitive nodes and channels, it is improper to exploit the traditional routing protocols for SCRNs. Since there is no need for determining next hops in advance in OR, it is more suitable for SCRNs.

Recently, several solutions have been proposed on opportunistic routing in CRNs. Lin *et al.* [3] induced a novel OR for regular and large-scale multi-channel CRNs, which exploits spectrum map established on local sensing information. In the first scheme SMOR-1, it exploits relay selection based on link transmission qualities. For the SMOR-2, it induces stochastic geometry for geographic OR for cooperative diversity. In [4], we proposed a novel OR scheme, CANCOR, for multi-channel CRNs, which incorporates channel assignment in OR protocol for multi-channel multi-radio CRNs. However, all above mentioned works do not systematically discuss how to exploit OR to improve the performance of CRNs. Until comparatively recently, Lin *et al.* [5] proposed a novel statistical QoS control mechanism through cooperative relaying from a network coded opportunistic routing perspective, realizing virtual MIMO communications at session level. Lin *et al.* [6] presented a cognitive and opportunistic relay selection scheme for cognitive M2M networks, which can mitigate detractive interference and efficiently selection the forwarders. However, they did not exploit the features of social networks to improve the performance of SCRNs.

Until comparatively recently, researchers begin to pay attention to investigate the performance of CRNs from the social network perspective [7–16]. They mainly focus on spectrum sensing/sharing [7–13], or queue control [14]. To the best of our knowledge, only two papers [15, 16] consider social networks in designing routing for CRNs. Reference [15] exploits the concept of PU community in designing SUs' routing, ignoring SUs' social behaviors. Reference [16] proposed a social-relationship-aware routing scheme for CRNs. It uses the predicted link reliability for routing and relay decision. However, they did not consider the SUs' energy efficiency and social similarity. Inspired by this, we propose an energy aware coded OR (ECOR) for SCRNs, which jointly considers energy efficiency and social feature. The contributions of this article can be summarized as follows. Firstly, we present a new routing metric, which jointly considers social features and energy. And then, the novel forwarding candidate selection is proposed for SCRNs, which is based on auction model, maximizing payoff. Moreover, the optimal bid price has been proved, which is related to the number of candidates and social features. Finally, we validate the effectiveness of the ECOR protocol by extensive simulations.

The remainder of this paper is organized as follows. The proposed routing protocol ECOR is introduced in Sect. 2, which mainly contains three key components: network model, candidate decision based on auction model, and data transmission based on network coding. Section 3 gives the performance evaluation of ECOR. Finally, Sect. 4 concludes this paper.

2 ECOR Design

In this section, we will present a coded OR for SCRNs, called energy aware coded opportunistic routing, ECOR. Next we will describe the network model, candidate selection and prioritization and data transmission based network coding.

2.1 Network Model

In this paper, we exploit an interweave model [4], in which the SUs can only transmit data in the channel that there is no PU activity occurs. In this model, it consists of C channels, num_s SUs and num_p PUs. Each SU is provided with the same number of radios R and exploits a half-duplex model. And also, a time-slotted model is exploited for SU, with a fixed slot duration T . Each slot includes a sensing period with duration T_s and a data transmission period with duration T_t . The usage pattern of a given channel follows an independent ON/OFF state model with the lengths of busy and idle periods in the exponentially distributed with rate parameters λ_{busy} and λ_{idle} over busy and idle transition respectively. Note that, the SUs have social relationships between them and are heterogeneous.

2.2 Candidate Decision Based on Auction Model

In this subsection, the candidate decision strategy is presented, which includes social ties, energy consumption, and auction model.

(1) Social ties

In real life, people who carry smart mobile devices (i.e., SUs for SCRNs) always have social relationship among themselves. We called that the SUs have social features in SCRNs, which have the same interests, or purpose, or family relationship. Individuals belonging to the same community will meet each other with high probability and regularly. Compared with dynamic information, social ties and behaviors between nodes in the same community tend to be stable over time. Hence, we can characterize the social ties between two nodes according to the history information of these two nodes, which can be expressed:

$$ST_{i,j}(T) = \chi SPM_{i,j}(T) + (1 - \chi) socsim_{i,j}(T) \quad (1)$$

where $SPM_{i,j}(T)$ means the social pressure metric (SPM) of the nodes i and j [17] during time T , $\chi (\in [0, 1])$ is the weight factor, which is set to be 0.5 in simulation, $socsim_{i,j}(T)$ means the social similarity between nodes i and j during time T , which can be reflected by formula (2).

$$socsim_{i,j}(T) = com_{i,j}(T) / (n_i(T) + n_j(T)) \quad (2)$$

where $com_{i,j}(T)$ means the number of common neighboring nodes for node i and node j during time T , $n_i(T)$ denotes the number of node i 's one-hop neighbors during time T , and $n_j(T)$ denotes the number of node j 's one-hop neighbors during time T .

(2) Energy consumption

Let $E_{iC}(T)$ as the energy consumption of the node i for successfully sending one packet to its downstream nodes during time T . It includes three parts: the energy $E_{iF}(T)$ (used to forward a packet), the energy $E_{iR}(T)$ (used to receive/hearing a packet), and the energy $E_{iACK}(T)$ (consumed to send an ACK). Thus, we can obtain

$$E_{iC}(T) = E_{iF}(T) + N_c \times E_{iR}(T) + E_{iACK}(T) \quad (3)$$

where N_c is the i 's one-hop neighbors during time T . Also, we assume it subject to (0, 1) uniform distribution.

(3) Auction model

Suppose in our proposed OR, we select two classes of candidate sets CFS_1 and CFS_2 , which CFS_1 is a primary set, CFS_2 is a backup selection. In proposed model, let source S denote the auctioneer and the forwarding nodes denote the bidders. The i^{th} bidder's cost is v_i , and the bidder offers price of node i is b_i^p which i is in the first class CFS_1 and the b_i^s is the bidder price of node i which i is in the second class CFS_2 . Note that we have $CFS_1 \cap CFS_2 = \emptyset$. Hence, the payoff function of the node i can be expressed as:

$$u_i = \begin{cases} b_i^p - v_i & i \text{ is in the first class } CFS_1 \\ b_i^s - v_i & i \text{ is in the second class } CFS_2 \\ 0 & \text{otherwise} \end{cases} \quad (4)$$

So, the forwarding cost can be expressed as

$$\theta_i = \frac{1}{|N(i)|} \sum_{j \in N(i)} ST_{i,j}(ETX_i + \alpha E_{iC}) \quad (5)$$

where ETX_i is the ETX of node i to the destination D , $N(i)$ is the i 's one-hop neighbors. Hence, we have

$$v_i = \frac{\theta_i}{\frac{1}{|N(i)|} \sum_{j \in N(i)} ST_{i,j}(ETX_s + \alpha E_{initial})} \quad (6)$$

which ETX_s is the ETX of source S to the destination D , and $E_{initial}$ is the initial energy. It is easy to know that the distribution of v_i is uniformed. So, the expected payoff of i can be calculated

$$u_i = (b_i - v_i) \prod_{j \neq i} P(b_i < (b(v_j))) \quad (7)$$

where $P(b_i < (b(v_j)))$ denotes the probability that node i has minimum bid.

According to the characteristics of v_i , we have

$$P(b_i < (b(v_j))) = P(\Phi(b_i) < v_j) = 1 - \Phi(b_i) \quad (8)$$

and

$$\prod_{j \neq i} P(b_i < (b(v_j))) = [1 - \Phi(b_i)]^{N(i)-1} \quad (9)$$

So we have

$$\max u_i = \max_{b_i} ((b_i - v_i)[1 - \Phi(b_i)]^{N(i)-1}) \quad (10)$$

After derivation, we can obtain

$$\begin{aligned} b^*(v_i) &= \frac{1}{|N(i)| - 1} - \frac{|N(i)| - 2}{|N(i)| - 1} v_i \\ &= \frac{1}{|N(i)| - 1} - \frac{|N(i)| - 2}{|N(i)| - 1} \frac{\theta_i}{\frac{1}{|N(i)|} \sum_{j \in N(i)} ST_{i,j}(ETX_s + \alpha E_{initial})} \end{aligned} \quad (11)$$

The bidding node i bids $b^*(v_i)$ such that all bidders payoff are maximized. In addition, the prioritization of forwarding candidates are set according the price, the node with low price has high priority.

2.3 Network Coding Based Data Transmission

In ECOR, we exploit network coding (NC) [18] for data transmission between selected trust nodes which is to improve the transmission performance. The ECOR uses the intra-session NC (IaSNC) in which the coding operations are based on intra-session (the packets are from the same session).

In IaSNC, the S will divide data into small generations of k packets, PKT_1, \dots, PKT_k , which are called original packets. The S linearly combines the k packets in current generation and keeps sending the linear combinations from the current generation until the destination feedbacks the generation acknowledgement. After receiving the generation acknowledgement from the destination, it moves to the next generation. When the node receives a coded packet, it will check to determine whether or not there exists the linearly independent between the received coded packet and the previously received packets of the same generation. If so, it will store it, otherwise, it drops it. In addition, the node can re-code received coded packets base on linear combination operations. After receiving any k linearly independent coded packets, the D can recover the k native packets, and then returns an acknowledgement to the source. So, the source will stop sending the linear combinations of the current generation, and moves to the next generation. In our simulation, the maximal k is set to be 10.

Similar to Ref. [19], we exploit the credit counter for coding and forwarding condition. Each credit counter is used for a channel in multi-channel wireless networks. Hence, for each node, we should maintain $|C|$ credit counters. In addition, we take channel availability into account for credit calculating in ECOR. Next, we will give a novel method for calculating the value of credit for node i corresponding to the channel c , which can be expressed

$$credit_i(c) = \frac{z_i(c)}{\sum_{c \in C} (u(c) \sum_{j > i} z_j(c)(1 - \rho_{ji}(c)))} \quad (12)$$

where $u(c)$ is the channel availability, $\rho_{ji}(c)$ denotes the packet loss rate from node j to node i on the channel c , and $z_i(c)$ is the expected number of transmissions that j must make on channel c .

If the value of $credit_i(c)$ is larger than zero, node i generates a coded packet, and broadcasts it on channel c , decreasing the credit counter. Next, we describe the data forwarding process, which includes three key components.

Source node: It continues seeds the encoding packets of the current generation size until it receives corresponding ACK feedback or reach current generation size k .

Relay node: When a relay node receives a coded packet, it will check to determine whether or not there exists the linearly independent between the received coded packet and the previously received packets of the same generation. If so, it will store it, otherwise, it drops it. As well as, the node can re-code received coded packets base on linear combination operations. As we know in SCRNs, there are multiple types of flows. Suppose that there are multiple unicast flows at the relay node, so we can determine the forwarding priority of these flows according to the following rule:

- (1) For different types of flows, the forwarding priority is set according to the preset priority.
- (2) For the same type flows, we exploit a new metric ς_{f_i} ($\varsigma_{f_i} = \delta_1 n_{f_i(pkt)} + \delta_2 n_{f_i(times)}$ where δ_1 and δ_2 are weight factors, and have $\delta_1, \delta_2 \in [0, 1]$, $\delta_1 + \delta_2 = 1$, in the simulation, we set them to be 0.5 and 0.5, respectively, $n_{f_i(pkt)}$ is the total number of packets of flow f_i currently at the node, and $n_{f_i(times)}$ is the total times that the flow f_i goes through the node in the past time). The flow f_i with higher ς_{f_i} has a forwarding priority.

Destination node: It feedbacks an ACK to the source by short path routing as soon as it can recover the whole generation. When two nodes meet, the ACK of the generation of the flow should be inserted into their packet header exchange before data transmission, which can avoid the transmission of ACKed generation of the flow.

For channel selection, the channel m with higher $u(m)$ is considered as a better channel. Thus, it is given a higher rank. In each channel assignment decision, we choose the channel with highest rank for data transmission.

3 Performance Evaluation

In this section, we present the performance evaluation of ECOR protocol using NS2 [20] and CRCN model [21]. The simulation settings are: the SUs mobility model is random waypoint model in a square area, whose node density is 400 nodes/Km². The propagation model is the Two-Ray Ground model. The CBR data packets are 1000 bytes and the data traffic is active in the interval [60, 1000] seconds. Each node generates one data flow to a destination node selected randomly. For each experiment we performed 100 runs computing both the average value, i.e., packet delivery ratio (PDR) and hop count.

In addition, the energy parameters $E_{iF}(T)$, $E_{iR}(T)$, and $E_{iACK}(T)$ are set to $3.6e-3$ eu, $1.8e-3$ eu, and $0.16e-3$ eu. The initial energy of the node is 300 eu. The number of flows is 5. Finally, we give three types of flows, the priorities and parameters are shown in Table 1.

Table 1. MAC parameters for 3 classes

Class	Priority	AIFSN	CWmin	CWmax
Class 1	2	2	3	7
Class 2	1	2	7	15
Class 3	0	3	15	1023

Table 2. Simulation parameters

Number of channels	10
Number of Radios	2
Weight factor α	0.2
Max SU speed	2 m/s
Number of PUs	[2, ..., 18]
Number of SUs	[20, ..., 100]
PU coverage	300 m
SU transmission range	120 m
PU transmission range	150 m
Channel data rate	5.4 Mbps
Per channel sensing time	5 ms
Channel changing time	70 μ s
Packet size	1000 bytes
Bandwidth	5.4 Mb/s
PU activity parameter $\hat{\lambda}$	[50, ..., 400]
Run time	1000 s

The simulation parameter settings are listed in Table 2. We compare ECOR with the following two protocols: CAODV [22] and SoRoute [16] in terms of PDR and hop count.

The first experiment (Figs. 1 and 2), we study the impact of SU number on packet delivery ratio (PDR) and hop count. In this experiment, the number of PU is set to be 10 and the PU active parameter is 200 s. As the number of SU number increases, the PDR will increase as well as shown in Fig. 1. In Fig. 2, we can see that the hop count will increase when the number of SU increases. However, the proposed scheme always achieve better performance that other two routing protocols. The reason is that we consider network coding technology and the social feature in SU’s communication, and exploit an auction based candidate selection scheme.

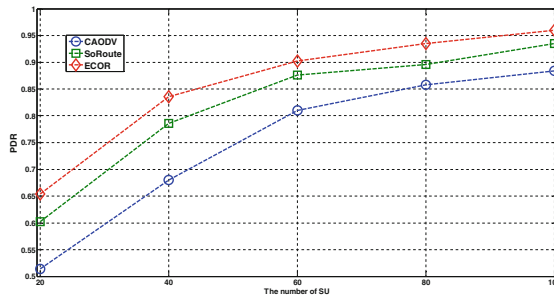


Fig. 1. PDR vs. the number of SU.

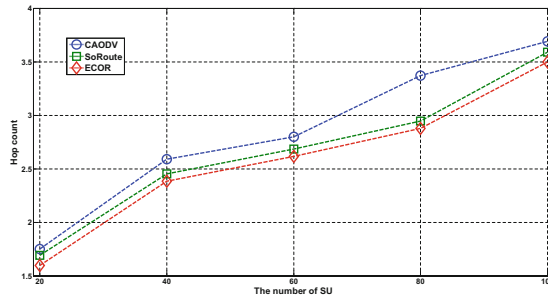


Fig. 2. Hop count vs. the number of SU.

The second experiment (Figs. 3 and 4), we analyze the impact of the number of PU on packet delivery ratio (PDR) and hop count. The number of SU is set to be 50 and the PU active parameter is set to be 200 s. From the figures, we can see that the PDR of all schemes will decrease with increasing the number of PU, the reason is that increasing the number PU means the duration of the free channels is shorter. Moreover, the hop count will increase and then decrease as increasing PU number. However, the proposed scheme will obtain better performance.

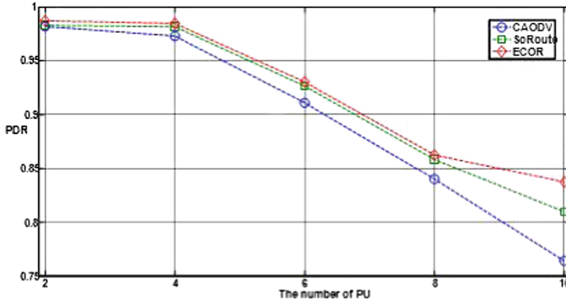


Fig. 3. PDR vs. the number of PU.

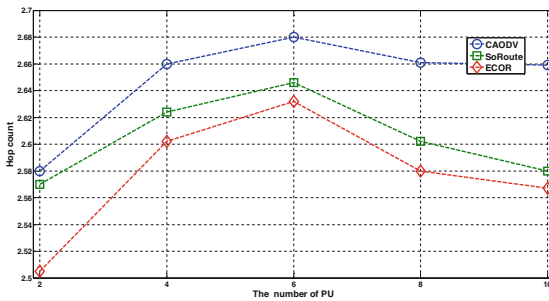


Fig. 4. Hop count vs. the number of PU.

4 Conclusion

Integrating OR with the features of social networks is an effective solution to improve network performance over multi-hop CRNs. This article provides a novel energy aware coded OR protocol for SCRNs, ECOR. In ECOR, we propose a novel method for model social feature of SCRNs. And then, we present an auction model based forwarding candidate selection which jointly considers social features, energy and ETX. In addition, the optimal bid price has been proved, which is related to the number of candidates and social features. In data transmission, we exploit network coding during selected candidate for multi-type flows, which can enhance data progressing. Furthermore, our extensive simulation results exhibit that ECOR performs better than CAODV and SoRoute.

Acknowledgments. This work was supported by the Natural Science Foundation of Guangxi Province under grant 2016GXNSFBA380010 and Innovation Project of GUET Graduate Education under grant 2017YJCX57. We would like to acknowledge the reviewers whose comments and suggestions significantly improved this paper.

References

1. Haykin, S.: Cognitive radio: brain-empowered wireless communications. *IEEE J. Sel. Areas Commun.* **23**(2), 201–220 (2005)
2. Biswas, S., Morris, R.: ExOR: opportunistic multi-hop routing for wireless networks. In: *Proceedings of the ACM SIGCOMM 2005*, vol. 35, pp. 133–144 (2005)
3. Lin, S.-C., Chen, K.-C.: Spectrum-map-empowered opportunistic routing for cognitive radio ad hoc networks. *IEEE Trans. Veh. Technol.* **63**(6), 2848–2861 (2014)
4. Qin, Y., Zhong, X., Yang, Y., Li, L., Ye, Y.: Combined channel assignment and network coded opportunistic routing in cognitive radio networks. *Comput. Electr. Eng.* **52**, 293–306 (2016)
5. Lin, S.-C., Chen, K.-C.: Statistical qos control of network coded multipath routing in large cognitive machine-to-machine networks. *IEEE Internet Things J.* **3**(4), 619–627 (2016)
6. Lin, S.-C., Chen, K.-C.: Cognitive and opportunistic relay for QoS guarantees in machine-to-machine communications. *IEEE Trans. Mob. Comput.* **15**(3), 599–609 (2016)
7. Li, H., Huang, W., Wu, C., et al.: Utility-maximizing data dissemination in socially selfish cognitive radio networks. In: *Proceeding of the IEEE MASS 2011*, pp. 212–221 (2011)
8. Li, S., Zheng, Z., Ekici, E., et al.: Maximizing social welfare in operator-based cognitive radio networks under spectrum uncertainty and sensing inaccuracy. In: *Proceeding of the IEEE INFOCOM 2013*, pp. 953–961 (2013)
9. Guven, C., Bayhan, S., Alagöz, F.: Effect of social relations on cooperative sensing in cognitive radio networks. In: *Proceedings of the IEEE BlackSeaCom 2013*, pp. 247–251 (2013)
10. Li, H., Song, J., Chen, C., et al.: Behavior propagation in cognitive radio networks: a social network approach. *IEEE Trans. Wirel. Commun.* **13**(2), 646–657 (2014)
11. Gopinathan, A., Li, Z., Wu, C.: Strategy proof auctions for balancing social welfare and fairness in secondary spectrum markets. In: *Proceedings of the IEEE INFOCOM 2011*, pp. 3020–3028 (2011)
12. Li, H., Wu, C., Li, Z.: Socially-optimal online spectrum auctions for secondary wireless communication. In: *Proceedings of the IEEE INFOCOM 2015*, pp. 2047–2055 (2015)
13. Chen, X., Huang, J.: Imitation-based social spectrum sharing. *IEEE Trans. Mob. Comput.* **14**(6), 1189–1202 (2015)
14. Li, H., Han, Z.: Socially optimal queuing control in cognitive radio networks subject to service interruptions: To queue or not to queue? *IEEE Trans. Wireless Commun.* **10**(5), 1656–1666 (2011)
15. Wu, H., Yu, R., Zhang, Y.: Exploiting primary user social features for reliability-driven routing in multi-hop cognitive radio networks. In: *Proceedings of the IEEE ICC 2014*, pp. 215–220 (2014)
16. Jing, T., Zhou, J., Liu, H., et al.: SoRoute: a reliable and effective social-based routing in cognitive radio ad hoc networks. *EURASIP J. Wirel. Commun. Netw.* **2014**, 200 (2014)
17. Bulut, E., Szymanski, B.K.: Exploiting friendship relations for efficient routing in mobile social networks. *IEEE Trans. Parallel Distrib. Syst.* **23**(12), 2254–2265 (2012)
18. Ahlswede, R., Cai, N., Li, S.-Y.R., Yeung, R.W.: Network information flow. *IEEE Trans. Inf. Theory* **46**(4), 1204–1216 (2000)
19. Wu, F., Vaidya, N.: Workload-aware opportunistic routing in multi-channel, multi-radio wireless mesh networks. In: *Proceeding of the IEEE SECON 2012*, pp. 344–352 (2012)
20. Network Simulator (ns2). <http://www.isi.edu/nsnam/ns/>
21. Michigan Technological University: Cognitive Radio Cognitive Network Simulator. <http://stuweb.ee.mtu.edu/ljialian/index.htm>
22. Cacciapuoti, A., Calcagno, C., Caleffi, M., et al.: CAODV: routing in mobile ad-hoc cognitive radio networks. In: *Proceedings of the IFIP Wireless Days 2010*, pp. 1–5 (2010)



Research on Anti PUE Attack Based on CAF Spectrum and Repeated-Game

Hong Chang^{1(✉)} and Yong Li²

¹ Department of Communication Engineering,
Xi'an University of Posts and Telecommunications, Xi'an, China
nuc_changhong@126.com

² School of Electronics and Information,
Northwestern Polytechnical University, Xi'an, China
liyong6@mail.nwpu.edu.cn

Abstract. High imitation of primary user (PU) signal, primary user emulation (PUE) signal is difficult for discrimination. First, a method based on cross ambiguity function (CAF) is proposed for determining PUE signal. For PUE signal different from PU signal in spatial but same in frequency in one sensing slot, the algorithm with two dimension search is reduced to one dimension search, having no inter-modulation signal influence. Moreover, for defending PUE attack (PUEA), a repeated game between malicious user (MU) and secondary user (SU) is formulated. By introducing credit discipline mechanism, the optimal strategies for both players are investigated. The stability of the strategies is analyzed with replicated dynamic equation, which indicates that the strategies are the final choice no matter what initial strategies they choose. Simulation results demonstrate that the method is effective for discriminating and defending PUEA in terms of lower computation, higher detection probability and greater payoff.

Keywords: PUE attack · Cross ambiguity function · Repeated game
Credit discipline mechanism · Replicated dynamic equation

1 Introduction

Nowadays, spectrum resource available cannot meet the needs of high development of communication. Cognitive radio (CR) is a technology for making dynamic spectrum access (DSA) by letting unlicensed user use white space of licensed bands. However, security vulnerabilities in cognitive radio systems is a key problem [1–5]. One specific type of attack is PUE attack which has been studied in many works. Emulating the characteristic of PU signals, PUEA signals deliberately send by MU during the sensing slot make SU produce wrong estimation of spectrum occupation. PUEA can be divided into two types, one of which occupies the attacked spectrum for own use called selfish PUE attack and the other is malicious PUE attack who wants to prevent the network working normally. Both of them would degrade the performance of CR system [6–10].

The existing works on PUEA are mainly grouped into attack detection and attack defense. The detection approaches are classified into two types: location-based method [11–13] and signal feature-based method [14–16]. Location based method is working

based on PU being a TV user, the location of which is known in a prior and fixed during the sensing time. By positioning the transmitter, it can decide whether the received signal is PUE attack signal or not. Signal feature-based method available is working for each signal has the unique characteristics due to the special transmitter and propagation path. The received signal having different features would not be considered as PU signal. The defense method is that SU intelligently chooses the spectrum bands to sense and access according to Nash equilibrium strategy of the game [17–21]. Since the DSA mechanism demanding that SU must periodically sense the spectrum bands and incur no violation of primary users, this work mainly investigates the optimal actions for both of the players under the circumstance of PU absenting.

The main work is formulated as follows: First, considering PU and MU separated in spatial, an estimation of Doppler frequency is made for PUEA detection by CAF spectrum. Then, since the competition between MU and SU is repeated and lasts a long time, formulation PUE attack and defense as a repeated game. By introducing credit discipline mechanism, the optimal strategies for both players are obtained. Also, the stability of the optimal strategy is analyzed by using replicated dynamic equation to assure that is the final strategy they choose for higher payoff. Finally, simulation results are presented to confirm the conclusion.

2 System Model

The study is working for IEEE 802.22 networks. Before the analysis, the specific assumptions need to be made as given below.

- (1) PU is assume to be a TV broadcast Tower placed at fix location.
- (2) SU and MU are mobile users placed at random location. It is assumed that no changes (including frequency and location) happen to PU and MU during the sensing slot.
- (3) SU has the ability of self positioning [22].
- (4) The working time for SU is consist of discrete periods, one of which is divided into sensing slot and transmission slot. Without loss of generality, SU performs spectrum sensing and MU launches PUE attack signal all in sensing slot. If no PU signal presents, SU transmits signal or if MU grabs the spectrum band successfully, MU transmits signal in the transmission slot.

Consider detection problem as a hypothesis testing problem

$$u(t) = \begin{cases} n(t) & H_0 \\ A_{MX_M}(t) + n(t) & H_1 \\ A_{PX_P}(t) + n(t) & H_2 \\ A_{PX_P}(t) + A_{MX_M}(t) + n(t) & H_3 \end{cases} \quad (1)$$

where $n(t)$ is a white Gaussian noise of unknown power. $A_{MX_M}(t)$ and $A_{PX_P}(t)$ corresponds to PUE signal and PU signal SU received.

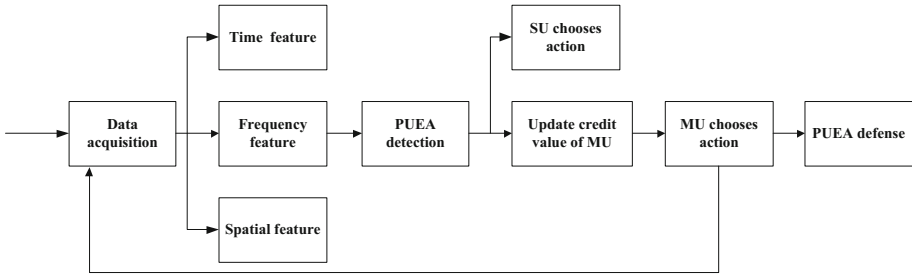


Fig. 1. Architecture of PUEA defense

Architecture of our proposed method is shown in Fig. 1. The main work is divided into two parts:

- (1) PUEA detection. Assume that the signals SU received are composed of simultaneous multi signals with uncertain parameters. The signals are firstly separated by FFT filter Banks in frequency domain. Since PUE signal highly mimic PU signal, the frequency of PUE signal is same with PU's. Obviously, it is difficult for separating PUE signal from PU signal in frequency domain. Owing to different in location but same in working time of PU and MU, CAF spectrum derived by mobile SU is effective for discriminate PUE signal from PU signal.
- (2) PUEA defense. After analyzing payoffs of SU and MU in one stage of the game, it is found that equilibrium strategy is not the optimal strategy. Since the game lasts over a long period of time and each stage of game is of same structure, repeated game is formulated. By introducing credit discipline mechanism, the optimal strategies for both of players are derived. The credit value of MU minus one if attack is detected. Given that the credit value is lower than the threshold, punishment such as gain smaller benefits despite no attack signal emitted will be put on MU in the penalty slot. Thereby, comparing with the payoffs achieved in short time, MU prefers the long payoffs, which determine the optimal strategic tuples. The stability of the strategies is proved by replicated dynamic equation, which is used for guaranteeing the maximum efficiency of system.

3 PUEA Detection

3.1 System Description

This section details the mathematical proof of the proposed method (see Fig. 2). At first, the signal frequency estimation is performed by fast Fourier transform (FFT) at O. Then, the detection test is carried on each point of the frequency representation. The test over a certain threshold represents the presence of a signal. As mentioned before, the fixed frequency of PU signal is known in prior and PUE signal effectively emulates the characteristics of PU signal such as frequency. The frequency equals to PU frequency, which the test is over the threshold, represents that PU or PUE transmission has worked. In the next section, we will determine the type of transmitter.

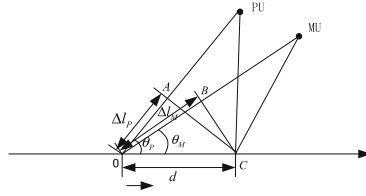


Fig. 2. PUEA detection system layout

Since the signal frequency varies slightly for the movement of SU, it is possible to discriminate PUE from PU by the Doppler frequency. Let v denotes the velocity of SU, θ_P and θ_M denote the yaw angle from PU and MU. $\Delta\varphi_P$ denotes the phase difference between O and A, which is the same with phase difference between O and C for PU signal. $\Delta\varphi_M$ is declared as the phase difference between O and B for MU signal. They can be expressed respectively as

$$\Delta\varphi_P = 2\pi\Delta l_P/\lambda = 2\pi v\Delta t \cos \theta_P/\lambda \quad (2)$$

$$\Delta\varphi_M = 2\pi\Delta l_M/\lambda = 2\pi v\Delta t \cos \theta_M/\lambda \quad (3)$$

Δt denotes the time for SU moving from O to C and $\Delta l_P, \Delta l_M, d$ all represent distance. Then, the Doppler frequency of the PU signal and PUE signal are shown respectively as

$$f_{dP} = \Delta\varphi_P/(2\pi\Delta t) = v \cos \theta_P/\lambda \quad (4)$$

$$f_{dM} = \Delta\varphi_M/(2\pi\Delta t) = v \cos \theta_M/\lambda \quad (5)$$

For PU's fix location, f_{dP} can be obtained in advance. The received signals are compared with PU signal in terms of time, frequency and Doppler frequency. The signal who has the same time duration and frequency with PU signal but different in Doppler frequency would be judged as PUE attack signal. Obviously, CAF spectrum works on the time difference and frequency difference representation and can be implemented effectively for PUE detection.

3.2 CAF Spectrum Representation and PUEA Detection

The CAF spectrum is defined as

$$A(\tau, f_d) = \int_0^T C_{uu}^{(n)}(\tau, t) e^{j2\pi f_d t} dt \quad (6)$$

Where $C_{uu}^{(n)}$ is the n th order cumulant. For the sake of low computation, n is set to be 2, the express becomes $C_{uu}^{(2)} = u_1(t)u_2^*(t - \tau)$. T refers to the integration length. $u_1(t)$ represents the signal SU received at O.

$$u_1(t) = s_1(t) + n_1(t) = \alpha A_P x_P(t) + \beta A_M x_M(t) + n_1(t) \tag{7}$$

After SU moving to the C, the signal obtained as follows:

$$u_2(t) = s_2(t) + n_2(t) = \alpha B_P x_P(t + \tau_P) e^{j2\pi f_{dP}(t + \tau_P)} + \beta B_M x_M(t + \tau_M) e^{j2\pi f_{dM}(t + \tau_M)} + n_2(t) \tag{8}$$

Where τ_P and τ_M are respectively the duration time of PU signal and PUE signal and assume $\tau_P \approx \tau_M \leq \tau_S < T_0$. Let τ_S be the time difference defined by SU moving from O to C and T_0 be the time of sensing slot. f_{dP} and f_{dM} are the Doppler frequency of PU signal and PUE signal due to the movement of SU. $n_1(t)$ and $n_2(t)$ are real-valued zero-mean white Gaussian noise. Index α and β refer to the probability of PU signal and PUE signal present. As PUE signal and PU signal exhibit the same time and frequency arrangement, $u_1(t)$ is rewritten as follow $u_1(t) \approx (A_P + A_M)x_P(t) + n_1(t)$. For no inter-modulation signals exist in $A(\tau, f_d)$, it is just the method for performing signal discrimination. Then, the duration time and Doppler frequency can be estimated using separate optimizations as

$$\hat{\tau} = \arg \max_{\tau} \int_0^T u_1(t) u_2^*(t - \tau) e^{j2\pi f_{dP} t} dt \tag{9}$$

$$\hat{f}_d = \arg \max_{f_d} \int_0^T u_1(t) u_2^*(t - \hat{\tau}) e^{j2\pi f_d t} dt \tag{10}$$

The signal detection based on CAF spectrum is mainly working in three steps:

- (1) Detection in frequency. First, filter the received signal by FFT. Then, the FFT outputs of the considered channel i having the same frequency as PU's is tested with the threshold. If lower, the channel is considered has no signal output, namely H_0 . If higher, the signal is considered to be present and judged as similar PU signal.
- (2) Detection in time. The CAF spectrum can be analytical computed by the signals respectively received by SU at O and C. As f_{dP} is known in prior, the two dimensional research in time and Doppler frequency reduce to one dimensional research in time, the method of which is considered to be more efficient. The signal is determined as PUE signal for no dominate peak corresponding to the f_{dP} in CAF spectrum but having the same frequency with PU's proved by the output of FFT channel, namely H_1 . If one dominate peak corresponding to the f_{dP} can be seen, which can be concluded that the signals are consist of at least PU signal.
- (3) Detection in spatial. Determine the duration time of the signals from the dominate peak in time. For simultaneous signals, perform the search for the Doppler frequency that is included in the same duration time. The estimated Doppler frequency derived from dominate peak of new search is f_{dM} , namely H_3 . In contrast, no peak presence demonstrates the signal is only PU signal, namely H_2 , when one dominate peak corresponding to the f_{dP} has been seen.

Procedure 1 Procedure of Setting Threshold for Signal Detection

- (1) In the free spectrum band, group the noise-only samples in descending order.
 - (2) Sample pairs are obtained by collecting first N_0 samples from the ordered samples, which is selected as threshold $T(n) = u'(n)$, and defining local PFA by $P_{fa}(n) = n/N_1$, $n = 1, 2, \dots, N_0$.
 - (3) By using CAF, the smoothed spectrogram obtained by non coherent integration in time and Doppler frequency is used to realize the signal detection according to above work. Using the appropriate Gaussian relation between threshold and the probability of false alarm P_{fa} , the threshold model is obtained as

$$T = \hat{k}_a \sqrt{-\ln P_{fa}} + k_b.$$
 - (4) The least square method performs properly on sample pairs, based on which the linear relationship between $\sqrt{-\ln P_{fa}}$ and T is shown.
-

4 Anti PUE Scheme

4.1 Nash Equilibrium Analysis for Single Stage

PUEA is formulated as a dynamic game between SU and MU, who choose its action respectively from the strategy space $A_S = \{\text{Switch, Stay}\}$ and $A_M = \{\text{Attack, No Attack}\}$. The payoff matrix of both players as shown in Table 1 and the

Table 1. Payoff matrix of single stage of the game

PU off	Attack	No attack
Switch	$-c_s, R_c + G - c_m + R_f$	$-c_s, R_f$
Stay	$G, R_c - c_m + R_f$	G, R_f

notation that will be used listed in Table 2. The game has unique pure strategy Nash equilibrium as $\{\text{Attack, Stay}\}$, which is not optimal for resisting attack. By introducing credit discipline mechanism, the optimal strategy $\{\text{No Attack, Stay}\}$ for defending against PUE is proposed based on repeated multistage game between SU and MU.

4.2 Repeated Game Model

It is noted that MU gains access to the spectrum band exclusively by launching PUE signal, which is severely degrade network performance. Therefore we introduce credit discipline mechanism for defending against PUEA, based on which MU adjust strategy as the credit value refers to the degree to gain the spectrum access. We consider the working period for MU to be divided by normal slot and penalty slot, and set a credit for every MU. The credit value is directly influenced by his action during the sensing time. The credit value goes down each time the MU launches attack. Normal slot represents MU can receive a spectrum gain from using free spectrum band because the credit value of MU is high. When the credit value is lower than the threshold T_C , MU is penalized for prohibiting from using the free spectrum band in the penalty slot.

Based on the game model presented before, we now consider PUEA defending as a multistage game. Assume that PU is absent, MU launches attack for every single stage leading the credit value of MU goes from R_0 down to T_C . We denote R_0 as the initial value of credit. In such case, the payoff for MU related with attack is $R_c - c_m + R_f$ during the normal slot. In penalty slot, the MU would suffer a penalty resulting in a

payoff $-R_f$ when the credit value is lower than T_C . The total payoff associated with always attack and always no attack respectively expressed as

$$R_A = (R_c - c_m + R_f)R_0 + (-R_f)\frac{\delta(1 - \delta^K)}{1 - \delta} \tag{11}$$

$$R_{NA} = R_f\left(R_0 + \frac{\delta(1 - \delta^K)}{1 - \delta}\right) \tag{12}$$

The payoff of attack is more than no attack in a single stage of game if $-R_f < R_f < R_c - c_m + R_f$ is satisfied. When it is true, the MU would be willing to launch attack which is the driving force behind. However, from the perspective of competing over a long period, MU is unwilling to attack if $R_A < R_{NA}$ exists because the overall gain attained from no attack is greater. Such that penalize factor K should satisfy the following constraints

$$\frac{\delta(1 - \delta^K)}{1 - \delta} > \frac{(R_c - c_m)R_0}{2R_f}. \tag{13}$$

The larger K is, the more loss is gained due to the long time for prohibited from using the free spectrum band. Thus, no attack is the optimal choice for MU such that more benefits can be obtained by MU with minimum costs. That is, if R_0 is too small, the MU may be penalized mistakenly for making wrong decisions (false alarm and misdetection). If R_0 is too large, the MU still willing to chose attack for the penalty mechanism not working effectively.

4.3 Optimal Strategy Stability Analysis

Since the pure-strategy equilibrium obtained by repeated game would not provide procession for dynamic competition, we introduce the evolution game model and replicated dynamic equation to show the strategies evolution and the stability analysis. Let the PU absent, the total payoff for both players in multistage game as shown in Table 3.

A PUEA is launched while the SU chooses stay the band where it is because SU successfully discriminate PUE from PU. Let the credit threshold T_C be zero. The total payoff regarding to always attack for MU and always stay for SU are respectively shown as

Table 2. Notations

Notation	Explanation
G	Indirect Attack gain for MU due to SU mistakenly interfere with PU
R_f	Gain for MU received from other available spectrum band
c_m	Attack cost
c_s	Switching cost
R_c	Indirect Attack gain for MU for SU consuming energy to discriminating PUEA
δ	Discount value
K	Penalty time
R_0	Initial credit value
T_C	Threshold for credit value

$$R_{A2} = R_A = (R_c - c_m + R_f)R_0 + \sum_{k=1}^K \delta^k (-R_f) \tag{14}$$

$$R_{St1} = GR_0 + \sum_{k=1}^K \delta^k (R - c_s). \tag{15}$$

Under the same circumstance, SU vacated the spectrum band and switch to a different free band as SU mistakes the PUE. Thus, MU attacks successfully resulting in the total payoff for MU is given by

$$R_{A1} = (R_c + G - c_m + R_f)R_0 + \sum_{k=1}^K \delta^k (R_c + G - c_m + R_f). \tag{16}$$

The total payoff for SU relating to stay strategy is given by

$$R_{Sw1} = (-c_s)R_0 + \sum_{k=1}^K \delta^k (-c_s) \tag{17}$$

Table 3. Total payoff matrix of multistage game

PU off	Attack	No attack
Switch	R_{Sw1}, R_{A1}	R_{Sw2}, R_{NA1}
Stay	$R_{St1}, R_{A2},$	R_{St2}, R_{NA2}

In case of no attack happening, SU falsely detects the PUE and chooses switch as the strategy. The total payoff for SU and MU regarding strategic tuples {Switch, No Attack} are given by

$$R_{Sw2} = (-c_s)R_0 + \sum_{k=1}^K \delta^k (-c_s) \tag{18}$$

$$R_{NA1} = R_fR_0 + \sum_{k=1}^K \delta^k R_f. \tag{19}$$

Supposed that no attack occurs, SU correctly detects the PUE and chooses stay the band where the SU is. The total payoff for SU and MU regarding strategic tuples {Stay, No Attack} are given by

$$R_{NA2} = R_{NA} = R_fR_0 + \sum_{k=1}^K \delta^k R_f \tag{20}$$

$$R_{St2} = GR_0 + \sum_{k=1}^K \delta^k G. \tag{21}$$

Let x be the ratio of number of attack to the total stage of repeated game. $1 - x$ denotes the percentage of no attack. Similar, let y be the ratio of number of switch to

the total stage. $1 - y$ denotes the percentage of stay. The expected payoff for switch strategy and stay strategy for SU respectively are expressed by

$$U_{ssw} = xR_{Sw1} + (1 - x)R_{Sw2} \tag{22}$$

$$U_{sst} = xR_{St1} + (1 - x)R_{St2}. \tag{23}$$

The total expected payoff for SU is given by

$$\bar{U}_{SU} = yU_{ssw} + (1 - y)U_{sst}. \tag{24}$$

The replicated dynamic equation for SU is given by

$$F_{SU}(y) = y(U_{ssw} - \bar{U}_{SU}) = y(1 - y)(U_{ssw} - U_{sst}). \tag{25}$$

- (1) When $U_{ssw} = U_{sst}$, any $y \in [0, 1]$ is said to be equilibrium by imposing $F_{SU}(y) = 0$.
- (2) When $U_{MA} \neq U_{MNA}$, from equilibrium $y = 0$ to $y = 1$, only $y^* = 0$ can be determined as evolution stable strategy (ESS), because $F'_{MU}(y = 0) = -(U_{ssw} - U_{sst}) < 0$ exists. For $U_{ssw} < U_{sst}$, we have constraints

$$R_{St1} = R_{St2} > R_{Sw2} = R_{Sw1}. \tag{26}$$

Using the same logic, we derive the expected payoffs for attack strategy and no attack strategy for MU expressed respectively as

$$U_A = yR_{A1} + (1 - y)R_{A2} \tag{27}$$

$$U_{NA} = yR_{NA1} + (1 - y)R_{NA2}. \tag{28}$$

The total expected payoff for MU is given by

$$\bar{U}_{MU} = xU_{MA} + (1 - x)U_{NA}. \tag{29}$$

The replicated dynamic equation for MU is derived as follows:

$$F_{MU}(x) = x(U_A - \bar{U}_{MU}) = x(1 - x)(U_A - U_{NA}). \tag{30}$$

If $U_A = U_{NA}$, any $x \in [0, 1]$ would be equilibrium according to $F_{MU}(x) = 0$. When $U_A \neq U_{NA}$ exists, both $x = 0$ and $x = 1$ are equilibrium. For $y^* = 0$ is ESS proved before, it is obvious that $R_A < R_{NA}$. Thus, we have $U_A < U_{NA}$, and in this case $x^* = 0$ would be ESS.

Based on the ESS analysis of evolution game, we can concluded that no matter what initial state both players are working on, MU and SU will finally choose the optimal strategic tuples {No Attack, Stay} based on the proposed game model.

5 Results and Discussion

5.1 Simulation of CAF Spectrum

We now only consider the case that PU is present who has priority license for the spectrum, SU must vacant the spectrum when PU is returned. We have blurred signal with a Gaussian centered white noise such that the SNR is 10 dB. The sampling rate is 330 Hz. In the Fig. 3(a) and (b), CAF spectrum is shown for estimating duration time and Doppler frequency based on peak detection in the presence of noise. It can be observed that the estimator is a good choice for depicting the composition of the signal and time –Doppler frequency structure for PUE detection.

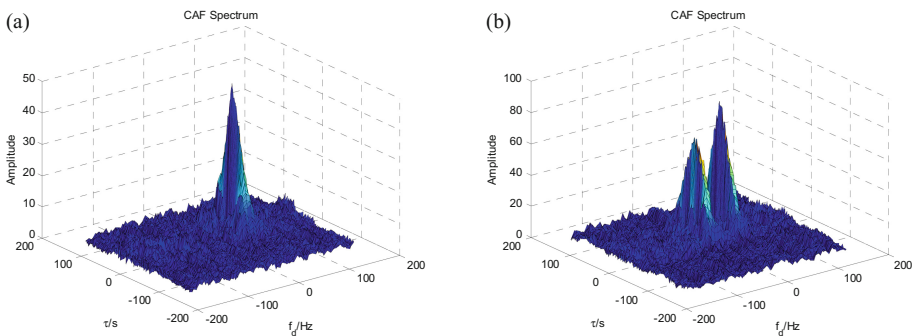


Fig. 3. (a) CAF spectrum for one PU signal ($f_{dP} = 40$, $\tau_S = 15T_s$), (b) CAF spectrum for simultaneous multi-signals ($f_{dP} = 40$, $f_{dM} = -10$, $\tau_S = 20T_s$)

5.2 Simulation for Constant False Alarm Rate (CFAR) Detection

For each value N , the threshold corresponding to every non coherent cumulative spectrum is obtained by the proposed method. In Fig. 4(a), the threshold of the detector increases as N increases. For signals with a Gaussian centered white noise, the threshold can become lower since the SNR is greater as shown in Fig. 4(b).

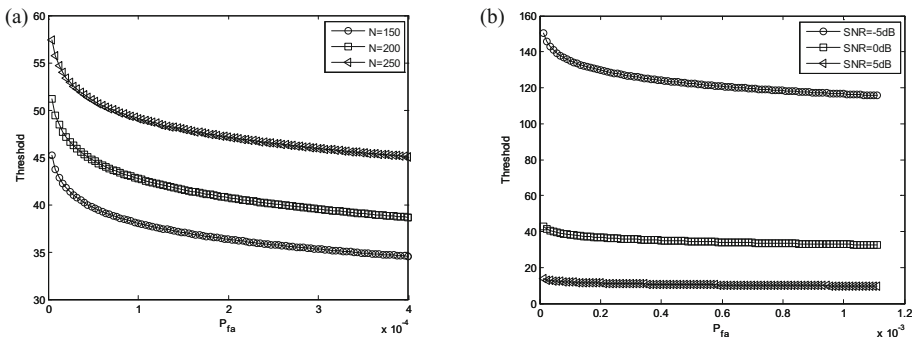


Fig. 4. (a) Threshold estimation versus P_{fa} for selected values of SNR = 0 dB obtained by varying N to take the values: 150, 200, 250, (b) Threshold estimation versus P_{fa} for selected values of $N = 150$ obtained by varying SNR to take the values: -5 dB, 0 dB, 5 dB

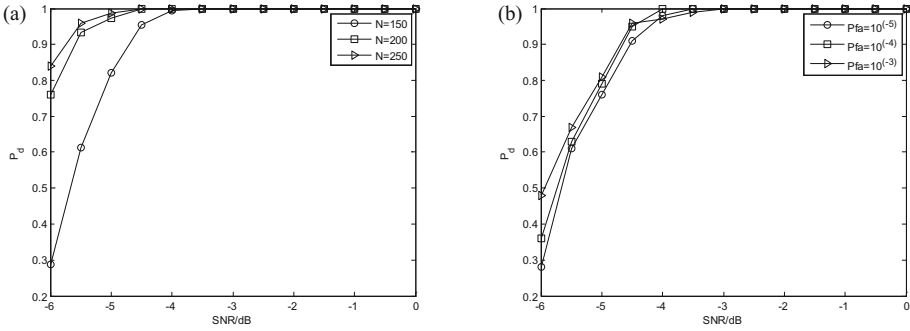


Fig. 5. (a) P_d estimation versus SNR obtained by varying N to take the values: 150, 200, 250, (b) P_d estimation versus SNR for selected values of $N = 150$ obtained by varying P_{fa} to take the values: 10^{-5} , 10^{-4} , 10^{-3}

In Fig. 5, we show the probability of detection as a function of SNR, T and N . We use the system configuration which has different samples N and different T (as different P_{fa}). As can be noticed, the signals are properly detected as the SNR increases. The probability of detection approaches 100% for SNRs above 0 dB.

5.3 Simulation of Repeated Game with Credit Discipline Mechanism

The parameters satisfied for the constraints are: $R_c = 110$, $c_m = 60$, $R_f = 90$, $G = 80$, $c_s = 50$, $R = 100$, $K = 50$, $T_C = 0$. Figure 6 shows the attack probability versus different δ . We observe that the attack probability decreases as δ increases or R_0 decreases although the attacker retards this trend. As the repeated game evolves, we observe that penalty mechanism yields attack probability degradation and slightly better performance in security for the system.

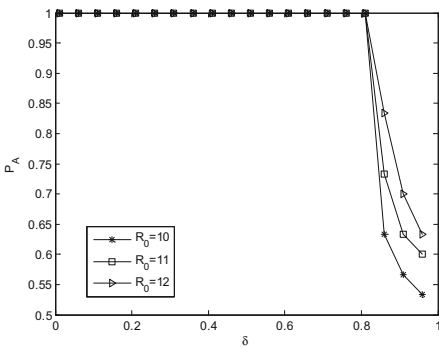


Fig. 6. The distribution of attack probability versus δ obtained by varying R_0 to take the values: 10, 11, 12

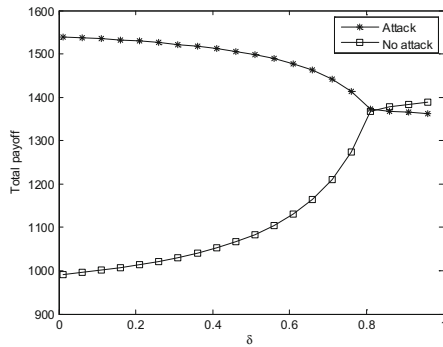


Fig. 7. The respectively total payoffs of MU choosing attack and no attack in one working time

Figure 7 shows the expected payoff of MU with the δ varying between 0 and 1. The curves are plotted corresponding to the procession for dynamic competition. With δ increasing, the payoff of attack is decreasing and no attack is increasing. When δ is above 0.8, MU is willing to choose no attack as optimal strategy instead of attack for $R_{NA} > R_A$ satisfied. And that is corresponding to the point $P_A < 1$ in Fig. 6.

6 Conclusion

PUEA signal emulates the characteristics of PU signal to obtain exclusive spectrum usage, which seriously degrades the performance of cognitive radio systems. Since PUE signal is same with PU signal in time and frequency but in spatial, a detection method based on CAF spectrum received by mobile SU is presented. For thwart PUEA, the optimal strategies for both players are studied. By incorporating credit discipline mechanism, MU would rather choose no attack as dominant strategy than attack by comparing the short payoff with long payoff during the repeated game. Under the circumstance of PU absent, the stability of dominant strategic tuples {No Attack, Stay} for MU and SU is analyzed. Thereby, both players would work in policy-abiding for larger payoffs in the long term. Simulation results show that the method is effective for defense PUEA and the proposed system is proved to have a more efficient and flexible spectrum assignment.

Acknowledgment. This research was supported in part by the Science Foundation of Shaanxi Provincial Education Office (15JK1649).

References

1. Mai, T.V., Molnar, J.A., Rudd, K.: Security vulnerabilities in physical layer of cognitive radio, pp. 1–4 (2011)
2. Baldini, G., Sturman, T., Biswas, A.R., Leschhorn, R.: Security aspects in software defined radio and cognitive radio networks: a survey and a way ahead. *IEEE Commun. Surv. Tutorials* **14**(2), 355–379 (2012)
3. Soto, J., Queiroz, S., Nogueira, M.: Taxonomy, flexibility, and open issues on PUE attack defenses in cognitive radio networks. *IEEE Wirel. Commun.* **20**(6), 59–65 (2013)
4. Rizvi, S., Mitchell, J., Showan, N.: Analysis of security vulnerabilities and threat assessment in Cognitive Radio (CR) networks, pp. 1–6 (2014)
5. Sharma, R.K., Rawat, D.B.: Advances on security threats and countermeasures for cognitive radio networks: a survey. *IEEE Commun. Surv. Tutorials* **17**(2), 1023–1043 (2015)
6. Naqvi, B., Rashid, I., Riaz, F., Aslam, B.: Primary user emulation attack and their mitigation strategies: a survey, pp. 95–100 (2013)
7. Blesa, J., Romero, E., Rozas, A., Araujo, A.: PUE attack detection in CWSNs using anomaly detection techniques. *EURASIP J. Wirel. Commun. Netw.* 1–13 (2013)
8. Jin, Z., Anand, S., Subbalakshmi, K.P.: Performance analysis of dynamic spectrum access networks under primary user emulation attacks, pp. 1–5 (2010)
9. Jin, Z., Anand, S., Subbalakshmi, K.P.: Impact of primary user emulation attacks on dynamic spectrum access networks. *IEEE Trans. Commun.* **60**(9), 2635–2643 (2012)

10. Zhang, C., Yu, R., Zhang, Y.: Performance analysis of primary user emulation attack in cognitive radio networks, pp. 371–376 (2012)
11. Chen, R., Park, J.M.: Ensuring trustworthy spectrum sensing in cognitive radio networks, pp. 110–119 (2006)
12. Chen, R., Park, J.M., Reed, J.H.: Defense against primary user emulation attacks in cognitive radio networks. *IEEE J. Sel. Areas Commun.* **26**(1), 25–37 (2008)
13. Jin, F., Varadharajan, V., Tupakula, U.: Improved detection of primary user emulation attacks in cognitive radio networks, pp. 274–279 (2015)
14. Pu, D., Wyglinski, A.M.: Primary user emulation detection using frequency domain action recognition, pp. 791–796 (2011)
15. Pu, D., Wyglinski, A.M.: Primary-user emulation detection using database-assisted frequency-domain action recognition. *IEEE Trans. Veh. Technol.* **63**(9), 4372–4382 (2014)
16. Xin, C., Song, M.: Detection of PUE attacks in cognitive radio networks based on signal activity pattern. *IEEE Trans. Mob. Comput.* **13**(5), 1022–1034 (2014)
17. Thomas, R.W., Komali, R.S., Borghetti, B.J., Mahonen, P.: A Bayesian game analysis of emulation attacks in dynamic spectrum access networks, pp. 1–11 (2010)
18. Thomas, R.W., Borghetti, B.J., Komali, R.S., Mahonen, P.: Understanding conditions that lead to emulation attacks in dynamic spectrum access. *IEEE Commun. Mag.* **49**(3), 32–37 (2011)
19. Hao, D., Sakurai, K.: A differential game approach to mitigating primary user emulation attacks in cognitive radio networks, pp. 495–502 (2012)
20. Tan, Y., Sengupta, S., Subbalakshmi, K.P.: Primary user emulation attack in dynamic spectrum access networks: a game-theoretic approach. *IET Commun.* **6**(8), 964–973 (2012)
21. Nguyen-Thanh, N., Ciblat, P., Pham, A.T., Nguyen, V.T.: Surveillance strategies against primary user emulation attack in cognitive radio networks. *IEEE Trans. Wirel. Commun.* **14**(9), 4981–4993 (2015)
22. Chen, S., Zeng, K., Mohapatra, P.: Hearing is believing: detecting wireless microphone emulation attacks in white space. *IEEE Trans. Mob. Comput.* **12**(3), 401–411 (2013)



Multi-modal Transmission Strategies with Obstacle Avoidance for Healthcare Applications

Tiong Hoo Lim^(✉)

Universiti Teknologi Brunei, Tungku Highway, Gadong, Brunei Darussalam
lim.tiong.hoo@utb.edu.bn

Abstract. This paper presents a novel energy-efficient MAC Protocol designed for Body Sensor networks (BSN) focusing towards pervasive healthcare applications. BSN nodes are usually attached to the human body to track vital health signs such as body temperature, activity or heart-rate. Unlike traditional wireless sensor networks, the nodes in BSN are not deployed in an adhoc manner. The network connectivity is usually centrally managed and all communications are single-hop. The BSN has to be dependable in order to ensure the availability and reliability of the data received. Hence, it is necessary to reduce energy consumption in order to prolong the operation of the network without frequent outage. It is common to duty cycle the sensor nodes to preserve the battery utilization. However, the communication between the sensing node and receiving node can be interfered by human movement that can lead to energy wastage. In this paper, A Multi-Modal Opportunistic Transmission with Energy Saving (M-MOTES) is proposed. M-MOTES uses the opportunistic transmission approach and the human kinematics to duty-cycling the node. Extensive experiments performed on real hardware show that M-MOTES can reduce the battery power consumption without affecting the packet reliability.

Keywords: Body Sensor Networks · Body shadowing
Multi-hop transmission · Duty cycle · Multimodal

1 Introduction

With the decrease in the cost and miniaturization of these electronic devices and biomedical sensors, it is possible to attach physiological sensing devices on the different body parts to form Body Sensor Networks (BSN). These devices allow non-obtrusive monitoring and capture of the vital health parameters of the human body and its environment in a decentralized manner [1]. Each device is usually consist of one or more sensors attached to or implanted in the human body with a micro-controller, a wireless radio and a power supply. These sensors can capture different physiological parameters such as body temperature, nerve

impulses, ECG, blood pressure, and blood oxygen level. The sensory data collected can be transmitted wirelessly to the medical clinic or hospital for analysis and to monitor the patient's coordination and activity level.

However, a major hurdle for the wide adoption of BSN technology is the potential of service disruption due to radio interference [2] and battery depletion [3]. These sensor nodes usually operate under limited battery supply and in an environment where other medical devices using the same radio frequency that can interfere with the radio communication of between nodes. Communication can also be obstructed due to body part movement especially when BSNs are applied in medical health monitoring system [4]. Experimental work by Lim et al. has shown that radio interference can lead to severe packet drop and packet retransmission by the nodes [2]. As the power consumed during data transmission is higher than the combined power utilizations for both data processing and sensing, it necessary to reduce or eliminate radio communication due to packet retransmission and enable the node to sleep during non-transmission period in order to conserve energy [5]. One approach is through duty cycling. In these schemes, the device wake-ups only when necessary, otherwise it sleeps thereby saving energy. Coordinated and controlled data transmission can reduce energy consumption. Coordinate transmission can be achieved if the human activities can be predicted and the radio transmission cycle can be adapted based on the activity patterns.

In this work, we propose a Multi-Modal Opportunistic Transmission with Energy Saving (M-MOTES) Protocol that uses the opportunistic transmission approach with the ability to toggle between single-hop and multi-hop communication depending on the activities of the users. The main contributions of the paper are:

- We present the system design and implementation of the M-MOTES protocols
- We perform a comprehensive analysis of the proposed protocol.
- We evaluate the packet reliability and energy efficiency of the M-MOTES based on the current measurements.

The rest of this paper is organized as follows. The MOTES is introduced in Sect. 3. In Sect. 4, we describe the experimental setup to analysis the performance of four different transmission protocols with the nodes attached to a student attending one day lecture. The Packet Delivery Rate (PDR) and current measurements are compared and discussed in detail. Section 6 describes the future work and concludes.

2 Related Works

Over the last, a number of previous researches have been proposed to investigate use of wearable sensors for motion analysis, activity classification, and monitoring athletic performance [6, 7]. Sensors devices such as the accelerometer and gyro-meter are usually used to assess the human kinematic and track different activities body movement. Prabh et al. [8] proposes the BANMAC based on

the radio frequency signal fluctuation to schedule for packet transmission. The RF signal fluctuations are measured through the periodic exchange of probing packets in every 12 s. The authors reported that the BANMAC can reduce the packet loss rate (>30%) in comparison to the standard IEEE 802.15.4 MAC protocol. However, the exchange of periodic messages can increase the energy consumption and the computation of the FFT can be time consuming in the BSN node.

The distance and relative antenna orientation between the BSN transmitter and receiver can change periodically during walking and running [9]. As a result, the signal strength in BSN exhibits periodic fluctuations due to obstruction, reducing the probability of a packet being transmitted successfully. To overcome this issue, an Optimistic Medium Access Control (OMAC) has been proposed in [10] to detect the maximum forward foot position and to overcome the transmission failure caused by body parts obstruction during walking. OMAC assumes that the walking stride and paces are similar for all the test participants and a predetermined accelerometer threshold is applied to detect the best transmission period. However, previous work by Barclay et al. [11] has shown that male and female exhibit different walking patterns with different accelerometer readings. As results, the OMAC may miss or unable to detect the transmission window if the walkers have a smaller or dynamic stride.

To support different operating environments, multi-modal approaches are usually applied. Kandukuri et al. [12] investigate novel channel access schemes for packetized wireless networks, which can dynamically switch between specific transmissions modes in order to match the channel state and success delivery rate. They proposed the multimodal dynamic multiple access (MDMA) schemes based on the observed state of the channel and the transmitter queue where each user can autonomously select the best transmission mode and power level to transmit at. In [13], A Multimodal Routing Protocol (MRP) is implemented and evaluated in WSNs to tolerate between different failures. The results have shown the MRP can tolerate failures with different durations. An application-aware event-oriented MAC protocol (App-MAC) to support prioritization, fairness, and reduce energy consumption is proposed in [14]. App-MAC leverages the advantages of contention- and reservation-based medium access control (MAC) protocols to coordinate channel access and propose channel contention and reservation algorithms to adaptively allocate the time slots according to application requirements and current events status.

3 The Multi-modal Opportunistic Transmission with Energy Saving (M-MOTES)

To address the multi-scenario environments, we present the Multi-Modal Opportunistic Transmission with Energy Saving (M-MOTES) that uses the built-in accelerator and the Received Signal Strength Indication (RSSI) measurements to switch between the single-hop and multihop transmission protocol depending on the user activities, and adjust the duty cycle of the transmission protocol accordingly to avoid packet collision.

3.1 M-MOTES Hardware Architecture

The M-MOTES architecture consists of three main components namely: the collector, the sensing nodes and a base node. The collector is used to gather the information send by the sensing nodes. The sensing node is used to capture the sensor reading and store the data temporary in the memory buffer until a sufficient number of readings is collected. Once the minimum threshold is met, the node can begin to determine the operating mode and the best time for transmission. The base node is used to collect the data from the collector. The base node can be in the form of mobile phone or laptop.

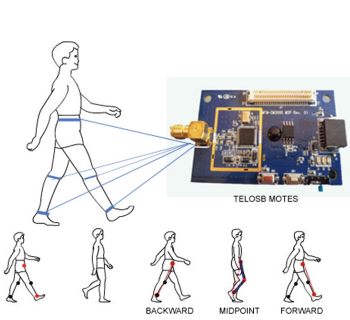


Fig. 1. The placement of the sensing nodes and the collector.

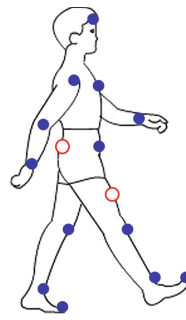


Fig. 2. Suitable node placement to ensure packet delivery

In M-MOTES architecture, it is critical to ensure the sensing node are attached at the right locations to ensure maximum radio signal. Maximum RSSI occurs when there is a direct LoS between the nodes. The node’s placements are usually restricted to the subject’s body parts and the most common locations are the waist, wrist, thigh, ankle and head [6, 7]. We have conducted a preliminary experiment to determine the best location to attach the sensing node in order to achieve maximum packet delivery. Figure 2 shows the good, bad or placement with no significant benefit when communicating with a node placed in the waist. In this work, we will attach the node on the knee, ankle and waist as shown in Fig. 1.

3.2 Algorithm Design

The M-MOTES consists of three modules:

Opportunistic Transmission: It is common to duty cycle the node to reduce the energy consumption. In M-MOTES, each sensing node is designed to operate in two cycles namely: sleep and awake modes. During sleep mode, the energy consumption is the lowest as each sensing node only reads and processes the sensor data and stores them in its buffer with its radio interface is switch off.

The sensing node will continue to be in the sleep mode until the node is ready for transmission. The node will turn its radio on when these two conditions are satisfied:

- When the transmitting queue or buffer is 50% utilization and
- When the GKA is showing the foot is in the forward position.

However, the aggregation node will always keep its radio in the awake mode to ensure that it will not miss any packet transmitted by the sensing nodes. The CSMA/CA is enabled in all the nodes with a maximum of 3 retransmissions.

Multimodal Function: To support multi-modal approach, M-MOTES uses its node’s outgoing transmitting buffer size to toggle between single-hop or multihop communication. The single-hop is initially applied as the node can use its accelerometer and radio signal to determine when there is a direct LoS based on the packet outgoing buffer. Otherwise, M-MOTES switches to a multihop when no direct LoS is available. To toggle between the transmission modes, the sensing node will switch to a specific mode and transmit all the packets in its buffer based on the following conditions:

$$Tx(mode) = \begin{cases} Tx(OTP_{Singlehop}) & \text{If Buffers} \geq 50\% \\ Tx(OTP_{Multihop}) & \text{If Buffers} \geq 75\% \\ Tx(Max_{Singlehop}) & \text{If Buffers} \geq 90\% \\ Tx(Sleep) & \text{Otherwise} \end{cases}$$

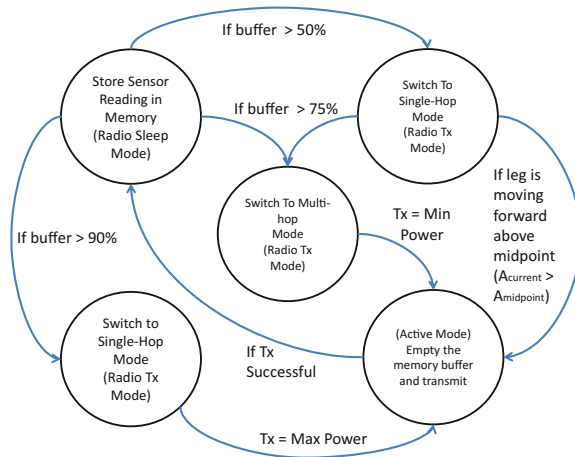


Fig. 3. The state chart representing the different operating modes of M-MOTES

In a typical medical application, the data is usually sensed frequently (every 10ms) [15]. As the variations in the data collected are minimum, it is not necessary to send every data immediately. Instead, each sensing node will store the

data in its buffer and switch to single-hop mode when the data buffer is 50%. By delaying and reducing transmission frequency, it will conserve its battery and switch off its radio. If no direct LoS is available and the buffer reaches 75%, the node will switch to multihop mode. However, it is necessary to install a routing protocol in the node to operating in multi-hop. A static route table is configured in the forwarding node as the physical node position is not moved or changes. Finally, if it is still not possible to send the packet in either modes, the node will increase its transmission power to the maximum and transmit the packets to the aggregation node for up to three retransmission before dropping the packets. The flow diagram for the M-MOTES is shown in Fig. 3.

Gait Kinematic Analysis: To allow transmission in a single-hop mode with minimum transmission power, it is necessary to determine when there is a direct LoS between the foot and the waist. This can be achieved by analyzing the build-in accelerometer and RSSI of the radio. When the foot is at the most forward position, the RSSI value is usually higher and the x-y reading from the accelerometer gives a sine wave. Using these values, the node can detect and transmit its packets in the buffer when the foot is in the most forward position. The transmission period can be determined by each node attached on the foot. As the node will only transmit when the foot is moving forward, packet collision can be avoided as the transmission cycle will alternate between both feet.

4 Evaluation of the M-MOTES

To evaluate the performance of the M-MOTES, we conduct a comprehensive analysis on the performance of M-MOTES against OTP, E-OTP and CSMA/CA on multihop using TelosB motes.

4.1 Experiment Setup

A group of 40 students are selected in mixed gender to perform the experiment over 20 days. Each student is requested to wear the TelosB motes on his or her feet with the aggregation node attached to the waist and four sensing nodes on the knees and ankles. A base station is used to collect the data for the experiments. The sending nodes are configured to transmit at the same power for all the four different transmission protocols and to collect the daily temperature. Each of the temperature data collected is time-stamped and is used to evaluate the reliability of the protocol to provide continuous data.

To ensure that proposed protocol can support different activities, each participant is requested to perform the following tasks: walking, running, climb up the stairs, and doing normal daily activities from 8:00 to 16:30.

5 Results and Discussions

To compare the performance between the four different protocols, a box-and-whiskers plot showing the median and upper and lower quartiles of the PDR is presented in Figs. 4, 5, 6 and 7 for each of the activities conducted. We also performed and showed the statistical test results to measure the statistical and scientific significance of the results using the Conceptual Statistical Test Framework (CSTF) proposed by [16]. Two tests have been applied namely the Rank-Sum and A-Tests. The results from the tests are shown in Table 1. For energy efficient, we computed the current utilization in milli-amp in Table 2.

5.1 Activities: Walking

From Fig. 4, more data packets were received by the aggregation node in a multi-hop network than single-hop network. The maximum PDR for the multihop CSMA/CA and M-MOTES is above 98% compared to single-hop OTP and E-OTP where both is 95%. The M-MOTES has a higher median compared to M-CSMA due to the ability to delay the transmission after the buffer is above 50% utilized. In term of different between the multihop CSMA/CA and M-MOTES, the values computed from the statistical tests have shown that the higher median observed in M-MOTES is not significant and there are differences between M-CSMA and M-MOTES. However, the current consumption for M-MOTES is significantly less than the other three protocols as shown in the Table 2. Hence, it is more energy efficient when it is applied when the users are walking.

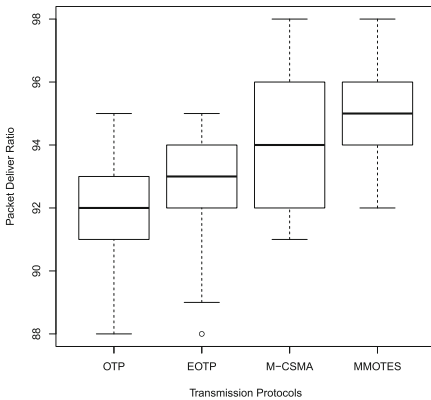


Fig. 4. PDR distributions for walking.

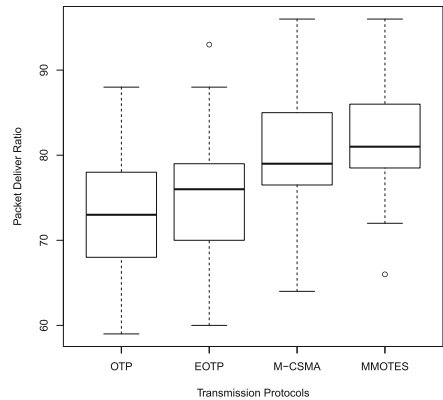


Fig. 5. PDR distributions for running

5.2 Activities: Running

The Boxplot in Fig. 5 shows the performance of multi-hop networks is higher than single-hop networks as the PDR is significantly higher. The median for

running is 82% compared to 95% while walking in M-MOTES. This is due the foot movement in running is more chaotic and faster than walking causing the radio frequency unstable. A higher PDR is also observed in M-MOTES than M-CSMA. However, the statistical tests shows the performance improvement is not significant as the p-test and a-test show values of 0.0743 and 0.6023. To achieve a significance difference, the values have to be ≤ 0.05 for p-test and the a-test should give a value of < 0.29 or > 0.71 . A larger distribution of PDR is also observed for all protocols when running. We believe the larger range of PDR observed is caused by the speed of the foot movement is moving too fast and the aggregation may not be able to receive the packets.

5.3 Activities: Climbing the Stairs

We have tested the transmission protocol to support a more challenging and dynamic movement of climbing the stair. The results presented in Fig. 6 has shown that the M-MOTES can deliver more packet than OTP and EOTP. This is because when the two communicating nodes are always within the line of sight. When compare against M-CSMA/CA, the median for M-MOTES is slight higher than M-CSMA/CA. The statistical tests have shown that the PDR differences between M-CSMA and M-MOTES is statistical significance but not scientifically significance.

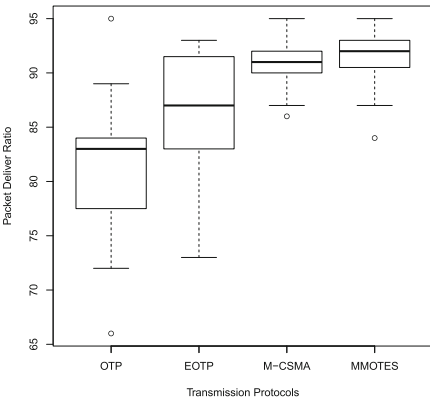


Fig. 6. PDR for climbing stairs

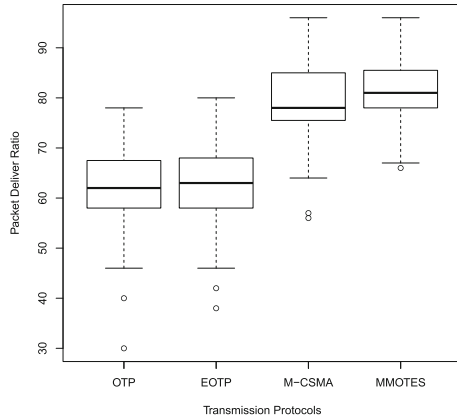


Fig. 7. PDR for normal daily routine

5.4 Activities: Normal Student Activities

For the last set of results, we evaluated the performance of the protocol based on students performing their normal daily activities from the time they come to the university to the time they left the campus. This set of experiments attempt to evaluate the a comprehensive of set of daily activities taken by the students that

includes tea break, lunch break outside campus, driving a car, walking, climbing the stairs, and sitting down attending lectures. The result of these experiments also show the ability of the nodes to provide the information without restricting the participant’s activities.

Table 1. Statistically (P-test) and scientifically (A-test) significant tests on the differences between the transmission protocols

Activities	Walk		Run		Stair		All day	
Protocols	p-test	a-test	p-test	a-test	p-test	a-test	p-test	a-test
OTP:EOTP	0.0012	0.3185	0.1578	0.4189	1.14E-06	0.2254	0.3759	0.4491
OTP:MMOTES	3.57E-12	0.1065	6.15E-07	0.2141	9.11E-17	0.0290	3.09E-14	0.0640
OTP:M-CSMA	1.63E-07	0.2049	4.95E-10	0.1432	5.48E-17	0.0251	1.40E-16	0.0256
EOTP:MMOTES	3.74E-08	0.1884	0.0002	0.2860	0.0003	0.2977	8.05E-14	0.0711
EOTP:M-CSMA	0.0019	0.3239	1.37E-07	0.1980	1.21E-06	0.2261	5.36E-16	0.0348
EOTP:MMOTES	3.74E-08	0.1884	0.0002	0.2860	0.0003	0.2977	8.05E-14	0.0711
M-CSMA:MMOTES	0.0837	0.4018	0.0743	0.6023	0.0094	0.6450	0.0406	0.6175

5.5 Energy Consumption in Term of Current Reading

In term of energy consumption, the average current consumed by the nodes is lower in M-MOTES than the other three protocols. Although both CSMA/CA and M-MOTES use multihop communication, M-MOTES only utilized half the amount of the current in the battery for most of the activities as tabulated in Table 2. This is because the packets are collected and queued until it the buffer is half full. The packets are only transmitted when the foot is in the forward position. Hence, the number of transmissions made in each foot is reduced and the number of packet collisions resulting in a lower energy consumption in M-MOTES.

Table 2. Average current consumption for nodes for 8 h

Activities	OTP	EOTP	M-CSMA	MOTES
Walking	0.711 mA	0.680 mA	0.821 mA	0.347 mA
Running	1.126 mA	0.741 mA	0.845 mA	0.571 mA
Climbing stairs	0.994 mA	0.710 mA	0.882 mA	0.477 mA
Attending classes	3.131 mA	2.540 mA	1.721 mA	0.965 mA

6 Conclusion

In this paper, we have shown that by the transmitting the packets in the multi-hop network, it is much more energy efficient than using single hop network as a

higher transmission power is required to reach the aggregation node. More packets can also be delivered in the multi-hop environment as there is less obstruction created by body movement. By buffering of packets before transmission in M-MOTES, the transmission frequency is reduced. Although the packet transmission duration increases as the number of transmitted packet increase, energy consumption within the nodes reduces. Hence, the proposed M-MOTES is more reliable and energy efficient than traditional CSMA/CA networks. However, as the forward foot position relies on the movement and speed of users, it maybe necessary to adjust the transmission duration to ensure the node stop transmitting when the nodes is moving backward and adjust the minimum buffer size to prevent overflow.

References

1. Yang, G.-Z. (ed.): *Body Sensor Networks*. Springer, London (2014). <https://doi.org/10.1007/978-1-4471-6374-9>
2. Lim, T., Lau, H., Timmis, J., Bate, I.: Immune-inspired self healing in wireless sensor networks. In: Coello Coello, C.A., Greensmith, J., Krasnogor, N., Liò, P., Nicosia, G., Pavone, M. (eds.) *ICARIS 2012*. LNCS, vol. 7597, pp. 42–56. Springer, Heidelberg (2012). https://doi.org/10.1007/978-3-642-33757-4_4
3. Schwiebert, L., Gupta, S., Weinmann, J.: Research challenges in wireless networks of biomedical sensors. In: *Proceedings of the 7th Annual International Conference on Mobile Computing and Networking*, pp. 151–165. ACM (2001)
4. Phunchongharn, P., Hossain, E., Niyato, D., Camorlinga, S.: A cognitive radio system for e-health applications in a hospital environment. *IEEE Wirel. Commun.* **17**(1), 20–28 (2010)
5. Chipcon, A.S.: *CC2420 2.4 GHz IEEE 802.15. 4/ZigBee-ready RF Transceiver Data Sheet (rev. 1.3), Rev. 3* (2011)
6. Bourke, A.K., O'Brien, J.V., Lyons, G.M.: Evaluation of a threshold-based tri-axial accelerometer fall detection algorithm. *Gait Posture* **26**(2), 194–199 (2007)
7. Kangas, M., Konttila, A., Lindgren, P., Winblad, I., Jamsa, T.: Comparison of low-complexity fall detection algorithms for body attached accelerometers. *Gait Posture* **28**(2), 285–291 (2008)
8. Prabh, K., Royo, F., Tennina, S., Olivares, T.: BANMAC: an opportunistic MAC protocol for reliable communications in body area networks. In: *Proceedings of the 8th International Conference on Distributed Computing in Sensor Systems*, pp. 166–175 (2012)
9. Miluzzo, E., Zheng, X., Fodor, K., Campbell, A.T.: Radio characterization of 802.15.4 and its impact on the design of mobile sensor networks. In: Verdone, R. (ed.) *EWSN 2008*. LNCS, vol. 4913, pp. 171–188. Springer, Heidelberg (2008). https://doi.org/10.1007/978-3-540-77690-1_11
10. Lim, T.H., Weng, T., Bate, I.: Optimistic medium access control using gait analysis in body sensor networks. In: *Proceedings of the 5th International Conference on Wireless Mobile Communication and Healthcare*, pp. 1–4, November 2014
11. Barclay, C., Cutting, J., Kozlowski, L.: Temporal and spatial factors in gait perception that influence gender recognition. *Percept. Psychophys.* **23**(2), 145–152 (1978)

12. Kandukuri, S., Bambos, N.: Multimodal dynamic multiple access (MDMA) in wireless packet networks. In: Proceedings of the Twentieth Annual Joint Conference of the IEEE Computer and Communications Societies, vol. 1, pp. 199–208. IEEE (2001)
13. Lim, T., Bate, I., Timmis, J.: Multi-modal routing to tolerate failures. In: Proceedings of the International Conference on Intelligent Sensors, Sensor Networks and Information Processing, pp. 211–216 (2011)
14. Du, J., Shi, W.: App-MAC: an application-aware event-oriented MAC protocol for multimodality wireless sensor networks. *IEEE Trans. Veh. Technol.* **57**(6), 3723–3731 (2008)
15. Vahdatpour, A., Amin, N., Xu, W., Sarrafzadeh, M.: On-body device localization for health and medical monitoring applications. *Pervasive Mob. Comput.* **7**, 746–760 (2011)
16. Lim, T.H., Bate, I., Timmis, J.: Validation of performance data using experimental verification process in wireless sensor network. In: Proceedings of the 17th Conference on Emerging Technologies Factory Automation, pp. 1–8, September 2012



A BP Neural Network Based Self-tuning for QoS Support in AVB Switched Ethernet

Dong Chen and Ang Gao^(✉)

Northwestern Polytechnical University, Xi'an 710027, Shaanxi, China
chendongcharlie@mail.nwpu.edu.cn, gaoang@nwpu.edu.cn

Abstract. To support QoS of time-sensitive services in Ethernet, IEEE has proposed a set of standards for transporting and forwarding real-time content over Ethernet known as Audio Video Bridging (AVB) with bandwidth reservation and priority isolation. AVB traffic is granted highest priority to ensure its transmission while low-priority traffic follows Strict Priority (SP). However, due to restrictions of SP algorithm, low-priority traffic may suffer a problem of starvation. To solve the problem, we propose a BP neural network based self-tuning controller (BPSC) over a probability selector to manage the transmission of best effort (BE) traffic in AVB switched Ethernet. This paper introduces the model of BPSC, followed by a simulation to demonstrate that BPSC could operate effectively and dynamically. The result shows that BPSC not only has the ability to manage the transmission precisely, but also shows both effectiveness and robustness.

Keywords: AVB · BP neural networks · Self-tuning
Machine learning · QoS

1 Introduction

In recent years, digital audio and video transmitted through Ethernet is increasing rapidly as the process of audio and video becomes a fundamental technology in many fields, laying a higher demand on network system. With high bandwidth, high flexibility and low cost, switched Ethernet Network has become a satisfying solution for transmission. In order to adapt audio and video data onto Ethernet Network, AVB technology was introduced. An AVB network implements a set of protocols developed by IEEE 802.1 Audio/Video Bridging Task Group (AVB TG). The core protocols include an Audio Video Bridging system (IEEE 803.2BA), timing and synchronization for time-sensitive applications (IEEE 802.1AS), stream reservation protocol (IEEE 802.1Qat) and forwarding and queuing for time-sensitive streams (IEEE 802.1Qav).

IEEE 802.1Qav standard introduced a specific mechanism to ensure the real-time audio/video transmission that is highly time-sensitive. The principle is to separate the network traffic into different classes, each with their respective

priority. There would be a portion of bandwidth reserved for AVB traffic, while other classes obey the rule of best effort transmission by appending traffic of each class into respective FIFO queue and generally being scheduled by a selector. 802.1Qav supports 2 selection algorithms in a switched Ethernet network: Credit Based Shaper (CBS) and Strict Priority (SP). CBS algorithm uses a token to manage the transmission by allowing only the queue that gets the token from the token bucket to transmit data for a limited length, while SP algorithm only transmits data from the queue that has (1) frames to transmit and (2) the highest priority among all queues that have frames to transmit at the same time.

AVB has become a research focus recently. Paper [1] purposed to use a new mechanism to reduce the guard band by accurately calculating the size of frame that can preempted. Paper [2–4] worked on analysis of worst-case scenarios of AVB network for multiple applications. However, most of these papers focused on resource reservation and the transmission of AVB traffic, while BE traffic not taken into consideration. Typically, SP algorithm is used for BE transmission, and networks exploiting SP are very likely to encounter starvation of low-priority traffic in which traffics with very low priority are not granted enough resources for transmission while high-priority traffics are allocated too much resources. In practice, there does exist situations that low-priority frames has little chance to transmit because high-priority queues have sustaining frames to transmit.

In this paper, we propose a probability selection model for non-AVB classes transmission based on a BP neural network controller to replace typical SP algorithm. This BP neural network based controller shows a ability to adjust the system dynamically and robustness for different traffic environment. It enables high-priority frames to transmit with less delay, while low-priority frames still have a chance to send so that over-sacrifice of them can be prevented.

2 BPSC Architecture

2.1 System Modeling

Suppose there are I classes of BE traffics in AVB switched Ethernet, each with a priority parameter δ set by upper layer protocol indicating the priority. The goal of the controller is to maintain all parameters to meet Eq. 1:

$$\frac{\zeta_i}{\zeta_j} = \frac{\delta_i}{\delta_j}, i, j = 1, 2, \dots, I \quad (1)$$

where ζ_i is the measured average queuing delay of class i . Apparently, class with a smaller δ would expect a lower delay and thus a higher priority. Moreover, the proportional relationships can be simplified by setting ζ_1 as the standardization factor, thereby we can obtain the condition illustrated in Eq. 2:

$$y_i = \frac{\zeta_i}{\zeta_1} = \frac{\delta_i}{\delta_1}, i = 2, 3, \dots, I \quad (2)$$

where y_i is defined as desired relative index (RI) for each class to maintain. Note that this equation illustrates that there are $I - 1$ independent constraints for this

system. As for the selector, we define the probability of transmission p_i for class i at the k^{th} sample period. The probabilities of all class obey the constraint in Eq. 3:

$$\sum_{i=1}^I p_i(k) = 1 \text{ for all } k \tag{3}$$

This enables frames in high-priority classes to have a relative small delay, while frame in low-priority classes still have a chance to transmit as long as $p_i(k) > 0$. Due to nonlinearity between selector probability and the delay, the probability cannot be settled based on desired relative index only: frame arriving rate and the throughput should be considered.

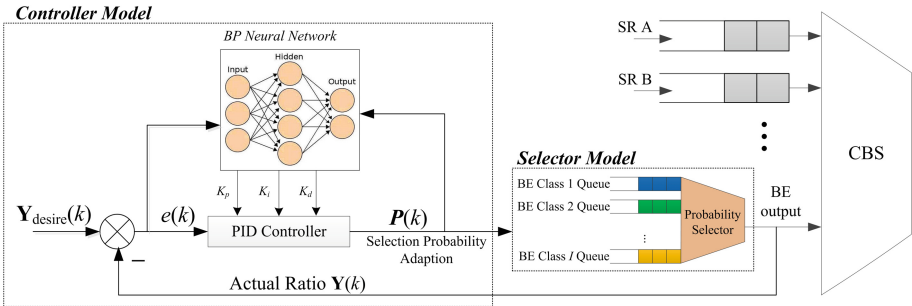


Fig. 1. System model of BPSC

Figure 1 shows our model of BPSC. It is composed of 2 parts: a selector model and a controller model. As for the selector, the input is a probability vector with $I - 1$ independent variables used for next sample period while the output is the measured RI, $Y(k)$, of this sample period. This measured RI, together with the preset desired RI, $Y_{\text{desire}}(k)$, are sent into the controller as its input. The controller will adjust its BP neural network accordingly so that all parameters will automatically change to a suitable value. And then, controller computes $P(k)$, the update of selection probability for next sample period, and sends it to selector.

By implementing this model, the measured RI is expected to adjust dynamically in accordance with frame arriving rate, and such a feedback mechanism could maintain the stability of the system so that the uncertainty of traffic flow can be well handled.

2.2 Core of BPSC: BP Neural Network

Artificial Neural network (ANN or NN) has been widely used in many disciplines including robotics, recognition and computer vision. It is a computational model simulating human being’s neural network to solve problems in the similar way as a human.expressrelationship because of its nonlinearity. The basic element of

NN is the single recurrent neuron which adds all its input with different and variant weight, as well as the threshold, as its primary output:

$$S_j(k) = \frac{1}{2} \sum_{i=1}^N w_i x_i - \theta_j \tag{4}$$

and then the $S_j(k)$ is taken to the activation function, the result being exported:

$$f_j(k) = f(S_j(k)) \tag{5}$$

In Eqs. 4 and 5, j denotes the label of the neuron, N is the total number of neuron’s input, w is the weight foreach input, θ is the threshold and f is the activation function of the neuron. The common activation functions in practice include sigmoid, hyper tangent and Rectified Liner Units (ReLu) (Fig. 2).

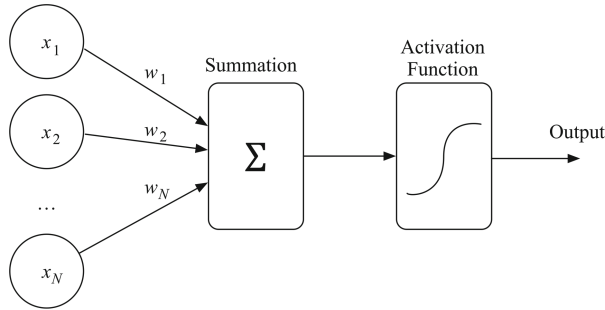


Fig. 2. The model of a neuron

A simpler representation of Eq. 4 is to combine inputs and delayed outputs together as the input of a single neuron, i.e.,

$$S(k) = \mathbf{W}^T \mathbf{X} \tag{6}$$

where

$$\mathbf{X} = \begin{bmatrix} x_1 \\ x_2 \\ \vdots \\ x_N \end{bmatrix}, \mathbf{W} = \begin{bmatrix} w_1 \\ w_2 \\ \vdots \\ w_N \end{bmatrix}$$

With multiple neurons in different layer, a network can be established. In a typical neural network, an input layer and a output layer are necessary. Each layer would contain one or more neurons, which enables parallel computing. A simple way of supervised learning to use NN is to feed the network with abundant datum, each with a label indicating the desired output. Then the NN uses optimization algorithm to approach the labels as close as possible. This

whole process is called training. After training (and validation, in most cases, to check if NN after training operates as we expect), all parameters in the NN will be settled and we can feed the NN with raw data and use its output for further work. However, in real network environment, most channel parameters such as channel quality and speed rate are time-varying and thus a pre-trained NN cannot fully satisfy our requirement.

BP neural network is a commonly used algorithm based on error back propagation algorithm of multilayer feedforward neural network. A typical BP neural network contains not only the input and output layer, but one or more hidden layer to process the data. The whole process starts from the input layer that spread the input data to hidden layer, then the hidden layer would put the summation from input layer to the activation function, and finally the output layer would collect the output of hidden layer to form the output of the system. Though there is no upper limit of layers, in this paper we propose to use only 3 layers, the first and the last being the input and output layer respectively, while second one being the hidden layer. This is because a 3-layer neural network is able to learn any function theoretically [6], and the computation amount would increase exponentially as more hidden layers are added. The BP neural network implemented in our system is shown in Fig. 3.

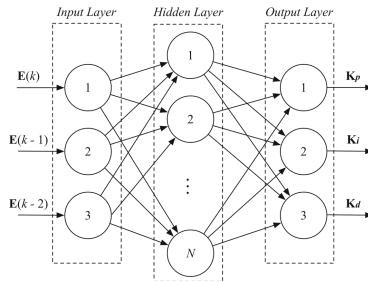


Fig. 3. BP neural network model

$\mathbf{E}(k)$ is the error between the desired RI and the measured RI of class i to class 1, i.e.,

$$\mathbf{E}(k) = \mathbf{Y}(k) - \mathbf{Y}_{\text{desire}}(k) \tag{7}$$

$\mathbf{K}_p, \mathbf{K}_i, \mathbf{K}_d$ are self-tuning coefficient vectors with $I - 1$ elements each, and N is the number of neurons in hidden layer.

The BP neural network calculates the self-tuning coefficients based on pre-trained weights, and at the same time, is trained with data from last sample period by back propagating the error to weights. Therefore, the network is able to handle a system with dynamic traffic arriving rate by adapting the selector accordingly.

Assume that the numbers of neurons in these layer are n_1, n_2 and n_3 respectively. When an example used for training is obtained, the first process is forwarding, which requires 2 matrix multiplications, and the computation amount

is $n_1 * n_2 + n_2 * n_3$. Since n_1 and n_3 are determined by the problem while n_2 is set by users, the time complexity is $O(n^2)$ given that time complexity for each neuron is $O(1)$. The second process, back propagation, has a similar computation amount as forwarding. Therefore, the time complexity of training BP neural network is $O(n_2)$.

2.3 Model Algorithm

Table 1 shows the process of complete BE transmission system, including BPSC and possibility selector model.

Table 1. Algorithm of selector with BPSC

Step 1	Initialize: $P(0) \leftarrow [\frac{1}{T}, \frac{1}{T}, \dots, \frac{1}{T}]^T$; $w_{ij} \leftarrow$ for all i, j ; $k \leftarrow 0$
Step 2	Set $\mathbf{Y}_{\text{desire}}$ as required and learning rate η for NN
Step 3	Check the queues of all classes, use an indicator vector \mathbf{A} to record if there is traffic, i.e., $A_i = \begin{cases} 0 & \text{if class } i \text{ has frame(s)} \\ 1 & \text{if class } i \text{ has no frame} \end{cases}$
Step 4	$M \leftarrow \mathbf{A}^T \mathbf{P}$
Step 5	Generate a pseudorandom number m that obeys uniform distribution in the range of $(0, M)$
Step 6	Decide that frame in class i to transmit if $A(i) = 1$ and $m \in (p_i \text{ lower}, p_i \text{ upper})$, where $p_i \text{ lower} = \sum_{j=1}^{i-1} p_j$ and $p_i \text{ upper} = \sum_{j=1}^i p_j$
Step 7	Transmit the frame selected in step 6 and collect its delay: $D_i = D_i + d, R_i = R_i + 1$ where i is the class of frame, \mathbf{D} is a vector that saves the summation of each class's delay, d is the delay of the frame transmitted and \mathbf{R} is a vector that saves the total number of frames transmitted in this sample period
Step 8	After transmission, if current sample period is not expired, go to step 3, else goto step 9
Step 9	$\zeta_i(k) \leftarrow \frac{D_i(k)}{R_i(k)}, Y_i(k) \leftarrow \frac{\zeta_i(k)}{\zeta_i(k)}$
Step 10	Feed NN with $\mathbf{Y}(k), \mathbf{Y}_{\text{desire}}(k), \mathbf{E}(k) \leftarrow \mathbf{Y}_{\text{desire}}(k) - \mathbf{Y}(k)$
Step 11	NN forward: obtain self-tuning parameters with NN
Step 12	Update possibility vector $\mathbf{P}(k+1)$ with self-tuning parameters
Step 13	NN error back propagation: update w_{ij} in negative gradient direction with learning rate η
Step 14	$k \leftarrow k + 1$
Step 15	Go to step 3 and continue transmission

3 Experiments and Results

3.1 Configuration

An software simulation is taken to test our BPSC for frame forwarding in AVB switched Ethernet. In our simulation, the total output bandwidth of switcher is 50 Mbps, 60% of which is allocated for frame transmission of AVB frames. Besides AVB traffics, there are other 4 kinds of BE traffics marked class 1, 2, 3 and 4 in the order of descending priority. Due to the fact that bandwidth reservation strictly isolates the transmission of AVB and BE, the following analysis focuses on the transmission of BE.

The interval of each frame arriving at the queue for each class obeys Gaussian distribution with $\sigma_i = 1/v_i$, where i is the label of class and v denotes the expected frame arriving rate. Meanwhile, the length of each frame obeys Pareto distribution with an average of 400 bytes.

In our simulation, we set $\mathbf{Y}_{\text{desire}}(k) = [1.3, 1.4, 1.7]^T$ for all k and we run dynamic and static test separately. By running a dynamic test we would like to observe how BPSC deals with burst change of communication environment; with a static test we hope to see if BPSC could manage the transmission to meet our requirement, i.e., desired RI.

3.2 Dynamic Performance

To illustrate how BPSC operates in changing environment, and to make the comparison between BPSC with existing algorithm, we exploit an off-and-then-on mechanism by dividing the whole simulation into 5 consecutive stages, in which the details of each stage are listed in Table 2.

Table 2. Simulation details of 5 stages

Stage	Arriving rate of class 1 (fps)	Arriving rate of class 4 (fps)	Arriving rate of class 2 & 3 (fps)	Selector algorithm	Controller online or not	Length of this stage (second)
1	1100	1100	1100	SP	N/A	100
2	1100	1100	1100	Possibility selector	N	100
3	1100	1100	1100	Possibility selector	Y	100
4	1600	600	1100	Possibility selector	Y	100
5	600	1600	1100	Possibility selector	Y	100

The frame arriving rate at the queue is shown in Fig. 4(a), while Fig. 4(b) and (c) shows the mean delay and RI of each class respectively.

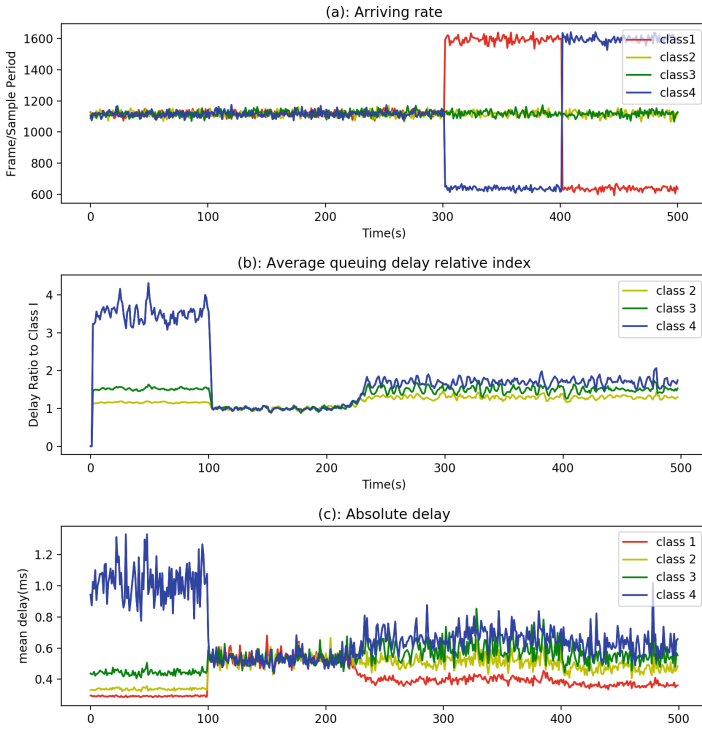


Fig. 4. Result of dynamic test

1. In the first stage (0–99 s), the mean delay of class 1 to 3 traffic is much shorter than class 4 traffic. This indicates that SP algorithm, though it could manage the transmission of traffic with different priority, may have the problem of over-sacrifice.
2. In the second stage (100–199 s) when possibility model is applied, the mean delay of each class traffic quickly stabilized and the measured RI is fluctuating around 1, showing that our possibility selection model could quickly stabilize the system.
3. Our controller is launched in the third stage (200–299 s), after 100 s of simulation. The controller takes about 20–30 s before its stabilization. After that, the measured RIs fluctuate slightly around the desired RI due to randomness of traffic. However, compared with first stage, our controller well manages the fluctuation in a smaller degree and maintains desired RIs.
4. In the fourth stage (300–399 s), the increase of frames in class 1 and decrease in class 4 make RI of class 2, 3 and 4 go up, especially class 4. A big fluctuation at the beginning of stage 2. But this situation settled very quickly. Similarly, in the last stage (400–499 s) all classes of traffic suffered an drop of RIs but being controlled quickly.

During the whole process, contingency of the length and interval of frames may disturb our system but our system shows robustness by adjusting itself dynamically and controlling the probability accordingly. Furthermore, by comparing the first and third stage, we can observe a better performance due to the implementation of our controller in respective of fluctuation, absolute delay and RI.

3.3 Static Performance

To evaluate the static performance of our controller, we collect the data of delay when the system turns stable with varying arriving rate which changes between 1100 and 1500 fps for each class. We first run the simulation using SP algorithm, then BPSC. The result of each controller is shown in Figs. 5 and 6 respectively.

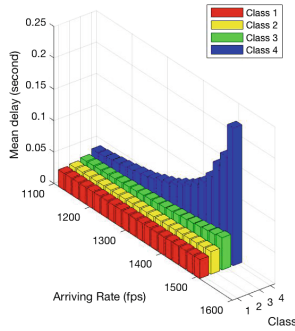


Fig. 5. Relation of delay and frame arriving rate using SP algorithm

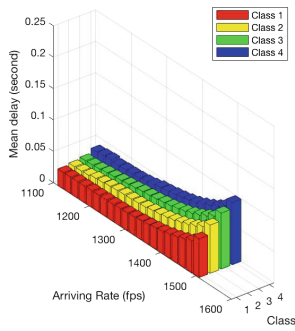


Fig. 6. Relation of delay and frame arriving rate using BPSC

1. As we can see in Fig. 5, when we are using SP algorithm for traffic management, it is inevitable that low-priority traffic has the problem of starvation as arriving rate increases while traffic with high priority barely increase their delay.
2. As shown in Fig. 6, when arriving rate is relatively low, system using BPSC cannot fulfill the desired RI. This is because the low arriving rate creates a situation such that frames arriving at the queue would be transmitted immediately: in most cases there is no other frames being transmitted.
3. However, frame in low-priority class still has a higher mean delay, and as the arriving rate increases, delays of 4 classes all increase at different speeds, suggesting that BPSC could manage to adjust the system to work as expected.
4. Since congestion control is not covered in this paper, the output data rate should always be larger than the frame arriving rate, which restricts the growth of input data rate. Nevertheless, this comparison illustrate that BPSC could control the traffic precisely without wasting throughput.

4 Conclusion

Our paper provides a new approach to support QoS for BE traffic in AVB switched ethernet by exploiting a BP neural network based self-tuning controller. As AVB technology developing rapidly, it is expected to be implemented in typical Ethernet to enable further management of traffic control. The controller we purpose in this paper, BPSC, is capable to manage the BE traffic in AVB switched ethernet. It could not only provide QoS service, but also maintain mean delay of each class that satisfies desired RI without reduction of throughput. Furthermore, in our simulation, BPSC shows its effectiveness and robustness, as well as the ability to prevent over-sacrifice problem that commonly happens using SP algorithm. Therefore, such BPSC has a great advantage over typical SP algorithm and could be implemented for BE traffic management.

Acknowledgments. This work was supported by the Natural Science Basic Research Plan in Shaanxi Province of China under Grant 2016JM6062, in part by the Aerospace Science and Technology Innovation Fund of China Aerospace Science and Technology Corporation, and in part by the Shanghai Aerospace Science and Technology Innovation Fund under Grant SAST2016034 and the China Fundamental Research Funds for the Central Universities under Grant No. 3102017ZY029.


References

1. Wang, Y., Shen, H., Duan, D.: On stabilization of quantized sampled-data neural-network-based control systems. *IEEE Trans. Cybern.* **PP**(99), 1–12 (2017)
2. Cao, J., Cuijpers, P.J.L., Bril, R.J., Lukkien, J.J.: Tight worst-case response-time analysis for ethernet AVB using eligible intervals. In: 12th IEEE World Conference on Factory Communication Systems, WFCS 2016, 3–6 May 2016, Aveiro, Portugal (2016)

3. Park, J.-D., Cheoun, B.-M., Jeon, J.-W.: Worst-case analysis of ethernet AVB in automotive system. In: 2015 IEEE International Conference on Information and Automation, ICIA 2015 - In Conjunction with 2015 IEEE International Conference on Automation and Logistics, 8–10 August 2015, Yunnan, China (2015)
4. Diemer, J., Rox, J., Ernst, R., Chen, F., Kremer, K.-T., Richter, K.: Exploring the worst-case timing of ethernet AVB for industrial applications. In: 38th Annual Conference on IEEE Industrial Electronics Society, IECON 2012, 25–28 October 2012, Montreal, QC, Canada (2012)
5. Liang, J., Qu, Y.: Intelligent Control Technology. Harbin Institute of Technology Press, Harbin (2016)
6. Funahashi, K.: On the approximate realization of continuous mappings by neural networks. *Neural Netw.* **2**(3), 183–192 (1989)
7. Gao, A., Hu, Y., Li, L., Li, X.: A feedback based probability selection for frame forwarding in AVB switched ethernet. In: 4th International Conference on Information Systems and Computing Technology (2016)
8. IEEE Standard for Local and Metropolitan Area Networks-Timing and Synchronization for Time- Sensitive Applications in Bridged Local Area Networks, IEEE Std 802.1As, November 2010
9. IEEE Standard for Local and Metropolitan Area Networks, Virtual Bridged Local Area Networks, Amendment 14, IEEE Std 802.1Qat, September 2010
10. IEEE Standard for Local and Metropolitan Area Networks, Virtual Bridged Local Area Networks, Amendment 12: Forwarding and Queuing Enhancements for Time-Sensitive Streams, IEEE Std 802.1Qav, January 2010
11. Diemer, J., Rox, J., Ernst, R.: Modeling of ethernet AVB networks for worst-case timing analysis. *Math. Model.* **45**(1), 848–853 (2012)
12. Zhang, X.Y., Gao, P.J., Liu, Y.: The researching and simulation of BP neural network PID controller in industrys control system. *Tech. Autom. Appl.* **37**, 9–12 (2010)
13. Diemer, J., Thiele, D., Ernst, R.: Formal worst-case timing analysis of ethernet topologies with strict-priority and AVB switching. In: International Symposium on Industrial Embedded Systems (2012)
14. Lim, H.T., Herrscher, D., Chaari, F.: Performance comparison of IEEE 802.1Q and IEEE 802.1 AVB in an ethernet-based in-vehicle network. In: International Conference on Computing Technology and Information Management (2012)
15. Alhwaide, A.A.Z., Doulat, A.S., Khamayseh, Y.M.: Performance evaluation of different scheduling algorithms in WiMAX. *Int. J. Comput. Sci. Eng. Appl.* **1**(5), 81 (2011)
16. Lee, H., Lee, J., Park, C., Park, S.: Time-aware preemption to enhance the performance of audio/video bridging (AVB) in IEEE 802.1 TSN. In: IEEE International Conference on Computer Communication and the Internet. IEEE (2016)
17. Wang, T., Gao, H., Qiu, J.: A combined adaptive neural network and nonlinear model predictive control for multirate networked industrial process control. *IEEE Trans. Neural Netw. Learn. Syst.* **27**(2), 416–425 (2016)



Optimal Power Splitting in a Full-Duplex Wireless Powered Network with a Bidirectional Relay

Yingting Liu¹ , Hongwu Yang¹, Chunman Yan¹, and Li Cong²

¹ The College of Physics and Electronic Engineering,
Northwest Normal University, No. 967 Anning East Road, Lanzhou, China
{ytl, yanghw}@nwnu.edu.cn, yancha02@163.com

² The Information and Communication Company,
Jilin Electric Power Company Limited, Baishan, China
congli8462@163.com

Abstract. This paper studies the optimal power splitting strategy in a full-duplex wireless powered communication network (WPCN). This wireless powered network contains three nodes, which are the access point (AP), the relay node (R) and the user. We divide the communication process into two phases that each one has the same duration time. The AP transmits the energy to the relay node and the user, and the user transmits the information to the relay node and the AP simultaneously in the first phase. In the second phase, R relays the energy to the user and simultaneously decodes the information and forwards the information signal to the AP. We study how R splits its harvested energy into two parts separately for energy harvesting (EH) and information forwarding, respectively, to maximize the achievable information rate from the user to the AP, when a direct link between AP and the user exists or does not. We get the mathematical results of optimal power splitting factor in two models. Numerical results show that the variation trend of the maximum achievable rate with the distance between the AP and R, and the rate with direct link is not always larger than the rate without direct link.

Keywords: Wireless powered communication network · Energy harvesting
Full-duplex · Power splitting · Relay

1 Introduction

In conventional wireless networks, concluding sensor networks and cellular networks, wireless devices are usually powered by replaceable or rechargeable batteries, therefore the operation time of these systems are usually limited since the battery power is always limited [1, 2]. In recent years, energy harvesting (EH) becomes an attractive

Y. Liu—This work was supported by the National Natural Science Foundation of China (Grant Nos. 11664036 and 61741119) and the Fundamental Research Funds for the Universities of Gansu Province.

approach to take the place of conventional wireless networks since the lifetime of the system using the EH technology is theoretically infinite [1–4]. The communication system which uses energy harvesting technology has the potential to provide a perpetual power supply via harvesting the energy from radiated wireless signal in the surrounding environment [5]. Current wireless power transfer (WPT) technology can effectively transfer tens of microwatts of radio frequency (RF) power to destination node from a distance of more than 10 m [6]. For the above reasons, wireless powered communication networks (WPCNs), in which wireless devices are powered only by WPT, is currently a hot research topic.

The authors developed a noncoherent simultaneous wireless information and power transfer (SWIPT) framework for energy harvesting relay networks, in which relay nodes are operated in decode-and-forward (DF) mode [7] and amplify-and-forward (AF) mode [8], respectively.

In [9], the authors proposed a protocol termed “harvest-then-transmit” for the WPCN, where the hybrid access point (H-AP) first broadcasts wireless energy to all users in the downlink (DL), and then the users transmit their independent information to the H-AP in the uplink (UL) using their individually harvested energy by time-division-multiple-access (TDMA). In [10], the authors studied user cooperation in the WPCN for throughput optimization. In [11], the authors first investigated the bidirectional wireless information and power relaying by the relay node in the WPCN in published papers. The relay node operated in the AF mode simultaneously needs to serve dual roles in the second phase, one is energy relaying in the DL from the AP to the user and another is information relaying in the UL from the user to the AP. They proposed two practical protocols for the considered system based on the power splitting (PS) and time switching (TS) strategies at the relay for maximizing the achievable information rate from the user to the AP. But in [11], the authors have ignored the direct link between the user and the AP both in the information transmission and energy transmission.

In this paper, we consider how the relay node splits harvested energy to maximize the achievable information rate from the user to the AP when the direct link between the user and the AP exists or does not on the basis of [11]. The relay node adopts the decode-and-forward instead of the amplify-and-forward depicted in [11].

2 System Model

As shown in Fig. 1, we consider a WPCN in which the user sends information to the AP via a helping relay **R**. It is assumed that both the user and **R** are only powered by energy harvested from the RF signal radiated by the AP. The AP is assumed to have a

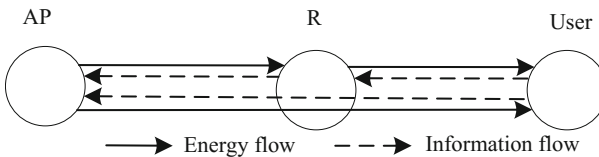


Fig. 1. Bidirectional wireless information and power transfer.

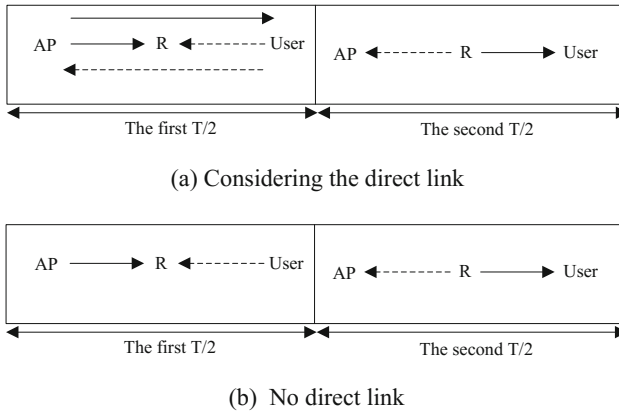


Fig. 2. The energy and information transmission process when the direct link exists or does not.

stable energy supply. It is defined that energy flowing direction is the DL and information direction is the UL and are denoted by the solid line and dashed line depicted in Fig. 1, respectively. \mathbf{R} has the double roles including energy and information relaying in the DL (from the AP to the user) and UL (from the user to the AP), respectively.

The whole transmission is divided into two equal duration phases each denoted by $T/2$ with T denoting the block length. The WPCN is operated in dual-duplex mode when we consider the direct link between the AP and the user. In this mode, the AP sends the RF energy signal to the user and \mathbf{R} and receives the information signal from the user at the same band in the first phase, and the user receives the energy signal from the AP and sends the information signal to \mathbf{R} and the AP simultaneously as shown in Fig. 2(a). In the second phase, \mathbf{R} relays the energy signal to the user and decodes the information then sends it to the AP simultaneously. The AP and the user only receive the information signal and the energy signal, respectively. It is also worth pointing out that the full-duplex concept is simultaneous DL and UL information transmission in the conventional communication system, but in our paper it refers to the simultaneous DL energy transfer and the UL information transmission. Every node equipped with two antennas that one is used for information transfer and another is used for energy transfer, respectively [2].

For full-duplex systems, the self-interference (SI) from the transmitting antenna to the receiving antenna is an important issue. Digital cancellation and analog cancellation can reduce the SI to a negligible level or noise level if the receiving antenna has a good estimate of the transmitted signal [12–15]. So the SI can be easily handled by using existing digital or analog cancellation techniques. For this reason, we assume perfect self-interference cancellation between the two antennas in this paper as in [2, 16].

If ignored the direct link between the AP and the user, the WPCN is operated in half-duplex mode as shown in Fig. 2(b). In the first phase, the AP transmits the energy signal to the user and \mathbf{R} , the user simultaneously transmits the information signal to \mathbf{R} . \mathbf{R} relays the information and energy signal to the AP and the user using different antenna,

and the user and the AP receive the energy and information signal in the second phase, respectively. So in half-duplex mode the user and the AP both have one antenna.

In both modes it is assumed that perfect channel state information (CSI) is available at \mathbf{R} , our objective is maximize the information rate from the user to the AP by ensuring that the energy consumed at both the user and \mathbf{R} does not exceed the harvested energy. For simplicity, we assume that the circuit and signal processing power consumption are negligible as compared to the radiation power, which could be the case for energy-efficient wireless devices (such as wireless sensors, tags, etc.) with simple electronics and low signal processing requirement. Furthermore, we assume that both \mathbf{R} and the user are equipped with a battery with sufficiently large initial energy. Therefore, signal transmission could be initialized before energy harvesting by using the existing energy stored in the battery without violating the energy-causality constraint [11].

3 Power Splitting Scheme in Different Situation

In this section, we derive the maximum achievable rate from the user and the AP when the direct link exists or does not.

3.1 The Direct Link into Consideration

When a direct link between the user and the AP exists, \mathbf{R} uses two directional antennas respectively pointing to the user and the AP, that one is used for the energy and information transmission to the AP and another is used for the energy and information transfer to the user. As described in Sect. 2, the signal received at \mathbf{R} during the first phase is thus given by

$$\begin{aligned} y_{ra}^1 &= \sqrt{P_a}hx_a + n_r \quad (a) \\ y_{ru}^1 &= \sqrt{P_u}gx_u + n_r \quad (b), \end{aligned} \quad (1)$$

where y_{ra}^1 and y_{ru}^1 represent the energy signal and the information signal received by \mathbf{R} at each antenna, which are sent by the AP and the user, respectively. P_a and P_u denote the transmit power of the AP and the user, respectively. h and g represent the channel gain coefficients from the AP and the user to \mathbf{R} , respectively. We assume channel reciprocity so that the DL and UL have the identical channel gain. It is assumed that both the DL and UL channels are quasi-static flat-fading, where channel coefficients remain constant during each block transmission. n_r denotes the additive white Gaussian noise received at \mathbf{R} ; x_a and x_u denote the energy and information signals sent by the AP and the user, respectively. We assume that x_a is a unit-power deterministic signal that is known to \mathbf{R} and the user, whereas x_u is a random signal following zero-mean unit-variance circularly symmetric complex Gaussian (CSCG) distribution, denoted as $x_u \sim CN(0, 1)$.

The signals received by the user and the AP in the first phase are given by the Eqs. (2) and (3).

$$y_u^1 = \sqrt{P_a}lx_a + n_u \quad (2)$$

$$y_{AP}^1 = \sqrt{P_u}lx_u + n_{AP} \quad (3)$$

l denotes the channel coefficient from the AP and the user. n_u and n_{AP} denote additive white Gaussian noise received at the user and the AP, respectively. P_u is connected with the sum of harvested energy in the first phase from the AP and in the second phase from \mathbf{R} , which expression is shown in the Eq. (9).

Considering $P_u \ll P_a$ in practice, \mathbf{R} only harvests energy from y_{ra}^1 , so the average energy harvested at \mathbf{R} during each block is then given by

$$E_r = \eta E[|y_{ra}^1|^2](T/2) = \eta P_a |h|^2 (T/2) \quad (4)$$

where $E[\cdot]$ denotes the statistical expectation, and $0 < \eta \leq 1$ denotes the energy conversion efficiency for the energy harvesting circuit at \mathbf{R} and the user. The received energy signal given in (1.a) at \mathbf{R} is split into two parts: one for energy relaying to the user, and the other for information relaying to the AP, both in the second phase. In the second phase, \mathbf{R} simultaneously relays energy signal x_a to the user using the energy ρE_r and information signal x_u to the AP using the residual energy $(1 - \rho)E_r$ with different directional antennas, where ρ is the power splitting ratio factor for energy harvesting and its value is between 0 and 1. Considering the fact that \mathbf{R} adopts the decode-and-forward mode and assuming that the bit error rate is zero, we obtain the received signal at the AP in the second phase is shown as

$$y_{AP}^2 = \sqrt{\eta(1 - \rho)P_a} |h|^2 x_u + n_{AP} \quad (5)$$

and the received signal at the user is shown as

$$y_u^2 = \sqrt{\eta\rho P_a} h g x_a + n_u \quad (6)$$

Since the energy harvested by the user is equal to the sum of the energy harvested from the AP and \mathbf{R} , combining the Eqs. (2) and (4), we can obtain the energy harvested by the user in the whole transmission block which is shown as

$$E_u = \eta \left(\eta \rho P_a |h|^2 |g|^2 + P_a |l|^2 \right) T/2 \quad (7)$$

So the power P_u of the user is shown as

$$P_u = \sqrt{\eta \left(\eta \rho P_a |h|^2 |g|^2 + P_a |l|^2 \right)} \quad (8)$$

Combining the equations from (1) to (8), the achievable rate among nodes in the whole block transmission are shown as

$$R_{U-AP} = 1/2 \log \left(1 + \frac{\eta(\eta\rho P_a |h|^2 |g|^2 + P_a |l|^2) |l|^2}{\sigma_{AP}^2} \right) \tag{9}$$

$$R_{R-AP} = 1/2 \log \left(1 + \frac{\eta(1-\rho) P_a |h|^4}{\sigma_{AP}^2} \right) \tag{10}$$

$$R_{U-R} = 1/2 \log \left(1 + \frac{\eta(\eta\rho P_a |h|^2 |g|^2 + P_a |l|^2) |g|^2}{\sigma_r^2} \right) \tag{11}$$

R_{U-AP} denotes the information rate from the user to the AP through the direct link in the first phase, and R_{U-R} is the information rate from the user to **R** in the first phase, respectively. R_{R-AP} is the information rate from **R** to the AP through the relaying link in the second phase, and the achievable information rate R' from the user to the AP in a transmission block time denoted by T is expressed by [10]

$$R' = \min(R_{U-AP} + R_{R-AP}, R_{U-R}) \tag{12}$$

Considering the value domain of ρ , the problem of maximizing the information rate from the user to the AP in a block time can be formulated as

$$R = \max \min(R_{U-AP} + R_{R-AP}, R_{U-R}), 0 \leq \rho \leq 1 \tag{13}$$

It is assumed that the received noise powers of all nodes are equal to σ^2 for simplicity of analysis. Considering the nature of the logarithmic function, we can get the following equation with some simple manipulations

$$f(\rho) = -a\rho^2 + b\rho + c, 0 \leq \rho \leq 1 \tag{14}$$

In Eq. (14),

$$a = \eta^3 P_a^2 |h|^6 |g|^2 \tag{15}$$

$$b = \left(\eta^2 |h|^2 |g|^2 \sigma^2 - \eta |h|^4 - \eta^2 |h|^4 |g|^4 \right) P_a + \left(\eta^3 |h|^6 |g|^2 - \eta^2 |h|^4 |l|^4 \right) P_a^2 \tag{16}$$

and

$$c = \sigma^4 - \sigma^2 + \left(\eta|h|^4\sigma^2 + \eta|l|^4\sigma^2 - \eta|l|^2|g|^2 \right) P_a + \eta^2|h|^4|l|^4P_a^2 \quad (17)$$

Now the problem of maximizing the achievable rate described in (13) is converted into finding the extreme value of the function (14). According to the nature of the parabolic function and the range of ρ , we can finally get the value of ρ meeting the requirement of the Eq. (13). Because calculating the value of the power splitting factor is a little tedious, we can get the maximum achievable rate through computer simulation using the method of exhausting searching.

3.2 Without the Direct Link

In this case, due to space limit, we omit the derivation process and give the results directly using the same analysis process which is depicted as part 1. The achievable rate from the user to the AP is shown as

$$R_{NO} = 1/2 \log\left(1 + \frac{(1-\rho)\eta P_a h^4}{\sigma^2}\right) \quad (18)$$

Observing the Eq. (18), it is obviously that the maximum achievable rate is obtained when ρ is equal to zero. This means that the achievable rate is maximized if **R** utilizes the whole harvested energy for relaying information signal. This is not possible in practice. It is explained that the bit error and outage probability when transmitting the information signal between nodes are both ignored in the paper [11]. So **R** can receive the information signal complete correctly even if the transmission power of the user is equal to zero. Obviously, the achievable rate from the user to the AP is maximizing when **R** relay the information signal to the AP utilizing the whole harvested energy, since **R** is closer to the AP than the user and the corresponding channel power attenuation is lower than the user. The results presented in this paper can be used as performance ceiling for similar systems.

4 Numerical Results

The parameters selected in this paper are the same as in [16]. The distance between the user and the AP is set to 10 m. **R** is located in the line connecting the AP and the user. η is equal to 0.8. For each user, the DL and UL channel power gains are modeled as $|h|^2 = 10^{-3}\theta d_{ar}^{-\alpha}$, $|g|^2 = 10^{-3}\theta d_{ur}^{-\alpha}$, and $|l|^2 = 10^{-3}\theta d_{au}^{-\alpha}$, respectively, in which θ represents the channel short-term fading in the DL and UL and is independent exponential random variables with unit mean. d_{ar} , d_{ur} and d_{au} denote the distance between the AP and **R**, between the user and **R**, and between the AP and the user, respectively. In the above channel model, a 30 dB average signal power attenuation is assumed at a reference distance of 1 m. It is assumed the received noise power spectral density of all nodes is -160 dBm/Hz and the bandwidth is set as 1 MHz. P_a is set to 20 dBm.

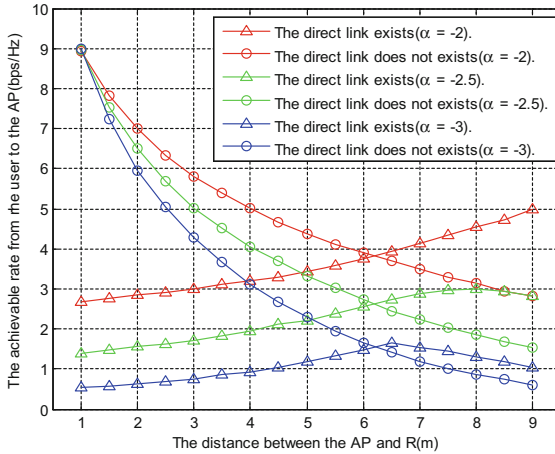


Fig. 3. The maximum achievable information rates when the direct link exists or not.

Figure 3 shows the maximum achievable information rates between the user and the AP when the direct link exists or does not. It is observed an interesting phenomenon that the maximum achievable information rates with the direct link are significantly less than when there is no direct path, when the distance between the AP and \mathbf{R} is less than 6 m. This is in contradiction to our intuition. In fact, when a direct link exists, the user is far away from the AP, so the power attenuation is very large via the direct link. If \mathbf{R} is closer to the AP, the relaying power is lower because the power experiences a greater attenuation from \mathbf{R} to the user, although harvested energy by \mathbf{R} is larger in this case. Considering the above reasons, the received energy of the user is very low when the distance between the AP and \mathbf{R} is short. But the achievable rate from the user to AP is shown in the Eq. (13), the transmission power of the user directly limits the achievable rate at this time. When we ignore the direct link, because we neglect both the outage probability and the bit error rate at this time, \mathbf{R} can utilize the whole harvested energy to relay the information signal. When \mathbf{R} is closer to AP, the power attenuation is lower and accordingly the achievable rate is larger. This is why the maximum achievable rate with the direct link existing is lower than the rate ignored the direct link when \mathbf{R} is closer to the AP than the user. The achievable rate with the direct link is larger than with the direct link not existing when \mathbf{R} is closer to the user, and \mathbf{R} helps the user to increase the achievable rate to the AP at this time.

The achievable rate monotonically decreases along with the increase of the distance between the AP and \mathbf{R} when the direct link does not exist as shown in Fig. 3, no matter what the value of α is, and the achievable rate decreases more quickly as α is lower. Obviously, the achievable rate when α is larger is always larger than when α is lower no matter whether the direct link exists or not.

With the increase of the distance between the AP and \mathbf{R} , the achievable rate monotonically increases when α is equal to -2 , and first monotonically increases and then monotonically decreases when α is equal to the other values. When \mathbf{R} is closer to the user, the relaying information signal power experiences a larger attenuation.

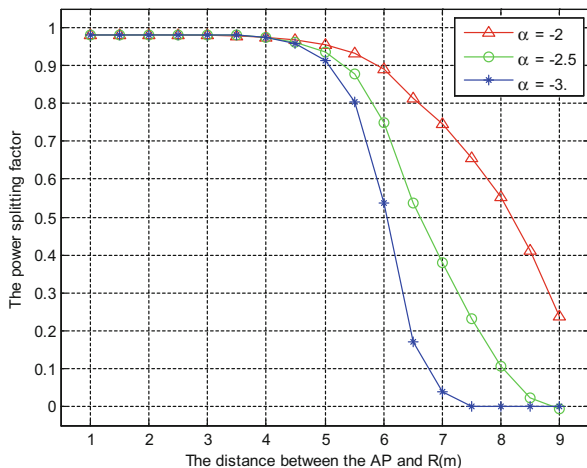


Fig. 4. The different values of the power splitting factor with the different values of α .

Although the whole harvested energy by \mathbf{R} ($\rho = 0$) is used to forward the information signal at this time, it is still difficult to change the trend of the rate of decline and the influence of power attenuation plays a major role in this situation, as shown in Figs. 3 and 4. The power splitting factor when \mathbf{R} is closer to the user decreases more quickly, and the trend is more obvious when α is lower.

5 Conclusions

In this paper, we study a WPCN system with a bidirectional information/energy forwarding relay operated in the decode-and-forward mode when the direct link exists or not. The corresponding achievable rate maximization problems are formulated and optimally solved ignoring the outage probability. Numerical results show that the relay node can only help the user increase the achievable rate to the AP when the relay node is closer to the user when the direct link exists. The results presented in this paper can be used as performance ceiling for similar systems.

References

1. Ozel, O., et al.: Transmission with energy harvesting nodes in fading wireless channels: optimal policies. *IEEE J. Sel. Areas Commun.* **29**, 1732–1743 (2011)
2. Kang, X., et al.: Full-duplex wireless-powered communication network with energy causality. *IEEE Trans. Wirel. Commun.* **14**, 5539–5551 (2015)
3. Ho, C.K., et al.: Optimal energy allocation for wireless communications with energy harvesting constraints. *IEEE Trans. Sig. Process.* **60**, 4808–4818 (2012)
4. Kang, X., et al.: Cost minimization for fading channels with energy harvesting and conventional energy. *IEEE Trans. Wirel. Commun.* **13**, 4586–4598 (2014)

5. Bi, S., et al.: Wireless powered communication: opportunities and challenges. *IEEE Commun. Mag.* **53**, 117–125 (2015)
6. Bi, S., et al.: Wireless powered communication networks: an overview. *IEEE Wireless Commun.* **23**, 10–18 (2016)
7. Liu, P., et al.: Energy harvesting noncoherent cooperative communications. *IEEE Trans. Wirel. Commun.* **14**, 6722–6737 (2015)
8. Liu, P., et al.: Noncoherent relaying in energy harvesting communication systems. *IEEE Trans. Wirel. Commun.* **14**, 6940–6954 (2015)
9. Ju, H., et al.: Throughput maximization in wireless powered communication networks. *IEEE Trans. Wirel. Commun.* **13**, 418–428 (2014)
10. Ju, H., et al.: User cooperation in wireless powered communication networks. In: *Proceedings of IEEE Global Communications Conference*, pp. 1430–1435. IEEE Press, Austin (2014)
11. Zeng, Y., et al.: Bidirectional wireless information and power transfer with a helping relay. *IEEE Commun. Lett.* **20**, 862–865 (2016)
12. Chen, Z., Dong, Y., Fan, P., Letaief, K.: Optimal throughput for two-way relaying: energy harvesting and energy co-operation. *IEEE J. Sel. Areas Commun.* **34**, 1448–1461 (2016)
13. Duarte, M., et al.: Full-duplex wireless communications using off-the-shelf radios: feasibility and first results. In: *Proceedings of 44th Asilomar Conference on Signals, Systems and Computers*, pp. 1558–1562. IEEE Computer Society, Asilomar (2010)
14. Radunovic, B., et al.: Rethinking indoor wireless mesh design: low power, low frequency, full-duplex. In: *5th IEEE Workshop on Wireless Mesh Networks*, pp. 25–30. IEEE Computer Society (2010)
15. Jain, M., et al.: Practical, real-time, full duplex wireless. In: *Proceedings of the Annual International Conference on Mobile Computing and Networking*, pp. 301–312. Association for Computing Machinery (2011)
16. Ju, H., et al.: Optimal resource allocation in full-duplex wireless-powered communication network. *IEEE Trans. Commun.* **62**, 3528–3540 (2014)

Advances and Trends of V2X Networks



Design and Implementation of an Intelligent Shipborne Terminal System

Wenqiu Chen¹, Rongbin Yao^{2(✉)}, Jincal Ye^{1,2}, Xin Tang¹, and Xiaohuan Li^{1,2,3}

¹ Guangxi Cooperative Innovation Center of Cloud Computing and Big Data, Guilin University of Electronic Technology, Guilin, China

² Key Laboratory of Cognitive Radio and Information Processing, Ministry of Education, Guilin University of Electronic Technology, Guilin, China
yao.guet@foxmail.com

³ Beihang University, Beijing, China

Abstract. To solve the problem that network services provided by ships can't distinguish different users and the Quality of Service (QoS) is poor, an intelligent shipborne terminal system which combines advanced positioning technology and wireless communication technology is designed in this paper. The overall design of the system including hardware design and software design is proposed. The test results show that the system can distinguish between different users' Wi-Fi connection, intelligentize the management of system users, realizes the function of GPS positioning navigation and has a rich local resource storage, which all proved its good application value.

Keywords: QoS · Shipborne terminal · Wi-Fi · GPS positioning

1 Introduction

In recent years, the Internet of Vessels has become an emerging field after the Internet of things and the Internet of Vehicles. The Europe proposed an inland waterway shipping integrated River Information Services (RIS) in the literature [1]. Through the integration, synergy and standardization of RIS, it provided all the users with a comprehensive and convenient information services and realized the safety, economy, efficiency, energy saving and environmental protection of inland navigation. In [2,3], these studies showed that GPS and wireless communication technology successfully realized the real-time monitoring of the ship's running status and position. The authors studied the main challenges of developing wide area Wi-Fi access to RIS in the Danube with the location and variety of antennas in [4]. Another study proposed an integrated wireless network system consisting of mobile ad hoc networks, cellular mobile communications networks and satellite mobile networks to provide richer maritime services for mobile users in [5]. However, none of these documents refers to the Wi-Fi sharing function and provides different quality of service for different users.

In 2014, the number of smartphone users in China has exceeded 500 million, and it is expected to reach 700 million in 2018. The popularization of intelligent terminals and the development of mobile Internet have brought the rapid expansion of Wi-Fi access requirements. As one of the indispensable transportation, tens of thousands of passengers' travel by vessels every day. Their demand for the internet is very large, they want to use their mobile phones, tablets to get news, use social media, listen to music, watch videos and so on. However, most of the ships are not equipped with enough network terminals for passengers' entertainment or handling official business, and other ships equipped with Wi-Fi equipment also have some annoying problems in network supply. There are still many drawbacks in existing shipboard terminal system:

- There are few ships that can provide Wi-Fi network service which cannot provide Internet access services.
- The existing shipborne Wi-Fi system only provides Wi-Fi access with poor QoS, but does not distinguish different users with their different network requirements.
- The bandwidth of existing wireless access is too low, so the speed of loading or browsing video or audio resources is very slow, which strongly affects the user experience.

Therefore, this paper designs an intelligent shipborne terminal system. The hardware part designs the function module and interface circuit according to the demands. The software part designs the GPS positioning function [6] and Wi-Fi connection with WeChat authentication [7]. Through this system, passengers will enjoy the stability network services and rich information contained in system, and the different needs of users will experience a different Qos, which can greatly enhance the passenger travel experience.

The rest of this paper is organized as follows: Sect. 2 overviews the design of the system. Section 3 introduces the system function. The system test results and analysis are presented Sect. 4. Finally, Sect. 5 concludes this paper.

2 System Design Overview

In order to show the feasibility of our designs, we build a system topology model that is detailed description in Fig. 1. Mobile intelligent terminals (such as smart phones, laptops, etc.) and intelligent shipborne terminal system (equipment designed in this paper) connect through wireless Wi-Fi connection. After the successful connection, passengers can access the intelligent multimedia database in the shipborne terminal system, and it can connect to the Internet through the intelligent shipborne terminal system, which makes network services available for mobile intelligent terminal equipment. At the same time, the intelligent terminal system can connect the shipborne camera and LED display to provide shipborne TV advertising and video services through the Ethernet port, through the serial port and shipborne sensor, it can obtain ship status and provide business like GPS positioning service, authentication charging and advertising push.

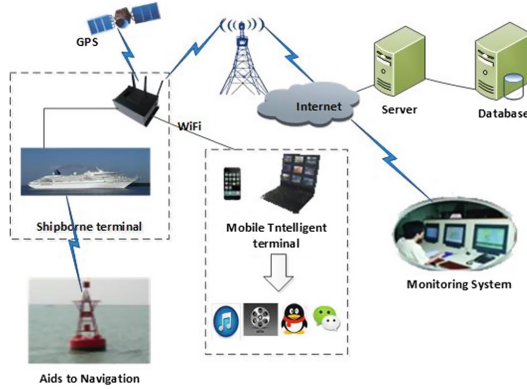


Fig. 1. The network topological structure of intelligent shipborne terminal system

2.1 Hardware Design

Considering the principle of the intelligent shipborne terminal system, the hardware system of intelligent shipborne terminal mainly includes power module, master control module, routing module, 4G communication module. Hardware framework of intelligent shipborne terminal system can be seen in Fig. 2.

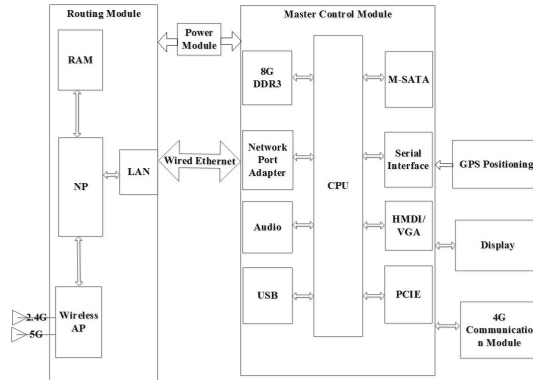


Fig. 2. Hardware framework of intelligent shipped terminal

Power module uses Cincon Electronics CHB100W-24S12, the input voltage of the module is broad, ranging from 9 V to 36 V, and the output voltage and current are 12 V, 8.3 A, and the power is 100 W, so it can provide a stable power supply for the system modules.

The main control module is the core module, using the PCM3-QM77 industrial mainboard with high performance and high reliability onboard IntelQM77 chip. The board has strong compatibility and abundant interface, which is convenient for system development and expansion.

The routing module is composed of dedicated network processor, memory and radio frequency antenna. The module is mainly used as an access point (AP)

for the intelligent terminal connect to local resources and Internet. This module communicates with the master control module using wired Ethernet and then accesses the Internet through the 4G communication module. Users can access to the multimedia database contained in the system by accessing the intelligent shipborne terminal system through its Wi-Fi signal.

The 4G communication module is SIM7100CE, it is an ultra-compact, highly reliable wireless module based on the Qualcomm MDM9215 multi-mode.

LTE platform network adapter module uses the MPCIE-RJ45, this module uses half-height Mini PCIE slot to Gigabit Ethernet interface RJ45 and integrated RTL8111E chip.

2.2 Software Design

According to the functional requirements of intelligent shipborne terminal system, the software system framework is composed of Linux operating system and embedded route operating system.

The main operating system uses Linux operating system, it is a multi-user, multitasking and multi-threaded operating system, which is based on POSIX and UNIX [8]. It can run the major UNIX tool software, applications and network protocols, and supports 32-bit and 64-bit hardware. The routing operating system [9] is an embedded operating system which using a transplant Linux kernel, so it has the best scalability, the fastest speed for routing support, and works well in support of routing CPU. It mainly achieves wireless routing and providing network access for intelligent terminals.

3 System Function Design

The system focuses on providing local multimedia services. There are massive multimedia resources stored in the local server, users can access the resources through the local area network, thus avoiding the congestion caused by the large number of users accessing the Internet through the 3G/4G channel at the same time. In this way of enjoying the multimedia services through the local area network, on the one hand it can improve the communication capacity of the intelligent shipboard terminal system, providing users with a good service experience, on the other hand, the decreasing number of users who accessing the Internet through 3G/4G channel also cut down the traffic of 3G/4G channel, thereby reducing the operating costs.

3.1 System User Status Query

The system user status query can query the IP, MAC address, uplink rate, downlink rate, total traffic, downlink total traffic, connection duration, and connection type of the user connected to the intelligent shipborne terminal system, also can monitor the network status of each user, and pass the data in the POST format to the database for subsequent operations. Implementation of the system user status query flow chart is shown in Fig. 3.

3.2 GPS Data Acquisition and Processing

GPS data is collected through the serial port system, so it must initialize the serial port and set the basic parameters of the serial port to provide GPS positioning information. Implementation of the GPS data acquisition and processing flow chart is shown in Fig. 4.

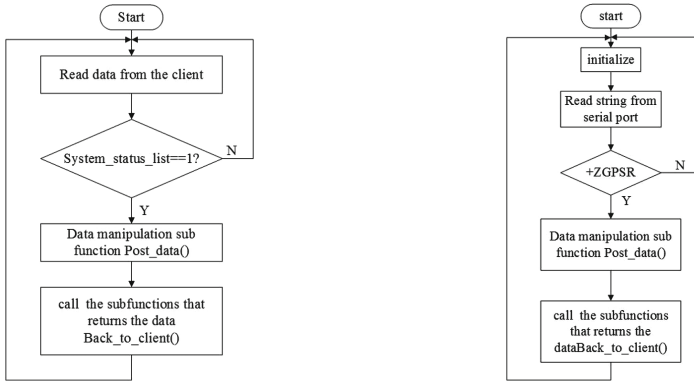


Fig. 3. System user status query flow chart Fig. 4. Flow chart of GPS data acquisition

3.3 System User QoS Control

System user QoS control can give users different bandwidth based on different needs, it can control the priority of user (IP address), selection of access to 3G/4G line, maximum upload rate, minimum upload rate, average upload rate, maximum download rate, minimum download rate, and average download rate to bring users different experience, so as to improve the QoS. Figure 5 shows the QoS control flow chart of the system user.

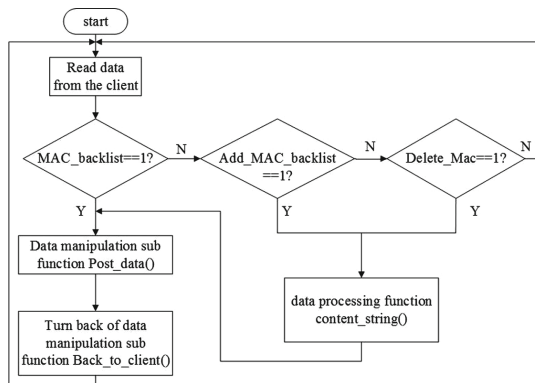


Fig. 5. QoS control flow chart of the system user

3.4 System User MAC Address Blacklist

System user status query can query the user’s physical address (MAC address) [10], the system user MAC address blacklist can restrict the user access to the Internet by adding the MAC address to the blacklist, and user is only allowed to access to the LAN server, which can further distinguish different users, reduce the flow pressure of 3G/4G channel, and enhance the user experience. Implementation of the system user MAC address blacklist flow chart is shown in Fig. 6.

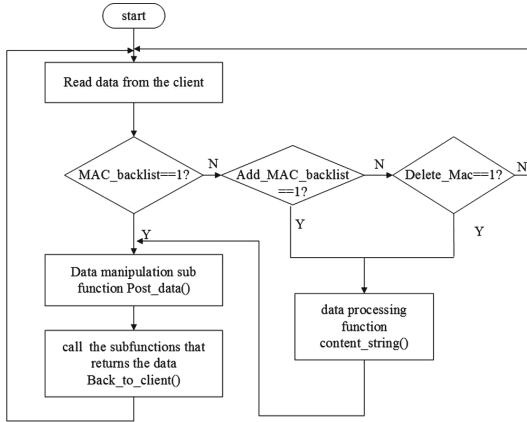


Fig. 6. System user MAC address blacklist flow chart shown

4 System Test and Analysis

The test of intelligent shipborne terminal system includes system user management function test, GPS positioning information test, automatic disconnection function test and system software login platform test, because the development of this system is the infrastructure development, so we use the code to realize the test. The material object of intelligent shipborne system is as shown in Fig. 7.



Fig. 7. The material object of intelligent shipborne system

4.1 System User Management Function Test

To accurately control the user information of each shipborne terminal and provide different service quality for different users, the system has the function module of system user management. In the testing of the system user management function, a client test program was written, through the client test program can connect system user management module, query information and accept the information returned by the system management module. When reading the system connection status through the client, the result of test is shown in Fig. 8.

```
time:2017-03-19 17:39:54
ip_addr:192.168.15.1
mac:2c:30:33:41:95:2b
connect:1
upload:0
download:0
total_up:0
total_down:0

time:2017-03-19 17:39:57
ip_addr:192.168.15.14
mac:00:e0:4c:68:0d:05
connect:379
upload:1102
download:0
total_up:9184120
total_down:0
```

Fig. 8. The parsed data

From the analysis of the data we can see that there are two users connected, where the user whose IP is 192.168.15.1 has no data communication and there is only one connection, this is the IP of the routing module itself. While another users IP, MAC address, connection time, connection number and the total flow can completely output.

When users use the mobile phone to connect the intelligent terminal, the system did not make any control to the user and use client test program to send users control commands to the system, the measured user speed is as shown in Fig. 9. Figure 10 shows that after data processing, the user with IP 192.18.15.11 had QOS control in wlan1 port and control time is 24h, the allowed minimum, maximum and average upload and download speed are: 80, 120, 100 KB/s, respectively.

When using the MAC blacklist to control users, the client receives the processed data returned by the system is as shown in the Fig. 11, it can be found that the user whose ID is 1 and the MAC address is a4:44:d1:33:2f:27 was intercepted by MAC. When we use mobile phone to connect the system, it can be connected, but cannot access to the Internet.

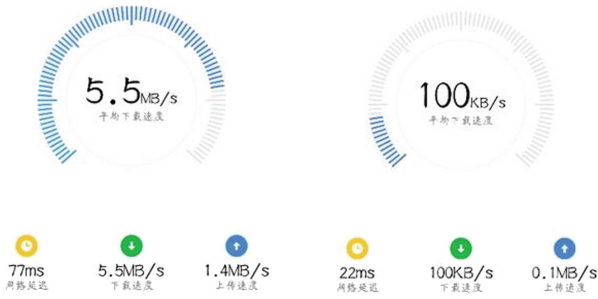


Fig. 9. No speed limit/speed limit test results

```
name:192.168.15.11
ip_addr:192.168.15.11
interface:wan1
time:00:00-23:59
week:1234567
min_up:80 max_up:120 avg_up:100
min_down:80 max_down:120 avg_down:100
```

Fig. 10. The results after system QOS analysis

```
id:1
mac:a4:44:d1:33:2f:27
```

Fig. 11. The MAC interception information

4.2 GPS Location Information Test

The master control module receives GPS data through the serial ports, and the analytical function will read and extract the useful positioning information, then output those information in a special format to other functions. The positioning information display result is as shown in Fig. 12. Positioning information includes date, time, latitude, longitude, altitude and direction angle. In this case, the date is March 19, 2017, time is 9 p.m. and 50 s, the north latitude is 25.2825933333 degrees, the east longitude is 110.3209633333 degrees, the height above sea level is 135.9 m and the direction angle is 149.00833 degrees.

```

/*****GPS information*****/
UTC date: 2017-03-19
Time: 21:00:50
Lat: 25.2825933333 deg, Latitude:N
Lon: 110.3209633333 deg, Longitude:E
Altitude mean-sea-level:135.9 m
Course over ground:149.00833 deg

```

Fig. 12. The GPS positioning information

4.3 Automatic Disconnection Function Test

The function of automatic disconnection can end the connection between the user and the intelligent shipborne terminal system and provide better service quality for the users in need. This function is connecting the routing module through the client test program client, then querying the disconnect network user list in routing module and receiving the return information of the routing module for test. The client test results is as shown in Fig. 13, when the client sends a GET command, the routing module will return the information about disconnect the user's MAC list, when using the ADD and MAC address to add user, the routing module will return OK, however if using a mobile phone connect the routing module, the routing module SSID can be seen but cannot connect.

```

GET
00:0C:29:4B:E5:F7
00:E0:4C:68:0D:05
ADD ,A4:44:D1:33:2F:27
OK!
GEET
Please enter the correct command!
GET
00:0C:29:4B:E5:F7
00:E0:4C:68:0D:05
A4:44:D1:33:2F:27
DELETE ,00:0C:29:4B:E5:F7
OK!
GET
00:E0:4C:68:0D:05
A4:44:D1:33:2F:27

```

Fig. 13. The command and return messages

4.4 Software Login Platform Test

The system software login platform test is done by using a mobile phone to connect the intelligent shipborne terminal system. As shown in Fig. 14, the mobile

phone will pop up the authentication information after connecting intelligent shipborne terminal system (as shown in a), when clicking the trial certification, the time of trial certification and the number of daily certification will be set, and the authentication failure will happen while the set limit exceeds, at that time only the intranets can be accessed (as shown in b). However, clicking the WeChat certification, the page will skip to the enterprise WeChat official account. After finishing the authentication, the various resources in the local server can be accessed via mobile phone. The “Wi-Fi + WeChat” authorization mode will automatically skip to the WeChat public number (as shown in c), it can avoid the complicated operation process of traditional web authentication. Making Wi-Fi connection process more concise, and not hinder the service provider information display and the opportunities of push advertisements (as shown in d), bring users a new experience in the mobile Internet era.



Fig. 14. Example of placing a figure with experimental results.

5 Conclusions

In this paper, an intelligent shipborne terminal system is proposed. First, we gave a detailed introduction of its hardware and software design scheme. The system can provide the wireless network sharing services, multimedia services, GPS positioning services for the end users and it also has the advantage of distinguishing different users. Then the test results shows that the system is easy to use, it has low configuration cost and stable operation. Users can enjoy local storage of videos, music, news, games and other multimedia entertainment information programs for free. This can better meet the demands of different users for the network and makes the journey on board be more pleasant. So it has good application value and practical significance.

Acknowledgment. This work was supported by the National Natural Science Foundation of China (61762030,61661016), Natural Science Foundation of Guangxi Province under Grant (2015GXNSFBA139247, 2016GXNSFGA380002), the Key Laboratory of Cognitive Radio and Information Processing, Ministry of Education (Guilin University of Electronic Technology), CRKL160106, and the Guangxi Colleges and Universities Key Laboratory of cloud computing and complex systems.

References

1. Schilk, G., Seemann, L.: Use of ITS technologies for multimodal transport operations - river information services (RIS) transport logistics services. *Proc. - Soc. Behav. Sci.* **48**(2307), 622–631 (2012)
2. Ten Broeke, I.A.A., Willems, C.P.M., Glansdorp, C.C.: River information services: a joint European effort to enhance safety and usability of the inland waterway. In: *Intelligent Transportation Systems*, pp. 1108–1115 (2001)
3. Zhao, Z., Zhou, W., Wang, N.: Shipping monitoring system based on GPS and GPRS technology. In: *2009 WASE International Conference on Information Engineering*, Taiyuan, Chanxi, pp. 346–349 (2009)
4. Xinglong, L., Xiumin, C., et al.: Portable ship information querying system based on Android. In: *International Symposium on Distributed Computing and Applications to Business, Engineering & Science*, Guilin, pp. 371–374 (2012)
5. Minea, M.G., Niculescu, M.C.M.: Challenges in developing WiFi wide coverage access for river information services on the Danube river. In: *12th International Conference on Telecommunication in Modern Satellite, Cable and Broadcasting Services (TELSIKS)*, Nis, pp. 141–144 (2015)
6. Shao, M., Yang, X.: Programming to achieve the reception extraction and translation of GPS positioning information. In: *2015 International Conference on Computer Science and Mechanical Automation (CSMA)*, Hangzhou, pp. 226–230 (2015)
7. Zhang, S., Wu, Y., Cai, X.: WeChat traffic profile and impact on mobile networks. In: *CIC International Conference on Communications in China (ICCC)*, Shanghai, pp. 334–338 (2014)
8. Du, W., Zhengxin, M., Bai, Y., Shen, C., Chen, B., Zhou, Y.: Integrated wireless networking architecture for maritime communications. In: *11th ACIS International Conference on Software Engineering, Artificial Intelligence, Networking and Parallel/Distributed Computing*, London, pp. 134–138 (2010)

9. May, P., Ehrlich, H.-C., Steinke, T.: ZIB structure prediction pipeline: composing a complex biological workflow through web services. In: Nagel, W.E., Walter, W.V., Lehner, W. (eds.) Euro-Par 2006. LNCS, vol. 4128, pp. 1148–1158. Springer, Heidelberg (2006). https://doi.org/10.1007/11823285_121
10. Abedi, N., Bhaskar, A., Chung, E.: Bluetooth and Wi-Fi MAC address based crowd data collection and monitoring: benefits, challenges and enhancement. Australasian Transport Research Forum (2013)



A Positioning Method Based on RSSI and Power Spectrum Waveform Distinction

Yuyang Lin, Zunwen He^(✉), Jiang Yu, and Yan Zhang

School of Information and Electronics, Beijing Institute of Technology, Beijing
100081, People's Republic of China

{ginieu, jiangy, zhangy}@bit.edu.com,
hezunwen@bit.edu.cn

Abstract. In this paper, we propose a positioning method based on the dual-complex fingerprint, which consists of the Received Signal Strength Indication (RSSI) and the Power Spectrum Waveform (PSW), including three stages. First, generate fingerprint library by data collected offline. For each reference point, RSSI and PSW are both stored in the library. Then make pre-positioning by RSSI fingerprint and the location of reference points. These points will be selected twice to remove the single points away from the others. Final positions are estimated by taking PSW Distinction (PSWD) and RSSI into consideration. In addition, we introduce an idea of evaluating PSWD by the Kullback-Leibler Distance (KLD). The MATLAB simulation results show that, comparing to other algorithms such as KNN and WKNN, the proposed method leads to lower number of observable misestimated points, and approximately 5% improvement in cumulative distribution function (CDF) of position error within 1.3 m.

Keywords: Positioning · RSSI · PSWD · KLD

1 Introduction

With rapid development of information technology in modern society, individuals are increasingly concerned about the derivative demand of wireless communication, such as positioning and confidentiality. So far, according to the different needs of the positioning range and accuracy, there have been varieties of sophisticated positioning measures, such as Satellite positioning, base station positioning, and Wi-Fi assisted positioning.

Nevertheless, these outdoor technologies cannot meet all the needs of customers on Location-Based Services (LBS). For instance, when the vehicles enter underground parking lots, tunnels and garages from the open area, the GPS signal received by on-board communication equipment will have enormous attenuation. Thus, it is difficult to maintain the relationship between received GPS signal strength and vehicle

This work was supported by National Nature Science Foundation of China under Grants No. 61201192 and the National High Technology Research and Development Program of China (863 Program) under Grants No. 2015AA01A708.

position, as the propagation channels become completely different. Therefore, driven by the demands for development of smart home and intelligent management systems, such as Vehicle-to Everything (V2X), positioning schemes based on infrared, ultrasound, RFID, Bluetooth, WI-FI, ZigBee, ultra wideband and other similar projects have been proposed. However, these mentioned schemes have their respective shortcomings, especially the expensive cost of equipment, so that most of them are unworthy to achieve large-scale popularization.

RF fingerprint technology comes up with a new idea for indoor positioning. The RSSI fingerprint keeps inherent law of changing with propagation distance and easy to achieve in low-cost acquisition. In this case, with Wireless Local Area Network (WLAN), which is the lowest cost, the most extensive coverage and most convenient to deployment, the RSSI positioning becomes the primary choice for indoor fingerprint positioning.

Whereas RSS values are affected by time variability and terminal heterogeneity, and prone to fluctuate in the same position, resulting in significant deviation in positioning results [1, 2]. For this reason, researchers pay attention to make improvement of RSSI fingerprint scheme. The targets of amelioration are improving accuracy and reducing cost. The improvement is mainly based on two aspects: the offline aspect is to ameliorate RSS values for fingerprint library while the online stage is to optimize positioning estimation algorithms. Considering the huge amount of measurements collected for the positioning accuracy in offline stage, interpolation technique is presented to decrease the amount of collected data [3]. Simple linear regression technique is used to facilitate under-trained location systems [4]. To reduce operation time, a method combines a little new feedback and some necessary old RSS values to build new RSS fingerprint library when environment changes [5]. Moreover, a method without offline stage is proposed, using only RSS measurements obtained in real time by dynamically estimating the propagation models [6]. On the other aspect, positioning algorithms develop from K-Nearest Neighbor (KNN) or Bayesian decision to diverse categories, and emerge in endlessly all these years, such as weighted centroid location algorithm [7], Kalman Smoothers [8], random forest classifier [9], neural network positioning algorithm [10], etc.

In this paper, we propose a method based on the weighted combination of signal PSW and RSSI. In the method, we introduce a new concept of PSWD outside the original signal fingerprint algorithms. Signals from same source inevitably maintain some certain inherent characteristics in the frequency spectrum as well as power spectrum. When a signal arrives at receiver via a wireless channel, its PSW will change correspondingly to the characteristic of channel. This results in the homologous signal PSW diverse in different locations. Therefore, it is feasible to reduce the interference of RSS fluctuation by comprehensively considering PSWD among the test point and reference points of each Access Point (AP), and comparing the summarized distinction.

The remainder of the paper is organized as follows: in Sect. 2, we present the existing theoretical knowledge we used. In Sect. 3, we describe the details of the method proposed in this paper. In Sect. 4, we record the experiment settings and present the results of performance evaluation with comparison to other schemes. Finally, a conclusion is outlined in Sect. 5.

2 RSSI and Channel in WLAN Network

The environment in which we want to optimize scheme and deploy the positioning system is a WLAN wireless network. The target of us is matching the location of a Mobile Station (MS) with signals it received, and estimating where the MS is. Assuming that there are M APs in WLAN network, the simplest RSS fingerprint at position l can be expressed as:

$$RSS_{l,n} = [rss_{l,1,n}, \dots, rss_{l,m,n}, \dots, rss_{l,M,n}]_{1 \times M}. \quad (1)$$

where $rss_{l,m,n}$ means the RSS value measured by MS in l position at n th time from AP m . As mentioned in Sect. 1, RSS values are affected by the time variability and environmental conditions changes, and prone to fluctuate in the same position, especially when staffs walk around and switch doors and windows. Thus, we need to measure several times at same position for each AP, in order to get reasonable and effective values as referential RSS fingerprints via some certain fingerprint algorithms.

RSSI fingerprints generated by different algorithms are generally formed as vectors consisting of M values. These M values represent the effective average of preprocessed RSS samples for M APs at the reference points. Nevertheless, some fingerprints appear in form of matrix. No matter how the fingerprint is, it is certain that the data measured in real-time should be manipulated into the same form of referential data stored in the library.

2.1 Channel Model and Signal Attenuation

Even in a precise spotting, the measured RSS values are affected by a large number of predictable and unpredictable factors. The distance between AP and MS (d) is the main factor of attenuation in RSS values, and keeps positive correlated with the attenuation. Of course, penetration loss is the other main reason for reduction of RSS value. If ignoring the unpredictable interference from time and space fluctuation, the RSS value of an AP measured in a certain position can be represented by the distance between AP and spotting, the path penetration loss and transmitting power. There are several Indoor empirical path loss prediction models raised these years [11–13]. When taking logarithmic unit, the primary RSS values, P_r , can be modeled by following expression:

$$P_r = P_t + G_t + G_r - L. \quad (2)$$

where P_t is the transmitted power, G_t and G_r are the transmitter and receiver gains, and L represents total attenuation during transit, respectively. The attenuation L can be described as different expressions according to different models [12]. A classic model, Keenan-Moltey (KM) model, describes the indoor propagation attenuation as follow:

$$L = L(d_0) + 20 \log \left(\frac{d}{d_0} \right) + \sum_{j=1}^{jj} N_{wj} L_{wj} + \sum_{i=1}^{ii} N_{Fi} L_{Fi}. \quad (3)$$

where d_0 (d_0 generally takes 1 m) is a standard reference point, $L(d_0)$ is the attenuation at d_0 , N_{Wj} and N_{Fi} denote the number of different types of walls and floors, L_{Wj} and L_{Fi} denote the penetration loss factors corresponding to these types of walls and floors, jj and ii mean the number of types of walls and floors, respectively.

Equation (3) shows that when we consider the question in a meter-level area, the penetration loss can be regarded as constant. Then the only closely related factor is d . Moreover, it can be easily found that the RSSI should be more similar when the test points are closer, which can be viewed as the spatial correlation of RSS. To maintain such correlation away from unpredictable factors, it is essential to measure a number of samples for RSSI generation process.

3 Positioning Algorithm Design

3.1 Measurement for PSWD—KLD

Same to correlation between RSSI and sampling position, there is correlation between signal frequency domain waveform and position. However, it is tough to measure the true instantaneous frequency waveform at real time. We choose the PSW as the substitute from the time average perspective. In the certain sampling point, the PSW of signals from different APs exist distinctions. Meanwhile the signal PSW from an identical AP share variations as well, due to the heterogeneity of wireless propagation channels influenced by changeable test positions. In addition, this method asks the APs to transmit same signal when working in positioning mode. In Fig. 1(a), we can know that the PSW are quite distinct among different Aps at the same position.

Furthermore, Fig. 1(b) and (c) show that the PSWD will be smaller along with the decrease of channel difference, when choosing from nearby location. The correlation between them provides a theoretical possibility of using PSWD as position fingerprint. This paper employs KLD to measure the distinction between two SPW, as a feature of position. There is no doubt that the signal PSW are measured and processed in discrete. The discrete form of KLD is defined as [14]:

$$KLD(P||Q) = \sum_{i \in N} P(i) \log P(i)/Q(i). \quad (4)$$

where P and Q represent two discrete distributions, ordinarily P is real distribution while Q is the ideal one or for comparison. In addition, N is the same length of two sequences. Almost all result of (4) is greater than zero, if and only if $P = c * Q$ ($c \neq 0$) it can equal to zero.

At each position, each AP keeps a valid sequence of PSW, which is obtained by processing a number of measured data. Prior to use, these sequences need to be normalized as follow:

$$Pu_{l,m}(i) = p_{l,m}(i) / \sum_{x \in N} p_{l,m}(x), i = 1, 2, \dots, N. \quad (5)$$

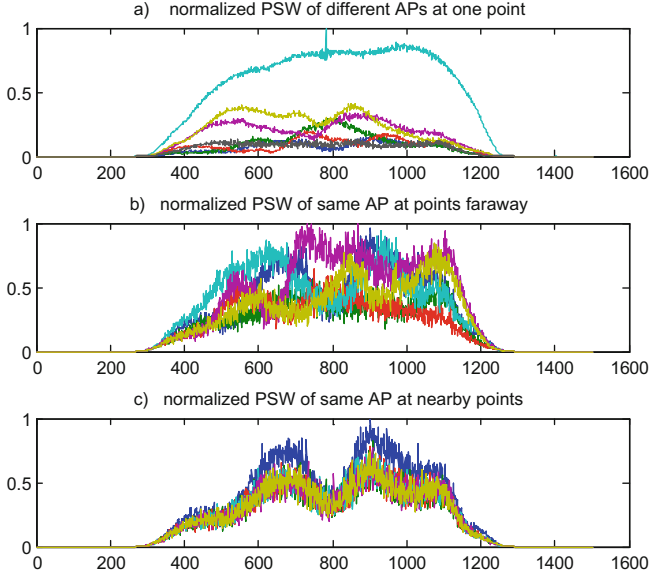


Fig. 1. Different normalized PSW collected by the same MS. Three different situations here: (a) PSW of different APs in same point, (b) PSW of same AP in positions faraway, (c) PSW of same AP in positions nearby.

where $Pu_{i,m}$ means the normalized result of PSW of AP m at the reference point l , and N is the length of waveform sequences. Therefore, the PSD between point i and j can be quantified by *KLD* from (4) and (5):

$$KLD(Pu_{i,m}, Pu_{j,m}) = \sum_{x \in N} Pu_{i,m}(x) \log Pu_{i,m}(x) / Pu_{j,m}(x). \quad (6)$$

3.2 Details of Combination of RSSI and PSD in the Scheme

In this paper, we simultaneously consider RSSI spatial correlation and PSD to optimize the accuracy and robustness of positioning algorithm.

During the offline stage, multiple sets of RSS samples and PSW sequences from each AP need to be collected at each reference point as original data of position fingerprint. However, considering the PSW existing as a long sequence, it has much larger data size than RSSI. Therefore, it has no possibility to employ the PSW as a whole-area discrepancy measurement tool like RSSI, because of enormous computation complexity and unpredicted time cost.

Thus, we assign RSSI and PSD for different purposes. In the real-time stage, RSSI is used as the first level fingerprint for whole-area preliminary orientation. Then PSD is used as the secondary fingerprint for re-weighting the reference points in pre-orientation range. In the final coordinate estimation, the RSSI weighting and the PSD weighting are taken into account simultaneously.

Most of indoor positioning algorithms are based on KNN algorithm and offline RSSI fingerprint library. Once the library is set up, an adaptive distance metric function is presented immediately, by which we can use to find out the K reference points nearest to the real-time test point and estimate the positioning result based on the coordinates of these reference points. Generally, the estimate methods employ arithmetic average (for KNN), weighted coordinates average (for WKNN) or correlation coefficient weighted average to obtain the test point position. Our work make some differences.

Work in offline stage. First, we need to make sure the space size of the room, and then select the appropriate numbers of APs (M) and reference points (L) as well as their reasonable distributions. Meanwhile the coordinates of reference points need to be obtained, and it is better to set points spacing as constant. After the preparatory work, use a MS to collect the original data at each reference point. The effective information we need has mentioned in previous Sect. 3.2. Then RSS values and PSW are pre-processed by respective filter rules to eliminate significant distortion samples for each AP at each reference point. RSS values are treated by limit average filter that is united by limit breadth filter and moving average filter, while the processing of PSW is to obtain the average waveform after removing large discrepant sequences. The final fingerprint stored for a reference point consists of a vector composed of M RSS values and a matrix of M PSW sequences. Each line of the matrix represents a representative PSW of one AP.

Preliminary orientation of real-time stage. The aim of this part is to catch a small area from the whole space, and to make ensure the reference points that will be included in the next stage. At first, a number of sampling data should be measured at test point by the MS. Then this data are transformed into the same form with fingerprints saved in library via the same means, as mentioned in Sect. 2.1.

We use Euclidean distance as a metric to denote the distances of RSS vectors (DR) among test point and reference points. The DR between test point A and reference point l , is defined as follow:

$$DR_{A,l} = \sqrt{\sum_{m \in M} (rss_{A,m} - rss_{l,m})^2}. \quad (7)$$

where $rss_{l,m}$ presents the stored RSS value for AP m in point l , while $rss_{A,m}$ is analogously for test point A .

Then we can choose K reference points by seeking the smallest K values for DR . From The perspective of theory analysis, these reference points should be in close proximity. However, when testing in real scene, the points usually keep near but not adjacent. Here we use “two-centric” cluster algorithm to optimize selection of reference points. After reselection of K points, the first weighting representations (named WFF) are given to these selected references according to the values of DR . The WFF between test point A and K reference points is built by DR :

$$WFF_A(k) = 1 / \left(DR_{A,k} \sum_{x \in K} 1 / DR_{A,x} \right), k \in K. \quad (8)$$

Final estimate stage. In this phase, we calculate the *KLD* between test point and selected points of each AP by (6), separately. In addition, when calculating *KLD*, the waveforms of test point should be the former ones. Then we recreate a set of weighting identifications (named *WSF*) according to the size of these *KLD* values. Analogously, *DK*, the summary of *KLD*, and *WSF* at each reference point can be calculated as:

$$DK_{A,k} = \sqrt{\sum_{m \in M} KLD_{A,k,m}^2} \quad (9)$$

$$WSF_A(k) = 1 / \left(DK_{A,k} * \sum_{x \in K} 1 / DK_{A,x} \right), k \in K. \quad (10)$$

where $KLD_{A,k,m}$ means the PSWD between test point A and reference point k of AP m .

The last few steps of this scheme are to integrate *WFF* and *WSF* together and to estimate the coordinate of test point by the integrated weighting factor *WF* in the end. The *WF* and estimated position for test point A affected by a scale factor α are calculated as follows:

$$WF_A(k) = (WFF_A(k) + \alpha * WSF_A(k)) / (1 + \alpha), k \in K. \quad (11)$$

$$X_A = \sum_{k \in K} WF_A(k) * X_k, Y_A = \sum_{k \in K} WF_A(k) * Y_k. \quad (12)$$

4 Experiment, Results and Analysis

The experimental data in this paper are collected in an office condition with an overall test area of 15.63 m * 15.86 m. There are seven APs distributed in the center position (Tx7) and the edge of office work area (Tx1-6). In order to avoid the interference among the different sources of signals at the same location, this paper adopts the means of sending and receiving antenna one-to-one correspondence to carry out data collection. The height of the transmitting antenna of the APs is fixed at 1.2 m. The receiving antennas are centrally placed on a pushcart, with the antenna height at 1.08 m and the pitch at half a wavelength. There are four main walkways available in the office for data collection.

First, we choose 91 reference points in each main walkway and record their coordinates. The process of reference data collection has mentioned in Sect. 3.4. In real-time test stage, the positions of APs remain unchanged, and the pushcart is moved at a speed of about 0.5 m/s. The sampling interval is set as 0.52 s. In each path, 45 points are selected as test points, and the device records the coordinates, the signal strength and PSW collected for each point. After sampling, all sampled data are imported into the computer equipment, read and processed by the MATLAB software. Then we use them to form the library of RSSI and PSW fingerprints and to perform the positioning accuracy test, respectively.

4.1 Estimation, Comparison and Analysis

In data processing, we realize the essentiality of the K value selection. By comparison, things are better when K varies from 3 to 5 than others. Thus, we choose 3 as the value of K for reducing computational complexity. Furthermore, we adopt the “two-centric” cluster algorithm for the nearest 2 * K-1 points to optimize selection of K points by the RSSI and location distribution of them. The accuracy becomes much better after the reselection of the reference points. In addition, the scale factor α is set to one as we keep the equal position of WFF and WSF.

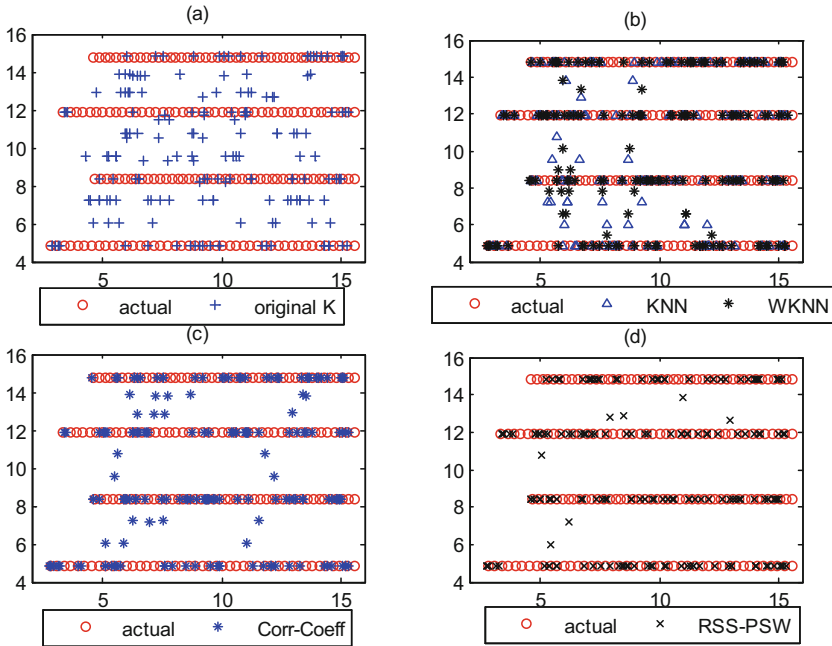


Fig. 2. The estimated locations of test points by different algorithms: (a) original K points average, (b) KNN and WKNN with reselected K points, (c) RSSI correlation-coefficient algorithm, and (d) the optimized algorithm based on RSSI and PSWD. The unit in Fig. 2 is meter.

Use KNN algorithm, WKNN algorithm, RSSI correlation-coefficient algorithm, and RSSI-PSWD algorithm respectively to estimate positions of test points. Then make a comparison among them through MATLAB simulation. The different estimated positions of test points by different schemes are shown in Fig. 2, in which the red circles represent the actual positions of test points. We can easily find from Fig. 2(a) that, if there is no weighted algorithm, the number of misestimated position points will be more. The effect of WFF can be seen in Fig. 2(b) that estimated positions by WKNN move near to the more similar reference points and the bias distance decreases. Moreover, the RSSI correlation-coefficient algorithm showed in Fig. 2(c) has quite different mismatched points with WKNN algorithm due to the different process during

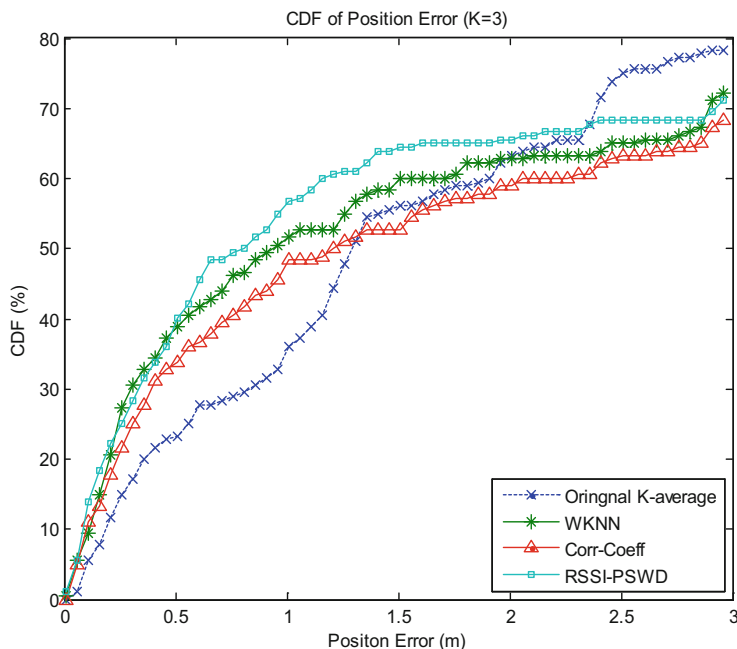


Fig. 3. Cumulative distribution function of errors in the estimated distance by comparing RSSI-PSWD algorithm with other methods. ($\alpha = 1$).

the selection step of K points. However, they have similar number of observable mis-estimated positions. Overall, when comparing Fig. 2(d) to the others, the number of observable mismatched points is much lower.

The CDF of error for mentioned algorithms is presented in Fig. 3. We adopt 3 m as the ceiling of position error for Fig. 3, because it is big enough in this indoor room, whose length and width are both less than 16 m. From this figure, because of so many mis-estimated points, the CDF of original K -average algorithm is much lower than the others when position error is less than 1.3 m. The other three have similar curves, as they all use the tool of weighting. The RSSI-PSWD is the best as it uses two kind of weighting factors, and there is about 5% improvement in accuracy when position error varies from 0.6 m to 1.3 m. In addition, the reason for these three curves increasing slowly after 2 m is the process of reselection of K reference points. In that step, we use “two-centric” cluster algorithm to optimize the accuracy for low position error scene, but it has an imperfection as well. If the data collection is not accurate enough, some selected good reference points settled far from other points may be considered as bad ones and be ignored.

5 Conclusion

This paper proposes an optimized algorithm of indoor positioning by using RSSI-PSWD weighting. The methods used such as RSSI, evaluation for PSW distinction, and weighted centroid estimation are introduced. The simulation results shows

it has higher accuracy than other mentioned algorithms. The downside is that we need to collect an extra data set of PSW during offline stage. The next research aims consist of three directions. One is finding how to retain the key features of PSW while simplifying the amount of data size. The second aim is to optimize weighting algorithm combined by WSF and WFF. Moreover, the last is seeking a better method to reselect the K reference points by DR and spatial distribution.

References

1. Lui, G., Gallagher, T., Li, B., Dempster, A.G., Rizos, C.: Differences in RSSI readings made by different Wi-Fi chipsets: a limitation of WLAN localization. In: 2011 International Conference on Localization and GNSS (ICL-GNSS), Tampere, pp. 53–57 (2011)
2. Chang, N., Rashidzadeh, R., Ahmadi, M.: Robust indoor positioning using differential Wi-Fi access points. *IEEE Trans. Consum. Electron.* **56**(3), 1860–1867 (2010)
3. Lee, M., Han, D.: Voronoi tessellation based interpolation method for Wi-Fi radio map construction. *IEEE Commun. Lett.* **16**(3), 404–407 (2012)
4. Hossain, A.K.M.M., Van, H.N., Jin, Y., Soh, W.S.: Indoor localization using multiple wireless technologies. In: 2007 IEEE International Conference on Mobile Adhoc and Sensor Systems, Pisa, pp. 1–8 (2007)
5. Koweerawong, C., Wipusitwarakun, K., Kaemarungsi, K.: Indoor localization improvement via adaptive RSS fingerprinting database. In: The International Conference on Information Networking 2013 (ICOIN), Bangkok, pp. 412–416 (2013)
6. Mazuelas, S., et al.: Robust indoor positioning provided by real-time RSSI values in unmodified WLAN networks. *IEEE J. Sel. Top. Sig. Process.* **3**(5), 821–831 (2009)
7. Wang, Z.M., Zheng, Y.: The study of the weighted centroid localization algorithm based on RSSI. In: 2014 International Conference on Wireless Communication and Sensor Network, Wuhan, pp. 276–279 (2014)
8. Paul, A.S., Wan, E.A.: RSSI-based indoor localization and tracking using sigma-point Kalman smoothers. *IEEE J. Sel. Top. Sig. Process.* **3**(5), 860–873 (2009)
9. Jedari, E., Wu, Z., Rashidzadeh, R., Saif, M.: Wi-Fi based indoor location positioning employing random forest classifier. In: International Conference on Indoor Positioning and Indoor Navigation (IPIN), Banff, AB, pp. 1–5 (2015)
10. Xuhui, Z., Baojiang, G., Yukun, L., Juan, W., Huimin, C.: The optimization of RSSI-neural network positioning algorithm. In: 2014 Fourth International Conference on Instrumentation and Measurement, Computer, Communication and Control, Harbin, pp. 633–637 (2014)
11. Aragon-Zavala, A., Belloul, B., Nikolopoulos, V., Saunders, S.R.: Accuracy evaluation analysis for indoor measurement-based radio-wave-propagation predictions. In: *IEEE Proceedings - Microwaves, Antennas and Propagation*, vol. 153, no. 1, pp. 67–74, 6 February 2006
12. Molisch, A.F.: Channel models. In: *Wireless Communications*, vol. 1, pp. 125–143. Wiley-IEEE Press (2011)
13. Solahuddin, Y.F., Mardeni, R.: Indoor empirical path loss prediction model for 2.4 GHz 802.11n network. In: 2011 IEEE International Conference on Control System, Computing and Engineering, Penang, pp. 12–17 (2011)
14. Do, M.N., Vetterli, M.: Wavelet-based texture retrieval using generalized Gaussian density and Kullback-Leibler distance. *IEEE Trans. Image Process.* **11**(2), 146–158 (2002)



A Network Coding Collaborative Download Scheme for Platoon-Based VANETs

Jincai Ye^{1,2}, Xuewen Huang², Xiaohuan Li^{1,2(✉)}, Guan Wang³,
Rongbin Yao², and Xin Tang²

¹ Beihang University, Beijing, China
xhuan.lee@126.com

² Key Laboratory of Cognitive Radio and Information Processing,
Ministry of Education (Guilin University of Electronic Technology), Guilin, China

³ The 34TH Research Institute of CETC, Guilin, China

Abstract. Platoon-based Vehicular Ad-hoc Networks (VANETs) can significantly improve the road capacity and facilitate the potential cooperative communication applications. However, the communication links between platoon-based vehicles and the roadside unit (RSU) are unstable, which decrease the throughput and increase the delay, and cause the infotainment resources cannot be downloaded quickly. In this paper, we propose a collaborative download strategy in platoon-based VANETs to solve the problems. On the basis of RSUs support simultaneous communication with multiple vehicles, when a demand vehicle need to download multimedia files, we use the collaborative download request management mechanism to request other vehicles in the same RSU coverage area to participate in the collaborative download process. Besides, to decrease the download time, we divide the required multimedia files into multiple data packets. After the RSUs encode the data packets via linear network coding, the cooperative vehicles forward the received encoded packets to the demand vehicle. We also research the impact of speed and file size on the performance of cooperative download strategy. The simulation results show that the proposed cooperative download strategy can effectively increase throughput and reduce the downloading completion time when download multimedia files, especially when the size of multimedia files is large and the speed of platoon-based vehicles is fast.

Keywords: Platoon-based VANETs · Collaborative download
Request management · Network coding · File segment

1 Introduction

The platoon-based driving pattern [1] can significantly enhance the traffic efficiency, safety and entertainment applications performance for Vehicular Ad-hoc Networks (VANETs). In the platoon, the follower vehicles can trace the road

without driving operation, so it also known as the formation of semi-automatic driving mode [2,3]. Platoon-based VANETs is committed to providing vehicles with high quality, accurate, real-time vehicle services, which consist of active safety applications [4] and non-safety applications [1], such as traffic safety information and automotive multimedia entertainment resources.

In platoon-based VANETs [5], the drivers and passengers in the follower vehicles have enough time to enjoy the infotainment services, so the demand for multimedia resources is more prominent. However, in the platoon-based VANETs, many of the data services, especially the multimedia infotainment services are usually with large volumes of data, which need a long time to download these resources. Moreover, the low throughput and the unstable communication link between the vehicles and roadside unit (RSU) [5] effect the performance of download, which cannot meet the passengers requirements on multimedia entertainment information.

To solve the problem that the communication links between platoon-based vehicles and RSU are unstable, which decreases the throughput and increases the delay during the downloading process, we propose a network coding cooperative download scheme in platoon-based VANETs. First, a collaborative download request management mechanism is designed, which focuses on the communication protocol between a vehicle in the platoon and other cooperative node, i.e. vehicles or RSU, to support the collaborative download. Then we propose a file segment strategy based on the collaborative download request management mechanism to divide the required files into multiple data packets. Besides, RSU use the linear network coding to encode these data packets and send them to all cooperative vehicles. Finally, a data forwarding mechanism between the vehicle and cooperative vehicles is proposed to ensure that the cooperative vehicles forwards all the received coded packets to the demand vehicle before entering the next RSU coverage area.

The rest of this paper is organized as follows. Section 2 overviews the related work. Section 3 presents our platoon-based VANETs system model for collaborative downloading. We propose a network coding cooperative download strategy in platoon-based VANETs in Sect. 4. Performance evaluation is presented in Sect. 4.3. Finally, Sect. 5 concludes this paper.

2 Related Works

In some earlier works, different collaborative download schemes has been proposed for platoon-based VANETs. Most of them studied collaborative download strategy for traditional VANETs. In [6], the authors proposed a new model for analyzing the connectivity probability to provide better performance in terms of multi-hop delay and there exists an optimal one-hop transmission range to minimize the multi-hop delay. In [7], the authors divided the file into a number of data packets and then used the peer-to-peer (P2P) or BitTorrent methods to collaborative download. In [8,9], instead of considering data distribution from RSU to vehicles, the authors researched Vehicle-to-Vehicle (V2V) data forwarding and

information sharing in the RSU coverage blind area. Besides, researchers have introduced network coding into the traditional collaborative download scheme to reduce the data transmission error rate and communication protocol costs. In [10], the authors investigated the application of network coding in collaborative downloading. It analyzed the derive probability distribution and the expected value of the amount of time necessary to deliver all of the information from RSU to the vehicles with network coding, but it only considered the collaboration downloading between the two vehicles. Based on the theory of [10], in [11], the authors extended the two vehicles to multiple vehicles to study the collaborative downloading. However, the above study results cannot be directly applied into platoon-based VANETs. Hence, in [5], the connectivity probabilities are analyzed for the V2V and Vehicle-to-RSU (V2R) communication scenarios for different driving speed in platoon-based VANETs to improve system throughput. In [12], the authors proposed a cooperative retransmission scheme to deliver multimedia data from a traveling vehicle to RSU reliably. But these works did not involve collaborative download studies. Besides, the problems of low system throughput and high downloading delay still exist and are not solved.

Therefore, in this paper, we propose a network coding collaborative download scheme for platoon-based VANETs, which can effectively increase throughput and reduce the downloading completion time when download multimedia files.

3 System Model

The cooperative download system model in platoon-based VANETs is shown in Fig. 1. The system consists of RSU, vehicles that driving in a platoon-based pattern, central control center, etc. Each vehicle is equipped with two independent broadcasting stations to transmit data, which referred to as On-Board Unit (OBU). The RSU has multiple independent broadcasting stations, each of which adopts the beamforming to communicate over the respective channels,

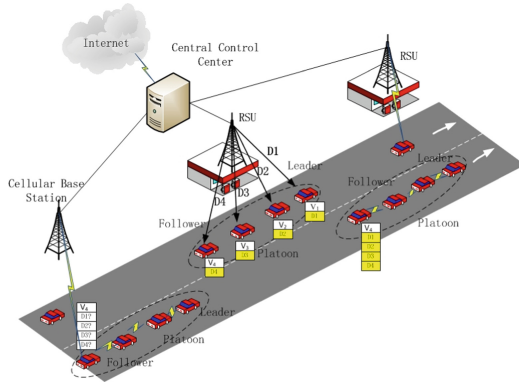


Fig. 1. Collaborative download model for platoon

and supports simultaneously communication with multiple vehicles. Short range communication between OBU of vehicles and RSU can be achieved using IEEE 802.11p [13] protocol in the Dedicated Short Range Communication (DSRC) [14] band. RSU uses optical fiber or microwave technology to access the Internet. When a vehicle want to obtain a specified multimedia resource, the central control center will send the source that vehicle required to RSU, so that RSU can be seen as providers of multimedia resources.

4 Collaborative Download Strategy for Platoon

The collaborative download strategy via network coding in platoon-based VANETs is composed of cooperative download request management mechanism, file segment strategy, V2R data distribution mechanism and V2V data forwarding mechanism. The detailed algorithm is described as follows.

- Step 1: When a vehicle in the platoon needs to download the p Mb multimedia files (we call it the demand vehicle), it sends the downloading request to RSU, and then the system executes the collaborative download request management mechanism. The central control center needs to obtain the speed of platoon, the number of collaborative vehicles, the multimedia filename need to be downloaded, and the geographic information of vehicles, etc.
- Step 2: Then the central control center executes the multimedia file segment mechanism. It divide the multimedia file into multiple data packets, after calculating the size of each packet, the central control center sends all these packets to RSUs, so that the RSUs are the resource providers.
- Step 3: When the platoon driving into the coverage area of the RSU, the RSU will encode the data packets via network coding and send the encoded packets to all collaborative vehicles in platoon, that is the V2R data distribution process. It can also be called V2R data distribution phase.
- Step 4: When the last vehicle in platoon leaves the RSU coverage area, the collaborative downloading vehicles will send the encoded packets that they downloaded during the V2R phase to the demand vehicle, which executes the V2V packets forwarding mechanism. It can also be called V2V packets forwarding phase.
- Step 5: When the size of encoded packets that the demand vehicle obtained can decode out of the original multimedia file, the download is completed; otherwise, when the vehicles enter the range of the next RSU, they try to obtain the remaining packets. This continues until the demand vehicle can decode the original file.

We call each V2R data distribution phase and its following V2V packets forwarding phase as a round, due to the size of the multimedia file is large, it is obvious that the collaborative downloading strategy cannot download the whole file in one round. The number of rounds that required sending all the encoded packets from RSUs to the vehicles can be used to reflect the time needed

to download the whole file. The following subsections provide more detailed information on the proposed collaborative download strategy.

4.1 Collaborative Download Request Management Mechanism

In this subsection, the collaborative download request management mechanism is described detailed. We assume that the vehicle in platoon is the demand vehicle, which needs to download the Mb multimedia file. The operations of the collaborative download request management mechanism are as follows:

- Step 1: The demand vehicle V_k sends collaborative download request to the leader vehicle of the platoon.
- Step 2: The leader vehicle agrees to the request and sends the message to other follower vehicles, which including the information about the demand vehicle, the filename and size of the multimedia file need to be downloaded.
- Step 3: If the vehicle V_p in the platoon owns the needed multimedia resource, it will reply to the leader vehicle and go to Step 4; Otherwise, if other follower vehicles are free now, they reply to the leader vehicle that they will participate in the collaborative download and go to Step 6.
- Step 4: Leader vehicle inform the vehicle that the vehicle V_p owns the resource and cancel the collaborative download request.
- Step 5: The vehicle V_k directly sends the file to the vehicle V_p until the file is downloaded completely.
- Step 6: Leader vehicle collects the information about the follower vehicles that participates in the collaboration, including the MAC address, geographical location, and then sends the information to the demand vehicle V_k .
- Step 7: The demand vehicle V_k sends the downloading request to the central control center through the cellular network.
- Step 8: If the central control center owns the needed file resource, it agrees to download, and go to Step 9, otherwise the collaborative downloading cannot be completed.
- Step 9: The demand vehicle V_k sends the related collaborative download information, such as the collaborative vehicles, the speed of platoon and geographical location to the central control center.
- Step 10: According to the received collaborative download information, the central control center executes the file segment mechanism to divide the original multimedia file into multiple data packets. After calculating the size of each data packet and estimating the rounds needed to complete download, the central control center packages the file segment information, platoon driving information and collaboration information into a collaborative information packet, and then sends the packet to RSUs.
- Step 11: When the vehicles enters the coverage of these RSUs, they connect to RSUs and download the resource immediately. From the above

description of the proposed mechanism, the collaborative download request management mechanism regulates the collaborative request-related operations to make it more systematic, standardized.

4.2 Multimedia File Segment Mechanism

After considered the collaborative download request management mechanism, when a vehicle in platoon requests to download the multimedia file, the central control center will divide the file into multiple data packets and send to RSUs, and then RSUs send the packets to multiple collaborative vehicles. Therefore, in this section, we will describe the multimedia file segment mechanism in detail.

When the RSU simultaneously sends data to multiple vehicles, the signal-to-interference ratio of vehicle V_k can be expressed as:

$$SINR_k = \frac{|h_{k,m}|^2 p_k}{\sum_{i=1, i \neq k}^K |h_{i,m}|^2 p_i + \sigma_k^2} \quad (1)$$

where $h_{k,m} = \sqrt{s_{k,m}} h'_{k,m}$ is the composite channel between the RSU and vehicle V_k , $S_{k,m} = (d_{k,m}/d_0)^{-\alpha} 10^{(\mu/10)}$ corresponds to small-scale fading from RSU to the V_k , which includes path loss and shadowing fading. The shadow fading for RSU is modeled as an independent log-normal random variable with standard deviation σ . $d_{k,m}$ denotes the distance between the RSU and V_k , d_0 is used as the reference distance. α indicates the path-loss exponent and μ is a normally distributed random variable with mean σ^2 . Also, $h'_{k,m}$ stands for the frequency-flat Rayleigh fading channel coefficient, which is modeled as independent and identically distributed (i.i.d.) complex Gaussian random variable with unit variance. P_k is the transmit power for vehicle V_k , n_k denotes an additive noise whose entries are i.i.d., complex Gaussian, with zero mean and variance. Then the throughput of vehicle can be expressed as σ_k^2 :

Then the throughput C_k of vehicle V_k can be expressed as:

$$C_k = W_k \log_2(1 + SINR_k) \quad (2)$$

where W_k is the channel bandwidth.

We set the platoon driving at a constant speed of v kilometers an hour, when the vehicle V_k in platoon driving through the coverage area of the RSU, the distance between the vehicle V_k and the RSU is $d_k = R - vt$, in which t is the running time of vehicle in RSU coverage area, and then the total time that the vehicle V_k driving through the area is $T = 2R/v$. Then the total size of data downloaded by V_k during the period can be expressed as:

$$S_k = 2 \int_0^{\frac{T}{2}} C_k dt \quad (3)$$

To ensure the transmission bandwidth is fully utilized, we will adopt a file segment strategy to divide the file into multiple data packets to simultaneous

transmission, in which the size of each data packet after division is smaller than 10Mb. The process of file segment strategy is elaborated as follows.

First of all, after vehicles in platoon driving through a RSU, the size of file downloaded by vehicles are S_1, S_2, \dots, S_K , and then we compare the size of each file and obtain the minimize one S_{min} , if S_{min} is larger than 10Mb, we make the become half of it until $S_{min} < 10$. Finally, S_{min} is the size of data packet.

4.3 V2R Data Distribution Mechanism Based on Network Coding

Based on the data distribution mechanism in [10,11], in this section, we focus on encoding the original data packets using random linear network coding to implement V2R data distribution. The performance of the cooperative download strategy is demonstrated by calculating the probability distribution and expected value of the number of rounds required for RSUs to send data packets to the vehicles in platoon.

The number of coded packets that vehicle download from an RSU during its coverage is m_k , and the size of m_k is determined by the speed of the vehicle, the transmission rate and the coverage area of the RSU. We assume that the size of data packet m_k obtained from any RSU is constant, according to the file segment mechanism described above, the size of coded packet is $m_k = \lceil S_k/S_{min} \rceil$, and the total number of coded packets from all the vehicles in each round is $m_{sum} = \sum_{k=1}^K m_k$. n Linear network coding is a block code conducted over a finite field F_q , where $q = 2^n$, and n is a positive integer [15]. During any transmission opportunity, the RSU will encode the segmented data packets (X_1, X_2, \dots, X_M) , where $M = P/S_{min}$. Besides, the packets after linear coding can be expressed as $\sum_{z=1}^M \beta_{i,k,z} X_z$, where $\beta_{i,k,z}$ is the random network coding coefficient selected uniformly in F_q at the i th round for the k th vehicle.

During the collaborative download process, the vehicle can represent a linear combination of M original packets in any received encoded packet. In order to enable the demand vehicle to decode the original packets, it needs to know the random coding coefficient matrix used for all distributions, thus the RSUs embed these coding coefficients in each coded packet. In the t th rounds, the vehicle V_k receivest $\times m_k$ packets, which is $y_1, y_2, \dots, y_{t \times m_k}$. With the perfect forwarding between cooperating vehicles in the platoon, the demand vehicle can obtain the encoded packets received by all other vehicles. Therefore, after the t th rounds, the number of coded packets D obtained by the demand vehicle can be expressed as

$$D = t \cdot m_{sum} \tag{4}$$

All the data packets obtained by the demand vehicle can be expressed in the form of vector, which is

$$X = (X_1, X_2, X_3, \dots, X_M) \tag{5}$$

$$Y = A_{D \times M} \cdot X \tag{6}$$

where $A_{D \times M}$ is the coefficient matrix containing all network coding coefficients. Only when $A_{D \times M}$ is full rank that the demand vehicle can recover the original data packets, which is

$$X = A^{-1}Y \quad (7)$$

When the rank of $A_{D \times M}$ is M , the number of total encoded packet D that demand vehicle obtained should require $D \geq M$, from the Eq.(4), we can know. The probability of matrix $t \geq M/m_{sum}$ is full rank increases with t , so we define the time that needed to download all the data packets is $\Gamma = \min_t \{rank(A_{D \times M}) = M\}$. It is obvious that $\Gamma \geq M/m_{sum}$. We will use the probability distribution and expected value of Γ to present the performance of the proposed scheme, and the following lemma gives the probability of rank of matrix $A_{D \times M}$ with random entries in a finite field.

Lemma 1. $A_{t \times n}$ is a random matrix over finite field F_q , and the entry $a_{i,j}$ is picked uniformly in F_q . Suppose that $t \geq n$, the probability of the rank of matrix $A_{t \times n}$ is can be expressed as

$$P(rank(A_{t \times n}) = n) \approx 1 - \frac{1}{q^{(t-n+1)}} \quad (8)$$

where the above approximation is valid when the q is sufficiently large.

According to the approximation of the probability distribution in Lemma 1, the upper limit of the probability of the cooperative download completion time can be further calculated in the following Lemma 2.

Lemma 2. Since $\Gamma = \min_t \{rank(A_{D \times M}) = M\}$ is the coordinate download complete time, then

$$P(\Gamma = t) \leq (1 - \frac{1}{q})(1 - P(rank(A_{(m_{sum}t-1) \times M}) = M)) \quad (9)$$

where the above inequality is valid when the q is sufficiently large.

According to Lemmas 1 and 2, we can estimate the expected value of the completion time of the coordinate download based on network coding, which satisfies the following condition:

$$\frac{M}{m_{sum}} \leq \Gamma \leq \frac{M}{m_{k_max}} \quad (10)$$

where $m_{k_max} = S_{max}$ indicates the largest number of encoded packets received by the vehicle in platoon. The expected value of completion time can be expressed as

$$\begin{aligned} \mathbf{E}(\Gamma) &= \sum_{U_{min}}^{U_{max}} tP(\Gamma = t) \\ &= (1 - \frac{1}{q})q^M \sum_{U_{min}}^{U_{max}} t \frac{1}{q^{m_{sum}t}} \end{aligned} \quad (11)$$

where $U_{max} = M/m_{k_max}$, and $U_{min} = M/m_{sum}$. Then the system throughput during the entire collaborative download process is as follows.

$$C = \mathbf{E}(\Gamma) \cdot m_{sum} \cdot S_{min} \quad (12)$$

4.4 V2V Data Packet Forwarding Mechanism

In order to execute V2V data packets forwarding mechanism smoothly, we assume that the network topology and the communication link is stability and there are no selfish vehicles in the platoon, so the cooperative vehicles will selflessly forward the data packets. The general steps are as follows. First, when the last vehicle leaves the RSU coverage area, each cooperative vehicle forwards the received encoded packet to the demand vehicle. Since each vehicle is equipped with 2 transceivers, it can communicate with two vehicles simultaneously to ensure the packets downloaded from RSU forward to the demand vehicle in the RSU blind zone. Then, the demand vehicle extracts the random coding coefficients from the received encoded data packets and adds them to the coefficient matrix $A_{D \times M}$ as a new row, and then vehicles are able to recover original RSU information when the rank of matrix $A_{D \times M}$ is M .

4.5 Simulation Results and Analysis

In this section, simulation results are shown to demonstrate the efficiency of the proposed cooperative download strategy. For the sake of simplification, we set three vehicles to participate in the collaboration, and they communication with RSUs simultaneously. To verify the performance of our proposed strategy, we will compare the proposed scheme with that without using the collaborative download strategy. In the simulation, we considered the path-loss, shadow fading factors that affect the wireless communication. The simulation parameters are set as shown in Table 1.

Table 1. Simulation parameters

Parameters	Value
Path-loss exponent	3
Shadowing standard deviation	8 dBm
Noise power	0.01 W
Cooperative vehicles power	2.5 W
Limited field space	512
RSU coverage radius	500 m
Initial request file size	700 Mb

Figure 2 describes the size of data that can be download per round when vehicles driving through the RSU coverage area with different speeds. It is obvious that after adopting the cooperative download strategy, more data packets can be obtained in each round, which shows that our proposed cooperative download strategy can reduce the downloading time and improve system throughput.

Figure 3 shows the average number of rounds that needed to complete download with different speeds. It can be seen that no matter the download process

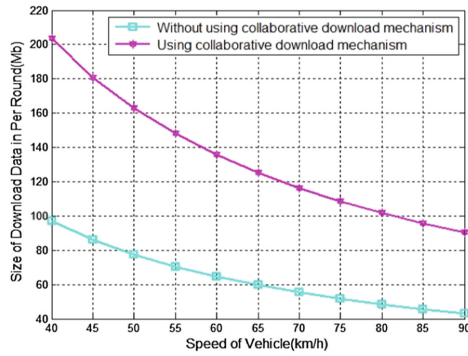


Fig. 2. Size of downloaded data per round with different vehicle speeds

adopts the cooperative download strategy or not, the average number of rounds increase with vehicle speed, but the rounds that cooperative download strategy needed is significantly smaller than that without using the strategy, which shows the advantage of our proposed scheme.

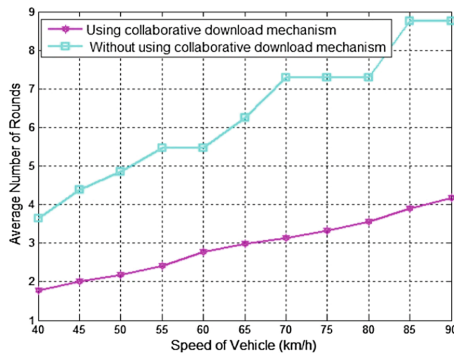


Fig. 3. Average number of rounds for different speed of vehicles

Figure 4 shows the average number of rounds is linearly increase with the amount of demand file data. Comparing the two scenes, it is obvious that the rounds collaborative download strategy needed is smaller than that without using the collaborative download. Besides, the gap of rounds between the two schemes is larger, which shows that when the size of multimedia files is large, the performance of cooperative download strategy is more prominent comparing with download scheme without collaboration.

Figure 5 describes the number of download rounds needed with different file segment mechanisms and the file size. The average number of rounds needed to complete download in our proposed file segment mechanism is less than the size

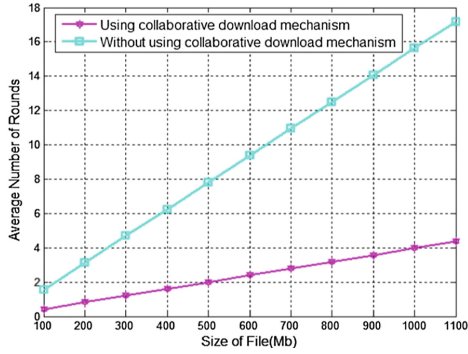


Fig. 4. Average number of rounds with different size of file

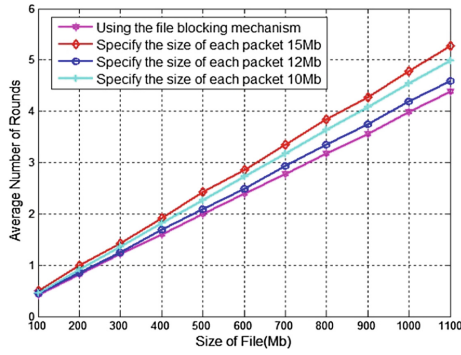


Fig. 5. Average number of rounds for different the size of each packet and file

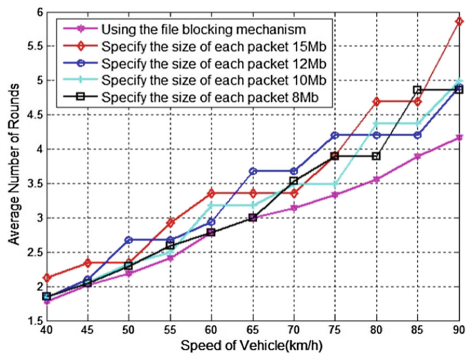


Fig. 6. Average number of rounds for different size of each packet and speed of vehicle

of the packets are directly set to be 15 Mb, 12 Mb and 10 Mb, which can reduce the downloading completion time effectively.

Figure 6 shows the number of download rounds needed under different file segment mechanisms with different speeds. Due to the fact that using the file segment mechanism can make the system stable, when the speed of vehicle is different, our proposed file segment mechanism need less time to complete download.

5 Conclusions

In order to solve the problem of low throughput and long delay in the process of downloading multimedia files, we studied the collaborative download strategy in platoon-based VANETs. The strategy includes collaborative download request management mechanism, file segment mechanism, V2R data distribution mechanism based on network coding and V2V package forwarding mechanism. The simulation results demonstrate that by using the collaborative download strategy, the system throughput is significantly improved and the downloading completion time is reduced.

Acknowledgment. This work was supported by the National Natural Science Foundation of China (61762030, 61561014), Natural Science Foundation of Guangxi Province under Grant (2015GXNSFBFA139247, 2016GXNSFGA380002), the Key Laboratory of Cognitive Radio and Information Processing, Ministry of Education (Guilin University of Electronic Technology), CRKL160106, and the Guangxi Colleges and Universities Key Laboratory of cloud computing and complex systems.

References

1. Hall, R., Chin, C.: Vehicle sorting for platoon formation: impacts on highway entry and throughput. *Transp. Res. Part C Emerg. Technol.* **13**(5), 405–420 (2005)
2. Kenney, J.B.: Dedicated short-range communications (DSRC) standards in the United States. In: *IEEE*, vol. 99, no. 7, pp. 1162–1182 (2011)
3. Jiang, D., Taliwal, V., Meier, A., Holfelder, W., Herrtwich, R.: Design of 5.9 GHz DARC-based vehicular safety communication. *IEEE Wirel. Commun.* **13**(5), 36–43 (2006)
4. Jia, D., Lu, K., Wang, J., Zhang, X., Shen, X.: A survey on platoon-based vehicular cyber-physical systems. *IEEE Commun. Surv. Tutor.* **18**(1), 263–284 (2016)
5. Shao, C., Leng, S., Zhang, Y., Vinel, A., Jonsson, M.: Performance analysis of connectivity probability and connectivity-aware MAC protocol design for platoon-based VANETs. *IEEE Trans. Veh. Technol.* **64**(12), 5596–5609 (2015)
6. Li, X., Hu, B.: Multi-hop delay reduction for safety-related message broadcasting in vehicle-to-vehicle communications. *IET Commun.* **9**(3), 404–411 (2015)
7. Shrestha, B., Niyato, D., Han, Z., Hossain, E.: Wireless access in vehicular environments using BitTorrent and bargaining. In: *IEEE Global Telecommunications Conference*, pp. 1–5 (2008)
8. Chen, B.B., Chan, M.C.: MobTorrent: a framework for mobile Internet access from vehicles. In: *IEEE INFOCOM*, pp. 1404–1412 (2009)

9. Fiore, M., Barcelo-Ordinas, J.M.: Cooperative download in urban vehicular networks. In: 6th IEEE International Conference on Mobile Adhoc and Sensor Systems, pp. 20–29 (2009)
10. Firooz, M.H., Roy, S.: Collaborative downloading in VANET using network coding. In: IEEE International Conference on Communications ICC, pp. 4584–4588 (2012)
11. Zhu, W., Li, D., Saad, W.: Multiple vehicles collaborative data download protocol via network coding. *IEEE Trans. Veh. Technol.* **64**(4), 1607–1619 (2015)
12. Jia, D., Zhang, R., Lu, K., Wang, J., Bi, Z., Lei, J.: Improving the uplink performance of drive-thru Internet via platoon-based cooperative retransmission. *IEEE Trans. Veh. Technol.* **63**(9), 4536–4545 (2014)
13. Taliwal, V., Jiang, D.: Mathematical analysis of IEEE 802.11 broadcast performance in a probabilistic channel. DaimlerChrysler Technical Paper (2005)
14. Kenney, J.B.: Dedicated short-range communications (DSRC) standards in the United States. *IEEE* **99**(7), 1162–1182 (2011)
15. Ho, T., Medard, L., Shi, J., Effros, L., Karger, D.: On randomized network coding. In: Allerton Conference on Communication, Control, and Signal Processing, pp. 1–10 (2003)



Analysis of Conditional Connectivity Based on Two Lanes for VANETs

Bin Pan^{1,2,4}  and Hao Wu^{1,3,4} 

¹ State Key Laboratory of Rail Traffic Control and Safety,
Beijing Jiaotong University, Beijing 100044, China
{binpan, hwu}@bjtu.edu.cn

² School of Electronic and Information Engineering,
Beijing Jiaotong University, Beijing 100044, China

³ Beijing Key Laboratory of Intelligent Traffic Data Safety and Privacy
Protection Technology, Beijing Jiaotong University, Beijing 100044, China

⁴ Beijing Engineering Research Center of High-Speed Railway Broadband
Mobile Communications, Beijing Jiaotong University, Beijing 100044, China

Abstract. Conditional connectivity is important for the design of the upper layer communication protocol and the network deployment in different scenarios. This paper analyzes the performance of conditional connectivity with the network topology change by establishing the model of inter-vehicle communication. The paper aims at the two-lane highway scenario for vehicular ad hoc networks (VANETs), considering the factors of communication range, vehicle flow characteristics and moving speed. The main conditional connectivity performance index is the conditional connectivity probability. Based on the simulation, the correctness of the theoretical analysis is verified. We also make an explanation of the simulation results.

Keywords: VANETs · Conditional connectivity performance
Two lanes · User level

1 Introduction

As a realization form of distributed wireless network, mobile ad hoc networks (MANETs) have received extensive attention from numerous institutes and researchers around the world in recent years. MANETs don't rely on the support of fixed infrastructure, consisting of mobile communication nodes which can form the networks quickly and have the ability of storing and computing information. MANETs can complete the transmission of information through the multi-hop communication between nodes. As a special kind of MANETs, vehicular ad hoc networks (VANETs) are formed with self-organizing vehicle nodes. Vehicles in VANETs can perform the multi-hop communication by vehicle-to-vehicle (V2V) and vehicle-to-infrastructure (V2I), completing information transmission and data distribution [1]. VANETs can ensure traffic safe and improve transportation efficiency, and therefore it has aroused people's wide attention in the field of transportation.

Compared with the traditional MANETs, the communication vehicles in VANETs can provide enough electric energy. However, its trajectory is limited by the geometry

of the road. Hence, it has certain predictability and regularity. Unlike traditional ad hoc networks, the high speed mobility of the vehicle nodes can cause the network topology to change dynamically, making the inter-vehicle communication links prone to interrupt and reducing the effective coverage and transmission performance. In recent years, a large number of scholars have carried out research on the connectivity of VANETs [2–4]. Based on the assumption that nodes obey the uniform distribution, the connectivity performance of vehicular networks is analyzed by [5]. However, the mobility of nodes is not considered. Literature [6] has verified the basic characteristics connectivity performance in VANETs through a lot of simulations and how the change of the relative position between the vehicle and the road can affect the connectivity performance has been discussed. In [7], a new type of mobility model is established, and the connection probability was derived based on this model. The author discussed how the mobility of vehicle nodes will affect the performance of the connectivity. In [8], a vehicle flow mobility model is established which is more close to the actual highway scenario. The paper analyzed the statistical characteristics of multiple connectivity performance indexes, considering the effects of different system parameters. In this system model, the vehicle arrival rate depends on the speed of vehicles. Therefore, this hypothesis does not apply to general scenarios for VANETs. These papers mentioned above have not considered the influence of the network topology change on the stability of data transmission. And most of the papers have analyzed the impact of vehicle mobility on the whole network connectivity performance from the system level. Literature [9] analyzes the influence of the vehicle movement characteristics and the network topology change on the conditional connectivity performance based on the model of freeway scene from the user level. However, its scene is restricted to the single-lane highway, which can't adapt to the more complex reality scene, therefore it has certain limitations.

In order to meet the need of continuous data service for a long time, this paper establishes a model in the two-lane highway scenario based on literature [9]. The influence of the system parameters such as the vehicle flow arrival rate, the speed of the vehicle, the communication range and the data transmission time on the conditional connectivity performance is considered. The main performance index is conditional connectivity probability. First, we derive the statistical distribution characteristics of the initial inter-vehicle distance in the two-lane scenario. The initial inter-vehicle distance represents the distance between the two vehicles when they enter the highway entrance. Then we calculate the distribution characteristics of the relative speed of the vehicles in the two-lane scenario. Finally, we obtain the analytical expression for the conditional connectivity probability in the two-lane scenario. The conclusions of this paper can provide theoretical guidance for the design and deployment of VANETs in the two-lane highway scenario.

The remainder of the paper is organized as follows. The system model in two-lane highway scenario is briefly described in Sect. 2. In Sect. 3, the conditional connectivity performance is analyzed by the theoretical derivation. In Sect. 4, we verify the correctness of the theoretical analysis by the system simulation and make an explanation for the results. Section 5 summarizes the whole paper and gives a conclusion.

2 System Model

In this paper, a two-lane highway scenario is modeled based on Poisson Point Process. The main model assumptions are as follows.

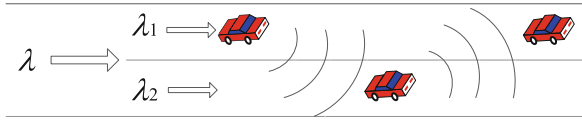


Fig. 1. Two-lane highway communication model

- Each vehicle node in the network is assumed to have the same ability to communicate with others. It is the same as the communication radius of each node, which is called R . When the distance between the two vehicles is less than R , the communication link can be considered connected.
- As shown in Fig. 1, the arrival of vehicles in the two-lane highway entrance follows a Poisson process with λ (vehicles per second). After the arrival at the highway, each vehicle will choose a lane to enter, based on the wishes of the driver. According to the drivers' choices, we assume that the arrival rate in the fast lane is λ_1 and the arrival rate in the slow lane is λ_2 . Hence, we can get the relation $\lambda = \lambda_1 + \lambda_2$. When the vehicle enters the fast or the slow lane, it will choose a constant speed v_i , which is independent uniformly distributed. If the vehicle enters the fast lane, the distribution interval of speed is $[v_{min1}, v_{max1}]$. If the vehicle enters the slow lane, the interval is $[v_{min2}, v_{max2}]$. In order to facilitate the calculation, assume that the minimum speed of the fast lane v_{min1} is equal to the maximum speed of the slow lane v_{max2} and the total arrival rate of two lane entrances is a constant 1 veh/sec. Therefore, the probability density function (pdf) of the speed v_i is given as:

$$f_{v_i}(x) = \begin{cases} \frac{1}{v_{max1} - v_{min1}} & v_{min1} \leq x \leq v_{max1} \\ \frac{1}{v_{max2} - v_{min2}} & v_{max2} \leq x \leq v_{min2} \\ 0 & \text{otherwise} \end{cases} \quad (1)$$

- Random variable T_i represents the arrival time interval of vehicles. According to the stochastic process theory, the arrival time interval T_i is independent identically distributed (i.i.d) with exponential distribution with parameter λ . Therefore, the pdf of T_i can be expressed as:

$$f_{T_i}(y) = \begin{cases} \lambda e^{-\lambda y} & y \geq 0 \\ 0 & y < 0 \end{cases} \quad (2)$$

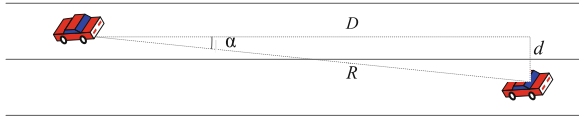


Fig. 2. Different-lane communication model

- As shown in Fig. 2, we discuss the critical situation of communication interruption when the two vehicles run in different lanes. The distance d between the adjacent lanes is very small compared with the communication radius R . That is α is approximately equal to zero. Therefore, this model can be simplified as the communication model that vehicles run in the same lane.
- Assume that the mobility of each vehicle is independent and is not affected by other vehicles. There can be the overtaking phenomenon without lane-changing to simplify the theoretical analysis.

According to [9], at the initial observation time $t = 0$, the vehicle i arrives at the highway entrance. Then it will choose a lane to enter according to the driver and choose a constant speed v_i in the speed range of the lane. After a period of time T_i , another vehicle j arrives at the entrance of the highway. It will also choose a lane to enter according to the driver and choose a constant speed v_j in the speed range of the lane. Assuming the vehicles i and j begin to transmit data, the communication distance between them at present is about $d_i = v_i T_i$. d_i is defined the initial inter-vehicle distance. Assuming the whole transmission time is T_t , if the link between i and j stay stable during the whole transmission, the packet can be received successfully at the time $t = T_i + T_t$. At this time, the distance between vehicles is defined d_t .

3 Performance Analysis

3.1 Initial Inter-vehicle Distance

After the vehicle i arriving at the entrance of the highway, the vehicle chooses a lane and continues moving with a speed of v_i . After a time interval T_i , another vehicle j arrives at the entrance. At the moment, two vehicles are d_i apart, which can be expressed as:

$$d_i = v_i T_i \tag{3}$$

v_i and T_i are independent random variables, therefore their joint probability density can be expressed as:

$$f_{v_i, T_i}(x, y) = f_{v_i}(x) f_{T_i}(y) \tag{4}$$

By combining (1) (2) with (3), the pdf of initial inter-vehicle distance d_i can be calculated as:

$$\begin{aligned}
 f_{d_i}(z) &= \int_{-\infty}^{+\infty} \frac{1}{|z|} f_{v_i}\left(\frac{z}{y}\right) f_{T_i}(y) dy = \begin{cases} \frac{\lambda}{v_{max1} - v_{min1}} \int_{z/v_{max1}}^{z/v_{min1}} \frac{1}{y} e^{-\lambda y} dy \\ \frac{\lambda}{v_{max2} - v_{min2}} \int_{z/v_{max2}}^{z/v_{min2}} \frac{1}{y} e^{-\lambda y} dy \end{cases} \\
 &= \begin{cases} \frac{\lambda}{v_{max1} - v_{min1}} \int_{\lambda z/v_{max1}}^{\lambda z/v_{min1}} t^{-1} e^{-t} dt & \text{the front vehicle in fast lane} \\ \frac{\lambda}{v_{max2} - v_{min2}} \int_{\lambda z/v_{max2}}^{\lambda z/v_{min2}} t^{-1} e^{-t} dt & \text{the front vehicle in slow lane} \end{cases} \tag{5}
 \end{aligned}$$

By analyzing (5), we can notice that the pdf $f_{d_i}(z)$ of initial inter-vehicle distance d_i is related to the Exponential Integral $E_I(z)$ [10]. The special function $E_I(z)$ can be expressed as:

$$E_I(z) = \int_z^{\infty} e^{-t} t^{-1} dt \tag{6}$$

Hence, we can get the pdf $f_{d_i}(z)$ of initial inter-vehicle distance d_i through calculating (5) with $E_I(z)$.

$$f_{d_i}(z) = \begin{cases} \frac{\lambda}{v_{max1} - v_{min1}} \left[E_I\left(\frac{\lambda z}{v_{max1}}\right) - E_I\left(\frac{\lambda z}{v_{min1}}\right) \right] & \text{the front vehicle in fast lane} \\ \frac{\lambda}{v_{max2} - v_{min2}} \left[E_I\left(\frac{\lambda z}{v_{max2}}\right) - E_I\left(\frac{\lambda z}{v_{min2}}\right) \right] & \text{the front vehicle in slow lane} \end{cases} \tag{7}$$

According to (7), the cumulative distributed function (CDF) $F_{d_i}(x)$ of d_i can be given as:

$$F_{d_i}(x) = Pr\{d_i \leq x\} = \int_0^x f_{d_i}(z) dz \tag{8}$$

Therefore, we can get the probability that the initial inter-vehicle distance is not more than the communication range R according to (8), which can be expressed as:

$$Pr\{d_i \leq R\} = \int_0^R f_{d_i}(z) dz \tag{9}$$

3.2 Conditional Connectivity Probability

Conditional connectivity probability is defined as the probability that two vehicles are constantly connected during the whole data transmission time T_t , given that the vehicles begin to communicate when they arrive at the highway entrance. Therefore, the conditional connectivity probability can be considered as the probability that the vehicles are always within the communication range of each other until the transmission is finished successfully.

The initial inter-vehicle distance is d_i , when the vehicle i and j begin to transmit data. After the complete data transmission, the vehicle communication link still keeps connected, and at the moment two vehicles are d_t apart. That is

$$d_t = |d_i + (v_i - v_j)T_t| = |d_i + \Delta v T_t| \tag{10}$$

Hence, the conditional connectivity probability P_{con} is the probability that i and j stay connected during the whole data transmission, given that i and j are within the communication range of each other at the beginning of transmission.

$$P_{con} = \Pr\{d_t \leq R | d_i \leq R\} = \frac{\Pr\{d_t \leq R, d_i \leq R\}}{\Pr\{d_i \leq R\}} \tag{11}$$

It can be found that P_{con} depends on initial inter-vehicle distance d_i , relative speed Δv , data transmission time T_t and communication range R .

As for relative speed Δv , we can get the derivation results with reference to [9].

- When the two vehicles are all in the fast lane, the pdf of Δv is

$$f_{\Delta v_1}(u) = \begin{cases} \frac{u + v_{max1} - v_{min1}}{(v_{max1} - v_{min1})^2} & v_{min1} - v_{max1} \leq u \leq 0 \\ \frac{-u + v_{max1} - v_{min1}}{(v_{max1} - v_{min1})^2} & 0 \leq u \leq v_{max1} - v_{min1} \\ 0 & \text{otherwise} \end{cases} \tag{12}$$

- When the two vehicles are all in the slow lane, the pdf of Δv is

$$f_{\Delta v_2}(u) = \begin{cases} \frac{u + v_{max2} - v_{min2}}{(v_{max2} - v_{min2})^2} & v_{min2} - v_{max2} \leq u \leq 0 \\ \frac{-u + v_{max2} - v_{min2}}{(v_{max2} - v_{min2})^2} & 0 \leq u \leq v_{max2} - v_{min2} \\ 0 & \text{otherwise} \end{cases} \tag{13}$$

- When i is in the fast lane and j is in the slow lane, the pdf of Δv is

$$f_{\Delta v_3}(u) = \begin{cases} \frac{-v_{min2} - u + v_{max1}}{(v_{max1} - v_{min1})(v_{max2} - v_{min2})} & 0 \leq v_{max1} - v_{max2} \leq u \leq v_{max1} - v_{min2} \\ \frac{u - v_{min1} + v_{max2}}{(v_{max1} - v_{min1})(v_{max2} - v_{min2})} & 0 \leq v_{min1} - v_{max2} \leq u \leq v_{min1} - v_{min2} \\ 0 & \text{otherwise} \end{cases} \tag{14}$$

- When i is in the slow lane and j is in the fast lane, the pdf of Δv is

$$f_{\Delta v_4}(u) = \begin{cases} \frac{u-v_{min2}+v_{max1}}{(v_{max1}-v_{min1})(v_{max2}-v_{min2})} & v_{min2} - v_{max1} \leq u \leq v_{min2} - v_{min1} \leq 0 \\ \frac{-u-v_{min1}+v_{max2}}{(v_{max1}-v_{min1})(v_{max2}-v_{min2})} & v_{max2} - v_{max1} \leq u \leq v_{max2} - v_{min1} \leq 0 \\ 0 & \text{otherwise} \end{cases} \quad (15)$$

Due to the randomness of two vehicles' speed, the vehicle i and j may be far away from each other or may be close to each other. We discuss the two cases respectively. We assume that $|\Delta v_{max} T_t| \leq R$ to simplify the analysis, where the $|\Delta v_{max} T_t|$ represents the upper limit to the variation of the inter-vehicle distance.

When i and j are far away from each other, the conditional connectivity probability can be expressed as the joint probability of $\{d_t \leq R\}$, $\{d_i \leq R\}$ and $\{v_i \geq v_j\}$.

$$\begin{aligned} p_1 &= \Pr\{d_t \leq R, d_i \leq R, v_i \geq v_j\} \\ &= \Pr\{0 \leq d_i \leq R - \Delta v T_t, \Delta v \geq 0\} \\ &= \frac{\lambda_1^2}{\lambda^2} \int_0^{v_{max1}-v_{min1}} \int_0^{R-\Delta v T_t} f_{d_i}(z) f_{\Delta v_1}(u) dz du + \frac{\lambda_2^2}{\lambda^2} \int_0^{v_{max2}-v_{min2}} \int_0^{R-\Delta v T_t} f_{d_i}(z) f_{\Delta v_2}(u) dz du \\ &\quad + \frac{\lambda_1 \lambda_2}{\lambda^2} \int_{v_{max1}-v_{max2}}^{v_{max1}-v_{min2}} \int_0^{R-\Delta v T_t} f_{d_i}(z) f_{\Delta v_3}(u) dz du + \frac{\lambda_1 \lambda_2}{\lambda^2} \int_{v_{min1}-v_{max2}}^{v_{min1}-v_{min2}} \int_0^{R-\Delta v T_t} f_{d_i}(z) f_{\Delta v_3}(u) dz du \end{aligned} \quad (16)$$

When i and j are close to each other, the conditional connectivity probability can be expressed as the joint probability of $\{d_t \leq R\}$, $\{d_i \leq R\}$ and $\{v_i \leq v_j\}$.

$$\begin{aligned} p_2 &= \Pr\{d_t \leq R, d_i \leq R, v_i \leq v_j\} \\ &= \Pr\{|d_i + \Delta v T_t| \leq R, d_i \leq R, \Delta v \leq 0\} \\ &= \frac{\lambda_1^2}{\lambda^2} \int_{v_{min1}-v_{max1}}^0 \int_0^R f_{d_i}(z) f_{\Delta v_1}(u) dz du + \frac{\lambda_2^2}{\lambda^2} \int_{v_{min2}-v_{max2}}^0 \int_0^R f_{d_i}(z) f_{\Delta v_2}(u) dz du \\ &\quad + \frac{\lambda_1 \lambda_2}{\lambda^2} \int_{v_{min2}-v_{max1}}^{v_{min2}-v_{min1}} \int_0^R f_{d_i}(z) f_{\Delta v_4}(u) dz du + \frac{\lambda_1 \lambda_2}{\lambda^2} \int_{v_{max2}-v_{max1}}^{v_{max2}-v_{min1}} \int_0^R f_{d_i}(z) f_{\Delta v_4}(u) dz du \end{aligned} \quad (17)$$

According to the law of total probability and combining (16) with (17), we can get the joint probability of $\{d_t \leq R\}$ and $\{d_i \leq R\}$.

$$\begin{aligned} &\Pr\{d_t \leq R, d_i \leq R\} \\ &= \Pr\{d_t \leq R, d_i \leq R, v_i \geq v_j\} + \Pr\{d_t \leq R, d_i \leq R, v_i < v_j\} \\ &= p_1 + p_2 \end{aligned} \quad (18)$$

Hence, substituting (9) and (18) to (11), we can get the analytical result of P_{con} .

4 Simulation Results

In this section, we will give the analytical and simulation results of the initial inter-vehicle distance and the conditional connectivity performance for different system parameters, such as the communication range and the vehicle flow arrival rate in each lane. System simulation parameters are set as shown in Table 1. In this paper, we adopt the Monte Carlo simulation method. For different simulation parameters, 10^5 trials are generated.

Table 1. Simulation parameters.

Parameters	Values
v_{min1}, v_{max2}	25 m/s
v_{max1}	35 m/s
v_{min2}	15 m/s
T_t	5 s
λ_1	0, 0.2, 0.5, 0.8, 1 veh/sec
λ	1 veh/sec

In Fig. 3, we can acquire the analytical and simulation results of $F_{di}(x)$ with different vehicle flow arrival rates $\lambda_1, \lambda_2 (\lambda_2 = \lambda - \lambda_1)$ in two lanes. As shown in the figure, the value of the cumulative distribution function $F_{di}(x)$ will increase with the increase of the initial inter-vehicle distance d_i . In addition, with the increase of the vehicle flow arrival rate λ_1 in the fast lane, the value of the cumulative distribution function $F_{di}(x)$ will be decreased. For example, the probability that d_i is not more than 50 meters is about 0.9 when the value of λ_1 is 0.2. However, that probability can decrease to 0.83 when the λ_1 increased to 0.8. This is because the higher proportion of vehicles in the fast lane, the higher mobility of the whole vehicles. Hence, the initial inter-vehicle distance gets larger and the connectivity performance becomes worse. We can also notice that when the value of λ_1 increased, the change of the value of $F_{di}(x)$ is not large, because the total vehicle flow arrival rate λ in two lanes is constant. When the value of λ_1 is 0, the result is the same as the $F_{di}(x)$ in [9] (when $\lambda = 1, v_{max} = 25$ m/s, $v_{min} = 15$ m/s).

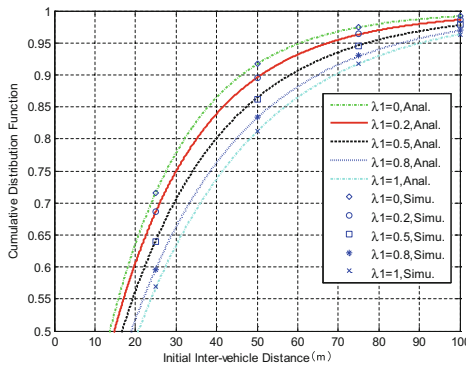


Fig. 3. CDF of initial inter-vehicle distance with various λ_1

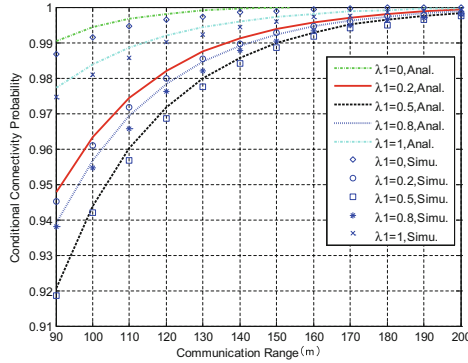


Fig. 4. Conditional connectivity probability with various λ_1

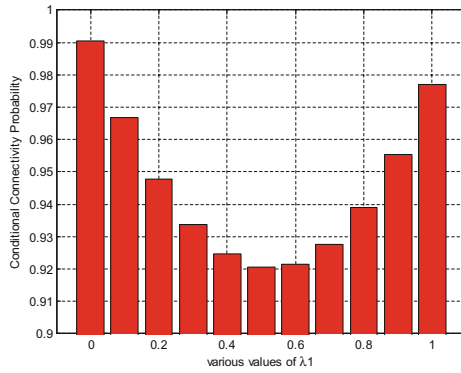


Fig. 5. Conditional connectivity probability with various λ_1 when R is 90 m

In Fig. 4, we can acquire the performance of conditional connectivity probability P_{con} in different communication range R and vehicle flow arrival rate λ_1 and λ_2 . According to the curve in the figure, we can find that P_{con} increases with the increase of R . That is, the improvement of the node communication ability is helpful to achieve the link connected constantly. P_{con} can't keep increasing or decreasing at all time with the increasing of λ_1 , but performs decreasing previously and increasing later as shown in Fig. 5. This is because when the proportions of the vehicles in the fast and slow lane are the same, the mean value of the speed difference among the vehicles is the largest, which will result in the worst conditional connectivity performance. In addition, we consider the cases that the proportions of vehicles in the fast and slow lane are different. P_{con} with $\lambda_1 = 0.1$ is higher slightly than the P_{con} with $\lambda_1 = 0.9$. This is because while in these two cases the mean values of the speed difference among the vehicles are the same, the low-speed vehicles with $\lambda_1 = 0.1$ are more than $\lambda_1 = 0.9$. The communication link between the vehicles with low speed is more stable, therefore the conditional connectivity performance is better when $\lambda_1 = 0.1$. When the value of λ_1 is 0, the result is the same as the P_{con} in [9] (when $\lambda = 1$, $v_{max} = 25$ m/s, $v_{min} = 15$ m/s).

5 Conclusion

According to the demand of the users' service in VANETs, this paper analyzes the influence of the distribution characteristics of the two-lane vehicle flow and the parameters of the communication system on the conditional connectivity performance. The main conditional connectivity performance index is the conditional connectivity probability. First, a system model in two-lane highway scenario is established. Then we derive the analytical expressions for the initial inter-vehicle distance and the conditional connectivity probability. Finally, we verify the theoretical results by software simulation and make an analysis of the conditional connectivity performance of the communication link. The results of this paper can be applied to design the upper layer communication protocol. For example, in the two-lane routing protocol, the conditional connectivity performance can be used as a routing criterion to determine whether the link can be selected as the next-hop communication link.

Acknowledgments. This work was supported by the New Century Excellent Talent Support Program (NCET-13-0657), 863 Program (2015AA016005) and the State Key Laboratory of Rail Traffic Control and Safety (RCS2016ZT015).

References

1. Hafeez, K.A., Zhao, L., Ma, B., Mark, J.W.: Performance analysis and enhancement of the DSRC for VANET's safety applications. *IEEE Trans. Veh. Technol.* **62**(7), 3069–3083 (2013)
2. Sharif-Nassab, A., Ashtiani, F.: Connectivity analysis of one-dimensional ad hoc networks with arbitrary spatial distribution for variable and fixed number of nodes. *IEEE Trans. Mob. Comput.* **11**(10), 1425–1435 (2012)
3. Wang, B.X., Yin, K., Zhang, Y.: An exact markov process for multihop connectivity via intervehicle communication on parallel roads. *IEEE Trans. Wirel. Commun.* **11**(3), 865–868 (2011)
4. Abuelenin, S.M., Abul-Magd, A.Y.: Effect of minimum headway distance on connectivity of VANETs. *AEU Int. J. Electron. Commun.* **69**(5), 867–871 (2015)
5. Yan, Z., Jiang, H., Shen, Z., Chang, Y.: k -connectivity analysis of one-dimensional linear VANETs. *IEEE Trans. Veh. Technol.* **61**(1), 426–433 (2012)
6. Shioda, S., Harada, J., Watanabe, Y., Goi, T., Okada, H., Mase, K.: Fundamental characteristics of connectivity in vehicular ad hoc networks. In: *IEEE 19th International Symposium on Personal, Indoor and Mobile Radio Communications*, pp. 1–6, September 2008
7. Hafeez, K.A., Zhao, L., Liao, Z., Ma, N.W.: Impact of mobility on VANETs' safety applications. In: *Global Telecommunications Conference*, pp. 1–5 (2010)
8. Yousefi, S., Altman, E., El-Azouzi, R., Fathy, M.: Analytical model for connectivity in vehicular ad hoc networks. *IEEE Trans. Veh. Technol.* **57**(6), 3341–3356 (2008)
9. Chen, R., Zhong, Z., Chang, C.Y., Ai, B., He, R.: Performance analysis on network connectivity for vehicular ad hoc networks. *Int. J. Ad Hoc Ubiquit. Comput.* **20**(2), 67–77 (2015)
10. Gradshteyn, I.S., Ryzhik, I.M.: *Table of Integrals, Series, and Products*, 7th edn. Academic Press, London (2007)



Optimized Workload Allocation in Vehicular Edge Computing: A Sequential Game Approach

Dongdong Ye, Maoqiang Wu, Jiawen Kang, and Rong Yu(✉)

Guangdong University of Technology, Guangzhou, China
dongdongye8@163.com, maoqiang.wu@vip.163.com,
kjwx886@163.com, yurong@ieee.org

Abstract. With the development of Vehicle-to-Everything (V2X) communication technologies, Vehicular Edge Computing (VEC) is utilized to speed up the running of vehicular computation workload by deploying VEC servers in close proximity to vehicular terminals. Due to resource limitation of VEC servers, VEC servers are unable to perform a large number of vehicular computation workloads. To improve the performance of VEC servers, we propose a new workload allocation framework where vehicular terminals are divided into Resource Provision Terminals (RPTs) and Resource Demand Terminals (RDTs). In this framework, we design an optimized workload allocation strategy through a sequential Stackelberg game. With the sequential Stackelberg game, a VEC server, RDTs, and RPTs achieve an efficient coordination of the workload allocation. The sequential Stackelberg game is proven to reach two sequential Nash Equilibriums. The simulation results validate the efficiency of the optimized workload allocation strategy.

Keywords: Vehicular edge computing · Workload allocation
Sequential Stackelberg game

1 Introduction

With the development of Vehicle-to-Everything (V2X) communication technologies, vehicular networks have gained extensive attention in recent years [1]. Meanwhile, vehicular terminals in vehicular networks can run various new applications such as real-time navigation, interactive gaming and augmented reality. However, vehicular terminals have relatively limited resources due to the physical size constraint. Therefore, it is difficult for vehicular terminals to support real-time and low-latency applications.

In order to meet the requirement of resource-constraint vehicular terminals, Vehicular Edge Computing (VEC) was proposed for vehicular network. VEC is similar to the concept of vehicular fog computing which has been proposed in [2]. VEC locally deploys light-weight cloud servers in close proximity to vehicular

terminals. Therefore, vehicular terminals can get realtime interaction and low delay services from VEC servers. Due to resource limitation of VEC servers, VEC servers are unable to perform a large number of vehicular computation workloads [3]. Thus, an optimized workload allocation strategy is essential for a VEC server in vehicular network.

Many researchers engaged in studying the efficient workload allocation strategies. In [3], the authors studied delay constrained offloading for vehicular edge computing in cloud-enabled vehicular networks and designed an efficient computation offloading scheme with a contract theoretic approach. In [4], the authors proposed to combine the vehicular cloud with the infrastructure-based cloud to expand the current available resources for task requests from smartphones, and designed an algorithm to select the suitable cloud service provider to perform the requested task. In [5], the authors proposed a non-cooperation matrix game to balance the workload of multiple local servers for vehicular terminals. In [6], the authors used Semi-Markov Decision Process method to optimize computation resource allocation scheme in vehicular cloud computing.

Vehicular terminals, having idle computation resources, are normally distributed within the coverage of the VEC server. However, few work has considered utilizing idle computation resources of vehicular terminals as the compensation of the VEC server. In addition, the mobility of vehicular terminals has been ignored in those work. In this paper, we propose a new workload allocation framework in vehicular network. The main contributions of this paper are summarized as follows.

- We propose a new workload allocation framework. In this framework, vehicular terminals are divided into Resource Provision Terminals (RPTs) and Resource Demand Terminals (RDTs). We design an optimized workload allocation strategy for the combination of RPTs, RDTs, and a VEC server.
- We elaborately use a sequential Stackelberg game to analyze and solve the optimized workload allocation. With the sequential Stackelberg game, the VEC server, RPTs and RDTs can maximize their utilities, respectively.
- The sequential Stackelberg game is proven to reach two unique sequential Nash Equilibriums. We propose a sequential algorithm to find out the unique solution for the Nash Equilibriums.

The rest of this paper is organized as follows. System model is introduced in Sect. 2. Problem formulation is presented in Sect. 3. We present the workload allocation strategy and propose a sequential algorithm for the sequential Stackelberg game in Sect. 4. The simulation results are presented in Sect. 5. We conclude the paper in Sect. 6.

2 System Model

Figure 1 shows the new workload allocation framework. The framework consists of a VEC server and vehicular terminals within the communication radius of the VEC server. In one cycle, when vehicular terminals are executing real-time and

low-latency applications, they become Resource Demand Terminals (RDTs) who require computation resources for computation services. We denote N as the set of RDTs. When vehicular terminals are under low-loaded condition, they become Resource Provision Terminals (RPTs) who have idle computation resources. We denote M as the set of RPTs. We denote K as the set of total vehicular terminals. The roles of the RDTs and RPTs may be converted under different conditions ($K = N + M$).

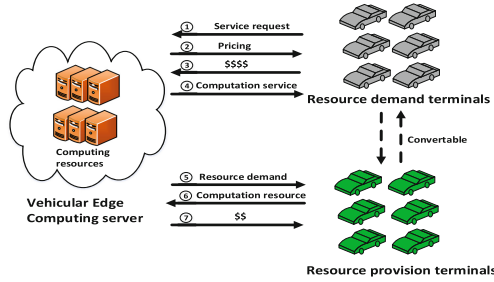


Fig. 1. The workload allocation framework.

RDT $n \in N$ wants to purchase computation amount x_n from the VEC server. The unit price charged by the VEC server for computation resource is denoted as p_n . Taking the payment into consideration, each RDT adjusts its required computation amount. After collecting the required computation amount from RDTs, the VEC server adjusts the unit price for its own maximum utility. Finally, the VEC server and RDTs reach a coordination with mutually satisfactory unit price and computation amount. Further, to improve the performance of the VEC server, the VEC server offers an incentive R_0 to recruit idle computation resources from M to serve RDTs. The computation amount that the RPT $m \in M$ provides is denoted as y_m . Considering the cost and obtained incentive, each RPT adjusts its offered computation amount. After collecting the offered computation amount from RPTs, the VEC server adjusts the incentive. Finally, the VEC server and RPTs reach a coordination with mutually satisfactory incentives and computation amount.

3 Problem Formulation

3.1 Utilities of RDTs and RPTs

The satisfaction function monotonically increases on x_n . Therefore, we define the satisfaction function of RDT n as $\varphi_n \log(x_n + 1 - x_n^{\min})$, where φ_n is a parameter and x_n^{\min} is the minimum demand computation amount. The cost of RDT n is the payment to the VEC server, which is given by $p_n x_n$. Therefore, the utility of RDT n is denoted as

$$u_n = \varphi_n \log(x_n + 1 - x_n^{\min}) - p_n x_n. \tag{1}$$

Following the principle of proportional sharing, the incentive amount of RPT m is proportional to its offered computation amount. For convenience, the incentive of RPT m is given by $\frac{y_m}{\sum_{m \in M} y_m} R_0$. Therefore, the utility of RPT m is denoted as

$$u_m = \frac{y_m}{\sum_{m \in M} y_m} R_0 - e_m y_m, \tag{2}$$

where e_m is unit energy consumption. According to the realistic measurements in [7,8], we can set $e_m = 10^{-11}(s_m)^2$, where s_m is computation capability of RPT m .

3.2 Utility of VEC Server

The total cost includes the computation energy consumption and transmission energy consumption of the VEC server.

Firstly, the VEC server serves RDTs with computation amount $\sum_{n \in N} x_n$. To reduce the energy consumption, the VEC server pays R_0 to recruit computation amount $\sum_{m \in k} y_m$ from RPTs. From [9], the computation energy consumption of the VEC server is denoted as $c_0 = \sigma_0(z_0)^2 + \eta_0 z_0 + \alpha_0$, where $z_0 = \sum_{n \in N} x_n - \sum_{m \in k} y_m$. It is provided by the VEC server.

Secondly, the transmission energy consumption of the VEC server is related to the mobility of RPTs. From [4,10], we know that the wireless channel would fade when RPT m is driving at high speed. When the speed of RPT m is less than a threshold speed, the bandwidth resource of m is B_m^{in} . When the speed of RPT m exceeds the threshold speed, the fading rate of RPT m is proportional to its speed and denoted as $r_m = wv_m$, where w is a constant factor. Therefore, the bandwidth resources consumed by RPT m are denoted as $B_m = B_m^{in} + \int r_m dt$, where t is the residence time of RPT m within the communication coverage of the VEC server. From [11], the transmission rate of RPT m can be obtained by $R_m = B_m \log_2(1 + \frac{P_m d_m^{-\eta} |h_0|^2}{N_0})$, where η is a parameter and d_m is the average distance between the VEC server and RPT m . P_m is the transmit power of the VEC server. h_0 is the complex Gaussian channel coefficient that follows the complex normal distribution $CN(0, 1)$. N_0 is the additive white Gaussian noise (AWGN) at the RPT receivers. Therefore, the transmission energy consumption is denoted by $q_m = \frac{y_m}{R_m} P_m$. The utility of the VEC server is denoted as

$$u_0 = \sum_{n \in N} p_n x_n - c_0 - R_0 - \beta_0 \sum_{m \in M} q_m, \tag{3}$$

where β_0 is unit cost per energy consumption.

All the RPTs, the VEC server, and the RDTs are assumed to be rational and want to make multilevel independent decision to maximize their utilities. It is impossible that the utilities of three-party are satisfied simultaneously, due

to the heterogenous framework of the workload allocation. A sequential stackelberg game studies the sequential decision of the players. Therefore, we model the sequential decision as the sequential stackelberg game [12]. The problem is formulated to

$$\max_{R_0}(u_0), \tag{4}$$

$$s.t. \max_{x_n \in X}(u_n | p_n, R_0), \tag{5}$$

$$\max_{y_m \in Y}(u_m | R_0). \tag{6}$$

The optimal decisions of the three-party including the VEC server, the RDTs and the RPTs are analyzed based on their utilities. In the first stage, the VEC server is the leader and the RDTs are the followers. Their optimal decisions are charged prices and requested computation amount respectively. In the second stage, the VEC server is the leader and the RPTs are followers. Their optimal decisions are optimal incentives and offered computation amount.

4 Solution and Algorithm

In this section, we use the backward induction method to prove the existence and uniqueness of the sequential Nash Equilibriums for problem (6). We propose a sequential algorithm for the sequential Stackelberg game.

4.1 Stackelberg Equilibrium Solution

4.1.1 Nash Equilibrium Between VEC Server and RDTs

Theorem 1. A unique Nash Equilibrium exists between the RPTs and the VEC server.

Proof: by taking the derivative of the utility function u_n with respect to x_n , we obtain

$$\frac{d^2u_n}{dx_n^2} = -\frac{\varphi_n}{(x_n + 1 - x_n^{\min})^2} < 0. \tag{7}$$

Clearly, the utility function u_n of n is concave function, which indicates that the maximum value of the utility function exists. Using first order optimality condition $\frac{du_n}{dx_n} = 0$, we get the optimal computation amount $x_n^* = \frac{\varphi_n}{p_n} + x_n^{\min} - 1$.

From the above equation, we know the relationship between the price and the optimal computation amount. We derivative the optimal price, denoted as $p_n^* = \frac{\varphi_n}{x_n + 1 - x_n^{\min}}$, based on the interaction between RDT n and the VEC server. We substitute p_n^* into Eq. (3) and get

$$u_0 = \sum_{n \in N} \frac{\varphi_n}{x_n + 1 - x_n^{\min}} x_n - c_0. \tag{8}$$

The second derivative of the function can be obtained as

$$\frac{\partial^2 u_0}{\partial x_n^2} = -2 \frac{\varphi_n}{(x_n + 1 - x_n^{\min})^3} - 2\beta_0\sigma_0 < 0. \quad (9)$$

Clearly, the second-order derivative of the utility of the VEC server is negative and strictly convex function. Therefore a unique Nash Equilibrium exists in the game. ■

4.1.2 Nash Equilibrium Between VEC Server and RPTs

In the stage, the VEC server is the leader and the RPTs are the followers. We prove that it exists an Nash Equilibrium. The Nash Equilibrium is unique.

Definition 1. When the other followers' strategies \mathbf{y}_{-m} are given, the best response function $\mathbf{f}_m(y_m, \mathbf{y}_{-m})$ of RPT can be defined by

$$\mathbf{f}_m(y_m, \mathbf{y}_{-m}) = \arg \max u_m(y_m, \mathbf{y}_{-m}). \quad (10)$$

Theorem 2 (Existence). An Nash Equilibrium exists among RPTs.

Proof: give the second order condition of the RPT's utility $u_m(y_m, \mathbf{y}_{-m})$ as

$$\frac{\partial^2 u_m(y_m, \mathbf{y}_{-m})}{\partial y_m^2} = -2 \left(\frac{1}{y_m + \sum_{j \in k \setminus m} y_j} \right)^3 R_0 < 0. \quad (11)$$

Since the second-order derivative of u_m is negative, the utility u_m is a strictly convex function in y_m . Therefore an Nash Equilibrium exists in the game. ■

The Nash Equilibrium is unique. The key of the Nash Equilibrium is to prove that the best response function of each RPT is a standard function [14].

Definition 2. $\mathbf{f}(\mathbf{p}) = (\mathbf{f}_1(\mathbf{p}), \mathbf{f}_2(\mathbf{p}), \dots, \mathbf{f}_M(\mathbf{p}))$, where $\mathbf{p} = (p_1, \dots, p_M)$. $\mathbf{f}(\mathbf{p})$ is said to be standard if it satisfies the following properties for all $\mathbf{p} \geq 0$

- *Positivity:* $\mathbf{f}(\mathbf{p}) > 0$.
- *Monotonicity:* for all \mathbf{p} and \mathbf{p}' , if $\mathbf{p} > \mathbf{p}'$ then $\mathbf{f}(\mathbf{p}) > \mathbf{f}(\mathbf{p}')$.
- *Scalability:* for all $\mu > 1$, $\mu \mathbf{f}(\mathbf{p}) \geq \mathbf{f}(\mu \mathbf{p})$.

Theorem 3. The best response function $\mathbf{f}_m(y_m, \mathbf{y}_{-m})$ of RPT m is a standard function of \mathbf{y}_{-m} .

Proof: from the Theorem 1, we know that the utility function $u_0(y_m, \mathbf{y}_{-m})$ is strictly concave. Let $\frac{\partial u_0}{\partial x_i} = 0$, we get the best function $\mathbf{f}_m(y_m, \mathbf{y}_{-m})$ of m ,

$$\mathbf{f}_m(y_m, \mathbf{y}_{-m}) = \begin{cases} \sqrt{\frac{\sum_{i \in k/m} y_i R_0}{e_m}} - \sum_{i \in k/m} y_m, \\ 0, R_0 \leq e_i \sum_{i \in k/m} y_m. \end{cases} \quad (12)$$

Next, we prove that the best function $\mathbf{f}_m(y_m, \mathbf{y}_{-m})$ satisfies the three properties of a standard function.

- *Positivity*: when $y_m > 0$ and $R_0 \leq e_i \sum_{i \in k/m} y_i$ are satisfied, we get

$$f_m(y_m, \mathbf{y}_{-m}) = \sqrt{\frac{\sum_{i \in k/m} x_i R_0}{e_m}} - \sum_{i \in k/m} x_i > 0. \tag{13}$$

- *Monotonicity*: given the first order condition of $f_m(y_m, \mathbf{y}_{-m})$ with respect to y_i , we obtain

$$\frac{\partial f_m(y_m, \mathbf{y}_{-m})}{\partial y_i} = \sqrt{\frac{\sum_{i \in k/m} y_i R_0}{4e_m}} - 1 > 0. \tag{14}$$

We get the constrain $\sum_{i \in k/m} y_i > \frac{4E_m^{consu}}{R_0}$. When it is satisfied, the monotonicity is satisfied.

- *Scalability*: based on (12), we obtain

$$\lambda f_m(y_m, \mathbf{y}_{-m}) - f_m(\lambda y_m, \mathbf{y}_{-m}) = (\lambda - \sqrt{\lambda}) \sqrt{\frac{R_0 \sum_{i \in k/m} y_i}{e_m}}. \tag{15}$$

For $\forall \lambda > 1$, we have $(\lambda - \sqrt{\lambda}) > 0$. Therefore, it is positive.

Based on Eq.(12), we get the total amount computation of the RPTs as $\sum_{m \in k} y_m = \frac{(k-1)}{\sum_{m \in k} e_m} R_0$. We substitute $\sum_{m \in k} y_m$ into Eq.(6). The problem can be written as

$$\min(c_1), \tag{16}$$

$$s.t. k > 1, \tag{17}$$

$$R_0 > 0, \tag{18}$$

$$\beta_0, \sigma_0, \eta_0, \alpha_0 > 0, \tag{19}$$

where

$$c_1 = R_0 + \beta_0 \sigma_0 \left(\sum_{n \in N} x_n - \frac{(k-1)}{\sum_{m \in k} e_m} R_0 \right)^2 + \beta_0 \alpha_0 + \beta_0 \eta_0 \left(\sum_{n \in N} x_n - \frac{(k-1)}{\sum_{m \in k} e_m} R_0 \right) + \frac{(k-1)R_0}{\sum_{m \in k} e_m} \sum_{m \in k} \frac{P_m}{R_m}. \tag{20}$$

We give the second order condition and get $\frac{\partial^2 c_1}{\partial R_0^2} = 2A^2 \sigma_0 \beta_0 > 0$, where $A = \frac{k-1}{\sum_{m \in k} e_m}$. Clearly, the cost of the VEC server is convex, which indicates that the

minimum value of this function exists. Therefore, given first order optimality condition $\frac{dc_1}{dR_0} = 0$, we get the optimal R_0^*

$$R_0^* = \frac{2A \sum_{n \in N} x_n + \beta_0 \eta_0 A - 1 - A \sum_{m \in k} \frac{P_m}{R_m}}{2A^2 \sigma_0 \beta_0}. \quad (21)$$

4.2 Sequential Distributed Algorithm

To reach two sequential Nash Equilibrium, we propose a sequential algorithm. Details are given in Algorithm 1.

Algorithm 1. Reach the Nash Equilibrium

Input: $\bar{e} = (e_1, e_2, \dots, e_n)$
Output: $\bar{X} = (x_1, x_2, \dots, x_n)$, $\bar{Y} = (y_1, y_2, \dots, y_m)$
Initialize parameters e , \bar{N} , \bar{M} , U_0^{up} , U_0 , R_0 , k' , $error = (u_o^{up} - u_o)^2$
for RPT $m \leftarrow 1$ **to** M **do**
 if $E_i^{consu} < \frac{\sum_{m \in k} E_m^{consu}}{(k-1)}$ **then**
 | $k' \leftarrow k' \cup \{m\}$, $m \leftarrow m + 1$
 end
end
for RPT $m \leftarrow 1$ **to** k' **do**
 | $y_i^* = \frac{(k-1)}{\sum_{m \in k} E_m^{consu}} R_0 (1 - \frac{(k-1)}{\sum_{m \in k} e_m} e_i)$
end
for RDT $n \leftarrow 1$ **to** n **do**
 if $x_n = \frac{\varphi_n}{p_n} + x_n^{\min} - 1 > 0$ **then**
 | $n' \leftarrow n' \cup \{n\}$, $n \leftarrow n + 1$
 end
end
return $(y_1^*, y_2^*, \dots, y_j^*)$ $j \in k'$
return $(x_1^*, x_2^*, \dots, x_q^*)$ $q \in n'$
return $\sum_{z \in N'} x_z$
while $(u_o^{up} - u_o)^2 > error$ **do**
 The VEC server calculates the total utility.
 if $(u_o^{up} - u_o)^2 < error$ **then**
 | The algorithm ends.
 | **Output:** $\bar{X} = (x_1, x_2, \dots, x_n)$, $\bar{Y} = (y_1, y_2, \dots, y_m)$
 |
 end
 $R_0 \leftarrow R_0 + 1$; $u_o^{up} = u_o$.
end

5 Numerical Results

We evaluate the performance of the proposed workload allocation strategy by simulations. The VEC server is assumed to be located in (500, 500) (in m). We use the following parameter settings as that in [4, 5, 7, 9]: $\beta \in [2, 50]$, $\sigma = 2$, $\eta \in (0, \frac{3}{2})$, $\alpha \in [1, 10]$, $\varphi \in [10, 20]$, $v \in [1, 10]$, $s_m = 50$ to 100 GZ, $B_m = 6$ to 10 Mbps.

Figure 2 shows the total energy consumption of the VEC server with respect to the number of computation resource. The energy consumption of the VEC server increases as the number of computation resource increases. The energy consumption of the VEC server by our proposed workload allocation strategy consumes less energy for the same computation resource. It is because the VEC server utilizes idle computation resource of the RPTs to reduce its energy consumption. Figure 3 shows the cost of the VEC server in computation resources for two values of β_0 . The VEC server has higher cost with larger β_0 . With our proposed strategy, the VEC server consumes lower cost in computation resources. It is because the VEC server consumes lower cost and cooperates with the RPTs. Figure 4 shows the impact of the speed of RPTs on the cost of the VEC server. The cost of the VEC server n increases as the speed of RPTs increases. It is because that RPTs provide less computation resources as the cost of RPTs increases.

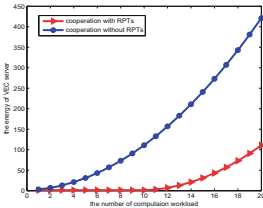


Fig. 2. Impact of computation resources on the VEC server

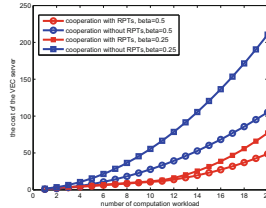


Fig. 3. Cost of the VEC server with different β_0

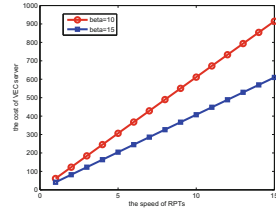


Fig. 4. Impact of the speed of RPTs on the VEC server.

6 Conclusion

In this paper, we propose a workload allocation framework in VEC. In the framework, RPTs are recruited to improve the performance of computation services which serve the RDTs. An optimized workload allocation strategy is proposed to maximize the utilities of the VEC server, the RPTs and the RDTs. We use a sequential Stackelberg game to design the strategy. The sequential Stackelberg game is proven to reach two sequential Nash Equilibriums. The simulations validate the efficiency of the optimized workload allocation strategy.

Acknowledgment. This work was supported in part by programs of NSFC under Grant nos. 61422201, 61370159 and U1301255, U1501251, the Science and Technology Program of Guangdong Province under Grant no. 2015B010129001, Special-Support Project of Guangdong Province under grant no. 2014TQ01X100, High Education Excellent Young Teacher Program of Guangdong Province under grant no. YQ2013057, Science and Technology Program of Guangzhou under grant no. 2014J2200097.

References

1. Yu, R., Zhang, Y., Gjessing, S., Xia, W., Yang, K.: Toward cloud-based vehicular networks with efficient resource management. *IEEE Netw.* **27**(5), 48–55 (2013)
2. Hou, X., Li, Y., Chen, M., Wu, D., Jin, D., Chen, S.: Vehicular fog computing: a viewpoint of vehicles as the infrastructures. *IEEE Trans. Veh. Technol.* **65**(6), 3860–3873 (2016)
3. Zhang, K., Mao, Y., Leng, S., Vinel, A., Zhang, Y.: Delay constrained offloading for mobile edge computing in cloud-enabled vehicular networks. In: 2016 8th International Workshop on Resilient Networks Design and Modeling (RNDM), pp. 288–294. IEEE (2016)
4. Zhang, H., Zhang, Q., Du, X.: Toward vehicle-assisted cloud computing for smartphones. *IEEE Trans. Veh. Technol.* **64**(12), 5610–5618 (2015)
5. Yu, R., Ding, J., Maharjan, S., Gjessing, S., Zhang, Y., Tsang, D.: Decentralized and optimal resource cooperation in geo-distributed mobile cloud computing. *IEEE Trans. Emerg. Top. Comput.* (2017)
6. Zheng, K., Meng, H., Chatzimisios, P., Lei, L., Shen, X.: An SMDP-based resource allocation in vehicular cloud computing systems. *IEEE Trans. Ind. Electron.* **62**(12), 7920–7928 (2015)
7. Chen, X.: Decentralized computation offloading game for mobile cloud computing. *IEEE Trans. Parallel Distrib. Syst.* **26**(4), 974–983 (2015)
8. Wen, Y., Zhang, W., Luo, H.: Energy-optimal mobile application execution: Taming resource-poor mobile devices with cloud clones. In: INFOCOM, 2012 Proceedings IEEE, pp. 2716–2720. IEEE (2012)
9. Deng, R., Lu, R., Lai, C., Luan, T.H., Liang, H.: Optimal workload allocation in fog-cloud computing towards balanced delay and power consumption. *IEEE Internet Things J.* **3**(6), 1171–1181 (2016)
10. Yu, R., Huang, X., Kang, J., Ding, J., Maharjan, S., Gjessing, S., Zhang, Y.: Cooperative resource management in cloud-enabled vehicular networks. *IEEE Trans. Ind. Electron.* **62**(12), 7938–7951 (2015)
11. Zhang, Y., Pan, E., Song, L., Saad, W., Dawy, Z., Han, Z.: Social network aware device-to-device communication in wireless networks. *IEEE Trans. Wire. Commun.* **14**(1), 177–190 (2015)
12. Zhang, H., Xiao, Y., Bu, S., Niyato, D., Yu, R., Han, Z.: Fog computing in multi-tier data center networks: a hierarchical game approach. In: 2016 IEEE International Conference on Communications (ICC), pp. 1–6. IEEE (2016)
13. Lee, J., Guo, J., Choi, J.K., Zukerman, M.: Distributed energy trading in microgrids: a game-theoretic model and its equilibrium analysis. *IEEE Trans. Ind. Electron.* **62**(6), 3524–3533 (2015)
14. Nisan, N., Roughgarden, T., Tardos, E., Vazirani, V.V.: *Algorithmic Game Theory*, vol. 1. Cambridge University Press, Cambridge (2007)



Navigation Route Based Stable Clustering for Vehicular Ad Hoc Networks

Zhiwei Yang, Weigang Wu, Yishun Chen, Xiaola Lin,
and Xiang Chen^(✉)

School of Data and Computer Science, Sun Yat-sen University,
Guangzhou 510006, China

{yangzhw, wuweig, chenys35, linxl,
chenxiang}@mail.sysu.edu.cn

Abstract. Due to high mobility of vehicles, stability has been always one of the major concerns of vehicle clustering algorithms. In this paper, we propose a novel clustering algorithm based on the information of route planned by vehicular navigation systems. Including route information into cluster mechanism is not trivial due to two issues: (i) stability is a property of time rather than position, (ii) route diversity may cause high re-clustering overhead at road intersections. To address the first issue, we propose a function to quantitatively calculate the overlapping time among vehicles based on route information, with which a novel clusterhead selection metric is designed. To address the second issue, we design a mechanism of future-clusterhead, which can help avoid message exchanges at intersections. The simulation results show that, compared with similar works, our algorithm can cluster vehicles with higher stability and at the same time lower communication cost.

Keywords: VANET · Clustering · Mobile computing
Information dissemination · Ad hoc networks

1 Introduction

Vehicular Ad hoc NETWORK (VANET) [1, 2] enables vehicles to communicate with roadside (V2R) or other vehicles (V2V) via wireless communications. VANETs can help drivers to acquire real-time information about road traffic status. One of major challenges in VANETs is the rapid change of network topology due to high mobility of vehicles. Establishing a cluster based hierarchy [3] is an effective and popular approach to cope with topology dynamics in ad hoc networks, including VANETs.

Most clustering algorithms use leadership metrics based on (relative) speed and distance. The SP-Clustering algorithm [4] is a typical example of this category, where the relative speed is calculated by the change of distance. More precisely, the distance of two vehicles is calculated using the signal strength of hello messages. Based on distance change, the algorithm can determine whether two nodes are closing to each other, and then delay cluster re-organization if possible. The affinity propagation (AP) algorithm [5, 6] is a distance-based clustering algorithm, which requires a lot of iterative loops that increase the delay time of cluster construction. Another type of leadership metric is

based on connection/link duration time. A vehicle needs to estimate the duration of the links with its neighbors and such a value is used to evaluate the priority of being clusterhead. The algorithms in [7, 8] choose the node with the longest connection duration as clusterhead, while the MA-Clustering algorithm in [9] takes the distance to destination points into consideration. The MA-Clustering algorithm takes into account the destination of vehicles, including the current location, speed, relative destination and final destination of vehicles, as parameter to arrange the clusters. The metric for clusterhead selection is the weighted sum of three parts: current distance of two vehicles, current speed difference of two vehicles and distance between their destination points.

Although navigation route has not been considered in clustering algorithms, it has been used in selecting data forwarding nodes in [10], where the term “trajectory” rather than “route” is adopted. Li et al. [11] propose a network coding with crowd sourcing-based trajectory estimation method to transmit data in vehicular networks. The estimation is completed by every node based on the pre-trajectory of GPS navigation. Network coding is used for data transmission according to the result of trajectory estimation. The STDFS algorithm proposed in [12] makes use of route information in a shared way. Such information is used to predict the encounters between vehicles, and a predicted encounter graph is constructed accordingly. Based on the encounter graph, STDFS optimizes the forwarding sequence to minimize delivery delay under a specific delivery ratio threshold. The TMC algorithm in [13] considers navigation route based multicasting. Route information is used to predict the chance of inter-vehicle encounter between two vehicles, and then the prediction result is further used to characterize the capability of a vehicle to forward a given message to destination nodes.

In this paper, we consider to improve the stability of clusters by making use of navigation route information. The route of a vehicle can be planned in advance by the navigation system. Such a route obviously indicates the future movement path of the corresponding vehicle [13, 14]. To improve the stability of clusters, vehicles with similar routes should be grouped into one cluster.

To construct a better cluster, we design a residual route time function, which quantitatively calculates the time during which two vehicles may keep to be neighbors. With this function, we design a metric to evaluate the priority of leadership (being clusterhead). Our metric also includes the number of neighbors as input, to guarantee the effectiveness of the cluster structure in terms of topology control.

To reduce the cost of cluster maintenance, we design a mechanism of future-clusterhead. Considering that some nodes in a new cluster may previously come from the same old cluster and have known routes of each other, we let only one of them exchange route data with nodes from other clusters for possible merging. Such a vehicle is called a future-clusterhead. Future-clusterheads are also elected based on route information collected during cluster forming.

To examine the performance of our algorithm, we conduct simulations using ns-3. The results show that, our navigation route based clustering algorithm can achieve higher stability and at the same time reduce communication cost.

The rest of the paper is organized as follows. Section 2 presents the system model and assumptions involved in our design. The proposed clustering algorithm is presented in Sect. 3. Performance evaluation is reported in Sect. 4 and finally Sect. 5 concludes the paper with future directions.

2 System Model and Assumption

In our work, we assume that each participating vehicle is equipped with a navigation system. The system can provide information like position (via GPS) and speed of the vehicle. Each vehicle has a predefined start location and destination location. The route of a vehicle is planned by the navigation system. A route should be set at the starting system and may be dynamically changed on the way according to traffic conditions, but such changes should be infrequent.

The route data of a vehicle is a sequence of road segments and turn directions (turn left, turn right, no turn) at intersection between two adjacent segments. In each route, there is no repeated segment, and also no loops. For the simplicity of presentation, we assume the intersection is the typical cross of two roads. The traffic light is placed at the intersection to control the passing of vehicles. Intersections of other types, i.e. crossing of more roads, can be handled similarly.

Each vehicle is also equipped with a wireless communication device. Two vehicles are connected in ad hoc way. The wireless link is assumed to be reliable and no packets will be lost. Two vehicles within transmission range of each other can communicate directly and they are neighbors of each other. The transmission range is less than the length of a road segment. Heartbeat messages are periodically exchanged among neighbors to probe neighbors, so each vehicle knows its neighbors and maintain a neighbor list. A heartbeat message also carries the speed and position information of the sender.

The route of a vehicle consists of a sequence of road segments, and each segment can be represented by the corresponding intersection ID (or number) and direction to go. Such information is with small size, so it can also be included into the heartbeat messages when it is necessary. On the other hand, if the route information is too large to be integrated into heartbeat message, vehicles can exchange route information via special messages. Since navigation route of a vehicle is seldom changed after selected, exchange of route information can be done with a much longer period than heartbeat, and the overhead of route information exchange would be quite small.

3 The Proposed Algorithm

Same as most existing clustering algorithms, our proposed algorithm consists of two phases: cluster formation and cluster maintenance. However, our algorithm has an additional mechanism of future-cluster. Future-clusters are formed in the cluster formation phase and used in cluster maintenance phase to save communication cost.

In the following, we first present the definition and calculation of *RRT*, and then describe operations of cluster formation, future-cluster formation and cluster maintenance.

The status of a node may be:

- *Undecided state (UN)*: the node is not in any cluster.
- *Clusterhead (CH)*: the node is a clusterhead.
- *Cluster member (CM)*: the node is a member of some cluster, but not a clusterhead.
- *Future-clusterhead (FCH)*: the node is a future-clusterhead, which is in charge of coordinating the merge of clusters.

3.1 The Metric of Residual Route Time

In our design, we define RRT, which is the representation of the “overall” time duration of neighborhood between a vehicle and its current neighbors. Table 1 lists the notations used in the definition of RRT.

Table 1. Notations used

Notations	Meaning	Notations	Meaning
R	The transmission range	l_i	The current position of node i
N_i	The set of neighbor nodes of i	v_i	The current speed of node i
n_i	Number of neighbors, i.e. $n_i = N_i $	v^k	The expected speed of vehicles at road segment k
Γ_i	The planned route of node i	p_{ijk}	The probability that nodes i and j being neighbors at road segment k
r_k	The length of road segment k		

For a pair of neighbor nodes i and j , we can estimate t_{ij} , the time they will keep to be neighbor in future trip:

$$t_{ij} = \frac{R \pm |l_j - l_i|}{|v_j - v_i|} + \sum_{k \in \Gamma_i \cap \Gamma_j} \left(\frac{r_k}{v^k} p_{ijk} \right) \tag{1}$$

The calculation of t_{ij} consists of two parts. The first part is the short-term estimation, which estimates the time that two vehicles will keep to be neighbors in the current road segment. It can be calculated using the current speed and position information. The second part is the long-term estimation, which is the time that two vehicles may be neighbors of each other in the future overlapping road segments. Since the vehicles have not entered these segments yet, such a time duration can only be calculated based on the expected speed obtained from historical data v_{ik} . We introduce the parameter p_{ijk} to denote the probability that two neighboring nodes become disconnected at road k . Such a value can be obtained by historic data analysis.

Then, considering all neighbor nodes of i , we have the total time of neighborhood, and the number of neighbor nodes. Therefore, we add two parameters in the final value of residual route time RRT, i.e.:

$$RRT = \theta_i t_i \text{ where : } \theta_i = \frac{1}{n_i} \sum_{j \in N_i} \frac{n_i}{n_j} = \sum_{j \in N_i} \frac{1}{n_j}, t_i = \sum_{j \in N_i} t_{ij} \tag{2}$$

Finally, we have the complete definition of *RRT*:

$$RRT = \sum_{j \in N_i} \frac{1}{n_j} \sum_{j \in N_i} \left[\frac{R \pm |\ell_j - \ell_i|}{|v_i - v_j|} + \sum_{k \in \Gamma_i \cap \Gamma_j} \left(\frac{r_k}{v^k} P_{ijk}^k \right) \right] \quad (3)$$

The above calculation of *RRT* focuses on the effect of vehicle movement and the quality of wireless link between neighboring nodes.

3.2 Cluster Formation

Initially, there are no clusters and all the vehicles are in undecided (UN) state. The clustering algorithm is initiated by the upper layer application or other mechanisms. The first step is exchanging HELLO messages with its neighbors to collect information used in the calculation of *RRT*. More precisely, the HELLO message contains neighbor number and route data. Notice that in the beginning, the nodes do not know their neighbors and the neighbor number in the HELLO message is set to be zero. Later, the number of neighbors is changed according to the HELLO messages from neighbors.

Upon receiving HELLO messages from neighbors, a vehicle *i* will calculate its *RRT* accordingly, and then includes its *RRT* value into its HELLO message. To adapt the dynamic changes of network topology and navigation route, *RRT* value is updated upon the detection of such changes. Obviously, *i* will receive HELLO messages containing *RRT* value from its neighbors in the third and later rounds.

In the initial state, each node is in the UN state, so there is no clusterhead in the neighbor list of any node. When an UN node detects no clusterhead in its neighborhood, it will start the clusterhead election procedure. It will firstly include all UN neighbors into a CH election list, excluding those without sharing/overlapping navigation road segments. Notice that the CH election list contains only UN nodes, and a non-UN node will not be included, even though it has a greater *RRT*. If vehicle *i* has a greater *RRT* value than all its neighbors in the CH election list, *i* itself is selected as a clusterhead by switching to the CH.

In later rounds, when one or more HELLO messages from clusterhead are received, *i* will choose to join the cluster with the highest *RRT* value by sending a *JOIN(CH_{id}, UN_{id})* message. The corresponding clusterhead will send an *ACK(CH_{id}, UN_{id})* message to confirm the join. Vehicle *i* then switches to be in the CM state.

On the other hand, if the UN node *i* does not receive HELLO message from clusterhead (all neighbors with higher *RRT* join clusters of other vehicles), *i* will wait for more rounds until a suitable CH is found or it has the greatest *RRT* among all the UN neighbors.

Since at each round, at least one UN node changes its status to CH or CM, eventually each UN node will decide its status and the cluster formation procedure stops.

3.3 Future-Cluster

The vehicles in one cluster may turn to different directions at the next intersection. Accordingly, we divide one cluster into multiple future-clusters, each of which contains vehicles that will turn to the same direction. Then, after passing the intersection, vehicles in the same future-cluster can simply form a new, even without exchanging node status information. This can help reduce the overhead of cluster maintenance, in terms of both message and time.

Since each cluster is coordinated and managed by its clusterhead, the formation of future-clusters is also conducted by clusterhead. After a cluster is formed, the clusterhead must have collected route data from all members.

The future cluster formation is triggered each time the clusterhead detects that it has entered a new road. By checking the route of cluster members, the clusterhead can divide them into future-clusters according to their direction at the next intersection. At a typical intersection with two roads cross with each other (other intersection scenarios can be handled similarly), vehicles will take one of three directions: LT (left turn), RT (right turn) or NT (no turn). Then, at most three future-clusters may be formed within one cluster.

Accordingly, the clusterhead can compare *RRT* values of all members and assign the vehicle with the largest *RRT* in a future-cluster to be the future-clusterhead. To keep stable, the clusterhead will choose itself as the future-clusterhead of its own future-cluster. After the clusterhead of a cluster determines future-clusters and assigns future-clusterhead, it will broadcast the results to all members, via a *FCH(fch_list, fch_fcm_list)* message. And each member will learn about its own future-cluster and future-clusterhead.

Notice that a node assigned to be future-clusterhead will not start the cluster merging procedure until it passes the corresponding intersection. On the other hand, the cluster member maintenance mechanism of a future-cluster, which is similar to the mechanism of a cluster, will begin immediately after the future-clusterhead is assigned.

3.4 Cluster Maintenance

After clusters are already formed, the cluster members and clusterhead of a cluster monitor each other via HELLO messages. The HELLO message of a cluster member is different from common HELLO messages. It contains the ID of the cluster it belongs to, which may be in fact the ID of the clusterhead. When a cluster member is disconnected from its clusterhead due to speed difference or turning at intersections, it needs switch to another cluster. On the other hand, new clusterhead may be selected due to split and merging at intersections. Moreover, a cluster should be destroyed if there are too few members or a clusterhead with higher *RRT* value is in the neighborhood. Such cases are handled by cluster maintenance mechanism.

Cluster switch. When a cluster member i detects disconnection from its current clusterhead, it will switch to UN state, and try to switch to some cluster with the clusterhead that is currently in neighbor list by sending a *JOIN(CH_{id}, UN_{id})* message.

The following operations are the same as in the cluster formation procedure. When the target clusterhead j receives the $JOIN(CH_{id}, UN_{id})$ message, it will reply with an $ACK(CH_{id}, UN_{id})$ message and i becomes a new member of cluster j .

Cluster merging. The case of cluster change at intersection is more complex. After passing an intersection, one cluster will be split into three or less future-clusters. Once a future-clusterhead passes the intersection, it will start the procedure of cluster merging with other cluster/future-clusters that enter the same lane.

The future-clusterhead will first try to merge with other clusters. It will prepare the candidate clusterhead list by adding the clusterhead neighbors and excluding those without overlapping route and those not entered the current lane yet. Then, the future-clusterhead will select the node with the greatest RRT , say CH_{id} , from candidate clusterhead list, and send a $QUERY(CH_{id}, FCH_{id}, fcm_list)$ message to CH_{id} , which carries future-clusterhead id and future-cluster member list. Upon receiving a $QUERY(CH_{id}, FCH_{id}, fcm_list)$ message, the clusterhead will reply by broadcasting $RESPONSE(CH_{id}, FCH_{id})$. Corresponding to the $RESPONSE(CH_{id}, FCH_{id})$, a cluster member can join the clusterhead CH_{id} , along with future-clusterhead FCH_{id} . Notice that we let only clusterhead respond to a query to reduce message cost.

On the other hand, if no clusterhead is in the candidate clusterhead list, clusterhead re-election is unavoidable. To reduce role changes and simplify operations, clusterhead re-election is done among only future-clusterheads. The future-clusterhead with the greatest RRT is elected as the new clusterhead, and other future-clusterheads will join the new cluster together with their members.

Cluster destruction. A cluster may be destroyed if there are too few members. A clusterhead keeps monitoring its members and neighbor RRT value via HELLO messages. If the number of members decreases and becomes less than a predefined threshold for a time long enough, the clusterhead will destroy the cluster by switching to be a future-clusterhead and try to join another cluster. The rest operations are the same as cluster merging.

4 Performance Evaluation

To evaluate the performance of our algorithm, we conduct simulations using ns-3. The mobility of vehicles is simulated via SUMO. To accurately examine the effect of our proposed future-clusterhead mechanism, we simulate our algorithm under two different variants: RT-Clustering is the variant without future-clusterhead and RTF-Clustering is the variant with the future-clusterhead mechanism. For comparison purpose, we also simulate three representative existing algorithms: ID-Clustering [15], SP-Clustering [4], and MA-Clustering [9]. We set a road network of a grid topology, with 4 horizontal roads and 4 vertical roads. Each road has eight lanes, four for each direction. The crossing point of two roads is viewed as an intersection. Each road segment between two crossing points is set to be 1 km. The maximum speed of vehicles is varied from 10 m/s to 35 m/s. The value of p_{ijk} plays a significant role in our algorithm. In our simulation, we adopt the value 0.8 in the discussion of simulation results.

We adopt four metrics to measure the performance of clustering algorithms.

- *Average clusterhead lifetime (CHT)*: the average consecutive time a node acts as a clusterhead.
- *Average cluster member lifetime (CMT)*: the average consecutive time a node acts as a cluster member. This metric is similar to *CHT*.
- *Average cluster size (ACS)*: the average number of nodes in a cluster.
- *Number of messages sent per node (NMS)*: the average number of messages of a node sent to form and maintain the cluster architecture.

We now present and discuss simulation results according to metrics. The confidence interval with confidence level 90% is shown in the result figures.

(1) *Lifetime of Clusters*

The stability of clusters is indicated by the lifetime of clusters, i.e. *CHT* and *CMT*, as shown in Figs. 1 and 2 respectively.

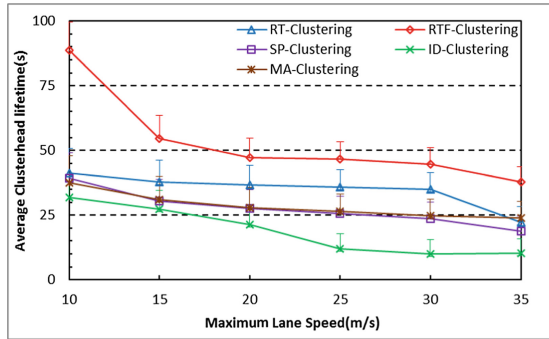


Fig. 1. Average clusterhead lifetime

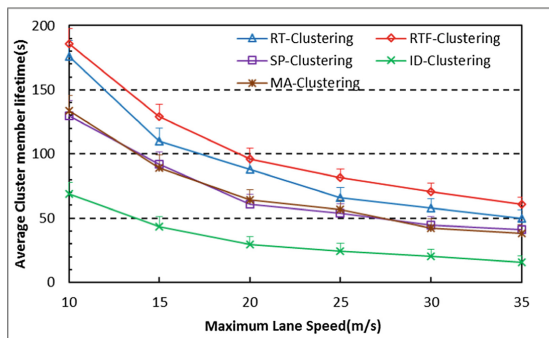


Fig. 2. Average cluster member lifetime

From both figures, we can easily see that, with the increase of lane speed, the lifetime of both clusterhead and cluster member decreases significantly. Among the three algorithms, ID-Clustering achieves the shortest lifetime. This is because ID-Clustering does not consider the movement of vehicles at all. Our proposed algorithm outperforms the others in both CHT and CMT. SP-Clustering and MA-Clustering considers the speed and direction of vehicles, but only the current movement status is considered. With the help of navigation route information, our algorithm can select clusterheads with more stable links, where the lifetime in CHT/CMT can be as high as twice of that of SP/MA-clustering. The different performance of RTF and RT shows clearly the benefit of our future-cluster mechanism.

Moreover, compared with RT/RTF-Clustering and ID-Clustering, SP-Clustering is more sensitive to lane speed, which is shown in both CHT and CMT. That is, with lane speed increases, the lifetime of SP-Clustering decreases faster than the other two algorithms. This can be explained as follows. Since SP-Clustering considers only the current speed and direction status of vehicles, under a higher lane speed, such information is valid for a shorter time, then more cluster switches will occur. In our RT-Clustering algorithm, however, we consider future segment and speed, and the effect of current speed and direction will be reduced.

(2) Average Cluster Size

Figure 3 shows the average cluster size (ACS) of different clustering algorithms. The cluster size of ID-Clustering is the smallest, with a value always less than 2.0. The cluster in RT-Clustering has about 4.0 members in average, and SP-Clustering's cluster size is about 3.0. With the consideration of route information, our algorithm constructs larger clusters than other algorithms do. This may be the benefit of future cluster merging at intersections, which try to merge future clusters into a large one.

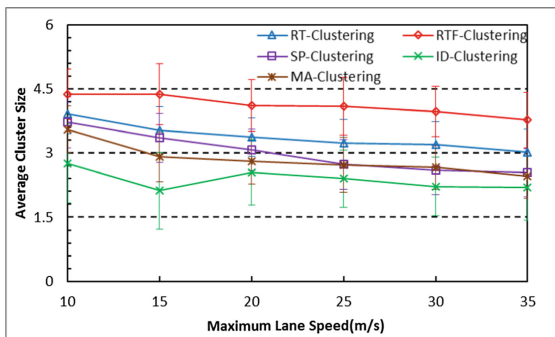


Fig. 3. Average cluster size

(3) Number of messages sent per node

NMS measures the communication cost for constructing and maintaining clusters. Figure 4 shows the cost of all the algorithms. Our algorithm performs better than all

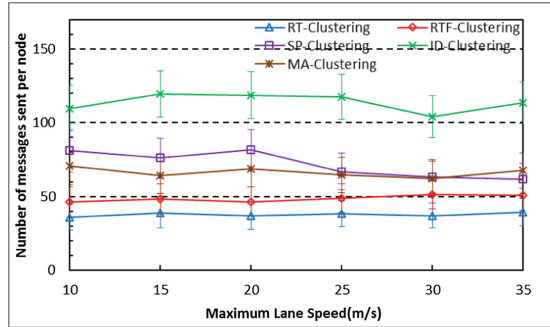


Fig. 4. Number of messages sent per node

others in all cases. This is certainly the benefit of high stability of clusters constructed. Since our algorithm can construct clusters with high stability, the message cost of cluster construction and maintenance should be much less than SP/MA-Clustering.

It is more interesting to compare RT-Clustering and RTF-Clustering. RTF-Clustering, the variant with Future-cluster mechanism, causes more communication cost than RT-Clustering, although the difference is not very large. We explain the additional communication cost of RTF as below. Future-clusterhead mechanism needs to exchange messages for merging future-clusters. On the other hand, RT-Clustering may simply keep future-clusters run individually to avoid re-clustering overhead. This is consistent with the results of cluster size in Fig. 3.

5 Conclusion and Future Work

In this paper, we propose a novel clustering algorithm for VANETs by considering navigation route of vehicles. Based on the overlapping road segments of routes from different vehicles, we design a function to estimate the time that two vehicles may keep to be neighbors in future trip. Clusterheads are elected based on the overall time that a vehicle can keep its neighborhood in future. Compared with existing clustering algorithms, our solution can improve cluster stability, in terms of various performance metrics.

Further study is certainly necessary. Possible directions include constructing models to estimate the probability of being neighbor in future road, optimizing the cluster size with respect to the upper layer applications.

References

1. Jaiswal, P.K., Jaidhar, C.D.: Location prediction algorithm for a nonlinear vehicular movement in VANET using extended Kalman filter. *Wirel. Netw.* **23**(7), 2021–2036 (2017)
2. Nasr, M.M., Abdelgader, A.M., Wang, Z., et al.: VANET clustering based routing protocol suitable for deserts. *Sensors* **16**(4), 1–23 (2016)

3. Caballerogil, C., Caballerogil, P., Molinagil, J., et al.: Self-organized clustering architecture for vehicular ad hoc networks. *Int. J. Distrib. Sens. Netw.* **11**(8), 1–12 (2015)
4. Souza, E.D., Nikolaidis, I., Gburzynski, P.: A new aggregate local mobility (ALM) clustering algorithm for VANETs. In: *International Conference on Communications*, pp. 1–5 (2010)
5. Shea, C., Hassanabadi, B., Valaee, S., et al.: Mobility-based clustering in VANETs using affinity propagation. In: *Global Communications Conference*, pp. 1–6 (2009)
6. Hassanabadi, B., Shea, C., Zhang, L., et al.: Clustering in vehicular ad hoc networks using affinity propagation. *Ad Hoc Netw.* **13**, 535–548 (2014)
7. Bononi, L., Felice, M.D.: A cross layered MAC and clustering scheme for efficient broadcast in VANETs. In: *International Conference on Mobile Adhoc and Sensor Systems*, pp. 1–8 (2007)
8. Ni, M., Zhong, Z., Zhao, D., et al.: MPBC: a mobility prediction-based clustering scheme for ad hoc networks. *IEEE Trans. Veh. Technol.* **60**(9), 4549–4559 (2011)
9. Morales, M.M., Hong, C.S., Bang, Y., et al.: An adaptable mobility-aware clustering algorithm in vehicular networks. In: *Asia-Pacific Network Operations and Management Symposium*, pp. 1–6 (2011)
10. Cunha, F.D., Villas, L.A., Boukerche, A., et al.: Data communication in VANETs: protocols, applications and challenges. *Ad Hoc Netw.* **44**, 90–103 (2016)
11. Li, L., Yang, Z., Wang, J., et al.: Network coding with crowdsourcing-based trajectory estimation for vehicular networks. *J. Netw. Comput. Appl.* **64**, 204–215 (2016)
12. Xu, F., Guo, S., Jeong, J., et al.: Utilizing shared vehicle trajectories for data forwarding in vehicular networks. In: *International Conference on Computer Communications*, pp. 441–445 (2011)
13. Jiang, R., Zhu, Y., Wang, X., et al.: TMC: exploiting trajectories for multicast in sparse vehicular networks. *IEEE Trans. Parallel Distrib. Syst.* **26**(1), 262–271 (2015)
14. Jeong, J., Guo, S., Gu, Y., et al.: TBD: trajectory-based data forwarding for light-traffic vehicular networks. In: *International Conference on Distributed Computing Systems*, pp. 231–238 (2009)
15. Lin, C., Gerla, M.: Adaptive clustering for mobile wireless networks. *IEEE J. Sel. Areas Commun.* **15**(7), 1265–1275 (1997)



A Social-Aware Routing Protocol for Two Different Scenarios in Vehicular Ad-Hoc Network

Zhixiao Zhu, Binjie Hu^(✉), Haina Song, and Xiaotao Liu

School of Electronic and Information Engineering,
South China University of Technology, Wushan Road 381,
Guangzhou 510640, China
eewszzx2015@mail.scut.edu.cn, eebjiehu@scut.edu.cn,
405186814@qq.com, liuxt_ee@qq.com

Abstract. Vehicular Ad-hoc Network (VANET) has recently attracted wide public attention. A key challenge is to design suitable routing protocols for VANET. In order to get high packet delivery ratio and low end-to-end delay, this paper proposes a social-aware routing protocol based on the “store-carry-forward” strategy, called Tie and Duration Based Routing Protocol (TDRP). To select the best relay node, TDRP takes two social metrics into consideration: community and centrality. We adopt a distributed K-Clique community detection to divide vehicles into different communities, and calculate global and local centralities of vehicles by making full use of strong and weak ties, as well as the duration of historical connections. The ONE simulator is used to evaluate the performance of TDRP and Bubble Rap, a typical social-aware routing protocol. Experimental results show that TDRP outperforms Bubble Rap in both city and highway scenarios in terms of packet delivery ratio and end-to-end delay.

Keywords: VANET · Social-aware routing protocol · Strong and weak ties
City and highway scenarios · The ONE

1 Introduction

As an important part of Intelligent Transportation System (ITS) [1], Vehicular Ad-hoc Network (VANET) works in a self-organized way with short-range communication devices installed on vehicles to improve traffic safety and efficiency. Each vehicle is not only a host, but also a router with a specific routing protocol. However, due to the high mobility of vehicles and the complexity of communication environment, it is difficult to maintain the stable communication links between vehicles. So, it is vital to have a suitable routing protocol for vehicular scenarios.

Opportunistic transmission is based on the “store-carry-forward” strategy, which is first adopted in the Delay Tolerant Network (DTN) [2]. In this strategy, a message is forwarded by multiple relay nodes to the destination, without requiring an end-to-end message routing path. The features of “Delay Tolerant” can meet the demand of VANET, applying to VANET called Vehicular Delay-Tolerant Network (VDTN) [3].

In VDTN, though the movement of nodes greatly improves the possibility of connection establishment, it is vital to determine when the best time to send the message and which the best relay node is.

In order to solve these problems, people in the study of routing protocols, make full use of dynamic network information (e.g. location information, traffic information and neighbor information) to make decisions. As we all know, in Social Networks (SN) [4], the link between people is largely dependent on the social relationship between them. Liu et al. [5] explored social properties in Vehicular Ad-hoc Networks by using two traces of mobile vehicles from San Francisco and Shanghai. Further, Vegni and Loscri [6] introduced the concept of Vehicular Social Networks (VSN), exploiting the great impact of social characteristics and human behavior on Vehicular Ad-hoc Networks. Since the movement and communication of vehicles are impacted greatly by human social behavior and social relationships, there are many social characteristics can be used, e.g., community, similarity, centrality, selfishness and so on. Moreover, these social attributes are much more stable than dynamic network information.

Recently, many routing protocols based on social properties have been proposed. Wei et al. [7] had made a survey of social-aware routing protocols in DTN. The properties of social ties such as positive and negative social characteristics are utilized to design social-aware routing protocols. However, in VANETs, high-speed movement of vehicles and frequent changes in the topology make it difficult to extract the social properties from the connection history. Thus it leads to poor performance for most social-aware routing protocols in the V2V communication.

To address the issue, this paper proposes a social-aware routing protocol called Tie and Duration Based Routing Protocol (TDRP). In TDRP, each vehicle records a neighbor list within the transmission range, as well as a connection history list. Then, we use strong and weak ties, as well as duration of historical connections to calculate global and local centralities to make protocol more suitable for VANET, compared with Bubble Rap protocol a typical social-aware routing protocol [8].

The organization of this paper is structured as follows. We briefly review related work in Sect. 2, and then propose the new centrality algorithm based on strong and weak ties and duration of historical connections in Sect. 3. In Sect. 4, we use The ONE simulator [9] to evaluate the performance of TDRP and Bubble Rap routing protocols in two different scenarios. Finally, we conclude our work briefly in Sect. 5.

2 Related Work

There are some typical social-aware routing protocols in DTN. Daly and Haahr proposed the SimBet algorithm [10]. In [10], the utility of a relay node is evaluated by the centrality and similarity of nodes, according to a standard rule. Then, the message will be forwarded to a node with higher utility until to the destination. Hui [11] proposed the LABEL algorithm using the community of nodes, which assigns each node a label to distinguish it from different communities. Note that the nodes with the same label are regarded to belong to the same community. However, the protocol can only improve the message delivery ratio when the message is in the same community as the destination, but ignores the situation where the message is transferred from different

communities to the destination. Moreover, there is a lack of the mechanism for transmitting the message to different communities. To fill this gap, Hui et al. [8] proposed a Bubble Rap algorithm combining with community and centrality of nodes to design forwarding strategy based on LABEL protocol. The algorithm forwards the message to the node with higher global centrality until the message arrives at the same community as the destination, and thus improves the message delivery ratio. After that, in the local community, message will be forwarded to the neighbor node with the higher local centrality until to the destination.

In Bubble Rap algorithm, the community detection and the centrality calculation are the most important parts. In the community detection part, the paper [12] proposes three typical algorithms of community detection: Simple, K-Clique and Modularity. In the centrality calculation part, Pan Hui proposed two ways to calculate centrality: S-Windows, and C-Windows, both of which are based on connection history. However, they ignore the current links, which are more important for highly mobile vehicles.

In this paper, we propose a new protocol by considering strong and weak ties of neighbor vehicles with the transmission range as well as the duration of historical connections to make it more suitable for VANET.

3 Design of TDRP Protocol

Due to the features of highly mobile vehicles, in this section, we design a social-aware routing protocol for vehicular scenarios, called Tie and Duration Based Routing Protocol (TDRP). Learning from Bubble Rap algorithm, TDRP takes the “community” and “centrality” into consideration to select the best next relay node. In the community part, since K-Clique algorithm performs the best, we choose it to detect communities. In the centrality part, TDRP uses strong and weak ties of neighbor vehicles with the transmission range, as well as duration of historical connections to calculate global and local centralities.

When the transmission occurs in the same community, the vehicle carrying the message chooses the next relay vehicle with the highest local centrality among its neighbors and higher local centrality than itself. Otherwise, the vehicle carrying the message selects the next hop with the highest global centrality among its neighbors and higher global centrality than itself.

3.1 Centrality Calculation

In the social network, the strength of the connection refers to the degree of intimacy among people, such as the relationship between friends and relatives. This connection is generally considered as a strong tie. However, if the person is an acquaintance, but contacts with each other are not so frequent, this connection is considered as a weak tie. Many studies show that there are a lot of similarities between nodes in the network in this aspect. There are different standards for measuring the strength of connection, according to the specific environment, but the form of expression is the same. Strong ties are gathered into a community, while weak ties exist between communities, as shown in Fig. 1.

There are only two cases of message transmission, to the same community and different communities. In Fig. 1, when the source node a (S) sends a message to node d (D1), since both of them are in the same community 3, node f with the most of strong ties is the best choice for next relay. The path of transmission is $a \rightarrow f \rightarrow d$. So, local centrality can be calculated by strong ties. However, when the source node a (S) sends a message to node o (D2), since they are in different communities, global centrality works, and a weak tie is required as a bridge to send the message out the community first. If node f is still chosen as a relay node, it won't forward message to other nodes with lower centrality, and the message will be stuck in the community 3.

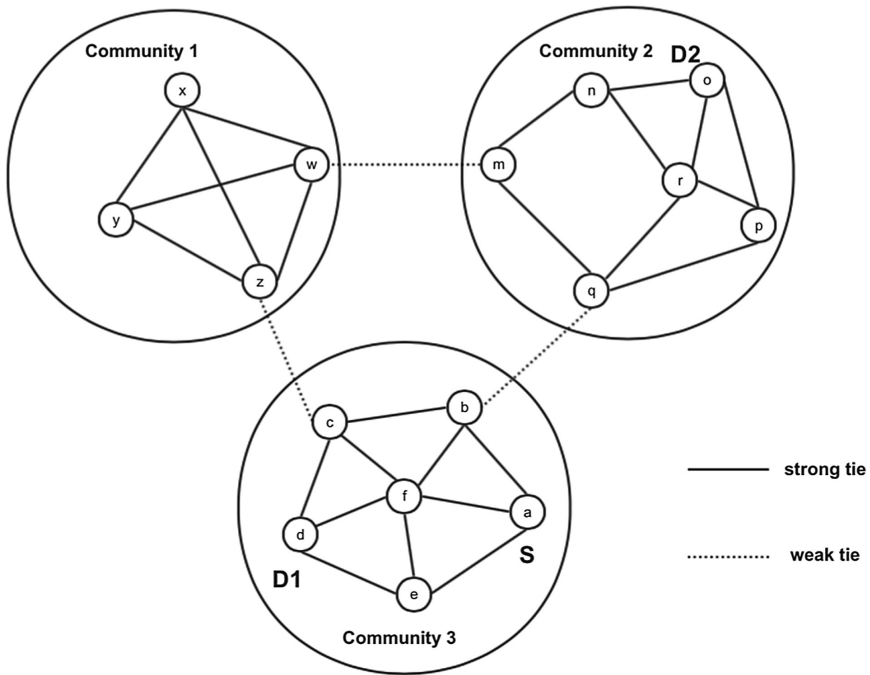


Fig. 1. The strength of ties, weak ties between different communities and strong ties in the same community

In this case, the weak ties between different communities are important. Node b and node c both have weak ties, but only node b has a strong tie with node a . Node b should be chosen as the next relay node. The path of transmission is $a \rightarrow b \rightarrow q \rightarrow r \rightarrow o$. So, global centrality should take full account of weak ties. In our real life, the route of taxi is usually based on the driver's preferences and the passengers' requirements, and the bus has a fixed route. Typically, the route of private car is entirely determined by the owner, such as work place, home, and shop stores. Therefore, buses and cars are more likely to constitute communities, while the taxis are more likely to be the bridges between these communities.

In addition, due to high-speed mobility of vehicles, network topology changes frequently in VANET. Hence, the duration of connections becomes very important. The duration has to be longer than the time of message transmission at least. So, in TDRP, we will also consider the duration of historical connections in both global and local centralities.

In order to calculate centrality, we assume every vehicle maintains a neighbor list within the transmission range and a connection history list recording vehicles that had ever connected and the meeting time.

The centrality of a node is calculated by *TieUtil* and *DurationUtil*. As for node u , it has a neighbor list. $E(u)$ denotes the set of these neighbor nodes, and node v is in $E(u)$. Besides, it has a connection history list, *connHistory*.

For Global Centrality of node u , we just consider the neighbor nodes in different communities. *TieUtil* is the number of communities, which the neighbor nodes belong to.

$$TieUtil(u) = \sum_{v \in E} c(u, v). \tag{1}$$

$$c(u, v) = \begin{cases} 1 & \text{if } u \text{ and } v \text{ are in different communities} \\ 0 & \text{otherwise} \end{cases}. \tag{2}$$

$$DurationUtil(u) = \sum_{v \in E \& \& c(u,v)=1} \frac{LongDuration}{LongDuration + ShortDuration}. \tag{3}$$

$$TieDurationUtil(u) = \alpha TieUtil(u) + \beta DurationUtil(u). \tag{4}$$

When node u and node v are in different communities, and they have met at least once time before, *DurationUtil* is calculated by Formula (3). There is a *threshold* for historical connections to distinguish long or short duration connections for every encounter. The threshold is preferably several times larger than the time of message transmission. The bigger *DurationUtil* is, the more *LongDuration* connections node u has.

Finally, Global Centrality is denoted by *TieDurationUtil(u)*, which is given by combining the normalized relative weights of the attributes, as shown in Formula (4). Wherein α and β are tunable parameters, and $\alpha + \beta = 1$. Thus, these parameters can be adjusted according to the relative importance of these two utility values in different scenarios.

For Local Centrality of node u , we just consider the neighbor nodes in the same community:

$$c(u, v) = \begin{cases} 1 & \text{if } u \text{ and } v \text{ are in the same community} \\ 0 & \text{otherwise} \end{cases}. \tag{5}$$

Only $c(u, v)$ is changed from Formula (2) to Formula (5), the others are the same as the Global Centrality.

3.2 Centrality Algorithm

Since the algorithms of calculating the Global Centrality and Local Centrality are similar, we only show the algorithm of Global Centrality of node u as follows:

Algorithm 1. Calculate the Global Centrality of Node u

```

1: Begin:
2: if ( $COMPUTE\_INTEVAL < 6$ )
3:   return  $GlobalCentrality$ 
4: else if ( $E(u) \neq NULL$ )
5:   for all node  $v \in E(u)$  do
6:     if (node  $u$  and node  $v$  are in different communities)
7:        $c(u, v) = 1$ 
8:     else
9:        $c(u, v) = 0$ 
10:    end if
11:    $TieUtil(u) = \sum c(u, v)$ 
12:   if node  $v \in E(u)$  &&  $v \in connHistory$  &&  $c(u, v) == 1$ 
13:     for all duration of node  $v$  in  $connHistory$  do
14:       if ( $duration(u, v).end - duration(u, v).start > threshold$ )
15:          $LongDuration++$ 
16:       else
17:          $ShortDuration++$ 
18:       end if
19:        $DurationUtil(u) = LongDuration / (LongDuration + ShortDuration)$ 
20:     end if
21:   end if
22:    $TieDuration(u) = \alpha * TieUtil(u) + \beta * DurationUtil(u)$ 
23:    $GlobalCentrality = TieDuration(u)$ 
24: return  $GlobalCentrality$ 
25: end.

```

4 Performance Evaluation

In this section, we analyze and compare the performance of the proposed TDRP to Bubble Rap in two different vehicular scenarios. The ONE simulator is used to evaluate the performance of routing protocols. We mainly consider Packet Delivery Ratio (PDR) and End-To-End Delay (E2ED) metrics.

- Packet Delivery Ratio (PDR) is the ratio of the number of successfully delivered packets to that of generated data packets.
- End-To-End Delay (E2ED) is the average latency that delivered packets are sent from the source node to the destination node.

4.1 City Scenario

In the city scenario, we use the map of Flower City Square in Guangzhou, which is imported from Open Street Map [13] and edited with JOSM tool to remove redundant information (see Fig. 2). The ONE simulator only supports *.wkt* format, so we need to use *osm2wkt* tool to transform *.osm* file into *.wkt* format. In addition, TDRP needs to be

imported to The ONE simulator, with $\alpha = 0.5$, $\beta = 0.5$, and threshold = 10 s. Based on some test experiments, we set K to be 22 and familiar threshold to be 970 in the K-Clique algorithm under the vehicular scenarios. The simulation time lasts 14000 s, and the topology size of the map is 2200 m * 2200 m. We deploy 100 vehicles in the network, with the speed between 10–50 km/h. The interface transmission speed is set to 6 Mbps and the interface transmission range is set to 500 m, which are commonly used in VANET. The message is set to 750 kB, generated every 50 s. The simulation parameters are shown in Table 1.



Fig. 2. Flower City Square in Guangzhou imported from OSM and edited with JOSM

Table 1. The simulation parameters for the city scenario

Parameters	Values
Map size	2200 m * 2200 m
Simulation time	14400 s
Number of vehicles	100
Vehicles speed	10–50 km/h
Buffer size	25 MB
Interface transmission speed	6 Mbps
Interface transmission range	500 m
Message size	750 kB
Event interval	50 s
Message TTL	5, 10, 15, 20, 25, 30, 35, 40, 45, 50 min

We compare the TDRP with the typical social-aware routing protocol, i.e., Bubble Rap, and run each experiment 10 times to get the average in all the following simulations.

Figure 3 compares the PDR of two protocols in different Time to Live (TTL) of the message. Both the PDR of two protocols has first increased as TTL increases. Until TTL reaches to 30 min, it begins to become stable, and almost unchanged. In all cases, TDRP consistently outperforms Bubble Rap, with a maximum of 25% improvement. With the increment of TTL, PDR of TDRP significantly raises, even to be 93%, which shows good performance. This is because that the longer a message survives in the network, the more likely it is to reach the destination.

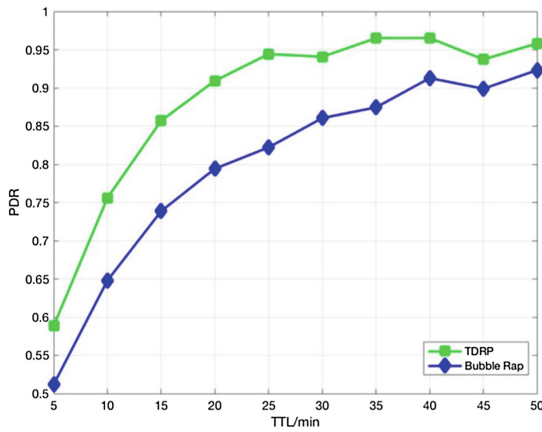


Fig. 3. PDR versus TTL when buffer size is set to 25 MB in the city scenario

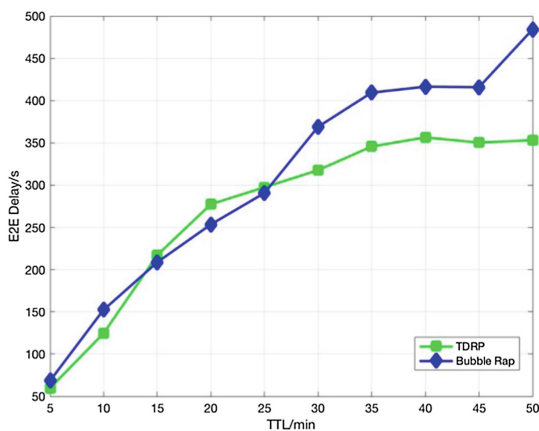


Fig. 4. E2ED versus TTL when buffer size is set to 25 MB in the city scenario

Figure 4 shows the E2ED of TDRP and Bubble Rap, when TTL of messages varies. At the beginning, E2ED of the two protocols increases with TTL and is almost equal. After TTL up to 30 min, although TDRP outperforms Bubble Rap, E2ED of both protocols still keeps increasing, while the corresponding PDR of both protocols approaches to be stable. In addition, the message with higher TTL means that it consumes more resources of the network. Consequently, from the Figs. 3 and 4, it concludes that setting TTL to 30 min is a good choice.

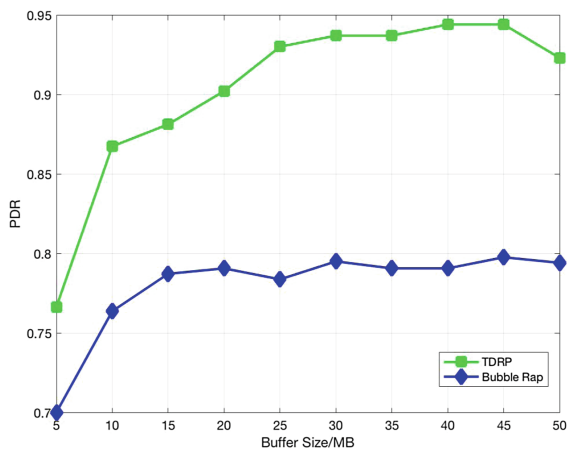


Fig. 5. PDR versus buffer size when TTL is set to 30 min in the city scenario

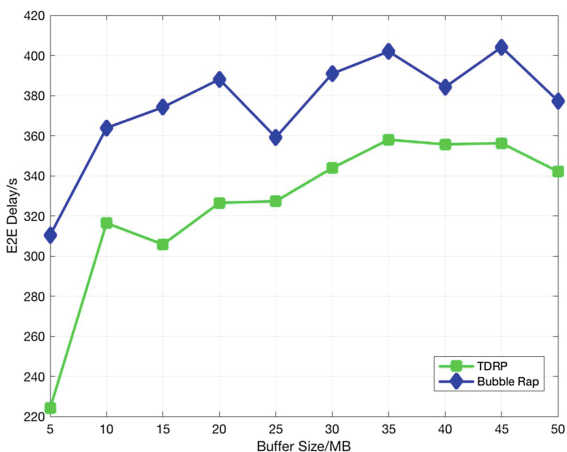


Fig. 6. E2ED versus buffer size when TTL is set to 30 min in the city scenario

In order to find the relation between the performance of protocols and buffer size of the vehicle, another simulation with the same parameters in Table 1 except TTL and buffer size has been done. Figure 5 compares the PDR of two protocols in different buffer sizes of the vehicles when TTL is set to 30 min. TDRP obviously outperforms Bubble Rap in all cases. When buffer size is up to 25 MB, PDR of TDRP is up to 93%, while PDR of Bubble Rap keeps almost unchanged at around 80% after buffer size up to 15 MB. The reason is that every vehicle maintains a neighbor list and a connection history list in TDRP, while only a connection history list in Bubble Rap. Hence, buffer size has a greater impact on TDRP. Figure 6 illustrates E2ED of two protocols in different buffer sizes. It is observed that E2ED of TDRP is lower than that of Bubble Rap in all cases. Given that the buffer of the vehicle becomes bigger and bigger, it follows that TDRP is more promising than Bubble Rap in the city scenario.

4.2 Highway Scenario

In the highway scenario, we use the map of airport expressway in Guangzhou, and choose a section of 4.5 km long highway with two-way eight lanes (see Fig. 7). The speed of vehicles is between 60–100 km/h. Other simulation parameters are the same with the city scenario, which are shown in Table 2.

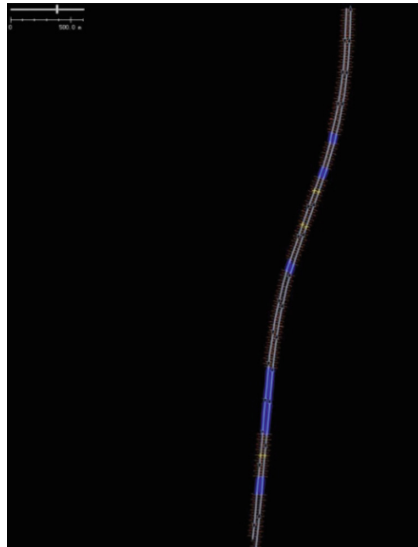


Fig. 7. Airport expressway in Guangzhou imported from OSM and edited with JOSM

Table 2. The simulation parameters for the highway scenario

Parameters	Values
Map size	4500 m * eight-lane
Simulation time	14400 s
Number of vehicles	100
Vehicles speed	60–100 km/h
Buffer size	25 MB
Interface transmission speed	6 Mbps
Interface transmission range	500 m
Message size	750 kB
Event interval	50 s
Message TTL	1, 2, 3, 4, 5, 6, 7, 8, 9, 10 min

Taking the length of this section of highway and the speed of the vehicle into account, it typically takes 2.7–4.5 s for one vehicle to cover this section of highway. This section is not circular, but the movement mode of the vehicle in the simulation is a circle mode, which is very different from the real life. Therefore, TTL of messages can not be large in the highway scenario. Figure 8 compares the PDR of two protocols when TTL is gradually increasing from 1 min to 10 min. It is shown that TDRP outperforms Bubble Rap slightly. When TTL is up to 5 min, PDR is over 95% for both protocols.

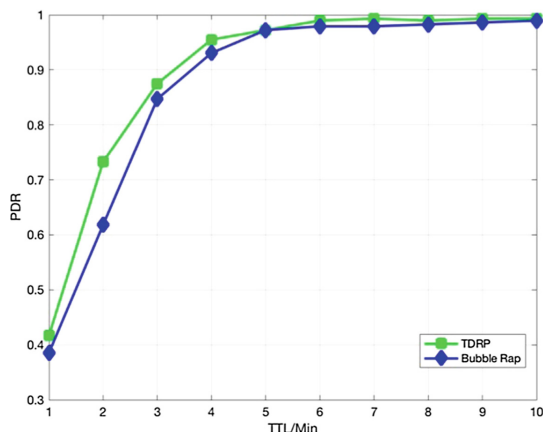
**Fig. 8.** PDR versus TTL when buffer size is set to 25 MB in the highway scenario

Figure 9 illustrates the E2ED of two protocols, when TTL varies from 1 min to 10 min. We find E2ED of TDRP is less than that of Bubble Rap in all cases, especially when TTL up to 5 min, reducing by 27%. In summary, TDRP not only has the slight higher PDR than Bubble Rap, but also reduces the end-to-end delay significantly. It effectively testifies that TDRP is also a more promising protocol in the highway scenario.

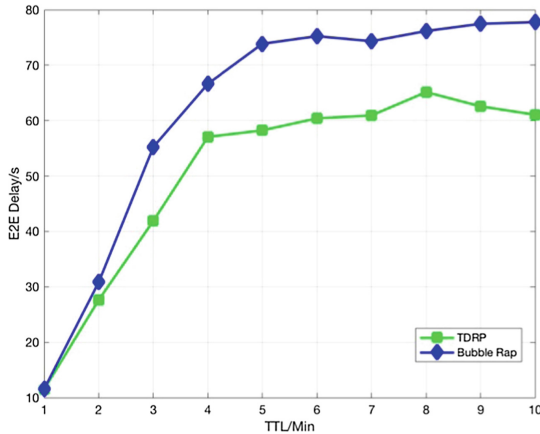


Fig. 9. E2ED versus TTL when buffer size is set to 25 MB in the highway scenario

5 Conclusion

In this paper, we propose a social-aware routing protocol, called Tie and Duration Based Routing Protocol (TDRP), to optimize the performance of vehicular ad-hoc network in terms of PDR and E2ED for two different scenarios. It improves the typical Bubble Rap routing protocol by making full use of the strength of ties and the duration of connections to calculate global and local centralities of nodes. The proposed algorithm is particularly applicable to the transmission of messages between different communities, with taking the features of highly mobile vehicles into account. Simulation results further validates the effectiveness of the proposed protocol. In particular, TDRP obviously outperforms Bubble Rap both in PDR and E2ED performance in the city scenario. While in the highway scenario, TDRP can improve the PDR performance slightly, but still maintains its distinct advantage on the E2ED performance. In conclusion, TDRP is more suitable and more promising than Bubble Rap for VANET.

Acknowledgment. This work was supported by the IOT Key Project of the Ministry of Industry and Information Technology ([2014]351), Guangzhou key science and technology project of Industry-Academia-Research collaborative innovation (2014Y2-00218), and University-Industry Key Project of Department of Education of Guangdong Province (CGZHSD1102).

References

1. Yan, X., Zhang, H., Wu, C.: Research and development of intelligent transportation systems. In: Proceedings of the 11th International Symposium on Distributed Computing and Applications to Business, Engineering and Science, pp. 321–327. IEEE Press, Guilin (2012)
2. Fall, K., Farrell, S.: DTN: an architectural retrospective. *IEEE J. Sel. Areas Commun.* **26**(5), 828–836 (2008)
3. Cruzcunha, M.M., Moreira, F.: *Vehicular Delay Tolerant Networks* (2011)

4. Dunbar, R.I.M., Arnaboldi, V., Conti, M., Passarella, A.: The structure of online social networks mirrors those in the offline world. *Soc. Netw.* **43**, 39–47 (2015)
5. Liu, X., Li, Z., Li, W., Lu, S., Wang, X.: Exploring social properties in vehicular ad hoc networks. In: *Proceedings of the Fourth Asia-Pacific Symposium on Internetware, Qingdao*, pp. 1–7. ACM (2012)
6. Vegni, A.M., Loscri, V.: A survey on vehicular social networks. *Commun. Surv. Tutor. IEEE* **17**(4), 2397–2419 (2015)
7. Wei, K., Liang, X., Xu, K.: A survey of social-aware routing protocols in delay tolerant networks: applications, taxonomy and design-related issues. *IEEE Commun. Surv. Tutor.* **16**(1), 556–578 (2014)
8. Hui, P., Crowcroft, J., Yoneki, E.: BUBBLE rap: social-based forwarding in delay-tolerant networks. *IEEE Trans. Mob. Comput.* **10**(11), 1576–1589 (2011)
9. Keranen, A., Ott, J., Karkkainen, T.: The ONE simulator for DTN protocol evaluation. In: *Proceedings of the 2nd International Conference on Simulation Tools and Techniques, Rome*, p. 55. ACM (2009)
10. Dely, E.M., Haahr, M.: Social network analysis for routing in disconnected delay-tolerant MANETs. In: *Proceedings of the 8th ACM International Symposium on Mobile Ad Hoc Networking and Computing, Montreal, Quebec*, pp. 32–40 (2007)
11. Hui, P., Crowcroft, J.: How small labels create big improvements. In: *Proceedings of the Fifth Annual IEEE International Conference on Pervasive Computing and Communications Workshops, White Plains, NY*, pp. 65–70 (2007)
12. Hui, P., Yoneki, E., Shu, Y., Crowcroft, J.: Distributed community detection in delay tolerant networks. In: *Proceedings of the 2nd ACM/IEEE International Workshop on Mobility in the evolving internet architecture, Kyoto*, pp. 1–8 (2007)
13. Open Street Map. <http://www.openstreetmap.org/>

Author Index

- Bai, Baoming I-460, II-122
Bie, Zhisong I-146
Bouras, Taha II-383
- Cai, Hui I-206, I-254
Chai, Yuan I-186
Chang, Hong II-450
Chang, Jianxin II-102
Chang, Jun II-405
Chang, Shuhao I-332
Chen, Daqing II-61
Chen, Dong II-474
Chen, Hang II-3
Chen, Jun II-132
Chen, Min-Rong II-153
Chen, Ping I-37
Chen, Qinbo I-206, I-254
Chen, Wei II-292
Chen, Wenqiu II-497
Chen, Xi I-332
Chen, Xiancai I-254
Chen, Xiang I-64, II-552
Chen, Xiaoming II-271
Chen, Yishun II-552
Chen, Zhaoxuan II-331
Cheng, Ran II-373
Cong, Li II-485
Cui, Panpan II-176
- Dai, Man I-27
Dan, Zesheng I-297
Deng, Der-Jiunn II-182
Deng, Su I-492
Deng, Yichen II-82
Ding, Zhihao I-95
Dong, Jian I-524
Dong, Wenqian I-381
Dong, Zhenjiang II-312
Du, Jianchao I-443
Du, Qinghe I-84, I-95, I-341, II-283
Duan, Aoqin I-84
- Fan, Shuquan I-448, I-546
Fan, Wei II-271
Fan, Weiqiang II-72
Fan, Yangyu I-274
Fang, Li I-37
Fang, Shu I-512
Feng, Hong I-195
Feng, Shixuan I-106, I-409
Fu, Zhi II-112
- Gan, Jiefu II-373
Gang, Hui-Seon I-361
Gao, Ang II-474
Gao, Jinchun I-176
Gao, Ling II-95
Gao, Meng II-102
Gao, Tianrun II-3
Gao, Zibin II-323
Gong, Qianyun I-206, I-254
Guo, Lantian II-302
- Han, Yuanchao I-512
Hao, Ming I-3
He, Chen I-264
He, Di II-383
He, Zunwen II-509
Hou, Bo II-132
Hu, Binjie II-563
Hu, Wei II-302
Huang, Di I-216, II-215
Huang, Hongbin I-492
Huang, Kaizhi I-557
Huang, Si I-226, II-352
Huang, Xin II-102
Huang, Xuewen II-519
Hui, Leifang I-425
Huo, Yuehua II-72
- Ji, Baihua II-323
Ji, Hong I-195, I-433, II-341, II-395
Ji, Xiang I-27

- Jialiang, Lu II-165
 Jiang, Guofeng I-274
 Jiang, Jichen II-395
 Jiang, Lei II-250
 Jiang, Wan I-481

 Kang, Jiawen II-542
 Ke, Sheng I-186
 Ke, Tenghui II-323
 Kuang, Rongjie II-323

 Lei, Miao II-312
 Leng, Supeng II-239
 Li, Bo II-61
 Li, Dantao I-240, II-141
 Li, Dong II-72
 Li, Guoquan II-155
 Li, Haili II-13
 Li, Hongxing I-37
 Li, Huaan I-460
 Li, Hui II-312
 Li, Jieqi I-351, I-372
 Li, Lei I-388, II-176
 Li, Lizhao I-381
 Li, Longjiang II-239
 Li, Qi II-199
 Li, Qingying II-61
 Li, Shuyun I-186
 Li, Weibin I-443
 Li, Xi I-195, I-433, II-341, II-395
 Li, Xiaohuan II-497, II-519
 Li, Xiaohui I-226, I-240, II-141, II-227,
 II-352
 Li, Xiaoya II-95
 Li, Xiongfei I-54
 Li, Yanchao II-41, II-51
 Li, Yi I-37
 Li, Yong II-450
 Li, Zhengxue I-351, I-372
 Lian, Baowang I-297
 Liang, Zhonghua I-114, I-125, I-135
 Liao, Guiwen II-405
 Liao, Han II-426
 Lim, Tiong Hoo II-463
 Lin, Chun-Cheng II-182
 Lin, Jinzhao I-155
 Lin, Rongheng I-448, I-546

 Lin, Xiaola II-552
 Lin, Yuyang II-509
 Ling, Zheng I-470
 Liu, Chunxu I-166
 Liu, Cong I-398
 Liu, Danli I-114, I-125, I-135
 Liu, Haojie I-114
 Liu, Hui I-284
 Liu, Jinjin I-125
 Liu, Lei I-166
 Liu, Pan I-54
 Liu, Peilin II-383
 Liu, Xiao II-323
 Liu, Xiaotao II-563
 Liu, Yiming I-166, II-112
 Liu, Yingting II-485
 Liu, Yinlong II-72
 Liu, ZiYao I-216
 Liu, Ziyao II-215
 Lu, Baicen II-13
 Lu, Liang-Yi II-182
 Lu, Renhao II-440
 Lu, Xuming I-64
 Lu, Yueming II-373
 Luo, Danyan I-524
 Lv, Guoyun II-13, II-23
 Lv, Pin II-331
 Lv, Shanshan I-307
 Lyu, Chao I-341

 Ma, Dong I-502
 Ma, La'ning I-114, I-135
 Ma, Lixiang II-250
 Ma, Mingyang I-372
 Ma, Wei I-425
 Mao, Baolei II-302
 Mao, Di I-323
 Martins, Philippe II-165
 Mbom, Christian Ango II-189
 Mei, Shaohui I-351, I-372
 Meng, Danfeng I-240, II-141
 Meng, Xiangyang I-54
 Mu, Dejun II-302

 Niu, Jinping II-95
 Niu, Meng I-21, II-207
 Nyarko, James Kweku Nkrumah II-189

- Pan, Bin II-532
 Pan, Di I-481
 Pan, Siyu II-331
 Pang, Yu I-155
 Park, June-Buem I-361
 Peng, Yang I-524
 Pyun, Jae-Young I-361
- Qian, Yueyan II-260
 Qin, Maoyuan II-302
 Qin, Tao II-292
 Qiu, Xiaofeng I-264
 Qiu, Xunjie II-132
 Qu, Jiahui I-381
- Ren, Jie I-535, II-95
 Ren, Pinyi I-95, I-341, II-283
- Shen, Weiqiang II-153
 Sheng, Jie I-502
 Shi, Chaoxiang II-102
 Shi, Jinglun II-153
 Song, Haina II-563
 Song, Huansheng I-135
 Song, Ke-Pu I-21, II-207
 Song, Tianming I-433
 Song, Yingjie I-3
 Song, Yingshuan II-341
 Su, Luo-Hui I-21, II-207
 Su, Yun I-546
 Sun, Bo I-84
 Sun, Chengjun II-199
 Sun, Hanwen I-425
 Sun, Jinhua I-307
 Sun, Li I-341
 Sun, Yin I-64
- Tai, Yu II-302
 Tan, Feiyang I-388
 Tan, Hongzhou I-64
 Tang, Chengkai I-46
 Tang, Xin II-497, II-519
 Tian, Maoxin I-206, I-254
 Tian, Zhongqi I-351
 Tong, Yan II-292
- Wan, Shuai I-372
 Wang, Binbin I-481
 Wang, Daoce II-323
- Wang, Guan II-519
 Wang, Hai II-95
 Wang, Hao I-307
 Wang, He II-199
 Wang, Hongzhi II-416
 Wang, Huichao II-239
 Wang, Jiacheng I-155
 Wang, Jun I-216, II-215
 Wang, Liangliang I-64
 Wang, Lihong I-106, I-409
 Wang, Linlin II-23
 Wang, Menglu I-332
 Wang, Rong I-492
 Wang, Ruonan II-405
 Wang, Shikai II-13
 Wang, Tonghui II-13
 Wang, Wei II-312
 Wang, Xia II-33
 Wang, Xinluo II-312
 Wang, Yu I-13
 Wang, Zhaowei I-166
 Wang, Zhifei I-492
 Wang, Zhijie I-216, II-215
 Wang, Zulin I-535
 Wei, Fang I-481
 Wei, Juan I-106, I-409
 Weitao, Pan I-470
 Wen, Fei II-383
 Wu, Budan I-448, I-546
 Wu, Daolong I-317
 Wu, Fan II-239, II-250
 Wu, Hao II-532
 Wu, Jibing I-492
 Wu, Jung-Chao II-182
 Wu, Luqi II-33
 Wu, Maoqiang II-542
 Wu, Peng I-297
 Wu, Weigang II-552
 Wu, Wenjing I-125
 Wu, Xiaofei I-481
 Wu, Yahui I-492
 Wu, Zhibo I-524
- Xiao, Shoubai II-440
 Xiao, Song I-381, I-388, II-176
 Xie, Gang I-176
 Xu, Fan I-502
 Xu, Hengzhou I-75, I-284, I-460
 Xu, Jia II-331
 Xu, Mai I-535

- Xu, Mengmeng I-75
 Xu, Mingdi II-292
 Xu, Yunjia I-557
- Ya, Gao I-470
 Yan, Chunman II-485
 Yan, Dawei I-398
 Yan, Yongfei II-416
 Yan, Zhengqing II-82
 Yang, Chunlei II-362
 Yang, Fei I-146
 Yang, Fuzheng I-417
 Yang, Hongwu II-485
 Yang, Mao II-112
 Yang, Qinghai I-75
 Yang, Qiong I-46, I-297
 Yang, Xiaojun I-125
 Yang, Xu II-227
 Yang, Xuetao I-443
 Yang, Yunchuan II-199
 Yang, Zhiwei II-552
 Yao, Mingwu II-260
 Yao, Rongbin II-497, II-519
 Ye, Dongdong II-542
 Ye, Jincan II-497, II-519
 Yin, Wei II-362
 Yong, Shaowei I-398
 You, Peng I-398
 You, Yang I-502
 Yu, Bin II-199
 Yu, Jiang II-509
 Yu, Ke I-481
 Yu, Rong II-542
 Yu, Wenxian II-383
 Yu, Yanggege II-23
 Yu, Yanping II-82
 Yu, Zhong-yang II-122
 Yuan, Hongbo I-274
 Yuan, Ruiyang I-226, II-227, II-352
 Yuchen, Wang II-165
- Zeng, Guo-Qiang II-153
 Zeng, Yu I-512
 Zhang, Anxue II-271
 Zhang, Bo I-284, I-460
 Zhang, Chuanlin II-153
- Zhang, Heli I-433, II-341
 Zhang, Jian II-292
 Zhang, Ke II-239, II-250
 Zhang, Liang II-260
 Zhang, Meng I-3
 Zhang, Mengjun I-176
 Zhang, Nangen II-215
 Zhang, Ningxin II-23
 Zhang, Qiang II-122
 Zhang, Qilin II-132
 Zhang, Xing-Long I-21, II-207
 Zhang, Yan II-509
 Zhang, Yanqiu I-512
 Zhang, Yi I-46
 Zhang, Yong I-351, I-372
 Zhang, Yuexia II-3
 Zhao, Mengdi I-37
 Zhao, Sai I-206
 Zhao, Yanbin I-226, I-240, II-141, II-227, II-352
 Zhao, Zhe I-425
 Zhen, Jiaqi II-41, II-51
 Zheng, Jie II-95
 Zhong, Xiaoxiong II-440
 Zhou, Bin I-226, I-240, II-141, II-227, II-352
 Zhou, Gang I-274
 Zhou, Hongjian II-362
 Zhou, Kaixiong II-102
 Zhou, Mingyue II-416
 Zhou, Shiqi I-448, I-546
 Zhou, Xiangyun I-155
 Zhou, Xianwen II-283
 Zhou, Ying I-155
 Zhou, Yuan I-27
 Zhu, Canyon I-502
 Zhu, Chunsheng I-433, II-341
 Zhu, Hai I-284
 Zhu, Hongyu I-155
 Zhu, Min I-460
 Zhu, Zhixiao II-563
 Zi, Ran II-405
 Zong, Rong II-405
 Zou, Hua I-448, I-546
 Zou, Wenjie I-417
 Zou, Yi I-557
 Zuo, Xiaoya I-351